Forschungszentrum Karlsruhe
in der Helmholtz-Gemeinschaft

Wissenschaftliche Berichte
FZKA 7442

From Hydrolysis to the Formation of Colloids - Polymerization of Tetravalent Actinide Ions

C. Walther

Institut für Nukleare Entsorgung

Oktober 2008

Forschungszentrum Karlsruhe
in der Helmholtz-Gemeinschaft
Wissenschaftliche Berichte
FZKA 7442

From hydrolysis to the formation of colloids - polymerization of tetravalent actinide ions

Clemens Walther

Institut für Nukleare Entsorgung

von der Fakultät Chemie, Pharmazie und Geowissenschaften
der Johannes Gutenberg - Universität Mainz
genehmigte Habilitation

Forschungszentrum Karlsruhe GmbH, Karlsruhe
2008

Forschungszentrum Karlsruhe GmbH
Postfach 3640, 76021 Karlsruhe

Mitglied der Hermann von Helmholtz-Gemeinschaft
Deutscher Forschungszentren (HGF)

ISSN 0947-8620

urn:nbn:de:0005-074421

FROM HYDROLYSIS TO THE FORMATION OF COLLOIDS

-

POLYMERIZATION OF TETRAVALENT ACTINIDE IONS

Habilitationsschrift

eingereicht dem Fachbereich
Chemie, Pharmazie und Geowissenschaften
der Johannes Gutenberg-Universität Mainz

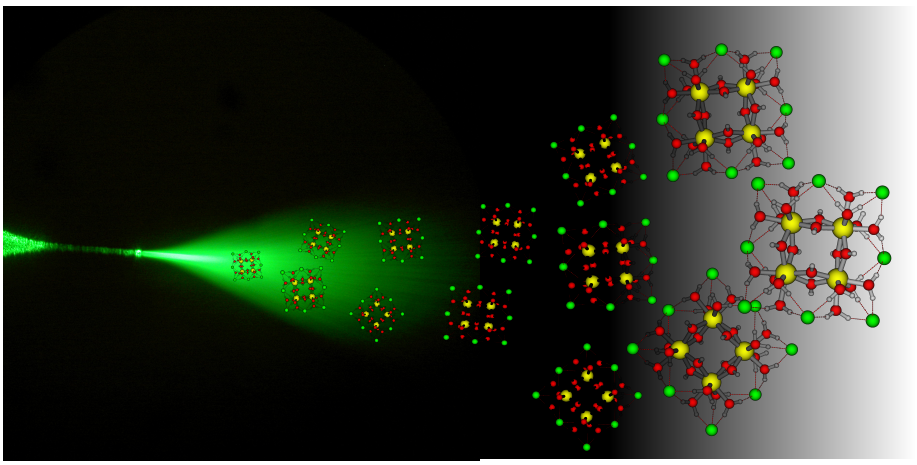

von Clemens Walther

geboren in Mainz

Karlsruhe 2007

Zusammenfassung

Von der Hydrolyse zur Kolloidbildung - Polymerisierung vierwertiger Actinoidionen

Polymerisierungsvorgänge in Lösungen vierwertiger Metallsalze erlangten in den letzten Jahren wieder vermehrte Aufmerksamkeit, jedoch sind die zugrundeliegenden Vorgänge noch lange nicht voll verstanden. Die Bedeutung dieser komplexen Chemie reicht von industriellen Anwendungen im Falle der Zirkon Salze bis zum nuklearen Brennstoffkreislauf aber auch umweltrelevanten Fragestellungen im Falle der Actiniden Thorium und Plutonium. Deren Wechselwirkungen in der Umwelt müssen bekannt sein, um mögliche Migrationswege dieser radiotoxischen Elemente in der Umwelt zu verstehen. In besonderem Maße gilt dies für den Langzeitsicherheitsnachweis potentieller Endlagerstandorte für hochradioaktiven Abfall. Die Relevanz von Polymer- und Kolloidbildung des vierwertigen Plutoniums trat zutage, als unvorhergesehen große Plutonium Kontaminationen viele Kilometer abseits von Bombenteststätten in Nevada (USA) und in der Nähe einer Wiederaufarbeitungsanlage bei Mayak (Rußland) gemessen wurden. In diesen Fällen war der Plutonium Transport durch die Bildung sogenannter Pseudokolloide, also chemisch an natürlichen Kolloiden gebundenen Plutoniums, verstärkt worden.

In der vorliegenden Arbeit wurden die Hydrolyse, die Polymerisieung und die Kolloidbildung mittels der spektroskopischen Techniken LIBD (Laser-induzierte Breakdown Detektion), TRLFS (zeitaufgelöste Laser Fluoreszenz Spektroskopie), UV-Vis (Absorptions-Spektroskopie) und XAFS (Röntgen-Absorptions-Feinstruktur Spektroskopie) untersucht. Die Reaktionskette, beginnend mit der Hydrolyse einkerniger ionischer Lösungsspezies hin zur Bildung aquatischer Kolloide auf der nm Skala, konnte durch direkte Beobachtung polynuklearer Komplexe mit der ESI-TOF-MS (nano Elektrospray Massenspektrometrie) komplettiert werden. Die Kombination dieser zum Teil speziell angepaßten oder verbesserten Methoden bedeutet einen wichtigen Schritt auf dem Weg zu einem Verständis des komplexen Wechselspiels von Redoxchemie, Hydrolyse und Polymerisierung in Lösungen vierwertiger Metallsalze.

Abstract

Polymerization reactions of tetravalent metal ions in solution gained considerable renewed interest in recent years but are still not fully understood. The relvance of their complex chemistry spans from industrial applications in the case of zirconium salts to the nuclear fuel cycle but also environmental research for the actinides thorium and plutonium. Their interactions in the environment must be known in order to understand potential migration pathways of the radiotoxic elements and in particular to perform safety assessments of prospective sites for high level nuclear waste repositories. The relevance of polymer and colloid formation, in particular of tetravalent plutonium, became obvious when unpredicted high levels of plutonium contaminations were found many kilometers off nuclear weapons test sites in Nevada (USA) and close to a nuclear reprocessing plant at Mayak (Russia). In these cases, plutonium transport was strongly enhanced by formation of so called pseudo colloids, *i.e.* plutonium ions chemically sorbed to natural colloids.

In the present work, hydrolysis, polymerization and colloid formation are investigated by the spectroscopic techniques LIBD (laser-induced breakdown detection), TRLFS (time-resolved laser-fluorescence-spectroscopy), UV-Vis (absorption spectroscopy) and XAFS (X-ray absorption fine structure spectroscopy). Observation of polynuclear complexes by ESI-TOF-MS (nano-electrospray mass-spectrometry) fills the gap in the reaction chain from the hydrolysis of monuclear ionic solution species to the formation of nm-sized aquatic colloids. Combining these to some extent especially taylored and improved methods allows making a step forward toward a molecular level understanding of the complex interplay of redox chemistry, hydrolysis reactions and polymer formation of tetravalent metal ions in solution.

Contents

In scientific research the most beautiful hypothesis always proves to be the right one.

But:

The most beautiful hypothesis can be murdered by one ugly fact

Thomas H. Huxley

1 Introduction

The use of nuclear energy for civil purposes lead to generation of a substantial amount of high level radioactive waste (HLRW). Until 2020 the spent fuel elements discharged from nuclear power reactors world wide will total 445.000 t [Amar06]. Given the number of 437 nuclear power plants under operation worldwide in 2006 [Reda07] the amount of spent fuel will increase by 11.000 t every year [Hoff01]. One ton of uranium based spent fuel has a radiotoxicity of approximately 10^8 Sv, which exceeds the corresponding toxicity of the same amount of natural uranium by a factor of 10^5. The spent fuel can either be reprocessed in order to reuse U and Pu [Fouq06] or, in a once through cycle, be disposed of in deep underground repositories [Alte06]. Presently the latter, *i.e.* the ultimate disposal of nuclear waste is favored by a number of countries, such as the USA, Sweden, Switzerland and Germany [Ewin02, Hoff01]. While the technical questions of building and operating a repository are solved, the long term safety of a repository cannot be guarantied by technical systems alone. Rather, the behavior of long lived radionuclides (RN) under geochemical conditions needs to be understood in order to provide tools for a long term safety assessment of HLRW.

In Germany the HLRW will be solidified (vitrified [Roth95, Quan03]) prior to disposal *i.e.* the radionuclides are dispersed and confined in a matrix of borosilicate glass [Hoff01]. The glass will be filled into stainless steel containers (coquilles), which will be buried in an underground repository. While a rock salt formation like Gorleben remained dry for geological time scales, accidents may lead to penetration of water into the repository. After a time scale of some 1000 years water might corrode the containers and cause leaching of the glass and release of radionuclides [Kim84a]. Fission producs account for the biggest fraction of radiotoxicity of the waste for the first few hundreds of years. After $>$ 1000 years, however, the minor actinides and Pu [Albr93] pose the biggest risk for environmental contamination, as illustrated in Fig. 1.1 where the radiotoxicity of one ton of spent fuel of a pressurized light water reactor after a burn up of 50 GWd is plotted as a function of time. Hence, a profound knowledge of the Pu chemistry under geochemical conditions is an indispensable prerequisite for a suitable risk analysis.

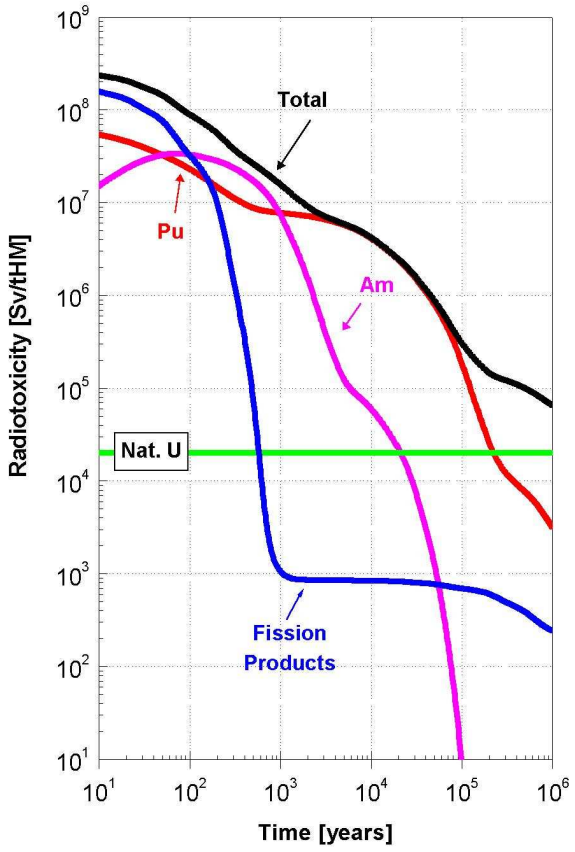

Figure 1.1: Radiotoxicity of one ton of spent fuel from a pressurized light water reactor (4% enrichment, 50 GWd) after an initial decay time of one year. The contribution of fission products, Pu and minor actinides varies strongly as a function of time [Hoff01].

It might be surprising that after more than 60 years of Pu chemistry there is still need for basic research but one needs to keep in mind that much of the early work on solution chemistry was driven by the requirement to separate and purify Pu in highly acidic solutions [Thiy90, Clar06]. It was of less relevance to understand the basic mechanisms of the Pu chemistry. One example is the polymerization of tetravalent Pu: Although polymerization was recognized in many experiments which focused on redox reactions of Pu [Kash49, Rabi53] and even some early attempts were made to characterize the polymers [Harv47, Ocke56, Krau56], emphasis lay on avoiding them because of their interference in process chemistry. In contrast, todays assessment of nuclear waste repositories where the low acidity of ground waters favors colloid formation and thus provides a potential transport pathway for migration of plutonium away from the repository [Kim84b, Kim94, Clar06] requires a comprehensive understanding of the

complex thermodynamics and redox chemistry of Pu in aqueous media. Since the tendencies for sorption, complexation or aggregation of polymeric species might differ considerably from those of the mononuclear ions and in turn be very different from the behavior of eigencolloids, precise predictions of species distributions are the prerequisite of a sound assessment of nuclear repositories under all possible conditions, including incident scenarios. However, databases are still lacking respective data, in particular many equilibrium constants for the formation of the most relevant polymers, the polynuclear hydroxide complexes are not yet known. Hence, the subject of the present work, the hydrolysis and polymerization of tetravalent actinides, is a very active area of research.

The concentration of Pu in solution under certain conditions is controlled by the solubility and precipitation of Pu(IV) hydroxide phases [Chop97, Efur98], which, as do the Pu colloids, span a wide range of structural features, crystallinities and stabilities and hence exhibit a wide range of solubilities [Rund00, Neck01a]: Crystalline PuO_2 ($\log K^o_{sp}(Pu(O)_2)$=- 64.0) is far less soluble than the amorphous hydrated hydroxide ($\log K^o_{sp}(Pu(OH)_{4(am,hyd)})$)=- 58.3) [Guil03]. Due to its high charge, the Pu^{4+} ion hydrolyzes readily even in very acidic conditions [Meti72] and these monomeric hydroxide complexes form polynuclear species at Pu(IV) concentrations $> 10^{-6}$ M [Rund00]. There is consensus that the hydrolysis of mononuclear Pu(IV) species is the first step towards colloid formation. The role of Pu(IV) polynuclear complexes, however, is still not clear. Their existence is generally accepted [Bell73a, John78, Toth81, Newt83, Katz86] and it is assumed that formation processes involve hydroxide or oxygen bridging of Pu nuclei [Katz86]. But the authors of two recent reviews [Lemi01, Guil03] within the Nuclear Energy Agency Thermodynamical Database Project (NEA-TDB) concluded that Pu(IV) polynuclear species are not thermodynamically stable but rather reaction intermediates and formation of colloids starts from mononuclear hydroxide complexes ($Pu(OH)_n^{4-n}$). In contrast, Toth *et al.* [Toth81] suggested a two step mechanism of colloid formation: In analogy to the behavior of Th(IV) [Katz86, Wick06], small polymeric species such as the Pu trimer were formed and after an induction period which depended on the degree of oversaturation of the solution [He94] the colloids grew rapidly.
The presence of a constant colloidal Pu(IV) level of $[Pu]_{coll} = 10^{-9}$M at pH 7 was explained by formation of chainlike polymers [Fuji01]: Cubic $Pu(OH)_4(H_2O)_4$ subunits aggregate and subsequent dehydration leads to formation of hydrated PuO_2:
$Pu(OH)_4(H_2O)_4 \rightarrow Pu_2(OH)_8(H_2O)_6 \rightarrow \{Pu_4O_2(OH)_{12}(H_2O)_4\}_n \quad \rightarrow PuO_2 \quad \cdot 2.5H_2O$
This model is extended in the present work (Sec. 2.6, [Roth04]) for describing the formation of colloids in acidic solutions: Cubic monomers ($[Pu(OH)_2(H_2O)_6^{2+}]$) form edge sharing dimers, trimers and larger polynuclear complexes by hydrolysis and the condensation reaction $2OH^- \rightleftharpoons H_2O + O^{2-}$ where oxide bridge links are formed. Further condensation of ($[Pu_pO_x(OH)_{4p-2x}(H_2O)_z]$ polymers culminates in the formation of large colloids with an ordered Pu-O-Pu backbone fcc (face-centered-cubic) structure.

Clearly, it is an oversimplification to speak of *the* Pu(IV) colloids in general. Structural investi-

gations over the last three decades indicate that the colloids in rather concentrated and highly acidic media [Bell73a, Bell73b, Lloy78] which were discussed above and are investigated in the present work [Roth04] (Sec. 2.7.5) differ from those at higher pH [Rai81, Silv02a, Hasc02b]. Fast neutralization of Pu(IV) solutions with a base or water leads to formation of lower ordered structures [Reed06], the number and size of colloids depend on growth rate (reaction limited aggregation) [Zhao97, Olss06]. If crystallization germs are present, *e.g.*, if Pu(IV) solutions are 'seeded' by addition of aged polymers, the colloid formation rate is enhanced by almost one order of magnitude [Newt83]. The size of Pu(IV) colloids ranges from a few nanometers [Krau56, Lloy78] to almost microns [Tria91] depending on the conditions of generation. Their density is $\rho = 9^{+2.1}_{-1.9}$ g/cm^3 [Rund88] which is slightly lower than the density of PuO_2. The geometry of the colloids seems to vary strongly depending on the conditions of formation and on the age of the solutions. Lloyd and Hair [Lloy78] observed by use of transmission electron microscopy that Pu(IV) forms small (2 nm), spherical PuO_2 colloids of fcc structure. These primary particles agglomerate and form larger entities which is in good agreement with the behavior of also spherical Th(IV) colloids [Krau56, Dzim85, Walt03a, Wick06]. However, small angle neutron scattering experiments of colloidal Pu(IV) suspensions after a few months of aging revealed the presence of thin rodlike Pu(IV) particles [Thiy90]. The geometry change is accompanied by structural transformations and pronounced changes of the chemical properties. Freshly formed colloids dissolve easily upon dilution at constant pH [Frie77, Kim84b, Hasc02a, Walt03b] or acidification [Ocke56, Clev79, Thiy90]. Aging leads to irreversible elimination of water [Ocke56, John78] *i.e.* transformation of hydroxide bonds to oxygen bonds (oxolation). These aged colloids are significantly less soluble [Zhao97, Clar06] and are often referred to as 'insoluble Pu(IV) polymer' [Clar06]. Two very thourough EXAFS studies on many Pu compounds and various solution species' including colloids by Conradson and coworkers [Conr04, Conr05] reveal the astonishing variety of structures and provide clear evidence for elimination of protonated species from freshly formed precipitates during aging and a contribution of higher oxidation states in aged 'Pu(IV) solid phases'. The presence of pentavalent Pu in these solid Pu-phases might help understanding why Pu(IV) colloids are in equilibrium with pentavalent Pu in near neutral solutions [Rai81] and why some of the redox reactions of Pu (the disproportionation of pure Pu(V) solutions) cannot be explained without Pu(IV) colloids as intermediate complexes [Newt86]. Very recent results show that Pu(IV) colloids and small polymeric species play an important part in the thermodynamic Pu equilibrium chemistry [Cho05a] (Sec. 2.7.3) and link the tri- and tetravalent Pu with the penta- and hexavalent oxo species PuO_2^+ and PuO_2^{2+} [Neck07].

However, polymerization is only one of the many facets of Pu aqueous chemistry. In their famous book on 'Chemistry of the actinide elements' J. Katz and G. Seaborg put it in the following words [Katz86]: *In a real sense, by virtue of its complexity, plutonium exhibits nearly all of the solution behavior shown by any of the other elements.* In particular, this remark may refer to the unique situation that up to four different oxidation states of Pu can be present in solution simultaneously due to the very similar redox potentials of the

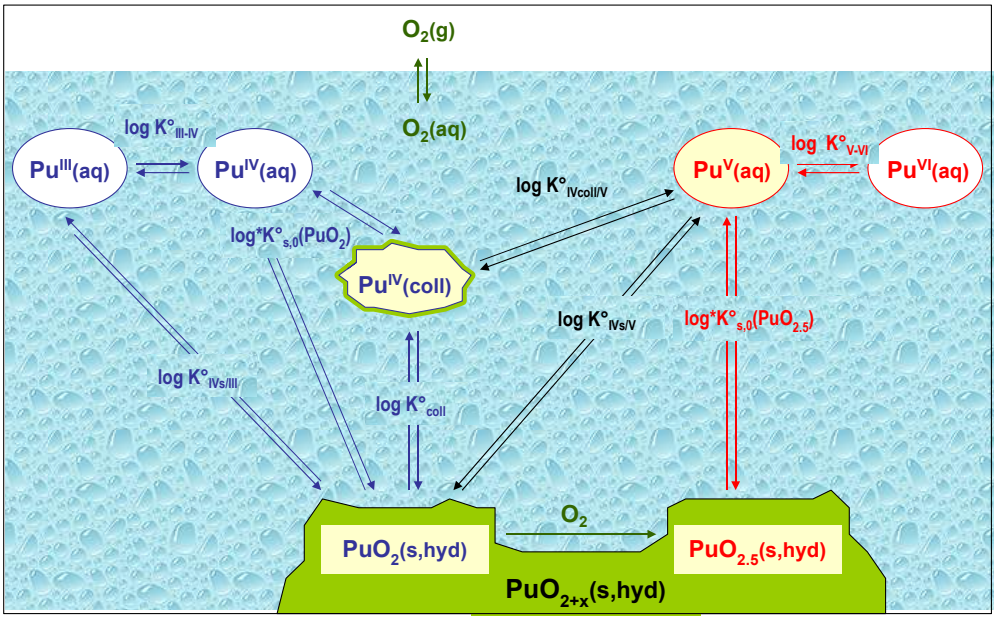

Figure 1.2: Solid-liquid and redox equilibria of Pu in the presence of oxygen. Polymeric and colloidal Pu species are in equilibrium with $Pu(IV)_{aq}$, PuO_2^+ and, if present, with precipitates such as $PuO_{2+x(s,hyd)}$ [Neck07]

couples Pu(III)/Pu(IV) and Pu(V)/Pu(VI) [Rabi56, Rigl89, Capd95]. Pu(V) and Pu(VI) form hydrated plutonyl ions (PuO_2^+ and PuO_2^{2+}) in solution, the heptavalent state is assigned a PuO_4^- stoichiometry. Pu(IV), Pu(VI), Pu(III) and Pu(V) have effective ion charges of +4, +3.3, +3, +2.3, respectively [Rund00], which causes their tendency towards complexation and, in particular, hydrolysis to decrease in the same order $Pu^{4+} > PuO_2^{2+} > Pu^{3+} > PuO_2^+$. Among the tetravalent actinides, Pu(IV) hydrolyzes most strongly[1]: Formation constants for $Pu(OH)_y^{4-y}$ are $\log {}^*\beta^o_{1,1} = 0.6 \pm 0.5$, $\log {}^*\beta^o_{1,2} = 0.6 \pm 0.3$, $\log {}^*\beta^o_{1,3} = -2.3 \pm 0.4$, $\log {}^*\beta^o_{1,4} = -8.5 \pm 0.5$ [Guil03] (for a discussion of these constants see Sec. 2.7.4). The high tendency for hydrolysis originates in the small ionic radius of Pu(IV) due to the so called actinide contraction [Katz86] ($r(Th^{4+})$= 1.0Å, $r(U^{4+})$= 0.93Å, ($r(Pu^{4+})$= 0.90Å [John78]). Hydrolysis of the Pu^{4+} ion leads to formation of the complex $Pu(OH)^{3+}$ which accounts for approximately half of the $Pu(IV)_{(aq)}$ concentration in media as acidic as 0.5 M hydrochloric acid [Meti72]. With increasing pH, further hydrolysis leads to formation of mononuclear ($Pu(OH)_y^{4-y}$) and, at concentrations $[Pu(IV)] > 10^{-6}$ M [Rund00], polynuclear ($Pu_p(OH)_y^{4p-y}$) complexes, which

[1]With the exception of Pa(IV), see Sec. 5.3

can grow into nm-sized colloids [Rabi53, Krau56, Chop83, Newt83, Clev79, Zhao97, Clar06] as mentioned above.

Last but not least, alpha radiolysis plays an important role [Conn53, Rabi57, Newt02, Clar02b, Korz04] not only for the short lived isotopes, but even for the rather long lived ^{239}Pu, $T_{1/2} = 2.4 \cdot 10^4$y. In particular, in the presence of a large amount of Pu solid (precipitate), reduction [Rabi55, Capd98, Yuso02] as well as oxidation [Nits94, Newt02] of aqueous Pu was reported due to radiolytic production of radicals such as H_2O_2. Use of ^{242}Pu, ($T_{1/2} = 3.75 \cdot 10^5$y) or ^{244}Pu, ($T_{1/2} = 8.0 \cdot 10^7$y) can reduce these effects and it is known that radiolysis is less pronounced in choride than in hypochloride or nitrate solutions [Rabi53, Newt02].

It is common praxis in radiochemistry to perform preliminary or preparatory experiments with stable or less radioactive analogs prior to the investigation of the element of interest. In the case of tetravalent Pu two elements were often and still are chosen: The stable element Zr and the extremely long lived isotope ^{232}Th ($T_{1/2} = 1.4 \cdot 10^{10}$y). Both metals form tetravalent ions in solution. Pu(IV) and Zr(IV) have similiar ionic radii ($r(Zr^{4+}) = 0.84$ Å for eightfold coordination [Shan76]) and hence similar formation constants for the mononuclear hydrolysis complexes (values for Pu(IV) in parantheses): The measured value for $Zr(OH)^{3+}$: $\log {}^*\beta^o_{1,1} = 0.32 \pm 0.22$ [Humm02, Curt02, Brow05] ($\log {}^*\beta^o_{1,1(Pu)} = 0.6$), and the estimated values for $Zr(OH)_y^{4-y}$, $\log {}^*\beta^o_{1,2}$=−0.4 ($\log {}^*\beta^o_{1,2(Pu)}$=0.6), $\log {}^*\beta^o_{1,3}$=−3.9 ($\log {}^*\beta^o_{1,3(Pu)}$=−2.3), $\log {}^*\beta^o_{1,4}$=−10.6 ($\log {}^*\beta^o_{1,4(Pu)}$=−8.5) according to [Cho05b] (Sec. 3.8.3). The behavior of Zr(IV) in solution is very well known, partly because Zr is a high priority element for the assessment of radioactive nuclear waste repositories. Thermodynamic data of Zr, (solubility and hydrolysis constants) were reviewed for a NAGRA/PSI database [Curt02] and recently, an extensive review of the Nuclear Energy Agency Thermodynamical Database Project (NEA-TDB) [Brow05] summarizes half a centuries work on aqueous zirconium chemistry since Blumenthals book of 1958 [Blum58] including hydrolysis reactions, polymerization and formation of halide complexes. Polymerization and colloid formation of Zr(IV) is of technical relevance for sol gel processes and in particular the tetramer $[Zr_4(OH)_8^{8+} \cdot 16H_2O]$ is well investigated by a number of studies [Blum58, Clea56, Rose03, Chia04]. The formation mechanisms of Zr(IV) colloids exhibit quite some similarity to the polymerization of Pu(IV), merely the solubility of amorphous Zr(IV) hydroxide considerably exceeds the one of Pu(IV) hydroxide ($\log K^o_{sp}(Zr(OH)_4)$=-53.1 [Cho05b]). Hence, it is not surprising that quite a few researchers who are well known for their work on Pu chemistry also contributed to the understanding of Zr(IV) in solution [Conn49b, Conn51, Ziel56, Pokr56, Curt02]. Two publiations of the present work follow this tradition to use Zr as a homologue. Formation and structure of Zr(IV) colloids in acidic solutions are investigated by a combined LIBD and EXAFS study (Sec.3.8.3) and the applicability of Electrospray Mass-Spectrometry (ESI-MS) for the direct quantification of polynuclear metal hydroxide complexes in solution is demonstrated in Sec. 3.8.4.

The second metal, Th, is an actinide and as such quite frequently compared to Pu. Besides its longer half life, the absence of redox reactions in solution makes Th a convenient analog for studying hydrolysis and colloid formation. Two recent reviews summarize available data on physics and chemistry of thorium [Wick06] and solution chemistry of thorium compounds [Rand07]. In acidic solutions, Th forms tetravalent ions, Th^{4+} (eff.charge 3.82 [Wick06]), which are slightly larger than Pu^{4+} ions ($r(Th^{4+})$=1.0Å[John78],1.08Å[Neck01a]) and are 10 fold coordinated (N=10.8[Wick06]). Due to the larger size, formation constants of mononuclear hydrolysis complexes are considerably smaller ($\log {}^*\beta^o_{1,1} = -2.2 \pm 0.2$, $\log {}^*\beta^o_{1,2} = -6.0 \pm 0.6$, $\log {}^*\beta^o_{1,3} = -11 \pm 1.0$, $\log {}^*\beta^o_{1,4} = -9.5 \pm 1.0$ [Neck01a]). The solubility of the amorphous hydroxide exceeds the values of the respective solids of Pu and Zr [Neck01a, Fang02, Rand07]. Over the last decade, detailed investigations on the colloid formation mechanisms of Th(IV) revealed that at least two regions with respect to pH and Th(IV) concentration have to be destinguished [Wick06] which correspond to different solid phases: $\log K^o_{sp}(ThO_{2(microcrys)})$=-52.8 [Neck01a] to -53.0±0.5 [Rand07], $\log K^o_{sp}(Th(OH)_{4(am,hyd)})$=-47.8 [Neck01a]. At high acidity (pH< 4), microcrystalline colloids form from oversaturated solutions [Bund00, Roth02, Neck03] whereas at higher pH, Th(IV) colloids are X-ray amorphous [Neck02], *i.e.* either represent an amorphopus hydroxide phase or consist of aggregates of small microcrystalline subunits most likely with a hydrated surface layer [Walt03a] (Sec. 3.8.1). The latter assumption is corroborated by a model, where the different solubilities of 'crystalline' ThO_2 and 'amorphous hydrated' $Th(OH)_4$ are attributed to the presence of particulates in the solids [Dzim85, Wick06, Rand07, Neck03] and the increasing solubility is explained by decreasing particulate size (Schindler effect [Schi67]). It is a surprising fact that solutions which are considerably oversaturated with respect to the solubility of crystalline ThO_2 are stable for years without any tendency to precipitation as long as the solubility of the amorphous $Th(OH)_{4(am,hyd)}$ is not exceeded. Th(IV) colloids are long time stable [Fang02] and, in analogy to the 'fresh Pu(IV) colloids', they are in equilibrium with Th(IV) ions [Katz86]. Reversible formation and dissolution of colloids proceeds on time scales of a few days [Bite03a] (Sec.3.8.2). Colloid formation is preceded by formation of polynuclear hydroxide complexes [Sill53, Krau56, John78, Kim94] such as $Th_2(OH)_2^{6+}$, $Th_2(OH)_3^{5+}$, $Th_4(OH)_8^{8+}$, $Th_4(OH)_{12}^{4+}$, $Th_5(OH)_{12}^{8+}$, $Th_6(OH)_{14}^{10+}$, $Th_6(OH)_{15}^{9+}$ [Neck01a, Wick06] which, in contrast to the polynuclear complexes of Pu(IV), are accepted as thermodynamically stable species [Rand07].

Profound understanding of the aqueous chemistry of each of the relevant radionuclides is a necessary prerequisite, but this information alone does not suffice to conduct a safety assessment of a repository. In addition, one needs to consider complex formation of radionuclides with various inorganic and organic ligands [Chop03], interaction with corroding container material (*e.g.*, secondary iron phases), backfill material [Mura02] (*e.g.*, bentonite) and host rock [Weij02] (granite, rock salt, clay). Surface sorption [Ditl78, Stum81, Dzom90, Seam00, Liu04, Stum06] and reversible or irreversible incorporation processes need to be considered (Fig. 1.3). One particularly important process is the sorption [Stum93, Chop99]

to aquatic colloids [Kral97], *i.e.* particles of submicron size [Nomi87] (per definition 1 nm $< D <$ 1 μm), which remain suspended in water [Buff95b, Atte98]. They are ubiquitous [Dick02, Gile04] in natural waters in large numbers [Kim88, Kral97, Degu97, Evan00] ranging from 10^6 particles per ml in granitic waters [Laak01, Haus03, Walt02] (Sec. 4.5.1) to 10^{12} particles per ml in near-surface waters [Kim84a, Kim94] rich in organics. The differential particle number density strongly depends on size (Paretos law [Buff95b, Buff95a, Degu96]: $\mathrm{d}N_{\mathrm{coll}}/\mathrm{d}D \propto D^{-\beta}$; $\beta = 3..5$).
The chemical composition may vary strongly [Kim94, File07]. Inorganic [Nomi89, Mavr94, Degu96, He96, Cont97] (silicates, alumo or iron phases) as well as organic [Kim92, Arti98,

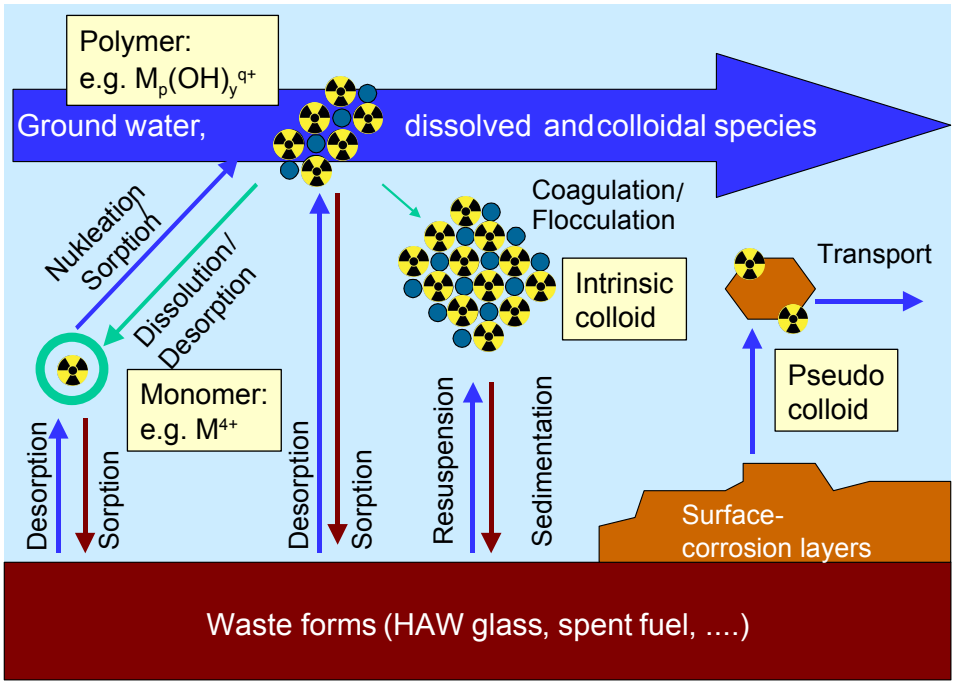

Figure 1.3: Leaching or dissolution of radioactive waste (*e.g.*, glass products) leads to formation of solvated species of radionuclides in solution. The monomeric ions may hydrolyze, form mononuclear or polynuclear complexes (polymers) up to colloidal size. These charged species are in equilibrium with each other and interact with corrosion products of containers, backfill material, and host rock. In addition, mono or polynuclear complexes of the radionuclides can sorb to natural colloids and form so called 'pseudo colloids'. They are mobile in the aquifer, and by colloid mediated transport, the risk of radionuclide release into the biosphere increases strongly.

Arti00, Arti02, Mons03] (humic acids, polysaccharides,...) and also mixed colloids, *e.g.*, inorganic particles with a stabilizing organic coating [Degu00, Roth00, Clar02a], are known. Additional colloids may be released from container surfaces due to erosion or from backfill material [Kall87, Ryan94]. The large surface to volume ratio of colloids in conjunction with often considerable surface charge [Kall00] makes them chemically reactive species [Town02]. It is well known that aquatic colloids migrate fast in the aquifer - under certain conditions even faster than conservative tracers [Puls92, Baum00, Mori03, Geck04, Delo07] and radionuclides that are incorporated into or sorb irreversibly (or with slow desorption kinetics [Pain02]) onto the colloids are transported equally fast [McCa93, Kim94, Ryan96, Klei96, Degu97, Kers99, Baum00, Flur02, Douc07]. The mobility enhancement [Rees91, Minc03] due to colloid mediated transport is most pronounced for substances of low solubility (particularly the tri- and tetravalent actinides [Mori03]) which are expected to form precipitates in or close to the repository. This effect has long been predicted [Avog84, Kim84a] and in dilute solutions, *i.e.* in natural waters, by far exceeds the transport due to formation of intrinsic colloids [Kim84b]. The high risk posed by colloid mediated transport was directly observed in contaminated areas such as the Nevada nuclear detonation sites [Kers99, Hone99], the U.S. Department of Energy's Hanford site [Flur02], or near Russian reprocessing plants [Novi06]. Ongoing efforts aim at the understanding of fundamental mechanisms in laboratory experiments with natural brines [Nits94, Efur98, Reed06] or in field experiments with trace amounts of radionuclides [Mori03, Geck04].

The detection and characterization of these colloids, however, still poses a major challenge [McCa93, Buff95a]. Of highest relevance for transport phenomena are colloids smaller than 50 nm due to their high mobility and large surface to volume ratio [Lead07]. At the same time, the small size fraction is hardest to characterize by commercial standard methods [Buff92, File93, Ledi95, Kral97, Walt03a]: Electron microscopy (Transmission Electron Microscopy, TEM or Scanning Electron Microscopy, SEM) require sample preparation and are destructive. Methods based on the interaction with visible light are non desturbing but cannot be applied to very dilute suspensions of small particles: static light scattering (*e.g.*, the Single Particle Counter, SPC [Knol92, Degu01, Ross03]), is a very sensitive method for detecting particles > 100 nm but due to the λ^{-6} amplitude decrease of Rayleigh scattering, it is limited to particles which are bigger than approx. one quart of the wavelength of visible light. Photon Correlation Spectroscopy (PCS) was shown to work for colloids of only a few nm in size but requires higher concentrations than are typically present in natural systems [Rees87, Ledi94, File97]. In the late 1980s, the very sensitive Laser-Induced Breakdown Detection (LIBD) [Kita88, Kita89b, Kita89a] was developed and improved continuously thereafter [Sche96, Kim96, Haus02, Bund01b, Bund01a]. The technique allows measuring very dilute (10^4 -10^5 particles/ml) suspensions of inorganic colloids down to ≈ 5 nm. In several papers of the present work, LIBD is used for colloids detection [Walt03b, Roth04, Bite03a, Cho05b, Walt02] (Sects. 2.7.1, 2.7.5, 3.8.2, 3.8.3, 4.5.1). Considerable effort was made to understand the fundamentals, model LIBD data [Kim07] (Sec. 4.5.2),

and extend the capabilities of LIBD in order to measure particle size *distributions* (PSD) [Walt04, Walt06] (Sects. 4.5.3, 4.5.4). Especially when the PSD extends over several orders of magnitude, a mere weighted mean size is not appropriate for describing a colloidal system.

However, the high chemical complexity of the systems under investigation, in particular those containing tri- and tetravalent actinides, requires additional analytical methods: Since, *e.g.*, in the case of Pu, complex formation, polymerization, solubility, and formation of precipitates depend very strongly on the oxidation state of Pu in solution. Monitoring and, if possible, controlling its redox state is an indispensable prerequisite for every measurement. For highly concentrated solutions ([Pu]$> 10^{-5}$M) visible absorption spectroscopy (UV-VIS) is a convenient speciation tool. Due to electronic intra band transitions in the 5f shell, each oxidation state exhibits several unique absorption bands [Katz86]. While the method is well established and frequently used since the very beginning of Pu chemistry, basic questions, such as how the absorption bands change upon hydrolysis are still a subject of discussion. The present work contributes a paper on the effect of hydrolysis on spectral absorption of $Pu(IV)_{aq}$ paying special attention to the influence of polymerization and colloid formation ([Walt07a], Sec. 2.7.2). When the redox potential of the solutions is carefully measured, hydrolysis constants can be obtained from the distribution of oxidation states ([Yun07], Sec. 2.7.4). A sensitivity increase of optical spectroscopy is achieved by extending the optical absorption path length. Recently, the detection limit was lowered by almost two orders of magnitude by use of liquid capillary waveguides of one meter length [Wils05, Walt07a, Yun07]. Of similar sensitivity is the Laser-Induced Photoacoustic Spectroscopy (LPAS) [Tam79, Stum84, Leto86, Kim90, Neck01b]: light of a tunable laser is absorbed by the solvated ions, locally heats the sample which expands and causes an acoustic wave which is detected by a piezo receiver. In contrast to UV-VIS, the measurement is not disturbed by light scattering signals, *e.g.*, in colloidal suspensions, since LPAS does not probe extinction but absorption. However, LPAS requires comparatively long measuring times of approx. 30 min for each oxidation state. In the present work, LPAS was used to observe dissolution of Pu(IV) colloids at low concentrations ([Walt03b], Sec. 2.7.1). Recently, detection limits for redox speciation below [Pu]=10^{-7} M were reported by combining capillary electrophoresis [Lu95] with Inductively-Coupled-Plasma Mass-Spectrometry (ICP-MS) [Kucz03, Amba05] and even lower, down to [Pu]=$< 10^{-10}$ M, for coupling [Bürg05] with Resonance-Ionisation Mass-Spectrometry (RIMS) [Pass97, Trau04]. In the past, speciation at such minute concentrations was reserved for solvent extraction [Meti72], ion exchange, or coprecipitation methods which always carry the risk of shifting chemical and redox equilibria [Chop03].

There are, however, some exceptions where nature provides very convenient tools for speciation: the trivalent actinide ions and the uranyl ion (Review [Yuso93]). The ones most frequently used are UO_2^{2+} [Bell68, Moul98, Ruts99, Bern01], Cm^{3+} [Beit80, Beit91, Kim91, Klen91], and, to some extent, Am^{3+} [Beit88, Thou93]. These ions exhibit fluorescence properties similar to those of some of the rare earth metals [Stei75] (Ce^{3+}, Sm^{3+}, Eu^{3+},Gd^{3+},Tb^{3+},

Dy^{3+}, Yb^{3+}). A rather large energy gap between the ground state and first excited state [Carn75b] within the 5f electronic configuration causes narrow, and due to the the Laporte (parity) forbiddance of the transition long lived, characteristic fluorescence bands (Cm^{3+} : $\tau = 4.8\,\mathrm{ms}$, Am^{3+} : $\tau = 1.875\,\mu\mathrm{s}$). The technique is very sensitive and allows speciation at concentrations [M]$< 10^{-8}$ M (mere detection is possible for [M]$> 10^{-10}$ M). In the case of Cm^{3+}, an electric field such as caused by ligand molecules (often denominated crystal field) shifts the energy levels and subsequently affects the emission wavelength. By observing the fluorescence, one obtains direct information on the chemical neighborhood of the metal ion. To these ligands (or a solvation shell of water molecules [Mare91]), energy can be transferred from the excited state [Stei75], which considerably decreases the lifetime. This effect is made use of by Time-Resolved Laser-Induced-Fluorescence Spectroscopy (TRLFS) [Beit80]. Excitation by a pulsed laser is followed by gated detection of the fluorescence emission and from the lifetime one concludes on the number of quenchers (Kimura equation [Horr79, Kimu94]). The present work comprises two applications of TRLFS. The ground state crystal field splitting of Cm^{3+} which substitutes the Y in a crystalline Yttrium chloride crown ether compound is investigated by TRLFS at low temperature [Lind05b] (Sec. 5.4.1). In contrast to earlier investigations on Cm^{3+} incorporated into crystalline hosts [Grub66, Liu93, Thou94, Murd96, Brun96] in the present case, the Cm^{3+} ion is hydrated, *i.e.* coordinated by eight water molecules ($[Cm^{3+}(H_2O)_8]Cl_3 \cdot 15-\mathrm{crown}-5$) . The spectroscopic results on this well defined system were used to attribute the temperature dependence of the fluorescence emission of the Cm^{3+} aquo ion to a decrease of the coordination number from nine at room temperature to eight at $T > 100^\circ$ C [Lind05a].
The last section of the present work focuses on TRLFS on tetravalent Protactinium. Pa^{4+} incorporated into solid compounds was investigated by TRLFS before [Edel88, Pieh91, Edel92, Edel93], but no TRLFS on Pa(IV) aquo species was reported so far. In [Marq04, Marq05] (Sects. 5.4.2, 5.4.3) a large shift of the emission spectrum of Pa(IV) upon hydrolysis is reported. Along with observation of U(IV) fluorescence, published shortly after [Kiri04], this is the first application of TRLFS to a tetravalent actinide ion in solution and opens up new possibilities of using Pa(IV) as a probe for the investigation of tetravalent actines which hitherto were not accessible by TRLFS.

2 Investigations on Redox Reactions, Hydrolysis and Colloid Formation of Tetravalent Plutonium

Hydrolysis, polymerization, and redox reactions of tetravalent Pu in acidic aqueous solution take place simultaneously and it is often difficult or even impossible to investigate one reaction without interference of the others. An example cited already in the introduction (Chapter 1) is the hydrolysis of Pu^{4+}. In millimolar solutions ([Pu(IV)] =0.1 - 1 mM) formation of polynuclear species starts between pH 0.5 and 0.7, which coincides with the predominance of the first and second mononuclear hydroxide complexes ($Pu(OH)^{3+}$ and $Pu(OH)_2^{2+}$). At the same time, redox reactions of Pu(IV) lead to a complex mixture of Pu^{3+}, Pu(IV), PuO_2^+, PuO_2^{2+}, possibly polynuclear complexes $Pu_x(OH)_y^{4x-y}$, and colloids ($Pu(IV)_{coll}$). Although the hydroxyl ion is the most important complexing ligand in acidic solution, complex formation with additional anions becomes relevant for increasing electrolyte concentration, not only for Pu^{4+} but also PuO_2^+ and PuO_2^{2+}. Formation of $\left[PuO_2^{2+} \cdot Cl^-\right]^+$ was directly observed spectroscopically at $I \gtrsim 0.2$ M [Rund99], and with increasing pH, also ternary complexes play a role. Incomplete characterization of the samples or misinterpretation of the origin of observed effects may very easily lead to erroneous results. In particular, the relevance of polynuclear complexes and colloids as part of the delicate balance between the many Pu species in solution is often underestimated. The present chapter focuses on the role of polynuclear and colloidal Pu(IV) species during hydrolysis and redox reactions of Pu(IV) in acidic solutions comprising optical spectroscopic investigations (UV-VIS, capillary absorption spectroscopy, LPAS), breakdown detection (LIBD) and X-ray absorption spectroscopy (XAFS).

2.1 INTRODUCTORY REMARKS

Throughout the present work, Roman numerals (*e.g.* Pu(IV)) designate the oxidation states without specifying the species, whereas the actual ions are written with Arabic numbers and charges (*e.g.* Pu^{4+}). The total concentration of, *e.g.*, Pu(IV) in solution results from the summation of the mono- and polynuclear hydrolysis complexes

$$[Pu(IV)] = \sum_{\substack{x=1-n \\ y=0-4x}} [Pu_x(OH)_y^{4x-y}] \,. \tag{2.1}$$

If the hydrolysis constants are known, Eq.2.1 can be written

$$[Pu(IV)] = \sum_{\substack{x=1-n \\ y=0-4x}} \beta'_{x,y} [Pu^{4+}]^x [OH^-]^y \,, \tag{2.2}$$

with ${\beta'}_{x,y}$ the conditional hydrolysis constant at finite ionic strength

$$ {\beta'}_{x,y} = \frac{[\mathrm{Pu_x(OH)_n^{4x-n}}]}{[\mathrm{Pu^{4+}}]^x[\mathrm{OH^-}]^n} = \beta^\circ_{x,y} \frac{(\gamma^{4+}_{Pu})^x(\gamma_{OH^-})^y}{(\gamma_{Pu_x(OH)_y^{4x-y}})} . \tag{2.3} $$

${\beta^o}_{x,y}$ is the hydrolysis coefficient at zero ionic strength, [i] denotes the concentration of species i, and γ_i its activity coefficient. Details on the calculation of hydrolysis constants and extrapolation to zero ionic strength are given in [Gren00], shortly summarized in the introduction of [Walt07a] (Sec. 2.7.2). A considerable number of experimental determinations of at least the first formation constant of mononuclear hydroxide complexes of Pu(IV) were published and some selected values are listed in Table 1 of [Walt07a] (Sec. 2.7.2).

Another aspect of plutonium which gained even more attention than its hydrolytic behavior is its complex redox chemistry, which has been studied for many decades. Due to the very similar redox potentials of the couples Pu(III)/Pu(IV) ($E^o = -1.047\,\mathrm{V}$), Pu(IV)/Pu(V) ($E^o = -1.031\,\mathrm{V}$) and Pu(V)/Pu(VI) ($E^o = -0.936\,\mathrm{V}$) (Standard potentials from [Lemi01]), an equilibrium of two or more oxidation states may form over time even in solutions which contain only one oxidation state of Pu in the beginning. In this case, Pu is oxidizing and reducing agent at the same time - a phenomenon called *disproportionation* [Conn49a]. More than a dozen plutonium disproportionation equations were published. However, they can be reduced to a set of a few reactions.

The formation of Pu(III), Pu(V) and Pu(VI) from Pu(IV) in solutions exposed to air is usually ascribed to the disproportionation of Pu(IV) into Pu(III) and Pu(V)

$$ \mathrm{2Pu^{4+} + 2H_2O} \quad \leftrightharpoons \quad \mathrm{Pu^{3+} + PuO_2^+ + 4H^+} \tag{2.4} $$

followed by the reaction of Pu(V) with Pu(IV) or the disproportionation of Pu(V) into Pu(IV) and Pu(VI)

$$ \mathrm{2PuO_2^+ + 4H^+} \quad \leftrightharpoons \quad \mathrm{Pu^{4+} + PuO_2^{2+} + 2H_2O.} \tag{2.5} $$

Combining reactions (2.4) and (2.5) leads to the reaction (2.6):

$$ \mathrm{3Pu^{4+} + 2H_2O} \quad \leftrightharpoons \quad \mathrm{2Pu^{3+} + PuO_2^{2+} + 4H^+.} \tag{2.6} $$

Values for the equilibrium constant (at zero ionic strength) of reaction (2.6) at rather high acidity (close to $[\mathrm{H^+}] = 1\,\mathrm{M}$) range from $\log K^o_{IV} = 2.38 - 2.43$ [Rabi53, Cost73, Capd92].

Use of the derived equilibrium constants facilitates the prediction of the equilibrium oxidation state distribution in plutonium solutions [Katz86, Newt02, Clar06] depending on total plutonium concentration, the initial oxidation state distribution and acidity (note the $\mathrm{H^+}$ concentration dependence of *e.g.* reaction 2.4). Silver published several papers on how to obtain

a system of balanced equations based on the disproportionation equations which are easily solved numerically [Silv99, Silv02b] (Details and equations see App. A). Results for acidic Pu solutions (pH 0-3, $[Pu]_{tot} < 1\,mM$) are visualized in figure 2.1. A pure Pu(IV) solution is only stable at very high acidities, whereas considerable fractions of Pu(III), Pu(VI) and Pu(V) form at pH > 0.

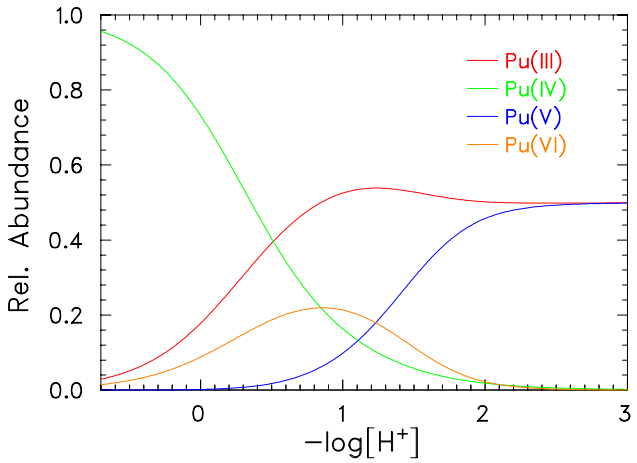

Figure 2.1: Equilibrium of Pu oxidation state distributions depending on -log $[H^+]$. Equations A.5 A.6 and A.8 with simultaneous consideration of mass and charge conservation were solved simultaneously using a FORTRAN routine (slatec mathematical library). Details see App.A

The *kinetics* of Pu disproportionation depends strongly on the initial oxidation state distribution and the acidity of the sample. In particular, those reactions involving formation or breaking of Pu-O bonds proceed quite slowly and it may take weeks or even months to reach a steady state. A considerable number of studies on this topic were performed since the 1950s (extensive reviews in [Newt02] and [Clar06]) and Pu reaction kinetics are still an active area of research (e.g. [Hasc07]). For the present example, the disproportionation of a pure Pu(IV) solution, the following reactions need to be considered:

$$2Pu^{4+} + 2H_2O \underset{k_{-1}}{\overset{k_1}{\rightleftharpoons}} Pu^{3+} + PuO_2^+ + 4H^+ \tag{2.7}$$

$$Pu^{4+} + PuO_2^+ \underset{k_{-2}}{\overset{k_2}{\rightleftharpoons}} Pu^{3+} + PuO_2^{2+} \tag{2.8}$$

$$Pu^{4+} + PuO_2^{2+} + 2H_2O \underset{k_{-3}}{\overset{k_3}{\rightleftharpoons}} 2PuO_2^+ + 4H^+ \tag{2.9}$$

Table 2.1: Reaction constants for Pu(IV) disproportionation

Reaction	Constant	value / $M^{-1}s^{-1}$	source
(2.7) back	k_1	$4.4 \times 10^{-2}[H^+]^{(a)}$	[Fult70]
(2.7) forward	k_{1-}	$3.8 \times 10^{-5}[H^+]^{-3(b)}$	[Fult70]
(2.8) back	k_2	2.7	[Rabi58]
(2.8) forward	k_{2-}	37.5	[Rabi58]
(2.9) back	k_3	$3.6 \times 10^{-3}[H^+]$	[Rabi57]
(2.9) forward	k_{3-}	$1.2 \times 10^{-7}[H^+]^{-3}$	[Rabi57]

a) Calculated from backward reaction
b) $k_{1-} = 2.9 \times 10^{-5}[H^+]^{-3}$ in [Newt02] and $k_{1-} = 2.7 \times 10^{-5}[H^+]^{-3}$ in [Rabi53]

The rate constants for the respective forward and backward reactions are named according to the convention in [Newt02] and summarized in Table 2.1. These reactions define a system of coupled differential equations which can be solved numerically. For instance the reaction (2.7) gives

$$\frac{\mathrm{d}[\mathrm{Pu(III)}]}{\mathrm{d}t} = k_1[\mathrm{Pu(III)}][\mathrm{Pu(V)}] - k_{-1}[\mathrm{Pu}^{4+}]^2 \tag{2.10}$$

(The hydrogen ion concentration dependence was included in the rate constants)

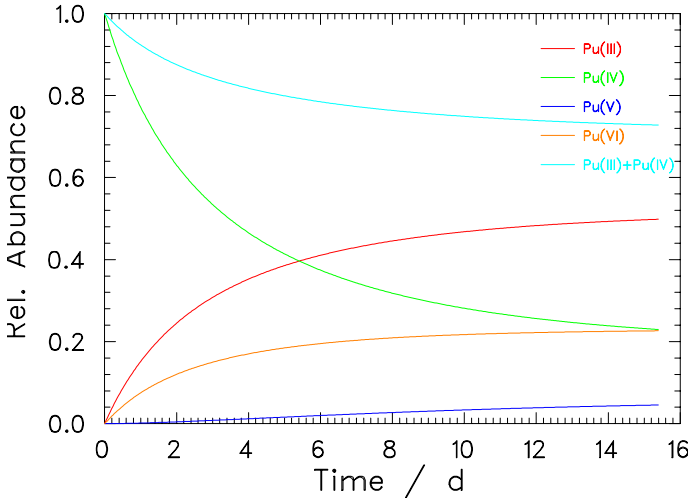

Figure 2.2: Kinetics of Pu(IV) redox reactions. Calculations were performed for $-\log[H^+] = 0.85$ using the rate constants of Table 2.1 and a first hydrolysis constant of $\log \beta^o_{1,1}$ =13.30 [Rabi60]. Details see text.

The reactant in (2.7) - (2.9) is the aquo ion Pu^{4+} but the measurable quantity is $[Pu(IV)_{aq}]$. Since for pH > 0 a considerable fraction of $Pu(IV)_{aq}$ forms hydroxide complexes, $[Pu^{4+}]$ has to be calculated according to Eq. 2.2 which requires knowledge of the hydrolysis constants $\beta'_{x,y}$.

It is hence not possible to determine rate constants k_i *and* hydrolysis constants independently on the basis of kinetic data alone. Usually, a set of hydrolysis constants is chosen from literature and the rate constants are determined from the kinetic data. The time evolution of an initially pure Pu(IV) solution is illustrated in Fig. 2.2. The graph was calculated following [Clar06] by use of the set of rate constants listed in Tab. 2.1 and a first hydrolysis constant of $\beta^o_{1,1}$ =13.30 [Rabi60]) which is in accordance with values obtained by spectrophotometric methods ($\beta^o_{1,1}$ = 13.37 [Krau50] , $\beta^o_{1,1}$ = 13.55 [Rabi51], $\beta^o_{1,1}$ = 12.81 [Clev68]). However, Metivier *et al.* obtained much higher constants by solvent extraction in very dilute solutions ($\beta^o_{1,1}$ = 14.6, $\beta^o_{1,2}$ = 28.6 [Meti72]) which were recommended in the NEA-TDB [Guil03] and whose use would yield rate constants differing by up to one order of magnitude. The paper [Yun07] (Sec. 2.7.4) of the present work suggests an alternative approach of measuring complex formation constants $\beta^o_{1,1}$ and $\beta^o_{1,2}$ and an estimate for $\beta^o_{1,3}$ by combining spectrophotometry with the measurement of the redox potential (Eh).

2.2 A NOVEL APPROACH TO DETERMINE THE SOLUBILITY OF PU(IV)

(Summary of [Walt03b] - Section 2.7.1)

The solubility of actinide oxides and hydroxides, in particular those of the tetravalent An, are rather low at neutral pH. However, the solubility increases by many orders of magnitude for acidic pH (and due to the formation of carbonate complexes also for very basic solutions). In the present study, the solubility of Pu(IV) is investigated for pH 0-2.

Most solubility measurements on plutonium were performed from undersaturation by contacting a defined Pu-solid with the aqueous phase. The amount of plutonium in solution after a certain contact time is measured by spectrophotometry [Kash49, Capd98, Kim89], liquid scintillation counting [Rai82, Fuji02], solvent extraction [Kim89, Rai84], cerimetry [Pere65] or combinations of these techniques. However, measurements from undersaturation can only be meaningful if the solid phase is well characterized. Even a minor contamination of the solid with a more soluble phase (for instance Pu(III) or Pu(VI) phases) may lead to an apparent increase in the total solubility. The same is true for the homogeneity of the solid. Small grains of the same solid have a higher solubility than larger ones [Schi65, Schi67] and hence the presence of only minute amounts of nm sized particulates may increase the apparant solubility of 'crystalline PuO_2' by orders of magnitude [Neck07] up to solubilities of X-ray

amorphous $Pu(OH)_4$. Radiolytic effects may play a role when 'short lived' isotopes of Pu are investigated, but in the presence of a large amount of precipitate even with ^{242}Pu α-reduction might lead to formation of Pu(III) which is much more soluble in acidic solutions.
Classical quantification methods of 'solvated Pu' like LSC do not distinguish mononuclear from oligomeric and colloidal species, as long as these remain suspended and do not precipitate. None of the techniques mentioned above can distinguish all of the species which might contribute to the 'solute phase' and only in some of the investigations, the contributions of colloids was quantified using filtration. In concentrated solutions ([Pu(IV)] > 0.1 M), the formation of polynuclear oxo-hydroxo-complexes starts as early as pH 0 and mononuclear species (solvated ions) are only observed in extremely acidic conditions (12M HCl). With increasing pH, small colloids form [Lloy78, Kim84b]. For lower concentrations, the domain of colloid formation shifts toward higher pH, nevertheless their presence remains of cardinal importance in the framework of solubility chemistry. Very small colloids can considerably contribute to the amount of Pu(IV) in solution and increase the apparent solubility by orders of magnitude. However, it remains a question of definition at what size one draws the line between solute (polymers) and precipitate (colloids and suspended particles).

Solubility measurements can be performed from two directions. Besides starting from *undersaturation* as described in the previous paragraph, one can start from *oversaturation*: An acidic solution with a well defined concentration of Pu(IV) is titrated to higher pH. Since in the case of Pu(IV), the solubility decreases as the pH increases (for the acidic domain) the solution becomes oversaturated and the amount of Pu(IV) exceeding the solubility forms a precipitate. If the starting point (pH) of precipitation is measured as a function of Pu(IV) concentration, a (crude) estimate of the solubility of the freshly formed precipitate - in this case amorphous $Pu(OH)_4$ - is obtained. The absence of precipitate reduces the amount of Pu in the sample so that α-induced redox reactions are basically absent particularly in HCl/NaCl solutions [Rabi55, Clar06]. A further advantage is that the results cannot be altered by possible contaminations or inhomogeneities of the precipitate.
In the present work, we refined this approach by detecting the precursor reaction of precipitation – the formation of colloids. With increasing pH, polynuclear Pu(IV) hydroxide complexes form and grow nm-sized colloids which can be detected using laser-induced breakdown detection (LIBD, described in detail in Chapter 4). A similar method was succesfully used for solubility measurements of $Th(OH)_{4(am)}$ / ThO_2 [Bund00, Neck02, Walt03a, Bite03a] and amorphous Np(IV) hydroxide [Neck01b]. Knopp et al. used LIBD combined with filtration for detection of colloids in solutions after reduction of Pu(VI) to Pu(IV) by addition of H_2O_2 but only data at -log $[H^+] = 1.0$ was obtained (see Fig.2.3).

For the present experiments, a $^{242}Pu(IV)$ stock solution in 0.5 M $HClO_4$ was prepared by electrolysis and fumed with HCl several times under UV VIS spectrometric control. Care was taken to achieve a colloid free solution. From this stock solution, several batch samples of constant ionic strength (HCl/NaCl) but different Pu(IV) concentration and different pH were

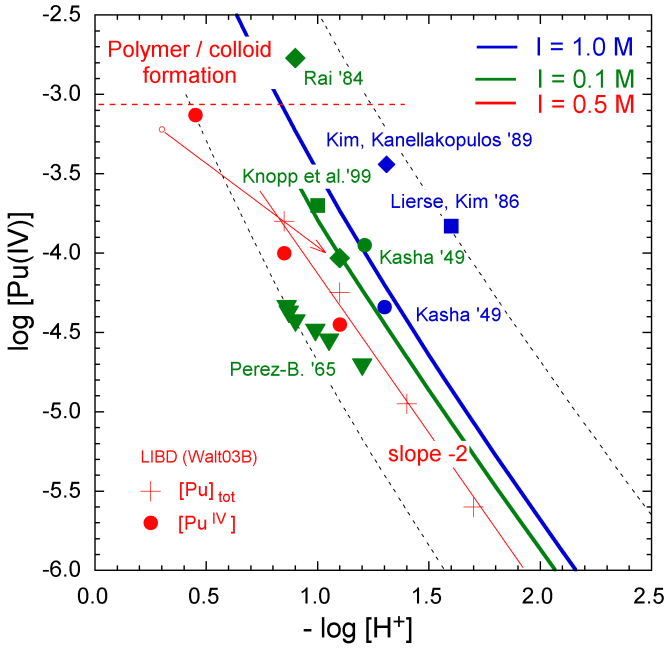

Figure 2.3: Solubility of amorphous Pu(IV) hydroxide, $Pu(OH)_4(am)$. Data of the present LIBD study (• , +) are compared to values from literature and calculations for I=0.1 M and I=1.0 M using $\log K^o_{sp} = -58.7$ [Neck01a] and the formation constants for mononuclear hydrolysis complexes from Metevier [Meti72]

prepared by dilution with 0.5M HCl and subsequent pH increase by slow (10μl/min) titration with 0.5 M NaCl: Pu concentration and acidity were lowered simultaneously (indicated for one of the samples by the arrow in Fig. 2.3). This pH increase ultimately lead to the formation of Pu(IV) colloids at the 'critical pH' (pH_{Crit}) observed by a sharp increase in the LIBD signal. Such colloid formation is the indication that the solubility limit has been exceeded. The critical pH was determined for four different Pu concentrations between $[Pu]_{tot} = 10^{-3}$ M and 2×10^{-6} M, visualized in Fig. 2.3 (red symbols). For the higher concentrations the fraction of Pu(IV) was determined by UV-VIS or LPAS [Kita82, Stum84, Kim90].

The essential result of this work is that the solubility curve has a slope $\Delta[Pu(IV)]/\Delta pH_{Crit} = -2$ in the considered range of concentration and acidity, which requires the dominant solution species being twofold charged as discussed in detail in Sec. 3.8.4 (Eqs.(30)-(32) of [Walt07b]). In the present case, if only mononuclear hydrolysis complexes are considered (*c.f.* Sect. 2.6), this is $Pu(OH)_2^{2+}$ which forms amorphous $Pu(OH)_4$ precipitate

or Pu(IV) oxyhydroxo colloids via

$$Pu(OH)_2^{2+} + 2H_2O \rightleftharpoons Pu(OH)_{4(coll)} + 2H^+ \quad . \tag{2.11}$$

The solubility product, extrapolated to zero ionic strength using hydrolysis constants and SIT coefficients from [Meti72] and [Knop99] respectively agrees well with the literature value of

$$\log K_{sp}^o = (\log[Pu^{4+}])(\gamma_{Pu}) + 4(\log[OH^-])(\gamma_{OH}) = -58.7 \pm 0.9 \tag{2.12}$$

within the errors.

A second, equally important finding concerns the redox reactions of Pu(IV). Using LPAS, the decrease of Pu(IV) and increase of Pu(III) over a 70 h period was monitored for a sample ($[Pu]_{tot} = 3.15 \times 10^{-5}$ M, $-\log[H^+] = 1.2$). Contradictory to what one would expect from disproportionation Equation (2.6), the decrease in [Pu(IV)] and increase in [Pu(III)] do not scale like 3:2 but rather $\Delta[Pu(III)] = -\Delta[Pu(IV)]$ anticipating the results of our more detailed investigations which are discussed below (Sec. 2.4): The solution is already slightly oversaturated with respect to $Pu(OH)_{4(am)}$ and Pu(IV) colloids are present in the sample. No Pu(V) or Pu(VI) was detected. From the difference of $[Pu]_{tot}$ and the sum of [Pu(III)]=6×10^{-6} M and [Pu(IV)]=2.15×10^{-5} M directly after titration, the colloid concentration is estimated as $[Pu(IV)]_{coll}] = 4 \times 10^{-6}$ M. LIBD measurements proved that these colloids which caused a strong signal in the fresh sample dissolved completely after 70 h and presumably formed Pu(V), which was not measured in this study. Accordingly, the Pu(IV) concentration decreases to [Pu(IV)]=1.35×10^{-5} M whereas the remainder is present in the more soluble tri- or pentavalent state which agrees very well with the $Pu(OH)_4$ solubility at $-\log[H^+] = 1.2$ in I=0.5 HCl/NaCl.

2.3 DO PU(IV) ABSORPTION SPECTRA CHANGE UPON HYDROLYSIS?

(Summary of [Walt07a] - Section 2.7.2)

Visible absorption spectroscopy is the most frequently used tool for measuring oxidation state distributions of Pu solutions. In order to evaluate the complex spectra resulting from a mixture of several oxidation states, it is necessary to know the spectra of the pure components. Furthermore, if the acidity dependence of Pu complex formation is investigated, the influence of pH on the spectra of each single oxidation state needs to be known. While it is generally accepted that in the range pH 0 to pH 3 the spectra of Pu(III), Pu(V) and Pu(VI) remain constant, the case of tetravalent Pu ($Pu(IV)_{aq}$) has been subject to intense discussions from the 1950 up to now. Shifts in the absorption spectra and decrease in absorptivity (ϵ) at seemingly constant $Pu(IV)_{aq}$ concentration were reported. These changes were attributed to

formation of the first Pu(IV) hydroxide complex $Pu(OH)^{3+}$. Based on the assumption that the $Pu(IV)_{aq}$ concentration remains constant, most authors concluded that the hydroxide complexes must have slightly different absorption spectra and some 20% lower maximum absorptivity ($\epsilon(471\,nm)$). Hydrolysis constants were calculated from these spectral changes as a function of pH [Krau50, Rabi60, Clev68, Nits96, Yuso04]. However, these data scatter considerably. In the present work, we show that the decrease in absorptivity does not originate in alterations of the absorption spectra due to hydrolysis but rather is caused by formation of Pu(IV) polymers or colloids ($Pu(IV)_{coll}$): As described in detail in Sec. 2.7.2, reference spectra of Pu(III), Pu(IV), and Pu(VI) in 0.1-1 M hydrochloric acid or perchloric acid at rather high concentration ($[Pu]_{tot} = 0.6 - 4\,mM$) were recorded and normalized to molar Pu concentration (details see Fig. 1 of [Walt07a]). The Pu(V) reference spectrum was recorded at lower acidity ([Pu(V)]=0.6 mM in 1 mM $HClO_4$).
The oxidation state distribution of an arbitrary sample is obtained by fitting the concentration weightet sum of all four reference spectra f^i

$$f(\lambda) = c^{III} f^{III} + c^{IV} f^{IV} + c^{V} f^{V} + c^{VI} f^{VI} \tag{2.13}$$

(Eq.(17) of [Walt07a]) to the absorption spectrum $f(\lambda)$ of the sample by a least squares method. The coefficients c^i are the absolute concentrations of the respective oxidation states i. In comparision to the widely used method of evaluating oxidation state concentrations from the absorbance at only one wavelength (*e.g.* at $\lambda = 471\,nm$ for Pu(IV)), the present technique of fitting the complete spectra is much more rubust against spectral noise and allows to evaluate even small (some percent) contributions of the weakly absorbing Pu(V). The pH dependence of the Pu(IV) absorption was investigated in the following way: Spectra were recorded at constant total Pu concentration as a function of pH. From the spectra $f(\lambda)$, the contributions of Pu(III), Pu(V), and Pu(VI) were subtracted and then normalized to molar Pu(IV) concentration ($f_{pH}^{IV} = \frac{1}{c^{IV}} \left(f_{pH}(\lambda) - c^{III} f^{III} - c^{V} f^{V} - c^{VI} f^{VI} \right)$). If the first hydroxo complex $Pu(OH)^{3+}$ had a spectrum different from Pu^{4+}, pH changes should give rise to spectral alterations, which were easliy seen by comparing f_{pH}^{IV} and the reference spectrum $f(IV)$. However, between pH 0.48 and 1.21 no significant deviations were found (Fig. 6 of [Walt07a]). While changes in the peak positions would be easily detected by the described method, an overall decrease of the molar absorptivity of Pu(IV) might remain unnoticed, as the decrease of f_{pH}^{IV} could be compensated by an apparent increase (*i.e.* an overestimation) of c^{IV}. However, for undersaturated solutions[1] containing little or no Pu(IV)-colloids/polymers, the sum of all Pu oxidation states must remain constant *i.e.* equal the total Pu concentration $[Pu]_{tot}$ as measured by LSC. An apparent increase of c^{IV} would lead to $\sum c^i > [Pu]_{tot}$. As evident from Table 4 of [Walt07a], this is not true which in turn proves that the absorption

[1] In the present case, this means undersaturation of the fraction of tetravalent Pu ([Pu(IV)]) with respect to Pu(IV) hydrous oxide. Since the solubilities of Pu(III), Pu(V), and Pu(VI) are much higher at pH and concentrations of the present study, a considerable fraction of the Pu might be present in oxidation states other than IV and hence the total Pu concentration in solution might exceed the solubility of $Pu(IV)(OH)_4(am)$ considerably. This is the case for the samples of pH > 0.8 listed in Table 4 of [Walt07a].

spectrum of Pu^{4+} does not change upon formation of the first two hydroxide complexes $Pu(OH)^{3+}$ and $Pu(OH)_2^{2+}$.

A very close look at the residuum spectra ($f_{pH}^{IV} - f^{IV}$) reveals that there is a weak spectral pattern around 620 nm (Figure 6 of [Walt07a]) which increases with decreasing acidity and which becomes more pronounced for aged solutions (after 70 days). This peak is evidence for the presence of small Pu(IV) colloids: various absorption spectra of Pu(IV) colloids were published depending on their age [Ocke56, Lloy78] and the way they were prepared [Clev68, Cost73, Lloy78, Toth81, Kim88] having in common more or less pronounced peaks around $\lambda = 620\,\text{nm}$. However, no precise values for the molar absorptivity is available. Estimates assume $\epsilon_{coll}(620\,\text{nm}) < 20\,\text{M}^{-1}\text{cm}^{-1}$ [Clev79]. For small polynuclear complexes containing only a few Pu ions, no absorption spectra are published at all and it is possible that these do not absorb visible light. In [Walt07a], an upper limit of 2% $[Pu]_{tot}$ is calcutated for the contribution of colloids in the present conditions. However, for highly oversaturated solutions, colloids are often the dominant Pu fraction. The weak absorption of the colloids leads to a decrease of Pu(IV) absorption without respective increase of any of the other oxidation states which was erroneously interpreted as a change the Pu(IV) absorptivity due to hydrolysis (*e.g.* in [Yuso04]). The present work unambiguously proves that the spectral absorption remains constant and any decrease of the optical absorption spectra in oversaturated solutions is due to colloid formation, similar to the case of Np(IV) [Neck01b].

The spectroscopic data obtained in the present work was not only evaluated with regard to potential spectral change upon hydrolysis of $Pu(IV)_{aq}$ but, in additon, allows to conclude on the solubility of amorphous Pu(IV) hydroxide. Similar to the solubility diagram (Figure 2.3) the absolute concentration of $Pu(IV)_{aq}$ of each sample is plotted in [Walt07a] Fig. 9 for $t = 0$ (*i.e.* directly after titration) and after redox equilibrium is established after some weeks or months (*c.f.* Fig. 2.4). Solutions which are oversaturated with respect to $Pu(OH)_{4(am)}$ in the beginning, adjust to concentrations $[Pu(IV)]_{aq}$ very close to the solubility limit of $Pu(OH)_{4(am)}$ measured by LIBD, *i.e.* the critical pH for colloid formation. The excess Pu concentration distributes among Pu(III), Pu(V), and Pu(VI) and/or $Pu(IV)_{coll}$. Whether Pu(IV) colloids or the ionic species Pu(III), Pu(V), Pu(VI) prevail depends on pH and pe of the solution according to the simultaneous balance of Equations (2.18) - (2.21).

2.4 INFLUENCE OF POLYNUCLEAR PU(IV)-HYDROXIDE COMPLEXES AND PU(IV) COLLOIDS ON THE REDOX REACTIONS

(Summary of [Cho05a] - Section 2.7.3)

Having proven that the Pu(IV) absorption spectrum remains unaffected by hydrolysis, UV-VIS was applied to study redox kinetics and equilibrium oxidation state distributions in acidic Pu solutions. Similar studies were performed since the early days of Pu chemistry and as long as no Pu(IV) colloids or polynuclear complexes are present, results can be described reasonably well by the theory of disproportionation (Sec. 2.1). However, discrepancies are found when polymerization comes into play. Connick and coworkers reported [Conn49c] that in solutions with approximately 5% polymeric plutonium, Eq. (2.4) was violated. Costanzo [Cost73] obeserved excess reduction of Pu(V) in rather concentrated solutions which were oversaturated with respect to formation of Pu(IV) hydrous oxide and most likely contained Pu(IV) polymers or colloids. Strong deviations of steady state distributions from the expected equilibria were reported by Romanovski *et al.* [Roma00] and Nitsche *et al.* [Nits94] over a wide range of acidity and Pu concentration. On the other hand, acceleration of redox reactions by Pu(IV) polymers was suggested [Newt83, Madi84] and Newton *et al.* [Newt86] assumed that Pu(V) disproportionation cannot proceed at all in the absence of Pu(IV) polymers.

Two examples illustrate how these small particles cause deviations of the redox kinetics and/or equilibria distributions from the predictions by the disproportionation equations (2.4) - (2.6). As described in [Walt07a], ^{242}Pu(IV) stock solutions were prepared by electrolysis and subsequently, pH and Pu concentration were adjusted by dilution with hydrochloric acid followed by very slow titration with 0.5 M NaCl. The presence or absence of Pu(IV) oxyhydroxide colloids > 5 nm was confirmed by laser-induced breakdown detection (LIBD, details see Chapter 4). As the fraction of polymeric or colloidal Pu(IV) cannot be quantified by spectroscopy, it was calculated from the difference

$$[\mathrm{Pu(IV)_{coll}}] = [\mathrm{Pu}]_{\mathrm{tot}} - \left\{[[\mathrm{Pu^{3+}}] + \mathrm{Pu(IV)_{aq}}] + [\mathrm{PuO_2^+}] + [\mathrm{Pu(VI)_{aq}}]\right\}. \tag{2.14}$$

The oxidation state distribution is measured as a function of time and compared to the prediction of equations (2.7) - (2.9) using the kinetic constants of Table 2.1. While the overall trend (velocity) of the redox reactions at [Pu]$= 3 \times 10^{-4}$ M, -log [H$^+$] = 0.48 (Fig.2.4, left) agrees quite satisfactorily with the disproportionation model (solid lines), the absolute concentrations of the oxidation states (symbols) deviate systematically: disproportionation (2.4) - (2.6) requires that 2 Pu(III) ions and 1 Pu(VI) ion are produced by consumption of 3 Pu(IV) ions, and hence

$$\mathrm{d[Pu(IV)aq]/dt} = \mathrm{d[Pu(III])/dt} + \mathrm{d[Pu(VI])/dt} \tag{2.15}$$

should be fulfilled, but instead, the formation of Pu(III) is always approximately equal to the

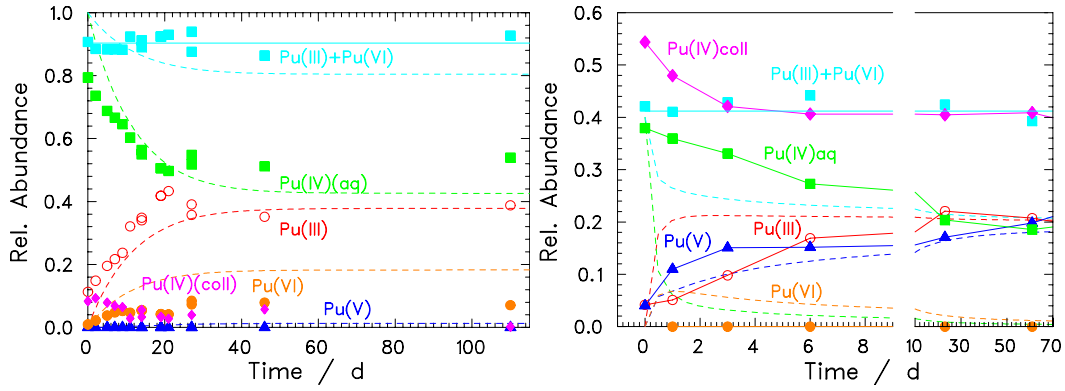

(a) $[Pu] = 3 \times 10^{-4}$ M, -log $[H^+] = 0.48$ (b) $[Pu] = 1 \times 10^{-5}$ M, -log $[H^+] = 2.1$

Figure 2.4: Kinetics of Pu redox reactions when Pu(IV) colloids are present. Symbols show measured data in HCl/NaCl solutions of I=0.5 M, dashed lines are calculated kinetics according to the disproportionation model described in the text.

simultaneous decrease of Pu(IV)aq:

$$d[Pu(III])/dt = d[Pu(IV)_{aq}]/dt \tag{2.16}$$

i.e., $\{[Pu(IV)_{aq}] + [Pu(III)]\}$ = constant (see cyan line) and, as a consequence:

$$d\{[Pu(V)] + [Pu(VI)]\}/dt = d[Pu(IV)_{coll}]/dt \quad . \tag{2.17}$$

From the decrease of $[Pu(IV)_{aq}]$, the disproportionation model predicts the formation (orange line) of twice as much $Pu(VI)_{aq}$ than actually observed (orange symbols). However, the increase of $Pu(VI)_{aq}$ correlates very well with the decrease of colloidal Pu(IV) strengthening the hypothesis that solutions containing colloids cannot be described by the disproportionation model.

The deviations become even more pronounced as the colloidal fraction increases for strongly oversaturated solutions. The right part of Fig.2.4 shows the kinetics of a sample at [Pu]= 1×10^{-5} M, -log $[H^+] = 2.1$. As for the higher concentrated but less oversaturated first example, the increase of trivalent Pu balances the decrease of (aquous) tetravalent Pu rather than that the expected 3:2:1 ratio (decrease Pu(IV), increase Pu(III), Pu(VI), respectively) would be observed. In addition, the reactions proceed much more slowly than predicted and - most important - Pu(V) builds up faster than Pu(III) and faster than $Pu(IV)_{aq}$ decreases. This can not be explained by the diproportionation model. Instead, the formation of Pu(V) correlates well with the decrease of the colloidal fraction $-\Delta[Pu(IV)_{coll}] = \Delta[Pu(V)]$ suggesting that

colloids are in equilibrium with both, Pu(IV) and Pu(V) and act as an intermediate for formation and breaking of the Pu-O bond.
Very recently, Haschke [Hasc07] suggested formation of Pu-trimers comprising two Pu(III) and one PuO_2^{2+} ion. The size (p=3) was inferred from slope analysis of kinetic data ([Rabi57, Arty59]). Although it is likely that, in addition to the trimer, additional polymers exist and although the Pu ions need not neccessarily be attributed to these exact oxidation states, it is interesting that the mean oxidation state of the trimer is IV=(2*III+VI)/3 and that the lower as well as the higer oxidation states contribute to the polymers which might explain the existance of equilibria with Pu(IV) and Pu(V) solution species.

As none of the solutions investigated in the present studies which contain colloids (four examples are shown in Figs. 1a-d of [Cho05a] and five more in Fig. 1 of [Yun07]) fulfills the 3:2:1 balance at reaction times < 10 days but rather behave according to the reactions (2.16) and (2.17), we suggest a more general model, which not only tolerates the presence of colloids but rather makes them an integral part of the Pu redox equilibrium system. All the reactions above can be represented by the summation or subtraction of the following half reactions. Firstly, there are the redox equilibria between Pu^{3+} and Pu^{4+} and between PuO_2^+ and PuO_2^{2+}. These reactions are fast because the electron transfer between two species of the same structure is rapid and reversible.

$$Pu^{3+} \quad \leftrightharpoons \quad Pu^{4+} + e^- \quad , \quad \log K^o = -17.74 \pm 0.051 \quad \text{[Lemi01]} \tag{2.18}$$

and

$$PuO_2^+ \quad \leftrightharpoons \quad PuO_2^{2+} + e^- \quad , \quad \log K^o = -15.86 \pm 0.085 \quad \text{[Lemi01]} \tag{2.19}$$

They do not depend on the pH of the solution. Secondly, there are the oxidation or reduction reactions between either of the two lower oxidation states (Pu(III) or $Pu(IV)_{aq}$) and either of the two upper oxidation states (Pu(V) or Pu(VI)). These reactions are slow since they require the formation or decomposition of Pu-O bonds and the reorganization of the solvent shell [Katz86], for example, is the oxidation of Pu(IV) to Pu(V),

$$Pu^{4+} + 2H_2O \leftrightharpoons PuO_2^+ + 4H^+ + e^- \quad , \quad \log K^o = -17.47 \pm 0.17 \quad \text{[Lemi01]} \tag{2.20}$$

This reaction (2.20) also reflects the fourth power dependence on the hydrogen ion concentration for the oxidation to plutonyl ions and explains the increasing stability of the Pu(V) state with decreasing H^+ concentration [Fuge76]. Finally, if Pu(IV) colloids or precipitates are present, then these Pu(IV) solid phases are in equilibrium with Pu(V) according to

$$PuO_2 \cdot xH_2O(am) \leftrightharpoons PuO_2^+ + xH_2O + e^- \quad , \quad \log K^o = -19.8 \pm 0.9 \quad \text{[Guil03].} \tag{2.21}$$

The present results indicate that the so-called 'disproportionation of Pu(IV)'is a two-step process. The initial step is the formation of PuO_2^+, either by the redox equilibrium with the

Pu(IV) colloids (see [Cho05a]Eq. (2.22))

$$PuO_{2(coll,hyd)} \Leftrightarrow PuO_2^+ + e^- \tag{2.22}$$

or by the oxidation of colloidal or smaller polynuclear Pu(IV) species by O_2, analogous to the water-catalysed oxidation of solid $PuO_{2(s,hyd)}$ to $PuO_{2+x(s,hyd)}$, [Hasc02b] followed by the dissolution of the oxidized Pu(V) fractions:

$$\begin{aligned} PuO_{2(coll,hyd)} + \frac{x}{2}O_2 + xH_2O &\rightarrow PuO_{2+x(coll,hyd)} + xH_2O \\ &\rightarrow 2x(PuO_2^+ + OH^-) + (1-2x)PuO_{2(coll,hyd)} \end{aligned} \tag{2.23}$$

The second step is the simultaneous equilibration of the redox couples Pu(V)/Pu(VI) (Eq. 2.19) and Pu(IV)/Pu(III) (Eq. (2.20) which are related by redox potential (pe) and pH (because of Pu(IV) hydrolysis equilibria).

This mechanism explains that the sum of tri- and tetravalent Pu $[Pu(III)] + [Pu(IV)_{aq}]$ always remains constant. It also explains the different behavior of undersaturated colloid-free solutions (*e.g.* [Cho05a] Fig. 1a) and those containing polynuclear complexes or colloids (*e.g.* [Cho05a] Fig. 1b). At $[Pu]_{tot} = 1x10^{-5}$ M and -log $[H^+] = 2.1$ (Fig. 2.4), considerably above the solubility of $PuO_{2(am,hyd)}$, Pu(V) is evidently formed faster than Pu(III), not simultaneously as required by the disproportionation reaction (2.4).

The presence of O_2 is not necessary for reaction (2.22), but a prerequisite for reaction (2.23). Analogous experiments under air and in an Ar glove box gave very similar results (*c.f.*, [Cho05a]Figs. 1b and d). However, the O_2 contamination (ca. 10 ppm) of the Ar box used might suffice to produce Pu(V) and Pu(VI) from colloidal or polynuclear Pu(IV) via reaction (2.23) preventing an unequivocal distinction at this time.
Recapitulating these facts, we conclude that the "disproportionation" reactions (2.4) and (2.5) describe correctly equilibrium state thermodynamics of undersaturated solutions, but not the underlying reaction mechanism, particularly not if polynuclear complexes or colloids are present.

2.5 DETERMINATION OF HYDROLYSIS CONSTANTS FOR THE MONONUCLEAR PU(IV)-HYDROXIDE COMPLEXES BY MEASUREMENT OF OXIDATION STATE DISTRIBUTION AND REDOX POTENTIAL (EH)

(Summary of [Yun07] - Section 2.7.4)

Although hydrolysis of Pu(IV) cannot be measured from a change of the absorption spectra directly, the formation constants of the first, second, and third Pu(IV) hydroxide complex can be determined by use of absorption spectroscopy: Equations (2.19) - (2.21) relate the abundance of two oxidaton states of Pu with the redox potential (more precisely the pe value) of the solution. For the reasoning below, one must keep in mind that Equations (2.19) - (2.21) refer to the uncomplexed ions ($Pu^{z+}, z = 3, 4$; $PuO_2{}^{z+}, z = 1, 2$) which is particularly relevant for Pu(IV) (hydrolysis) and Pu(VI) (chloride complexation) under the conditions of the present experiments (pH and ionic strength). The central quantity in Equations (2.19) - (2.21), the redox potential (pe=F/RT ln(10)Eh(V) $\approx$ 16.9 Eh(V)) can be measured directly, *e.g.*, using half cells. In the case of [Yun07], minituriazed Pt and Ag/AgCl electrodes were used. Samples of $0.3 < -\log[H^+] < 2.5$ were prepared as described in the previous sections and the oxidation state distribution was monitored spectroscopically by use of the algorithm desribed in [Walt07a] until a steady state was reached after days or weeks. The amount of colloids was calculated by Equation (2.14). Using Equations (2.19) and (2.21), pe values were obtained from the couple Pu(V)/Pu(VI) and the couple $Pu(V)/Pu(IV)_{coll}$ respectively, which agree excellently with the measured redox potentials (Fig. 2 of [Yun07]). In contrast, the pe values calculated from the Pu^{3+}/Pu(IV) couple by use of Equation (2.20) deviate systematically from the measured data. The calculated pe values fall below the measured data, the discrepancy being more pronounced for increasing pH. However, when the hydrolysis of Pu(IV) is taken into acount (Eq. 2.2), *i.e.* if only the fraction of Pu^{4+} instead of the total $[Pu(IV)]_{aq}$ enters Equation (2.20), good agreement with measured pe is achieved (Fig. 3 of [Yun07]). A fit to the data using the hydrolysis constants $\log \beta^o_{1,i}, i = 1, 2, 3$ as fit parameters in (Eq. 2.2) yields the following values extrapolated to zero ionic strength with the SIT: $\log \beta^o_{1,1} = 14.0 \pm 0.2$, $\log \beta^o_{1,3} = 26.8 \pm 0.6$, $\log \beta^o_{1,3} = 38.9 \pm 0.9$. These values fall between the lower value selected by Lemire *et al.* [Lemi01] ($\log \beta^o_{1,1} = 13.2 \pm 0.6$) and the significantly higher ones from the study of Metivier and Guillaumont [Meti72] ($\log \beta^o_{1,1} = 14.6 \pm 0.2$, $\log \beta^o_{1,3} = 28.6 \pm 0.3$, $\log \beta^o_{1,3} = 39.7 \pm 0.4$).

Another important conclusion of this work concerns the reaction mechanisms which lead to the observed oxidation state distribution. The consistency of measured redox potential and pe values calculated from the Pu(V)/Pu(VI) and $Pu(IV)_{coll}$/Pu(V) couples indicate that true thermodynamic equilibria of the different Pu oxidation states exist. In particular the latter proves that colloidal $PuO_{2(am,hyd)}$ is in equilibrium with pentavalent Pu and provides further evidence for the hypothesis made in [Cho05a] that the redox reactions of Pu(IV) proceed by

a two step meachanism, namely the formation of PuO_2^+ either by the redox equilibrium of colloidal $PuO_{2(am,hyd)}$ with Pu(V) or the oxidation of colloids (or small polynuclear species) by dissolved O_2 followed by simultaneous equilibration of the redox couples V/VI and III/IV.

Furthermore, this two step mechanism allows to explain findings first published by Rabideau *et al.* [Rabi56]. In equilibrated Pu solutions, the quantity

$$\frac{[Pu^{3+}][PuO_2^{2+}]}{[Pu^{4+}][PuO_2^+]} \tag{2.24}$$

was found to remain constant even for different ratios of Pu(III)/Pu(IV) and Pu(V)/Pu(VI). Using Equations (2.20) and (2.19), one calculates

$$\frac{[Pu^{3+}][PuO_2^{2+}]}{[Pu^{4+}][PuO_2^+]} = \frac{K^o_{III/IV}10^{-pe}}{K^o_{V/VI}10^{-pe}} = \frac{K^o_{III/IV}}{K^o_{V/VI}} = \text{const.} \tag{2.25}$$

which is independent of pe. The pH dependence is caused by the hydrolysis of Pu(IV) and the decrease of the Pu^{4+} fraction with increasing pH. The couples Pu(III)/Pu(IV) and Pu(V)/Pu(VI) adjust according to the redox potential of the solution and both couples are linked via the formation of amorphous oxyhydroxo Pu(IV) colloids ($PuO_{2(am,hyd)}$) or polynuclear complexes which are in equilibrium with Pu(V).

2.6 FORMATION AND STRUCTURE OF COLLOIDAL PU(IV) HYDROLYSIS PRODUCTS

(Summary of [Roth04] - Section 2.7.5)

With increasing evidence for the relevance of polynuclear Pu(IV) complexes and small Pu(IV) colloids for the Pu redox chemistry, the need for more detailed investigations of their formation mechanisms and structure became evident. From slope analysis of solubility measurements [Kash49, Pere65, Rai82, Rai84, Kim89, Knop99, Neck01a, Fuji02, Walt03b, Mori05], it is known that the dominating Pu(IV) species in saturated solutions of pH 0.3 - 2 are twofold charged (for a detailed discussion see [Walt07b]). In the present work, this species was assumed to be $Pu(OH)_2^{2+}$, although close to the solubility limit, polynuclear complexes might contribute a considerable fraction of the solution species, in particular, above millimolar concentration.
Samples between $0.2 < [Pu]_{tot} < 1.2$mM were prepared at acidities (HCl) $0 < -\log[H^+] < 1.75$ by dilution of a Pu(IV) stock solution with the addition of appropriate amounts of solutions of milli-Q water, HCl, and NaCl. After equilibration of 2-4 days, the samples were measured by XAFS and a second set of samples at $0.3 < -\log[H^+] < 0.75$ was probed for the presence of colloids by LIBD. The LIBD data once more confirms the slope =-2 of the solubility plot (Pu concentration versus acidity) and furthermore, an increase in weighted mean colloid size (see [Kim07]) with increasing degree of oversaturation with respect to amorphous Pu(IV)hydroxide from 12 nm at -log $[H^+]$ = 0.45 to 25 nm at -log $[H^+]$ = 0.73 is observed. This is much larger than the 2 nm mean size of cristalline PuO_2 colloids which form in highly concentrated solutions [Lloy78] or at high acidities (1.2 M HCl) [Kim84b]. However, the colloids formed in the present study must be of different structure: Slope analysis of the LIBD data proves that in the present case, the colloids are not crystalline PuO_2. The slope -2 suggests colloid formation via

$$Pu(OH)_2^{2+} + 2H_2O \rightleftharpoons Pu(OH)_{4(coll)} + 2H^+ \tag{2.26}$$

i.e. the colloids must contain a rather large fraction of amorphous hydroxide, but most likely with a high degree of disorder. Alternatively, they might be composed of small crystalline subunits covered by an amorphous hydroxide layer in analogy to Th(IV) colloids [Walt03a].

Evaluation of the EXAFS data yields direct information on the structure of Pu solution species, with the one limitation that coordination numbers and bond distances are averaged over all species which are present in solution: colloids and polymers as well as mononuclear species. In order to obtain data of the Pu(IV) mononuclear species, samples at high acidity were measured and the structure of colloids was inferred from highly oversaturated solutions, where colloids account for the largest fraction of Pu(IV). At molar acidity, no Pu-Pu backscattering was detected which complies with the expectation that mononuclear Pu(IV) species dominate the solution. Eight to nine water molecules coordinate the Pu(IV) at a 2.38 ± 0.02 Å

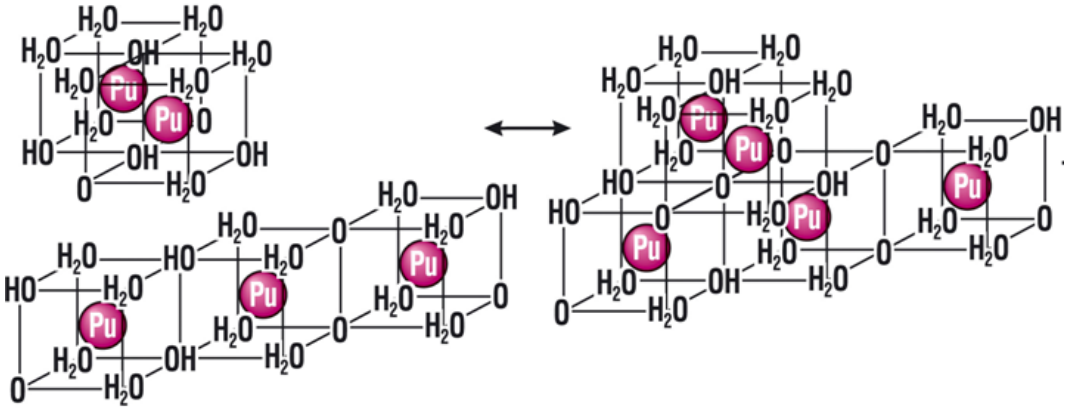

Figure 2.5: Model for polymerization of Pu(IV) from [Roth04]. Dimers and trimers form via edge sharing from $Pu(OH)_2^{2+}$. These subunits agglomerate and eventually form nm sized colloids. During this process, the cubic subunits [Anku98] are preserved and form a distorted fluorite like Pu lattice. With increasing size of the colloids, the disorder decreases, but even at the highest pH investigated in the present study (-log $[H^+]$ =1.75), a high number of defect sites leads to a mean Pu coordination number of only $N_{Pu} = 4.9$.

Pu-O bond distance in agreement with expectations [Anku98]. At higher pH, different Pu-O bond lengths indicate the formation of Pu(-O, OH, OH_2) coordination species. The shorter Pu-O distance (2.22 Å) is assigned to hydroxyl groups and a coordination number of below $N_{OH} < 2$ is found for all colloidal samples. With decreasing acidity, *i.e.* formation of larger colloids, the samples show a trend towards increasing Pu-Pu coordination number ($N_{Pu} = 4.9$ at -log $[H^+]$ =1.75) and increasing order of the Pu sublattice. In contrast, the Pu-Pu distance ($\approx 3.86 - 3.89$ Å) is hardly effected by the O-peak splitting, supporting the hypothesis of a rather rigid Pu-O-Pu 'backbone'. This result rules out that the Pu(IV) colloids in our samples at [Pu]= 1 mM are composed of pure amorphous Pu(IV) hydroxide or can be visualized by crystalline Pu oxide particles covered by a hydroxide layer since an amorphous Pu hydroxide precipitate has $N_{Pu} = 2.4$ (sample A in [Roth04]). It rather allows to conclude that colloid growth proceeds via agglomeration of ordered polymers from the mononuclear dihydroxo complex $Pu(OH)_2(H_2O)_6^{2+}$. Based on a model by Fujiwara and coworkers [Fuji01], we propose that polymerization proceeds via formation of edge sharing dimers and trimers followed by release of protons for charge compensation. While according to the model of Fujiwara *et al.*, polymerization should colminate in the formation of crystalline PuO_2, which is incompatible with the slope of the solubility measurements, our model suggests formation of a hydrated Pu oxide hydroxide phase with the general formula

$$Pu_nO_p(OH)_{4n-2p}(H_2O)_z \tag{2.27}$$

and a distorted fluorite-like strukture.

From the EXAFS spectra, no evidence was found for the presence of trivalent or hexavalent Pu which is contradictory to a very recent work from Haschke [Hasc07] who postulated the formation of linear Pu-trimers comprising two Pu(III) and one PuO_2^{2+} ions bridged by hydroxyl groups. Haschke reevaluated data from early studies on Pu redox kinetics [Rabi57, Arty59] which were performed in rather highly concentrated solutions ($[Pu]_{tot} > 1mM$) at $0.1\,M < [HNO_3] < 1\,M$. In one of the studies [Arty59], the authors stated themselves that in the low acidic samples, the disproportionation equation (2.6) was violated and a considerable fraction of the total Pu was not detectable spectroscopically allowing the conclusion that these samples were already oversaturated and contained Pu(IV) colloids or precipitate. In this case, the slope analysis made by Haschke might lead to erroneous results. However, even if the trimer might not be the only polynuclear species in these solutions and the structure might be different, the mean oxidation state of these polymeric species seems to be close to four (in the case of the trimers (3+3+6)/3=4).

A concluding comment concerns PuO_{2+x}, the formation of which was suggested by Haschke [Hasc00] and followed by a remarkably high number of theoretical and experimental studies [Hasc02b, Hasc02a, Conr03, Conr04, Hasc04, Korz04, Hasc05, Conr05, Neck07]. All samples which contained colloids show a small feature in the FT spectra at $R-\Delta = 1.9\,Å$. Since a Pu-O distance of less than 2 Å was considered physically implausible by that time, we attributed this peak to multielectron excitations. However, two detailed XANES and EXAFS studies by Conradson and coworkers [Conr04, Conr05] on various PuO_{2+x} solids and aged colloids revealed that in a $PuO_{2.26}$ solid, the small shoulder indicating the short interatomic distance near 1.9 Å evolves into the dominant spectral feature. As suggested by Clark [Clar06], the small shoulder in our FT spectra might indicate a small contribution of Pu(V) which does not alter the XANES spectra but nevertheless hints at a PuO_{2+x}-like stochiometry of the colloids. Upon aging, an increasing Pu(V) fraction (increasing x) causes this spectral feature to becomes even more pronounced. It is hence desirable to investigate the polymerization process further, in particular using direct speciation of the polynuclear complexes as is now possible, *e.g.*, using ESI-TOF MS (see Chapter 3.8.4).

2.7 PUBLICATIONS

2.7.1 Nanoscopic approaches to the aquatic plutonium chemistry [Walt03b]

Contributed Papers

Thomas Fanghänel

Thomas Fanghänel of the Institut für Nukleare Entsorgung, Karlsruhe Research Center, Germany, makes a point during his discussion of nanoscopic approaches to aquatic plutonium chemistry.

This article was contributed by Clemens Walther, Claudia Bitea, Jong Il Yun, Jae Il Kim, Thomas Fanghänel, Christian M. Marquardt, Volker Neck, and Alice Seibert of the Institut für Nukleare Entsorgung, Karlsruhe Research Center.

Predicting long-term actinide mobility

Nanoscopic approaches to aquatic plutonium chemistry

The Institut für Nukleare Entsorgung (INE) in Karlsruhe Research Center, Germany, focuses on the basic research relevant to the assessment of prospective repositories for radioactive waste, including both technical and scientific chemical aspects. The predictive modeling of long-term actinide mobility in the geosphere is contingent on basic knowledge of the aquatic chemistry of actinides. In this context, plutonium is of special interest.

Plutonium appears in spent fuel in small amounts (about 1 percent), but after the decay of short-lived fission products, plutonium-239 represents the dominant radioactive inventory for thousands of years.

On the one hand, the solubility constraints of plutonium have led to the perception that this element will be immobilized easily in the repository environment. On the other hand, this particular property of low solubility induces the formation of colloids (tiny, nano-sized particles—either real colloids or pseudo colloids), which may strongly enhance plutonium's potential for mobility in the aquifer. These characteristic properties are of cardinal importance for our work.

Challenges

Different oxidation states (typically III–VI) of plutonium can coexist in aqueous solution under the appropriate conditions, with the relative abundance of each oxidation state depending on the chemical conditions such as pH, Eh, and ionic strength. Plutonium exhibits a complicated redox behavior that permits transformation of one oxidation state into another. For example, the collision of two plutonium(IV) ions generates one plutonium(III) and one plutonium(V) ion, and the plutonium(V) ion subsequently can be oxidized to a plutonium(VI) ion by an additional collision with a plutonium(IV) ion.

Since different oxidation states exhibit different chemical properties, a reliable speciation (with regard to the oxidation states) is required. Our work focuses on the tetravalent plutonium ion, which, in aquatic solution, is known to be unstable even at low pH in dilute concentrations, not only because of disproportionation—the interconversion of its ionic species—but also because of colloid formation.

This instability of dilute plutonium(IV) has made the appraisal of its thermodynamic solubility in aquatic systems extremely difficult, resulting in a large number of controversial results. Thus, assessing the chemical reactions of plutonium(IV) in dilute concentrations in the low pH region requires sensitive speciation and colloid characterization methods.

Our present work combines two different laser spectroscopic speciation approaches, providing the possibility of assessing the chemical reactions of plutonium(IV) at concentrations of only a few micromoles per liter or even lower.

Researchers from the Karlsruhe Research Center Institut für Nukleare Entsorgung are using a "homebuilt" laser setup to study the colloidal transport of plutonium in aqueous solutions. In the front row, from left to right, are: Claudia Bitea and Alice Seibert. In the back row, from left to right, are: Christian Marquardt, Clemens Walther, and Jong Il Yun.

Experimental approaches

We use two methods in our research: laser-induced breakdown detection (LIBD) for colloid quantification and laser-induced photoacoustic spectroscopy (LPAS) for chemical speciation.

LIBD is based on nonlinear interaction of colloids with a tightly focused laser beam (see sidebar on page 14). This leads to the formation of a hot, dense plasma, detected either optically (via light emission) or acoustically (via its expansion-generation shockwave). Each plasma event corresponds to a single colloid and, when compared with the number of laser shots, this provides a measure of colloid concentration.

Compared with dynamic light scattering (the most frequently applied colloid detection technique), the sensitivity, particularly for colloids smaller than 50 nanometers, is enhanced by more than six orders of magnitude. Compared with the so-called single-particle counter, a static light-scattering device, the accessible size range is considerably extended toward smaller colloids.

For particles of 20-nanometer diameter, for instance, the sensitivity corresponds to detecting a pinhead one millimeter in diameter in a good-sized hotel swimming pool.

The speciation methods are based on linear light absorption. Plutonium's oxidation states III, IV, V, and VI exhibit characteristic absorption bands. The absorption strength is directly proportional to the amount of species present. From the (visible) absorption spectra, a quantitative speciation is obtained, typically by UV-visible (UV-Vis) spectroscopy, which measures the extinction (i.e., absorption plus scattering losses) of white light wavelength resolved after passing through the sample.

However, this method is limited to measuring plutonium(IV) concentrations of approximately 10 micromolar. LPAS lowers this limit by a factor of up to 100 by detecting the effects of the light absorbed by the plutonium ions (photothermal method) rather than the transmitted light. A 10-nanosecond light pulse of a tunable dye-laser is guided through the sample, and the energy of the absorbed photons gives rise to a rapid temperature increase with subsequent expansion and generation of an acoustic shock wave.

Analogous to the LIBD method, this acoustic wave is detected by a piezo detector, but because its energy content is rather low (less than one nanojoule), the signal is electronically amplified prior to data recording. The acoustic (and electronic) signal is linearly proportional to the absorption strength at the specific wavelength of the laser beam. Absorption spectra are obtained by scanning the laser over the desired spectral range. In addition to the increased sensitivity down to the micromole-per-liter range, LPAS (in contrast to UV-Vis) is not influenced by the presence of colloids, which give rise to light scattering in the blue end of the spectrum.

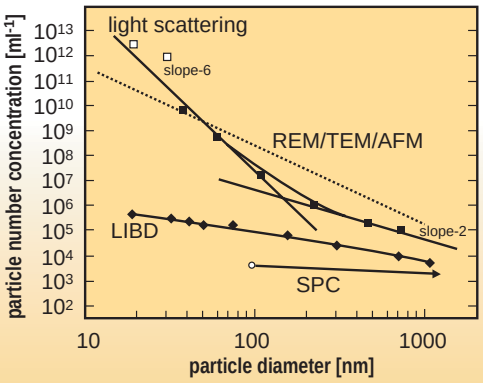

This figure shows the sensitivity of laser-induced breakdown detection (LIBD) compared with classical characterization methods. LIBD's sensitivity is enhanced by more than six orders of magnitude compared with dynamic light scattering, and the accessible size range is considerably extended toward smaller colloids when compared with the single-particle counter (SPC).

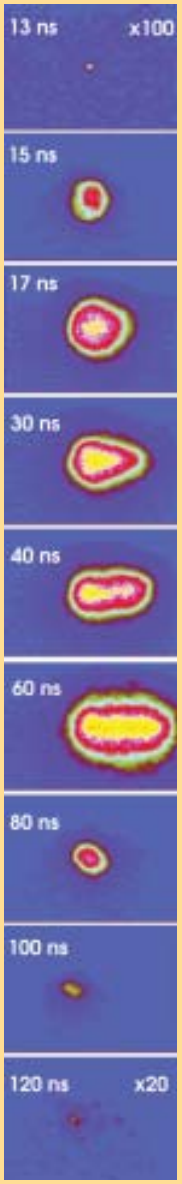

A time evolution of laser-induced plasma plumes incited on single colloids as observed by an ultrafast (200 picoseconds) charge-coupled device camera.

Actinide Research Quarterly

Contributed Papers

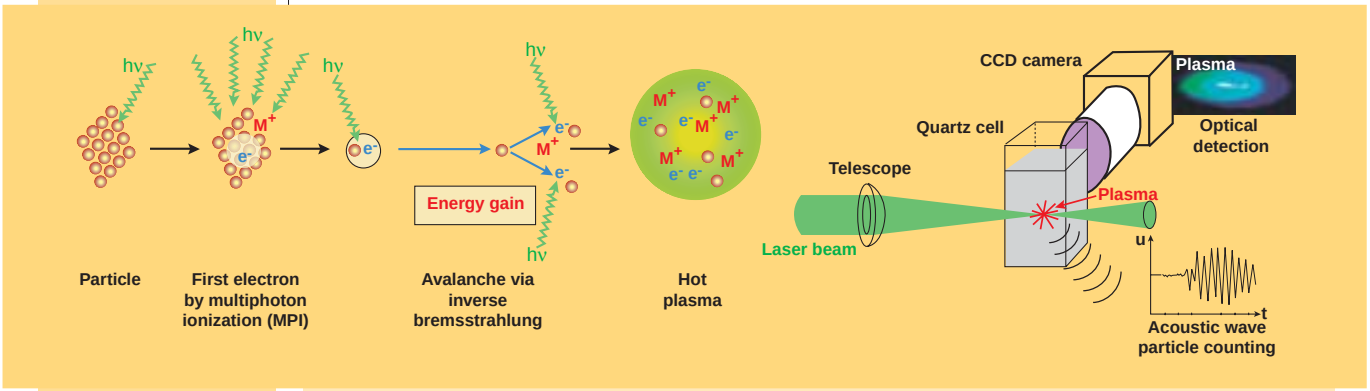

The basics of LIBD

Laser-induced breakdown detection (LIBD) is based on plasma formation due to dielectric breakdown in the high-field region of a focused pulsed laser beam when a colloid is present. We commonly experience low-energy plasmas in everyday life, ranging from "flames" over neon lights to the blinding flash of lightning.

The plasma used for LIBD begins with a single (so-called "lucky") electron, which is created by the high-electric field of the laser. In the language of quantum physics, this is equivalent to the nonresonant absorption of four to six photons (multiphoton ionization or MPI) within only some picoseconds. This process is very unlikely, and it takes on the order of 10^{15} photons to free one electron.

By interaction with the electric field, this electron is accelerated (by inverse bremsstrahlung) to energies sufficient to ionize neighboring atoms by means of collisions, resulting in a second electron (second "generation"), which undergoes the same process. Within typically only 30 such generations, a hot, dense plasma is created, which is observed by either its light emission or by detection of the acoustic shock wave generated by its rapid expansion.

Because each plasma event corresponds to one single colloid, the relative number of events per number of laser shots provides a measure of colloid concentration. The photon flux required for breakdown decreases with the increasing number of molecules inside the colloid. By making use of that dependence, the colloid size can be ascertained by varying the laser pulse energy.

A plutonium-242 solution of pure oxidation state (IV) was prepared by electrochemical reduction in 0.5-molar hydrochloric acid to plutonium(III), followed by careful re-oxidation back to plutonium(IV). The oxidation state was monitored by UV spectroscopy and the plutonium concentration was determined by liquid scintillation spectroscopy. The pH was increased with an associated decrease in plutonium concentration by very slow, stepwise dilution with 0.5-molar sodium chloride solution. The pH adjustment ultimately led to the formation of plutonium(IV) colloid kernels, as observed by a well-defined, sharp increase of the LIBD signal. Such colloid formation is the most sensitive indication that the solubility limit has been exceeded.

Macroscopically, the solubility limit is defined as the concentration at which the total amount of a substance is no longer present in ionic form but instead forms a precipitate. Here, our precipitate takes the form of colloids, which are so small that they remain suspended because of Brownian motion.

Analogous experiments were conducted at different concentrations of the plutonium stock solution. With decreasing plutonium(IV) concentration, the pH of colloid kernel formation increased.

Evaluation

Depending on pH, the tetravalent plutonium ion is more or less hydrolyzed, meaning that it is surrounded by up to four hydroxide (OH^-) molecules. Only in very acidic conditions (a pH less than zero), does a non-hydrolyzed Pu^{4+} aquo-ion exist in solution. The hydrolysis does not change the spectral properties of Pu^{4+}, and so it cannot be detected directly by LPAS. But from the crossing points of colloid formation—log of plutonium(IV) concentration versus pH, we obtain the solubility curve with slope = –2, indicating that the plutonium(IV) dihydroxo complex $Pu(OH)_2^{2+}$ represents the dominant species.

This mononuclear plutonium species undergoes further colloid formation and is thus in equilibrium with colloids. Knowing the hydrolysis constant of $Pu(OH)_2^{2+}$ from the literature, the solubility product (log Ksp = –59 at zero ionic strength) of plutonium colloids (presumably oxyhydrate) can be derived from our data.

Since the amount of plutonium(IV) colloids is relatively small at a given pH of colloid kernel formation, there remains a considerable quantity of (hydrolyzed) plutonium(IV) ionic species undergoing disproportionation with time. This reaction is directly observed by LPAS for plutonium(IV) and (III), at a plutonium concentration within the region of colloid formation above the solubility curve.

The disproportionation reaction can be written as $3Pu(IV) + 2H_2O \leftrightarrows 2Pu(III) + Pu(VI) + 4H^+$, which requires that, for three consumed plutonium(IV) ions, two plutonium(III) ions and one plutonium(VI) ion must be formed. The ratio of plutonium(IV) decrease and plutonium(III) / plutonium(VI) increase should scale as 3:2:1.

Our LPAS measurement however, corresponds to a ratio of 1, indicating a decrease of plutonium(IV) that is too low by at least 50 percent.

To explain this discrepancy, we must keep in mind that plutonium(IV) colloids are in equilibrium with the plutonium(IV) ionic species, and that the plutonium(IV) tied up in colloids is spectroscopically invisible in the LPAS experiment.

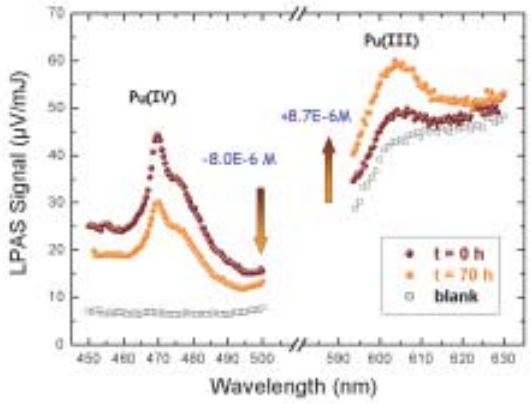

Laser-induced photoacoustic spectroscopy (LPAS) detects the oxidation states of plutonium ions in solution by means of light absorption. This figure shows plutonium(IV) undergoing disproportionation with time. The signal on the left at 470 nanometer (nm) is due to the electronic absorption of plutonium(IV). This signal decreases with time, while the plutonium(III) signal at 605nm increases by the same amount.

Contributed Papers

Diluting a plutonium-242 solution with 0.5-molar sodium chloride results in a decrease in plutonium concentration and an increase in pH (top), until the solubility is exceeded and plutonium(IV) colloid kernels are formed (crossing point). The formation of the colloid kernels is shown by a well-defined, sharp increase of the laser-induced breakdown detection (LIBD) signal (bottom).

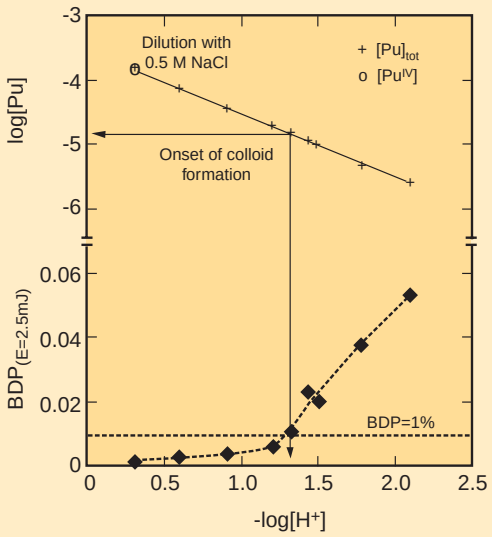

The solubility product of plutonium colloids can be derived from the experimental data. For decreasing plutonium concentration, the crossing point of colloid formation is shifted to higher pH. From the slope = –2, we infer the plutonium(IV) to be present as dihydroxo-complex, $Pu(OH)_2^{2+}$, in equilibrium with colloids.

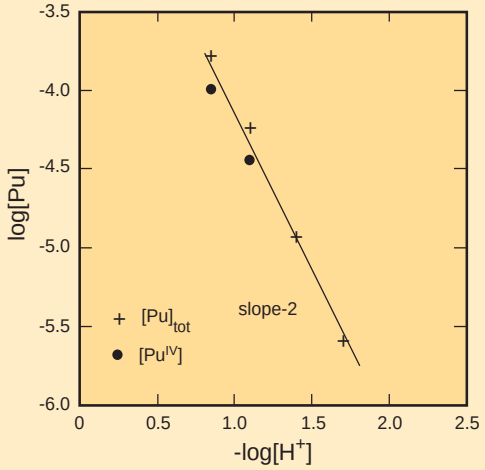

Over the course of 70 hours, as plutonium(IV) ionic species are consumed by the disproportionation reaction, the fraction of (spectroscopically invisible) plutonium(IV) present as colloids redissolved, and this addition to the spectroscopically observable plutonium(IV) fraction was sufficient to account for the discrepancy. Once this was taken into account, the true decrease of plutonium(IV) could be calculated, and satisfied the required 3:2 ratio of the reaction. This was confirmed by LIBD measurements, where the colloid dissolution with time was observed directly.

At lower concentrations (below 10 micromolar total plutonium concentration), LPAS is no longer capable of detecting small amounts of plutonium(IV) colloids present in the solution. However, such minute concentration of colloids (less than one micromolar) can still be detected by LIBD, and the dissolution with time has been demonstrated for solutions of one micromolar total plutonium.

A combination of LIBD and LPAS facilitates a sound assessment of chemical reactions of plutonium(IV) involved at a rim of its solubility-constrained pH for the total plutonium(IV) concentration down to micromoles per liter and for its colloids, about 100 times less (down to a particle concentration of 10 nanomoles per liter).

The present experiment shows how complicated the thermodynamic assessment of plutonium(IV) solubility is. For this reason, there is a wide scattering of the plutonium(IV) solubility product published in the literature—either for its oxide or for its hydroxide, with the differences being a few orders of magnitude. Our research has demonstrated how the use of novel spectroscopic approaches can reduce the uncertainties that have, up to now, hindered the assessment of plutonium(IV) solubility.

2.7.2 Hydrolysis of plutonium(IV) in acidic solutions: no effect of hydrolysis on absorption-spectra of mononuclear hydroxide complexes [Walt07a]

Radiochim. Acta **95**, 7–16 (2007) / **DOI** 10.1524/ract.2007.95.1.7

Hydrolysis of plutonium(IV) in acidic solutions: no effect of hydrolysis on absorption-spectra of mononuclear hydroxide complexes

By C. Walther[1,*], H. R. Cho[1], C. M. Marquardt[1], V. Neck[1], A. Seibert[2], J. I. Yun[1] and Th. Fanghänel[1,3]

[1] Forschungszentrum Karlsruhe, Institut für Nukleare Entsorgung, 76021 Karlsruhe, Germany
[2] European Commission, JRC, Inst. for Transuranium Elements, 76125 Karlsruhe, Germany
[3] Physikalisch-Chemisches Institut, Ruprecht-Karls Universität, Im Neuenheimer Feld 253, 69120 Heidelberg, Germany

(Received January 26, 2006; accepted in revised form July 7, 2006)

Plutonium / Tetravalent / Hydrolysis / Redox reaction / Disproportionation / Colloids / Polymer / UV-Vis / Capillary waveguide / LIBD

Summary. Tetravalent plutonium readily undergoes hydrolysis even in highly acidic aqueous solutions. In the past, many attempts were made to quantify hydrolysis species by means of optical absorption spectroscopy. In the present work solutions ranging from 10^{-5} M to 10^{-2} M (total Pu) concentration in 0.5 M HCl/NaCl ($0.3 < pH_c < 2.1$) are carefully investigated by combining absorption-spectroscopy (UV-Vis, liquid core waveguide capillary) and laser-induced breakdown detection, with special emphasis on the limited solubility of Pu(IV). The results clearly indicate that all changes in the absorption spectra originate from the formation of Pu-polyspecies and colloids. The molar absorptivity of mononuclear Pu(IV) hydroxide complexes does not vary with increasing pH_c and ongoing hydrolysis. The normalized absorption spectra of at least the first and the second hydroxide complex ($Pu(OH)_n^{4-n}$ $n = 1, 2$) do not differ from those of the hydrated Pu^{4+} ion.

1. Introduction

Highly charged metal ions undergo hydrolysis in aqueous solution, and some of them like $Pu^{4+}_{(aq)}$, even under very acidic conditions. The hydrolysis reaction is the primary complexation reaction of actinide elements in aqueous solution and is known to correlate with the electrostatic interaction energy between the actinide ion and the OH^- ligand [1–4]. For the tetravalent actinides the hydrolysis constant increases in the order Th(IV) < U(IV) < Np(IV) < Pu(IV) caused by the decreasing ionic radius (actinide contraction) and the resulting increase in Lewis acidity from Th(IV) to Pu(IV). Only at pH_c[1] < 0.5 Pu^{4+}_{aq} is the dominant species whereas with increasing pH in undersaturated solutions (with regard to plutonium hydroxide) the hydrolysis reaction leads to the quantitative formation of mononuclear complexes $Pu(OH)_n^{4-n}$ ($n = 1$–4). Above millimolar concentration and close to the solubility limit Pu forms polyspecies.

*Author for correspondence (E-mail: walther@ine.fzk.de).

[1] For the definition of pH_c see Sect. 4.

A number of studies on the hydrolysis constants for mononuclear species, $Pu(OH)_n^{4-n}$ ($n = 1$–4), were performed over the last 50 years which are well summarized in [5]. These investigations are based on spectroscopic techniques [6–10], solvent extraction [11], and potentiometry [12, 13]. However, the results are difficult to assess, since in some studies the thermodynamic equilibrium might not have been reached due to slow oxidation, disproportionation, radiolysis, or polymerization reactions. Values of the published hydrolysis constants are listed in Table 1.

The most frequently used method to investigate the first hydrolysis constant is spectrophotometry. In these studies, the decrease of the characteristic Pu(IV) absorption bands (mostly at 470 nm) is ascribed to the initial mononuclear hydrolysis step, the formation of $Pu(OH)^{3+}$. However, there are neither unique absorption bands for the respective hydroxide species $Pu(OH)^{3+}$ nor significant changes in the absorption bands of Pu^{4+} like a shift of the peak position. These studies might suffer from similar misinterpretation as was the case for Np as pointed out recently [4]. Pu studies are performed in the range pH_c 0–2 (for the definition of pH_c see Sect. 4) at relatively high concentrations and in many of these spectroscopic studies, the total $Pu(IV)_{aq}$ concentrations considerably exceed the solubility limit of amorphous Pu(IV) oxide/hydroxide at pH_c 1–2. Thus polymer species or colloids could be present in solutions and cause the decreasing absorption.

Especially in a recent work of Yusov *et al.* [10], the influence of colloid formation is obvious. This work was carried out in the pH_c range from 1.00 to 1.34 at 1.20×10^{-4} M Pu concentration in a 0.5 M ($HClO_4 + NaClO_4$) matrix. In the presented spectra, the absorption at 470 nm decreases with pH increase whereas at about 620 nm the absorption increases. The authors excluded colloid formation under the assumption that Pu(IV) colloids once formed do not depolymerize at room temperature after acidifying the solutions. While this is true for oxidic Pu polymer described *e.g.* by Lloyd *et al.* [14], amorphous hydroxo colloids formed in oversaturated solutions are in equilibrium with the ionic aqua species and may dissolve within minutes upon acidification [15]. Moreover, the Pu concentration used in the work of Yusov *et al.* already exceeds the solubility limit

Table 1. Pu(IV) hydrolysis constants at 20–25 °C and the values converted to $I = 0$ with the SIT[a] approach.

Medium/species	Pu(IV)/M	$\log K'_{1n}$	$\log K^{\circ}_{1n}$	$\log \beta^{\circ}_{1n}$	Methods	Ref.
1.0 M $HClO_4/NaClO_4$ [b]	10^{-8}				extr.	[11]
$Pu(OH)^{3+}$	10^{-8}	−0.45	0.60	14.6 ± 0.2	extr.	[11]
$Pu(OH)_2^{2+}$	10^{-8}	−1.2	0.63	28.6 ± 0.3	extr.	[11]
$Pu(OH)_3^{+}$	10^{-8}	−4.5	−2.25	39.7 ± 0.4	extr.	[11]
$Pu(OH)_4$(aq)	10^{-8}	−10.8	−8.54	47.5 ± 0.5	extr.	[11]
$Pu(OH)^{3+}$						
0.5 M HCl/NaCl, 25 °C	7.2×10^{-4}	−1.65	−0.63	13.37	spec.	[6]
0.5 M $HClO_4/NaClO_4$, 25 °C	7.2×10^{-4}	−1.60	−0.64	13.36	spec.	[6]
2.0 M $HClO_4/NaClO_4$, 25 °C	10^{-3}	−1.73	−0.70	13.30	spec.	[7]
0.19 M $HClO_4$, 23 °C	1.8×10^{-3}	−1.96	−1.19	12.81	spec.	[8]
0.06 M $HClO_4$, 23 °C	1.6×10^{-3}	−1.48	−0.94	13.06	spec.	[8]
0.5 M $HClO_4/NaClO_4$ [b] (pH 0.3–1.5)	1.3×10^{-4}	−1.57	−0.61	13.39	spec.	[9]
0.5 M $HClO_4/NaClO_4$ [b]	1.2×10^{-4}	−1.57	−0.61	13.39	spec.	[10]
0.1 M $HClO_4/NaClO_4$ [b]	1.2×10^{-4}	−1.20	−0.57	13.43	spec.	[10]
1.0 M $HClO_4/NaClO_4$, 25 °C	10^{-3}	−1.51	−0.45	13.55	redox.	[12]
2.0 M $HClO_4/LiClO_4$, 25 °C	8×10^{-3}	−1.27	−0.24	13.76	redox.	[13]
Model calculation	–	–	–	14.6	model	[18]
	–	–	–	28.3		[18]
	–	–	–	39.4		[18]
	–	–	–	47.5		[18]

a: Specific ion interaction theory (SIT) [3] is used for conversion to $I = 0$;
b: Room temperature.

at $pH_c > 1$ (cf. below Sect. 5, Fig. 9). Further evidence for the formation of colloidal plutonium is the absorption band at 620 nm in the 'Pu(OH)$^{3+}$' spectrum which is typical for colloidal Pu [16] (see Fig. 8) and the strong extinction in the blue range of the spectrum with increasing pH due to Rayleigh scattering of suspended particles. Since colloidal plutonium does no longer contribute to the absorption bands of Pu^{4+} or mononuclear $Pu(OH)_n^{4-n}$, in the following designated as $Pu(IV)_{aq}$, the characteristic Pu(IV) absorption bands decrease.

From the analogous study with Np(IV), it is obvious that Yusov *et al.* [10] misinterpreted colloid formation at increased pH as formation of $NpOH^{3+}$. The proposed pure component spectrum of $NpOH^{3+}$, consisting of double peaks, results from deconvoluting 'holes' into the broad Np(IV) colloid bands in the wavelength ranges 680–760 nm and 920–1000 nm (cf. [4]).

In the potentiometric studies of Rabideau *et al.* [12, 13], the redox potential was measured as a function of the pH at relatively high Pu concentrations ($[Pu] > 10^{-3}$ M). The first hydrolysis constant was determined by relating the measured redox potential (E_h), the redox equilibrium Pu(III)/Pu(IV) and the first hydrolysis reaction of Pu(IV). However, the pH range was very narrow and Pu concentrations were rather high so that colloid formation cannot be excluded. Stepwise hydrolysis equilibria for Pu^{4+} were determined in undersaturated solutions by the solvent extraction technique using ^{238}Pu in trace concentrations ($[Pu]_{tot} = 10^{-7}$ M $\sim 10^{-8}$ M) [11]. The hydrolysis constants exceed the value found potentiometrically in a similar medium by one order of magnitude [12]. This difference could be due to additional loss of Pu^{4+} by processes like disproportionation, polymerization or colloid formation. Actually, $Pu(IV)_{aq}$ redox reactions must not be neglected in solutions at any case. Thus, to stabilize $Pu(IV)_{aq}$ in this study, the distribution experiments were carried out with different redox agents depending on pH regions. However, the data were not corrected for effects on counting rate due to variations in scintillation quenching caused by varying concentrations of TTA in the organic phase. The experimental uncertainties were estimated to be about 0.2 logarithmic units for the first hydrolysis step [17, 18].

2. Hydrolysis, redox reactions and solubility

Three reaction pathways have to be considered when plutonium is studied in aqueous solution: hydrolysis, formation of polymers and colloids, and redox reactions of the various oxidation states.

The terminology used in the present work is reviewed shortly in the following.

The hydrolysis reactions of the Pu^{4+} ions are generally written as

$$x\mathrm{Pu}^{4+} + n\mathrm{H_2O} \leftrightarrows \mathrm{Pu}_x(\mathrm{OH})_n^{4x-n} + n\mathrm{H}^+ \tag{1}$$

or

$$x\mathrm{Pu}^{4+} + n\mathrm{OH}^- \leftrightarrows \mathrm{Pu}_x(\mathrm{OH})_n^{4x-n} \tag{2}$$

and the hydrolysis constants K'_{xn} in a given medium and K°_{xn} (at infinite dilution) are given by

$$K'_{xn} = \frac{[\mathrm{Pu}_x(\mathrm{OH})_n^{4x-n}]\,[\mathrm{H}^+]^n}{[\mathrm{Pu}^{4+}]^x} = \frac{K^{\circ}_{xn}(\gamma_{\mathrm{Pu}^{4+}})^x\,(a_w)^n}{(\gamma_{\mathrm{Pu}_x(\mathrm{OH})_n^{4x-n}})\,(\gamma_{\mathrm{H}})^n} \tag{3}$$

with the corresponding formation constants β'_{xy} and β°_{xy}

$$\beta'_{xn} = \frac{[\mathrm{Pu}_x(\mathrm{OH})_n^{4x-n}]}{[\mathrm{Pu}^{4+}]^x\,[\mathrm{OH}^-]^n} = \frac{\beta^{\circ}_{xn}(\gamma_{\mathrm{Pu}^{4+}})^x\,(\gamma_{\mathrm{OH}^-})^n}{(\gamma_{\mathrm{Pu}_x(\mathrm{OH})_n^{4x-n}})\,(\gamma_{\mathrm{H}})^n} \tag{4}$$

$[i]$ denotes the concentration of species i, γ_i its activity coefficient and a_w the activity of water. The hydrolysis constants $\log K^\circ_{xn}$ are related to $\log \beta^\circ_{xn}$ by the ion product of water ($\log \beta^\circ_w = -14.00 \pm 0.01$).

Neck and Kim [18] pointed out that at least the first formation constant β°_{11} should be known from an experiment where the presence of colloids is excluded in order to reliably calculate β°_{1n} ($n = 2$–4) by an electrostatic approach [19].

Therefore, the value $\log \beta^\circ_{11} = 14.6$, derived from experiments at trace levels of Pu [11] where the formation of polyspecies is less likely, is chosen for the estimation of the remaining hydrolysis constants. These values from the model calculation in [18] are in close agreement with the experimental values of [11].

In the present work, the knowledge of the solubility of $Pu(IV)_{aq}$ is of cardinal relevance, since in oversaturated solutions the formation of polyspecies and colloids takes place, which alters the absorption spectra and is easily misinterpreted for a change in $Pu(IV)_{aq}$ absorption due to hydrolysis. The solubility products K'_{sp} and K°_{sp} (at infinite dilution) of amorphous Pu(IV) oxide or hydroxide, $Pu(OH)_4$(am), refer to the following equilibrium

$$Pu(OH)_4(am) \leftrightarrows Pu^{4+} + 4OH^- \tag{5}$$

with

$$K'_{sp} = [Pu^{4+}]\,[OH^-]^4 \tag{6}$$

and

$$K^\circ_{sp} = K'_{sp}(\gamma_{Pu})\,(\gamma_{OH})^4 \quad \text{(for } Pu(OH)_4\text{(am))} \tag{7}$$

If there are neither complexes with other inorganic ligands nor colloidal species present in solution, the total Pu(IV) equilibrium concentration is given by

$$[Pu(IV)]_{tot} = [Pu^{4+}] + \sum_{n=1}^{4} [Pu(OH)_n{}^{4-n}] = (K'_{sp}[OH^-]^4)\left(1 + \sum_{n=1}^{4} \beta'_{1n}[OH^-]^n\right) \tag{8}$$

The solubility products of the amorphous An(IV) hydroxide decrease by orders of magnitude in the series Th(IV) > U(IV) > Np(IV) > Pu(IV) [18, 20], which correlates with the decreasing distance d_{An-O} in the lattice [21]. The same trend is shown for the solubility product of the crystalline An(IV) dioxide, calculated from thermochemical data [18, 20, 22]. For the calculation of the solubility product using Eq. (8) the concentration of each tetravalent plutonium hydroxo species or, respectively, the total $Pu(IV)_{aq}$ concentration and the hydrolysis constants ($n = 1$–4) must be known. There are a number of reports on the solubility of solids resulting from hydrolysis of plutonium(IV) [17, 23–29] summarized in Fig. 9. The reported solubility constants K°_{sp} scatter considerably with an uncertainty of several orders of magnitude due to various reasons, such as insufficient equilibration time, ignoring redox reactions which lead to formation of highly soluble Pu(V), lacking phase separation and apparent solubility enhancement due to the presence of colloids. The solubility data were reviewed [17, 18] and reinterpreted on the basis of the hydrolysis constants from [11] resulting in $\log K^\circ_{sp} = -58.7 \pm 0.9$ [17], from which the solubility curves in Fig. 9 are calculated. In a recent review [20], based on the solubility constants determined by [17, 30–32] who used three different, independent methods, $\log K^\circ_{sp} = -58.33 \pm 0.52$ is selected as unweighted mean value. All the values recently reported agree with this selected value within the uncertainty range which, however, remains relatively large.

The redox chemistry of Pu(IV) plays an important role [33], since many chemical properties of Pu, *e.g.* hydrolysis and solubility, depend strongly on the oxidation state and overall charge of the respective stable species at given conditions. Up to four oxidation states might be present simultaneously in solution at low pH [34].

Even in solutions which are carefully prepared to contain only one well defined oxidation state, equilibrium of two or more oxidation states may form over time. This phenomenon is explained in the literature by disproportionation of Pu(IV) [35],

$$2Pu^{4+} + 2H_2O \leftrightarrows Pu^{3+} + PuO_2{}^+ + 4H^+ \tag{9}$$

and further disproportionation of Pu(V) or the reaction of Pu(V) with Pu(IV) yielding Pu(III) and Pu(VI) which results in the total reaction

$$3Pu^{4+} + 2H_2O \leftrightarrows 2Pu^{3+} + PuO_2{}^{2+} + 4H^+ . \tag{10}$$

Alternatively, the above reactions can be represented by the summation or subtraction of two half reactions, the redox-equilibria between Pu^{3+} and Pu^{4+} and between $PuO_2{}^+$ and $PuO_2{}^{2+}$, which are fast because the electron transfer between two species of the same structure is rapid and reversible.

$$Pu^{4+} + e^- \leftrightarrows Pu^{3+} \quad \log K^\circ = 17.69 \pm 0.04\ [5] \tag{11}$$

and

$$PuO_2{}^{2+} + e^- \leftrightarrows PuO_2{}^+ \quad \log K^\circ = 15.82 \pm 0.09\ [5] \tag{12}$$

In addition there is the conversion of the lower oxidation states (Pu(III) or Pu(IV)) to the higher ones (Pu(V) or Pu(VI)) and *vice versa*. These reactions are slow since they require the formation or rupture of Pu−O bonds and the reorganization of the solvation shell [35]. The following reaction, for example, is the oxidation of Pu(IV) to Pu(V),

$$Pu^{4+} + 2H_2O \leftrightarrows PuO_2{}^+ + 4H^+ + e^- \quad \log K^\circ = -17.45 \pm 0.17\ [5] . \tag{13}$$

This reaction also reflects the fourth power dependence on hydrogen ion concentration and explains the increasing stability of the Pu(V) state with decreasing H^+ concentration [36]. Finally, if Pu(IV) oxyhydroxide colloids or precipitate are present, then solid Pu(IV) particles are in equilibrium with $Pu(V)_{(aq).}$ according to the oxidation reactions

$$Pu(OH)_4(am) \leftrightarrows PuO_2{}^+ + 2H_2O + e^- \tag{14}$$

or

$$PuO_2 \cdot xH_2O(am) \leftrightarrows PuO_2^+ + xH_2O + e^-$$
$$\log K^\circ = -19.78 \pm 0.89\ [20]\,. \qquad (15)$$

3. Experimental techniques

The detection of colloids is performed using laser-induced breakdown detection (LIBD) [37, 38]. This method has been successfully applied for solubility measurements of actinide hydroxides [4, 9, 29, 40–42]. The apparatus used in the present study is described in detail in [43]. Colloids larger than 5 nm are detected in ppt concentrations in situ and LIBD allows the appraisal of size distributions between 20 and 100 nm [44]. In the present work LIBD was only used as a supplementary method to detect the presence (or absence) of colloids in a relative manner as described in [45].

The oxidation state distribution of Pu in solution is quantified by absorption spectroscopy [35, 46–48]. Here, a combination of a commercial UV-Vis spectrometer (Varian Cary5) and a liquid core waveguide capillary spectrometer is presented and a spectra deconvolution routine is used which is described in the following.

The electronic intraband (f-f) transitions of plutonium are quite narrow, usually a few nanometers wide, and the wavelengths (λ) of the absorption peaks are uniquely characteristic of the respective oxidation states. The absorption spectra of Pu(III), $Pu(IV)_{aq}$, Pu(V), Pu(VI) and Pu(IV)-polymer species (colloids) are depicted in Fig. 1. Usually, the concentrations of the solution species are obtained from specific absorption bands for each oxidation state (listed in Table 2 [35]) by use of Beer's law,

$$A = \varepsilon\, c\, d \qquad (16)$$

where A is the absorption, ε the absorptivity (often referred to as molar extinction coefficient[2] or molar absorption coefficient) [$M^{-1}\,cm^{-1}$], c the concentration [M] and d the beam pathlength [cm]. For quantifying a certain oxidation state with a specific band, the other states must have an absorptivity as small as possible at the same wavelength, a condition which is well met for Pu(III), $Pu(IV)_{aq}$ and Pu(VI), but not for Pu(V) which suffers from interference with Pu(III) and $Pu(IV)_{aq}$ at 569 nm. If several oxidation states are present simultaneously, simple evaluation of the specific absorption bands only at the peak maxima is difficult and leads to large experimental errors. The preferred method is spectral deconvolution of a wide spectral range.

By use of a sample of $[Pu] = 4.03 \times 10^{-4}$ M at pH_c 0.9 in $I = 0.5$ M HCl/NaCl where all four oxidation states are present, the procedure is exemplified. The measured spectrum $f(\lambda)$ ($450\ \text{nm} < \lambda < 850\ \text{nm}$) is described as the

[2] In the present work the term extinction is used for the total loss of (monochromatic) light after passing a sample. The loss might be due to either absorption or scattering, which cannot be distinguished by UV-Vis spectroscopy. On the other hand, concentrations are obtained from the absorption of the sample only. This problem is most severe for samples containing colloids at short wavelengths ($\lambda < 500$ nm) due to the strong wavelength dependence of Rayleigh scattering.

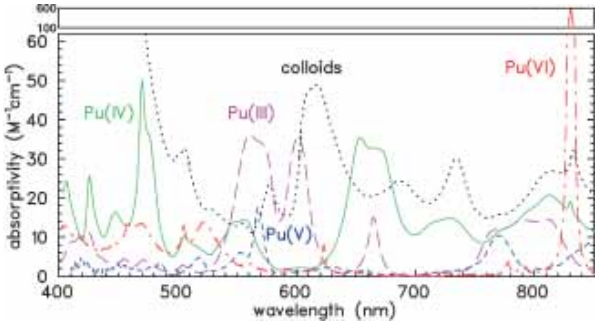

Fig. 1. Absorption spectra of four reference solutions are given in the molar absorptivity scale. The solutions were prepared at different concentrations and in different media: Pu(III) at 3.8×10^{-3} M in 1 M $HClO_4$, $Pu(IV)_{aq}$ at 4.3×10^{-3} M in 0.75 M $H(ClO_4/Cl)$, Pu(V) at 3×10^{-4} M in 0.001 M $HClO_4$ and Pu(VI) at 5.3×10^{-4} M in 0.1 M $HClO_4$, respectively. The colloid spectrum is taken from [14] and not to scale (see Sect. 5).

Table 2. The molar absorption coefficients (ε [$M^{-1}\,cm^{-1}$]) for different oxidation states of plutonium (summarized in [35]).

Wavelength (nm)	Molar absorption coefficients ε [$M^{-1}\,cm^{-1}$]			
	ε Pu(III)	ε $Pu(IV)_{aq.}$	ε Pu(V)	ε Pu(VI)
600	35.3	0.91	0.5	1.35
470	3.46	49.6	1.82	11.25
653	3.1	34.4	1.15	0.9
		37.8[a]		
		36.7[b]		
569	34.3	5.6	17.1	1.75
831	5.25	15.5	4	550

a: 0.5 M $(H/Na)ClO_4$, 25 °C, 7.2×10^{-4} M Pu(IV) from [6];
b: 2 M $HClO_4$, 1.2×10^{-4} M Pu(IV) from [10] Fig. 4.

weighted sum of four reference spectra $f^{(i)}(\lambda)$ representing the four pure oxidation states

$$f(\lambda) = c^{\mathrm{III}} f^{\mathrm{III}}(\lambda) + c^{\mathrm{IV}} f^{\mathrm{IV}}(\lambda) + c^{\mathrm{V}} f^{\mathrm{V}}(\lambda) + c^{\mathrm{VI}} f^{\mathrm{VI}}(\lambda) \qquad (17)$$

present at concentrations $c^{(i)}$. The deconvolution is carried out by a least squares fit (Gauss Newton) varying the four $c^{(i)}$-parameters. This method requires reliable and normalized reference spectra $f^{(i)}(\lambda)$ (Fig. 1) which are measured from carefully prepared pure solutions. The reference solutions are prepared in $HClO_4$ because perchlorate does not form complexes with aqueous Pu species [35].

The reference solution of $Pu(IV)_{aq}$ ($[Pu]_{tot}^{LSC} = 4.3 \times 10^{-3}$ M in 0.75 M $H(ClO_4/Cl)$) contains only small amounts of Pu(III) and Pu(VI) (1.30×10^{-4} M of $Pu(III)_{aq}$ and 2.18×10^{-5} M of Pu(VI), respectively). No spectral absorption band of Pu(V) was observed. The PuO_2^+ contamination was estimated to be about $[PuO^{2+}] = 9 \times 10^{-8}$ M (2×10^{-5} of $[Pu]_{tot}^{LSC}$) from the redox equilibria: The redox potential, or *pe*, of the solution is obtained from the measured concentrations of tri- and tetravalent plutonium (Eq. (11))

$$pe = \log \frac{[Pu^{4+}]}{[Pu^{3+}]} - \log K'_{\mathrm{III/IV}} \qquad (18)$$

The known equilibrium constant $K^\circ_{\mathrm{III/IV}} = -17.69$ [5] was corrected to ionic strength $I = 0.5$ M ($\log K'_{\mathrm{III/IV}} = -16.55$)

using the specific ion interaction theory, and the amount of Pu^{4+} was calculated from the $Pu(IV)_{aq}$ concentration, taking into account the first hydrolysis reaction ($\log \beta^{\circ}_{11} = 14.6$, [5]). Since both, the $Pu(III)/Pu(IV)_{aq}$ and the $Pu(V)/Pu(VI)$ redox couples equilibrate very fast, Eq. (12) allows to estimate the amount of Pu(V):

$$\log [PuO_2^{+}] = \log [PuO_2^{2+}] - \log K'_{V/VI} - pe \qquad (19)$$

with the equilibrium constant $\log K'_{V/VI} = -15.36$ calculated from $\log K^{\circ}_{V/VI} = -15.82$ [5]. In addition it is confirmed by LIBD that no colloids (> 5 nm) are present. This is particularly important, since colloids cause a strong increase in extinction for $\lambda < 500$ nm due to Rayleigh scattering (see footnote on p. 2), which can increase the apparent absorption at 470 nm and hinder a reliable evaluation of the 470 nm band of $Pu(IV)_{aq}$.When the concentration of $Pu(IV)_{aq}$ is calculated with ε (653 nm) = 36.7 M^{-1} cm^{-1} [10], then its concentration is obtained to be 4.14×10^{-3} M. The sum of all oxidation states of Pu agrees with the total Pu concentration 4.3×10^{-3} M measured by LSC. This shows that no considerable amounts of Pu(IV)-polymeric species smaller than 5 nm are present in the $Pu(IV)_{aq}$ reference solution. The reference spectra for Pu(III), $Pu(V)_{aq}$ and Pu(VI) aquo ions were obtained from solutions of Pu(III) at 3.8×10^{-3} M in 1 M $HClO_4$, Pu(V) at 3×10^{-4} M in 0.001 M $HClO_4$ and Pu(VI) at 5.3×10^{-4} M in 0.1 M $HClO_4$.

Fig. 2 (top) shows the total spectrum ('Sample') and the contribution of each of the oxidation states ('III', 'IV', 'V', 'VI'). The sum of all four, denominated as 'Fit', reproduces the measured spectrum well. Even the region below $\lambda = 500$ nm, which is sensitive to colloidal impurities shows no significant deviations. In a second step, the contribution of $Pu(IV)_{aq}$ is calculated by subtraction of the Pu(III), Pu(V) and Pu(VI) fractions from the total spectrum (Fig. 2 (bottom) 'Sample – III,V,VI'), normalized to the molar $Pu(IV)_{aq}$ concentration, and compared to the reference spectrum 'Reference IV' from Fig. 1. The 'Residue', defined as the difference between 'Sample' and 'Reference', shows some structure around $\lambda = 620$ nm (see Sect. 5) and a more distinct feature at $\lambda \sim 837$ nm, which is discussed in the following.

Complex formation of Pu aquo ions can cause significant shifts of the absorption bands, an effect which may lead to an underestimation of the Pu concentration if not taken into account properly. The relevance for $Pu(VI)_{aq}$ is demonstrated in the following. All reference spectra are recorded in $HClO_4$ which does not form complexes with aqueous Pu species, but all present experiments are carried out in 0.5 M (Na/H)Cl media. In the case of $Pu(VI)_{aq}$, spectroscopic studies indicate the formation of at least three chloride complexes with increasing hydrochloric acid concentration [35]. In 0.5 M (Na/H)Cl media, only the first chloride complex is observed and its spectrum is shown in Fig. 3. The maxima of the bands are 830.6 nm (FWHM: 2.5 nm) for PuO_2^{2+} and 837.6 nm (FWHM: 5.6 nm) for PuO_2Cl^{+}. No absorption from PuO_2Cl_2 at 843 nm is observed in the present work which is in good agreement with Runde *et al.* [49] (Table 3) who reported the formation of the dichloro species only at higher chloride concentration. The monochloro complex contributes 15% of the total $Pu(VI)_{aq}$ concentration in 0.5 M (Na/H)Cl. Since the Cl^{-} concentration is kept

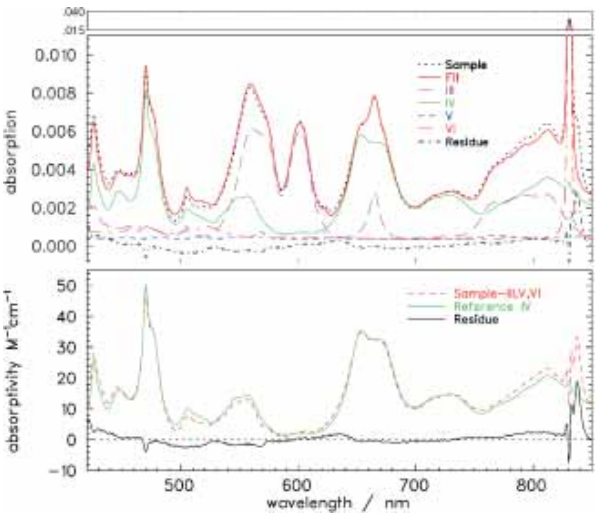

Fig. 2. Top: Oxidation state distribution of an aged sample at pH_c 0.9, $[Pu]_{tot} = 4.03 \times 10^{-4}$ M according to LSC (100%). The spectral deconvolution yields 1.60×10^{-4} M Pu(III) (39.6%), 1.55×10^{-4} M $Pu(IV)_{aq}$ (38.4%), 2.05×10^{-4} M Pu(V) (5.0%) and 5.73×10^{-4} M Pu(VI) (14.4%). The sum of the four oxidation states equals 3.97×10^{-4} M which is in good agreement with the LSC measurement. Bottom: The $Pu(IV)_{aq}$ fraction of the spectral absorption (*i.e.* after the contributions of Pu(III), Pu(V) and Pu(VI) are subtracted) is normalized to molar concentration and compared to the reference spectrum of $Pu(IV)_{aq}$. The residue shows some minor structure and a small peak due to PuO_2Cl^{+} at 837 nm (see text).

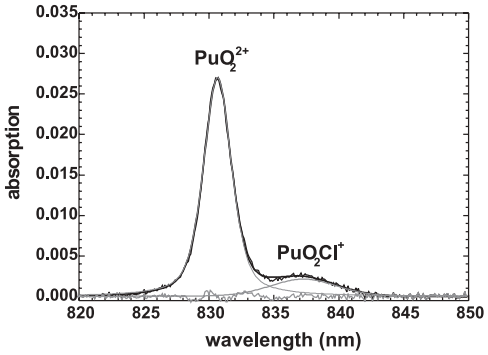

Fig. 3. In order to obtain the correct concentration of Pu(VI) from the absorption spectrum, the fraction of chloride complexes has to be known, as complexation shifts the absorption band from 830.6 nm to the red. The spectrum of $Pu(VI)_{aq}$ in 0.5 M (H/Na)Cl contains $[PuO_2^{2+}] = 4.86 \times 10^{-5}$ M (85%) and $[PuO_2Cl^{+}] = 0.734 \times 10^{-5}$ M (15%) calculated with the molar absorption coefficients in Table 3.

Table 3. The spectroscopic parameters of the predominant $Pu(VI)_{aq}$ species in NaCl [49].

Species	Peak maximum	Full width at half maximum height	(Molar) absorptivity, ε (M^{-1} cm^{-1})
PuO_2^{2+}	830.6 ± 0.1 nm	2.5 ± 0.2 nm	555 ± 12
PuO_2Cl^{+}	837.6 ± 0.2 nm	5.6 ± 0.3 nm	290 ± 23
PuO_2Cl_2	843.0 ± 0.4 nm	7.6 ± 0.4 nm	140 ± 80

constant in the present experiments, the peak at 837 nm is not included in the deconvolution but rather the fit stops at 833 nm and the $Pu(VI)_{aq}$ concentration is corrected by a factor of $1.18(= 1/0.85)$. No effect of chloride complex formation is observed for Pu(III), $Pu(IV)_{aq}$, and PuO_2^+.

Due to the low molar absorption coefficients ($< 50\ M^{-1}\ cm^{-1}$ for Pu(III), $Pu(IV)_{aq}$, and Pu(V)) absorption spectroscopy with 1 cm absorption path length proves to be inadequate for studies at dilute concentrations. However, the sensitivity can be improved by extending the optical path length. Making use of total reflection, the sample is probed in a liquid core waveguide (LCW) which constrains the light propagation within a liquid medium which has a higher refractive index (RI) than the surrounding solid tubing [50]. The coating material outside of the fused silica capillary is Teflon AF whose RI is about 1.29. This capillary (length 100 cm, diameter 550 μm, volume 240 μl) enhances the sensitivity by two orders of magnitude as compared to a 1 cm cell. A similar instrument was recently applied for plutonium speciation [51]. In the present work, a LCW (WPI, World Precision Instruments) coupled with a diode array spectrometer (Zeiss) is used for analysis of Pu aqueous species at relatively low concentration ($[Pu]_{tot} = 10^{-5}$ M).

The absorption spectrum of a plutonium solution containing different oxidation states ($[Pu]_{tot}^{LSC} = 1.9 \times 10^{-4}$ M in 0.5 M $HClO_4$, $[Pu(III)] = 3.11 \times 10^{-5}$ M, $[Pu(IV)_{aq}] = 1.53 \times 10^{-4}$ M and $[Pu(VI)] = 0.69 \times 10^{-5}$ M, no Pu(V)) is measured twice: a) with a 1 cm quartz cell (Fig. 4, bottom) and b) with the 100 cm LCW (Fig. 4, top) coupled to the diode array spectrometer. The two spectra are almost identical and the setup using the capillary shows 100 times higher sensitivity.

However, a problem independent from the LCW arises due to the poor resolution of the diode array spectrometer. While the broad spectral features used for the quantification of Pu(III), $Pu(IV)_{aq}$ and Pu(V) are uncritical, the reproduction of the narrow peak of Pu(VI) at 831 nm depends strongly on the resolving power of the spectrometer. Recently, Wilson *et al.* [51] reported molar absorption coefficients and detection limits for each plutonium aquo species using a 100 cm LCW. In this study, a molar absorption coefficient of $\varepsilon = 288\ M^{-1}\ cm^{-1}$ for Pu(VI) at 831 nm was obtained. The authors were aware of the peak broadening effect due to the limited spectral bandwidth of the spectrometer and used this absorption coefficient as an "operative" value. In our system, the "operative" molar absorption coefficient is about $\varepsilon = 302\ M^{-1}\ cm^{-1}$ which differs strongly from reference spectra using high resolution spectrometers (*e.g.* the CARY). A low resolution instrument convolutes its spectrometer function with the line profile which results in broadened spectra of lower peak absorption. However, the peak area (oscillator strength) is independent of resolution: $A = \int \varepsilon \mathrm{d}nm$. In order to avoid "operative" molar absorption coefficients, the spectra are deconvoluted [52]. A measured line profile $h(\lambda)$ can be described as a convolution of the initial line profile $f(x)$ (which is $f^{VI}(\lambda)$ in the present case) and the spectrometer function $g(x)$, which is obtained experimentally by measuring a sharp emission line (*e.g.* of a Hg or Ne discharge lamp). In the present case this is a Gaussian curve of FWHM = 4.2 nm. By deconvolution, the initial profile is obtained from the measured spectrum by solving the equation

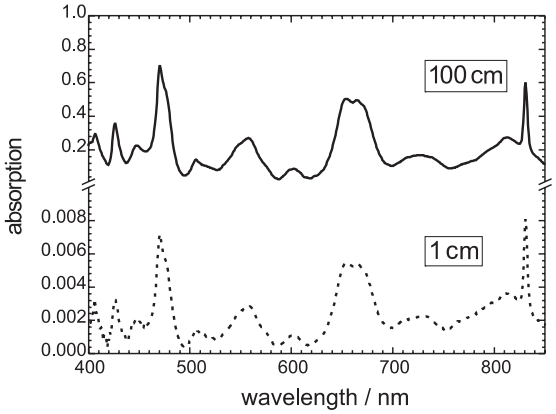

Fig. 4. The absorption spectrum of plutonium solution $[Pu]_{tot} = 1.9 \times 10^{-4}$ M in 0.5 M $HClO_4$. The dashed line shows the spectrum obtained with 1 cm quartz cell and the solid line shows the one measured with the LCW using diode array spectrometer.

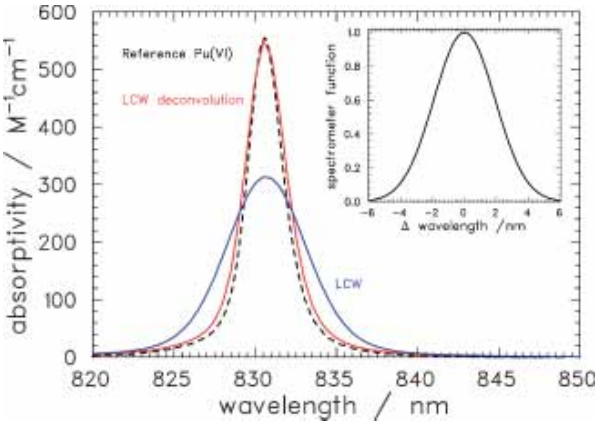

Fig. 5. Deconvolution of absorption spectra recorded by a diode array spectrometer coupled to a liquid core waveguide

$$h(\lambda) = \int_{-\infty}^{\infty} f(x)\, g(\lambda - x)\, \mathrm{d}x \qquad (20)$$

e.g. by use of the FFT [53] or B-spline method [52].

Fig. 5 shows how the broad measured line due to Pu(VI) of the diode array spectrometer ('LCW') by use of the spectrometer function (inlay) is deconvoluted ('LCW deconvolution') and reproduces the initial line profile obtained by the high resolution spectrum ('Reference Pu(VI)') obtained by the Cary UV-Vis spectrometer (resolution 0.1 nm).

4. Sample preparation

$^{242}PuO_2$ (brown powder) is diluted in 14 M HNO_3/0.1 M HF and then heated for several hours until all powder is dissolved. In order to remove hydrofluoric acid, the solution is evaporated several times in 8 M HNO_3 and subsequently dissolved in 8 M HNO_3. The metal contaminations (*e.g.*, americium and iron) are removed from the plutonium solution

(Pu(IV)) using an anion exchange column with Dowex 1 × 4 (50–100 mesh) in 8 M HNO_3. Subsequently, Pu(IV) is reduced to Pu(III) and eluted with 0.35 M HNO_3/0.02 M HN_2OH-HCl solution. To remove organic contaminations, the Pu(III) solution is evaporated in concentrated $HClO_4$ solution until the volume is reduced to one third of the original volume and subsequently diluted in 5 ml of 1 M $HClO_4$. The solution is characterized using α- and γ-spectroscopy as well as ICP-MS. The stock solution contains ^{242}Pu (99.39 atom %), $^{239/240}$Pu (0.6 atom %) and ^{238}Pu (5.3×10^{-3} atom %). Pu(IV) stock solutions are prepared by electrolysis at constant potential as described by Cohen [54].

The mixture of different Pu oxidation states in 1 M $HClO_4$ or 0.5 M HCl is reduced to Pu(III) ($E_{cathode} = ca. -0.2$ V) and subsequently oxidized to Pu(IV) ($E_{anode} = ca.$ 0.8). For the mixing of solution in the working cell during the electrolysis the Pu solution is bubbled with argon gas. After electrolysis the Pu(IV) stock solution is filtered through a cellulose membrane microfilter (Amicon, 10 kD, average pore size about 1.5 nm). Even if no true Pu(IV) colloids are present, pseudocolloids may act as crystallization germs and cause premature precipitation. Hence it is important to remove colloids of any composition from the stock solutions. The successful removal of colloids is confirmed by LIBD, and the oxidation state distribution is measured by UV-Vis absorption spectrometry.

Samples are prepared batchwise by slow dilution with colloid-free 0.5 M (H/Na)Cl. Pu(IV) colloids can be formed inadvertently under conditions of transient instability, and once formed, they might be stable for days or weeks. Dilution of an acidic plutonium solution with neutral solution (*e.g.* water) may cause polymerization in locally oversaturated areas of low acidity, even when the final acidity of the solution is too high for polymerization to occur [16]. For this reason, the 0.5 M (H/Na)Cl diluent solution is added very slowly, 10 µl per minute, under stirring to avoid local oversaturation. All samples are prepared in quartz cells. The total Pu concentrations are determined by LSC. Stock solutions in the range from 1×10^{-3} to 4×10^{-3} M in 1 M $HClO_4$ or 0.5 M HCl are diluted to concentrations between 1×10^{-5} and 10^{-3} M at acidities between pH_c 0.3 and 2.1. To determine the concentration of each oxidation state, the concentrated solutions are measured by Cary 5E with a 1 cm quartz cell and the lower concentrated solutions are measured using LCW coupled with a diode-array spectrometer as described in the summary.

The H^+ concentration ($pH_c = -\log[H^+]$) is determined with combination glass electrodes (type Ross, Orion) as described in [22, 39–41]

5. Results and discussion

Five different Pu(IV) solutions, with total plutonium concentrations of 3×10^{-4} M are prepared, measured and evaluated as described in the summary. The measurement is performed several times during a period of > 70 days in order to observe the time evolution of the oxidation state distribution due to redox reactions (often denominated by the term 'disproportionation') of $Pu(IV)_{aq}$, which follow the equations [15]

$$[Pu(IV)_{aq}] + [Pu(III)] = \text{const.}, \quad (21)$$

$$[Pu_{polymer}] + [Pu(V)] + [Pu(VI)] = \text{const.} \quad (22)$$

Fig. 6 shows the $Pu(IV)_{aq}$ fraction from the deconvoluted absorption spectra (analogous to Fig. 2 (bottom)) at different pH_c (from 0.5 to 1.2) for solutions after 1 day (a) and after equilibration > 70 days (c). The ε_0 values at the peak maxima (470 nm and 653 nm) are listed in Table 4. The spectrum of the sample at pH_c 1.21 shows noise because of the low concentration of $Pu(IV)_{aq}$ left after equilibration; the major fraction of Pu is reduced to Pu(III). The spectra indicate neither peak shifts nor a systematic decrease of the absorption coefficients in contrast to earlier work [10] (see Sect. 5).

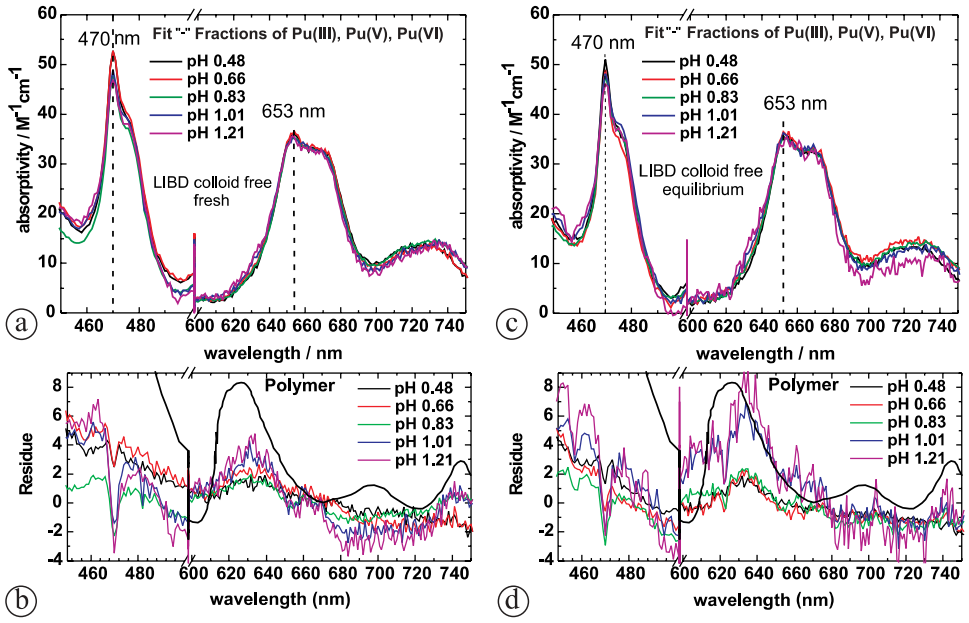

Fig. 6. The molar absorption spectra of Pu(IV) (**a**,**c**) and residual spectra (**b**,**d**) after subtraction of the Pu(IV) reference spectrum as a function of pH in the range from $0.5 < pH_c < 1.2$ at a concentration [Pu] = 3×10^{-4} M, after 1 day (**a**,**b**) and after 70 days (**c**,**d**). The solutions have no colloidal fraction > 5 nm detectable by LIBD. However, for $pH_c > 1$ a small fraction of polymer species is present in the aged solutions (**c**,**d**) (reference polymer spectrum from [14]). The concentrations of all oxidation states of Pu in the aged solutions are listed in Table 4.

Table 4. The distribution of Pu oxidation states (%) in equilibrium at different pH according to the analysis of the absorption spectrum. The total Pu concentration is 3×10^{-4} M. The absorption coefficients of the deconvoluted spectra of the Pu(IV) fraction are given at two specific absorption positions.

pH_c	Pu(III) (%)	$Pu(IV)_{aq}$ (%)	Pu(V) (%)	Pu(VI) (%)	Sum (%)	ε_0 at 470 nm (M^{-1} cm^{-1})	ε_0 at 653 nm (M^{-1} cm^{-1})
0.48	38.88	54.07	0	7.07	100.03	51.1	35.2
0.66	46.45	39.87	0	10.92	97.24	48.9	36.1
0.83	50.03	28.5	348	15.57	97.57	47.8	35.1
1.01	58.54	17.42	698	16.83	99.77	48.1	35.9
1.21	60.83	11.32	1372	15.06	100.93	47.2	36.9[a]

a: The value is taken after the smoothing of the spectrum at pH_c 1.21 by averaging adjacent 5 points.

The distributions of oxidation states at each pH, which are obtained through fitting, are listed in Table 4. LIBD measurements indicate that none of the samples contains colloids larger than 5 nm. The normalized spectra at different pH resemble each other closely. For a closer inspection the reference spectrum of $Pu(IV)_{aq}$ (Fig. 1) is subtracted from each of the normalized spectra and the differences are plotted in Fig. 6b (1 day) and d (30 days). With increasing pH, the spectra indicate a band around 620 nm and a weaker feature around 740 nm. For the fresh samples the absorption remains below 4 normalized units for all pH values. In contrast to this, the aged samples at $pH_c > 1$ exhibit a significantly increasing absorption. The sums of all Pu aqueous species obtained by fitting are close to 100% (100% corresponds to $[Pu]_{tot}$ measured by LSC).

5.1 Mononuclear hydrolysis

As already discussed in Sect. 1 and Sect. 2, the Pu^{4+} ion has a strong tendency to form hydroxide complexes even at low pH. The distributions of Pu(IV) hydrolysis products as a function of pH are shown in Fig. 7, calculated using the hydrolysis constants of Metivier *et al.* [11], which were selected in [17, 18, 20] for the reasons given earlier. According to these hydrolysis constants, at pH_c 0 about 30%, and at pH_c 1 over 90% of Pu is already hydrolyzed (Fig. 7). If the absorption of $Pu(OH)^{3+}$ would differ from the absorption of the hydrated Pu^{4+} ion, it should be clearly noticeable from a comparison of the spectra at pH_c 0.3 and pH_c 1.2. However, the normalized spectra in Fig. 6 show no shift and the absorptivities calculated as described in the summary do not change. If the absorption coefficient decreased with increasing hydrolysis of the Pu^{4+} ion, the calculated sum of Pu(III), $Pu(IV)_{aq}$, Pu(V) and Pu(VI) should fall short of the total concentration detected by LSC. This is not the case.

Earlier attempts to determine the hydrolysis constant β_{11} by spectroscopic methods were based on the assumption that the molar absorption coefficients for the Pu hydrolysis species were different from that of the Pu^{4+} ion, thus the decrease of the characteristic $Pu(IV)_{aq}$ absorption bands was ascribed to the initial mononuclear hydrolysis. However, this is not correct. If no colloids and polymeric species are present in solution, then the absorption of $Pu(IV)_{aq}$ does not depend on pH even if the Pu^{4+} aquo ion is a minor species. The Pu(IV) hydrolysis species dominant in the pH range investigated in the present work, $Pu(OH)_n^{4-n}$ ($n = 0$–2), have equal molar absorption coefficients.

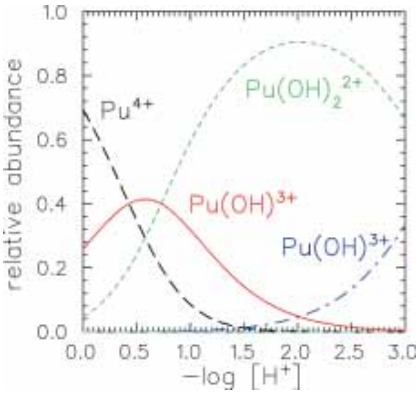

Fig. 7. Mononuclear hydrolysis-species distribution calculated with the hydrolysis constants from [11] summarized in Table 1.

5.2 Polynuclear and colloidal Pu(IV) species

A closer discussion is needed to understand the small differences between the reference spectrum and the normalized absorption of the $Pu(IV)_{aq}$ fraction (residues) in Fig. 6. The absorption peak at 620 nm and the weak band at 740 nm are known very well from literature and are ascribed to the absorption of Pu(IV) polymer or colloids [14, 16]. The characteristics of the spectrum is independent of pH as demonstrated in Fig. 8, where the absorption spectra of colloidal Pu(IV) solutions at $[Pu] = 1.1 \times 10^{-2}$ M in 1 M $HClO_4$ and at $[Pu] = 5.6 \times 10^{-4}$ M in 0.5 M HCl/NaCl at pH_c 2.0 are

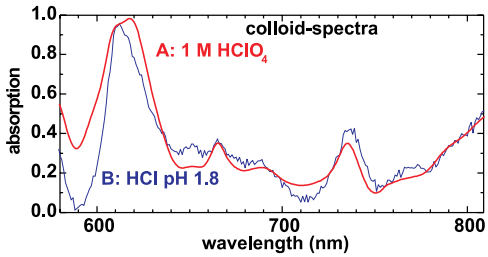

Fig. 8. The absorption spectra of colloidal Pu(IV) solutions (A) $[Pu]_{tot} = 1.1 \times 10^{-2}$ M in 1 M $HClO_4$ (after 5 days) and (B) $[Pu] = 3.6 \times 10^{-4}$ M in HCl at pH_c 2.0 (after 6 months) are very similar, which shows that the absorption feature at 620–630 nm cannot be ascribed to $Pu(OH)^{3+}$, since in 1 M $HClO_4$ $Pu(OH)^{3+}$ is a minor species.

compared. Both are very similar and show the absorption feature at 620–630 nm which is further proof that this peak cannot be ascribed to $Pu(OH)^{3+}$. In 1 M $HClO_4$ $Pu(OH)^{3+}$ is only a minor species and should cause only a small change with regard to a Pu^{4+} absorption spectrum. However, the Pu^{4+} absorption bands are completely absent in the spectra of Fig. 8.

Although the spectral characteristics of Pu(IV)-colloids/polymer absorption are reported by many groups and are well reproducible, no reliable molar absorption coefficients exist. The values reported in literature scatter considerably, which might be due to the intrinsic difficulty of measuring colloid size distributions. It is most unlikely, that only one well defined size of polymeric species is present in solution, but rather one expects a broad size distribution and particles of different size having different absorptivity to volume ratio. Hence, if equal amounts of Pu (measured by LSC) are present in different colloidal size, the absorptivity might be very different. Consequently, the colloid reference spectrum plotted in Fig. 1 which was taken from [14] cannot be normalized, and the absolute absorptivity might be in error by a factor of 3. A further consequence is, that from the residues of Fig. 6d only limited information can be drawn on the amount of colloidal Pu(IV). For pH_c 1.2, the residue amounts to 8 units which is 20% of the Pu(IV) absorption. The amount of $Pu(IV)_{aq}$ present in the sample at pH_c 1.2 is 11% of the total Pu concentration and hence the colloid content is of the order of only 2%. A different approach of determining the colloid content is possible from the spectroscopic measurement of all ionic Pu species. If the sum of all ionic species $(Pu(III) + Pu(IV)_{aq} + Pu(V) + Pu(VI))$ is subtracted from the total amount of Pu determined by LSC, the rest should account for the colloidal/polymer species Pu_{coll}. As it is obvious from Table 4, the ionic species sum up to 100% to good approximation, and an upper limit of $< 3\%$ Pu(IV) for the colloid fraction is estimated from the uncertainties of the respective measurements.

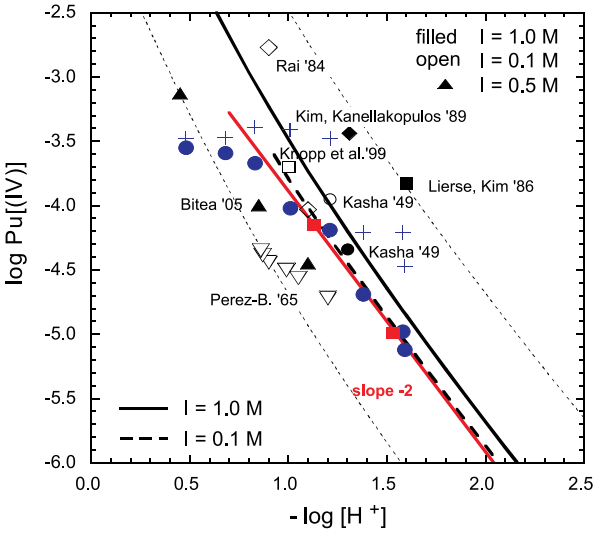

Fig. 9. Solubility data of $Pu(OH)_4$(am) at $0 < pH_c < 2.5$. The solubility curves are calculated for 0.1 and 1 M $NaClO_4$ with $\log K^\circ_{sp} = -58.7 \pm 0.9$ [17] and included are solubility data of an earlier LIBD study (▲) [29] and the present work: LIBD (■) and spectroscopy (●). The crosses (+) mark the total Pu concentration of the spectroscopic data $[Pu]_{tot}$.

For the aged samples at $pH_c > 1$, a clear increase of the absorption band at 620 nm is observed. This effect coincides with the solubility limit at $[Pu(IV)_{aq}] = 3 \times 10^{-4}$ M (cf. Fig. 9). The Pu(IV) concentrations in the aged samples of two series at $[Pu]_{tot} = 3 \times 10^{-4}$ M and $[Pu(IV)]_{tot} = 1 \times 10^{-5}$ M are plotted in Fig. 9 (solid circles). When the pH is increased, the $Pu(IV)_{aq}$ concentration decreases until an equilibrium state is reached which coincides with the solubility. However, as mentioned in Sect. 1 there are two reactions, which decrease the amount of $Pu(IV)_{aq}$ in solution; redox reactions (for example, reduction of Pu(IV) to Pu(III)) and colloid/polymer formation.

When the solubility is exceeded in the course of pH titration by dilution with NaCl solution, the samples of two series (at $[Pu]_{tot} = 3 \times 10^{-4}$ M and at $[Pu]_{tot} = 1 \times 10^{-5}$ M) form colloids directly observable by LIBD, as was reported in earlier work [29, 45]. but in three more experiments, the one shown in Fig. 6 ($[Pu]_{tot} = 3 \times 10^{-4}$ M) and two experiments at $[Pu]_{tot} = 3 \times 10^{-4}$ M and $[Pu]_{tot} = 3 \times 10^{-5}$ M only small amounts of polymeric species were formed but no colloids detectable by LIBD (> 5 nm). The different behavior probably originates from the competition between redox reactions and colloid formation of Pu(IV) or the reductive dissolution reaction

$Pu(OH)_4(coll) + 4H^+ + e^- \Longleftrightarrow Pu^{3+} + 4H_2O$. In the final steady state, Pu(III) is in equilibrium with $Pu(IV)_{aq}$ The final ratio $[Pu(IV)_{aq}]/[Pu(III)]$ and hence the pe value is lower in the present study. The reason for the more reducing conditions is not clear. In both cases, the small fraction of oxidized plutonium consists of PuO_2^+ in equilibrium with PuO_2^{2+}. Details of the oxidation state distributions and the underlying mechanism are reported in [15].

A similar spectroscopic study of the hydrolysis, colloid formation and solubility of Np(IV) combining LPAS with LIBD was carried out by Neck *et al.* [4]. They observed the steep drop of $[Np(IV)_{aq}]$ as a function of pH along the solubility curve due to Np(IV) colloid formation confirmed by LIBD. In the present investigations, the concentrations of $Pu(IV)_{aq}$ (filled circles,Fig. 9) directly after dilution (fresh sample, not yet equilibrium) decrease as a function of pH until they reach the solubility curve obtained by LIBD (solid squares and solid line, Fig. 9).

The slope of the solubility curve provides further evidence that the dihydroxo-complex ($Pu(OH)_2^{2+}$) is the prominent species in the range $1.0 < pH_c < 1.6$. Recent EXAFS investigations [55] support the assumption that under the present conditions oxy-hydrate colloids are formed and $Pu(OH)_4$ is the solubility limiting phase. The slope $= -2$ for the solubility curve in Fig. 9, infers that colloid formation proceeds from $Pu(OH)_2^{2+}$ *via* consumption of 2 OH^- per Pu(IV) ion suggesting the reaction

$$Pu(OH)_2^{2+} + 2OH^- \leftrightarrows Pu(OH)_4(am/coll) \qquad (23)$$

By use of Eqs. (6)–(8) in conjunction with the hydrolysis constants from [11] and SIT coefficients from [18], the solubility product for the reaction

$$Pu^{4+} + 4OH^- \leftrightarrows Pu(OH)_4(am/coll) \qquad (24)$$

is calculated in the range proposed by Knopp *et al.* [17] ($\log K^{\circ}_{sp} = -58.3$ at zero ionic strength).

6. Conclusions

Solutions of tetravalent Pu at concentrations between 10^{-5} M and 10^{-2} M (total Pu) in HCl/NaCl ($0.3 < pH_c < 2.1$) are investigated by combining spectroscopy (UV-Vis, liquid core waveguide capillary) and laser-induced breakdown detection. Spectral deconvolution allows to compare the molar absorptivity of Pu^{4+} with the hydrolysis products $Pu(OH)_n^{4-n}$ ($n = 1, 2$). While the absorption spectra of $Pu(IV)_{aq}$ remain unaffected by mononuclear hydrolysis, characteristic contributions of polymeric or colloidal Pu are observed by calculation of spectral residues. For equilibrated samples, the appearance of these polymer-patterns coincides with the exceeding of the solubility of Pu(IV)-hydroxide observed directly by LIBD and allows the calculation of the solubility product. The amount of $Pu(IV)_{aq}$ in solution always adjusts to amounts below the solubility after a certain equilibration time, and the decrease in $Pu(IV)_{aq}$ solute species proceeds either by redox reactions (mainly to Pu(III)) or by formation of colloids, which can be regarded as suspended Pu(IV)-oxyhydroxide precipitate.

References

1. Baes, C. F., Mesmer, R. E.: *The Hydrolysis of Cations*. Wiley, New York (1976).
2. Choppin, G. R.: Radiochim. Acta **32**, 43 (1983).
3. Grenthe, I., Puigdomenech, I.: *Modelling in Aquatic Chemistry*. OECD/NEA, Paris (1997).
4. Neck, V., Kim, J. I., Seidel, B. S., Marquardt, C. M., Dardenne, K., Jensen, M. P., Hauser, W.: Radiochim. Acta **89**, 439 (2001).
5. Lemire, R. J., Fuger, J., Nitsche, H., Potter, P., Rand, M. H., Rydberg, J., Spahiu, K., Sullivan, J. C., Ullman, W. J., Vitorge, P., Wanner, H.: (OECD, NEA-TDB). *Chemical Thermodynamics Vol. 4, Chemical Thermodynamics of Neptunium and Plutonium*. Elsevier, North-Holland, Amsterdam (2001).
6. Kraus, K. A., Nelson, F.: J. Am. Chem. Soc. **72**, 3901 (1950).
7. Rabideau, S., Kline, R. J.: J. Phys. Chem. **64**, 680 (1960).
8. Cleveland, J. M.: Inorg. Chem. **7**, 874 (1968).
9. Nitsche, H., Silva, R. J.: Radiochim. Acta **72**, 65 (1996).
10. Yusov, A. B., Fedosseev, A. M., Delegard, C. H.: Radiochim. Acta **92**, 869 (2004).
11. Metivier, H., Guillaumont, R.: Radiochem. Radioanal. Lett. **10**, 27 (1972).
12. Rabideau, S. W., Lemons, J. F.: J. Am. Chem. Soc. **73**, 2895 (1951).
13. Rabideau, S. W.: J. Am. Chem. Soc. **79**, 3675 (1957).
14. Lloyd, M. H., Haire, R. G.: Radiochim. Acta **25**, 139 (1978).
15. Cho, H. R., Marquardt, C. M., Neck, V., Seibert, A., Walther, C., Yun, J. I., Fanghänel, T.: Redox Behaviour of Plutonium(IV) in Acidic Solutions. In: *Recent Advances in Actinide Science*. (May, I., Alvarez, R., Bryan, N., eds.) The Royal Society of Chemistry, Spec. Publ. No. 305 (Proc. of the Conference Actinides 2005, Manchester, UK), RCS Publishing, Cambridge, UK (2006).
16. Cleveland, J. M.: *The Chemistry of Plutonium*. American Nuclear Society, La Grange Park, IL (1979).
17. Knopp, R., Neck, V., Kim, J. I.: Radiochim. Acta **86**, 101 (1999).
18. Neck, V., Kim, J. I.: Radiochim. Acta **89**, 1 (2001).
19. Neck, V., Kim, J. I.: Radiochim. Acta **88**, 815 (2000).
20. Guillaumont, R., Fanghänel, T., Fuger, J., Grenthe, I., Neck, V., Palmer, D. A., Rand, M. H.: (OECD, NEA-TDB). *Chemical Thermodynamics Vol. 5, Update on the Chemical Thermodynamics of Uranium, Neptunium, Plutonium, Americium and Technetium*. Elsevier, North-Holland, Amsterdam (2003).
21. Shannon, R. D.: Acta Cryst. **32**, 751 (1976).
22. Neck, V., Altmaier, M., Müller, R., Bauer, A., Fanghänel, T., Kim, J. I.: Radiochim. Acta **91**, 253 (2003).
23. Rai, D.: Radiochim. Acta **35**, 97 (1984).
24. Rai, D., Hess, N. J., Felmy, A. R., Moore, D. A., Yui, M., Vitorge, P.: Radiochim. Acta **86**, 89 (1999).
25. Perez-Bustamante, J. A.: Radiochim. Acta **4**, 67 (1965).
26. Kasha, M.: In: *The Transuranium Elements*. McGraw-Hill Inc., New York (1949), p. 295.
27. Lierse, Ch., Kim, J. I.: Chemisches Verhalten von Plutonium in natürlichen aquatischen Systemen: Hydrolyse, Carbonatkomplexierung und Redoxreaktionen; Report RCM 02286, Institut für Radiochemie, Technische Universität München (1986).
28. Kim, J. I., Kanellakopulos, B.: Radiochim. Acta **48**, 145 (1989).
29. Bitea, C.: PhD. Thesis, Fakultät für Maschinenbau, Universität Karlsruhe, Karlsruhe (2005).
30. Capdevila, H., Vitorge, P.: Radiochim. Acta **82**, 11 (1998).
31. Fujiwara, K., Yamana, H., Fujii, T., Moriyama H.: J. Nucl. Fuel Cycle Environ. **7**, 17 (2001).
32. Rai, D., Gorby, Y. A., Fredrickson, J. K., Moore, D. A., Yui, M., J. Solut. Chem. **31**, 433 (2002).
33. Hoffman, D. C.: *Advances in Plutonium Chemistry, 1967–2000*. Am. Nucl. Soc., La Grange Park, IL (2002).
34. Hecker, S. S.: MRS Bull.**26**, 672 (2001).
35. Katz, J. J., Seaborg, G. T., Morss, L. R.: *Chemistry of the Actinide Elements*. Chapman Hall., London (1986).
36. Fuger, J., Oetting, F. L.: The chemistry thermodynamics of actinide elements and compounds. *Part 2. The Actinide Aqueous Ions*. IAEA, Vienna (1976).
37. Scherbaum, F. J., Knopp, R., Kim J. I.: Appl. Phys. B **63**, 299 (1996).
38. Kitamori, T., Yokose, K., Sakagami, M., Sawada, T.: Japanese J. Appl. Phys. **28**, 1195 (1989).
39. Bundschuh, T., Knopp, R., Müller, R., Kim, J. I., Neck, V., Fanghänel, T.: Radiochim. Acta **88**, 625 (2000).
40. Bitea, C., Müller, R., Neck, V., Walther, C., Kim, J. I.: Coll. Surf. A **217**, 63 (2003).
41. Neck, V., Müller, R., Bouby, M., Altmaier, M., Rothe, J., Denecke, M. A., Kim, J. I.: Radiochim. Acta **90**, 485 (2002).
42. Walther, C.: Coll. Surf. A **217**, 81 (2003).
43. Walther, C., Bitea, C., Hauser, W., Kim, J. I., Scherbaum, F. J.: Nucl. Instrum. Methods B **195**, 374 (2002).
44. Walther, C., Cho, H. R., Fanghänel, T.: Appl. Phys. Lett. **85**, 6329 (2004).
45. Bitea, C., Walther, C., Yun, J. I., Kim, J. I., Fanghänel, T., Marquardt, C. M., Neck, V., Seibert, A.: Actinide Research Quarterly 11 (2003).
46. Rossotti, F. J. C., Rossotti, H. S.: *The Determination of Stability Constants*. McGraw-Hill, New York (1961).
47. Bauman, R. P.: *Absorption Spectroscopy*. Wiley, New York (1962).
48. Keller, C.: *The Chemistry of the Transuranium Elements*. Verlag Chemie, Weinheim, Germany (1971).
49. Runde, W., Reilly, S. D., Neu, M. P.: Geochim. Cosmochim. Acta **63**, 3443 (1999).
50. Wei, L., Fujiwara, K., Fuwa, K.: Anal. Chem. **55**, 951 (1983).
51. Wilson, R. E., Hu, Y.-J., Nitsche, H.: Radiochim. Acta **93**, 203 (2005).
52. Brablec, A., Trunec, D., Stastny F.: J. Phys. D **32**, 1870 (1999).
53. James, F., *Minuit, Function Minimization and Error Analysis*. CERN Program Library (1994).
54. Cohen, D.: J. Inorg. Nucl. Chem. **18**, 207 (1961).
55. Rothe, J., Walther, C., Denecke, M. A., Fanghänel, T.: Inorg. Chem. **43**, 4708 (2004).

2.7.3 Redox behavior of plutonium(IV) in acidic solutions [Cho05a]

REDOX BEHAVIOUR OF PLUTONIUM(IV) IN ACIDIC SOLUTIONS

H.R. Cho,[1] C.M. Marquardt,[1] V. Neck,[1] A. Seibert,[1] C. Walther,[1] J.I. Yun[1] and Th. Fanghänel[1,2]

[1]Forschungszentrum Karlsruhe, Institut für Nukleare Entsorgung,
PO Box 3640, D-76021 Karlsruhe, Germany
[2]Physikalisch-Chemisches Institut, Ruprecht-Karls Universität,
Im Neuenheimer Feld 253, D-69120 Heidelberg, Germany

1 INTRODUCTION

The redox behaviour of plutonium in acidic solutions has been studied for many decades. The formation of Pu(III), Pu(V) and Pu(VI) in Pu(IV) solutions exposed to air is usually ascribed to the disproportionation of Pu(IV) into Pu(III) and Pu(V), followed by the reaction of Pu(V) with Pu(IV) or the disproportionation of Pu(V) into Pu(III) and Pu(VI).[1-4] As the measured oxidation state distributions led to doubts on this reaction path,[3,5] we have revisited this topic and studied 10^{-5} to $5 \cdot 10^{-4}$ M Pu(IV) solutions (pH_c = 0.3 - 2.1 in 0.5 M HCl/NaCl, 22°C) as a function of time. Most of the solutions, obtained by dilution of electrochemically prepared Pu(IV) stock solutions, were kept under air in closed vials or cuvettes. Part of the experiments were performed in an Ar glove box. The concentrations of $Pu^{IV}(aq)$, Pu^{3+}, PuO_2^+ and PuO_2^{2+} were determined by UV/Vis/NIR absorption spectroscopy, using a capillary cell (path length 1 m) for low concentrations. Partly the solutions were colloid-free, partly they included Pu(IV) colloids, in particular at Pu(IV) and H^+ concentrations above the reported solubility of PuO_2(am, hyd).[6] The presence or absence of Pu(IV) oxyhydroxide colloids > 5 nm was confirmed by laser-induced breakdown detection (LIBD) as described previously.[5,6] As the fraction of polymeric or colloidal Pu(IV) cannot be quantified by spectroscopy it was calculated from the difference $[Pu]_{tot}$ - $\{[Pu^{IV}(aq)] + [Pu^{3+}] + [PuO_2^+] + [PuO_2^{2+}]\}$.

2 DISCUSSION OF EXPERIMENTAL RESULTS

2.1 Disproportionation of Pu(IV) ?

The disproportionation of Pu(IV) solutions at pH 0 - 2 leads to Pu(III) and, depending on pH, to Pu(V) (1), Pu(VI) (2) or both:[1-4]

$$2\ Pu^{4+} + 2\ H_2O \Leftrightarrow Pu^{3+} + PuO_2^+ + 4\ H^+ \quad (1)$$
$$3\ Pu^{4+} + 2\ H_2O \Leftrightarrow 2\ Pu^{3+} + PuO_2^{2+} + 4\ H^+ \quad (2)$$

Accordingly and independent of whether an equilibrium state is reached or not, the following balance must be valid for Pu(III), Pu(V) and Pu(VI) formed from Pu(IV):[3]

$$[Pu(III)] = [Pu(V)] + 2\,[Pu(VI)] \quad (3)$$

However, none of the solutions investigated in the present study (four examples are shown in Figs. 1a-d) fulfils this balance at reaction times < 10 days. Instead, the formation of Pu(III) is always approximately equal to the simultaneous decrease of Pu(IV)aq:

$$D[Pu(III])/dt = - d[Pu(IV)aq]/dt \quad (4)$$

i.e., $\{[Pu(IV)aq] + [Pu(III)]\}$ = constant and, as a consequence:

$$D\{[Pu(V)] + [Pu(VI)]\}/dt = - d[Pu(IV)coll]/dt. \quad (5)$$

2.2 A mechanism accounting for the observed oxidation state distributions

The present results indicate that the so-called "disproportionation of Pu(IV)" is a two-step process. The initial step is the formation of PuO_2^+, either by the redox equilibrium with PuO_2(am, hyd) [7,8] which is equal to $PuO_n(OH)_{4-2n}\,xH_2O$ colloids > 5 nm:

$$PuO_2(coll, hyd) \Leftrightarrow PuO_2^+ + e^- \quad (6)$$

or by the oxidation of colloidal or smaller polynuclear Pu(IV) species by O_2, analogous to the water-catalysed oxidation of solid PuO_2(s, hyd) to PuO_{2+x}(s, hyd),[9] followed by the dissolution of the oxidised Pu(V) fractions:

$$PuO_2(coll, hyd) + x/2\ O_2 + x\ H_2O \rightarrow \{PuO_{2+x}(coll, hyd)\} + x\ H_2O \rightarrow 2x\ (PuO_2^+ + OH^-) + (1-2x)\ PuO_2(coll, hyd) \quad (7)$$

The second step is the simultaneous equilibration of the redox couples Pu(V)/Pu(VI) and Pu(IV)/Pu(III) which are related by pe (and pH because of Pu(IV) hydrolysis equilibria):

$$PuO_2^+ \Leftrightarrow PuO_2^{2+} + e^- \quad (8)$$

$$Pu^{4+} + e^- \Leftrightarrow Pu^{3+} \qquad (Pu(OH)_n^{4-n} + n\ H^+ + e^- \Leftrightarrow Pu^{3+} + n\ H_2O) \quad (9)$$

This mechanism explains that the sum $\{[Pu(III)] + [Pu(IV)aq]\}$ always remains constant. It also explains the different behaviour of a colloid-free 3.8×10^{-4} M Pu(IV) solution at pH = 0.3 (Fig. 1a), i.e., far below the solubility of PuO_2(am, hyd),[6] and at pH = 1.0 (Fig. 1b) where polynuclear and colloidal Pu(IV) is formed immediately. In the experiment at $[Pu]_{tot} = 1.0 \times 10^{-5}$ M and $pH_c = 2.1$ (Fig. 1c), considerably above the solubility of PuO_2(am, hyd),[6] Pu(V) is evidently formed faster than Pu(III), not simultaneously as required by the disproportionation reaction (1).

The presence of O_2 is not necessary for reaction (6), but a prerequisite for reaction (7). Analogous experiments under air and in an Ar glove box gave very similar results (*c.f.*, Figs. 1b and d). This favours reaction (6) as the initial step. However, the Ar box used had a certain O_2 contamination (ca. 10 ppm), possibly sufficient to produce Pu(V) and Pu(VI) from colloidal or polynuclear Pu(IV), so that a final decision is not yet possible.

The oxidation state distributions and pe values measured after equilibration times of more than 20 days are consistent with the known redox equilibria (6), (8) and (9).[7,8,10] The "disproportionation" reactions (1) and (2) also describe correctly equilibrium state thermodynamics, but not the underlying reaction mechanism.

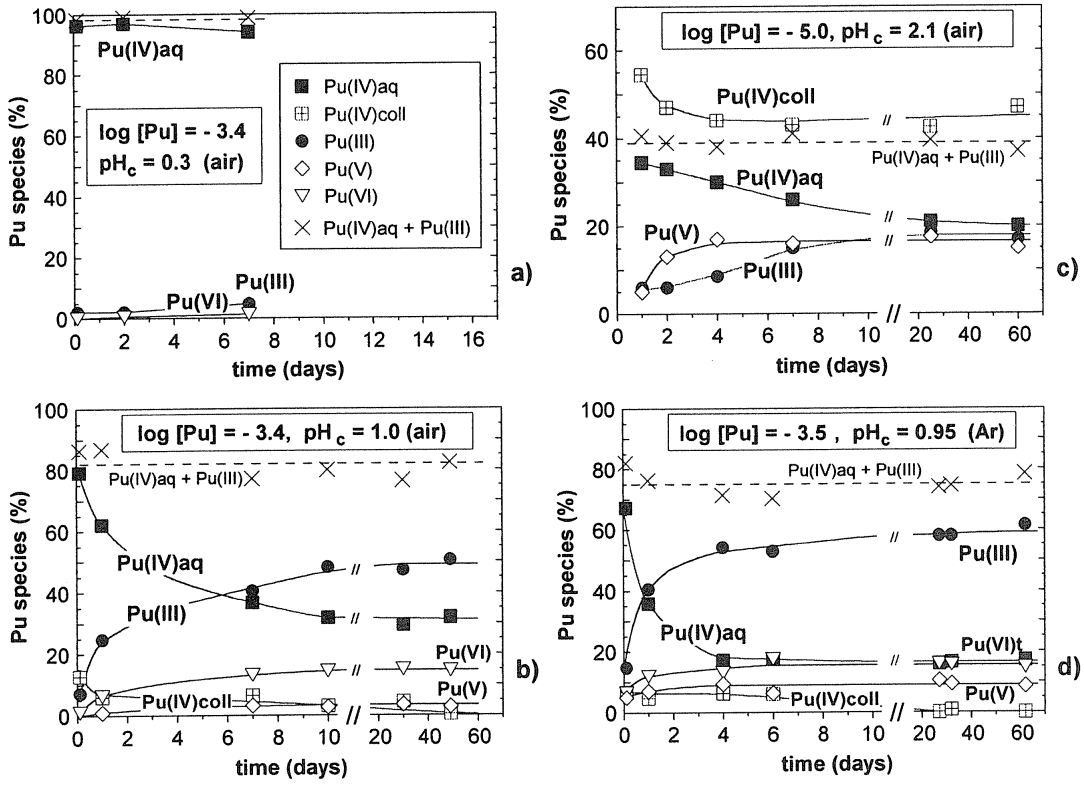

Figure 1 *Oxidation state distributions of initially Pu(IV) solutions as a function of time; a - c) solutions exposed to air, d) solution kept in an Ar glove box containing ca. 10 ppm O_2(g)*

References

1 R.E. Connick and W.H. McVey, *J. Am. Chem. Soc.*, 1953, **75**, 474.
2 S.W. Rabideau, *J. Am. Chem. Soc.*, 1953, **75**, 798 and 1957, **79**, 6350.
3 D.A. Costanzo, R.E. Biggers and J.T. Bell, *J. Inorg. Nucl. Chem.*, 1973, **35**, 609.
4 H. Capdevila, P. Vitorge and E. Giffaut, *Radiochim. Acta*, 1992, **58/59**, 45.
5 C. Walther, C. Bitea, J.I. Yun, J.I. Kim, Th. Fanghänel, C.M. Marquardt, V. Neck and A. Seibert, *Actinides Research Quarterly*, Los Alamos Natl. Lab., 2003, **11**, 12.
6 R. Knopp, V. Neck and J.I. Kim, *Radiochim. Acta*, 1999, **86**, 101.
7 D. Rai, *Radiochim. Acta*, 1984, **35**, 97.
8 H. Capdevila and P. Vitorge, *Radiochim. Acta*, 1998, **82**, 11.
9 J.M. Haschke and V.M. Oversby, *J. Nucl. Mat.*, 2002, **305**, 187.
10 R.J. Lemire, J. Fuger, H. Nitsche, P. Potter, M.H. Rand, J. Rydberg, K. Spahiu, J.C. Sullivan, W.J. Ullman, P. Vitorge, H. Wanner (OECD, NEA-TDB). *Chemical Thermodynamics of Neptunium and Plutonium*. Elsevier, North-Holland, 2001.

2.7.4 Investigation of the hydrolysis of plutonium(IV) by a combination of spectroscopy and redox potential measurements [Yun07]

Radiochim. Acta **95**, 89–95 (2007) / **DOI** 10.1524/ract.2007.95.2.89

Investigation of the hydrolysis of plutonium(IV) by a combination of spectroscopy and redox potential measurements

By J.-I. Yun*, H.-R. Cho, V. Neck, M. Altmaier, A. Seibert#, C. M. Marquardt, C. Walther and Th. Fanghänel#

Forschungszentrum Karlsruhe, Institut für Nukleare Entsorgung, 76021 Karlsruhe, Germany

(Received June 19, 2006; accepted in revised form September 12, 2006)

Plutonium(IV) / Hydrolysis / Formation constants / Redox potential / Spectroscopy

Summary. The hydrolysis of tetravalent plutonium in 0.5 M HCl/NaCl has been investigated by a combination of spectroscopy and redox potential measurements in the concentration range from 10^{-5} to 4×10^{-4} M and at pH_c 0.3–2.1. Redox potentials were both measured and calculated from the plutonium oxidation state distributions using well-known equilibrium constants for the redox reactions of plutonium. The plutonium oxidation states in solution were quantified by spectroscopy. The p_e values calculated from the plutonium redox couples Pu(V)/Pu(VI) and PuO_2(am,hyd)/Pu(V) were found to be consistent with the measured p_e values whereas those calculated from the Pu(III)/Pu(IV) couple were found to deviate, suggesting that the formation constants selected in recent reviews for the mononuclear hydroxide complexes of Pu(IV) are overestimated. Combining the redox potentials and the spectroscopically determined Pu(III) and Pu(IV) concentrations, the formation constants of the first, second, and third mononuclear hydroxide complexes $Pu(OH)_n^{4-n}$ at $I = 0.5$ M and 23 ± 2 °C are calculated and corrected to zero ionic strength using the specific ion interaction theory (SIT): $\log \beta_{11}^\circ = 14.0 \pm 0.2$, $\log \beta_{12}^\circ = 26.8 \pm 0.6$, and $\log \beta_{13}^\circ = 38.9 \pm 0.9$.

1. Introduction

Due to a high toxicity and long half-life, plutonium is one of the most important actinides to consider for the safety assessment of radioactive waste disposal. Reliable thermodynamic data of Pu(IV) are difficult to obtain because of the redox chemistry of plutonium with multiple oxidation states, *i.e.*, Pu(III), Pu(IV), Pu(V), and Pu(VI), known to co-exist in aqueous solutions. The determination of thermodynamic data of Pu(IV) is further complicated by hydrolysis even at low pH (pH < 1) and the formation of polymeric/colloidal species. It is relatively easy to maintain aqueous plutonium species in the Pu(III) or Pu(VI) oxidation states by adding strong reducing or oxidizing agents. It is more difficult, however, to study plutonium in the Pu(IV) and Pu(V) states, in particular under conditions relevant to geologic environments.

As discussed in the NEA-TDB reviews [1, 2], there are a number of solubility experiments and potentiometric, solvent extraction, and spectroscopic studies of the hydrolysis of Pu(IV). Contrary to the solubility constant of Pu(IV) hydrous oxide, which is well-known from different kind of experiments [2], the equilibrium constants $\log {}^*\beta_{1n}$ or $\log \beta_{1n}$ for the reactions

$$Pu^{4+} + nH_2O \Longleftrightarrow Pu(OH)_n^{4-n} + nH^+ \quad (1)$$

or

$$Pu^{4+} + nOH^- \Longleftrightarrow Pu(OH)_n^{4-n} \quad (2)$$

respectively, are not well ascertained [1, 2] and there are no data available for polynuclear hydroxide complexes $Pu_m(OH)_n^{4m-n}$. The reported values for the first hydrolysis constant of Pu(IV) differ by about 1.5 orders of magnitude due to various reasons, such as slow equilibration, formation of polymers/colloids, and redox reactions interfering in solvent extraction studies. In many spectroscopic studies at pH 0–2 [4–8], the authors interpret a steady decrease in the characteristic absorption band of the Pu^{4+} aquo ion at 470 nm in terms of mononuclear hydrolysis, *i.e.*, formation of $Pu(OH)_3^+$. Combining absorption spectroscopy with the laser-induced breakdown detection (LIBD) for the detection of Pu(IV) colloids, our recent study [9] clearly demonstrates that the decrease of the Pu(IV) absorption band is caused by the formation of Pu(IV) colloids or polymers, not by mononuclear hydrolysis reactions. This becomes also evident from the recent spectroscopic study of Yusov *et al.* [8], where the peak deconvolution yielded an "apparent pure component spectrum" for $Pu(OH)_3^+$ which is very different from that of the Pu^{4+} ion but similar to known spectra for Pu(IV) polymers (c.f., discussion in [9]).

As none of the available studies provides reliable thermodynamic data for higher hydrolyzed species of Pu(IV), Lemire *et al.* [1] selected only an equilibrium constant for the formation of $Pu(OH)^{3+}$: $\log {}^*\beta_{11}^\circ = -0.78 \pm 0.60$ ($\log \beta_{11}^\circ = 13.22 \pm 0.60$). A model calculation based on an electrostatic approach (Neck and Kim [3]) exhibits close agreement with experimental values of Metivier und Guillaumont [10] determined by solvent extraction with Pu-238 trace concentrations, *i.e.*, under conditions excluding Pu(IV)

*Author for correspondence (E-mail: yun@ine.fzk.de).

Present address: European Commission, Joint Research Center, Institute for Transuranium Elements, 76125 Karlsruhe, Germany

polymers and colloids. The stepwise hydrolysis constants in 1.0 M (H/Li)ClO_4 ($\log {}^*K'_n = -0.45$, -0.75, -3.3, and -6.3 for $n = 1$–4 [10]), extrapolated to $I = 0$ with the SIT, correspond to $\log \beta^\circ_{11} = 14.6 \pm 0.2$, $\log \beta^\circ_{12} = 28.6 \pm 0.3$, $\log \beta^\circ_{13} = 39.7 \pm 0.4$, and $\log \beta^\circ_{14} = 47.5 \pm 0.5$ if an uncertainty of ± 0.2 log-units is ascribed to each of the stepwise constants [2, 3]. In the recent reviews of Neck and Kim [3] and Guillaumont *et al.* [2], these hydrolysis constants were considered as the best available and selected, despite of some ambiguities in the interpretation of the solvent extraction data commented in [1].

The formation constant $\log \beta^\circ_{14}$ is reasonably consistent with the solubility product of $\log K^\circ_{sp}(PuO_2(am, hyd)) = -58.33 \pm 0.52$ [2] and experimental solubility data in neutral to alkaline solution, $\log[Pu(OH)_4(aq)] = -10.4 \pm 0.5$ [11, 12]. However, there are no other experimental data to verify the values of $\log \beta^\circ_{12}$ and $\log \beta^\circ_{13}$ from [10]. Hence, there remains a need for additional well-constrained and well-designed experiments to establish the hydrolysis constants of Pu(IV).

In the present work, the mononuclear hydrolysis of Pu(IV) is studied at pH_c 0.3–2.1 in 0.5 M (H/Na)Cl, in the concentration range from 10^{-5} to 4×10^{-4} M. For this purpose we used a combination of spectroscopy and redox potential measurements on the Pu(III)/Pu(IV) couple. This method is based on the fact that the Pu^{3+} ion is the only aqueous Pu(III) species in the pH range investigated whereas the Pu^{4+} ion undergoes hydrolysis reactions which affect the redox potential. Similar studies on the Pu(III)/Pu(IV) couple were performed by Rabideau in 1.0 M (H/Na)ClO_4 [13] and 2.0 M (H/Li)ClO_4 [14]. However, because of the rather high plutonium concentrations used (1×10^{-3} and 8×10^{-3} M, respectively), these studies cover only a very limited range of $pH_c \leq 1$ below the onset of colloid formation or precipitation of $Pu(OH)_4$(am). In addition, it is doubtful whether the activity coefficients of the plutonium species remain constant when the medium is changed, *e.g.*, from 1.0 M $HClO_4$ to 0.1 M $HClO_4$/0.9 M $NaClO_4$ or whether a certain variation of $\log \gamma_{Pu^{3+}}$ and $\log \gamma_{Pu^{4+}}$ also contributes to the small changes in $E'(Pu^{3+}/Pu^{4+})$ observed in these studies.

2. Experimental section

2.1 Sample preparation

Preparation, handling, and characterization of the plutonium samples are described in detail in [9, 15]. A brief summary shall be given here. The purity of the plutonium with regard to daughter nuclides is controlled by α- and γ-spectrometry and by ICP-MS. The purified plutonium consists of 99.4% Pu-242 ($t_{1/2} = 3.75 \times 10^5$ a) by weight; the remainder of the mass is composed of Pu-239 and Pu-240. Stock solutions of Pu(IV) in 1 M $HClO_4$ are prepared electrochemically as described in [16]. The original plutonium solution containing a mixture of different oxidation states is reduced on a platinum cathode at $E_{cathode} = -0.2$ V to Pu(III). The Pu(IV) stock solution is prepared by subsequent electrochemical oxidation of Pu(III) at $E_{anode} = 0.8$ V. The oxidation state purity of the Pu(IV) stock solutions is confirmed by spectroscopy. The total plutonium concentration is determined by liquid scintillation counting (LSC). Prior to each experiment, the stock solutions are filtered through a cellulose membrane microfilter (Amicon, 10 kD) and the success in removal of colloids is confirmed by laser-induced breakdown detection (LIBD) as described in [15, 17]. Batch samples at a constant ionic strength of $I = 0.5$ M, plutonium concentrations in the range of 10^{-5} to 4×10^{-4} M and pH_c 0.3–2.5 are prepared by slow dilution of the Pu(IV) stock solution with 0.5 M (H/Na)Cl solutions. The HCl and NaCl solutions used are examined for the presence of colloidal impurities after purification by ultrafiltration and recrystallization. Most of the solutions are kept in closed vials or quartz cuvettes under air, part of the experiments are performed in a glove box under Ar atmosphere containing trace amounts of O_2 (around 10 ppm).

2.2 Oxidation state speciation of plutonium

The oxidation state distributions in solution are measured as a function of time by UV/Vis/NIR absorption spectroscopy using a Cary 5E for concentrations above 10^{-4} M and a 1-meter liquid capillary waveguide combined with a diode-array spectrometer for lower concentrations [9, 18]. The spectral deconvolution routine has been described in detail in our recent paper [9].

2.3 Measurements of pH and E_h

The H^+ concentrations in the 0.5 M (H/Na)Cl test solutions are measured in small aliquots of 250 µl with a combination glass electrode (Ross electrode, Orion Co.) calibrated against standard pH buffers (pH 1–3, Merck) and 0.5 M (H/Na)Cl standard solutions covering the range of $pH_c = -\log[H^+]$ in the experiments (pH_c 0.3–2.0 in 0.5 M HCl – 0.01 M HCl/0.49 M NaCl). Redox potentials are measured with a micro-Pt electrode and a micro-Ag/AgCl reference electrode (Kurt Schwabe Institut für Meß- u. Sensortechnik e.V., Meinsberg, Germany). Commercial redox-buffers (220 mV and 640 mV, Schott Instruments GmbH) are used for calibration, and the measured potential is converted into E_h *versus* standard hydrogen electrode (SHE) by correction for the potential of the Ag/AgCl reference electrode. The value of $p_e = -\log a_{e^-}$ is calculated from $E_h = -(RT/F) \ln a_{e^-}$ according to the relation: $p_e = 16.9\, E_h(V)$ at 25 °C. The E_h electrode response usually reached a steady reading of the redox potential with a negligibly limiting drift rate, especially for solutions below the onset of colloid formation, with a reproducibility of about ± 5 mV. In samples containing Pu(IV) polymers/colloids the uncertainty of the redox potential measurements becomes larger due to a slow drift with time. Possibly these Pu(IV) species are adsorbed on the Pt electrode or undergo slow redox reactions contributing to the redox potential of the solution.

3. Results and discussion

3.1 Spectroscopic speciation

The spectroscopic determination of the Pu(III), Pu(IV), Pu(V), and Pu(VI) concentrations requires the knowledge

whether or how the absorption spectra of the corresponding aquo ions are affected by the change of pH_c in the range 0.3–2.5 and by the constant chloride concentration of 0.5 M used in the present work. Contrary to Pu(IV) which forms hydroxide complexes already at pH < 1, the trivalent, pentavalent and hexavalent actinide ions do not undergo hydrolysis reactions at pH < 4 [1, 2], *i.e.*, the change of pH has no effect on the absorption spectra of the Pu^{3+}, PuO_2^{+}, and PuO_2^{2+} aquo ions. The effect of hydrolysis on the absorption spectrum of the Pu^{4+} ion is discussed controversially. Different from interpretations given in previous spectroscopic studies [4–8], our recent study [9] indicates unmistakably that the characteristic molar absorptivity of the Pu(IV) aqueous species at 470 nm remains unaffected by mononuclear hydrolysis reactions. The absorption spectra of at least the first and the second hydrolyzed species $(Pu(OH)_n^{4-n}$, $n = 1, 2)$ normalized to the molar plutonium concentration do not differ from that of the hydrated Pu^{4+} aquo ion. The observed decrease in the molar absorptivity of Pu(IV) when pH is increased from 0 to 2 [4–8] is undoubtedly caused by the formation of Pu(IV) polymers/colloids [9].

The chloride concentration of 0.5 M has no effect on the absorptions spectra of Pu(III), Pu(IV) and Pu(V). Pentavalent actinide ions have generally an extremely weak tendency to form chloride complexes. Neither Np(V) nor Pu(V) chloride complexes have been identified experimentally [1, 19, 20]. In the case of the trivalent actinide ions Pu^{3+}, Am^{3+}, and Cm^{3+} the formation of chloride complexes can be observed spectroscopically only at high chloride concentrations above 4 M [2, 21, 23, 24]. The effect of chloride on the absorption spectrum of Pu(IV) is negligible as well [19, 20, 22]. The tendency to form chloride complexes is certainly higher for tetravalent actinides than for trivalent actinides [1, 2], but as indicated by the observations for Pu(IV) hydroxide complexes [9], the characteristic Pu(IV) absorption bands seem to be rather insensitive to complex formation with one or two OH^- or Cl^- ligands. In the case of Pu(VI), however, spectroscopic studies indicate the formation of at least three different chloride complexes with increasing chloride concentration in 1 M H(ClO_4/Cl) [23]. There is also spectroscopic evidence for the formation of Pu(VI) chloride complexes in 0.5 M (H/Na)Cl [9]. The chloride complex observed at 837.6 nm is in agreement with the spectral parameters of the first Pu(VI) chloride complex, PuO_2Cl^+, reported by Runde *et al.* [25]. This monochloro complex of Pu(VI) accounts for 15% of the total Pu(VI) concentration in 0.5 M (H/Na)Cl, *i.e.*, $[Pu(VI)(aq)] = 1.18\,[PuO_2^{2+}]$.

With this analytical background, the concentrations of Pu^{3+}, Pu(IV)(aq), PuO_2^{+}, and Pu(VI)(aq) are determined by absorption spectroscopy using the spectral deconvolution routine described in [9]. As the fraction of polymeric or colloidal Pu(IV) cannot be quantified by spectroscopy it is calculated from the difference of the total plutonium concentration measured by LSC and the sum of the spectroscopically determined plutonium concentrations:

$$[Pu(IV)_{coll}] = [Pu]_{tot} - ([Pu^{3+}] + [Pu(IV)(aq)] + [PuO_2^{+}] + [Pu(VI)(aq)])\,. \quad (3)$$

3.2 Plutonium oxidation state distributions and redox potentials

The plutonium oxidation state distribution of the initially pure Pu(IV) solutions, obtained by diluting the electrochemically prepared Pu(IV) stock solution in 1 M $HClO_4$ with 0.5 M (H/Na)Cl, was pursued spectroscopically as a function of time until the plutonium concentrations in the different oxidation states approached constant values after some days or weeks. In this steady state the plutonium oxidation states are in equilibrium and the redox potential remains at a constant value. The final (steady state) concentrations and p_e values of all samples are listed in Table A1 (Appendix). Fig. 1a–e show typical examples for the changes in the plutonium oxidation state distribution as a function of time. It should be noted that the oxidation state distributions and redox potentials in the samples kept under Ar atmosphere were not significantly different from those observed at comparable pH values in closed samples kept under air (Fig. 1).

In the samples at $pH_c < 1$, Pu(IV)(aq), *i.e.*, $Pu(OH)_n^{4-n}$, and Pu^{3+} are the predominant aqueous plutonium species. Only small fractions of Pu(VI) and Pu(V) are formed. With increasing pH and beyond the solubility of Pu(IV) hydroxide/hydrous oxide, *i.e.*, at pH > 1.5–2 for Pu(IV) concentrations of 10^{-4}–10^{-5} M, Pu(IV) colloids are formed as well. In the final steady state, these Pu(IV) polymers/colloids are in equilibrium with Pu^{4+} and its hydroxide complexes, with Pu^{3+}, PuO_2^{+}, and PuO_2^{2+}. The $PuO_n(OH)_{4-2n}\cdot xH_2O$ colloids detectable by LIBD (particle size > 5 nm) have thermodynamic properties similar to amorphous precipitates called $Pu(OH)_4$(am), $PuO_2\cdot xH_2O$(am) or PuO_2(am, hyd). Similar oxidation state mixtures including Pu(IV) colloids were observed by Capdevila and Vitorge [26] who used the Pu(III)/Pu(IV) and Pu(V)/Pu(VI) equilibria to calculate a solubility product of $\log K^\circ_{sp} = -58.3 \pm 0.5$ which is in excellent agreement with the values determined by classical solubility measurements [2].

In the following the p_e values derived from the measured redox potentials are compared with p_e values calculated from the Pu(III)/Pu(IV) and Pu(V)/Pu(VI) equilibria:

$$Pu^{3+} \Longleftrightarrow Pu^{4+} + e^-$$
$$(\log K^\circ_{III/IV} = -17.69 \pm 0.04\ [1, 2]) \quad (4)$$

$$PuO_2^{+} \Longleftrightarrow PuO_2^{2+} + e^-$$
$$(\log K^\circ_{V/VI} = -15.82 \pm 0.09\ [1, 2]) \quad (5)$$

using the spectroscopically determined concentrations. For samples with an appreciable fraction of Pu(IV) colloids the p_e values are additionally calculated from the equilibrium

$$PuO_2(am, hyd) \Longleftrightarrow PuO_2^{+} + e^-$$
$$(\log K^\circ_{IV(s)/V} = -19.78 \pm 0.89\ [2])\,. \quad (6)$$

In the case of the Pu(III)/Pu(IV) couple (reaction Eq. (4)), the concentration of the Pu^{4+} aquo ion has to be calculated from the measured Pu(IV)(aq) concentration according to

$$[Pu^{4+}] = [Pu(IV)(aq)]/\left(1 + \sum \beta'_{1n}[OH^-]^n\right) \quad (7)$$

where β'_{1n} are the formation constant of $Pu(OH)_n^{4-n}$ in 0.5 M (H/Na)Cl. The specific ion interaction theory (SIT) [27]

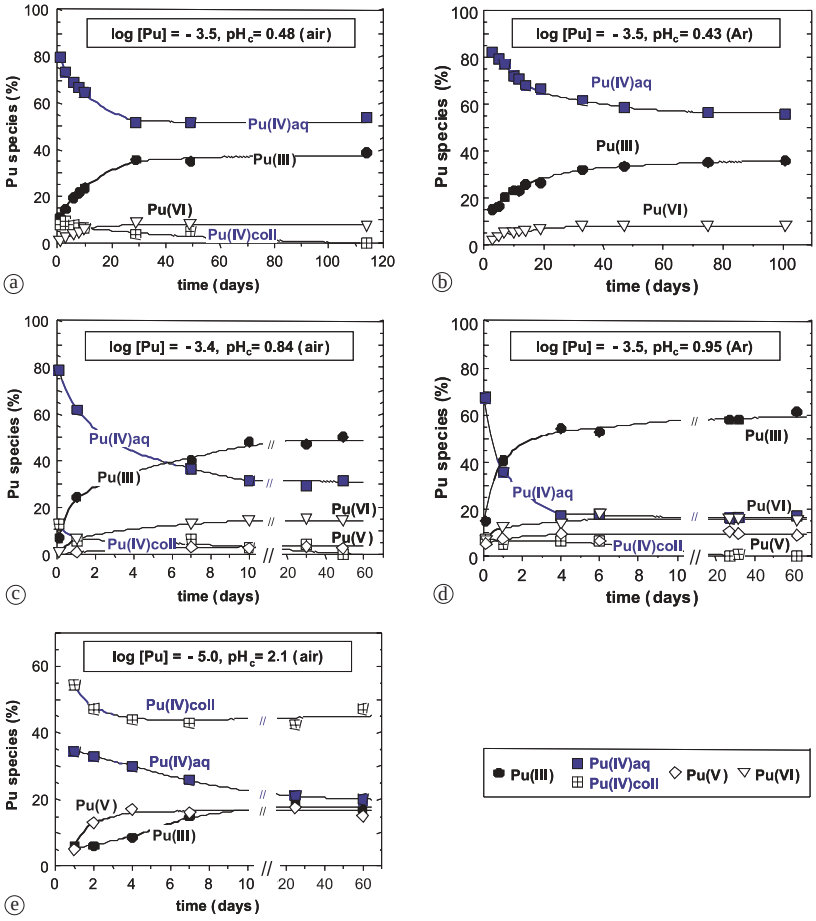

Fig. 1. Typical examples of plutonium oxidation state distributions measured as a function of time in initially 1×10^{-5}–4×10^{-4} M Pu(IV) solutions at pH$_c$ 0.43–2.1. The samples in Fig. 1a, c, and e were kept under air, those in Fig. 1b and d were kept under Ar atmosphere.

recommended in the NEA-TDB reviews [1, 2] for ionic strength corrections is used to calculate the activity coefficients γ_i of the species involved:

$$\log \gamma_i = -z_i^2 D + \sum \varepsilon_{ij}\, m_j \qquad (8)$$

where z_i is the charge of ion i, ε_{ij} is the interaction parameter for a pair of oppositely charged ions, m_j (mol/kg H_2O) is the molal concentration of ion j, and D is the Debye–Hückel term: $D = A\sqrt{I_m}/(1 + Ba_j\sqrt{I_m})$, where A and Ba_j are assigned the values of 0.509 kg$^{1/2}$ mol$^{-1/2}$ and 1.5 kg$^{1/2}$ mol$^{-1/2}$ at 25 °C and 1 bar, respectively. I_m is the molal ionic strength. The SIT coefficients ε_{ij} used are summarized in Table 1.

Combining and re-arranging Eq. (4)–Eq. (8), p_e can be calculated from the redox couples Pu(III)/Pu(IV), Pu(V)/Pu(VI), and PuO_2(am,hyd)/Pu(V) according to:

$$p_e = -\log K'_{III/IV} + \log[\mathrm{Pu(IV)(aq)}] - \log\left(1 + \sum \beta'_{1n}[OH^-]^n\right) - \log[\mathrm{Pu(III)(aq)}] \qquad (9)$$

$$p_e = -\log K'_{V/VI} + \log[\mathrm{Pu(VI)(aq)}] - \log[\mathrm{Pu(V)(aq)}] \qquad (10)$$

$$p_e = -\log K'_{IV(s)/V} + \log[\mathrm{Pu(V)(aq)}] \qquad (11)$$

with $\log K'_{III/IV} = -16.55 \pm 0.04$, $\log K'_{V/VI} = -15.36 \pm 0.09$, and $\log K'_{IV(s)/V} = -19.65 \pm 0.89$ in 0.5 M (H/Na)Cl.

Table 1. Ion interaction (SIT) coefficients at 25 °C used in the present work (from the NEA-TDB [1, 2], except otherwise stated)

i	j	ε_{ij} (kg mol^{-1})
H^+	Cl^-	0.12 ± 0.01
OH^-	Na^+	0.04 ± 0.01
PuO^{2+}	Cl^-	0.09 ± 0.05 [a]
PuO_2^{2+}	Cl^-	0.21 ± 0.02 [a]
Pu^{3+}	Cl^-	0.23 ± 0.02 [a]
Pu^{4+}	Cl^-	0.4 ± 0.1 [b]
$Pu(OH)_3^+$	Cl^-	0.2 ± 0.1 [b]
$Pu(OH)_2^{2+}$	Cl^-	0.1 ± 0.1 [b]
$Pu(OH)_3^+$	Cl^-	0.05 ± 0.1 [b]
$Pu(OH)_4^\circ$	Na^+, Cl^-	0

a: The values for PuO_2^+, PuO_2^{2+}, and Pu^{3+} are adopted from the analogous values for NpO_2^+; UO_2^{2+}, and Am^{3+}, respectively [2].
b: Estimated in [3] according to charge-type analogies and systematics in the actinide series as outlined in the NEA reviews [1, 2].

The formation constants $\log \beta'_{11} = 13.3$, $\log \beta'_{12} = 26.4$, $\log \beta'_{13} = 36.8$, and $\log \beta'_{14} = 44.3$ are calculated from the $\log \beta^\circ_{1n}$ values selected in [2, 3] and log[OH^-] is calculated from log[H^+] and the ion product of water, $\log K'_w = -13.74$ in 0.5 M NaCl [1, 2].

As shown in Fig. 2, the p_e values calculated from the redox couple Pu(V)/Pu(VI) are consistent with the measured p_e values (+). The p_e values calculated from the re-

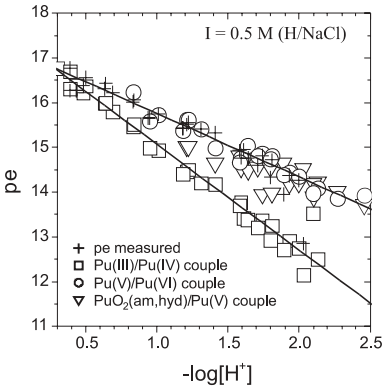

Fig. 2. Redox potentials ($p_e = 16.9\,E_h(V)$) calculated from the redox couples Pu(III)/Pu(IV) (squares), Pu(V)/Pu(VI) (circles), and PuO_2(am,hyd)/Pu(V) (triangles) and the oxidation state distributions determined by spectroscopy in comparison with measured values (crosses +).

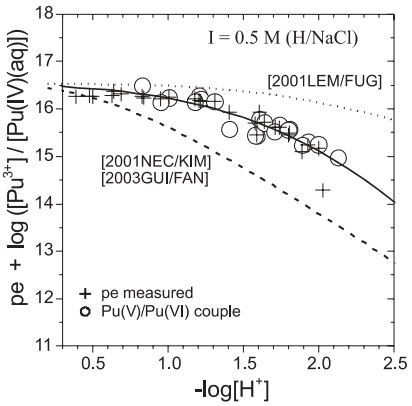

Fig. 3. Calculation of the Pu(IV) hydrolysis constants from the present experimental data: Best fit (solid line) in comparison with calculations using the hydrolysis constants selected in recent reviews [1] (dotted line) and [2, 3] (dashed line).

dox couple PuO_2(am,hyd)/Pu(V) are more scattered, but also in reasonable agreement with the measured values, in particular with regard to the large uncertainty of ± 0.9 log-units for the equilibrium constant $\log K'_{IV(s)/V}$. However, the p_e values calculated from Pu(III)/Pu(IV) couple deviate systematically from the measured data, indicating that the Pu(IV) hydrolysis constants used to calculate $[Pu^{4+}]$ from [Pu(IV)(aq)], *i.e.*, the values selected in recent reviews [2, 3] from the solvent extraction study of Metivier and Guillaumont [10], are too large.

It is to note that the E_h values measured in solutions with Pu(IV) polymers/colloids as predominant species (pH > 2) are markedly lower than those calculated from the Pu(V) and Pu(VI) concentrations (c.f., measured p_e value (+) at pH 2.03 in Fig. 2). The reason, possibly the adsorption of polymeric/colloidal Pu(IV) species on the surface of the E_h electrode, is not yet understood. Therefore these values are not included in the data evaluation discussed below.

3.3 Determination of the hydrolysis constants of Pu(IV)

Combining Eq. (4) and Eq. (7), the hydrolysis constants of Pu(IV) can be calculated from the experimental p_e values and the spectroscopically determined concentrations of Pu^{3+} and Pu(IV)(aq) according to the following relation:

$$p_e + \log([Pu^{3+}]/[Pu(IV)(aq)]) = -\log K'_{III/IV} - \log\left(1 + \sum \beta'_{1n}(K'_w/[H^+]^n)\right) \quad (12)$$

Fig. 3 shows the experimental data, *i.e.*, the left hand term of Eq. (12), applying both the measured redox potentials and those calculated from the Pu(V)/Pu(VI) couple as function of the H^+ concentration. The solid line shows the right hand term of Eq. (12), calculated by nonlinear least squares fitting of the first, second, and third hydrolysis constants of Pu(IV) in 0.5 M (H/Na)Cl:

$$\log \beta'_{11} = 12.7 \pm 0.2 \; (\log \beta^\circ_{11} = 14.0 \pm 0.2)$$
$$\log \beta'_{12} = 24.5 \pm 0.6 \; (\log \beta^\circ_{12} = 26.8 \pm 0.6)$$
$$\log \beta'_{13} = 36.0 \pm 0.9 \; (\log \beta^\circ_{13} = 38.9 \pm 0.9)$$

The equilibrium constant $\log K'_{III/IV} = -16.55 \pm 0.04$ [1, 2] is used as fixed value and the uncertainties correspond to the 2σ level. The large uncertainty of $\log \beta'_{13}$ is due to the lack of data at $pH_c > 2.1$ where the solubility of Pu(IV) and hence the concentration of Pu(IV)(aq) decreases to values below the analytical detection sensitivity. The hydrolysis constants at zero ionic strength (given in parenthesis) are calculated with the SIT. The $\log {}^*\beta^\circ_{1n}$ values selected in [2, 3] for $n =$ 1–3 from the study of Metivier and Guillaumont [10] are higher than those determined in the present work whereas $\log {}^*\beta^\circ_{11}$ selected by Lemire *et al.* [1] is lower (c.f., Table 2). For comparison the right hand term of Eq. (12) is calculated using the formation constants of Pu(IV) hydroxide complexes selected in [2, 3] (dashed line in Fig. 3) and also using only the formation constant of $Pu(OH)^{3+}$ selected in [1] (dotted line in Fig. 3). The calculated curves are either lower or higher than our experimental data.

4. Conclusions

The plutonium oxidation state distributions in acidic solutions containing predominantly Pu(III) and Pu(IV), based on a precise and correct spectroscopic evaluation and combined with the redox potentials in these solutions, allow the determination of the hydrolysis constants of Pu(IV). The formation constants $\log \beta^\circ_{1n}$ determined in the present study for

Table 2. Pu(IV) hydrolysis constants at $I = 0$ and 25 °C; present results in comparison with the values selected in the NEA-TDB reviews [1, 2].

	$\log \beta^\circ_{1n}$		$\log {}^*\beta^\circ_{1n}$	
	p.w.	p.w.	Lemire *et al.* [1]	Guillaumont *et al.* [2]
$Pu(OH)_3^+$	14.0 ± 0.2	0.0 ± 0.2	-0.8 ± 0.6	0.6 ± 0.2
$Pu(OH)_2^{2+}$	26.8 ± 0.6	-1.2 ± 0.6		0.6 ± 0.3
$Pu(OH)_3^+$	38.9 ± 0.9	-3.1 ± 0.9		-2.3 ± 0.4
$Pu(OH)_4^\circ$				-8.5 ± 0.5

the species $Pu(OH)_n^{4-n}$ ($n = 1$–3) indicate that the values selected in recent reviews [2, 3] from the only experimental study hitherto available [10] are overestimated.

As the method used in the present study is not applicable beyond the acidic pH range, the formation constant of $Pu(OH)_4(aq)$ could not be determined. However, the value of $\log \beta^\circ_{14} = 47.5 \pm 0.5$ selected in [2, 3] from the stepwise constants determined in the solvent extraction study of [10] is expected to be overestimated as well. Even if the stepwise equilibrium constant between $Pu(OH)_3^+$ and $Pu(OH)_4(aq)$, $\log K^\circ_{14} = 7.8 \pm 0.2$ [2, 3], is correct, the maximum value of $\log \beta^\circ_{14}$ is 46.7 ± 0.9. If this value is considered as an upper limit and combined with the solubility constant of $\log K^\circ_{sp}(PuO_2(am, hyd)) = -58.33 \pm 0.52$ [2], which is ascertained by experimental data from different authors [26, 28–30] and different type of experiments, the maximum concentration of the Pu(IV) tetrahydroxo complex is calculated to be $\log[Pu(OH)_4(aq)] < -11.6 \pm 1.0$. Accordingly, the solubility determined with Pu(IV) hydroxide or hydrous oxide in neutral and alkaline solution, $\log[Pu] = -10.4 \pm 0.5$ [11, 12] is probably not caused by mononuclear species $Pu(OH)_4(aq)$ but by small polynuclear species $Pu_m(OH)_n^{4m-n}(aq)$ or by plutonium species at other oxidation states.

Another important conclusion concerns the reaction mechanism leading to the observed oxidation state distributions in the initially pure Pu(IV) solutions at pH_c 0.3–2.5. The redox potentials measured in the final steady state exhibit consistency with those calculated from the spectroscopic data and known equilibrium constants [1, 2, 26] for the redox couples Pu(V)/Pu(VI) and PuO_2(am,hyd)/Pu(V) if solid or colloidal Pu(IV) particles are present. This indicates that an equilibrium state is reached between the different plutonium oxidation states, which is usually ascribed to the disproportionation of Pu(IV). However, a closer look at the oxidation state distributions, in particular after short reaction times, shows that the underlying mechanism is a two-step process. The initial step is the formation of PuO_2^+, either by the redox equilibrium with colloidal PuO_2(am,hyd) or by the oxidation of colloids or smaller polynuclear Pu(IV) species by dissolved O_2. The second step is the simultaneous equilibration of the redox couples Pu(V)/Pu(VI) and Pu(III)/Pu(IV) which are related by p_e (and pH because of Pu(IV) hydrolysis equilibria). This is discussed in a separate paper [31].

Appendix

Table A1. Final (steady state) values of the samples investigated in the present work.

Sample	pH_c	p_e	$\log[Pu]_{tot}$ (M)	Pu^{3+} (%)	Pu(IV)(aq) (%)	PuO^{2+} (%)	Pu(VI)(aq) (%)	$Pu(IV)_{coll}$ (%)
Air	0.30	–	−5.0	24.9	59.4	15.7	0	0
	0.48	16.4	−3.5	40.7	53.4	0	5.9	0
	0.50	16.6	−3.4	32.0	62.4	0	5.6	0
	0.63	16.3	−3.4	43.9	47.2	0	8.8	0
	0.69	16.2	−3.5	49.0	41.7	0	9.4	0
	0.83	16.0	−3.4	52.2	32.9	1.7	13.2	0
	0.84	16.1	−3.4	52.8	34.9	0	12.3	0
	1.01	15.7	−3.4	59.9	18.4	6.1	14.2	1.5
	1.21	15.5	−3.5	62.3	13.3	7.0	12.7	4.8
	1.22	15.6	−3.5	57.1	14.1	8.0	14.3	6.6
	1.31	15.4	−3.4	60.9	10.8	11.3	12.5	4.7
	1.41	15.3	−4.2	52.4	13.2	16.3	6.8	11.4
	1.58	14.9	−4.2	50.8	8.7	23.6	4.9	12.2
	1.59	14.8	−4.5	50.2	10.5	23.0	5.7	10.7
	1.61	14.9	−3.5	53.7	5.6	26.4	7.4	7.0
	2.10	–	−5.0	16.3	19.8	14.3	0	49.5
Ar	0.39	16.8	−3.6	21.4	70.6	0	8.0	0
	0.39	16.3	−3.5	38.9	54.1	0	7.0	0
	0.43	16.3	−3.5	34.0	59.6	0	6.4	0
	0.64	16.4	−3.6	38.4	43.3	0	18.3	0
	0.95	15.7	−3.5	60.3	16.8	8.5	14.4	0
	1.18	15.4	−3.5	59.2	9.8	15.2	15.7	0
	1.28	15.4	−4.6	51.7	13.8	8.1	14.2	12.3
	1.44	15.2	−4.6	56.8	9.9	9.8	11.2	12.3
	1.64	14.8	−4.6	54.0	5.8	13.7	6.6	19.9
	1.71	14.6	−4.6	55.0	5.3	16.2	4.6	19.0
	1.74	14.8	−4.8	51.3	8.4	13.8	4.5	22.1
	1.80	14.3	−4.6	53.8	4.1	15.7	3.8	22.5
	1.81	14.7	−4.9	52.2	8.8	16.0	4.5	18.4
	1.89	13.9	−4.6	51.9	3.6	20.7	2.2	21.5
	1.93	14.4	−4.9	51.9	7.0	24.9	3.0	13.2
	2.00	14.3	−4.9	51.3	6.4	25.2	2.5	14.6
	2.03	12.9	−4.8	54.9	2.0	21.8	0	21.2
	2.10	–	−4.9	43.1	0	27.9	1.1	27.9
	2.27	–	−5.1	38.0	0	30.5	1.0	30.5
	2.46	–	−5.4	42.6	0	28.1	1.1	28.1

References

1. Lemire, R. J., Fuger, J., Nitsche, H., Potter, P., Rand, M. H., Rydberg, J., Spahiu, K., Sullivan, J. C., Ullman, W. J., Vitorge, P., Wanner, H.: Chemical Thermodynamics of Neptunium and Plutonium. OECD NEA-TDB, Elsevier Science Publ., North-Holland, Amsterdam (2001).
2. Guillaumont, R., Fanghänel, Th., Fuger, J., Grenthe, I., Neck, V., Palmer, D. A., Rand, M. H.: Update on the Chemical Thermodynamics of Uranium, Neptunium, Plutonium, Americium and Technetium. OECD NEA-TDB, Elsevier Science Publ., North-Holland, Amsterdam (2003).
3. Neck, V., Kim, J. I.: Solubility and hydrolysis of tetravalent actinides. Radiochim. Acta **89**, 1 (2001).
4. Kraus, K. A., Nelson, F.: Hydrolytic behavior of metal ions. I. The acid constants of uranium(IV) and plutonium(IV). J. Am. Chem. Soc. **72**, 3901 (1950).
5. Rabideau, S., Kline, R. J.: A spectrophotometric study of the hydrolysis of plutonium(IV). J. Phys. Chem. **64**, 680 (1960).
6. Cleveland, J.: Sulfamate complexes of plutonium(IV). Inorg. Chem **7**, 874 (1968).
7. Nitsche, H., Silva, R. J.: Investigation of the carbonate complexation of Pu(IV) in aqueous solution. Radiochim. Acta **72**, 65 (1996).
8. Yusov, A. B., Fedosseev, A. M., Delegard, C. H.: Hydrolysis of Np(IV) and Pu(IV) and their complexation by aqueous $Si(OH)_4$. Radiochim. Acta **92**, 869 (2004).
9. Walther, C., Cho, H. R., Marquardt, C. M., Neck, V., Seibert, A., Yun, J. I., Fanghänel, Th.: Hydrolysis of plutonium(IV) in acidic solutions: No effect of hydrolysis on absorption-spectra of mononuclear hydroxide complexes. Radiochim. Acta **95**, 7 (2007).
10. Metivier, H., Guillaumont, R.: Hydrolyse du plutonium tetravalent. Radiochem. Radioanal. Lett. **10**, 27 (1972).
11. Lierse, Ch., Kim, J. I.: Chemisches Verhalten von Plutonium in natürlichen aquatischen Systemen: Hydrolyse, Carbonatkomplexierung und Redoxreaktionen. Report RCM 02286, Institut für Radiochemie, Technische Universität München (1986).
12. Rai, D., Hess, N. J., Felmy, A. R., Moore, D. A., Yui, M., Vitorge, P.: A thermodynamic model for the solubility of PuO_2(am) in the aqueous K^+-HCO_3^--CO_3^{2-}-OH^--H_2O system. Radiochim. Acta **86**, 89 (1999).
13. Rabideau, S. W., Lemons, J. F.: The potential of the Pu(III)-Pu(IV) couple and the equilibrium constants for some complex ions of Pu(IV). J. Am. Chem. Soc. **73**, 2895 (1951)
14. Rabideau, S. W.: The hydrolysis of Pu(IV). J. Am. Chem. Soc. **79**, 3675 (1957)
15. Bitea, C.: Laser-induzierte Breakdown Detektion (LIBD): Quantifizierung der Kolloidbildung vierwertiger Actiniden und Homologen. Ph.D. thesis, Fakultät für Maschinenbau, Universität Karlsruhe, Germany (2005).
16. Cohen, D.: Electrochemical studies of plutonium ions in perchloric acid solution. J. Inorg. Nucl. Chem. **18**, 207 (1961).
17. Bitea, C., Walther, C., Yun, J. I., Kim, J. I., Fanghänel, Th., Marquardt, C. M., Neck, V., Seibert, A.: Nanoscopic approaches to the aquatic plutonium chemistry. Actinide Research Quarterly **11**, 12 (2003).
18. Wilson, R. E., Hu, Y.-J., Nitsche, H.: Detection and quantification of Pu(III, IV, V, and VI) using a 1.0-meter liquid core waveguide. Radiochim. Acta **93**, 203 (2005).
19. Cleveland, J. M.: *The Chemistry of Plutonium*. Am. Nucl. Soc., La Grange Park, IL (1979).
20. Katz, J. J., Seaborg, G. T., Morss, L. R.: *The Chemistry of the Actinide Elements*. Vol. 1, Chapman Hall, London, New York (1986).
21. Shiloh, M., Marcus, Y.: A spectrophotometric study of trivalent actinide complexes in solution II: neptunium and plutonium. J. Inorg. Nucl. Chem. **28**, 2725 (1966).
22. Marcus, Y.: Metal-chloride complexes studied by ion-exchange and solvent-extraction methods. Part I. Non-transition-metalions, lanthanides, actinides, and *d* transition-metal ions. Coord. Chem. Rev. **2**, 195 (1967).
23. Giffaut, E.: Influence des ions chlorure sur la chimie des actinides. Ph.D. thesis, Université de Paris-Sud, Orsay, France (1994).
24. Fanghänel, Th., Kim, J. I., Klenze, R., Kato, Y.: Formation of Cm(III) chloride complexes in $CaCl_2$ solutions. J. Alloys Compd. **225**, 308 (1995).
25. Runde, W., Reilly, S. D., Neu, M. P.: Spectroscopic investigation of the formation of PuO_2Cl^+ and PuO_2Cl_2 in NaCl solutions and application for natural brine solutions. Geochim. Cosmochim. Acta **63**, 3443 (1999).
26. Capdevila, H., Vitorge, P.: Solubility product of $Pu(OH)_4$(am). Radiochim. Acta **82**, 11 (1998).
27. Ciavatta, L.: The specific interaction theory in evaluating ionic equilibria. Ann. Chim. (Rome) **70**, 551 (1980).
28. Knopp, R., Neck, V., Kim, J. I.: Solubility, hydrolysis and colloid formation of plutonium(IV). Radiochim. Acta **86**, 101 (1999).
29. Fujiwara, K., Yamana, H., Fujii, T., Moriyama, H.: Solubility product of plutonium hydrous oxide. J. Nucl. Fuel Cycle Environ. (Japan) **7**, 17 (2001).
30. Rai, D., Gorby, Y. A., Fredrickson, J. K., Moore, D. A., Yui, M.: Reductive dissolution of PuO_2(am): The effect of Fe(II) and hydroquinone. J. Sol. Chem. **31**, 433 (2002).
31. Cho, H. R., Marquardt, C. M., Neck, V., Seibert, A., Walther, C., Yun, J. I., Fanghänel, Th.: Redox behaviour of plutonium(IV) in acidic solutions. In: Recent Advances in Actinide Science. (May, I., Alvarez, R., Bryan, N., eds.), pp. 602–604, The Royal Society of Chemistry, Spec. Publ. No. 305 (Proc. of the conference Actinides 2005, Manchester, UK), RCS Publishing, Cambridge, UK (2006).

2.7.5 XAFS and LIBD investigation of the formation and structure of colloidal Pu(IV) hydrolysis products [Roth04]

Inorg. Chem. **2004**, *43*, 4708–4718

XAFS and LIBD Investigation of the Formation and Structure of Colloidal Pu(IV) Hydrolysis Products

Jörg Rothe, Clemens Walther, Melissa A. Denecke,* and Th. Fanghänel

Institut für Nukleare Entsorgung, Forschungszentrum Karlsruhe, Postfach 3640, D-76021 Karlsruhe, Germany

Received February 3, 2004

Pu(IV) oxyhydroxide colloid growth is investigated with XAFS and LIBD. From combined results a model of colloid formation is proposed, which leads to a face-centered cubic Pu sublattice having cation defects, as observed with EXAFS, and a linear dependency of log [Pu(IV)] on –log [H^+] with slope –2, in accord with LIBD. The solubility for Pu(IV) measured with LIBD is close to the lower limit of the solubility curve from previously reported data.

Introduction

Reports of X-ray absorption fine structure (XAFS) studies on the formation of actinide oxyhydroxide "eigen-colloids" including Pu L-edge XAFS investigations of Pu(IV) eigen-colloids are sparse. Conradson[1] describes a low-temperature XAFS investigation of Pu(IV) oxyhydroxide colloids, isolated from solution via centrifugation, reporting observation of multiple, distinct Pu−O bonds due to the presence of different Pu−O moieties. Understanding the mechanism of Pu(IV) "eigen-colloid" formation is important, e.g., for understanding the origin of variations in results of Pu(IV) solubility studies reported in the literature[2−5] and why apparent nonlinear behavior of Pu(IV) solubility in the millimole range at −log [H^+] approaching zero has been reported.[4] Such information is not solely of interest to basic research but has technological significance. For example, the solubility of Pu(IV) in groundwater is an important aspect in the performance and safety of sites for nuclear waste disposal in deep geological formations.

In this paper we report on the structures of colloids formed upon increasing the −log [H^+] of an aqueous Pu(IV) solution through dilution and, in one case, addition of NaOH, characterized from their Pu L3 extended X-ray absorption fine structure (EXAFS) spectra. In addition, their valence and electronic structure near the continuum are evaluated from their Pu L3 X-ray absorption near edge structure (XANES). The colloids are studied without prior separation from solution and compared to results for freshly precipitated amorphous $Pu(OH)_4$(am) and the Pu^{4+} aquo ion.

Independently, Pu(IV) oxyhydroxide colloids are investigated by laser induced breakdown detection (LIBD). We have studied the onset of eigen-colloid formation in an initially colloid free Pu(IV) solution as it is continually diluted. The −log [H^+] and Pu(IV) concentration at which colloids form, as detected by an increase in the LIBD signal, is an indicator as the point crossing over the solubility limit.

Experimental Section

XAFS Sample Preparation. The samples investigated are indicated with capital, bold-face letters in the solubility diagram for Pu(IV) in Figure 1 and summarized in Table 1. Samples **C** through **H** are prepared from a Pu(IV) solution designated sample **A**. Solution sample **A** is prepared from a ^{242}Pu(VI) stock solution by bubbling NO through it. The concentration of the Pu(VI) stock solution is determined prior to reduction from its UV/vis absorption spectrum to be 16.1 mM Pu(VI). Utmost care was taken to avoid oxygen in the samples. All of the aqueous reagents were prepared from oxygen free water. The Pu(IV) solution samples are prepared in a N_2 purged glovebag by appropriate addition of aqueous solutions of milli-Q water, 0.5 M HCl, 1.25 M NaCl, and (only for sample **G**) 1 M NaOH. Sample **F** is prepared by dilution of 111 μL acidic aqueous 16.1 mM Pu(IV) with 889 μL of 0.5 M NaCl. The −log [H^+] values for XAFS samples in Table 1 are measured with a Ross electrode following calibration with commercial reference buffer solutions having −log [H^+] of 4.00 and 7.01. Following the experiments, a control UV/vis measurement of sample **A** is performed. The spectra indicate that the solution contains colloids, but no evidence of oxidation is observed. Sample **B** is produced by electrochemical reduction of a mixture of a different

* To whom correspondence should be addressed. Tel: +49 7247 82 5536. Fax: +49 7247 82 3927. E-mail: Melissa.Denecke@ine.fzk.de.

(1) Conradson, S. D. *Appl. Spectrosc.* **1998**, *52* (7), 252−279.
(2) Fujiwara, K.; Yamana, H.; Fujii, T.; Moriyama, H. *J. Nucl. Fuel Cycle Environ. (Japan)* **2001**, *7*, 17−23.
(3) Capevila, H.; Vitorge, P. *Radiochim. Acta* **1998**, *82*, 11−16.
(4) Kim, J. I.; Kanellakopulos, B. *Radiochim. Acta* **1989**, *48*, 145−150.
(5) Rai, D. *Radiochim. Acta* **1984**, *35*, 97−106.

10.1021/ic049861p CCC: $27.50
Published on Web 06/24/2004

XAFS and LIBD Study of Pu(IV) Hydrolysis

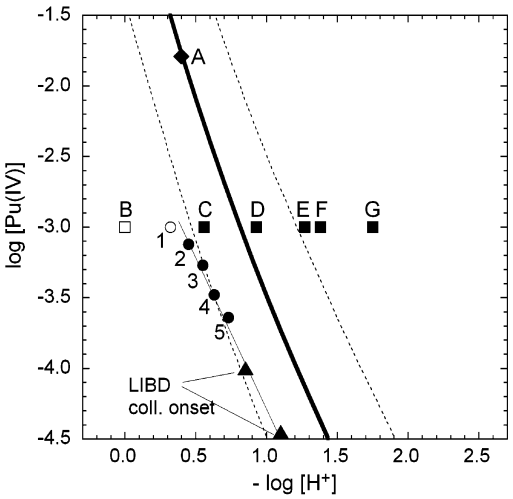

Figure 1. Solubility curve of Pu(IV) using log $K^{\circ}_{sp} = -58.7 + -0.3$ from ref 32. Square symbols marked with letters indicate composition (Pu(IV) concentrations and $-\log [H^+]$) of XAFS solution samples, and circles marked with numbers LIBD samples investigated. Triangles show points of colloid formation observed in analogous dilution series LIBD studies at Pu concentrations lower than 1 mM. See text for details.

Table 1. Summary of Samples Examined by XAFS and LIBD in This Study

ID	sample description
A	16.1 mM Pu(IV) in 0.4 M HCl
B	1 mM Pu(IV) in 1 M $HClO_4$, $-\log [H^+] = 0$
C	1 mM Pu(IV) in 0.5 M NaCl, $-\log [H^+] = 0.56$
D	1 mM Pu(IV) in 0.5 M NaCl, $-\log [H^+] = 0.93$
E	1 mM Pu(IV) in 0.5 M NaCl, $-\log [H^+] = 1.27$
F	1.22 mM Pu(IV) in 0.5 M NaCl, $-\log [H^+] = 1.38$
G	1 mM Pu(IV) in 0.5 M NaCl, $-\log [H^+] = 1.75$
H	precipitated $Pu(OH)_4$ (am)
1	1 mM Pu(IV), I = 0.5 M, $-\log [H^+] = 0.32$
2	0.76 mM Pu(IV), I = 0.5 M, $-\log [H^+] = 0.45$
3	0.54 mM Pu(IV),, I = 0.5 M, $-\log [H^+] = 0.55$
4	0.33 mM Pu(IV), I = 0.5 M, $-\log [H^+] = 0.63$
5	0.23 mM Pu(IV), I = 0.5 M, $-\log [H^+] = 0.73$

^{242}Pu stock solution in 1 M $HClO_4$ to Pu(III) and subsequent oxidation to Pu(IV). The total Pu concentration is assayed by liquid scintillation counting and the tetravalent oxidation state purity also verified by absorption spectroscopy. The amorphous $Pu(OH)_4$(am) (sample **H**) is freshly precipitated from approximately 1 mM Pu(IV) solution by addition of 1 M NaOH to $-\log [H^+]$ between approximately 2.0 and 2.3. The solid is separated from the aqueous solution by ultrafiltration and collected on a cellulose triacetate membrane microfilter (Amicron, area: 10 kDalton, average pore size radius ~1.5 nm). The filter with the wet solid is encased inside a thin latex bag. The solution samples are contained in capped polyethylene vials (4 mm inner diameter), with the caps taped with a thick layer of Parafilm to prevent oxygen intrusion or evaporation. XAFS measurements are performed two to four days after sample preparation.

XAFS Data Acquisition and Analysis. XAFS measurements of samples **A** and **C** through **H** are performed at the Advanced Photon Source (APS), at the BESSRC beamline 12BM, using a Si(111) double-crystal monochromator (DCM). The 12BM beamline is equipped with a collimating and focusing mirror, and the beam spot used is 0.5 mm^2. The incident beam is free of higher harmonic reflections, as is shown by the absence of the corresponding inelastic scattering peaks recorded with an energy dispersive detector. The spectra are calibrated against the first derivative XANES spectrum of a Zr foil, defined as 17.998 keV. Spectra are recorded in both transmission and fluorescence mode. Argon filled ionization chambers are used for transmission spectra detection, and a 13-element energy dispersive solid state Ge detector is used for fluorescence spectra. Samples are studied mounted in the Actinide Facility sample changer[6] for transport and measurement. Three to seven scans are collected and averaged for each sample.

Pu L3 edge XAFS data for sample **B** is collected at the Rossendorfer Beamline (ROBL), BM20, at the European Synchrotron Radiation Facility (ESRF). A 5-element energy dispersive solid state Ge detector is used for fluorescence detection. A Si(111) crystal pair is used in the DCM, and the energy scale is also calibrated against the first derivative XANES spectrum of a Zr foil, as for the samples measured at APS.

EXAFS data analysis is based on standard least-squares fit techniques[7] using the WinXAS[8] and the UWXAFS[9] program packages. The region up to about 700 eV above the Pu L3 edge ($k \sim 13$ Å^{-1}) is investigated. The atomic background function $\mu_0(E)$ is optimized with respect to spurious contributions below ~1 Å in the k^2-weighted Fourier transform (FT) of the data using WinXAS. The ionization energy E_0, the origin for calculation of the $\chi(k)$ function, is fixed at the maximum of the most intense absorption feature—the white line (WL)—in the individual spectra at ~18068 eV. Metric parameters (neighboring atomic distances R_i, mean square radial displacements or EXAFS Debye−Waller factors σ^2_i, and coordination numbers N_i for the different coordination shells i) are determined using the feffit code. Backscattering amplitude and phase shift functions for single scattering paths in a 3-shell PuO_2 cluster (*Fm*3*m* fluorite structure with a lattice constant of 5.396 Å[10]) are obtained from FEFF8.2[11,12] calculations. Prior to analysis, the k^2-weighted EXAFS spectra are Fourier transformed over a k-space range of ~2.7−12.5 Å^{-1}, using symmetric square windows with $\Delta k = 0.2$ Å^{-1} "Hanning sills". All fitting operations are performed in R-space over the individual radial distance ranges given in Table 2. Special care is taken to avoid overinterpretation of the data beyond the limits defined by the number of independent points.[13] The amplitude reduction factor[14] S_0^2 is fixed at 1. Martin et al.[15] applied S_0^2 0.9 in order to reproduce the theoretical coordination number (8) for the first oxygen neighbor shell in the PuO_2 fluorite structure.

The *feffit* code evaluates randomly distributed fit uncertainties as the amount by which a given parameter changes, when values for all other parameters remain fixed, while maintaining the sum of squares of the difference between data and model (Chi^2) below a certain limit (as suggested by Teo[13]). This procedure yields uncertainty values for the nearest neighbor oxygen shell of $\Delta R_O \leq 0.02$ Å and $\Delta N_O \leq 0.4$ for samples **B**, **C**, and **H**, which are modeled

(6) See: http://chemistry.anl.gov:80/heavy-element/actinide/multiple.html (accessed June 2004).
(7) Sayers, D. E.; Bunker, B. A. In *X-Ray Absorption: Techniques of EXAFS, SEXAFS and XANES*; Koningsberger, D. C., Prins, R., Eds.; J. Wiley & Sons: New York, 1988; pp 211−253.
(8) Ressler, T. *J. Phys. IV* **1997**, *7-C2*, 269.
(9) Stern, E. A.; Newville, M.; Ravel, B.; Yacoby, Y.; Haskel, D. *Physica B* **1995**, *208&209*, 117−120.
(10) See: http://www.mrw.interscience.wiley.com/ueic/articles/a21_133/frame.html.
(11) Ankudinov, A. L.; Ravel, B.; Rehr, J. J.; Conradson, S. D. *Phys. Rev. B* **1998**, *58*, 7565−7576.
(12) Ankudinov, A. L.; Rehr, J. J. *Phys. Rev. B* **1997**, *56*, 1712.
(13) Teo, B.-K. *EXAFS: Basic Principles and Data Analysis*; Springer-Verlag: Heidelberg, 1988.
(14) Lee, P. A.; Citrin, P. H.; Eisenberger, P.; Kincaid, B. M. *Rev. Mod. Phys.* **1981**, *53*, 769−806.
(15) Martin, P.; Grandjean, S.; Ripert, M.; Freyss, M.; Blanc, P.; Petit, T. *J. Nucl. Mater.* **2003**, *320*, 138−141.

Table 2. Data Range and Metric Parameters Extracted by Least-Squares Fit of EXAFS Spectra to the EXAFS Equation[a]

ID	fit range $R-\Delta$ (Å)	shell	R (Å)	N	σ^2 (Å^2)	ΔE (eV)	R-factor
A	1.34−4.02	O1	2.24	3.3	0.0031	3.07	0.005
		O2	2.42	0.8	0.0099	3.07	
		Pu	3.86	2.1	0.0076	3.19	
B	1.32−2.67	O	2.38	8.4	0.0077	8.3	0.004
C	1.32−4.08	O	2.35	7.2	0.0094	1.06	0.007
		Pu	3.90	1.9	0.0067	4.64	
D	1.35−4.0	O1	2.20[b]	1.1	0.0004	3.10	0.007
		O2	2.42	4.4	0.0068	3.10	
		Pu	3.90	3.0	0.0085	4.52	
E	1.32−3.96	O1	2.22	0.7	0.0012	2.77	0.013
		O2	2.38	5.6	0.0122	2.77	
		Pu	3.85	4.3	0.0090	2.08	
F	1.35−3.99	O1	2.22	1.5	0.0017	2.51	0.008
		O2	2.39	4.0	0.0059	2.51	
		Pu	3.87	4.2	0.0075	1.71	
G	1.32−3.96	O1	2.29	1.4	0.0080	3.08	0.008
		O2	2.37	5.0	0.0136	3.08	
		Pu	3.87	4.9	0.0075	1.74	
H	1.35−3.99	O	2.32	4.0	0.0104	2.38	0.016
		Pu	3.87	2.4	0.0066	1.84	

[a] See text for error discussion. S_0^2 fixed at 1.0. [b] Denotes fixed value.

using a single oxygen shell. However, in the case of samples **A**, **D**, **E**, **F**, and **G** the strong correlation between the two oxygen shells required for modeling the highly asymmetric neighboring oxygen contributions leads to much higher ΔR_{O1}, ΔR_{O2}, ΔN_{O1}, and ΔN_{O2} values, reflecting the shallow minimum of the fit in a multiple parameter space. Determination of fit parameters for the more distant plutonium backscatterers yields $\Delta R_{Pu} \leq 0.04-0.08$ Å and $\Delta N_{Pu} \leq 1.2$ for samples **A**, **C**, **D**, **E**, **F**, **G**, and **H**. The overall goodness of the fit evaluated by *feffit* is given as the "*R*-factor" (listed in the last column in Table 2), which is Chi^2 scaled by the magnitude of data.[16] $R = 0.02$ signifies that the average deviation between theory and data is two percent.

XANES spectra for samples **A**−**H** are isolated from XAFS scans following subtraction of the preedge background absorption, approximated as a linear function, and normalization of the edge jump (average between 18100 and 18300 eV) to unity. In order to quantify the WL intensity in these spectra, curve-fitting is accomplished by modeling the experimental data using pseudo-Voigt (WL), Gaussian (feature near 18105 eV), and arctan (edge-step) functions. The arctan width is set to the natural Pu L3 line width,[17] whereas the arctan position for samples **A** and **C**−**H** is fixed to the fit value obtained for sample **B**.

LIBD Measurements. The LIBD technique has been described previously[18,19] and shall only be discussed briefly. A pulsed laser is focused into the colloidal suspension and a plasma is ignited selectively when the laser power is great enough and a colloid is present in the focal region. Detecting the plasma by means of its shock wave is hence equivalent to counting colloids. By varying the laser pulse energy, the mean size and number-concentration of colloids can be quantified.[20] Particles down to 5 nm in size can be detected at concentrations well below 10^{-8} M.

The colloid samples investigated with LIBD are indicated with boldface numbers **1** through **5** in Figure 1 and listed in Table 1. Solution **1** is prepared electrolytically similarly to the XAFS sample **B** but using a ^{242}Pu stock solution in 0.5 M HCl. This solution **1** is observed from LIBD measurements to be colloid free at log [Pu] −3.0 and −log [H$^+$] 0.32 (Figure 1, open circle). The −log [H$^+$] of the solution is increased very slowly by dilution with 0.5 M NaCl (<10 μL/min). At the same time, dilution with the NaCl solution also causes a decrease in Pu(IV) concentration. At −log [H$^+$] 0.45, the onset of Pu(IV) colloid formation is observed as a well-defined, sharp increase of the LIBD signal (sample **2**, filled circles). Further dilution of the Pu(IV) solution leads to the colloidal samples **3** through **5** in Figure 1. Analogous dilution series are measured beginning at Pu(IV) concentrations lower than log [Pu] −3.0, and the points of colloid formation are included in Figure 1 (filled triangles). We would like to stress that there is no precipitate or bulk plutonium phase in the classical sense present in these samples during LIBD measurements. The only solid plutonium present is the suspended colloids. Consequently, the thermodynamic equilibrium between solvated Pu(IV) and bulk in a classical solubility study is substituted by an equilibrium between colloidal fraction and solute species in an LIBD experiment.

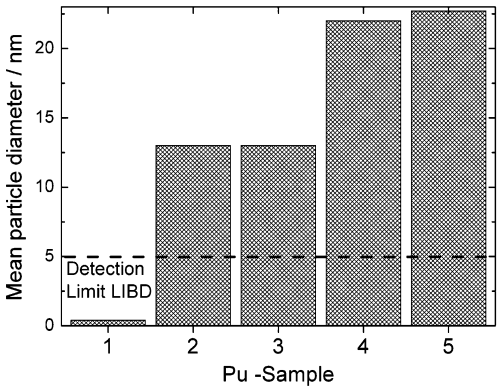

Figure 2. Mean particle diameter for colloids larger than 5 nm (limit of detection) in samples **1** through **5**, as determined with LIBD.

Results

LIBD Measurements. From the LIBD measurements a mean particle diameter for colloids larger than 5 nm (detection limit) is obtained. Figure 2 shows the mean colloid diameter found for samples **1** through **5**. Sample **1** is "colloid free" in the sense that no colloids larger than 5 nm are present. The colloids in samples **2** and **3** are around 12 nm in size. The ones in samples **4** and **5** are almost twice as large.

EXAFS Results. The k^2-weighted EXAFS-functions $\chi(k)$, extracted using WinXAS, are shown in Figure 3 at the left, and the corresponding FT magnitudes are shown at the right-hand side. All spectra exhibit an intense, more or less asymmetric FT peak at ~1.9 Å, corresponding to a phase corrected distance value of about 2.4 Å. This peak represents oxygen atoms comprising the first coordination sphere of the central absorbing Pu(IV) in all samples. Additional peaks or shoulders at about 1.15−1.2 Å, representing a low frequency contribution to the EXAFS, are obvious for all spectra. These features are apparently not an artifact of the μ_0 spline function subtraction, because they are persistent

(16) Newville, M. *FEFFIT—Using FEFF to model XAFS data*; Department of Physics, FM-15, University of Washington: Seattle, 1995.
(17) Krause, M. O.; Oliver, J. H. *J. Phys. Chem. Ref. Data* **1979**, *8*, 329.
(18) Scherbaum, F. J.; Knopp, R.; Kim, J. I. *Appl. Phys. B* **1996**, *63*, 299−306.
(19) Kitamori, T.; Yokose, K.; Sakagami, M.; Sawada, T. *Jpn. J. Appl. Phys.* **1989**, *28*, 1195−1198.
(20) Walther, C.; Bitea, C.; Hauser, W.; Kim, J. I.; Scherbaum, F. J. *Nucl. Instrum. Methods B* **2002**, *195*, 374−388.

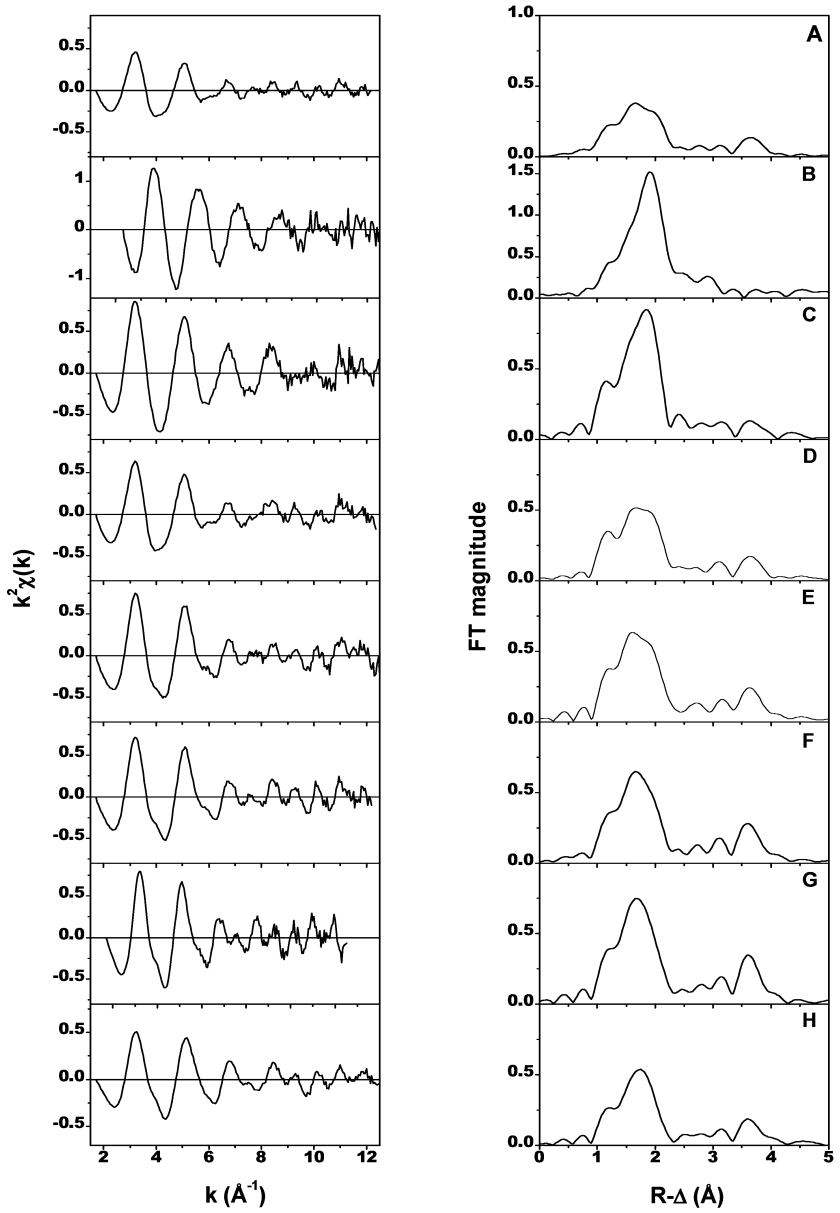

Figure 3. k^2-weighted $\chi(k)$-functions of the samples listed in Table 1 (left panel) and corresponding Fourier transform magnitudes (right panel). Note the different ordinate scale for sample **B**.

in the FT spectra, except for cases where the μ_0 spline is allowed to be flexible as to intolerably remove intensity from the Pu−O peak at $R - \Delta = 1.9$ Å. Other Pu L3 edge EXAFS presented in the literature, including data taken at different experimental stations, also show these low-R features in the FT spectra (see, e.g., ref 21). A Pu−O distance of less than 2 Å makes no physical sense (the sum of ionic radii is 2.26 Å for Pu(IV) with 6-fold coordination[22]), so that we expect these features to be due to atomic contributions or to multielectron excitations in the EXAFS regime.[23] Supporting the latter hypothesis, the FEFF8.2 calculation using a three-shell (45 atom) PuO_2 cluster in Cartesian coordinates displays an energy dependence of μ_0 with discontinuities, evidence for multielectron excitations.[24] Despite its continual presence, inclusion or omission of this low-R feature by broadening or narrowing the R-space fit range does not significantly influence the fit results.

The EXAFS metrical parameters obtained from fits of the EXAFS equation to the experimental data are summarized in Table 2. Figures 4 and 5 display experimental data and the fit results in R-space and backtransformed k-space for

(21) Richmann, M. K.; Reed, D. T.; Kropf, A. J.; Aase, S. B.; Lewis, M. A. *J. Nucl. Mater.* **2001**, *297*, 303−312.
(22) Greenwood, N. N.; Earnshaw, A. *Chemie der Elemente*; VCH Verlagsgesellschaft: Weinheim, 1988.
(23) Wang, W.-C.; Yu, C. *Phys. Status Solidi A* **1998**, *168*, 351−357.
(24) Rehr, J. J.; Zabinsky, S. I.; Ankudinov, A.; Albers, R. C. *Physica B* **1995**, *208&209*, 23−26.

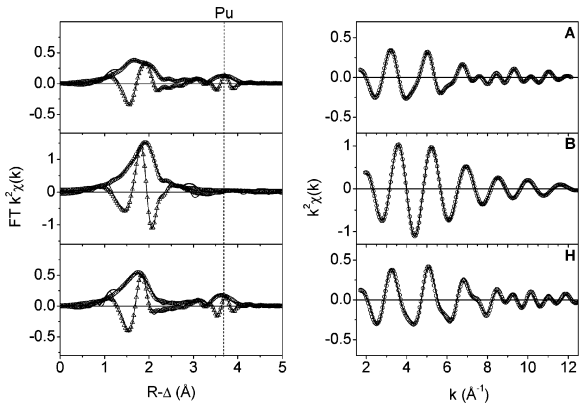

Figure 4. *R*-space fit results for samples **A**, **B**, **H**. Left panel: FT magnitude of EXAFS data (solid line), fit magnitude (open circles), FT imaginary part (thin solid line), and fit imaginary part (open triangles). Right panel: corresponding Fourier-filtered data (solid line, ranges given in Table 2) and backtransformed fit (open circles). Note the different ordinate scale for sample **B**. Dashed line marks Pu−Pu interaction.

the sample spectra, segregated into two groups. The first group (samples **A**, **B**, and **H**, Figure 4) includes the stock solution and reference compounds (Pu^{4+} aquo ion and solid $Pu(OH)_4$(am) precipitate), whereas the second group (samples **C**−**G**, Figure 5) tracks the fate of the colloidal suspensions after crossing the solubility threshold when successively increasing −log [H^+]. The presentation of the results below is structured according to these two groups of sample sets.

Only sample **B** (1 mM Pu(IV) in 1 M $HClO_4$, −log [H^+] 0) exhibits a spectrum dominated by a single sinusoidal contribution, originating from backscattering on a single shell of oxygen atoms. Sample **A,** the Pu(IV) stock solution, as well as the solid sample **H** and the colloidal suspensions **C**−**G** exhibit a more complex absorption fine structure. This includes the appearance of a high-frequency EXAFS contribution, which is found in the fit procedure to be associated with a Pu−Pu interaction.

Samples A, B, H. The experimental FT magnitudes and fits for samples **A**, **B**, and **H** and their corresponding Fourier-filtered data are shown in Figure 4. The EXAFS spectrum for solution **B** exhibits the signature of the Pu^{4+} aquo ion[25] with ∼8 oxygen atoms at 2.38 Å and $\sigma^2 = 0.0077$ Å^2 (Table 2). The spectra of the amorphous precipitate (sample **H**) and the aqueous stock solution (sample **A**, 16.1 mM Pu(IV) in 0.4 M HCl) exhibit more complex structures. Above the spurious low-*R* feature, the major oxygen FT peak appears strongly dampened and broadened as compared to the aquo ion (note the different ordinate scale for sample **B** in Figure 4). An additional FT peak surmounting the noise level is observed in both spectra between about 3.3 and 4.1 Å. In contrast to samples **B** and **H**, we did not succeed in modeling the FT of sample **A** between 1.34 and 2.32 Å using a single shell of oxygen backscatterers. Addition of a second oxygen scattering path (O2) leads to a reasonable fit for sample **A** with about three oxygen atoms at 2.24 Å and ∼1 further distant oxygen atom at 2.42 Å. ΔE_0 for the two adjacent oxygen shells is confined to the same value. The large asymmetry of the Pu−O shell in sample **H** is reflected by a σ^2 value of >0.01 Å^2. A large σ^2 value is also obtained in the fit when an additional asymmetry term is added (third cumulant). The apparent number of coordinating oxygen atoms (∼4) obtained for samples **A** and **H** is reduced by 50% compared to the aquo ion and the theoretical value of 8 expected for crystalline PuO_2. There is good agreement between FT imaginary part and magnitude of the fit and the experimental feature located between 3.3 and 4.1 Å (dashed line in Figure 4) using a Pu−Pu interaction for samples **A** and **H**. In both samples Pu coordination numbers (2.1 and 2.4) and Pu−Pu second next-neighbor distances (3.86 and 3.87 Å) are nearly identical.

Samples C, D, E, F, G. The experimental FT magnitudes and fits for samples **C**, **D**, **E**, **F**, and **G** and the corresponding Fourier-filtered data are shown in Figure 5. All spectra exhibit features similar to those of samples **A** and **H** described in the preceding paragraph. This is also reflected by the fit parameters listed in Table 2. However, a certain trend can be discerned going from sample **C** (1 mM Pu(IV) at −log [H^+] 0.56) to the precipitate sample **H**. The apparent splitting of the oxygen neighbor shell due to the inherent disorder in the colloidal hydroxide particles initially increases, to then decrease again with increasing −log [H^+]. This trend is also reflected by the shape of the oxygen peak in the FT spectra (Figure 5, left panel). The Pu second next-neighbor coordination number observed for the solution samples **C** through **G** increases with increasing −log [H^+].

Sample **C** at the onset of polynucleation and the precipitate sample **H** show a single oxygen distance value similar to that expected for PuO_2(cr) (2.33 Å). The mean square radial displacement is increased (and, hence, the apparent coordination number drops) for the amorphous solid. For samples **D**−**F** the nearest neighbor oxygen metrical parameters are grouped in a minor contribution at a shorter (2.20−2.24 Å) and a major contribution at a longer (2.38−2.42 Å) distance. This ratio seems to be reversed for the high concentration stock solution **A**. In the case of sample **G**, the distance differences between the shells O1 and O2 has decreased to 0.08 Å (2.29 and 2.37 Å, with a mean value of 2.33 Å). The Pu second next-neighbor positions obtained for samples **A** and **C**−**H** only slightly vary between a 3.86 and 3.90 Å distance from the absorber and seem to be barely affected by the disorder fluctuations present in the oxygen nearest neighbor shell. We observe Pu−Pu distances that are 0.05 to 0.09 Å elongated compared to the theoretical value of 3.81 Å for PuO_2(cr). Our results are visualized in Figure 6, where the coordination numbers obtained for the individual shells are plotted against the corresponding distance values for samples **A**−**H**.

XANES Results. The normalized XANES spectra for samples **B**, **C**, **E**, **F**, and **H** are depicted in Figure 7. No shift in the energy of the XANES WL is evident in any of the spectra, nor is there any structure at the high energy side of the WL characteristic for actinyl dioxo moieties, testimony for all samples being in the tetravalent state. An example of a fit result to the XANES, performed as described in the

(25) Ankudinov, A. L.; Conradson, S. D.; Mustre de Leon, J.; Rehr, J. J. *Phys. Rev B* **1998**, *57* (13), 7518−7525.

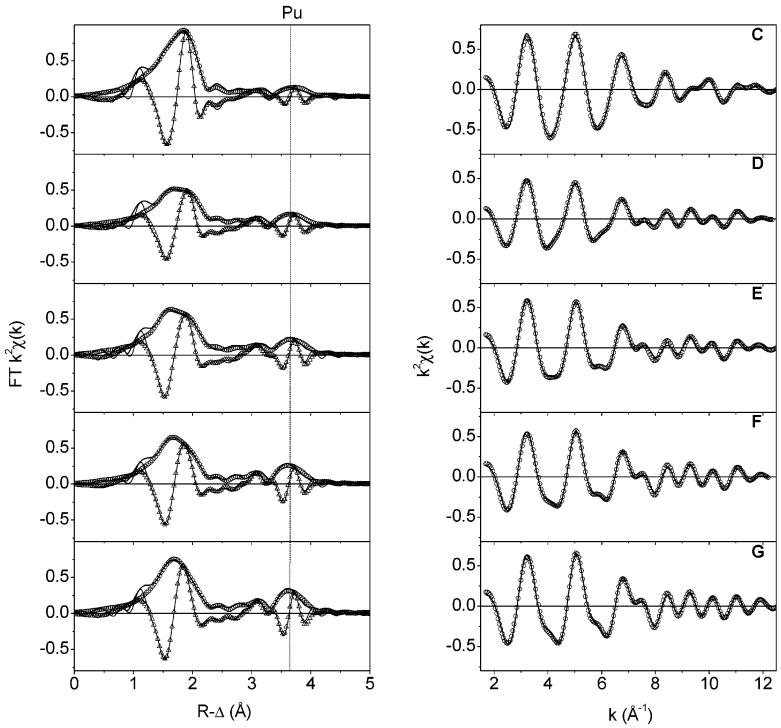

Figure 5. *R*-space fit results for aqueous colloidal suspension samples (**C**, **D**, **E**, **F**, **G**). Left panel: FT magnitude of EXAFS data (solid line), fit magnitude (open circles), FT imaginary part (thin solid line), and fit imaginary part (open triangles). Right panel: corresponding Fourier-filtered data (solid line, ranges given in Table 2) and back-transformed fit (open circles). Dashed line marks Pu−Pu interaction.

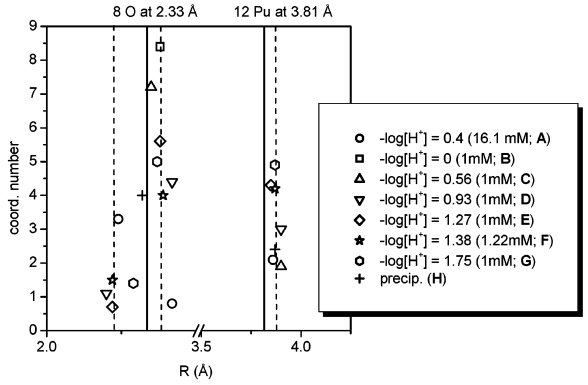

Figure 6. Graphical representation of EXAFS metrical parameters for samples **A** through **H**: coordination numbers N_i plotted vs interatomic distances R_i (see text for details). Solid vertical lines mark theoretical PuO_2 first and second next Pu neighbor distances.

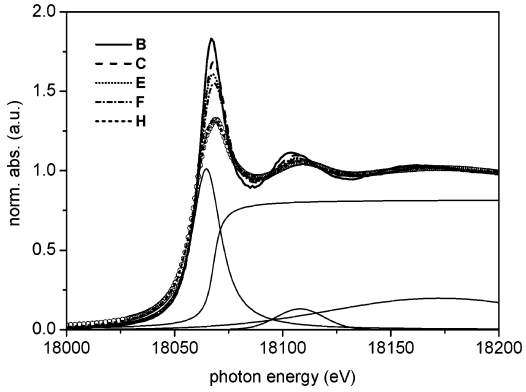

Figure 7. Pu L3 edge XANES spectra for Pu^{4+}(aq) (**B**), Pu(IV) hydroxide colloids (**C**, **E**, **F**), and precipitated $Pu(OH)_4$(am) (**H**), including least-squares fit (open circles) and fit components for sample **H** (see text for details).

Experimental Section, for sample **H** is shown in the same figure. A significant change in the intensity of XANES features is observed, which is predominant for the WL. The WL intensity decreases going from the Pu^{4+} aquo ion (**B**) to the amorphous $Pu(OH)_4$(am) precipitate (**H**). Figure 8 shows that there is an almost linear correlation between the decrease of WL peak height (determined as the pseudo-Voigt profile height in the XANES fit result) and −log [H^+]. Note that the pseudo-Voigt profile area, reflecting the integral $2p_{3/2} \rightarrow 6d$ transition probability, remains constant for all samples. Sample **A** and the solid $Pu(OH)_4$(am) sample **H** exhibit the lowest WL intensities.

Discussion

EXAFS. The metric parameters obtained for 1 mM Pu(IV) at −log [H^+] 0 (sample **B**) fully agree with results obtained in previous EXAFS investigations of the Pu^{4+} aquo ion.[25] Eight to nine water molecules (depending on the uncertainty in the S_0^2 value) coordinate Pu(IV) at a 2.38 ± 0.02 Å Pu−O bond distance.

The highly asymmetric oxygen coordination in the colloid samples **A** and **C**−**G** and the amorphous precipitate **H** unambiguously indicates the presence of different Pu−O bond lengths from different coordinating oxygen atoms ($-O^-$, −OH, OH_2). However, we cannot use these metric

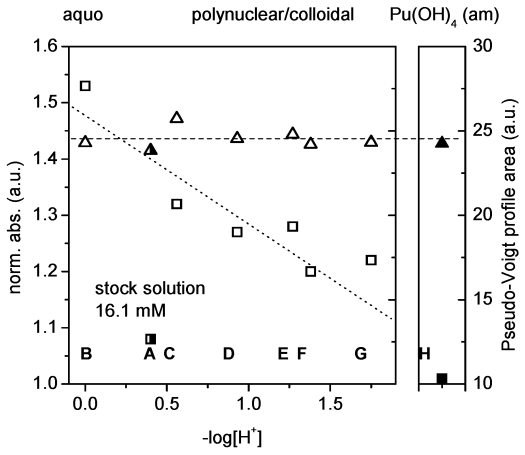

Figure 8. Pseudo-Voigt profile height (squares) as a measure of the white line intensity and integrated area (triangles) from fit results to the XANES for samples **A**−**H**. Sample **A** is marked with a different symbol to accentuate its different behavior, as it is an oversaturated solution.

parameters obtained specifically for formulating a precise structure model, as does Conradson.[1] This is because the bond length resolution in EXAFS is limited by $\Delta R \approx \pi/2k_{max}$ and is 0.13 Å in this study. This renders it difficult, and for some distances impossible, to separate contributions from multiple, closely spaced backscatterers. We can and will further below, however, postulate a model of colloid growth, which agrees with the trends in the EXAFS and XANES data, combined with LIBD and UV/vis spectroscopy results.

In the case of samples **D**−**G** one can observe the splitting between a dominant oxygen contribution at average distances slightly larger than that for PuO_2(cr) and a smaller contribution at a significantly shorter distance (around 2.22 Å). Only for sample **A**, the colloids formed in the more concentrated stock solution, the short distance contribution seems to be dominant. In agreement with refs 1 and 26, we assign this shorter Pu−O distance to hydroxyl groups. The Pu−Pu distances remain hardly influenced by the splitting in the nearest neighbor oxygen shell, supporting the hypothesis of the presence of a rather rigid −Pu−O−Pu− "backbone" in the nanoparticle lattice as the basis of the polynuclear and/or colloidal Pu(IV) hydrolysis species. This is also corroborated by FEFF8.2 simulations presented in Figure 9. In this figure a 45-atom fluorite structure simulation of the PuO_2(cr) EXAFS (top row) is compared to results obtained for a defect and distorted cluster (bottom row), where Pu voids in the Pu sublattice represent Pu defect sites. The agreement between the simulation and the EXAFS of the colloid species (e.g., sample **F**) is highly convincing.

XANES. There are two possible explanations for the WL intensity variations observed in the XANES regime. As already pointed out in our previous investigation of Th(IV) hydrolysis products,[27] one is an extrinsic effect, resulting from charge transfer, and the other an intrinsic effect, resulting from the variation in particle size. The WL feature is associated with a dipole allowed transition from a $2p_{3/2}$ core level into an empty 6d state, lying just above the continuum. Changes in the intensity of the WL can result from variations in the occupancy of d states caused by charge transfer between the central absorbing atom and its surrounding nearest neighbors, an extrinsic effect (e.g., refs 28 and 29). Intrinsic particle size effects leading to variations in L3 XANES WL intensities have been reported for, e.g., spectra of metallic nanoparticles (e.g., ref 30). The WL intensity variation, in this case, results from variation of the density of state (DOS) for atomic clusters as a function of the number of atoms in the cluster or the ratio of surface atoms to atoms in the bulk.

No significant variation in WL area, determined from least-squares fits to the data, is observed for the Pu(IV) samples (see Figure 8). The integral transition probability remains constant, excluding any charge transfer to the d-like final states. Again we conclude that the WL intensity variation is likely a particle size effect similar to that reported in ref 27. Of all the Pu(IV) samples investigated here, the Pu^{4+} aquo ion can be assumed to have the most molecular orbital (MO)-like 6d final state. Because the $2p_{3/2} \rightarrow$ 6d dipole allowed transition probability (or square root of the absorption coefficient) is proportional to the energy-dependent density of the 6d final states, the MO-like, more localized final state has the greatest transition probability of these samples and, hence, largest WL intensity. The 6d state of the condensed amorphous $Pu(OH)_4$(am) precipitate is better described as a band than as a discrete MO. The density of the 6d-like final state is spread over a larger energy interval. With it, the height of the WL is observed to be lower than for all other samples, due to the subsequent lower transition probability. At the same time, the width of the WL feature increases significantly (Figure 7). The colloid samples **C**−**G** represent an intermediate situation. Here the particle size, as reflected by the decreasing WL height, increases with increasing −log [H^+]. If small Pu colloid species exhibit 6d-like final states intermediary between the MO picture used for the aquo ion and the band structure picture describing the condensed system of sample **H**, the DOS of the colloids should tend toward that of a bulk sample's band structure for large clusters. This is obviously the case. Note that the WL height for sample **A**, which is at a strong oversaturation Pu(IV) concentration above the solubility limit, approaches that for the $Pu(OH)_4$(am) precipitate **H**. The interpretation of WL height decrease to result from photoelectron scattering on an increasingly disordered crystal lattice, as proposed by Conradson et al.,[31] does not hold here. The WL decrease in Figure 7 must be related to increasing particle size, as the EXAFS results demonstrate this decrease in WL height to be also associated with an increase in the ordering of the

(26) Denecke, M. A.; Marquardt, C. M.; Rothe, J.; Dardenne, K.; Jensen, M. P. J. *Nucl. Sci. Technol.* **2002**, *3*(Suppl.), 410−413.
(27) Rothe, J.; Denecke, M. A.; Neck, V.; Müller, R.; Kim, J. I. *Inorg. Chem.* **2002**, *41*, 249−258.
(28) Mansour, A. N.; Cook, J. W., Jr.; Sayers, D. E. *J. Phys. Chem.* **1984**, *88*, 2330−2334.
(29) Lee, Y. S.; Whang, C. N.; Jeon, Y.; Choi, B. S.; Han, T. J.; Woo, J. J.; Croft, M. *Nucl. Instrum. Methods Phys. Res. B* **1997**, *129*, 387−391.
(30) Bazin, D.; Sayers, D.; Rehr, J. J.; Mottet, C. *J. Phys. Chem. B* **1997**, *101*, 5332−5336.

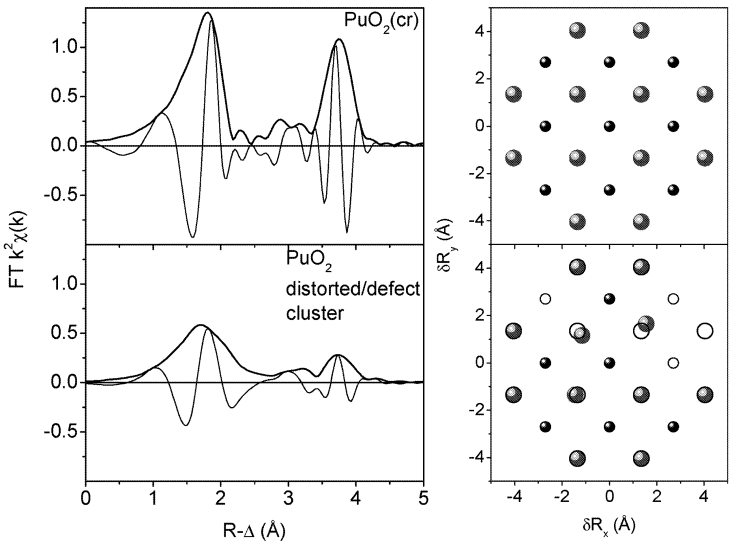

Figure 9. FEFF8.2 calculations for 3-shell fluorite structure PuO_2 cluster (left panel, top) and distorted cluster with defect sites (left panel, bottom) simulating local structure in the colloid samples. The right panel shows the projection of the clusters along the Cartesian *z*-axis. Small dark spheres represent metal cations, large spheres oxygen atoms, and circles "voids" or defect sites. See text for details.

−Pu−O−Pu− backbone structure of the colloids. It is also associated with an increase in order of the oxygen neighbor shell for solution samples at the highest −log [H^+]. The decrease in WL height is, hence, not associated with increasing disorder.

LIBD. Observation of colloid formation in the LIBD experiments is evidence for exceeding the solubility limit. Macroscopically, the solubility limit is defined as the concentration where the total amount of a substance is no longer present in ionic form but instead forms a precipitate. The "precipitate" found in the LIBD experiment is colloids, which are so small that they remain suspended due to Brownian motion. Plotted in Figure 1 (solid line) is the solubility curve of Pu(IV) according to ref 32 along with experimental errors (dashed lines) for

$$\log K^{\circ}_{sp} = (\log [Pu^{4+}])(\gamma_{Pu}) + 4(\log [OH^-])(\gamma_{OH}) = -58.7 + -0.3$$

the γ values being the ion activity coefficients. The points of colloid formation observed from LIBD (sample **2** and filled triangles) all lie close to the lower limit of the log K°_{sp} curve indicated. This might be expected since this nanoscopic LIBD approach for solubility determinations is more sensitive than most classical methods. A detailed description how to obtain solubility data from the LIBD experiments by using ion activity coefficients and hydrolysis constants is presented, e.g., in ref 33.

Clues to the formation mechanism of the colloids may also be extracted from this data. It is well-known that Pu(IV) undergoes hydrolysis even under very acidic conditions. For a HCl/NaCl solution of 0.5 M ionic strength and −log [H^+] 0.6, $Pu(OH)_1^{3+}$ and $Pu(OH)_2^{2+}$ should account for more than 80% of the solvated Pu(IV). The remaining 20% is Pu^{4+} aquo ion species, as calculated from the hydrolysis constants of Metivier et al.:[34]

$$Pu^{4+} + 2H_2O \leftrightarrow Pu(OH)_2^{2+} + 2H^+ \quad (1)$$

Colloids may form according to a generalized reaction

$$Pu(OH)_2^{2+} + 2H_2O \leftrightarrow Pu(OH)_{4(coll)} + 2H^+ \quad (2)$$

with $Pu(OH)_{4(coll)}$ designating the presumably oxyhydroxide complex $Pu_nO_p(OH)_{4n-2p}(H_2O)_z$ ($0 \le p \le 2n$). The presence of different oxygen atom types coordinating Pu(IV) indicated in the EXAFS results agrees with the formulation $Pu_nO_p(OH)_{4n-2p}(H_2O)_z$. The expression for the reaction for colloid formation according to reaction 2 is in agreement with the fact that the points of colloid formation in Figure 1 show a linear dependence on −log [H^+] with slope −2. The slope analysis alone only gives information on the ratio between the stoichometric coefficients of Pu(IV) and OH^- and does not allow one to distinguish between the mononuclear $Pu(OH)_2^{2+}$ and any polynuclear species of the form $[Pu(OH)_2]_n^{2n+}$ as actual reactant for colloid formation. However, additional information may be drawn from UV/vis investigations. We have spectroscopically detected a decrease in solvated Pu(IV) species considerably below the solubility limit, which is given in Figure 1, without any observable increase in another Pu oxidation state. The decrease in absorption cannot be due to hydrolysis, since

(31) Conradson, S. D.; Abney, K. D.; Begg, B. D.; Brady, E. D.; Clark, D. L.; den Auwer, C.; Ding, M.; Dorhout, P. K.; Espinosa-Faller, F. J.; Gordon, P. L.; Haire, R. G.; Hess, N. J.; Hess, R. F.; Keogh, D. W.; Lander, G. H.; Lupinetti, A. J.; Morales, L. A.; Neu, M. P.; Palmer, P. D.; Paviet-Hartmann, P.; Reilly, S. D.; Runde, W. H.; Tait, C. D.; Veirs, D. K.; Wastin, F. *Inorg. Chem.* **2004**, *43*, 116−131.
(32) Knopp, R.; Neck, V.; Kim, J. I. *Radiochim. Acta* **1999**, *86*, 101−108.
(33) Neck, V.; Müller, R.; Bouby, M.; Altmaier, M.; Rothe, J.; Denecke, M. A.; Kim, J. I. *Radiochim. Acta* **2002**, *90*, 485−494.
(34) Metivier, H.; Guillaumont, R. *Radiochem. Radioanal. Lett* **1972**, *10*, 27.

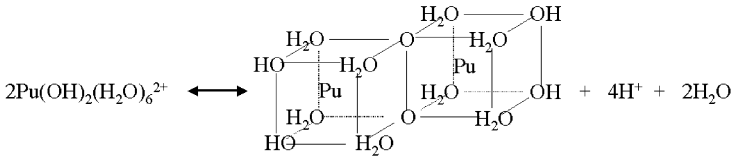

Figure 10. Hydrolysis and condensation of two monomeric $Pu(OH)_2(H_2O)_6^{2+}$ units to an edge sharing, charge-neutral, binuclear species.

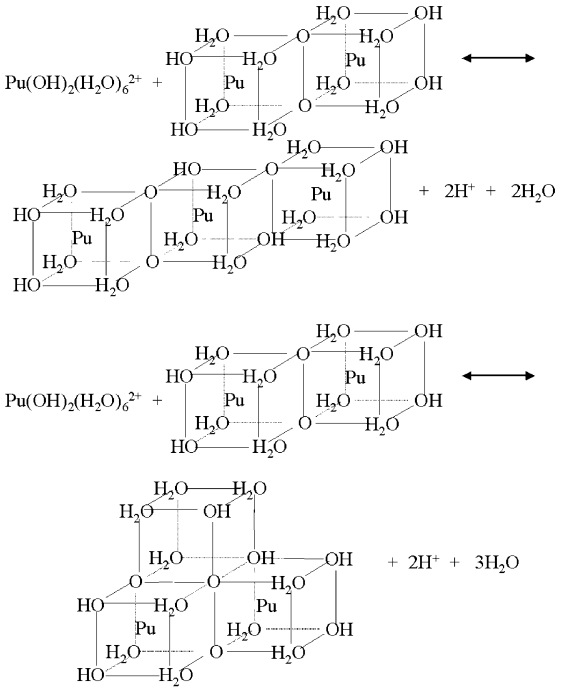

Figure 11. Formation of a trinuclear species through hydrolysis and condensation of a monomeric $Pu(OH)_2(H_2O)_6^{2+}$ unit with a binuclear species to form a single edge sharing, charge-neutral species as product (top) or a double edge sharing species with a common corner (bottom).

the optical absorption coefficient of Pu(IV) remains constant for all $Pu(OH)_n^{4-n+}$ complexes. Polynuclear species, however, do not exhibit strong spectral absorption features, and the decrease in signal is attributed to formation of small polynuclear oligomers, formed by a fraction of the Pu(IV). We will return to this fact in the discussion of our model for colloid growth. Two examples of the simplest of such oligomers (binuclear and trinuclear neutral species) are depicted in Figure 10 and Figure 11. With increasing $-\log [H^+]$, above the initial absorption decrease, a further decrease in the UV/vis absorption is observed, eventually leading to a complete disappearance of the Pu(IV) peak, which is due to quantitative formation of colloids, verified by LIBD. This behavior is analogous to measurements on Np(IV) with laser-induced photoacoustic spectroscopy (LIPAS).[35] Combined LIBD and UV/vis results give the following picture: colloid formation is preceded by formation of small polynuclear species, too small to be detected by LIBD (<5 nm), but causing the first UV/vis absorption decrease. A subsequent growth process with increasing $-\log [H^+]$ leads to the formation of colloids larger than 5 nm, which are detectable directly by LIBD.

Analogous LIBD solubility experiments on tetravalent thorium[36] proved the emerging colloids to be long term stable species, the size of which is determined by the amount of oversaturation of the solution (corresponding to the relative vertical distance from the solubility curve in Figure 1). A similar behavior for fresh Pu(IV) colloids follows from Figure 2. The mean colloid size increases from 12 nm in sample **2** to almost 25 nm in sample **5**. We cannot determine the structure of these colloids directly from the LIBD data, however. Lloyd et al.[37] suggested a cubic fluorite structure, inferring the chemical state $n(PuO_2)$, which is in contradiction with the equilibrium of these colloids with a $Pu(OH)_n^{(4-n)+}$ species. Fujiwara et al.[2] suggest formation of polynuclear species $Pu_{4n}O_{2n}(OH)_{12n}(H_2O)_{4n+5}$, which grow in a stepwise fashion from $Pu(OH)_4(H_2O)_4$ units under loss of water. Their model of colloid growth ultimately leads to PuO_2(cr) formation. Because we cannot explain the LIBD experimental results by the formation of colloids consisting of pure crystalline particles, as it would contradict the observed -2 slope, the polynuclear oligomers formed at low $-\log [H^+]$ below the solubility limit may serve as cores or crystallization centers for colloid formation, which become covered by an amorphous hydroxide layer when the solubility for $Pu(OH)_4$ is exceeded. The growth of an amorphous hydroxide layer would fulfill the slope -2. It would, however, contradict our EXAFS findings that show the structural order of the colloids to increase with size. That small PuO_2 oligomers form is supported by the findings of Kim et al.,[4] who measured a solubility product of PuO_2 (log [Pu] -3.6, 1 M $HClO_4$), 2 orders of magnitude lower than for $Pu(OH)_4$ (log [Pu] -1.5, 1 M $HClO_4$), and could not separate the colloidal fraction by filtration, probably due to their small size.

We now compare these proposed mechanisms of colloid formation with the EXAFS results. Sample **B**, well below the solubility of $Pu(OH)_4$ and at $-\log [H^+]$, where the mononuclear (hydrated) Pu^{4+} dominates (less than 50% hydrolyzed species), shows a single oxygen shell due to eight coordinated water molecules. No Pu−Pu interaction is observed, since there are little or no polynuclear species, further confirmed by UV/vis spectroscopy. The EXAFS sample **A** contains solvated $Pu(OH)_n^{(4-n)+}$ species along with a large fraction of colloids. Due to the strong oversaturation of solution **A** with respect to the solubility curve given by the LIBD experiments, the appearance of its UV/vis spectrum (not shown), and the XANES results, the colloids most likely are large in size and are composed of amorphous

(35) Neck, V.; Kim, J. I.; Seidel, B. S.; Marquardt, C. M.; Dardenne, K.; Jensen, M. P.; Hauser, W. *Radiochim. Acta* **2001**, *89*, 439−446.
(36) Bitea, C.; Müller, R.; Neck, V.; Walther, C.; Kim, J. I. *Colloids Surf. A* **2003**, *217*, 63−70.
(37) Lloyd, M. H.; Haire, R. G. *Radiochim. Acta* **1978**, *25*, 139.

$Pu(OH)_4(am)$ or at least have a thick outer layer of $Pu(OH)_4(am)$. The dominance of the short Pu−O distance associated with ligated hydroxyl groups and a small coordination number for the Pu shell in this sample's EXAFS, similar to that observed for the amorphous $Pu(OH)_4(am)$ precipitate (sample **H**), can be considered to support the conclusion that the colloids in **A** are $Pu(OH)_4(am)$-like.

Samples **C** through **G** show a trend toward increasing Pu coordination number up to N_{Pu} 4.9, while the Pu−Pu distance remains between 3.85 and 3.90 Å. The apparent order in the sample Pu sublattice increases with increasing $-\log [H^+]$ and colloid size. A mechanism of colloid formation and growth from agglomeration of ordered oligomers is consistent with the observed increase in Pu sublattice order; simple growth of a wholly amorphous layer on core centers is not. As we have shown, the presence of oligomers is indicated by the UV/vis absorption decrease. If a mechanism involving growth of an amorphous layer on core centers were valid, then the trend of the colloids from samples **C** to **G** should approach that of sample **H**, the amorphous precipitate. The Pu sublattice of sample **H** is presumably more disordered, as reflected in the fit value for N_{Pu} 2.4. The colloid solution samples do not become more disordered but more ordered as their size increases. An agglomeration of crystalline PuO_2 oligomers for colloid growth ($n(PuO_2)$) could explain the observed increase in Pu sublattice order with increasing particle size in the solution samples. However, this model is inconsistent with both the observed −2 slope of the LIBD solubility curve in Figure 1, with the observed splitting of the Pu−O coordination sphere (Table 2), and with the simulation presented in Figure 9, indicating the presence of defect sites in the Pu sublattice. The EXAFS analysis also indicates that −OH ligands are present in the colloid containing samples at relatively short distances. If the colloids were a cubic fluorite structure of $n(PuO_2)$, we would not expect the −OH distance to be observed throughout.

We propose a model of eigen-colloid formation, which is consistent with the XAFS, LIBD, and UV/vis data and similar to the model of Fujiwara et al.[2]. We envisage Pu(IV) eigen-colloid formation through growth and agglomeration of small oxyhydroxide $Pu_nO_p(OH)_{4n-2p}(H_2O)_z$ oligomers, which themselves form through condensation of monomeric units. For the model to be consistent with XAFS, LIBD, and UV/vis data, monomeric solvated Pu(IV) species must disappear before colloids >5 nm actually form, and colloid formation must entail splitting of the nearest-neighbor oxygen shell, provide for the presence of a −Pu−O−Pu− backbone having a face-centered cubic (fcc) Pu sublattice in the colloid structure, whose static order increases with colloid size, and involve a −2 slope dependency on solubility versus $-\log [H^+]$. The following model of Pu(IV) oxyhydroxide colloid formation through growth and agglomeration of small oligomers fulfills these requirements.

Let us begin by picturing condensation of monomeric units to form oligomers in our scheme of eigen-colloid formation. We consider here the smallest and simplest possible oligomers, binuclear and trinuclear species formation from monomeric units. These are the simplest and, hence, easiest to visualize. They also represent the smallest building blocks, from which we may conceive building the colloid structure. Consider a reaction of hydrolysis coupled with condensation of two monomeric species to form a dimer of cubic units connected at their edges:

$$2Pu(OH)_2(H_2O)_6^{2+} + xH_2O \leftrightarrow Pu_2O_p(OH)_{8-2p}(H_2O)_{6+p} + 4H^+ + (2+x)H_2O \quad (3)$$

An example of reaction 3 to one of the possible products ($p = 2$) is depicted in Figure 10. The units are connected at their edges, because a Pu−Pu distance near that observed in the EXAFS results; joining them at their faces or at their corners would result in distances too short or too long, respectively. We choose to formulate reaction 3 using the octacoordinate monomer as reactant, as EXAFS results suggests an average Pu(IV) coordination number of eight at low $-\log [H^+]$. Using a number of water molecules coordinating the monomeric charged species other than eight would merely change the stoichiometry factor for the number of water molecules in reaction 3. We also choose hydrated $Pu(OH)_2^{2+}$ as the reactant as it fulfills the −2 slope dependency needed to be in agreement with LIBD results. In reaction 3, oxide bridge links may form via the condensation reaction equivalent $2OH^- \leftrightarrow H_2O + O^{2-}$. The number of oxide links from this special condensation reaction is "*p*" in reaction 3.

Note that reaction 3 is a generalized reaction scheme for binuclear species formation. The actual mechanism may proceed by initial hydrolysis of monomeric units according to

$$Pu(OH)_2(H_2O)_6^{2+} \leftrightarrow PuO_p(OH)_{4-2p}(H_2O)_{4+p} + 2H^+$$

with subsequent condensation to $Pu_2O_p(OH)_{8-2p}(H_2O)_{6+p}$ under loss of two water molecules. It may also proceed via condensation of $Pu(OH)_2(H_2O)_6^{2+}$ units followed by release of protons to lower charged or noncharged species:

$$2Pu(OH)_2(H_2O)_6^{2+} \leftrightarrow Pu_2(OH)_4(H_2O)_{10}^{4+} + 2H_2O \leftrightarrow (p+x)H^+ + Pu_2O_p(OH)_{4-p+x}(H_2O)_{10-x}^{(4-p-x)+}$$

with $x \le 4$ and $p \le 4 - x$. This process would also fulfill the Pu(IV):OH^- ratio of 2 expected from LIBD results.

In visualizing formation of the next higher polynuclear species, a trinuclear species from a binuclear species and an additional monomeric unit (in effect equivalent to reaction of three monomeric units), we must again keep in mind that ultimately a fcc Pu sublattice with an approximate 3.87 Å distance between Pu atoms should form. This is possible through connection of a third monomeric $Pu(OH)_2(H_2O)_6^{2+}$ unit to a dimer either in the same pattern as for the formation of the binuclear complex (i.e., attachment along cube edges to form a chain with general formula $Pu_nO_p(OH)_{4n-2p}(H_2O)_{2n+2+p}$) leading to a $Pu_3O_p(OH)_{12-2p}(H_2O)_{8+p}$ species, or by attaching a third monomeric $Pu(OH)_2(H_2O)_6^{2+}$ unit along two edges of neighboring cubes of a dimer, resulting in a trimer of cubes

sharing one common corner, $Pu_3O_p(OH)_{12-2p}(H_2O)_{7+p}$. Examples of these two possibilities for the formation of trimers (both with $p = 3$) are shown in Figure 11. As for the dimer reaction, it is feasible that the actual mechanism involves hydrolysis with subsequent condensation, condensation of charged species followed by release of protons, or any combination thereof. It is not possible to say from our data which mechanism actually occurs, in what order, or if it occurs stepwise at all. The central factor in this scheme is that the structure of growing oligomers occurs in a manner resulting in Pu−Pu distances near 3.87 Å, that small oligomers form, as indicated by UV/vis results, and that the Pu(IV):OH^- ratio of 2 is adhered to.

We can imagine that growth to larger oligomers proceeds by condensation of dimeric and trimeric units either with one another or with other monomeric units, thereby uniting their cube edges. If we imagine continued linking together of such units at their edges in all dimensions, ultimately a fcc arrangement of Pu(IV) cations forms. This represents the Pu sublattice or −Pu−O−Pu− backbone in the colloid particle structure, in accord with our EXAFS results. The elongation of the Pu−Pu distance in the colloids over that for PuO_2(cr) observed in the EXAFS can be considered to result from the larger size of the hydrated primary building blocks comprising the colloids, compared to $Pu(O)_8$ cubic building blocks of the crystalline compound.

Note that the formation of polymeric oligomers via condensation of monomeric units at their corners or cube faces is also feasible. However, the Pu sublattice of the resulting oligomers is no longer fcc. Such reactions may be the source of the defects in the Pu sublattice (cf. Figure 9 and related discussion). Introduction of a corner sharing polymer into a growing edge sharing oligomer breaks up the fcc Pu sublattice, because the unlike polymers do not fit together in a manner similar to matching puzzle pieces. This would lead to empty cubes or Pu defect sites. If the reader has ever played the computer game 3D Tetris, he or she can easily visualize how "lock and key" fitting of cubes connected in different fashions (at corners versus at their edges) into a three-dimensional network can affect holes in the structure. These holes or empty cubes could represent the defects in the colloid Pu sublattice observed in the EXAFS and whose presence is corroborated through the simulation presented in Figure 9. Attachment of units along their faces appears less likely, as this would result in interstitial Pu atoms in the fluorite fcc structure, as opposed to defect "holes" in the structure, as well as to a Pu−Pu distance much shorter than that observed.

Conclusions

The present paper describes the first combined XAFS/LIBD investigation of the formation and structure of Pu(IV) oxyhydroxide eigen-colloids in aqueous suspension. On the basis of our XAFS and LIBD results, a model for colloid formation via condensation of $Pu_nO_p(OH)_{4n-2p}(H_2O)_z$ oligomers is put forward. The resulting structure exhibits a −Pu−O−Pu− backbone with increasing order as the size of the colloids increase. The Pu−O coordination shell shows a variable degree of order, likely due to the variation in numbers of O^{2-}, OH^-, and H_2O ligands in the growing structural network. The highest degree of order is in the largest colloids (sample **G**), where the highest degree of condensation, correlated to the greatest degree of O^{2-} bridging in the cubic network, might be expected.

Further investigation is needed in order to corroborate this hypothetical model of colloid growth. Our data does not directly reveal the structure of the small oligomers formed. We postulate the structural compostion being cubic units, as this represents the basic units or building blocks comprising the larger colloids, which our EXAFS results indicate to have an ordered Pu−O−Pu− backbone fcc structure. The oligmers in reality may have a much different structure, which somehow totally reorganizes upon growth and agglomeration to colloids. Simultaneous LIBD and XAFS experiments and quantum chemical calculations of the stability of different oligomers will be performed. In addition, an alternative mechanism of increasing numbers of small polymeric, well-ordered solution species and simultaneous increasing size of amorphous colloids could also be considered to be in accord with our combined EXAFS and LIBD results. In order to differentiate between these two mechanisms, we will perform XAFS experiments on colloids filtered off the solution samples and on their filtrates in the future. Finally, experiments are now underway aimed at providing a reason for the decrease in amplitude for the Pu−Pu interaction in the $Pu(OH)_4$(am) precipitate (sample **H**) that otherwise is observed to increase with increasing colloid size in the solution samples **C**−**G**.

Acknowledgment. We thank Dr. A. Seibert for the preparation of sample **B**, Drs. K. Dardenne, P. Lindqvist-Reis, P. Panak, and A. Seibert for aiding in XANES/EXAFS data acquisition, and C. Bitea and Drs. C. Marquardt and V. Neck for assistance in planning and performing LIBD studies. Use of the APS was supported by the U.S. Department of Energy, Office of Science, Office of Basic Energy Sciences, under Contract No. W-31-109-ENG-38. We are grateful for beamtime allotment and experimental assistance by BESSRC and the BESSRC beamline staff and by the ESRF and the ROBL staff. Use of the infrastructures of the Actinide Facility for synchrotron research in the Chemistry Division of ANL and support by Chemistry Division staff is also acknowledged with gratitude.

IC049861P

3 Investigations on the Homologes Th(IV) and Zr(IV)

Investigations on radionuclides are often preceded by experiments on chemical homologues in order to validate new experimental methods, minimize radioactive dose or simply save expensive or rare material. In the case of tetravalent plutonium, the two most frequently used homologues are the stable element zirconium and the very long lived actinide isotope ^{232}Th. Both elements form exclusively tetravalent ions in solution and offer the possibility to study complexation processes and perform solubility experiments without interference of the complex redox chemistry which is typical for plutonium. The present chapter comprises four papers, two each on investigations on Th and on Zr, respectively. Short summaries are given on why Th and Zr are especially suited homologues for the particular objectives.

3.1 WHY THORIUM?

^{232}Th has the longest halflife among all actinides ($T_{1/2} = 1.4 \times 10^{10}$ y). Small amounts of millimolar solutions remain far below the permitted limit that can be handled in inactive laboratories, which opens up access to a wide manyfold of experimental methods. The solution chemistry of Th(IV) parallels the one of Pu(IV) in many respects, in particular, the formation of polynuclear species and small colloids are very similar. The effective charge of the Th(IV) ion in solution is 3.88 [Wick06] (Pu(IV) 4.0). Some eleven water molecules coordinate to the Th^{4+} ion (CN=10.8 [Moll99, Wick06], CN=10-12 [Roth02])[1] compared to Pu CN=9-10 [Clar06], CN=8.4 [Roth04] and CN=8 [Anku98]. As a result of the actinide contraction, the M-O bondlength is largest for Th(IV) among the tetravalent actinides (d(Th^{4+}-O) = 2.485 ± 0.01 Å [Joha91]; d(Th^{4+}-O) = 2.46 ± 0.02 Å [Neck00, Roth02]; d(Th^{4+}-O) =2.45 ± 0.02 Å [Moll99]), significantly larger than the value of d(Pu^{4+}-O) = 2.38 ± 0.02 Å [Alle96, Clar06]; d(Pu^{4+}-O) = 2.39 ± 0.01 Å [Neck00]. Accordingly, complexation with anionic ligands is much stronger for Pu(IV) than for Th(IV). The formation constants for the first mononuclear hydroxid complex $M(OH)^{3+}$ are Th(IV): $\log \beta^o_{1,1} = 11.8 \pm 0.2$ [Neck01a]; $\log \beta^o_{1,1} = 11.5 \pm 0.5$ [Rand07] and Pu(IV): $\log \beta^o_{1,1} = 14.6 \pm 0.2$ [Neck01a, Guil03], $\log \beta^o_{1,1} = 14.0 \pm 0.2$ [Yun07]. Th as well as Pu form crystalline MO_2 (see discussion on PuO_{2+x} in Chapter 2) and amorphous hydroxide ($M(OH)_{4(am)}$, in the case of Pu in [Guil03] more precisely denominated $PuO_{2(am,hydr)}$ solids. Both Th compounds are several orders of magnitude more soluble than their Pu pendants: $\log K^o_{sp}(ThO_2)$=-52.8 [Neck01a]; $\log K^o_{sp}(ThO_2) = -54.2 \pm 1.1$ [Rand07], $\log K^o_{sp}(Th(OH)_4)$=-47.8 [Neck01a]; $\log K^o_{sp}(Th(OH)_4) = -46.7 \pm 0.9$ [Rand07] compared to $\log K^o_{sp}(PuO_2) = -64.04 \pm 0.51$ [Guil03], $\log K^o_{sp}(Pu(OH)_4) = -58.33 \pm 0.52$ [Guil03]. Both elements form polynuclear hydroxide complexes when the solubility limit is

[1] An early result obtained form large angle X-ray scattering of CN=8.0±0.5 [Joha91] is no longer accepted

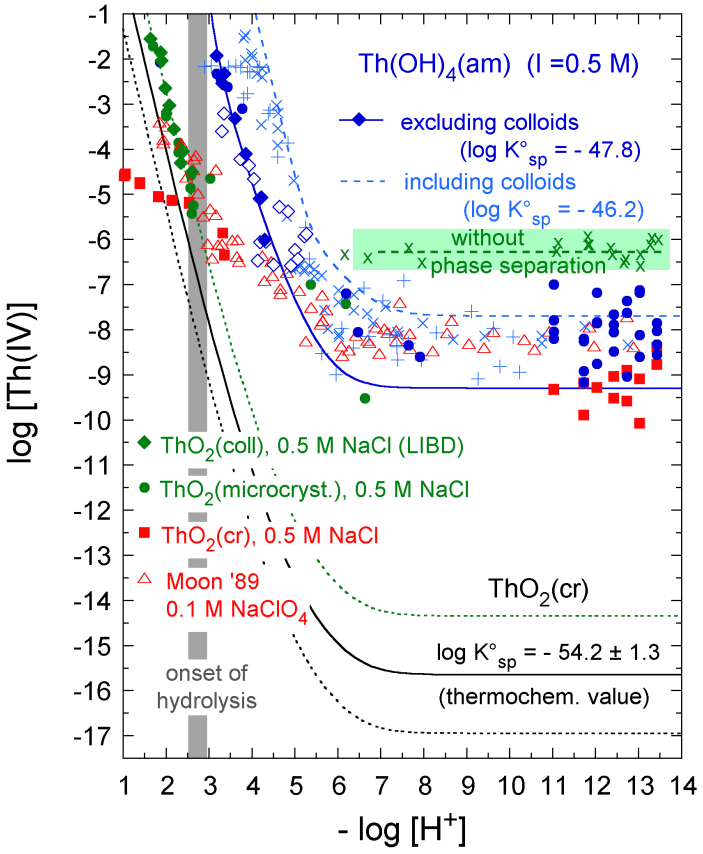

Figure 3.1: Th Solubility diagram from [Neck01a]

approached and amorphous oxyhydroxide colloids in solutions which are oversaturated with respect to the amorphous hydroxide. At near neutral pH, up to moderate basicity (pH 12), the solubility remains constant (Fig. 3.1). Neck et al. [Neck01a, Rand07] pointed out that experiments which are perfromed without separation (ultrazentrifugation, ultrafiltration) overestimate the solubility considerably (green shaded area in Fig. 3.1). This apparent increase is due to the presence of large polynuclear complexes (filterable by 1.5 nm filtration) or colloids at levels of $\log [\mathrm{Th(IV)}]_{\mathrm{tot}} = -6.2 \pm 0.5$ [Rand07] and $\log [\mathrm{Pu(IV)}]_{\mathrm{tot}} = -7.7 \pm 0.4$ [Guil03], respectively. In most models describing solubility and hydrolysis of Th(IV), the polynuclear hydroxide complexes ($\mathrm{Th_x(OH)_y^{4x-y}}$) are considered to be in equilibrium with the mononuclear ionic species [Katz86] and their formation is included particularly for near saturated solutions [Neck01a, Wick06, Rand07] (a summary of the proposed stoichiometries is given in Sec. 3.7). In a review on Pu(IV) and Th(IV) polymerization, Johnson and Toth [John78] concluded that although Pu(IV) begins to hydrolyze at considerably lower pH, the 'hydrolytic behavior of Th(IV) and Pu(IV) (*i.e.* the mechanism) is quite similar'. The extent of polymerization is greater for Pu(IV) and the transition from monomeric ionic complexes to the formation of colloids is expected to take place in a narrower pH region close to the solubility of amorphous hydroxide, but both form polymeric hydroxyl and oxygen-bridged species, eventually growing to colloids, which justifies the use of Th(IV) as a homologue for Pu(IV).

3.2 FORMATION OF TH(IV) OXYHYDROXIDE COLLOIDS IN ACIDIC SOLUTION

(Summary of [Walt03a] - Section 3.8.1)

The present work addresses the characterization of Th(IV) colloids. Written as an invited paper of the EMRS 2002 conference in Strasbourg on single particle analytical techniques for the characterization of aquatic colloids, this paper comprises discussions of various techniques used for colloid characterization and comparision of the respective advantages and limitations. The investigation of Th(IV) colloids is treated as a case study. Several investigations on the solubility of amorphous Th hydroxide [Neck02] and crystalline Th dioxide [Bund00, Neck03] suggested that the structure of the colloids strongly depends on the pH and concentration of the oversaturated solution: upon pH increase at $[Th]_{tot} \approx 0.1 - 10\,mM$, colloid formation was observed between pH 1 - 2 (Fig. 3.1, green filled symbols). The 'critical pH' values of colloid formation (definition see Sec. 2.2, p. 18) coincided with the solubility curve of crystalline ThO_2 and, therefore, the colloids were considered to have (micro-)crystalline composition (**A** in [Walt03a] Fig. 1). In the absence of impurities[2] which could act as crystallization germs for colloids, Th(IV) solutions can be prepared which are strongly oversaturated with respect to crystalline ThO_2 (*e.g.* at $[Th(IV)]_{tot} = 1\,mM$ at pH 3) but, nevertheless, do not show any tendency of precipitation or colloid formation over time periods of several months up to years. If the pH of one of theses solutions is further increased, a second domain of colloid formation is reached around pH 4-5 (Fig. 3.1, blue symbols) close to the solubility curve of amorphous $Th(OH)_4$ (**B,C** in [Walt03a] Fig. 1). Colloids from both domains were investigated by scanning and transmission electron microscopy (SEM and TEM), transmission electron diffraction (TED), atomic force microscopy (AFM), and LIBD.

A mean size of some 5-10 nm was obtained from AFM, SEM, and LIBD for the colloids of sample **A** ($[Th]_{tot} = 2.5 \times 10^{-3}\,M$, pH 1.9, two-fold oversaturated with respect to ThO_2), however, the LIBD s-curve[3] showed that the size distribution extended to somewhat bigger colloids. This was confirmed by the observation of up to 50 nm sized colloids by TEM, which exhibited a core-layer structure ([Walt03a] Fig. 9A). Transmission electron diffraction (TED) on single particles showed clear diffraction patterns ([Walt03a] Fig. 10) indicating a fluorite structure with a spacing of 3.1 Å in the (111) plane, slightly smaller than the spacing of crystalline ThO_2 (3.23 Å). We concluded that these particles were composed of a crystalline ThO_2 core layered by amorphous Th hydroxide or hydrated Th oxide.
Sample **B** ($[Th]_{tot} = 3 \times 10^{-3}\,M$, pH 3.8) which was > 50-fold oversaturated with respect to $Th(OH)_4$ contained larger colloids (50-100 nm). None of the colloids investigated by TED showed a diffraction pattern. TEM data revealed smaller subunits ([Walt03a] Fig. 9B) of

[2]Impurites (dust) of only a few parts per trillion (ppt) mass concentration were shown to induce formation of microcrystalline Th(IV) colloids.

[3]For a detailed discussion on laser-induced breakdown detection in general and in particular on the s-curve analysis, see Chapter 4.

approxiamtely 2 nm in size. Either the subunits were amorphous themselves or, if they were crystalline, spatial disorder or lattice distortion caused destructive interference of the diffraction patterns.

That in the case of region **A**, colloid formation defines the *upper* limit of the solubility curve of crystalline ThO_2 whereas in the second domain **B,C**, colloids are detected by LIBD close to the *lower* limit of the solubility curve of amorphous $Th(OH)_4$, might be related to the particle size effect [Schi65, Schi67]. Large particles have a lower solubility than small ones and applied to the case of thorium, both soulbility curves can be explained by assuming the same material (ThO_2) but particle sizes of 16-23 nm 'ThO_2(microcryst.)' and 2-4 nm '$ThO_{2(am,hyd)} \hat{=} Th(OH)_{4(am)}$', respectively [Neck07]. In the presence of a precipitate, the different solubilities might originate from particulates included in the solid. A perfect crystal would yield the solubility of ThO_2 (K^o_{sp}(cryst.) $= -54.2 \pm 1.1$)[Rand07]. With inclusion of 20 nm colloids, the solubility product would increase to (K^o_{sp}(microcryst.) $= -53 \pm 0.5$)[Rand07]. The 'amorphous, hydrated' Th oxide ($\hat{=}$amorphous hydroxide) would then be a solid including very small particles (≈ 2 nm) ($K^o_{sp}(\text{am, hyd}) = -47.8 \pm 0.6$)[Rand07] and freshly precipitated truely amorphous $Th(OH)_4$ would be the most soluble phase ($K^o_{sp}(\text{am}) = -46.7 \pm 0.9$)[Rand07].

3.3 STABILITY OF TH(IV) OXYHYDROXIDE COLLOIDS AND EQUILIBRIUM WITH IONIC SPECIES

(Summary of [Bite03a] - Section 3.8.2)

The second paper on Th-colloid chemistry in the EMRS 2002 proceedings volume focuses on the equilibrium between Th(IV) colloids and ionic Th(IV) species. In solutions of $[Th]_{tot} = 10^{-5}\,M - 10^{-2}\,M$ at pH $3-5$, Th(IV) colloids are stable over years without tendency towards agglomeration or precipitation ([Bite03a], Fig. 2 and 3). From the viewpoint of colloid chemistry (DLVO theory [Kral97]), this exceptional stability is surprising, all the more considering the high ionic strength (I=0.5 M HCl/NaCl) of the samples. Even if kinetically hindered, eventually agglomeration should take place and larger aggregates should form as pointed out by Smoluchowsky [Smol16]. His theory is well verified experimentally [Barr84, Lin90, Vird91, Holt96, Schu97, Kret98, Tomb99] and holds even for dilute solutions of < 10 ppb colloidal mass as demonstrated recently using ZrO_2 spheres ($[Zr(IV)]_{coll} < 10^{-7}$ M) [Bite03b]. That, nevertheless, the size distribution of Th(IV) colloids remains constant over extended time periods suggests that these Th(IV) colloids which form in dissolution experiments [Bund00, Neck02] must not be described as insoluble charged spheres in the sense of DLVO theory but rather are part of steady state precipitation and dissolution processses comparable to the thermodynamic solid-liquid equilibrium of amorphous $Th(OH)_4$ with ionic mono- and possibly polynuclear Th(IV) species.

To check this hypothesis, four aged suspensions prepared from dissolution of thorium nitrate in HCl/NaCl [Bund00, Neck02] were subjected to pH changes. The mean size and total amount of the colloids were determined by LIBD and ultrafiltration followed by photometric detection of the arsenazo III Th complex [Savv61], respectively. We started from a slightly oversaturated suspension (**A** in Fig. 4 of [Bite03a]) containing $[\mathrm{Th}]_{\mathrm{coll}} \approx 1 \times 10^{-3}\,\mathrm{M}$ colloids. One aliquot was diluted by adding a HCl/NaCl mixture such that acidity and ionic strength remained constant (**B** in Fig. 4 of [Bite03a]). The colloids dissolved completely after some 30 days, which lead to a pH increase according to

$$\mathrm{Th(OH)_{4(coll)}} \rightarrow \mathrm{ThOH^{3+}} + 3\mathrm{OH^-} \tag{3.1}$$

assuming the first hydrolysis complex $\mathrm{ThOH^{3+}}$ to be the dominant ionic species in solution. Subsequently, the sample was diluted by addition of pH neutral NaCl solution (**C** in Fig. 4 of [Bite03a]) until the solubility was exceeded and $\mathrm{Th(OH)_{4(coll)}}$ colloids formed (**D** in Fig. 4 of [Bite03a]). Complementary to reaction (3.1), the formation was accompanied by $\mathrm{H^+}$ release and acidification of the sample

$$\mathrm{ThOH^{3+}} + 3\mathrm{H_2O} \rightarrow \mathrm{Th(OH)_{4(coll)}} + 3\mathrm{H^+}\,. \tag{3.2}$$

The second aliquot was diluted along a different path in the solubility plot (**A,E,F,G** in Fig. 4 of [Bite03a]) which never left the region of oversaturation, *i.e.* the Th(IV) colloids never completely dissolved. The total dilution of both aliquots was chosen in a way to give equal $[\mathrm{Th}]_{\mathrm{tot}}$ concentrations in the final solutions. After equilibration of > 140 days, both samples adjusted to equal acidity and very similar total colloid content, supporting the conclusion of colloids being in thermodynamic equilibrium with the ionic Th(IV) species.

Assessment of amount and size of colloids (Fig. 1 of [Bite03a]) of three more aged samples revealed two more interesting results: Even after ultrafiltration (1 kD $\hat{=}$1 nm cutoff size) of the suspensions, the Th concentration in the filtrate slightly exceeded the equilibrium concentration of ionic Th(IV) species as given by the LIBD measurements. This suggests that ultrafiltration does not lead to a complete separation of colloids and probably small polymeric species exist which can pass the filter and contribute to the total Th concentration. A second finding concerns the size of the colloids. By that time, we were not yet able to extract the particle size distribution from the LIBD data but, nevertheless, the threshold of the s-curves is a measure of the weighted mean size of the colloids (with a higher weight of larger particles). This breakdown threshold is plotted as a function of the degree of oversaturation (defined by the ratio of the amount of Th(IV) in solution over equilibrium concentration of ionic Th(IV) species $[\mathrm{Th}]_{\mathrm{tot}}/[\mathrm{Th}]_{\mathrm{eq}}$) in Fig. 3.2. Though only limited data are available, there is a clear correlation of mean colloid size and oversaturation: With increasing degree of oversaturation, the threshold decreases which corresponds to increasing mean colloid size ranging from a few nanometers close to the solubility curve to $\approx$ 200 nm in a tenfold oversaturated solution, where the eigencolloids contribute the main fraction of Th(IV) concentration.

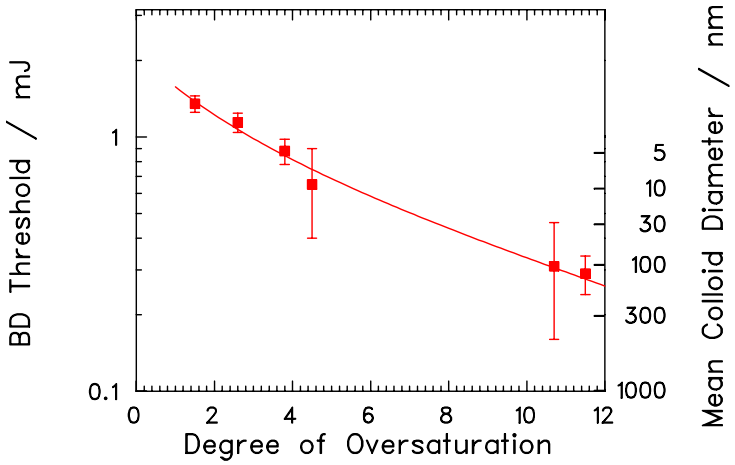

Figure 3.2: Mean colloid size as a function of oversaturation

These findings emphasize that the apparent solubility is considerably increased by the presence of Th(IV) eigencolloids. However, the question is allowed how to define the 'solubility'. Taking into account only small (possibly monomeric) ionic species, *i.e.* after phase separation, underestimates the total amount of Th(IV) in solution. On the other hand, simple integration over all species, ionic and colloidal, might not meet the requirements either. If, for instance, solubility data is required to predict groundwater transport, the interaction of each single species with ligands, secondary phases, and host rock might be very different and must be taken into account one by one in order to draw a complete picture. In near neutral pH, Th(IV) true colloids show strong sorption and will experience significant retention in man made or natural barriers around a repository and will not contribute significantly to the intake into the biosphere. Ionic $Th(IV)_{aq}$, however, strongly sorbs to natural colloids (form so called pseudocolloids) and will migrate fast over considerable distances [Haus02, Mori03] (see also Fig. 21 of [Kim07] in Sec. 4.5.2).

3.4 WHY ZIRCONIUM?

The most striking similarity of Zr(IV) and Pu(IV) ions in solution is their strong tendency towards hydrolysis. The first hydrolysis constants for $M(OH)^{3+}$ are $\beta^o_{1,1} = 14.3$ [Humm02] and $\beta^o_{1,1} = 14.0$ [Yun07] for Zr(IV) and Pu(IV), respectively (the full set of constants for $Zr(OH)^{4-y}_y$ is given in Table 1 of [Cho05b]). Figure 3.3 compares the species distribution in very dilute soultions at (I=1 M HCl/NaCl) when polynuclear complexes do not play a role. For both metal ions, the first hydroxide complex starts to form in 1 M acid (calculated for HCl), and the second complex $M(OH)^{2+}_2$ dominates up to pH 3. The Zr^{4+} ion is somewhat smaller, $r(Zr^{4+}) = 0.84$ Å for CN=8 and $r(Zr^{4+}) = 0.89$ Å for CN=9 [Shan76], than its Pu pendant with $r(Pu^{4+}) = 0.96$ Å for CN=8 [Shan76]. The Zr-O distance in solution is calculated as $d(Zr^{4+} - O) = 2.22$ Å for CN=8 and $d(Zr^{4+} - O) = 2.27$ Å for CN=9 using $r(OH^-) = 1.38$ Å which is significantly smaller than $d(Pu^{4+} - O) = 2.38$ Å for CN=9 [Alle96] (see Sec. 3.1). In solutions exceeding $[Zr]_{tot} = 1$ mM, Zr forms polymers already at molar acidity, primarily the tetramer $Zr_4(OH)^{8+}_8$ which was investigated in detail in the past [Ziel56, Muha60, Bert87, Aber93, Sing96, Rose03, Hagf04]. For increasing pH, the degree of polymerization increases leading to the formation of large polymers close to the solubility limit which is yet another parallel to Pu(IV). In recent times, the properties of Zr polyspecies in aqueous solutions gained renewed interest [Sout02, Ekbe04, Sasa06] due to the fact that Zr is a high priority element for the assessment of radioactive nuclear waste repositories: zirconium is used as fuel cladding material in nuclear light water reactors and, in addition, Zr has a high yield among the uranium-fission products. Thermodynamic data of Zr, (solubil-

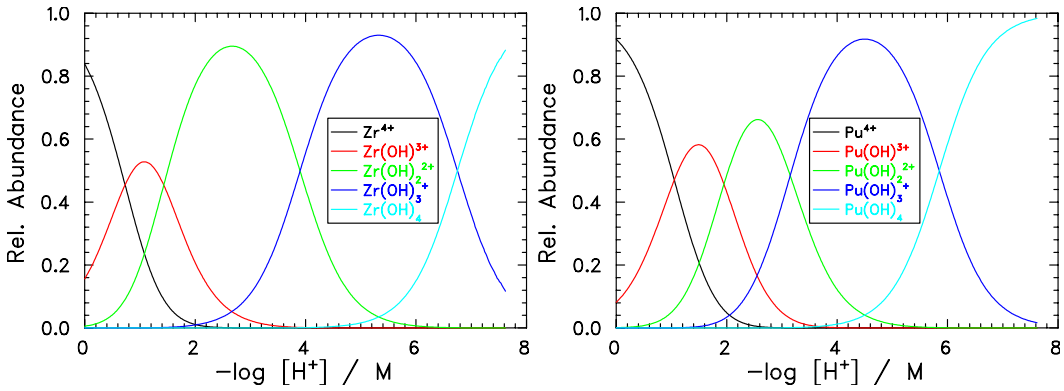

(a) Zr(IV) (b) Pu(IV)

Figure 3.3: Calculated distribution of mononuclear hydroxide complexes (HCl/NaCl solutions of I=0.5 M) in the absence of polynuclear species, *e.g.*, at very low metal ion concentration. (a) Zr(IV), hydrolysis constants from [Cho05b]. (b) Pu(IV), hydrolysis constants from [Yun07].

ity and hydrolysis constants) were reviewed for a NAGRA/PSI database [Curt02, Humm02] and recently, an extensive review of the NEA-TDB [Brow05] summarizes data on aqueous zirconium chemistry including hydrolysis reactions, polymerization, and formation of halide complexes. A compilation of literature with special emphasis on Zr(IV) polymerization and a discussion of the applied techniques is given in Appendix B of [Walt07b] (Sec. 3.8.4) and is hence not summarized here.
In analogy to Th(IV) and Pu(IV), Zr(IV) forms several oxide/hydroxide phases with solubilities ranging from $\log K^o_{sp} = -63 \pm 1.6$ for the crystalline ZrO_2 [Brow05] (Pu: $\log K^o_{sp} = -64.04 \pm 0.51$ [Guil03]) up to $\log K^o_{sp} = -52.8 \pm 0.1$ [Brow05] for the freshly formed amorphous $Zr(OH)_4$ (Pu: $\log K^o_{sp} = -58.33 \pm 0.52$ [Guil03]). Hence, solubility data scatters over many orders of magitude (Fig. 9 of [Cho05b]) depending on the precipitate used for investigations from undersaturation. Particulate inclusions, hydration, and aging effects play important roles, so that a thourough characterization of the solid is necessary for meaningful interpretation of the data. In experiments from oversaturation [Bili66], the formation of colloids and suspended particles is observed, which resemble amorphous $Zr(OH)_4$. The following paper adresses formation and structure of these colloids by combining LIBD and EXAFS measurements.

3.5 FORMATION AND STRUCTURE OF ZR(IV) COLLOIDS

(Summary of [Cho05b] - Section 3.8.3)

Undersaturated Zr(IV) solutions were prepared by dissolving $ZrOCl_2n(H_2O)$ in HCl/NaCl (I=0.5 M). By coulometric titration (CT) [Neck02], pH was increased until the solubility was exceeded. CT allows very slow pH increase and thus avoids local pH gradients which can cause preliminary colloid formation. In the present study, we did not use convential combination glass electrodes (Ross type) for pH measurement since it is not possible to completey avoid leaking of reference filling solution into the sample which may act as crystallization germs for the formation of microcrystalline colloids (*c.f.* discussion for the case of Th(IV) colloids in Sec. 3.1). Instead, pH was measured using two half cells: a H^+ sensitive glass electrode and a Cl^- sensitive electrode [Knau90]. We strictly used non sorbing materials (PEEK,PFA,quartz) in contact with the solutions, which allowed us to prevent colloid sorption and lower the detection limit two orders of magnitude as compared to earlier experiments, down to [Zr(IV)] $= 2.5 \times 10^{-8}$ M.

The solubility measurements were performed for 13 different concentrations between $[Zr(IV)]_{tot} = 2.5 \times 10^{-8} - 1 \times 10^{-3}$ M. The formation of colloids after exceeding the solubility of amorphous Zr(IV) hydroxide was observed by LIBD as described in Sec. 2.2. Beyond the mere detection of colloids, in the present work, LIBD was used for measuring the *particle size distribution* as described in Sec. 4.3. The capability of LIBD - in this case combined

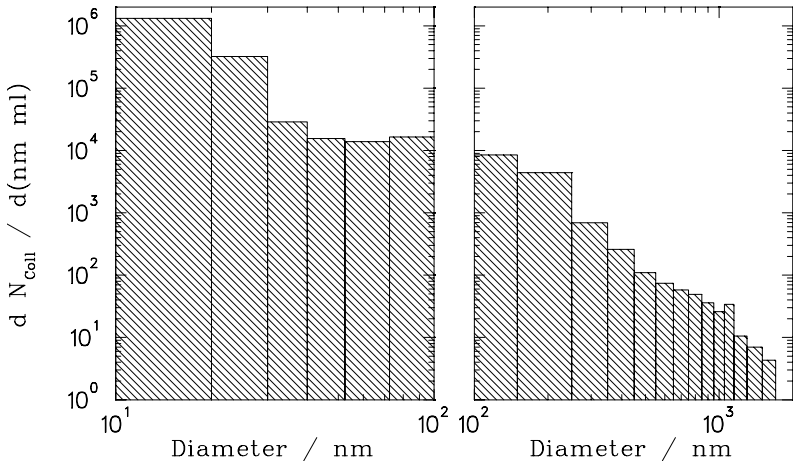

(a) LIBD (b) SPC

Figure 3.4: Colloid formation in a sample of [Zr(IV)]=3×10^{-7} M at pH 8.0. The particle size distribution (PSD) is measured by (a) LIBD for the small colloids < 100 nm and (b) by a commercial single particle counter (SPC) for particles up to 2.3 μm in size. From these data, the total colloid content is estimated to be 40 ppb :$[\mathrm{Zr(IV)}]_{\mathrm{coll}} = 2.5(3) \times 10^{-7}$ M.

with a single particle counter, which is a commercial instrument utilizing static light scattering - is illustrated by means of a solution of $[\mathrm{Zr(IV)}]_{\mathrm{tot}} = 3 \times 10^{-7}$ M at pH 8.0 (Fig. 3.4). This solution is 5-times oversaturated with respect to $\mathrm{Zr(OH)}_{4(\mathrm{am})}$, hence, only the fraction $[\mathrm{Zr(IV)}]_{\mathrm{aq}} = 6 \times 10^{-8}$ M should be present in ionic form. The particle size distribution shows a Pareto like character ($\mathrm{d}N_{coll}/\mathrm{d}d \propto d^{-\beta}$; $\beta = 3-5$). The mass of all sized fractions sums up to 40 ± 5 ppb which corresponds to a colloidal Zr concentration of $[\mathrm{Zr(IV)}]_{\mathrm{coll}} = 2.5(3) \times 10^{-7}$ M, which is in good agreement with the expectation of 80% being present as colloids.

The onset of colloid formation is plotted as a function of H^+ concentration in Figure 1 of [Cho05b]. At $[\mathrm{Zr}]_{\mathrm{tot}} > 3 \times 10^{-4}$ M, the solubility curve agrees well with data obtained under similar conditions by Bilinsky *et al.* [Bili66] who used tyndallometry as a measure of oversaturation. For decreasing Zr concentration, however, our data deviate significantly from Bilinskies which originates in the different methods used for colloid detection: tyndallometry measures the turbity of the solution. For a solution to becomes opaque, light must be scattered by a large number of big colloids (> 100 nm). However, with decreasing Zr(IV) concentration, the number of large colloids decreases. LIBD, in contrast, detects much smaller colloids (diameter of a few nm) at low concentrations and, hence, indicates colloid formation as a sign of oversaturation much earlier. From the slope $\mathrm{d}\log[\mathrm{Zr}]_{\mathrm{tot}}/\mathrm{d}(-\log[\mathrm{H}^+]) = -2$ of our data, we deduce that the dominating ionic species in solution, be it a monomer or polymer, carries charge $z = 2$. Unfortunately, reliable formation constants and SIT coefficients

of polynuclear hydroxide complexes in HCl/NaCl were not available and, hence, we could not model the species distribution along the measured solubiliy curve correctly. With the awareness that this model is probably not realistic for $[\mathrm{Zr(IV)}]_{\mathrm{tot}} > 10^{-5}\,\mathrm{M}$ we calculated the operative solubility product $\log K^{o}_{sp} = -53.1 \pm 0.5$ using only the hydrolysis constants for mononuclear species.

From the series at $[\mathrm{Zr(IV)}]_{\mathrm{tot}} = 1 \times 10^{-3}\,\mathrm{M}$, six aliquots at different pH were measured by EXAFS. Two addtional samples (monoclinic ZrO_2 and commercial ZrO_2 colloids) and a concentrated solution of $[\mathrm{Zr(IV)}]_{\mathrm{tot}} = 1 \times 10^{-1}\,\mathrm{M}$, which contained colloids of presumably microcrystalline structure served as reference materials.
The FT spectra of the microcrystalline colloids showed clear interference patterns from the backscattering of two oxigen shells. From comparision with published data on $HfOCl_2n(H_2O)$ followed that tetrameric subunits were present in these microcrystalline colloids. However, the polymeric and colloidal species in the samples at $[\mathrm{Zr(IV)}]_{\mathrm{tot}} = 1 \times 10^{-3}\,\mathrm{M}$ pH 2-3.3 could not be derived from stacked tetramers but exhibit more complex structures. At pH 1, the Zr-O distances agreed well with those of the tetramer but no Zr-Zr backscattering peak was identified which we attributed erroneously to the absence of polymeric species. From the results of [Walt07b], we know now that the opposite is true. A great variety of Zr polymers of different size form at pH 1 and the manyfold of different Zr-Zr distances causes destructive interference of the Zr-Zr backscattering peak. Simliar conclusions were drawn by Conradson*et al.* when interpreting XAFS spectra of Pu phases [Conr05].
For pH 2-2.8, Zr-Zr backscattering signals were present in the FT spectra but at significantly smaller Zr-Zr distances than expected for the tetramer and with relatively small amplitude. No colloids were detected in this pH range which lead to the conclusion that several different polymeric species of small size formed under theses conditions. For pH > 2.8, LIBD detected colloids and with decreasing acidity, their concentration and mean size increased. These colloids exhibited a disordered Zr-Zr coordination shell, which may result from the presence of more than one distance and defects in the Zr sublattice. The Zr-O coordination number remained close to or above CN=8. When taken together, we propose the following conclusions: The colloids might form from ZrO_8 building blocks or from polynuclear solution species of different geometry. It is well known that Zr forms several modifications of similar energy [MacD73]. By all means, the structures of both, solution species and colloids are highly disordered.

3.6 FORMATION OF POLYNUCLEAR ZR(IV) HYDROXIDE COMPLEXES

(Summary of [Walt07b] - Section 3.8.4)

The present work aims at answering one of the basic questions raised by the previous study (Sec. 3.5): Which metal hydroxide complexes form in near saturated solutions. Information on solution species often is deduced from potentiometric titration experiments which, however, only give meaningful results when the species which dominates the starting solution is known. Futhermore, information is restricted on the ratio of consumed metal ion and hydroxide ligand. Formation of, *e.g.*, $Zr(OH)_2^{2+}$ cannot be destinguished from formation of $Zr_2(OH)_4^{4+}$ without plausibility considerations from titration series at different concentrations. In the present work, we show that nano-electrospray mass-spectrometry [Yama84, Fenn02], a method which is well established for speciation of biomolecules [Dole68, Cole97, Pram02], is also suited for the direct detection of the species distribution of metal hydroxide complexes in aqueous solutions. Size (number of metal ions), number of ligands, and charge of the complex are unambiguously determined. Different species which are present simultaneously are well resolved down to contributions of only 0.2% of the total metal-ion concentration. In the present example, a fraction of only 3×10^{-6} M mononuclear Zr(IV) hydroxide complexes is detected at a the simultaneous presence of $[Zr]_{Zr_4(OH)_8^{8+}} \approx 1.5 \times 10^{-3}$ M. Only a few microliters of the sample is required for the speciation, which makes the method especially suited for investigation of radioactive material.

It is well known that in the course of the electrospray process, solvent evaporation [Cole97, Irib76] can cause an increase of less volatile species [Zhou00] (in the present case the metal ions). Electrolytic oxidation of water in the capillary due to the applied high voltage leads to H^+ generation and acidification of the solution [Zhou99, Zhou02]. In order to minimize influence of solvent evaporation, we used a nano-ESI capillary [Wilm96] which generates droplets of only ≈ 100 nm diameter. At low concentrations, one metal complex is expected to be present in such a droplet at most rendering aggregation impossible. But even at millimolar concentration where presumably several complexes will be in one droplet, the chance of preserving the original state is much better than in conventional ESI since droplet fission proceeds much faster and after a few μs [Wort05] the droplets shrink to a size of below 10 nm.
Acidification which was observed when using 'nano-ESI wire-in-capillaries' [VanB01] is not expected in our case since we use tips with outside metal coating where the metal is not in contact with the solution except at the very tip of the capillary. Moreover, an estimate of the maximum possible H^+ generation due to electrolysis given in [Walt07b] shows that the fairly high acidity of our samples would not be altered.
Finally, collisions with buffer gas might fragment delicate molecules. For the latter reason, we use very soft declustering conditions [Agne95] conserving part of the solvent shell of the complexes, *i.e.* the complex $Zr(OH)_y^{z+}$ gives rise to a cluster of peaks $[Zr(OH)_yCl_{4-y-1}n(H_2O)]^+$

(the chloride ions partly compensate the charge of the complex. See discussion in [Walt07b]). However, operation at these conditions requires a high mass resolution of the spectrometer (isobaric resolution). *E.g.*, the masses of the first and second monomeric hydrolysis complex $m([^{90}Zr(OH)_1^{35}Cl^{37}Cl\ 9(H_2O)]^+) = 340.937$ amu and $m([^{90}Zr(OH)_2^{37}Cl\ 10(H_2O)]^+) = 340.981$ amu embedded in a cluster of 9 and 10 water molecules, respectively, differ by less than 1/20th of a mass unit ($m/\Delta m \approx 7750$) which is well resolved by our spectrometer (Fig. 3 of [Walt07b]).

For direct proof that the species distribution is not altered by the electrospray process, (non-invasive) XAFS measurements were performed on selected samples. Though no species distribution can be deduced from the XAFS FT spectra, the Zr-Zr and Zr-O distances and the coordination numbers can be confronted with the size distribution measured by ESITOF. Increasing disorder of the coordination shells is always evidence for the presence of more than one polynuclear species.

Some 60 samples of [Zr]=1.5 - 10 mM at $0 < -\log[H^+] < 3$ were prepared by dissolving appropriate amounts of zirconyl chloride in hydrochloric acid of predefined pH and were allowed to equilibrate for at least one hour prior to the measurement by ESI-TOF MS. Typical mass spectra of this series are displayed in Figs. 4,5 of [Walt07b]. They contain up to 5000 peaks which are identified by a three step algorithm described in [Walt07b]. The large number of peaks originate from the natural isotope distribution of Zr (five stable isotopes) dividing the signal of each polymer $Zr_x(OH)_y^{z+}$ into many peaks according to the binomial distribution. Though spectra get complicated by this effect, these distributions serve as fingerprint allowing an unambiguous species identification, both, with regard to the degree of polymerization x, the number y of OH^- ligands and, as a consequence, the charge $z = 4x - y$ of the complex.

While tetramers and monomers account for $> 80\%$ of the species at molar acidity, larger polymers form with increasing pH (Fig. 7 of [Walt07b]). Polymers up to $x = 21$ were identified and most likely larger species form at lower acidity, eventually reaching the size of colloids. The XAFS measurements consistently corroborate the ESI results: The mean Zr-Zr distances of all samples pH< 1 at [Zr]=10 mM are in good agreement with the dominance of tetramers. With increasing variety of polymers, the peaks broaden and eventually vanish due to destructive interference. This important finding which parallels XAFS interpretations in [Conr05] allows us to reinterpret the data of [Cho05b], where the absence of a Zr-Zr signal at [Zr]=1mM, pH 1 was erroneously assumed to indicate the presence of monomers. Further evidence for the correctness of this explanation is given by the XAFS measurement at pH 1.8: the Zr-Zr signal reappears (d=3.66(3) Å with a mean coordination number close to two) in accordance with the ESI spectra showing that some 80% of the detected ions are octamers. The lower concentrated samples show a slightly larger mean Zr-Zr distance attributed to the pentamer which contributes a larger fraction than in the higher concentrated samples. The good correlation of XAFS findings with the species distributions measured by ESITOF suggests that

the species were not significantly disturbed by the electrospray process.

Keeping in mind the newly gained knowledge of the species distribution measured by ESI (Fig. 7(top) of [Walt07b]), we revisit the results of the previous section [Cho05b]: Broadening of the Zr-Zr backscattering peak suggested that for [Zr]=1 mM at pH > 2, several species with different Zr-Zr distances coexist in solution. ESI shows that these are the pentamer, the octamer and the decamer. Colloid formation was detected by LIBD between pH 2.8 and pH 3.0 ([Zr]=1.0 mM) in [Cho05b] explaining the clogging of the nano ESI capillary at pH> 2.7, an agreement which is very good considering that the ESI measurements were performed at slightly higher concentration ([Zr]=1.5 mM) and without addition of electrolyte (the measurements of [Cho05b] were performed in HCl/NaCl = 0.5 M).

As stated in Sec. 3.5 and discussed in detail in App. A of [Walt07b], close to the solubility limit, the charge of the dominating complex in solution must equal the slope of the solubility curve. The ESI-TOF results confirm the expectations: as the solubility limit is approached, the charges of the dominating complexes decrease approaching $z = 2$ (pentamer and octamer). Charge compensation proceeds indeed via stepwise hydrolysis of the complexes as suggested in [Tulo02]). In addition, chloride ions [Hagf04] coordinate to the complex - presumably in the outer shell. It is important to realize that no measurements can be performed in oversaturated solutions since immediate formation of a precipitate at the tip clogs the capillary. In this regard, ESI-TOF and LIBD complement each other, since colloids are detected by LIBD only in oversaturated solutions.

Finally, the data are compared to the species distribution calculated from the equilibrium constants selected in [Brow05] (Fig. 11 of [Walt07b])[4] . At high acidity ($-\log[H^+] < 0.7$), the tetramer dominates the species distribution which is well in line with the NEA model. For

[4]Unfortunately some typographic errors occured in Table 3 of [Walt07b].The correct table should read:

Species	$\log \beta^o_{p,y}$ a)	$\log {}^*\beta^o_{p,y}$	$\log \beta'_{p,y}$ c)	ϵ_{i,Cl^-}	ϵ_{i,OH^-}
Zr^{4+}	—	—	—	0.33 d)	0.64 g)
$Zr(OH)^{3+}$	14.1	0.32	13.5	0.18 e)	0.36 g)
$Zr(OH)_2^{2+}$	27.8	0.30	26.8	0.08 e)	0.18 g)
$Zr_3(OH)_4^{8+}$	55.4	0.4	56.3	0.18 e)	0.64 g)
$Zr_3(OH)_9^{3+}$	135.75	12.2	132.3	1.7 e)	0.38 g)
$Zr_4(OH)_8^{8+}$	117.8	7.95 b)	118.6	3.0 f)	0.64 g)
H^+	—	—	—	0.12 h)	—

a) Reaction $pZr^{4+} + yOH^- \rightleftharpoons Zr_p(OH)y^{4p-y}$
b) Taken from [Ziel56]. In [Brow05] ${}^*\beta^o_{p,y} = (6.52 \pm 0.65)$
c) Value (at $[H^+]$=2 M [Zr]= 10mM)
d) from [Brow05]
e) estimated from ϵ_{Zr^{4+},Cl^-} and quadratic charge/radius dependence [Brow05]
f) from [Brow05]
g) estimated from value in [Cho05b] and quadratic charge/radius dependence [Brow05]
h) from [Gren00]

increasing pH, the NEA model predicts the increasing dominance of a trimer ($Zr_3(OH)_9^{3+}$). In strong contrast, no trimer was observed in any of the samples investigated by ESI-TOF. However, as stated in the NEA review 'The species $Zr_3(OH)_9^{3+}$ has been introduced to increase the quality of the global fit of the hydrolysis data (...). This species has not yet been identified or proposed in the experimental literature.' And, as confirmed by one of the authors of [Brow05], it is not necessary to introduce $Zr_3(OH)_9^{3+}$ in order to obtain a good fit. This species may be substituted by the octamer or pentamer detected with ESI-MS which have similar x/z ratios and, in the case of the octamer, are also in agreement with X-ray scattering experiments [Sing96, Hu99].

In conclusion, the most important findings of the present work are, that the hydrolysis of polynuclear Zr(IV) complexes is a continuous process. The charge of the polymers is compensated through sequential substitution of H_2O molecules by hydroxide ligands. While tetramers account for the by far greatest fraction of Zr(IV) at high acidity, pentamers and octamers dominate the species distribution for increasing pH. From the ESI-TOF mass spectra, no evidence for the formation of trimers is found. Close to the solubility limit, the charges of the pentamers and octamers decrease and approache $z \approx 2$ as expected from slope analysis of the solubility curve. The tetramer behaves differently. Close to the solubility, the relative abundance of the eightfold charged tetramer strongly decreases but the formation of considerably lower charged teramers is not observed. This behavior is in line with the exceptional stability of the $Zr_4(OH)_8^{8+}$ complex [Turr95, Rose03].

3.7 RECENT ADVANCES

Recently, the investigations on polymerization processes by ESI-TOF were extended to Th(IV) solutions. The polynuclear hydroxide complexes of Th are considered to be in equilibrium with the mononuclear ionic species [Katz86]. The stoichiometry of many of them was deduced from potentiometric titration (earlier work) or from X-ray scattering experiments [Wils07]: using the nomenclature (x,y) for the complex $Th_x(OH)_y^{4x-y}$ those are (2,2); (5,12) [Krau56]; (2,4); (4,12); (6,15) [Neck01a]. (2,2); (2,3); (2,4); (4,8); (4,12); (5,12); (6,14); (6,15) [Wick06]. A general formula $Th[Th_x(OH)_3]_n^{n+4}$ *e.g.* (2,3), (3,6), (4,9); (5,12) was proposed by[Sill53]. In a review on Pu(IV) and Th(IV) polymerization, Johnson and Toth [John78] summarized that (2,2), (6,14), and (6,15) were proposed in nearly all cited studies but most likely, many additional species existed, particularly in concentrated solutions ($[Th]_{tot}$=0.01 - 0.1 M).

For the present work, freshly precipitated amorphous ^{232}Th hydroxide[5] was dissolved in 0.5 M hydrochloric acid, where necessary diluted with HCl (pH 0.3-3), and finally slowly titrated

[5]The Th hydroxide was precipitated from a concentrated thorium nitrate solution by pH increase and subsequently washed with destilled water and fumed several times in hydrochloric acid.

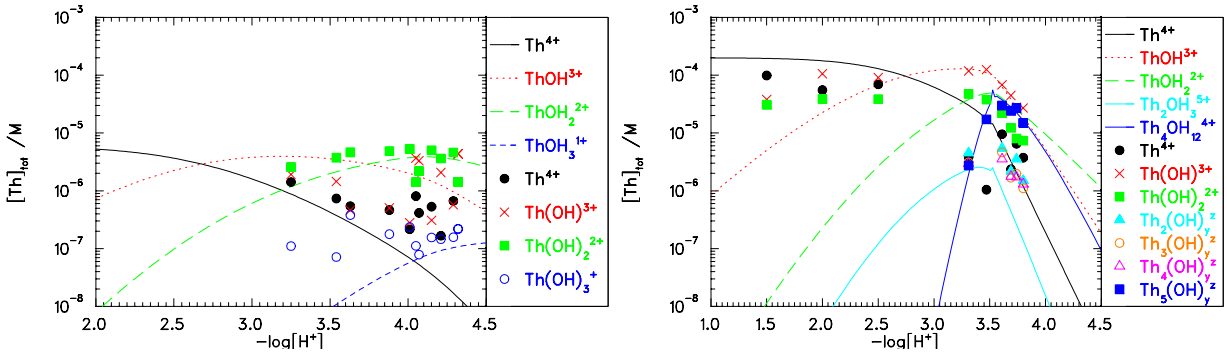

(a) $[\mathrm{Th(IV)}]_{\mathrm{tot}}=6\times10^{-6}\,\mathrm{M}$ (b) $[\mathrm{Th(IV)}]_{\mathrm{tot}}=2\times10^{-4}\,\mathrm{M}$

Figure 3.5: Species distribution in Th(IV) solutions measured by ESI-TOF: (a) At $[\mathrm{Th(IV)}]_{\mathrm{tot}}=6\times10^{-6}\,\mathrm{M}$ only monomeric hydroxide complexes $\mathrm{Th(OH)_y^{4-y}}$ are detected. (b) At higher concentration ($[\mathrm{Th(IV)}]_{\mathrm{tot}}=2\times10^{-4}\,\mathrm{M}$), a variety of polynuclear complexes is formed close to the solubility limit.

with MQ water. Samples of $[\mathrm{Th(IV)}]_{\mathrm{tot}}=6\times10^{-6}-10^{-3}\,\mathrm{M}$ were prepared at pH 0.3 - 4.0. Measurement and spectra evaluation were performed as described in [Walt07b] after equilibration of the samples for 24 h. Since only the very long lived isotope ^{232}Th is present in these solutions, the mass spectrometric signal of each polymer is distributed over a much smaller number of peaks $\left[^{232}\mathrm{Th_x(OH)_y^{37}Cl_p^{37}Cl_q}\,\mathrm{n(H_2O)}\right]^+$ than in the case of Zr with its five stable isotopes. Data evaluation is facilitated by the reduced number of peaks in the mass spectra and the detection limit is lowered by several orders of magnitude down to $[\mathrm{Th(IV)}]_{\mathrm{tot}}\approx1\,\mu\mathrm{M}$.

The species distributions of two series at $[\mathrm{Th(IV)}]_{\mathrm{tot}}=6\times10^{-6}\,\mathrm{M}$ and $[\mathrm{Th(IV)}]_{\mathrm{tot}}=2\times10^{-4}\,\mathrm{M}$ are compared to the model of [Rand07] in Figure 3.5. At the lower concentration (a) no polymers are detected. With increasing pH 3.0 − 4.3, ongoing hydrolysis shifts the weight from the hydrated ion $\mathrm{Th^{4+}}$ (●) and the first complex $\mathrm{Th(OH)^{3+}}$ (×) to the dihydroxide complex $\mathrm{Th(OH)_2^{2+}}$ (■) in agreement with the hydrolysis model of [Rand07] (solid, dotted and dashed lines, respectively). It also agrees with the model that no polymers are detected. The contribution of the most abundant polymer, the tetramer $\mathrm{Th_4(OH)_{12}^{4+}}$, is expected to be of the order of $[\mathrm{Th_4(OH)_{12}^{4+}}]=1\times10^{-8}\,\mathrm{M}$ which is below the detection limit of our ESI mass spectrometer. Attempts to extend the ESI measurements to higher pH were hindered by clogging of the needle. By LIBD, we confirmed that at $-\log[H^+]=4.6$, colloids form and account for $[\mathrm{Th(IV)}]_{\mathrm{coll}}=5.0(5)\times10^{-6}\,\mathrm{M}$ which is ≈80% of the total Th concentration ($[\mathrm{Th(IV)}]_{\mathrm{tot}}=6.0\times10^{-6}\,\mathrm{M}$). According to Neck *et al.* [Neck01a], the solubility of amorphous thorium hydroxide at $-\log[H^+]=4.6$ is approximately $[\mathrm{Th(IV)}]_{\mathrm{aq}}=5\times10^{-7}\,\mathrm{M}$ (Fig.3.1) which agrees quantitatively with the high colloid contribution.
In the second series at $[\mathrm{Th(IV)}]_{\mathrm{tot}}=2\times10^{-4}\,\mathrm{M}$, Figure 3.5 (b), polynuclear complexes play a

role for decreasing acidity. At $-\log[H^+] = 3.3$, dimer, trimer, tetramer, and pentamer form at approximately equal amounts, though they still are minor species. Around $-\log[H^+] = 3.5$, the relative abundance of the pentamer increases strongly and eventually accounts for almost 50% of the $[Th(IV)]_{tot}$ concentration at $-\log[H^+] > 3.6$. At $-\log[H^+] = 3.5$, the pentamer coordinates 16 hydoxide ligands, and 17 at $-\log[H^+] > 3.6$:$Th_5(OH)_{17}^{3+}$. In accordance with the slope of the solubility curve for amorphous Th hydroxide $d\log[Th]_{tot}/d(-\log[H^+]) = -3$ close to $-\log[H^+] = 4$ (Fig.3.1), the two most abundant species, $Th(OH)^{3+}$ and $Th_5(OH)_{17}^{3+}$ carry three charges.

It is quite obvious from Figure 3.5 and in agreement with what one would expect, that polymers become less important in dilute solutions. It is, however, surprising, how rapidly colloid formation proceeds in solutions of only micromolar Th concentration. Colloids form in the narrow range between $-\log[H^+] = 4.3$ where no polynuclear complexes are detectable by ESI TOF and $-\log[H^+] = 4.6$ where they contribute the dominating fraction of $[Th(IV)]_{tot}$. This might raise the question, whether polynuclear complexes are involved at all in the process of colloid formation at low concentration or if the amorphous thorium oxo hydroxide colloids form from the monomeric species' $Th(OH)_y^{4-y}$. A common model for crystallization phenomena called 'homogeneous coagulation' describes spontaneous formation of crystals from ionic solution species after a so called 'induction time' which depends on the degree of oversaturation [He94, Guo06]. Future investigations aim at these topics.

3.8 PUBLICATIONS

3.8.1 Comparision of colloid investigations by single particle analytical techniques - a case study on thorium-oxyhydroxides [Walt03a]

ELSEVIER

Colloids and Surfaces A: Physicochem. Eng. Aspects 217 (2003) 81–92

COLLOIDS AND SURFACES A

www.elsevier.com/locate/colsurfa

Comparison of colloid investigations by single particle analytical techniques—a case study on thorium-oxyhydroxides

C. Walther *

Institut für Nukleare Entsorgung, Forschungszentrum Karlsruhe, Postfach 3640, D76021 Karlsruhe, Germany

Abstract

Characterization of complex systems such as colloids calls for the combination of a multitude of analytical methods. This work reviews some of the most common techniques used to gain information on the particle size distribution of a colloidal suspension. Fractionation by filtration or centrifugation is discussed as well as flow field fractionation and electron- and atomic-force microscopy. Since these delicately balanced systems are to be characterized with as little perturbation as possible, this work lays special emphasis on non-invasive methods such as light scattering (photon correlation spectroscopy (PCS), static light scattering: single particle counter) and laser induced breakdown detection, an in-situ method, which opens up a wide operational dynamic range, covering three orders of magnitude in size (5–1000 nm) and seven orders of magnitude in particle concentration (1 ppt-several ppm). Advantages and shortcomings of each technique are illuminated by means of an example, the characterization of $ThO_n(OH)_m$-colloids in over-saturated thorium solutions. Results obtained by atomic force microscopy (AFM)-, scanning electron microscopy (SEM)-, transmission electron microscopy (TEM)-, PCS- and laser induced breakdown detection (LIBD) measurements are compared and discussed.

Keywords: Colloid; Aquatic; Thorium; Breakdown; Single particle

1. Introduction

Colloids are of common interest to many different research fields, and the methods applied to their characterization likewise are of diverse origins. While their presence is undesired in clean process liquids, e.g. for semiconductor manufacturing [1] or for the primary coolant of nuclear power plants [2–5], they are conveniently used for the design of 'new materials' [6,7] and also of catalysts [8]. In natural aquifers, aquatic colloids appear to play a carrier role for the migration of pollutants, in particular heavy metal ions [9] or radionuclides [10,11], which in addition show a strong tendency to form 'true' colloids [12,13].

In the aquifer the size regime spans several orders of magnitude (1 nm–several μm) and typical concentrations can vary from 10^5 to 10^{15} l^{-1} water [14]. However, due to their small size the surface to volume or mass ratio is very large (several 10 m^2 g^{-1}) and even at moderate concentrations the net surface involved in interactions with the chemical surrounding should not be

* Tel.: +49-7247-82-6064; fax: +49-7247-82-3927.
E-mail address: walther@ine.fzk.de (C. Walther).

0927-7757/02/$ - see front matter
PII: S0927-7757(02)00562-9

underestimated. In conjunction with very complex chemical properties the combination of many complementary methods is required to achieve a closed picture. Hence, colloid science represents a highly interdisciplinary field of research.

The particle size distribution (PSD) is one very important parameter of a colloidal suspension. Generally, samples show broad size distributions and since one single detection method might not cover this large range with adequate sensitivity and resolving power, several techniques have to be combined. Table 1 lists the techniques applied most frequently. The three classical separation (pre-fractionation) techniques, centrifugation, filtration, and sedimentation which are discussed in detail, e.g. in [15] and references therein, are listed along with sedimentation, which was shown to work for colloids as small as 10 nm [16]. Field flow fractionation (FFF) cannot be operated as 'stand alone' technique, but rather is to be considered a prefractionation stage followed by a particle detection unit which determines the sensitivity. A very detailed review is given in [17]. Three kinds of microscopy and four detection methods based on particle-light interaction, follow. The data on accessible sizes and concentrations may be understood as rules of thumb only. The detection limit (DL) may strongly depend on particle size (e.g. for photon correlation spectroscopy, PCS, the DL scales with the 6th power of the diameter). In many cases refined versions of the method exist, allowing the investigation of extended size ranges and the same holds for the particle concentration. The single particle counter (SPC), a method based on static light scattering, for instance, is capable of detecting colloids larger than 50 nm at very low concentrations ($< 10^4\ ml^{-1}$) [3,4,18]. Also particle composition may influence the detection limit (e.g. contrast in scanning electron microscopy, SEM, is strongly enhanced for heavy elements). For each method it is indicated whether the properties of single particles (S) or the mean values for the population (P) are mapped. S(P) indicates that the properties of the population are gained by detecting single particle events, but one event by itself cannot meaningfully be interpreted. Suitability for in-situ measurements and the extent of sample preparation necessary are itemized. Finally, the methods are categorized according to whether the system is strongly disturbed (invasiveness) and whether the same particle that has been used for size measurement is still available for further investigations (destructiveness).

One of the standard size characterization techniques nowadays is photon correlation spectroscopy (PCS), which allows in situ measurements,

Table 1
Methods for determination of colloid size and concentration

Method	Size (nm)	Concentration	Statistics	In situ	Preparation	Invasive	Destructive
Centrifugation	50–10^5	ppb	P	(x)	Med.	x	(–)
Filtration	> 1	ppb	P	(x)	Med.	x	(–)
Sedimentation	> 10	ppm	P	–	Med.	x	x
Field flow fractionation, FFF	> 2	DM	P	–	Low	x	–
Transmission electron microscopy, TEM	0.5–100	ppm	S	–	High	x	x
Scanning electron microscopy, SEM	> 10	ppm	S	–	High	x	x
Atomic force microscopy, AFM	1–1000	ppm	S	(x)	Med.	(x)	(–)
Static light scattering, SLS	> 100	ppm	S(P)	x	None	–	–
Single particle counter, SPC	> 30	ppq	S(P)	x	None	–	–
Photon correlation spectroscopy, PCS	2–2000	ppm	S(P)	x	None	–	–
Laser induced breakdown detection, LIBD	> 5	ppt	S(P)	x	None	–	x

Given sizes reflect the most common range of operation and the detectable concentrations may vary strongly with colloid size. For FFF the concentration range depends on the sensitivity of dectection method (DM). Column 'Statistics' indicates whether the properties of S)ingle particles or of the whole P)opulation are determined. S(P) means detection of single particles but statistical relevance only for an average over many measurements. Next, the suitability for in-situ measurements and the preparative work necessary are given. Finally the methods are classified, whether invasive (disturbing the system as a whole) and destructive (is the very particle measured available for additional investigations).

but is restricted to suspensions of large colloids or high number density. Electron microscopy certainly is the most powerful technique for investigating nanosystems, including element-composition and internal structure, but the initial state of aquatic colloids is disturbed during sample preparation. Atom force microscopy (AFM) is a non-destructive method of atomic resolution, but requires a relatively concentrated colloid suspension, which means that a condensation of sample might be necessary for the colloid characterization. Advantages and limitations of these methods are considered in the context of colloid formation in over-saturated solutions, a topic being investigated in the framework of gaining thermodynamic solubility data of actinides.

2. The colloids

In continuation of previous work the formation of colloids in over-saturated thorium solutions is studied [19,20]. Acidic solutions containing a well defined concentration of Th(IV) in 0.5 M HCl/NaCl were prepared. By coulometric titration the pH was increased in very small steps until the solubility was just exceeded, initiating the formation of small colloids. Fig. 1 shows the corresponding solubility diagram, where the Th(IV) concentration is plotted versus H^+ concentration on a log-log scale. Two domains have to be distinguished: Titrations in the pH range 1.5–2.5 lead to the formation of small microcrystalline $ThO_2 \cdot H_2O$(s) colloids which subsequently agglomerate to a microcrystalline precipitate [20]. At pH 3–5 hydrolysis and poly-nucleation causes the formation of amorphous thorium hydroxide colloids. The H^+ and Th(IV) concentrations at the onset of colloid formation define the solubility of $Th(OH)_4$(am).

Three suspensions are investigated in the following, denominated *A*, *B* and *C* in Fig. 1. *A* refers to the 'ThO_2 domain', at a Th(IV) concentration of 2.5×10^{-3} M at pH 1.9. Suspension *B* contains about the same amount of Th(IV) (3×10^{-3} M) at pH 3.8, hence being in the '$Th(OH)_4$ colloid domain', at strong oversaturation (vertical distance to the solubility curve) but still showing no

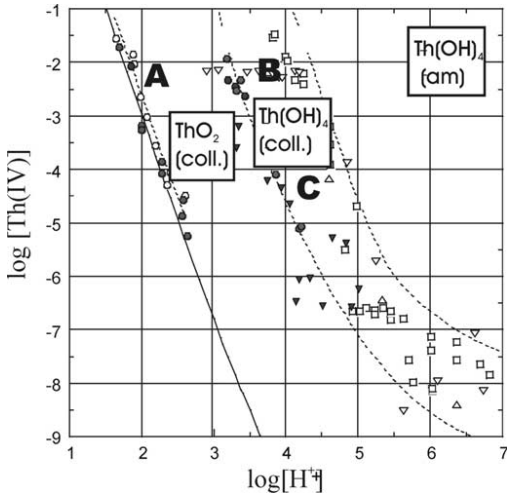

Fig. 1. Solubitity diagram of Th(IV). When the solubility is exceeded, colloids are formed: thorium dioxide at pH 1.5–2.5 (lower curve) and thorium hydroxide at pH > 3 (between the two dashed curves). Three samples *A*, *B*, and *C* are further investigated. Experimental data and investigations are taken from [19–21].

observable precipitation. Suspension *C* belongs to the same domain, but at lower concentration ($[Th(IV)] = 6.3 \times 10^{-5}$ M, pH 4.1) and closer to the solubility curve. Combination pH electrodes (type ROSS, Orion) are used to determine the H^+ concentration in 0.5 M NaCl solution. They are calibrated against standard pH buffers (pH 1–10, Merck) and standard solutions *x* M HCl/(0.5 − *x*) M NaCl with *x* in the range 0.001–0.1. This yields the relation between the H^+ concentration and measured pH_{exp} containing the activity coefficient '*A*' [21].

$$-\log[H^+] = pH_{exp} + A$$

All suspensions were aged for at least six months in order to reach equilibrium.

3. The analytical methods

3.1. Photon correlation spectroscopy

Since PCS is an easy to use in-situ method [22], allowing non-invasive, non-destructive colloid characterization without sample preparation, we tried to apply this method to our samples. Colloids

between ≈2 nm and 2 μm can be detected, however the sensitivity strongly depends on the particle size (Fig. 2) and decreases proportionally to the 6th power of the inverse particle diameter below 100 nm [23]. The suspension is available for further investigations, e.g. elemental analysis or can be measured again in order to observe time evolution. Instruments of many different manufacturers are commercially available allowing 'hands-off' operation without need for calibration. Single events are detected, but can only be evaluated to statistical relevance in large number and reflect values averaged over the sample. Typically more than 10^5 counts are summed up for the correlation function, which takes only minutes by use of intense laser light sources. A model suspension of 10 ppm ZrO_2-colloids of 100 nm diameter (Alfa Aesar, Zirconium(IV) oxide, colloidal dispersion) yields a smooth correlation function corresponding to a mean size of 92.7 nm, in good agreement with the specification of the manufacturer (100 nm). In contrast for all three thorium samples investigated here, the correlation function decays too fast due to either very small colloid diameter and/or low concentration (see below). This shows the most severe drawback of this method, the low sensitivity for particles below

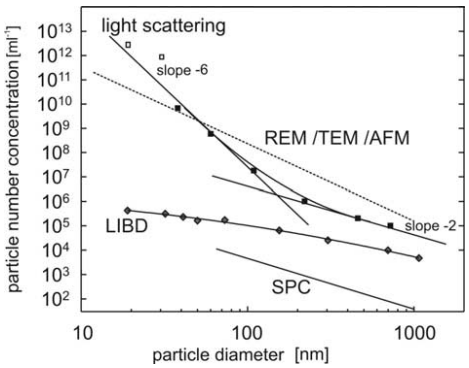

Fig. 2. Sensitivity of selected colloid characterization methods. In general light scattering methods suffer from a strong sensitivity-decrease for particles below 100 nm ($\lambda/4$). However, the SPC based on static light scattering allows to detect colloids >30 nm at ultratrace levels. LIBD shows a less pronounced size-dependence and is applicable to colloids >5 nm. The sensitivity of electron- and atomic force microscopy depends strongly on sample preparation and can deviate from the values given by the dotted curve.

100 nm. Furthermore, PCS is limited in resolving multimodal particle distributions. A comparatively small fraction of big particles can cause a large signal masking the presence of a vast surplus of small colloids. A number of sophisticated analysis and data filtering techniques were developed to gain information on size distributions. In all cases, in order to obtain concentration information from the scattered light intensity, a uniform shape of the particles must be assumed and the refractive index of the colloids must be known.

3.2. Electron microscopy

Next, the samples were investigated by electron microscopy (EM). Invented in the 1930s (TEM 1931: Knoll and Ruska [24]; SEM 1937 v. Ardenne [25]), nowadays EM plainly is *the* method of fine structure investigation [26] and widely used in the field of colloid characterization [27]. However, in general the method requires ultra high vacuum (UHV) conditions in order not to scatter the fast electrons via collisions with rest gas atoms. It is obviously not possible to study aquatic colloids in their natural surrounding, and a rather time consuming sample preparation has to be performed (coating of sample with a conductive layer). Recent developments called environmental scanning electron microscopes (ESEM) allow operation at rest gas pressures of ∼1 torr. The residual gas at the same time acts as an efficient charge carrier, allowing the investigation of *uncoated* samples [28]. There are also improved preparation techniques, conserving the structure as the sample is dehydrated [29]. In all cases the sample is heated by interaction with the high-energy electrons, causing structural changes (annealing) or evaporation of atoms.

The manifold of different types of electron microscopes [30] can be subdivided into two categories: transmission elelctron microscopes (TEM) and scanning electron microscopy (SEM), which creates a point to point image. Secondary products (secondary electrons, backscattered electrons and X-ray photons) serve as a measure of interaction strength. These emission products (X-rays from inner shell excitation or inelastically scatterd electrons) are detected from above, allow-

ing thick substrates. A very large depth of field is achieved, giving a three-dimensional impression of the objects. Particle counting and sizing is routinely performed by deposition of colloids onto a grid (or membrane after filtration) and evaluating the pictures [31]. It is a logical consequence to detect the X-rays energy-resolved by energy-dispersive spectrometry (EDS) and gain information on the elemental composition of the sample from the characteristic spectral patterns (K, L, M lines). The intensities are proportional to the respective mass concentration within the interaction volume, allowing quantitative determination of element abundance. Typical resolutions of $\Delta E \simeq 150$ eV suffice even to analyze complex colloid samples containing a multitude of elements like in natural ground-waters [31] or river and spring waters [32]. Automated micrograph evaluation algorithms allow mapping of several hundred colloids on a single particle basis as performed, e.g. for analysis of waste depository leachates [33] or natural colloids in sea sediments containing plutonium [34]. Scanning electron micrographs of suspension *C* are shown in Fig. 3. The suspension was dried on a substrate, rinsed with MQ-water in order to get rid of dissolved species (salt!) and coated with a thin chromium layer. Imaging at 25 keV reveals single colloids of 15–50 nm (top, B). Due to poor resolution, smaller structures are not resolved and it is not clear whether the observed colloids are representative of the complete sample. The large particles seen in the left part of Fig. 3 could either be due to agglomeration on the substrate or represent a very small fraction of large colloids that are not detectable with PCS. However, the large agglomerates can be probed by EDS, whereas this is not possible for single small colloids due to the limited resolution in EDS mode (several 100 nm) of the microscope used here (CamScan FE44). The large agglomerate at the bottom of Fig. 3(A) results in the EDS-spectra displayed on a log scale in the lower part of Fig. 3. The Th M-lines at 2.99 keV, 3.15 keV and the L-lines at 11.1, 15.6 and 16.20 keV are clearly visible. The background is due to the Al and Si of the mica substrate and the Cr of the coating. Summarizing, SEM is a convenient standard method to get an impression on colloid size and structure for particles larger than 5 nm. Vacuum requirements and sample drying call for some preparation and no in-situ measurements are possible. The method is both destructive and invasive, and a concentrated suspension has to be provided. There are no restrictions to substrate thickness, allowing the direct analysis of particles deposited on a filter or membrane.

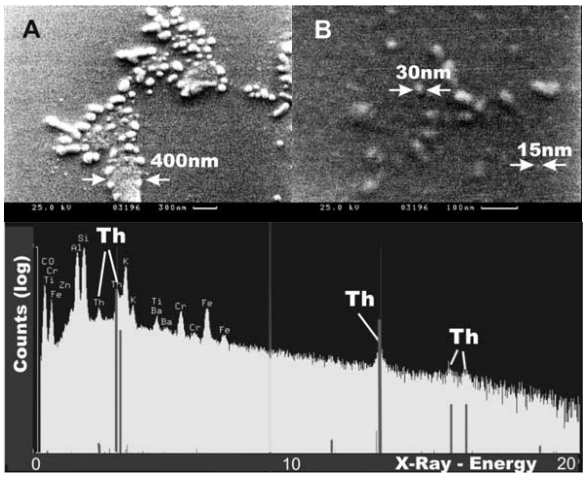

Fig. 3. The upper section shows two SEM micrographs of sample *C*. At regions of low coverage, single small colloids are resolved (B), whereas the particles form agglomerates at high coverage (A). The latter agglomerate results in the EDS spectra displayed at the bottom. The characteristic thorium X-ray-lines are clearly visible. Al, Si, Fe and Ti lines originate from the substrate (natural mica). Cr was used as conductive layer.

3.3. Atomic force microscopy

A completely different approach for surface investigations was introduced in 1981 by Binnig and Rohrer [35]. Imaging by use of electromagnetic radiation or particle beams was replaced by the direct interaction of an ultra-thin tip with the sample. The very first microscopes made use of the quantum mechanical tunneling effect, which allows electrons to 'tunnel' through a gap of several Å between two conductors. A voltage difference between tip and sample results in a current, which decreases exponentially with increasing barrier width, and serves as sensitive measure of separation. Moving the tip relative to the probe by use of piezoelectric actuators, the surface topography is

scanned. Like electron microscopy, AFM requires deposition of colloids on an atomically flat surface (e.g. mica or HOPG).

As an advantage, it can be operated in air or even in aqueous surrounding at room temperature, proving it especially suited for colloid investigations [36–40]. Although vibration isolation is recommended, resolution in the nm regime can be obtained without even a damped table. In contrast to the seemingly spatial impression SEM images offer, AFM data contain a three dimensional mapping of the surface. The vertical information is very reliable and atomic resolution is achieved, whereas lateral resolution is limited by the finite size and shape of the tip (tip artifact). Depending on the object-height and radius of the tip, the artefact may reach 50 nm, apparently increasing the diameter of a particle. The measured data has to be de-convoluted in order to obtain lateral particle dimensions as published in the case of bentonite colloids in [41]. A detailed discussion of AFM applied to investigation of colloids is given in, e.g. [27].

Samples *A* (Fig. 4) and *B* (Fig. 5) were investigated by AFM. In both images a cut along the solid line shows the vertical profile. It is

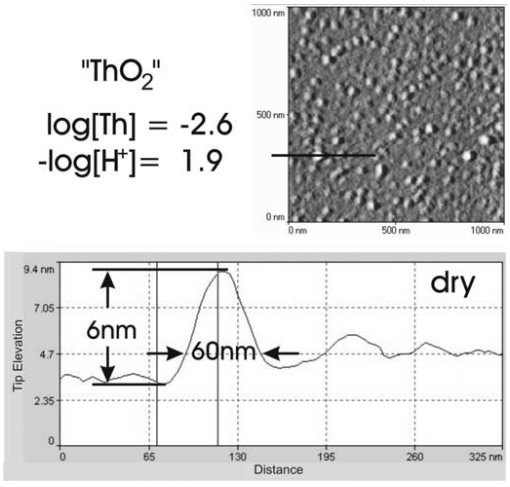

Fig. 4. AFM image of sample *A* (which was dried before measurement) and vertical profile along the solid line through one typical colloid. Averaging results in ≈4–5 nm, which agrees well with LIBD measurements, however, the lateral dimension after substraction of the tip artefact indicates agglomeration on the substrate (details see text).

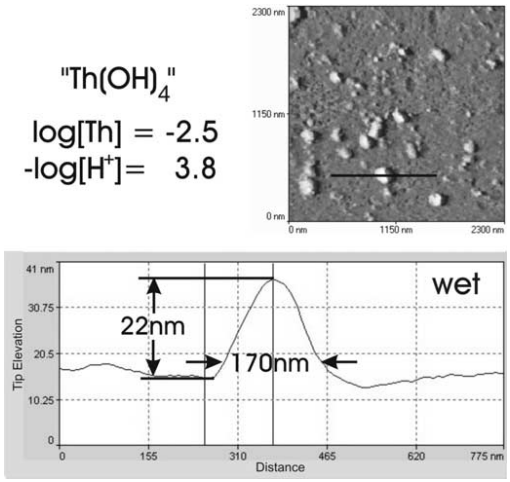

Fig. 5. AFM image of sample *B* (in wet state) and vertical profile along the solid line. As in Fig. 4, the lateral dimension does not match the height of the colloids.

obvious, that in both cases the width is much larger than the height of the particles, even after subtraction of the tip artefact. On the other hand, the vertical dimension (average 4–5 nm) is in line with the mean diameter obtained by laser induced breakdown detection (LIBD) for sample *A* (see below). For sample *B* the LIBD measurements showed a diameter of 100 nm, considerably larger than the average height in the AFM investigation (20–50 nm), but still smaller than the lateral dimension. Most likely, agglomeration occurs and small flat islands form on the charged mica substrate. The dimension of the tip (radius 50 nm) does not allow one to resolve a possible substructure.

3.4. Laser induced breakdown detection

In the late 1980s the lack of sensitive detection methods for small colloids in ultra-low concentrations (semiconductor manufacturing) lead to the development of LIBD [1,42]. When a pulsed laser is focused tightly into a medium (Fig. 6) exceeding a certain threshold irradiance, a so called breakdown occurs [43]: At least one atom is ionized by multi-photon ionization (MPI) early during the laser pulse, and the resulting seed electron is accelerated due to inverse bremsstrahlung in the high electric field of the laser focus. After gaining

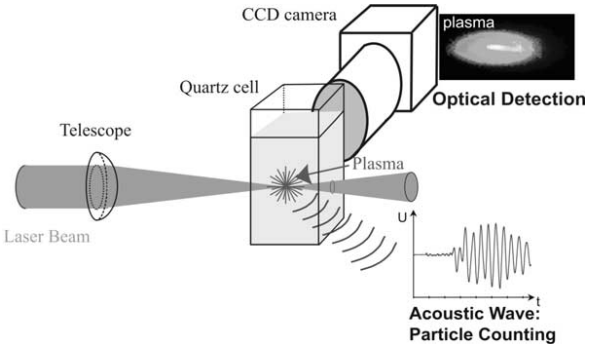

Fig. 6. LIBD, principle of operation: A plasma is ignited selectively on colloids in a suspension by a tightly focused pulsed layer. Its expansion causes an acoustic wave, which is detected by a piezo. In addition, the emitted light is observed spatially resolved by a CCD camera.

sufficient energy, additional atoms are ionized by collisions, multiplying the number of electrons. The density of free charge carriers increases in an avalanche after a few consecutive iterations and a plasma is created. However, the energy density to initiate the above process (threshold) depends on the phase of the matter in the focal region. It is highest for the gas phase, lower for liquids and lowest for bulk matter. This is made use of for particle detection: the pulse energy is adjusted such that no breakdown occurs in pure water [44]. Whenever a colloid enters the focal region, the threshold for the solid phase applies (which is exceeded) and a plasma is ignited, which can be detected by its optical emission [19,45] or by a piezo detector coupled to the sample cell, recording the acoustic signal of the plasma expansion [46,47]. By counting the number of breakdown events relative to a predefined number of laser shots (breakdown probability), the particle number density in the solution can be evaluated [48,49]. Size information is gained by determination of the breakdown probability at different energy densities: the ionization rate of a particle scales proportionally to the MPI-cross-section times the photon-flux density. The cross-section increases proportionally to the particle volume (proportional to the number of valence electrons in the particle), and hence the breakdown threshold decreases with increasing particle size and is used as a calibration curve for particle sizing. For an unknown sample the threshold is determined by recording the breakdown probability for increasing laser pulse energies (so called s-curves, Fig. 7) and converted to a mean particle diameter [50].

Within the focal region the intensity distribution decreases from the center outwards on length scales of 2 mm along the laser beam axis and 4–5 μm perpendicular to it (beam waist). This by far exceeds the size of the detected colloids and to good approximation the photon flux density a particle experiences is constant over its volume and does only depend on the position within the focus. By sorting the breakdown events according to their exact position within the focus, a flux dependency measurement and hence size determination is performed at a single fixed pulse energy [45]. Colloids down to ≈10 nm are detectable at concentrations as low as 10^4 ml^{-1}, with only a linear particle size dependence as shown in Fig. 2. Bimodal [50] or narrow [2] particle size distributions (20–100 nm) are accessible directly. Systems containing a large fraction of colloids >1000 nm have to be pre-fractionated, for instance by filtration or FFF [51].

It is important to note that the method requires some kind of calibration with monodisperse particles of well defined size (usually polystyrene

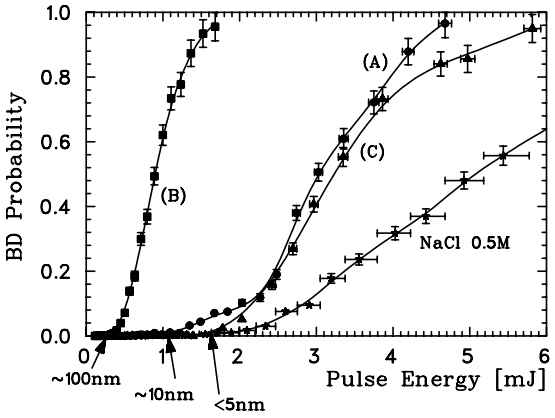

Fig. 7. All three samples are measured by LIBD without preparation or pre-fractionation and the breakdown (BD) probability as function of laser pulse energy, so-called s curves, are plotted. The energy threshold allows to determine the weighted mean particle size (arrows below x-axis). While *B* and *C* show a narrow size distribution, the saddle of *A* at low BD probability indicates a higher polydispersivity.

reference colloids). Strictly speaking, this calibration of threshold versus particle-size is only valid for this very material. For different materials the calibration might be wrong by up to a factor of 2 [49]. In consequence, the calibration has either to be repeated for the new material (if reference colloids are available), or the thresholds have to be converted using a model [48,50], which requires the ionisation potential and the MPI cross-section of the colloids. The former is easily found in standard literature [52] and can be corrected for small size and surface effects [53], but the latter generally is not known and must be calculated [54,55] by the Keldysh theory [56] or determined experimentally [57].

Summarizing, LIBD is a sensitive (ppt), method to detect single nanoparticles down to 5 nm diameter directly in liquid, without need for preparation. The method is non-invasive but destructive in the sense that the very particle measured is vaporized in the plasma. However, typically only a small fraction (10^5 particles) of the total particle content is decomposed, and the suspension as a whole is only marginally affected allowing consecutive observations of long term colloid alteration [58,59]. Reliable, even mobile systems were built and successfully applied to in-situ field studies of colloid migrations [60,61].

Applied to the $ThO_n(OH)_m$-colloids, LIBD confirms the large colloid size for *B*. The sample *A* (ThO_2 colloids) shows a breakdown threshold corresponding to $\sim$10 nm with a rather large saddle below 10% BD-probability, indicating some polydispersivity of the system. This is probably due to formation of small (2–5 nm) primary colloids which agglomerate over time. Suspension *C* exhibits a similar curve in the upper part, but with almost no saddle, hence suggesting a narrow size distribution of (2–5 nm). Due to the inherent high sensitivity of the method, LIBD measurements are also sensitive to colloidal contamination stemming from primary chemicals. It is indispensable to perform 'background measurements' of all chemicals used in the experiments. In our case this is the matrix, a 0.5 M NaCl solution. After twofold recrystallization and ultrafiltration the matrix is of sufficient purity and does not contribute considerably to the total colloid content (Fig. 7, 'NaCl').

Recently, a new LIBD apparatus was developed, applying an excimer-pumped dye-laser (Lambda Scanmate). The excitation wavelength can be tuned continuously, while the pulse energy is kept constant by a home built attenuator-feedback-loop. As described above, LIBD is based on multi-photon ionization, which, in general is a non-resonant process. Tuning the wavelength of the laser allows the use of material dependent resonances in analogy to the well known resonance enhanced multi-photon ionization process (REMPI) [62–64] used to investigate atoms and molecules in the gas phase. This 'REMPI-LIBD' was applied to samples *A* and *B* as shown in Fig. 8. While sample *B*, exhibits two pronounced absorption patterns at 480 and 450 nm, no significant enhancement is seen for the 'ThO_2' species (*A*). This result is surprising, because in both cases the thorium ion is bound in its tetravalent state. The difference is the coordination by two oxygen atoms in case *A* in contrast to four OH-groups in case *B*. Hence, REMPI-LIBD is not only sensitive to the valence state, but even to the first coordination shell of the thorium ion. A quantitative interpretation would involve spectroscopic information (absorption spectra, level schemes) on ThO_2 and $Th(OH)_4$. While the former is available in literature, to our knowledge no data exists on amorphous precipitates of the latter.

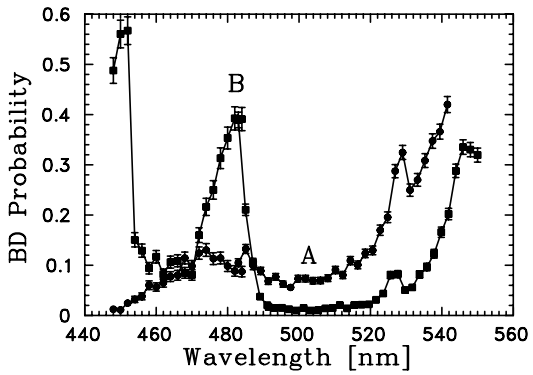

Fig. 8. Breakdown (BD) probability as function of excitation wavelength measured by an excimer pumped dye-laser system. The samples were neither prepared nor prefractionated. Sample *B* exhibits two pronounced absorption patterns at 480 and 450 nm, but no significant enhancement is seen for the 'ThO_2' species (*A*).

Hence, for the time being, this finding will only be of phenomenological nature.

A direct proof of the different composition of colloids *A* and *B* was found by transmission electron microscopy (TEM): In contrast to SEM, TEM makes use of electrons transmitted through the sample and calls for thin samples (of the order of 10–100 nm) in order not to absorb the electron beam and reduce multiple scattering of electrons. For the same reason the sample has to be water free. Suspensions *A* and *B* were dried on a TEM grid (carbon film on gold mesh) and imaged in a 300 keV transmission microscope. Due to the NaCl content of the suspension most colloids were embedded in NaCl crystals. Only a few single colloids were found, and hence the pictures might not be representative of the whole sample. The right part of Fig. 9 shows a $Th(OH)_4$-colloid of suspension *B* at 270 000-fold magnification. Its diameter of some 50 nm is still in line with the LIBD measurements, considering the low statistics of the TEM images. However, this particle exhibits substructure and seems to consist of small (3–5 nm) colloids. This confirms the assumption that the large particles of strongly over-saturated $Th(OH)_4$ suspensions are agglomerates of small primary colloids.

The left part of Fig. 9 shows a colloid of the 'ThO_2' domain. In contrast to the LIBD measurements, where the majority of particles was detected in the >10 nm regime, no such particles were observed. Only larger colloids (10–50 nm) from the 'saddle' of the breakdown curve were found. This could be due to low contrast. Even the 50 nm particle of Fig. 9(left) is hard to see against the substrate. Nevertheless the image allows the distinction of a core and a brighter outer layer of a few nanometer thickness. Both particles were further examined by transmission electron diffraction (TED). The spatial resolution of ≈ 100 nm allowed us to image diffraction patterns of the single colloids of Fig. 9. Particle *A* revealed a clear pattern (Fig. 10). The dark regions (high electron flux) correspond to strong diffraction of the (111) plane with a spacing of 3.1 Å. This is in qualitative agreement with the ThO_2 bulk value of 3.23 Å, but disagrees with findings of Dzimitrowicz et al., that the precipitate of Th(IV) has fluorite structure with a spacing of 3.4 Å [65]. While the latter group initiated rapid precipitation, great care was taken in our experiments to approach the solubility curve very slowly, so formation of colloids might proceed differently than in a precipitation experiment and lead to a more highly ordered structure. However, the diffraction patterns prove unambiguously the existence of a crystalline phase inside the colloid. For particle *B* no diffraction was observed. In consequence the particle either is completely amorphous, or it is composed of many small crystallites which are randomly oriented and

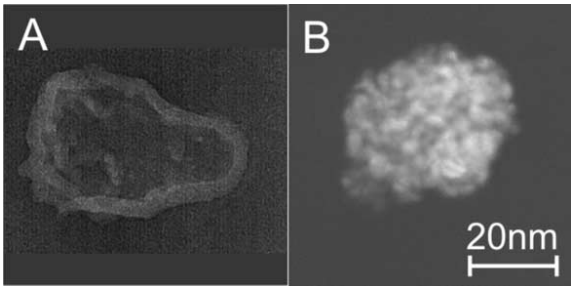

Fig. 9. TEM micrographs of samples *A* and *B*. Sample (*A*) shows a core-layer structure of presumably microcrystalline $Th(O)_2$ (see Fig. 10) surrounded by an amorphous phase containing additional water or hydroxo-species. The amorphous colloid of sample *B* is composed of small spherical 'subparticles', the structure of which is not known.

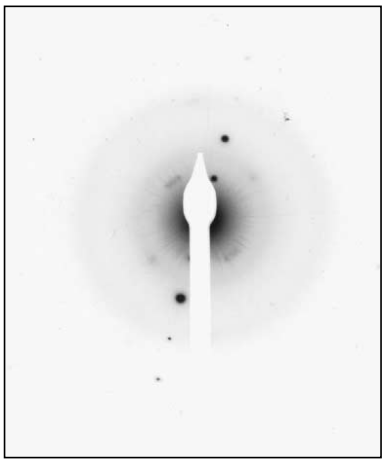

Fig. 10. Electron diffraction pattern of the single colloid shown in Fig. 9(A). The pattern indicates a lattice spacing of 3.1 Å in agreement with bulk crystalline ThO_2 (3.23 Å). The direct beam is shadowed in order to avoid saturation.

don't show a net diffraction, as is plausible from the substructure visible in Fig. 9.

4. Concluding remarks

Table 2 summarizes all data obtained for the three samples *A, B,* and C. The results for sample *A*, the crystalline colloids, are in satisfactory agreement: LIBD and SEM suggest 10 nm or below, while AFM yields an average value of 4–5 nm, and consistently PCS cannot detect any colloids since at this small size light scattering needs higher concentrations. In the TEM investigations we find a distribution of larger colloids. This is due to the low contrast of small particles and sample preparation. The suspension contains 0.5 M NaCl, and we cannot rinse the TEM grid after deposition without washing off the colloids as well. Hence, most colloids were embedded in NaCl crystallites, which was veryfied by electron-diffraction, and only very few clean thorium particles were found, leading to poor statistics. TED proved the crystallite structure of the particles with a (111) plane spacing of 3.1 Å in the core and an amorphous layer.

Sample *B* contains larger colloids due to the higher degree of oversaturation [66] (SEM: 50–100 nm, TEM 50 nm, LIBD $\approx$ 100 nm) of amorphous structure (TED), which are composed of smaller substructures (TEM), which in turn might have crystalline structure [65,21]. The AFM data of the vertical dimension, as for sample *A*, suggest smaller colloids. This might be due to a size selectivity of the adhesive forces and the attachment process to the mica, favoring smaller particles. The data of the lateral dimension shows a larger spread (up to several 100 nm), which cannot be explained by the tip artefact (50 nm). The reason most likely is the formation of agglomerates on the substrate, observed commonly during the drying process of substrates and attributed to capillary forces [67]. Had there been particles much larger than 100 nm preformed in the suspension, PCS should have given a clear signal, because the colloid-concentration of ≈ 1 ppm is just below the limit of detection for 100 nm and PCS is much more sensitive for larger colloids. In addition the breakdown threshold of LIBD would have been shifted to lower pulse energies considerably, even if only $< 1\%$ of all particles had been larger than 100 nm [50]. REMPI measurements show two resonance patterns at 450 and 480 nm which are not observed for sample *A* and indicate a difference in coordination. So far the peaks could not be assigned to known molecular resonances.

Table 2
Summary of the results for Samples *A*, *B* and *C* described in detail in the respective sections

	A	*B*	*C*
[Th]	2.5×10^{-3} M	3×10^{-3} M	6.3×10^{-5} M
pH	1.9	3.8	4.1
PCS	No signal	No signal	No signal
SEM	<10 nm	<50–200 nm	15–50 nm + agglomerates
EDS	No signal	No signal	Th lines (Fig. 3)
AFM	4–5 nm	20–50 nm	No signal
LIBD	≈ 10 nm	100 nm	2–5 nm
REMPI	No pattern	2 resonances	Not investigated
TEM	10–50 nm	≈ 50 nm	No signal
TED	X-tal 3.1 Å	Amorphous	No signal

The least information could be obtained for sample *C* due to the low thorium colloid concentration. Neither by TEM nor by AFM (wet state) were any colloids found on the substrate. The particles observed by SEM were agglomerates, which formed during the dehydration process and allowed us to perform EDS. LIBD suggests 2–5 nm size, which explains the lack of signal by PCS. REMPI investigations were not performed.

The above data are shown merely to demonstrate the capability of the respective methods. A detailed discussion on theoretical grounds will follow along with further long term investigations on colloid stability [66]. However, it should be evident that even the investigation of a relatively simple laboratory sample (only two colloidal species—ThO_2 and $Th(OH)_4$) requires a multitude of different methods. For natural samples which cover a much larger size range and in general have a complex chemical composition, this holds true all the more, emphasizing that colloid science is a highly interdisciplinary field.

Acknowledgements

I am indebted to many people who contributed to the work shown here. In alphabetical order I thank C. Bitea (LIBD), J.I. Kim (former head of the institute), V. Neck (Th-solubility), M. Plaschke (AFM), J. Römer and K. Spieler (SEM), T. Schäfer (PCS), P. Schlossmacher (TEM) and I. Yun (LIBD). In addition, I am grateful to H. Geckeis and F.J. Scherbaum for many valuable discussions and proof reading.

References

[1] T. Kitamori, K. Yokose, K. Suzuki, T. Sawada, Y. Goshi, Jpn. J. Appl. Phys. 27 (6) (1988) L983.
[2] M. Bolz, W. Hoffmann, W. Ruehle, F. Becker, Wat. Chem. Nucl. React. Sys. 7 (1996) 42.
[3] C. Degueldre, A. Bilewicz, H.P. Alder, Nucl. Sci. Eng. 120 (1995) 65.
[4] C. Degueldre, E. Schenker, H. Nobbenhuis-Wedda, Wat. Chem. Nucl. React. Sys. 7 (1996) 112.
[5] H.P. Alder, C. Degueldre, E. Schenker, Wat. Chem. Nucl. React. Sys. 7 (1996) 272.
[6] C.B. Murray, D.J. Norris, M.G. Bawendi, J. Am. Chem. Soc. 115 (1993) 8706.
[7] K. Riwotzki, H. Meyssamy, H. Schnablegger, A. Kornowsky, M. Haase, Angew. Chem. 113 (3) (2001) 574.
[8] W. Moser, Advanced Catalysts and Nanostructured Materials, Academic Press, San Diego, 1996.
[9] T. Baumann, N. Huber, S. Müller, R. Nießner, Vom Wasser 95 (2000) 151.
[10] J.I. Kim, Mater. Res. Soc. Bull. 19 (12) (1994) 47.
[11] A.B. Kersting, D.W. Efurd, D.L. Finnegan, D.J. Rokop, D.K. Smith, J.L. Thompson, Nature 397 (1999) 56.
[12] J.I. Kim, B. Kanellakopulos, Radiochim. Acta 48 (1989) 145.
[13] R. Knopp, V. Neck, J.I. Kim, Radiochim. Acta 86 (1999) 101.
[14] J.I. Kim, P. Zeh, B. Delakwitz, Radiochim. Acta 58 (1992) 147.
[15] H.G. Barth, B.E. Boyes, C. Jackson, Anal. Chem. 70 (1998) 215.
[16] T.F. Rees, Wat. Resourc. Res. 26 (11) (1990) 2777.
[17] H. Cölfen, M. Antonietti, Adv. Polym. Sci. 150 (2000) 67.
[18] C. Degueldre, H.-R. Pfeiffer, W. Alexander, B. Wernli, R. Bruetsch, Appl. Geochem. 11 (5) (1996) 677.
[19] T. Bundschuh, R. Knopp, R. Müller, J.I. Kim, V. Neck, T. Fanghänel, Radiochim. Acta 88 (2000) 625.
[20] J. Rothe, M.A. Denecke, V. Neck, R. Müller, J.I. Kim, Inorg. Chem. 41 (2002) 249.
[21] V. Neck, R. Müller, M. Bouby, M. Altmaier, J. Rothe, M.A. Denecke, J.I. Kim, Radiochim. Acta, 21 (2002) 485–494.
[22] A. Ledin, S. Karlsson, A. Düker, B. Allard, Wat. Res. 28 (7) (1994) 1539.
[23] L. Rayleigh, Philos. Mag. 41 (1871) 107.
[24] M. Knoll, E. Ruska, Ann. Phys. 12 (1932) 607.
[25] M. v. Ardenne, Z. Phys. 109 (1938) 553.
[26] S.L. Flegler, J.W. Heckman, K.L. Klomparens, Scanning and Transmission Electron Microscopy, Oxford University Press, Oxford, 1993.
[27] G.L. Hornyaka, S. Peschela, T. Sawitowskia, G. Schmid, Micron 29 (2–3) (1998) 183.
[28] H.E. Nuttal, R. Kale, Micr. Res. Techn. 25 (1993) 439.
[29] E. Balnois, K.J. Wilkinson, Coll. Surf. A, 207 (2002) 229–242.
[30] P. Rennert, H. Schmiedel, C. Weißmantel, Kleine Enzyklopädie Physik, i Editio, Harri DeutschThun, Frankfurt, 1987.
[31] C. Degueldre, I. Triay, J.I. Kim, P. Vilks, M. Laaksoharju, N. Miekeley, Appl. Geochem. 15 (2000) 1043.
[32] O. Atteia, D. Perret, T. Adatte, R. Kozel, P. Rossi, Environ. Geol. 34 (4) (1998) 257.
[33] T. Klein, R. Niessner, Vom Wasser 87 (1996) 373.
[34] M. Moring, T.K. Ikäheimonen, R. Pöllänen, E. Ilus, S. Klemola, J. Juhanoja, M. Eriksson, J. Radioanal. Nucl. Chem. 248 (3) (2001) 623.
[35] G. Binnig, H. Rohrer, C. Gerber, E. Weibel, Appl. Phys. Lett. 40 (1982) 178.
[36] C. Degueldre, Mater. Res. Symp. Proc. 465 (1997) 835.
[37] K.J. Wilkinson, E. Balnois, G.G. Leppard, J. Buffle, Colloid Surf. A 28 (1999) 155.
[38] P.H. Santschi, E. Balnois, K.J. Wilkinson, J. Zhang, J. Buffle, L. Guo, Limnol. Oceanogr. 43 (1998) 896.
[39] M. Plaschke, J. Römer, R. Klenze, J.I. Kim, Colloid Surf. A 160 (1999) 269.
[40] M. Plaschke, J. Römer, R. Klenze, J.I. Kim, Surf. Interface Anal. 30 (2000) 297.
[41] M. Plaschke, T. Schäfer, T. Bundschuh, N.M. Thang, R. Knopp, H. Geckeis, J.I. Kim, Anal. Chem. 73 (2001) 4338.
[42] T. Kitamori, K. Yokose, M. Sakagami, T. Sawada, Jpn. J. Appl. Phys. 28 (7) (1989) 1195.
[43] L.J. Radziemski, D.A. Cremers, Laser induced Plasmas and Applications, Marcel Dekker, Rochester, 1989.
[44] C.A. Sacchi, J. Opt. Soc. Am. B 8 (2) (1991) 337.
[45] T. Bundschuh, W. Hauser, J.I. Kim, R. Knopp, F.J. Scherbaum, Colloid Surf. A 180 (2001) 285.
[46] W. Hauser, FZK-Bericht 9057 (1998) 1.
[47] W. Hauser, R. Götz, Patent (Germany) DE 19602048C2.
[48] F.J. Scherbaum, R. Knopp, J.I. Kim, Appl. Phys. B 63 (1996) 299.
[49] T. Bundschuh, R. Knopp, J.I. Kim, Colloid Surf. A 177 (2001) 47.
[50] C. Walther, C.Bitea, W. Hauser, J.I. Kim, F.J. Scherbaum, Nucl. Instr. Methods B, 195 (2002) 374–388.
[51] N.G. Thang, R. Knopp, H. Geckeis, J.I. Kim, H.P. Beck, Anal. Chem. 72 (1) (2000) 1.

[52] D.R. Lide, Handbook of Chemistry and Physics, 75th Edition, CRC Press, Boston, 1995.
[53] H. Burtscher, U. Mueller, A. Schmidt-Ott, Z. Phys. D 12 (1–4) (1989) 563.
[54] J. Schwarz, P. Rambo, J.C. Diels, Appl. Phys. B 72 (3) (2001) 343.
[55] C.J.G.J. Uiterwaal, C.R. Gebhardt, H. Schröder, K.-L. Kompa, Phys. Rev. Lett., in press.
[56] L.V. Keldysh, Sov. Phys. JETP 20 (5) (1965) 1307.
[57] C. Walther, A. Herlert, J.I. Kim, F.J. Scherbaum, L. Schweikhard, M. Vogel, Chem. Phys. 265 (2001) 243.
[58] V. Neck, J.I. Kim, B.S. Seidel, C.M. Marquardt, K. Dardenne, M.P. Jensen, W. Hauser, Radiochim. Acta 89 (2001) 1.
[59] C. Bitea, C. Walther, J.I. Kim, H. Geckeis, T. Rabung, F.J. Scherbaum, D. Cacuci, Colloid Surf. A, in press.
[60] W. Hauser, H. Geckeis, J.I. Kim, T. Fierz, Colloid Surf. A 203 (1–3) (2002) 37.
[61] W. Hauser, R. Götz, H. Geckeis, B. Kienzler, Äspö progress report.
[62] U. Boesl, J. Grotemeyer, K. Walter, E.W. Schlag, Resonance ionisation and time-of-flight mass spectrometry: high resolution, involatile molecules, In: RIS 86, Vol. 84, Inst. Phys. Conf. Ser., pp. 223.
[63] J.C. Miller, C.S. Feigerle, Multiphoton ionization of transient species in supersonic jets, In: RIS 88, Vol. 94, Inst. Phys. Conf. Ser., pp. 101.
[64] T. Gibert-Legrand, T. Gonthiez, L. Vivet, P. Brault, Resonant ionisation mass spectrometry of ammonia, In: RIS 98, The American Institute of Physics, pp. 143.
[65] D.J. Dzimitrowicz, P.J. Wiseman, D. Cherns, J. Colloid Interface Sci. 103 (1) (1985) 170.
[66] C. Bitea, R. Müller, V. Neck, C.Walther, J.I. Kim, Colloid Surf. A, this issue.
[67] A. Thill, O. Spalla, Colloid Surf. A, this issue.

3.8.2 Study of the generation and stability of thorium(IV) colloids by LIBD combined with ultrafiltration [Bite03a]

ELSEVIER

Colloids and Surfaces A: Physicochem. Eng. Aspects 217 (2003) 63–70

COLLOIDS AND SURFACES A

www.elsevier.com/locate/colsurfa

Study of the generation and stability of thorium(IV) colloids by LIBD combined with ultrafiltration

C. Bitea [1], R. Müller, V. Neck *, C. Walther, J.I. Kim

Forschungszentrum Karlsruhe, Institut für Nukleare Entsorgung, P.O. Box 3640, D-76021 Karlsruhe, Germany

Abstract

The generation of Th(IV) colloids is investigated by laser-induced breakdown detection (LIBD) combined with ultrafiltration in the concentration range from 10^{-5} to 10^{-2} M at pH 3–5 in 0.5 M NaCl. The amount of colloids generated by coulometric titration of initially ionic thorium solutions depends on the total thorium concentration and the degree of over-saturation with regard to the thermodynamic solubility limit of solid Th(IV) hydroxide at given pH. These generated thorium colloids are found to be small in size and remain stable up to 400 days of investigation, without a tendency towards agglomeration or precipitation. A dilution of the suspension at constant pH downgrades colloids to ionic species, while a dilution with 0.5 M NaCl of neutral pH causes an increased over-saturation and colloid generation, leading to an equilibrium between colloids and ionic species. This equilibrium is comparable to the thermodynamic solid–liquid equilibrium of amorphous Th(IV) hydroxide. The present results allow a precise estimation of colloid generation in the dissolution of a Th(IV) hydroxide solid phase. Such a possibility may facilitate the practical solubility assessment of metal hydroxides in natural aquifer systems.

Keywords: Thorium hydroxide; Solubility; Colloid formation; Colloid stability; LIBD; Ultrafiltration

1. Introduction

The important role of colloids in solubility studies with x-ray amorphous Th(IV) precipitates, $Th(OH)_4(am)$ or $ThO_2 \cdot nH_2O(am)$, has recently been demonstrated [1,2]. As shown by laser-induced breakdown detection (LIBD) and extended X-ray absorption fine structure (EXAFS) spectroscopy [1,2], the large discrepancies between the reported solubility data of amorphous Th(IV) precipitates [1,3–8] are caused by the inclusion of colloids in the measured thorium concentrations. The objective of the present work is the investigation of colloid generation and stability as a function of time.

The applicability of LIBD to the detection of thorium colloids has been demonstrated and used in previous studies by our laboratory. Bundschuh et al. [9] combined coulometric pH titration with LIBD to detect initial colloid formation as a function the H^+ and Th(IV) concentration in 0.5 M HCl–NaCl. Exceeding the solubility limit of

* Corresponding author. Tel.: +49-7247-82-2592; fax: +49-7247-82-4308.

E-mail address: neck@ine.fzk.de (V. Neck).

[1] C. Bitea was awarded the Graduate Prize by E-MRS Colloid for this study.

0927-7757/03/$ - see front matter
doi:10.1016/S0927-7757(02)00559-9

ThO_2(cr) during the titration in the pH range of 1.5–2.5 led to the formation of small ThO_2 colloids, which subsequently agglomerate to a microcrystalline thorium dioxide precipitate [2]. When the same titration-LIBD method was applied in the higher pH range of 2.7–4.5, hydrolysis and polynucleation led to the formation of amorphous thorium hydroxide colloids [1,2]. The H^+ and Th(IV) concentrations at the onset of colloid formation define the solubility of $Th(OH)_4$(am) excluding colloidal thorium species. The solubility determined by this method is comparable with classical solubility data for an X-ray amorphous solid precipitated at pH 10 and dried at room temperature [1,8], while numerous solubility data for amorphous precipitates, not dried but only washed with water (e.g. those in [3–7]), exceed the threshold for colloid formation by 3–4 orders of magnitude. As the colloids, which are the prevailing Th(IV) species under these conditions, neither re-dissolved nor agglomerated to a precipitate, it was concluded that these Th(IV) colloids formed by chemical polynucleation reactions might be thermodynamically stable [1].

The long-time stability of the Th(IV) colloids in the suspensions produced by coulometric titration in our previous study [1] is now investigated over a period of up to 400 days. In addition, freshly prepared suspensions of Th(IV) colloids are investigated as a function of time up to 150 days. The recently improved laser system and LIBD apparatus [10] is used in combination with ultrafiltration to obtain more detailed information of the colloid size and concentration.

2. Experimental

2.1. Chemicals and analytical methods

$Th(NO_3)_4 5H_2O$ (p.a.), NaCl (p.a.) and HCl (ultrapure) are purchased from Merck. For further purification, NaCl is recristallized twice. Colloid-free thorium stock solutions are obtained by double filtrations through Amicon 10 kDa ultrafilters. All solutions are prepared in a ultrapure flow-box (class 100) with ultrapure water (spec. resistance: 18.2 MΩ cm). The aged suspensions of Th(IV) colloids have been prepared previously [1] by careful coulometric titration of 10^{-2}–10^{-5} M thorium nitrate solutions (60 ml) at $I = 0.5$ M (NaCl) and initial H^+ concentrations in the range $-\log[H^+] = 2.7$–4.1. Fresh colloidal suspensions are prepared by dilution of thorium solutions with 0.5 M NaCl of neutral pH, leading to a simultaneous decrease of [Th] and $[H^+]$ (increase of pH). In order to avoid local over-saturation the dilution experiments are performed by adding the diluent 0.5 M NaCl very slowly (20 μl min^{-1}) to the vigorously stirred thorium solutions. For this purpose, a titroprocessor (Metrohm, model 686) is used. The dilution factor is controlled by weighting the initial and final solutions. In previous experiments at low thorium concentrations $\leq 10^{-5}$ M and pH > 4, the thorium colloids were found to be sorbed almost completely onto the glass surface of the reaction vessel [1]. Therefore the colloidal Th(IV) suspensions are stored in perfluorated alkoxy (PFA) vessels. All experiments are performed at room temperature (22 ± 2 °C). It is important to note that none of the suspensions contained visible precipitates.

The total thorium concentration of the samples is determined from unfiltered aliquots and 1 kDa ultrafiltration (Filtron, pore size ca. 1.2 nm) is applied to determine the fractions of Th(IV) colloids and ionic species. Thorium concentrations are determined photometrically by the arsenazo III method [11].

A combination pH electrode (type ROSS, Orion) is used to determine the H^+ concentration in 0.5 M NaCl solution. The electrode is calibrated against x M HCl/$(0.5-x)$ M NaCl standard solutions with x in the range 0.001–0.1 and in addition against standard pH buffers (pH 1–4, Merck), using the relation $-\log[H^+] = pH_{exp} + A$ as described in [1,9].

2.2. LIBD measurements

The principle of LIBD is described in detail in [12,13]. A pulsed laser beam is focused tightly into the sample in a quartz cell. In the focal region free charge carriers are created due to multi photon ionization and inverse bremsstrahlung inducing a dielectric breakdown. Photon absorption during

the further course of the laser pulse leads to heating and expansion of the plasma. It can then be detected either optically or acoustically via its shock wave. The pulse energy density (threshold) necessary to induce a breakdown event is lower for solid matter than for water. By a suitable choice of pulse energy, breakdown events can be selectively initiated on particles in the focal volume. The ratio between the number of breakdown events and the given number of laser shots defines the breakdown probability (BDP). Information on size and concentration of colloids is gained by varying the laser pulse energy. The BDP increases with the laser pulse energy ('s-curves'). The onset of these curves ('threshold') depends on the particle size. Using latex reference colloids (polystyrene particles with a particle size of 19–1000 nm, Duke Scientific) a calibration curve is obtained, relating breakdown thresholds at BDP = 1% to particle size. The slope of the 's-curves' contains information on the mass concentration of colloids (number density).

The experimental setup used in the present study, a Nd-YAG laser with a TEM_{00} beam profile (Diva, Soliton; pulse repetition rate: 20 Hz, pulse width: 10 ns, max. pulse energy: 10 mJ at 532 nm) in combination with a piezoelectric acoustic detector [14], and its calibration with latex reference particles are described in detail elsewhere [10,15]. Time-resolved LIBD measurements are performed in a 450 μl flow-through quartz cuvette (flow rate of the suspension: 800 μl min^{-1}). The breakdown probability is derived from 500 laser shots.

3. Results and discussion

3.1. Long-time stability of Th(IV) colloids

In a recent study [1] the coulometric titration of 10^{-2}–10^{-5} M $Th(NO_3)_4$ solutions in the pH range of 2.7–4.5 in 0.5 M NaCl has been combined with LIBD for colloid detection. Contrary to the present study, the laser pulse energy was kept constant at a value somewhat below the threshold of the 0.5 M NaCl background medium. The onset of colloid formation is recognized by the steep increase of the breakdown probability. Considering colloids as small solid particles, the H^+ and thorium concentrations at the onset of colloid formation define the solubility of thorium hydroxide excluding colloidal thorium species (solid line in Fig. 1). The upper limit for the solubility of Th(IV) hydroxide (dashed line) is derived from solubility studies including colloidal contributions [3–7]. The calculations are based on the thermodynamic constants evaluated in [1,16]. Between the two curves colloidal Th(IV) suspensions can be prepared without precipitation of $Th(OH)_4$(am).

The thorium and H^+ concentrations of the colloidal suspensions at the end of the coulometric titrations performed in [1] and the corresponding values observed more than 200 days later are shown in Fig. 1 as open and filled circles, respectively. The slight increase of pH might be caused by the dissolution of a small excess of colloids provoked by local over-saturations during the titration. The colloidal thorium concentration

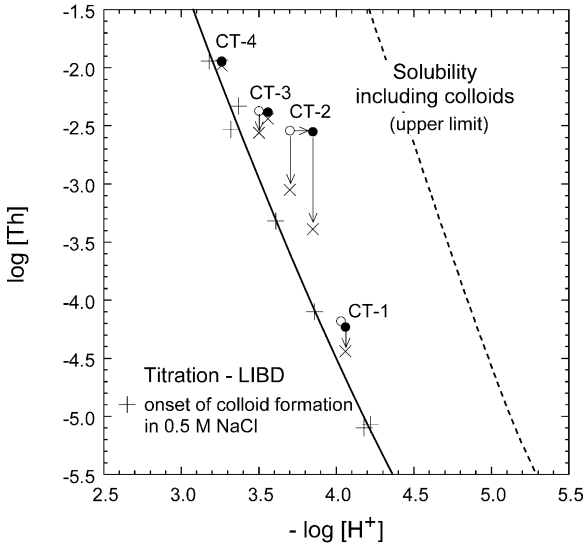

Fig. 1. Solubility of amorphous Th(IV) hydroxide in $I = 0.5$ M and 25 °C; the experimental data determined by coulometric titration combined with LIBD (+) [1] correspond to the lower solubility curve excluding colloids. The dashed line represents an upper limit referring to solubility data including colloids [3–7]. (The slope of about −4 arises from the complex $Th_4(OH)_{12}^{4+}$ included in the calculation, c.f. [1,16].) The colloidal suspensions at the end of the coulometric titrations performed in [1] are shown as open circles, those after 240–390 days as filled circles. The crosses (×) show the thorium concentration measured after 1 kDa filtration.

is calculated from the difference between the total thorium concentration $[Th]_{tot}$ and $[Th]_{filt.}$ measured after 1 kDa ultrafiltration (Filtron, pore size ca. 1.2 nm):

$$[Th]_{coll} = [Th]_{tot} - [Th]_{filt.} \quad (1)$$

The results are summarized in Table 1. As shown in Fig. 1, the thorium concentrations measured after ultrafiltration (x) are somewhat higher than $[Th]_{eq}$, the equilibrium concentration of ionic Th(IV) species at the solubility limit given by the onset of colloid formation. This indicates that ultrafiltration does possibly not lead to a complete separation of colloids.

Fig. 2 shows the LIBD measurements of these aged Th(IV) colloid suspensions in comparison to ultrapure water and the background medium 0.5 M NaCl. With increasing values of $[Th]_{coll}$ (the values determined by ultrafiltration are 2×10^{-5} M in CT-1, 4×10^{-4} M in CT-3, 8×10^{-4} M in CT-4 and 2×10^{-3} M in CT-2) both particle size and concentration increase, i.e. the threshold at BDP = 1% decreases and the slope of the 's-curves' increases. The values of $[Th]_{coll}$ increase (a) with the factor of over-saturation ($\log f_{ov} = \log[Th]_{tot} - \log[Th]_{eq}$, corresponding to the vertical distance to the solubility curve, solid line in Fig. 1) and (b) with the total thorium concentration.

Table 1
H^+ and thorium concentrations of samples prepared by coulometric titration (CT) or dilution (B–G) at $I = 0.5$ M (NaCl) and 22 ± 2 °C

Experiment/sample	Time (days)	$-\log[H^+]$	$\log[Th]_{tot}$ (unfiltered)	$\log[Th]_{filt.}$ (1 kDa filt.)	$\log[Th]_{coll}$
CT-1	1	4.03	−4.18	n.d.	
	348	4.06	−4.23	−4.44	−4.65
	489	4.07	−4.23	−4.35	−4.87
CT-2	1	3.70	−2.54	−3.05	−2.70
	117	3.85	−2.55	−3.39	−2.62
	242	3.87	−2.53	−3.09	−2.67
CT-3	1	3.50	−2.36	−2.57	−2.79
	384	3.56	−2.38	−2.42	−3.44
CT-4 = A	1	3.26	−1.95	−1.98	−3.11
A_1	111	3.28	−1.95	−1.98	−3.10
A_2	260	3.28	−1.94	−1.98	−3.05
B	26	3.36	−3.42		No colloids
C	1	3.54	−3.54		No colloids
D_0	0	4.13[a]	−4.13[a]		No colloids
D_1	3	3.92	n.d.	n.d.	
D_2	64	3.85	−4.13	−4.16	−5.27
D_3	141	3.77	−4.12	−4.15	−5.24
E_0	0	3.89[a]	−2.56[a]		−3.72[a]
E_1	3	3.70	n.d.	n.d.	
E_2	6	3.51	n.d.	n.d.	
E_3	66	3.47	−2.54	−2.57	−3.72
F_0	0	4.29[a]	−3.35[a]		−4.50[a]
F_1	1	3.83	n.d.	n.d.	
F_2	6	3.75	n.d.	n.d.	
F_3	56	3.66	−3.33	−3.39	−4.22
G_0	0	4.53[a]	−4.13[a]		−4.95[a]
G_1	1	4.16	n.d.	n.d.	
G_2	48	3.83	−4.14	−4.25	−4.78
G_3	125	3.78	−4.11	−4.21	−4.80

[a] The values at $t = 0$ are calculated from $\log[H^+]$, $\log[Th]_{tot}$ and $\log[Th]_{coll}$ measured in C, A_1, E_2 and F_2 prior to dilution with 0.5 M NaCl to suspensions D_0, E_0, F_0 and G_0, respectively, and from the corresponding factor of dilution.

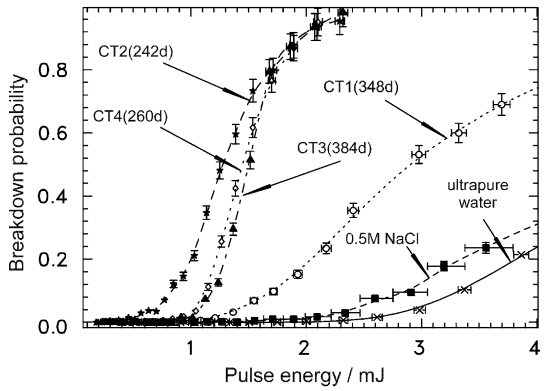

Fig. 2. LIBD measurements of aged Th(IV) colloid suspensions prepared by coulometric titration. The 's-curves' for ultrapure water and the background medium 0.5 M NaCl are shown for comparison.

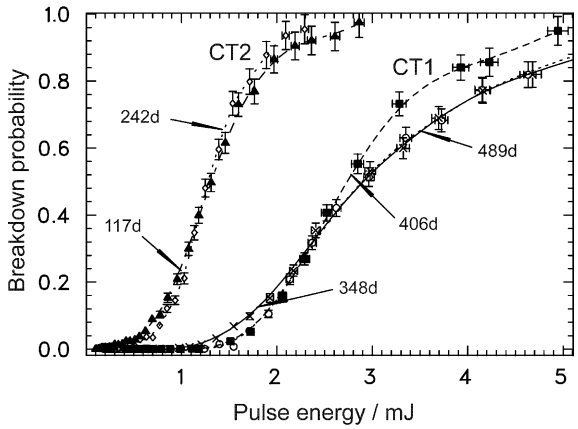

Fig. 3. LIBD measurements of aged Th(IV) colloid suspensions CT-1 and CT-2 measured after different storing times.

The 's-curve' of CT-2, the suspension with the highest Th(IV) colloid concentration, has a threshold corresponding to a particle size of $\sim$250 nm. Suspensions CT-1, CT-3 and CT-4, with considerably lower colloid concentrations $[Th]_{coll}$, contain smaller particles (about 2–10 nm). The latter particle sizes can only be estimated, because no polystyrene reference particles of this small size are available. In addition one has to be careful, applying the size calibration for the polystyrene particles directly to the thorium colloids. The sensitivity for Th(IV) hydroxide particles is found to be about 4 orders of magnitude lower than for the polystyrene particles (if the BDP measured at a given laser pulse energy is normalized to the molar concentration of Th and phenyl groups, respectively). This could be due to a very high ionization energy of the thorium colloids and a breakdown process of higher order than in the case of polystyrene particles. The size calibration could then be in error by a factor of about two. Nevertheless, the method gives information on relative differences or changes in size. The LIBD 's-curves' recorded after different storing times of suspensions CT-1 and CT-2 (Fig. 3) do no vary essentially. The small changes reflect rather the reproducibility of the measurements at different times than changes in the size and concentration of the colloids. (The shown error bars represent only statistical errors, not other uncertainties due to the possible instability of experimental parameters of the LIBD equipment.) As a first approximation, the colloids present in these suspensions can be considered as stable within the time period of investigation.

3.2. Dissolution and generation of Th(IV) colloids as a function of time

At first, the colloidal suspension A = CT-4 ($\log[Th]_{tot} = -1.95$, $\log[Th]_{coll} = -3.10$,

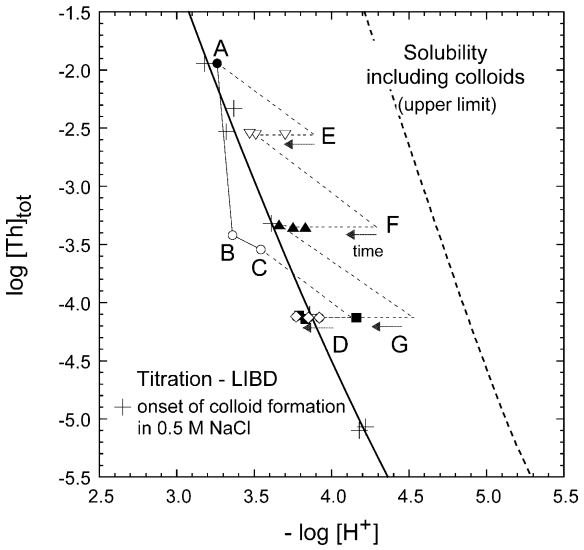

Fig. 4. Thorium and H^+ concentrations of solutions B and C and colloidal suspensions D, E, F, and G prepared by dilution of suspension A at constant pH and with 0.5 M NaCl. In suspensions D–G, the pH value is shifted with time (c.f. Table 1) to the solubility curve determined by coulometric titration combined with LIBD [1].

$-\log[H^+] = 3.26$) was diluted 1:30 with a HCl/0.5 M NaCl mixture of the same H^+ concentration. After 26 days the resulting solution B (c.f. Fig. 4) was completely free of colloids. Dilution of solution B with neutral 0.5 M NaCl yielded the colloid-free solution C, which is still below the solubility limit of Th(IV) hydroxide.

It should be noted that during the dilution of suspension A to colloid-free solution B, the H^+ concentration slightly decreased from $-\log[H^+] = 3.26$ to 3.36. This observation can be explained by the dissolution of the colloids. The colloids $Th_nO_{2n-x}(OH)_y^{nz+}$ with a charge of $0 < z < 1$ per Th unit may be written in the simplified form as 'Th(OH)$_4$(coll)' and at low Th concentrations, $ThOH^{3+}$ is known to be the predominant ionic hydroxide complex in the pH range of 3.2–4.5 [1,16,17]. Accordingly, the dissolution of colloids leads to an increase of pH:

$$\text{'Th(OH)}_4\text{(coll)'} \rightarrow ThOH^{3+} + 3OH^- \quad (2)$$

Conversely, the formation of colloids leads to an acidification of the solution:

$$ThOH^{3+} + 3H_2O \rightarrow \text{'Th(OH)}_4\text{(coll)'} + 3H^+ \quad (3)$$

The latter effect was observed when solution C was diluted with 0.5 M NaCl to obtain the colloidal suspension D above the solubility limit of Th(IV) hydroxide (c.f. Fig. 4). With increasing time the pH value is shifted to lower values. An analogous observation was made when suspension A was diluted with 0.5 M NaCl. As the resulting suspension E is highly over-saturated with regard to the solubility of Th(IV) hydroxide, small amounts additional colloids are formed shifting pH to lower values. Simultaneously with decreasing pH, the degree of over-saturation, i.e. the driving force for the formation of additional colloids, decreases as well until the final steady state is reached.

This procedure was repeated by diluting suspension E after 6 days to F and F after 6 days to G (c.f. Fig. 4). The observed decrease of pH is shown in Fig. 5 as a function of time. Steady state pH values are approached asymptotically, indicating that an equilibrium between colloids and ionic Th(IV) hydrolysis species is reached.

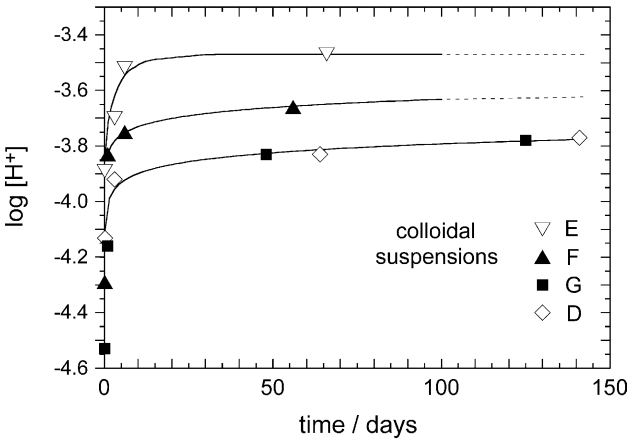

Fig. 5. Increase of the H^+ concentration (decrease of pH) as a function of time in the Th(IV) colloid suspensions D, E, F, and G.

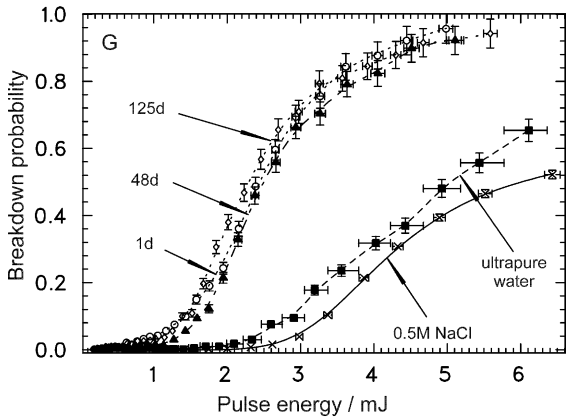

Fig. 6. LIBD measurements of suspension G ($\log[Th]_{tot} = -4.1$, $\log[Th]_{coll} = -4.8$) as a function of time.

A typical example of the LIBD measurements in the suspensions prepared by dilution is shown in Fig. 6. The 's-curves' measured for suspension G after different times show only small changes, because the colloidal thorium concentration in G_3 (measured after 125 days) is only slightly increased compared to that in G_0 at $t = 0$ (c.f. Table 1). It appears interesting to compare the steady state concentrations in suspensions D and G, because they are prepared in different ways but at the same value of $\log[Th]_{tot} = -4.13$. Suspension D is prepared by diluting the colloid-free solution B to C to D_0 of moderate over-saturation ($f_{ov} = 6$), while suspension G is obtained by dilu-

tion of suspension F_2 to G_0 at a high value of $f_{ov} = 81$. The measured steady state values of $-\log[H^+]$ (3.77 in D_3 and 3.78 in G_3) and $\log[Th]_{eq} \approx \log[Th]_{filtr}$ (-4.15 in D_3 and -4.21 in G_3) are very similar, while the amounts of colloids is somewhat larger in G_3 ($\log[Th]_{coll} = -5.24$ in D_3 and -4.80 in G_3). This observation also supports the conclusion that the final suspensions represent an equilibrium state between Th(IV) colloids and ionic species.

As the colloidal thorium concentrations $[Th]_{coll}$ in suspensions D–G are only 7–20% of $[Th]_{tot}$, (i.e. $\log[Th]_{tot} \approx \log[Th]_{eq}$), the final H^+ and thorium concentrations are found to be close to the solubility determined by coulometric titration combined with LIBD [1] (c.f. Fig. 4). Contrary to the suspensions D–G, in the aged suspensions CT-2 and CT-3 the total Th concentration largely exceeds the values of $[Th]_{eq}$ (c.f. Fig. 1) and hence $\log [Th]_{tot} \approx \log[Th]_{coll}$. In both type of experiments an equilibrium is reached between Th(IV) colloids and ionic species. The thorium concentrations measured after 1 kDa filtration in the colloidal steady state suspensions prepared by coulometric titration and by dilution with 0.5 M NaCl are comparable with the solubility data given by the onset of colloid formation as determined by the titration-LIBD method [1]. The different experimental approaches yield reasonably consistent results.

4. Conclusions

(1) From the coulometric titration experiments: the colloids formed when the solubility limit of Th(IV) hydroxide is exceeded by coulometric titration appear to be stable within the time period of investigation, i.e. up to more than 400 days. The 's-curves' measured with the LIBD show that neither the thorium colloid concentration nor the particle size changed significantly. The colloidal thorium concentration $[Th]_{coll}$ and the particle size increase with $[Th]_{tot}$ and the degree of oversaturation.

(2) From the dilution experiments: LIBD, ultrafiltration and the pH changes measured as a function of time indicate that freshly prepared Th(IV) hydroxide suspensions approach a steady state, where Th(IV) colloids are in equilibrium with ionic species. Dilution of a colloidal suspension at constant pH to a thorium concentration below the solubility limit of thorium hydroxide leads to the dissolution of the thorium colloids into ionic species.

The present results allow the quantification of colloidal thorium concentrations contributing to the total thorium concentration in solubility experiments with amorphous Th(IV) precipitates. The thermodynamic solubility given by the solubility product and the equilibrium constants of the ionic hydroxide complexes may be considerably increased by the formation of stable colloids. The modelling of the solubility increasing effect of colloids is of particular interest also for oxides/hydroxides of other highly charged metal ions.

Acknowledgements

The present work was financially supported by the European commission, in the frame of the ACTAF program within the 5th R&D framework program (contract No. FIKW-CT-2000-00035).

References

[1] V. Neck, R. Müller, M. Bouby, M. Altmaier, J. Rothe, M.A. Denecke, J.I. Kim, 90 (2002) 485–494.
[2] J. Rothe, M.A. Denecke, V. Neck, R. Müller, J.I. Kim, Inorg. Chem. 41 (2002) 249–258.
[3] B.I. Nabivanets, L.N. Kudritskaya, Ukr. Khim. Zh. 30 (1964) 891–895.
[4] H.C. Moon, Korean Chem. Soc. 10 (1989) 270–272.
[5] A.R. Felmy, D. Rai, M.J. Mason, Radiochim. Acta 55 (1991) 177–185.
[6] D. Rai, A.R. Felmy, S.M. Sterner, D.A. Moore, M.J. Mason, C.F. Novak, Radiochim. Acta 79 (1997) 239–247.
[7] D. Rai, D.A. Moore, C.S. Oakes, M. Yui, Radiochim. Acta 88 (2000) 297–306.
[8] E. Östhols, J. Bruno, I. Grenthe, Geochim. Cosmochim. Acta 58 (1994) 613–623.
[9] T. Bundschuh, R. Knopp, R. Müller, J.I. Kim, V. Neck, Th. Fanghänel, Radiochim. Acta 88 (2000) 625–629.
[10] C. Walther, C. Bitea, W. Hauser, J.I. Kim, F.J. Scherbaum, Nucl. Instr. Methods B, 195 (2002) 374–388.
[11] S.B. Savvin, Talanta 8 (1961) 673–685.

[12] T. Kitamori, K. Yokose, K. Suzuki, M. Sakagami, Y. Goshi, Jpn. J. Appl. Phys. 27 (1988) L983–L985.
[13] F. Scherbaum, R. Knopp, J.I. Kim, Appl. Phys. B63 (1996) 299–306.
[14] W. Hauser, R. Götz, Druckwellensensor, Deutsches Patentamt, Patentschrift DE 196 02048 C2 (1999).
[15] C. Bitea, C. Walther, J.I. Kim, H. Geckeis, Th. Rabung, F.J. Scherbaum, D.G. Cacuci, Time-Resolved Observation of ZrO_2-Colloid Agglomeration, accepted for publication, Colloids and Surfaces A.
[16] V. Neck, J.I. Kim, Radiochim. Acta 89 (2001) 1–16.
[17] C. Ekberg, Y. Albinsson, M.J. Comarmond, P.L. Brown, J. Solution Chem. 29 (2000) 63–86.

3.8.3 Combined LIBD and EXAFS investigation of the formation and structure of Zr(IV) colloids [Cho05b]

Anal Bioanal Chem (2005) 383: 28–40
DOI 10.1007/s00216-005-3354-6

ORIGINAL PAPER

**Hye-Ryun Cho · Clemens Walther · Jörg Rothe
Volker Neck · Melissa A. Denecke
Kathy Dardenne · Thomas Fanghänel**

Combined LIBD and XAFS investigation of the formation and structure of Zr(IV) colloids

Received: 22 March 2005 / Revised: 20 May 2005 / Accepted: 24 May 2005 / Published online: 5 July 2005

Abstract The solubility of $Zr(OH)_4$(am)—in other words hydrated Zr(IV) oxyhydroxide—is determined by means of coulometric titration (CT), and colloids are detected by laser-induced breakdown when the solubility limit is exceeded. Our results at pH 3–8 demonstrate that the solubility of $Zr(OH)_4$(am) is several orders of magnitude higher than reported classical solubility data for acidic solutions, determined from undersaturation with a less soluble microcrystalline Zr(IV) oxide precipitate. Analysis of extended X-ray absorption fine structure (EXAFS) data shows that the microcrystalline colloids in a 0.1 mol l^{-1} Zr aqueous solution at pH 0.2 contain tetrameric units, similar to those present in the structure of $ZrOCl_2.8H_2O$. Characterization of the CT solutions by means of EXAFS shows that oligomeric species form as the solubility limit is approached. The current lack of data on equilibrium constants for polynuclear hydroxide complexes prohibits the use of a realistic speciation model to describe the solubility of pH-dependent $Zr(OH)_4$(am). However, the solubility curve is obtained using the mononuclear hydrolysis constants estimated in the present paper, along with the solubility constant ($\log K'_{sp} = -49.9 \pm 0.5$ in 0.5 mol l^{-1} NaCl; $\log K°_{sp} = -53.1 \pm 0.5$ at $I = 0$).

Keywords LIBD · Colloids · EXAFS · Zirconium · Hydrolysis

Introduction

Due to its similar hydrolysis and colloid chemistry, Zr(IV) serves as a homologue for Pu(IV) and has been the focus of renewed interest in recent years [1]. However, literature data on Zr(IV) solubility in acidic aqueous media are controversial and there is considerable scatter [1–3 and references therein]. As known from investigations on Th(IV) [4], the size and nature of these colloids strongly depends upon the pH. Similar to Th(IV), recent work suggests that at least two different species of Zr(IV) colloids exist: a microcrystalline phase of very small size at low pH, and a less-ordered phase of larger particles, which determine the solubility of amorphous $Zr(OH)_4$ [5]. The microcrystalline phase, if it exists, could explain the low solubility reported by, for example, Ekberg et al [2] and Kovalenko et al [6].

In this investigation we follow the formation of Zr(IV) colloids using laser-induced breakdown detection (LIBD), while increasing the pH of the solution via coulometric titration (CT). The pH and Zr(IV) concentration at which colloids are observed to form, as detected by an increase in the LIBD signal, indicates the point at which the solubility limit is exceeded. Thus, a solubility curve is obtained, from which the solubility product is derived. In parallel investigations, we use X-ray absorption fine structure (XAFS) to characterize the structure of the Zr(IV) species in a $\sim 10^{-3}$ mol l^{-1} Zr aqueous solution as a function of pH from 1.0 to 3.3, in other words at pH values crossing the solubility limit. The XAFS studies were perfomed in order to investigate the relative importance of different structural and particle-size effects on Zr(IV) solubility. In addition, evidence for the presence of small, microcrystalline colloids at low pH is also sought, and so the structures of colloids in a 0.1 mol l^{-1} Zr aqueous solution at pH 0.2 are characterized. We use commercial reference zirconium oxide particles and monoclinic ZrO_2 as structural references for comparison. We also compare data with that for $HfOCl_2.8H_2O$ and monoclinic HfO_2.

H.-R. Cho · C. Walther (✉) · J. Rothe · V. Neck
M. A. Denecke · K. Dardenne · T. Fanghänel
Forschungszentrum Karlsruhe GmbH,
Institut für Nukleare Entsorgung,
PO Box 3640, 76021 Karlsruhe, Germany
E-mail: walther@ine.fzk.de

Zr(IV) hydrolysis and solubility

Zirconium has a strong tendency towards hydrolysis. Under the experimental conditions used here, the "free"

hydrated Zr^{4+} ion is not the dominant species. Therefore, to be able to interpret solubility data at high pH properly, the distribution of the Zr-hydrolysis species must be known. The hydrolysis reaction of the Zr^{4+} ions, in other words the formation of hydroxide complexes $Zr_x(OH)_y^{4x-y}$, is usually written as

$$xZr^{4+} + yOH^- \Leftrightarrow Zr_x(OH)_y^{4x-y} \quad (1)$$

The corresponding formation constants β'_{xy} (in a given medium) and β°_{xy} (at infinite dilution) are defined by

$$\beta'_{xy} = [Zr_x(OH)_y^{4x-y}]/[Zr^{4+}]^x[OH^-]^y \quad (2)$$

$$\beta^\circ_{xy} = \beta'_{xy}\left(\gamma_{Zr_x(OH)_y^{4x-y}}\right)\Big/\left(\gamma_{Zr^{4+}}\right)^x(\gamma_{OH^-})^y \quad (3)$$

[i] denotes the concentration of species i and γ_i its activity coefficient. The solubility products K'_{sp} (in a given medium) and K°_{sp} (at infinite dilution) of Zr(IV) oxides/hydroxides, formulated as $Zr(OH)_4$(am), refer to the reaction

$$Zr(OH)_4(am) \Leftrightarrow Zr^{4+} + 4\ OH^- \quad (4)$$

with

$$K'_{sp} = [Zr^{4+}][OH^-]^4 \quad (5)$$

and

$$K^\circ_{sp} = K'_{sp}\left(\gamma_{Zr^{4+}}\right)(\gamma_{OH^-})^4 \quad (6)$$

The specific ion interaction theory (SIT) [7, 8] is used to calculate activity coefficients, according to:

$$\log\gamma_i = -z_i^2 D + \Sigma\varepsilon_{ij}m_j \quad (7)$$

where z_i is the charge of ion i, ε_{ij} is the interaction parameter for ion i and an oppositely charged ion j, and m_j (mol/kg H_2O) is the molal concentration of ion j. D is the Debye–Hückel term at 25 °C: $D = 0.509\sqrt{I}/(1 + Ba_j\sqrt{I})$, where $Ba_j = 1.5$ and I (mol/kg H_2O) is the molal ionic strength. In order to convert the equilibrium constants from $I = 0$–1.0 mol l^{-1} $NaClO_4$ and 0.5 mol l^{-1} NaCl, the ion interaction coefficients for Zr(IV) species are set equal to those reported for analogous Pu(IV) species [9]. The SIT coefficients $\varepsilon(Zr_x(OH)_y^{4x-y}, Cl^-)$ $x > 1$ are not known, so the equilibrium constant $\log \beta^\circ_{xy}$ cannot be converted to 0.5 mol l^{-1} NaCl in order to calculate the solubility of $Zr(OH)_4$(am). Furthermore, the coefficients that are known have been determined under H^+ and Zr concentrations other than those used in this study. For these reasons, we refrain from including polynuclear species in our calculations and include only mononuclear Zr(IV) hydroxide complexes.

The first hydrolysis constant for the complex $Zr(OH)^{3+}$ is known from potentiometric studies [1, 3]. The formation constants of $Zr(OH)_n^{4-n}$ ($n = 2$–4) are estimated using the semi-empirical ligand repulsion model of Neck and Kim [10], and are listed in Table 1. The bond distance between Zr^{4+} and OH^- used in the model calculation is taken as the sum of the ionic radii, 2.22 Å ($r(OH^-) = 1.38$ Å and $r(Zr^{4+}) = 0.84$ Å for coordination number CN = 8 [11]).

If there are no complexes with other inorganic ligands or polynuclear/colloidal species present in solution, the total Zr(IV) equilibrium concentration is given by

$$[Zr]_{tot} = \left[Zr^{4+}\right] + \sum_y \left[Zr(OH)_y^{4-y}\right] \quad (8)$$

Combining Eqs. 8 with 2 and 5, we obtain

$$[Zr]_{tot} = K'_{sp}[OH^-]^{-4}\left(1 + \sum_y \beta'_{1y}[OH^-]^y\right) \quad (9)$$

We use this expression to determine the solubility product K'_{sp} from our experimental CT–LIBD data.

Experimental

Materials

The background medium in the solutions is 0.5 mol l^{-1} HCl/NaCl. A concentrated stock solution for the titration–LIBD experiments ($[Zr] = 5\times10^{-3}$ mol l^{-1} in 0.5 mol l^{-1} HCl) is prepared from ultra pure $ZrOCl_2 \cdot H_2O$ (Aldrich, 99.99%). Starting undersaturated solutions for the CT series are prepared by dilution of the stock solution with 0.5 mol l^{-1} NaCl containing 0–0.01 mol l^{-1} HCl. Zr concentrations are determined by ICP-MS. All chemicals and all stock solutions are ultrafiltrated (1.5 kDa) or, in the case of NaCl, recrystallized, in order to remove colloidal contamination; the absence of colloids > 5 nm is always confirmed by LIBD. The reference colloids (Table 3, **b**) are obtained from Postnova (ready-to-use suspension, colloid size 100 nm ± 2.5%, concentration 2.5 g l^{-1}) and diluted fivefold with ultrapure water prior to the EXAFS measurement. The monoclinic ZrO_2 (**c**) is a commercially-available sample (Fluka, p.a.).

Table 1 Equilibrium constants for mononuclear Zr(IV) hydroxide complexes

Complex	Log $\beta^{\circ a)}_{1y}$	Log $\beta'^{c)}_{1y}$
$ZrOH^{3+}$	14.3	13.02
$Zr(OH)_2^{2+}$	27.6[b)]	25.34
$Zr(OH)_3^{+}$	38.1[b)]	35.19
$Zr(OH)_4^{0}$	45.4[b)]	42.19

a) Reaction: $xZr^{4+} + yOH^- \Leftrightarrow Zr_x(OH)_y^{4x-y}$.
b) Estimated by applying the ligand repulsion model of [10].
c) Value at ionic strength 0.5 mol l^{-1} HCl/NaCl.

30

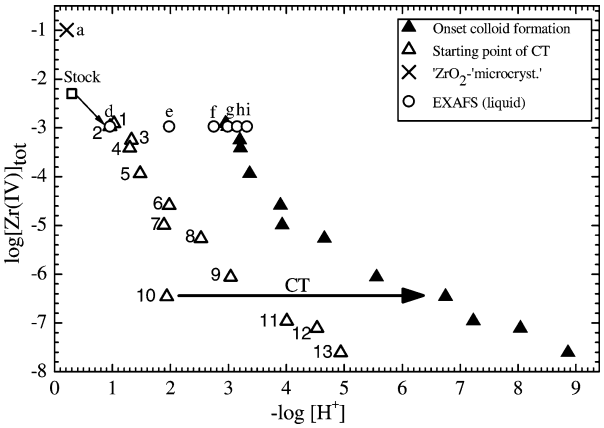

Fig. 1 Starting with the stock solution (*open squares*, pH 0.3 HCl, $[Zr] = 5\times10^{-3}$ mol l^{-1}), 13 starting solutions (*open triangles*) for the coulometric titrations (CT) are obtained by dilution with NaCl (0.5 mol l^{-1}). pH is increased by CT, as shown explicitly for series 10 (*arrow*) until colloids are formed (*closed triangles*). Six samples from series 2 are measured by EXAFS (**d–i**). In addition, a concentrated solution (pH 0.2, $[Zr] = 0.1$ mol l^{-1}) is investigated (*cross*)

Sample preparation

The Zr^{4+} concentrations and the pH values of the solutions used in the CT–LIBD experiments and the the XAFS investigations are indicated in Fig. 1. In addition, Tables 2 and 3 summarize these samples. Table 2 lists the titration–LIBD series, their Zr concentrations, starting pH and the pH values where colloid formation is observed to begin. Table 3 lists the EXAFS samples investigated, their identification letter (**a–i**) and the sample content. From the concentrated stock solution (Fig. 1, *open squares*), 13 starting solutions at concentrations ranging between $[Zr] = 1\times10^{-3}$ and 2×10^{-8} mol l^{-1} are prepared (Fig. 1, *open triangles*; Table 2: Series 1–13). The onset of colloid formation, detected by LIBD as pH is continuously increased, is indicated in Fig. 1 by *closed triangles*. EXAFS samples **d–i** belong to the CT series 2 ($[Zr] = 1.07\times10^{-3}$ mol l^{-1}). Six samples of this series 2 with increasing pH are investigated (Fig. 1, *open circles*, Table 3). For technical reasons the samples measured by EXAFS and LIBD could differ by up to ±0.03 pH units. An additional XAFS sample containing a concentrated solution at $[Zr] = 10^{-1}$ mol l^{-1} and pH 0.21 (*cross*, **a**) is also studied. Like the stock solutions for the titration experiments, it is prepared from ultrapure $ZrOCl_2.H_2O$ in HCl. No further treatment is applied. This solution is observed to be stable for >6 months and shows no evidence of precipitation.

Table 2 Summary of CT–LIBD series examined in this study (see Fig. 1)

Series	Log [Zr]	pH at CT start	pH colloid formation onset
1	−2.91	1.03	2.95
2	−2.97	1.0	3.0
3	−3.25	1.00	3.00
4	−3.41	1.3	3.21
5	−3.94	1.30	3.37
6	−4.59	1.98	3.9
7	−4.99	1.89	3.90
8	−5.27	2.53	4.66
9	−6.06	3.04	5.56
10	−6.46	1.94	6.75
11	−6.96	4.01	7.23
12	−7.11	4.53	8.04
13	−7.61	4.94	8.86

Table 3 Summary of samples examined by XAFS in this study

ID	Sample description	Colloids present
a	Concentrated "micro-crystalline" log[Zr] = −1, pH 0.2	~10 nm
b	Reference colloids	Yes
c	Monoclinic ZrO_2	–
d	log[Zr] = −2.97; pH 1.0	No
e	log[Zr] = −2.97; pH 2.0	No
f	log[Zr] = −2.97; pH 2.8	No
g	log[Zr] = −2.97; pH 3.0	Yes
h	log[Zr] = −2.97; pH 3.1	Yes
i	log[Zr] = −2.97; pH 3.3	Yes

LIBD measurements

Conventionally, solubility data is obtained by measuring the equilibrium amount of a solvated species in the presence of a precipitate starting from undersaturation. We apply a different (non-equilibrium) approach, similar to our previous study with Th(IV) [4], of using LIBD to detect the point at which colloids form in an acidic undersaturated Zr^{4+} solution upon increasing the solution pH slowly at constant Zr concentration. The colloids formed in the solution and detected with LIBD remain suspended by Brownian motion due to their small size (10–100 nm), and serve as a very sensitive indicator of when the solubility limit is exceeded. Solubility data obtained by this method [12] is of high quality and consistent with conventional solubility data of well characterized solubility limiting phases, provided pH is increased very slowly. A well suited method for this is CT [4, 13], where OH^- is generated in the (electrolyte) solution by an electric current between a Pt electrode and a Hg half cell electrode:

$$2H_2O + 2e^- \rightarrow 2OH^- + H_2$$

Typical currents of 50 μA generate $\sim5\times10^{-10}$ mol OH^- per second. A pH increase from 3.0 to 3.1 in a 50 ml solution, for instance, takes 320 min; an increase from pH 1.0 to pH 1.1 takes 540 h. Addition of a base (for example NaOH) in order to increase pH is not a good choice, as this leads to strong local gradients (regions of oversaturation) where colloids may form and may be metastable for weeks [14], even in undersaturated solution.

The LIBD technique has been described in detail previously [15, 16]. A pulsed laser is focused into the colloidal suspension and a plasma is ignited selectively when a colloid is present in the focal region and the laser power is great enough. Detecting the plasma by means of its shock wave is hence equivalent to counting colloids. The number of plasma events per number of laser shots (breakdown probability) is recorded as a function of increasing pulse energy (so called "s-curves"). From these data we can quantify the size distributions of the colloids [17]. Particles down to 5 nm in size can be detected at concentrations well below 10^{-8} mol l^{-1}.

The CT set-up during the LIBD experiments used is described in [4, 13]. Current control, pH detection, and LIBD measurements are fully automated and operated using remote-control for up to several weeks continuously for a single titration–LIBD series. pH is initially increased by (predefined) 0.1 units using an appropriate current (1,000–20 μA). After each incremental increase, the current is turned off and the solution allowed to equilibrate for 10 min, prior to the measurement of the colloid size distribution with LIBD. Once the LIBD measurement has finished, the current is switched on again, the pH is incremented again, and the procedure is repeated. Close to the expected solubility limit, the pH is increased more slowly by reducing the electric current down to 20 μA.

The following changes are made to the equipment described in [4]: in order to avoid sorption, quartz is used throughout; the reaction vessels are quartz and quartz housing is used for the salt bridge. Since a combination electrode (such as a ROSS electrode with a liquid junction) tends to leak when used for pH measurements, and so can cause colloidal contamination of the solution, two half cells (H^+-glass electrode and Ag/AgCl electrode) are used instead. We use a refined LIBD apparatus [18] so that the particle size distribution is obtained instead of merely a mean particle size. The combination of these improvements decreases the detection limit by two orders of magnitude to $[Zr] = 2\times10^{-8}$ mol l^{-1}.

XAFS measurements

Zr K XAFS measurements of samples **a–i** were performed at the Angströmquelle Karlsruhe (ANKA), Forschungszentrum Karlsruhe, Germany. Zr K edge spectra of samples **a**, **b**, and **d–i** are recorded at the INE-Beamline for actinide research [19] using a pair of Ge(422) crystals ($2d = 3.412$ Å) in the Lemonnier-type double crystal monochromator (DCM). The INE-Beamline is equipped with a collimating first and a focusing second mirror and the beam spot used was 4×2 mm^2. The data set represents the first comprehensive series of samples ever measured at this new experimental station. Sample **c** is measured at the ANKA-XAS endstation. The Si(311) ($2d = 3.274$ Å) crystal pair is used in the ANKA-XAS fixed-exit DCM. The standard beam spot size was 8×1 mm^2. Higher harmonic radiation in the incident beam is suppressed by detuning the parallel alignment of the DCM crystals to 60% of photon flux peak intensity. The spectra are calibrated against the first derivative X-ray absorption near-edge structure (XANES) spectrum of a Zr foil (17.998 keV). All spectra are recorded in fluorescence mode, with the exception of the microcrystalline colloid sample **a** and the monoclinic oxide sample **c**; these sample spectra are recorded in transmission mode. Fluorescence spectra are recorded by registering the normalized Zr $K\alpha_{1,2}$ fluorescence radiation (~15.7 keV) as a function of the incident photon energy using a 5-pixel energy dispersive solid state Ge detector (Canberra LEGe). Argon-filled ionization chambers are used. Three to six scans are collected and averaged for each sample.

XANES spectra for samples **a–i** (Fig. 4) are isolated from XAFS scans following subtraction of the pre-edge background absorption, approximated as a linear function and normalization of the edge jump (average between 18.100 and 18.300 keV) to unity.

Extended X-ray absorption fine structure (EXAFS) data analysis is based on standard least square fit techniques [20] using the WinXAS [21] (v3.0) and the UWXAFS [22] program packages. The region up to about 850 eV above the Zr K edge ($k \sim 14.5$ Å^{-1}) is investigated. The atomic background function $\mu_0(E)$ is optimized with respect to spurious contributions below ~1.1 Å (about half of the next-neighbor distance) in the k^3-weighted Fourier transform (FT) of the data using WinXAS. The ionization energy E_0, the origin for calculation of the $\chi(k)$ function, is fixed at the maximum of the most intense absorption feature—the white line (WL)—in the individual spectra at ~18.018 keV. The k^3-weighted $\chi(k)$-functions are displayed in the right panels of Figs. 5 and 6 as *thin solid lines*. Metric parameters (neighboring atomic distances R_i, mean square displacements or EXAFS Debye–Waller factors $\sigma^2{}_i$, and coordination numbers N_i for the different coordination shells i), are determined using the *feffit* code (v2.98). Backscattering amplitude and phase shift functions for single scattering (SS) paths in a 60-atom cluster in cartesian coordinates of monoclinic ZrO_2 (crystallographic data taken from [23]) are obtained from FEFF8.2 [24, 25] calculations. Hf L3 edge spectra are fit in the same manner using amplitude and phase functions calculated from crystallographic data in [26, 27] [1]. Prior to analysis, the k^3-weighted Zr K EXAFS spectra are Fourier-transformed over a k-space range of ~2.5–14.5 Å^{-1}, using symmetric square windows with $\Delta k = 0.2$ Å^{-1} "Hanning sills". All fit operations are performed in R-space over the individual radial distance ranges given in Table 4. The amplitude reduction factor [28] S_0^2 is fixed at 1.

[1] Cartesian coordinates for atoms up to 6 Å are calculated using the crystal structure in [26] and HfO_2 unit cell dimensions are taken from [27]

32

Table 4 Data range and metric parameters extracted by least-squares fit analysis of Zr K EXAFS spectra shown in Figs. 5 and 6. Values in parentheses are statistical uncertainties, except where *f* is given; in this case, the parameter is held constant during the fit procedure. Values in italics and square brackets are from the XRD crystal structure reported in [23]

ID	Fit range R–Δ (Å)	Shell	R (Å)	N	σ^2 (Å^2)	ΔE (eV)	R-factor
a	0.07–3.90	O	2.189(8)	8.8(9)	0.009(1)	1(1)	0.037
		Zr	3.59(2)	1.8(2)	0.005(f)	2(4)	
b	1.10–3.93	O	2.13(1)	7.2	0.011(1)	0(2)	0.033
		Zr	3.50(3)	4(2)	0.012(4)	5(4)	
c	0.86–3.19	O	2.16(2) *[2.168]*[7]	8.4 (1.5)	0.011(2)	–5(2)	0.018
		Zr	3.46(1) *[3.45]*[7]	6.0(1.3)	0.006(1)	–7(2)	
d	1.23–2.33	O	2.14(1)	3.2(5)	0.000(1)[a]	–2(2)[a]	0.007
pH 1.0		O	2.28(2)	3.4(4)	0.000(1)[a]	–2(2)[a]	
e	1.10–3.44	O	2.210(5)	8.8(9)	0.0053(6)	4.4(9)	0.013
pH 2.0		Zr	3.39(2)	2.2(9)	0.007(f)	8(4)	
f	0.86–3.44	O	2.201(5)	8.9(7)	0.0044(6)	3(1)	0.022
pH 2.8		Zr	3.43(2)	1.2(9)	0.004(3)	17(6)	
g	0.86–3.4	O	2.200(8)	11(1)	0.0065(9)	2(1)	0.034
pH 3.0		Zr	3.38(5)	1.0(4)	0.005(f)	11(10)	
h	0.61–3.44	O	2.200(6)	10.2(9)	0.0062(7)	–5(1)	0.021
pH 3.1		Zr	3.36(3)	3(2)	0.011(4)	–1(6)	
i	0.86–3.4	O	2.21(1)	10(1)	0.006(1)	4(2)	0.044
pH 3.3		Zr	3.42(7)	1(2)	0.006(8)	10(14)	

[a] Defined as a global parameter for both shells.

The *feffit* code evaluates randomly-distributed fit uncertainties as the amount by which a given parameter changes when values for all other parameters remain fixed, whilst maintaining the sum of squares of the difference between data and model (χ^2) below a certain limit. This procedure yields uncertainty values, which are listed in Tables 4 and 5 in parentheses. Uncertainties for the nearest-neighbor oxygen shell of $\Delta R_O \leq 0.02$ Å and $\Delta N_O = 0.4$–1.5 are obtained. Determination of fit parameters for the more distant zirconium (hafnium) backscatterers yields $\Delta R_{Zr} \leq 0.07$ Å ($\Delta R_{Hf} \leq 0.01$ Å) and $\Delta N_{Zr} \leq 2$ ($\Delta N_{Hf} \leq 1.6$). The overall goodness of the fit evaluated by *feffit* is given as the "*R*-factor" (listed in the last column in Tables 4 and 5), which is χ^2 scaled by the number of degrees of freedom in the fit of data [29]. $R = 0.02$ signifies that theory and data agree within 2%.

Simulations of Zr K EXAFS for monoclinic ZrO_2 and $ZrOCl_2.8H_2O$ are calculated using FEFF8 for a cluster of 24 and 13 atoms, respectively, with interatomic distances of up to 4.03 Å from a central Zr atom, using the XRD crystal structures reported in [26] and [30], respectively. σ^2 values for SS paths below 3 Å were set at 0.0035 Å^2, σ^2 for SS between 3 and 3.75 Å were set to 0.005 Å^2, and the remaining SS paths were given $\sigma^2 = 0.008$ Å^2. Three-legged multiple scattering (MS) paths were included in the simulation and given σ^2 values defined as the sum of σ^2 values for the individual paths involved. Hf L3 edge data for solid samples of $HfOCl_2.8H_2O$ and HfO_2 are taken from [31].

Results

LIBD

Our experimental approach, that uses CT–LIBD to determine the solubility limit, is exemplified with titration series 2, which also corresponds to the series of XAFS samples investigated. The LIBD s-curves showing the breakdown probability recorded as a function of increasing pulse energy are depicted in Fig. 2. The starting solution (**d**, $[Zr] = 1.07\times10^{-3}$ mol l^{-1}, pH 1.0) is obtained by diluting the stock solution with colloid-free NaCl. The LIBD s-curve for this solution (Fig. 2, **d**)

Table 5 Data range and metric parameters extracted by least-squares fit analysis of experimental Hf L3 EXAFS spectra shown in Fig. 7. Values in parentheses are statistical uncertainties. Values in italics and square brackets are from the XRD crystal structure reported in [26, 30]

Sample	Fit range R–Δ (Å)	Shell	R (Å)	N	σ^2 (Å^2)	ΔE (eV)	R-factor
HfO_2	1.10–3.56	O	2.12(2) *[2.148]*	7.1(1.5) [7]	0.011(3)	7(3)	0.042
		Hf	3.44(1) *[3.436]*	6.2(1.6) [7]	0.006(1)	9(2)	
$HfOCl_2.8H_2O$	1.10–3.80	O	2.154(6) *[2.184]*	6.3(5) [8]	0.0078(8)	7.8(8)	0.025
		Hf	3.55(1) *[3.539]*	2.3(9) [2]	0.005(2)	9(2)	

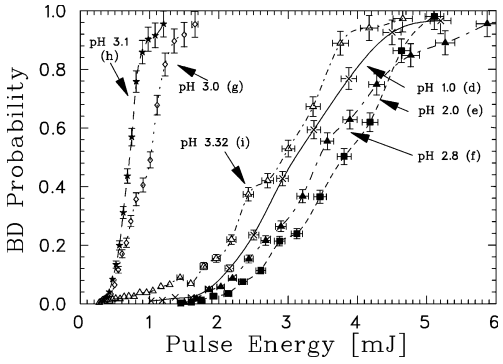

Fig. 2 LIBD measurements of titration series 2 ([Zr]$\sim 10^{-3}$ mol l^{-1}). Samples **d** (*crosses*), **e** (*filled squares*) and **f** (*filled triangles*) below pH 3 are colloid-free (high threshold of the s-curves), whereas the breakdown thresholds of samples **g** (*diamonds*), **h** (*stars*) and **i** (*open triangles*) are shifted toward lower pulse energy, which indicates the presence of colloids (for size distributions see Fig. 3)

exhibits a high pulse energy threshold (1.7 mJ), which corresponds to a mean colloid size below 5 nm, the detection limit of LIBD. Although particles smaller than 5 nm might be present, we refer to solution **d** as "colloid-free". As the solution pH is increased and LIBD measurements are made every 0.1 units (not all s-curves are shown in Fig. 2), the threshold in the s-curves at pH 2.0 (**e**) and pH 2.8 (**f**) do not significantly differ from the starting solution **d**, which proves that these solutions can also be considered to be colloid-free. When the solubility limit is exceeded at pH 3.0 (curve **g**), the breakdown threshold shifts to lower pulse energies, which is evidence for the presence of large colloids. At pH 3.1 (**h**) the colloid content is even higher. The slope of the s-curve at pH 3.3 (**i**) decreases due to a lower number of colloids. However, the shoulder of this s-curve starts at very low pulse energies, indicative of the presence of a small number of very large (>1 μm) colloids.

More detailed information is obtained from multimodal evaluation [17] of the LIBD data, from which the particle size distribution between 50 and 1000 nm can be obtained. Figure 3 depicts the differential particle number density d N_{coll}/d(ml nm) as a function of particle diameter for the starting solution (**d**), the two samples slightly above the solubility limit (**g** and **h**) and the titration-endpoint of series 2 (**i**). The colloid content of the starting solution (**d**) does not exceed the detection limit (shown as a *solid line*) throughout the size range 50–1,000 nm. The colloid size distribution of solution **g** is a near-Pareto-like shape (d N_{coll}/d(ml nm) $\propto D^{-\beta}$, $\beta = 4$, D is the colloid diameter) [32]. The missing size fraction around 300 nm is an artifact that is due to the poor statistical quality of the LIBD data, which shifts the fraction of colloids that should have been counted in this channel to 100–200 nm. The number of colloids increases in sample **h**. A further increase in pH (sample **i**) results in an apparently lower number of colloids, and colloids smaller than 200 nm were not detected at all due to size-screening effects. However, this result is misleading, and the total colloidal mass present in sample **i** most likely exceeds the one of **h** due to the presence of very large particles. These large particles cause the shoulder in the LIBD s-curve extending down to low laser pulse energies, but as a principal limitation no size information $>1{,}000$ nm can be obtained. LIBD is well suited to detecting colloids down to 5 nm in size, and the detection limit is only weakly size-dependent. However, due to the small detection volume of the laser focal region in LIBD ($\sim$100 pl), particles cannot be detected at concentrations below $\sim 10^4$ ml^{-1} even if they are very large and easily detected with light scattering.

The colloidal samples **a** and **b** were measured with LIBD and photon correlation spectroscopy (PCS). The colloids of sample **a** are $\sim$10 nm in size (LIBD: 9.8 nm, PCS 10.5 nm). The certification of the ZrO_2 colloids by Postnova (100 nm $\pm$ 2.5%) agrees well with LIBD (102 nm) and PCS (97.5 nm).

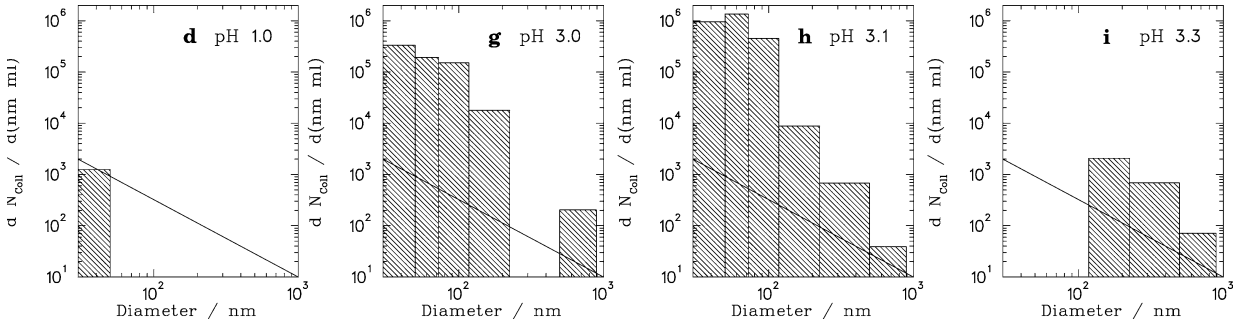

Fig. 3 Particle size distributions (PSD: number density as a function of size) for titration series 2 ([Zr]$\sim 10^{-3}$ mol l^{-1}) obtained form the s-curves of Fig. 2. The line depicts the detection limit of LIBD. *Left:* no colloids are detected in sample **d**. *Center left:* colloids form spontaneously when the solubility is exceeded (**g**). The PSD resembles a Pareto distribution, typical for natural colloidal systems. *Center right:* the number of colloids increases as the solution is titrated to higher pH (**h**) due to the higher degree of oversaturation. *Right:* the total colloidal (mass) concentration at pH 3.3 (**i**) is even higher than for sample **h**. However, the large fraction of particles >1 μm prevents the simultaneous detection of colloids <100 nm (size screening)

34

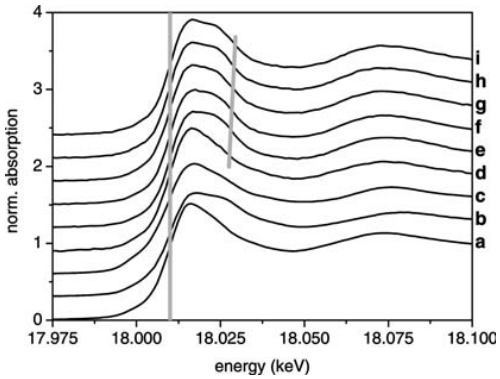

Fig. 4 Normalized Zr K-XANES spectra of samples **a–i**. See Table 3 for sample descriptions. The *gray lines* connect curve inflection points as a guide for the eye to demonstrate the peak broadening in titration samples **d–i**. Spectra have been shifted along the y-axis for clarity

XAFS

Comparison of the XANES features in Fig. 4 shows that there are slight but significant differences between the various samples. The spectra differ in the shape of their WL feature. The starting solution **d** exhibits the most intense, almost structureless WL. The remaining solution samples of titration series 2 (**e–i**) show a split WL, which broadens with increasing pH going from sample spectra **e–i** (see gray bars in Fig. 4). WL splitting in Zr K XANES spectra was reported by Li et al in their XAFS investigation of ZrO_2 polymorphs. These authors attributed the splitting and WL broadening to degenerate energy levels in the valence band, which increases with decreasing Zr absorber site symmetry [33]. The reference colloid sample (**b**) also exhibits a similar WL appearance. However, its amplitude is reduced in comparison to that of the other solution samples. The WL amplitude of the solid monoclinic ZrO_2 XANES (**c**) is also smaller than that of the solution spectra. The lower WL intensity for these two samples reflects the solid state or bulk-like density of states (final states for the excited photoelectron transition) of the solid monoclinic ZrO_2 and the reference colloids (compare [34] and [35]). Note that XANES features of the concentrated solution at low pH (**a**) do not resemble those of the solution samples **e–i**; its appearance is intermediate between that for monoclinic ZrO_2 and the starting solution **d**. This is the first indication that the Zr species in this sample is significantly different to the hydrolysis species formed during the CT. The spectrum for sample **c** is the same as that reported in [33] for monoclinic ZrO_2. None of the remaining XANES samples resemble any of the Zr K XANES for the polymorphs of ZrO_2 shown in [33].

The Zr K EXAFS and their corresponding FT spectra for samples **a** through **c** are shown in Fig. 5, those for solutions **d–i** in Fig. 6. Qualitative comparison of the spectra show that sample **d** shows one FT peak, whereas the rest of the samples exhibit two coordination shells (R–Δ peaks centered at ~1.7 and 3 Å). The titration-LIBD starting solution **d** exhibits a single damped sinusoidal EXAFS oscillation. This is not true for other samples; they show patterns resulting from interference of oscillations from backscattering on two shells. The interference pattern is especially evident in the spectra from samples **a**, **b**, and **c**. That this pattern is strong in

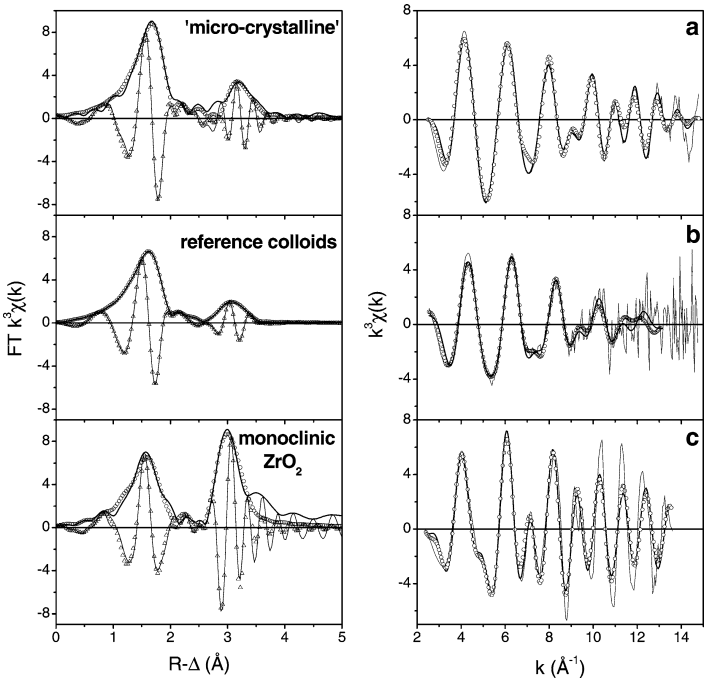

Fig. 5 Zr K EXAFS and *R*-space fit results for reference samples (**a**, **b** and **c**). *Left panel:* FT magnitude of EXAFS data (*solid line*), fit magnitude (*open circles*), imaginary part of FT (*thin solid line*) and imaginary part of fit (*open triangles*). *Right panel:* k^3-weighted raw data (*thin solid line*), back-transformed fit (*open circles*) and corresponding Fourier-filtered data (*solid line*, ranges given in Table 4)

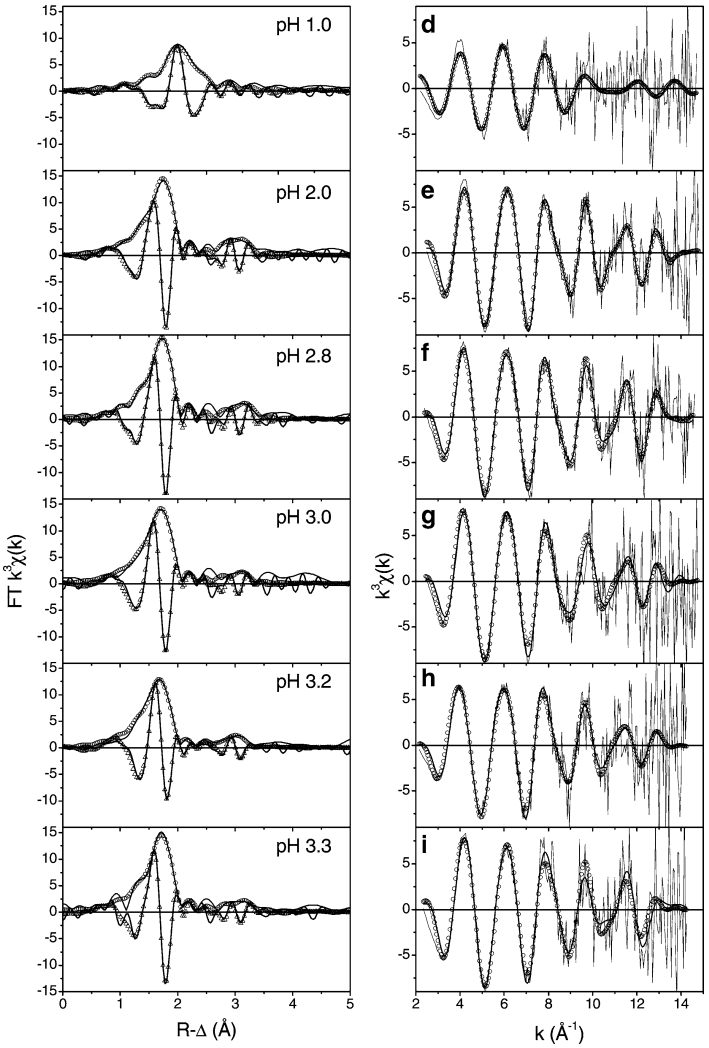

Fig. 6 Zr K EXAFS and *R*-space fit results for coulometric titration samples (**d–i**). *Left panel:* FT magnitude of EXAFS data (*solid line*), fit magnitude (*open circles*), imaginary part of FT (*thin solid line*) and imaginary part of fit (*open triangles*). *Right panel:* k^3-weighted raw data (*thin solid line*), back-transformed fit (*open circles*) and corresponding Fourier-filtered data (*solid line*, ranges given in Table 4)

the spectrum of sample **a**, the concentrated solution at low pH, is an indication that this sample indeed contains a major fraction of the Zr in the form of a "crystalline" component. This supports our hypothesis that Zr(IV) colloids exist as a microcrystalline phase of very small size at low pH. Upon comparing the oscillatory pattern of **a**, **b**, and **c**, we see that the pattern of **a** is unlike that of the reference colloids (**b**) and of the monoclinic ZrO_2 (**c**). The values for *N* and *R* obtained in fits to the data (Table 4) for the O and Zr shells in **a** are higher than those obtained for the reference colloids (differences being >0.03 Å and >0.14 Å for *R*(O) and *R*(Zr), respectively) and for monoclinic ZrO_2.

In order to explore what the structure of the microcrystalline particles is, we first compare its EXAFS with simulated data. Figure 7 depicts simulated Zr K EXAFS calculated for monoclinic ZrO_2 and for $ZrOCl_2.8H_2O$. Upon comparing the simulated spectra for $ZrOCl_2.8H_2O$ with the experimental spectrum obtained for the microcrystalline phase (**a**), also plotted in

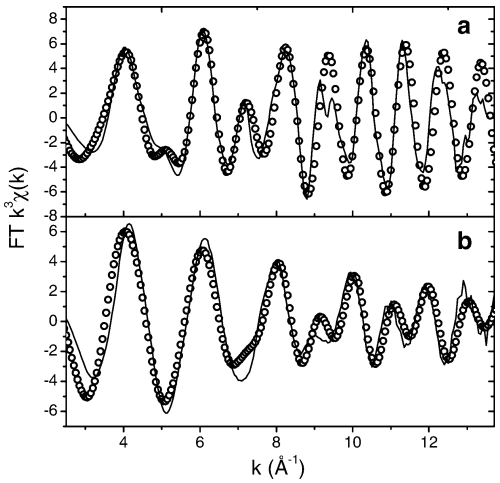

Fig. 7a–b Simulated Zr K EXAFS (*circles*) calculated using FEFF8 for monoclinic ZrO_2 (*panel a*) and $ZrOCl_2.8H_2O$ (*panel b*), compared to the experimental EXAFS for sample **c** and sample **a** (*continuous lines*)

Fig. 7, we find a good qualitative agreement. Of course, the simulated ZrO_2 spectrum exhibits the general qualitative features observed in the experimental spectrum for monoclinic ZrO_2 (**c**). The splitting of the oscillatory maximum in the experimental data near $k \sim 9.35$ Å^{-1} is due to contributions from MS paths [36]. These paths have effective lengths outside of that considered in the EXAFS simulation, so the splitting is not present in the simulated spectrum. Because MS paths are not included in the fits, it is also lacking in the back-transformed fit and the Fourier-filtered data for sample **c** (Fig. 4).

We then compare data (Fig. 8) for sample **a** to published Hf L3 EXAFS [31] for monoclinic HfO_2 (isostructural with monoclinic ZrO_2) and crystalline $HfOCl_2.8H_2O$ (isostructural with $ZrOCl_2.8H_2O$). Although the bond lengths are not the same in the two compounds, so that the interference pattern in the EXAFS is not exactly the same, the similarity between the FT spectra for ZrO_2 (Fig. 6) and HfO_2 is evident. The microcrystalline spectrum **a** is dissimilar to these monoclinic oxide spectra; its spectrum is more like that of $HfOCl_2.8H_2O$. Table 5 lists the results for fits to the $HfOCl_2.8H_2O$ and HfO_2 *R*-space data using a two shell model (O and Hf). The *R*(O) values obtained for both compounds are within 0.03 Å of the XRD values, those for *R*(Hf) the same in HfO_2 and within 0.01 Å for $HfOCl_2.8H_2O$. We now compare these results to those obtained for sample **a** (Table 4). Similar to our observations comparing sample **a** with ZrO_2, we find longer *R*(O) and *R*(Hf) in **a** compared to distances found for monoclinic HfO_2 (0.07 and 0.15 Å longer for O and Hf, respectively). The interatomic distances in **a** agree better with those in $HfOCl_2.8H_2O$. In fact, the value for *R*(O) of 2.19 Å in **a** is within experimental error the same as that reported for the average Zr–O distance in $ZrOCl_2.8H_2O$, 2.21 Å [30]. The EXAFS fit to sample **a** indicates the presence of a second next-neighbor Zr coordination shell with a coordination number of 2. This is the same as that found for fit results for $HfOCl_2.8H_2O$, as this compound's crystal structure contains tetrameric $[Hf_4(OH)_8(H_2O)_{16}]^{8+}$ structural units. The fit results for **a**, a comparison to Hf solid reference compound structures and the corresponding simulated Zr data allows us to conclude that the stable $[Zr] = 10^{-1}$ mol l^{-1} and pH 0.2 solution (**a**) contains microcrystalline particles (LIBD: ~10 nm in size), whose structure is comprised of tetrameric $[Zr_4(OH)_8(H_2O)_{16}]^{8+}$ units and which represent the major part of the Zr in solution. The Zr–Zr (Hf–Hf) distance at ~5 Å in the tetrameric unit is not visible in the spectra recorded here at room temperature.

The FT of the solution at pH 1 (spectrum **d**) exhibits one asymmetric peak. When spectrum **d** is modeled using a single shell, the fit result for the mean distance obtained is 2.21 Å . However, the phase of the model curve does not match that of the experimental data at *k* values above 10 Å^{-1}. This and the strong asymmetry of the FT peak for this sample indicate that the distribution of oxygen around Zr is non-Gaussian. When a third cumulant is added to the fit to compensate for this asymmetry, a large value for this parameter (0.0016 Å^3) is obtained. We therefore model spectrum **d** with two separate oxygen shells. With the *k*-range available, the statistically-available resolution ($\Delta R = \pi/2\Delta k$) is large enough to resolve these shells with an observed difference in bond distance of 0.14 Å . These Zr–O distances are within experimental error the same as the mean distances to hydroxyl and water ligands (Zr–OH^- and Zr–OH_2) in the tetrameric $[Zr_4(OH)_8(H_2O)_{16}]^{8+}$ structural unit in the crystal structure $ZrOCl_2.8H_2O$, 2.142 and 2.271 Å (mean = 2.207 Å), respectively. However, no indication of any Zr–Zr interatomic distance is found, not in the raw data (although noisy) nor in the residual after the fit (experimental data minus model curve; not shown). These results indicate that the starting sample **d** at pH 1 has significant amounts of hydrolyzed, likely mono-

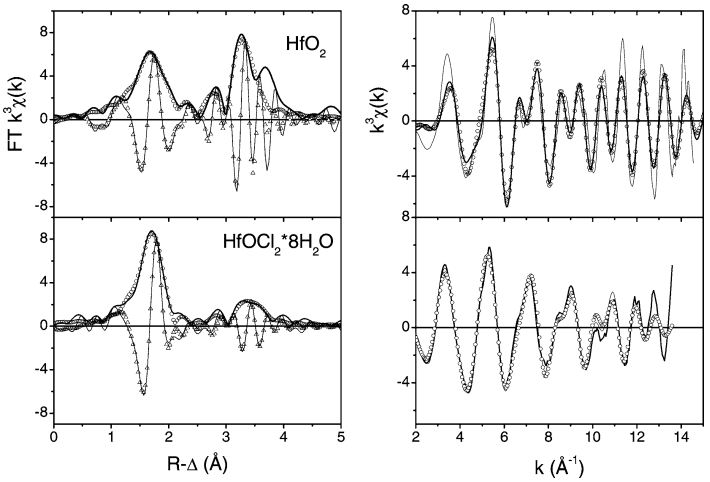

Fig. 8 Hf L3 EXAFS and *R*-space fit results for monoclinic HfO_2 and $HfOCl_2.H_2O$. *Left panel:* FT magnitude of EXAFS data (*solid line*), fit magnitude (*open circles*), imaginary part of FT (*thin solid line*) and imaginary part of fit (*open triangles*). *Right panel:* k^3-weighted raw data (*thin solid line*), back-transformed fit (*open circles*) and corresponding Fourier-filtered data (*solid line*, ranges given in Table 5)

meric, Zr(IV) species, in agreement with hydrolysis constants listed in Table 1.

None of the spectra for samples with pH 2 and higher resemble the reference colloid spectrum (**b**), that for monoclinic ZrO_2 (**c**), the stable colloids at low pH (**a**), or the starting solution at pH 1 (**d**). We conclude that the Zr in these titration samples must have a different structure than in these other compounds and solution samples. The XANES spectra discussed above suggest the same. The interference pattern between oscillations from the O and Zr shells in the titration samples **e–i** is not as strongly evident as for samples **a–c** (Fig. 4), but can easily be identified above k values of around 10 $Å^{-1}$. Metrical parameters obtained from fits to the data for samples **e–i** using a two shell (O and Zr) model are listed in Table 4. What we observe in the fit results is that the values for N(O) for these samples are all larger than for the samples **a–c**, that the R(O) value is invariant of pH (all ~2.21 Å), and that R(Zr) exhibits more scatter than the O shell but remains about 3.41 Å. The R(O) value of 2.21 Å nearly corresponds to the sum of ionic radii for octa-coordinated Zr(IV) [11], suggesting that N(O) should be eight. That the amplitude of the Zr–O shell is greater in the titration series than in the other samples suggests that there is a more inherent order in the Zr–O shell in these samples compared to the other compounds studied. However, the values for N appear to be unrealistically large. The fit to spectrum **c** yields 8.4, which is greater than the expected 7. The 8.4 value lies within the range of the error associated with N determinations with the EXAFS method, ~20%. However, we expect a priori a lower amplitude for this shell resulting from destructive interference of the EXAFS oscillations for the seven close-lying O distances (2.16 ± 0.09 Å), similar to that observed for HfO_2. From the 2.21 Å bond distance and through comparison of amplitudes observed for ZrO_2 we conclude that the N(O) values in Table 4 are over-estimated. The 3.41 Å Zr–Zr distance found in the fits is 0.18 Å shorter than that observed for sample **a**, 0.15 Å shorter than in $ZrOCl_2.8H_2O$ [30] and 0.09 Å shorter than in the reference colloids. A mechanism of simply joining tetrameric $[Zr_4(OH)_8(H_2O)_{16}]^{8+}$ units to form sheet or stacked octamers, which may grow further to form colloids as suggested in the literature for concentrated, acidic Zr(IV) solutions [37–40], appears unlikely. If tetrameric units condense to form the colloids, we would observe both an increase in N(Zr) and a longer R(Zr) than obtained in the fits. The amplitude of the Zr–Zr interaction does not increase, as would be expected for simple growth of octamers. The observed increase in coordination number over that of monoclinic ZrO_2, and the value obtained for R(Zr) of 3.41 Å in the titration solutions is in accord with XRD results reported by Zyusin et al for amorphous Zr(IV) precipitates obtained by adding ammonia to zirconium nitrate solutions [41]. These authors report a comparable Zr–Zr distance of 3.40 Å, but a Zr–O bond length of 2.14 Å (with a coordination number of eight), which is shorter than that observed for the titration samples.

The observed R(Zr) of 3.41 Å in the titration solutions does not match mean distances in known ZrO_2 polymorphs. This R(Zr) of 3.41 Å is smaller than that of monoclinic ZrO_2 (Table 4), shorter than in orthorhombic ZrO_2 with a mean Zr–Zr distance of 3.469 Å [42], as well as much shorter than the cubic [2] and tetragonal forms of ZrO_2 [43], both having interatomic Zr–Zr distances of ≥3.6 Å. Furthermore, the EXAFS oscillatory pattern for samples **e–i** does not match published data characteristic of these various individual phases [33]. The values for R(O) and R(Zr) for the titration series samples above pH 1 are also different to those reported for thin films of amorphous ZrO_2 reported in [36]. We note that the samples **e–i** are not well modeled with just two coordination shells (O and Zr). The metrical parameters obtained in the fits have large uncertainties in the parameters associated with the EXAFS amplitude. Some of the uncertainties for R(Zr) are even larger than what one usually finds (within ~0.03 Å). In particular, the Zr shell for the titration samples does not appear to be modeled well with one distance. The large uncertainties associated with the fit to this shell and the large fluctuations in its corresponding ΔE_0 values, as well as the partially unphysically low σ^2 values, suggest that there may be more than one distance near 3.41 Å in these samples. The signal-to-noise ratio in the spectra is not adequate to attempt to model this shell with more than one distance, however.

When taken together, all of these observations for the EXAFS of the titration samples **d–i** allow us to make the following conclusions. The observed Zr–Zr distance is evidence that polymeric, oligomeric species, or more condensed colloid species exist in all of the solutions investigated, with the exception of the starting solution **d** with pH 1. The structure of these solution species is not a simple ZrO_2; it has neither the monoclinic, cubic, orthorhombic, nor tetragonal ZrO_2 structure. Its structure also cannot be derived from simple stacking of tetrameric $[Zr_4(OH)_8(H_2O)_{16}]^{8+}$ units. The Zr–O coordination number of the polynuclear species in the samples with pH≥2 is likely near eight, and its distance shows little variation. At the same time, the Zr–Zr interaction is relatively small, and this coordination shell is possibly comprised of more than one distance. A possible interpretation of these apparent reverse trends in the O and Zr coordination is the following. We interpret these results as indicating that the species are built up of primarily ZrO_8 building blocks, but the associated Zr sublattice is highly disordered. The ZrO_8 building blocks can take on different geometries and related polyhedra (idealized polyhedra being cube, square antiprism, dodecahedron and hendecahedron). Zirconium exhibits a great variety of geometric variations in its primary coordination sphere. There is apparently a low energy difference between one geometry over another [44]. The order in the first O shell and the simultaneous variation in the Zr–Zr interaction may

[2] Calculated for the *Fm– 3m* space group; $a = 5.09$ Å

result from the polymerization of ZrO_8 building blocks with different geometries. Their polymerization and packing into a more condensed system would necessarily lead to a disordered and defect-rich Zr sublattice.

Discussion

Hydrolysis and solubility constants

The distribution of Zr hydroxide species ($Zr(OH)_n^{4-n}$; $n = 0$–4) as a function of pH is calculated assuming the absence of polynuclear species and using the hydrolysis constants listed in Table 1 after conversion of the constants for infinite dilution to constants for the present experimental conditions ($I = 0.5$ mol l^{-1} NaCl/HCl). The Zr and H^+ concentrations of the titration experiments and the onset of colloid formation detected by LIBD are illustrated in Fig. 9. The solubility curves defined by the onset of colloid formation observed in LIBD measurements are used to calculate the solubility product of $Zr(OH)_4$(am). The experimental data do not allow independent determination of the solubility product and the hydrolysis constants so that the log β'_{1y} for $I = 0.5$ mol l^{-1} are used as fixed values in the case of $y = 1$, 2 in Eq. 9. The log β'_{1y} ($y = 3$, 4) and solubility product K'_{sp} are obtained from a least squares fit (Gauss–Newton algorithm) to the LIBD-data.

Using the LIBD solubility curve, the following solubility product is obtained

$$\log K'_{sp} = -49.9 \pm 0.5 \quad (\text{in } 0.5 \text{ mol } l^{-1} \text{ NaCL/HCL}) \tag{10}$$

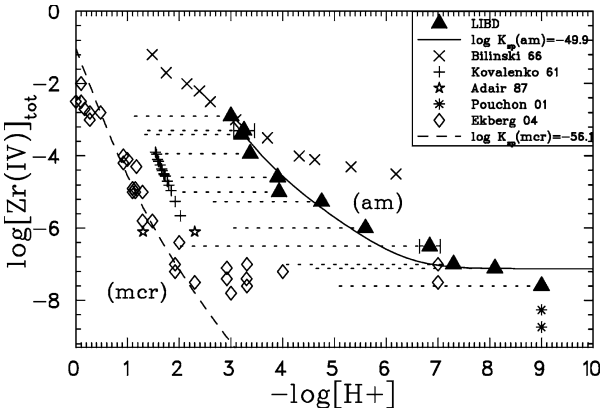

Fig. 9 Solubility plots showing two distinguishable regions. A low solubility is found in dissolution experiments of X-ray amorphous Zr-precipitates (mcr) [2, 6, 45]. However, solutions of much higher Zr concentrations are found to be stable and colloid free [46, this work LIBD, *dashed lines*]. The points of onset of colloid formation (am: amorphous zirconium-hydroxide) (*filled triangles*) are well reproduced (*solid line*) using the mononuclear hydrolysis constants (Table 1) and a solubility constant of log $K'_{sp} = -49.9 \pm 0.5$ (at $I = 0.5$ mol l^{-1}). *Asterisk* indicate data from [53]

Using Eq. 6 yields

$$\log K^{\circ}_{sp} = -53.1 \pm 0.5 \quad (\text{at } I = 0) \tag{11}$$

The LIBD solubility curve, depicted as *solid triangles* in Fig. 9, is well reproduced using mononuclear hydrolysis constants estimated using the ligand repulsion model of Neck and Kim [10] and these solubility products (Eqs. 10 and 11). However, polynuclear species are most likely present for concentrations $[Zr] > 10^{-5}$ mol l^{-1}, and hence the description using mononuclear species alone is not realistic for high concentrations.

Colloid and oligomer size and structure

In addition to the LIBD solubility curves determined in this work, Fig. 9 shows various literature solubility data. We can distinguish between two different types of data. Data obtained from undersaturation experiments [2, 6, 45] yield solubility products several orders of magnitude lower than data obtained under oversaturation conditions [46, present work]. A similar effect is also observed for solubility studies of Th(IV). The solubility of crystalline or microcrystalline Th(IV) oxide is reported to be log $K^{\circ}_{sp} = -54.2$ [47] and –53.2 [13]. The solubility of the amorphous phase $Th(OH)_4$(am) is log $K^{\circ}_{sp} = -47.8$ [4]. Titration–LIBD studies with Th(IV) [4, 12] show that colloid formation occurs immediately and reproducibly when the solubility of $Th(OH)_4$(am) is exceeded. In contrast, it is possible to prepare colloid-free solutions in Th and H^+ concentrations above the solubility limit for microcrystalline Th(IV) oxide but below the solubility of $Th(OH)_4$(am). Assuming that Zr(IV) exhibits a behavior similar to that of Th(IV), we turn to the interpretation of the EXAFS and LIBD measurements.

The most concentrated solution, sample **a** ($[Zr] = 0.1$ mol l^{-1}, pH 0.2) contains particles of ~10 nm (Table 3). These particles are slightly smaller than experimental findings for "microcrystalline ThO_2" colloids at lower concentration [34, 47] (16–23 nm) and calculations of particle size by means of Schindler's equation [48] from solubility data [4] (13–29 nm). The EXAFS measurements for **a** show a strong Zr–Zr interaction and a single oxygen shell with metrical parameters corresponding to those for tetrameric $[Zr_4(OH)_8(H_2O)_{16}]^{8+}$ units. Singhal et al report similar results, identifying the presence of tetrameric units at $[Zr] = 0.05$ mol l^{-1} and pH below 0.7 by means of small angle X-ray scattering experiments [37]. The $[Zr_4(OH)_8(H_2O)_{16}]^{8+}$ unit is also reported to exist by Hagfeldt et al [38] at higher H^+ concentrations. That a Zr–Zr interaction is observed at all contrasts with the earlier findings of Ekberg [49], where monomeric Zr^{4+} and $ZrOH^{3+}$ species were stated to dominate at this pH range.

The starting solution of the CT series (**d**, $[Zr] \sim 10^{-3}$ mol l^{-1}, pH 1) is colloid-free according to LIBD. No Zr–Zr interaction is observed in this sample by EXAFS. This means that, if polymeric species do exist, they are a

minority species. The interpretation of their solubility data by Ekberg et al [2] as referring to $Zr(OH)_4(am)$ cannot be correct, as it is possible to prepare a colloid-free solution in this Zr and H^+ concentration range, which exceeds Eckberg's reported solubility by more than one order of magnitude.

No colloids are detected by LIBD in the course of the titration up to pH values below 3.0 at $[Zr]\sim10^{-3}$ mol l^{-1}. However, analysis of the EXAFS data for sample **e** at pH 2.0 and sample **f** (pH 2.8) reveal the presence of a Zr–Zr distance. This indicates that, as the solubility limit is approached and before measurable colloids are present, oligomeric Zr species form. Several charge compensation mechanisms have been suggested in the literature for forming larger compounds from charged hydroxo species. Hagfeld et al [38] suggested a charge compensation by Cl^- ions, Tulock et al [50] formulated the hydrolysis reaction

$$[Zr(OH)_2, 4H_2O]_4^{8+} \leftrightarrow [Zr(OH)_{(2+x)}, (4-x)H_2O]_4^{(8-4x)+} + 4xH^+$$

for the formation of colloidal Zr as the pH is increased. Singhal [37] and Hu [51] found evidence for the formation of neutral octamers during forced hydrolysis. All effects may play a role during colloid formation, from sample **d** through **h**. At a pH close to 3 (**g**), colloids are detected by LIBD. These colloids grow in size, with size distributions extending to μm-size particles, as the titration proceeds and the pH increases (Fig. 3). The samples containing colloids investigated with EXAFS (**g–i**) are observed to exhibit a disordered Zr–Zr coordination shell, leading to small amplitudes. This may result from the presence of more than one distance near 3.41 Å and numerous defects in the Zr sublattice.

It is difficult to compare these findings on Zr(IV) with earlier investigations on Th(IV) [4] and Pu(IV) [35], since the earlier studies were not evaluated with regard to size distributions, only for a mean particle size. Colloids are observed to form as hydrolysis products of Pu(IV) at higher acidity due to the lower solubility product of Pu ($\log K^\circ_{sp} = -58.7$ [52]) and have a mean size of 10–15 nm. However, a small number of aggregates large enough to cause light scattering are also formed. Zr forms large aggregates within a few minutes after the solubility limit is exceeded and these colloids do not dissolve for several months. Further growth of the colloids is observed in the course of a few days until an equilibrium is reached. The colloid growth is accompanied by a slight increase in acidity due to the formation reaction

$$ZrOH_2^{2+} + 2H_2O \rightarrow Zr(OH)_4(coll) + 2H^+ \qquad (12)$$

in analogy to Th [14]. If colloids are formed due to fast titration and local oversaturation effects, then they are observed to dissolve within days.

Because we know from the EXAFS analysis that Zr oligomers form before the solubility limit is reached, the solubility products K'_{sp} and K°_{sp} extracted from the LIBD solubility curve, considering mononuclear species $Zr(OH)_n^{4-n}$ alone, are only empirical working values. However, the values for K'_{sp} and K°_{sp} can be used to determine the amount of "dissolved" Zr in solution under a set of given conditions. However, this "dissolved" Zr is in the form of hydrolyzed polynuclear species. A future task is to develop a model describing the equilibria of the species involved at the solubility limit.

Acknowledgements We gratefully acknowledge the beamtime allotment by ANKA/ISS for measuring the monoclinic ZrO_2 reference sample and experimental assistance by S. Mangold. We also acknowledge the analytic group of INE for ICP-MS concentration measurements.

References

1. Hummel W, Berner U, Curti E, Pearson FJ, Thoenen T (2002) Radiochim Acta 90:805–813
2. Ekberg C, Kallvenius G, Albinsson Y, Brown PL (2004) J Solution Chem 33:47–79
3. Curti E, Degueldre C (2002) Radiochim Acta 90:801–804
4. Neck V, Müller R, Bouby M, Altmaier M, Rothe J, Denecke MA, Kim JI (2002) Radiochim Acta 90:485–494
5. Cho H-R, Walther C, Neck V, Fanghänel T (2004) unpublished results
6. Kovalenko PN, Bagdasarov KN (1961) Russ J Inorg Chem 6:272–275
7. Ciavatta L (1980) Ann Chim (Rome) 70:551
8. Grenthe I, Fuger J, Konings RJM, Lemire RJ, Muller AB, Nguyen-Trung C, Wanner H (1992) Chemical thermodynamics of uranium. Elsevier, Amsterdam
9. Neck V, Kim JI (2001) Radiochim Acta 89:1–16
10. Neck V, Kim JI (2000) Radiochim Acta 88:815–822
11. Shannon RD (1976) Acta Cryst 32:751
12. Neck V, Kim JI, Seidel BS, Marquardt CM, Dardenne K, Jensen MP, Hauser W (2001) Radiochim Acta 89:1–8
13. Neck V, Altmaier M, Müller R, Bauer A, Fanghänel T, Kim JI (2003) Radiochim Acta 91:253–262
14. Bitea C, Müller R, Neck V, Walther C, Kim JI (2003) Colloids Surf A 217:63–70
15. Scherbaum FJ, Knopp R, Kim JI (1996) Appl Phys B 63:299–306
16. Kitamori T, Yokose K, Sakagami M, Sawada T (1989) Jpn J Appl Phys 28:1195–1198
17. Walther C, Cho H-R, Fanghänel T (2004) Appl Phys Lett 85:6329–6331
18. Walther C, Bitea C, Hauser W, Kim JI, Scherbaum FJ (2002) Nucl Instrum Meth B 195:374–388
19. Denecke MA, Rothe J, Dardenne K, Blank H, Hormes J (2005) Phys Scr T115:1001
20. Sayers DE, Bunker BA (1988) In: Koningsberger DC, Prins R (eds) X-ray absorption: techniques of EXAFS, SEXAFS and XANES. Wiley, New York, pp 211–253
21. Ressler T (1997) J Phys IV 7-C2:269
22. Stern EA, Newville M, Ravel B, Yacoby Y, Haskel D (1995) Physica B 208/209:117–120
23. Gualtieri A, Norby P, Hanson J, Hriljac J (1996) J Appl Cryst 29:707–713
24. Ankudinov AL, Ravel B, Rehr JJ, Conradson SD (1998) Phys Rev B 58:7565–7576
25. Ankudinov AL, Rehr JJ (1997) Phys Rev B 56:1712
26. Smith DK, Newkirk HW (1965) Acta Cryst 18:983–991
27. Adam J, Rodgers MD (1959) Acta Cryst 12:951
28. Lee PA, Citrin PH, Eisenberger P, Kincaid BM (1981) Rev Mod Phys 53:769–806

40

29. Newville M (1995) FEFFIT—using FEFF to model XAFS data. Department of Physics, FM-15, University of Washington, Seattle, WA
30. Mak TCW (1967) Can J Chem 46:3491–3497
31. Denecke MA, Geckeis H, Pohlmann C, Rothe J, Degering D (2000) Radiochim Acta 88:639–643
32. Degueldre C, Pfeiffer H-R, Alexander W, Wernli B, Bruetsch R (1996) Appl Geochem 11:677–695
33. Li P, Chen I-W, Penner-Hahn JE (1993) Phys Rev B 48(14):10063–10073
34. Rothe J, Denecke MA, Neck V, Müller R, Kim JI (2002) Inorg Chem 41:249–258
35. Rothe J, Walther C, Denecke MA, Fanghänel Th (2004) Inorg Chem 43:4708–4718
36. Winterer M (2000) J Appl Phys 88:5635–5644
37. Singhal A, Toth LM, Lin JS, Affholter K (1996) J Am Chem Soc 118:11529–11534
38. Hagfeldt C, Kessler V, Persson I (2004) Dalton Trans 2142–2151
39. Muha GM, Vaughan PA (1960) J Chem Phys 33:194–199
40. Southton PD, Bartlett JR, Woolfrey JL, Ben-Nissan B (2002) Chem Mater 14:4313–4319
41. Zyuzin DA, Moroz EM, Ivanova AS, Shmakov AN, Kustova GN (2004) Kinet Catal 45(5):780–783
42. Ohtaka O, Yamanaka T, Kume S, Hara N, Asano H, Izumi F (1990) Proc Jpn Acad B 66:193
43. Teufer G (1962) Acta Cryst 15:1187
44. MacDermott TE (1973) Coord Chem Rev 11:1–20
45. Adair JH, Denkewicz RP, Arriagada FJ (1987) Ceram Trans 1:135–145
46. Bilinski H, Branica M, Sillen LG (1966) Acta Chem Scand 20:853–861
47. Bundschuh T, Knopp R, Müller R, Kim JI, Neck V, Fanghänel T (2000) Radiochim Acta 88:625–629
48. Schindler PW (1967) Adv Chem Ser 67:196
49. Ekberg C, Brown P, Comarmond J, Albinsson Y (2001) Mater Res Soc Symp 663:1091–1099
50. Tulock JJ, Blanchard GJ (2002) J Phys Chem B 106:3568–3575
51. Hu MZC, Zielke JT, Lin JS, Byers CH (1999) J Mater Res 14:103–113
52. Knopp R, Neck V, Kim JI (1999) Radiochim Acta 86:101–108
53. Pouchon MA, Curti E, Degueldre C, Tobler LU (2001) Prog Nucl Energy 38:443–446

3.8.4 Investigation of polynuclear Zr-hydroxide complexes by nano-electrospray mass-spectrometry combined with XAFS [Walt07b]

Anal Bioanal Chem (2007) 388:409–431
DOI 10.1007/s00216-007-1223-1

ORIGINAL PAPER

Investigation of polynuclear Zr(IV) hydroxide complexes by nanoelectrospray mass-spectrometry combined with XAFS

Clemens Walther · Jörg Rothe · Markus Fuss · Sebastian Büchner · Sergei Koltsov · Thorald Bergmann

Received: 22 December 2006 / Revised: 14 February 2007 / Accepted: 16 February 2007 / Published online: 5 April 2007

Abstract Polynuclear species of zirconium in acidic aqueous solution are investigated by combining X-ray absorption spectroscopy (XAFS) and nanoelectrospray mass spectrometry (ESI-MS). Species distributions are measured between pH_C 0 and pH_C 3 for [Zr] = 1.5–10 mM. While the monomer remains a minor species, with increasing pH the degree of polymerization increases and the formation of tetramers, pentamers, octamers, and larger polymers is observed. The high resolution of the mass spectrometer permits the unambiguous determination of polynuclear zirconium hydroxide complexes by means of their isotopic patterns. The relative abundances of mononuclear and polynuclear species present simultaneously in solution are measured, even if one of the species contributes only 0.1% of the Zr concentration. For the first time it has been directly observed that the hydrolysis of polynuclear Zr species is a continuous process which leads to charge compensation through the sequential substitution of water molecules by hydroxide ligands until doubly charged polymers dominate at conditions (H^+ and Zr concentrations) close to the solubility of $Zr(OH)_4$(am). The invasiveness of the electrospray process was minimized by using very mild declustering conditions, leaving the polynuclear species within a solvent shell of approximately 20 water molecules.

Keywords Zirconium · Hydrolysis · Polymerization · Nanoelectrospray · EXAFS

C. Walther (✉) · J. Rothe · M. Fuss · S. Büchner
Institut für Nukleare Entsorgung,
Forschungszentrum Karlsruhe,
Postfach 3640,
76021 Karlsruhe, Germany
e-mail: walther@ine.fzk.de

S. Koltsov
Institute for Analytical Instrumentation,
Russian Academy of Sciences,
Rizhsky st. 26,
198103 St. Petersburg, Russia

T. Bergmann
BME KG,
Bahnhofstr. 14,
82418 Murnau, Germany

Introduction

Over the last few years the properties of Zr polyspecies in aqueous solutions have found renewed interest. For one, zirconia is an important ceramic product which finds application in fields such as ceramic engineering, piezo electronics, ion exchange, and catalysis. Production processes for these, often nanoscaled, materials from aqueous solutions are being investigated by the sol-gel community [1, 2]. On the other hand, zirconium metal is used as a fuel-cladding material in nuclear light water reactors and Zr has a high yield among the uranium-fission products. Hence, Zr is a high-priority element in assessments of radioactive nuclear waste repositories. Thermodynamic data for Zr (solubility and hydrolysis constants) were reviewed for a NAGRA/PSI database [3] and recently an extensive review of the Nuclear Energy Agency Thermodynamical Database Project (NEA-TDB) [4] summarized half-a-century's work on aqueous zirconium chemistry (since Blumenthals book of 1958) [5], including hydrolysis reactions, polymerization, and the formation of halogenide complexes. After the critical review process and the selection and refitting of data considered reliable, a consistent thermodynamical description was developed. It became evident that the Zr^{4+} ion is stable only under very acidic conditions ($pH_C<0$), and that mononuclear hydroxide complexes dominate only in very dilute solutions

([Zr] < 10^{-5} M). At higher concentrations or lower acidities, the solvated Zr^{4+} ion ([Zr^{4+}·$8H_2O$]) hydrolyzes and forms [Zr $(OH)^{3+}$·$7H_2O$] and [$Zr(OH)_2^{2+}$· $6H_2O$]. Condensation of the latter complex through olation leads to polymerization and the formation of a cyclic tetramer [$Zr_4(OH)_8^{8+}$ · $16H_2O$]. Each of the four zirconium dodecahedra in the tetramer shares two edges with its two zirconium neighbors [5, 6]. The tetramer and similar polynuclear species account for the largest mass fraction of Zr in solution.

In most studies on the solubility of zirconium oxide or amorphous zirconium hydroxide the presence of polynuclear species has been assumed. While it is common knowledge that these polynuclear species exist in concentrated solutions of zirconium salts ([Zr] > 10^{-5} M), even at rather high acidities, and the general trend of increasing polymer size and abundance with increasing pH is well known, most techniques do not allow the species distribution in solution to be assessed directly (for a discussion of the following references, see the "Appendix B"). Chemical structures were derived from X-ray scattering and EXAFS measurements [1, 2, 7–14], but these methods yield mean values which may be averaged over several different species. Only a few polynuclear complexes are used to model results obtained by phase equilibrium methods [15–19], spectrophotometric techniques [20–24] or potentiometric titration [25] for practical reasons. Neither larger polymers (p>4) nor the dimer were considered to be thermodynamically stable in the NEA-TDB review [4]. Because of the large number of possible complexes ([$Zr_p(OH)_y$·nH_2O]$^{4p-y}$, p=1 to >20, y=0 to 4p), the methods usually used to infer stoichiometry (potentiometry, spectrophotometry, solubility, etc.) always lead to ambiguous results. There is therefore a need for alternative methods that yield direct information on complex stoichiometries *and* the relative abundances of polynuclear Zr(IV) hydroxide complexes in solution.

In the present work, electrospray mass spectrometry (ESI-MS) is used to do this. The electrospray method was developed [26] to investigate macromolecules and coupled to MS for the first time in 1984 by Fenn and coworkers [27, 28]. The method is mainly used for biomedical applications and the detection of large organic molecules [29, 30]. However, there are a considerable number of studies on metal ions in aqueous solution that are mainly aimed at determining elemental speciation [31, 32] and at the interaction of metals with organic ligands (see the reviews of Gross [33] and, focusing on elemental speciation, Stewart [34]). A few studies focus on the interaction of the metal ion with water or on hydrolysis. The applicability of ESI for chromium speciation was demonstrated [35]. In the case of alkaline earth metals [36], the formation of doubly charged monomers with a solvation shell of up to seven water molecules was observed, but no polymeric species were found. The hydrolysis of Al^{3+} ions was investigated by ESI tandem TOF [37, 38], and very recently the detection of $Al_{13}(OH)_y^q$ and small Fe(III)hydroxide polymers in solution was reported [39]. Studies on hydrates of several metal ions aimed at understanding charge reduction mechanisms that occur during the electrospray process [40, 41]. Using high-resolution time-of-flight mass spectrometry, Hartke et al. [42] investigated the hydration of Na^+ ions embedded in clusters of up to 25 water molecules. The group of Moulin conducted several studies on the interaction of metal ions with various ligands [43], for instance Eu(III) complexation with acetic, glycolic, and 4-hydroxyphenylacetic acids [44], sulfate complexation of La(III) [45], and hydrolysis of uranium(VI) [46] and thorium [47]. The results obtained for UO_2^{2+} and Eu^{3+} ions agree well [48] with those obtained by time-resolved laser fluorescence spectroscopy (TRLFS).

There are also some ESI studies on zirconium complexes. Liquid–liquid extraction of zirconium ([Zr] = 1 − 20 mM in 3 M nitric acid) by dibutylphosphoric acid (HDBP) was followed using ESI-MS under conditions simulating the reprocessing of spent nuclear fuel [49]. A second work [50] was aimed at the investigation of Zr(IV) tetracarbonate complexes in 70 mM Zr solutions of near-neutral pH. The formation of the negative complex $[Zr(CO_3)_4]^{4-}$ was investigated by detecting $[Zr(CO_3)_4(HCO_3)]^{5-}$·$xH^+$$(6-x)K^+$ in the positive-ion mode of ESI. The presence of polymers was not mentioned in any of those works. By applying electrospray mass spectrometry to zirconium alkoxides [51] in pure ethanol, the polymers $[Zr_n(OEt)_{4n+1}]^-$ (n=1...5) were detected.

Experimental

Sample preparation

Samples of [Zr] = 1.5 − 10 mM at 0<pH_C<3 were prepared by dissolving appropriate amounts of zirconyl chloride in hydrochloric acid with a predefined pH_C. Zirconyl chloride hydrate ($ZrOCl_2$·xH_2O, 99.99%) from Aldrich (Sigma, St. Louis, MO, USA) was used without further purification. The hydrochloric acid was prepared by diluting HCl (Merck, Darmstadt, Germany; 37%, analytical grade) with ultrapure water (Millipore, Billerica, MA, USA; 18.2 MΩcm). No additional electrolyte was added. The solutions were kept in an ultrasonic bath for at least 15 min and allowed to equilibrate for at least one hour prior to the measurements. In the hydrolysis of $ZrOCl_2$·$8H_2O$ (see Eq. 36), the H^+ concentration increases after the dissolution of zirconyl chloride by approximately 1/Zr atom [25]. The H^+ concentration of the final solution (pH_C = −log [H^+]) was measured using a combination glass electrode (type

Ross, Orion, Thermo Scientific, Waltham, MA, USA) calibrated against standards of 1 M, 0.1 M, 0.01 M, and 1 mM HCl without additional electrolyte. The Zr concentrations of all samples were measured by ICP-MS with a precision of <2%.

The electrospray mass spectrometer

The time-of-flight mass spectrometer was built by one of the authors (T. Bergmann) and it is described in detail elsewhere [52–54]. The main components of the ALBATROS ESI-TOF are shown in Fig. 1. The nanospray ion source is homemade and equipped with spray capillaries from Proxeon (Odense, Denmark; borosilicate, thick metal coating, inner tip diameter 1 μm). The source can be operated in positive or negative ion mode. After passing differential pumping stages symbolized by the skimmer and the apertures, the ions are injected orthogonally into the time-of-flight mass spectrometer. The reflector then analyzes the ions. A maximum mass resolution of up to $m/\Delta m$= 26000 is achieved; typical values in the present work are $m/\Delta m$=15000.

In order to avoid fragmentation of the zirconium hydroxide polymers, the source is operated at low declustering conditions [31] (see "Discussion"). A static nitrogen pressure of <0.5 bar is applied at the end of the capillary and adjusted according to the mass spectrometric signal in order to achieve a stable flow. The sampling plate voltage is kept at 42 V. Nitrogen at room temperature is used for the gas curtain at a flow rate of <0.1 l/min. The sample flow rate is approximately 15 nl/min and the ESI current is between 50 and 100 nA. The addition of organic solvents such as methanol, which is often used in ESI investigations to reduce the surface tension, was strictly avoided in the present study.

XAFS data acquisition and analysis

Selected samples of [Zr] = 10 mM and [Zr] = 1.5 mM at $0.1<pH_C<1.8$ (Fig. 2, circles, and Table 1) were investigated by Zr KXAFS (X-ray absorption fine structure) measurements at the Angströmquelle Karlsruhe (ANKA), Forschungszentrum Karlsruhe, Germany, using the INE-Beamline for actinide research [55]. A pair of Ge(422) crystals ($2d$=3.412 Å) was used in the Lemonnier-type double-crystal monochromator (DCM). The monochromatic radiation (~3.5×10^{11} photons/s at Zr K-edge) was focused into a spot of size ~1 mm (h) × 0.5 mm (v) at the sample position. Higher harmonic radiation in the incident beam was suppressed by detuning the parallel alignment of the DCM crystals to 70% of the peak photon flux intensity. The spectra were calibrated against the first-derivative X-ray absorption near-edge structure (XANES) spectrum of a Zr foil (assigned as 17.998 keV). Spectra of samples a–f (Table 1) were recorded in transmission mode using Ar-filled ionization chambers at ambient pressure. To achieve a better signal-to-noise ratio, samples g–k were measured in fluorescence detection mode by registering the Zr $K_{\alpha1,2}$ fluorescence yield at ~15.7 keV using a five-pixel Ge solid state detector (Canberra LEGe, Meriden, CT, USA). 3–7 scans were collected and averaged for each sample. A summary of the samples examined by XAFS in this study is given in Table 1.

XANES spectra (Fig. 9) were isolated from XAFS scans following subtraction of the pre-edge background absorption and normalization of the edge jump to unity. Extended X-ray absorption fine structure (EXAFS) data analysis was based on standard data reduction and least squares fit techniques [56] performed using the ATHENA [57] (v0.8.050) and the UWXAFS [58] software packages. E_0, the origin used to calculate the EXAFS $\chi(k)$ function, was

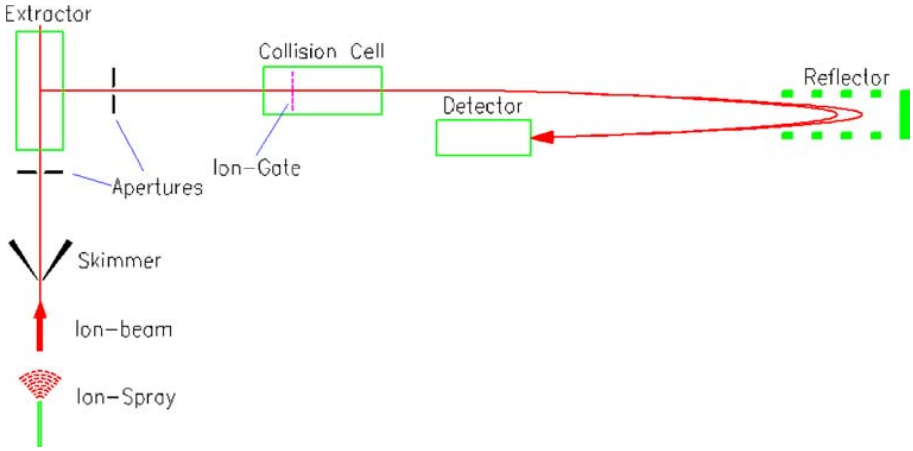

Fig. 1 The ALBATROS ESI-TOF consists of a homemade nano-ESI source and a high-resolution reflectron time-of-flight mass spectrometer

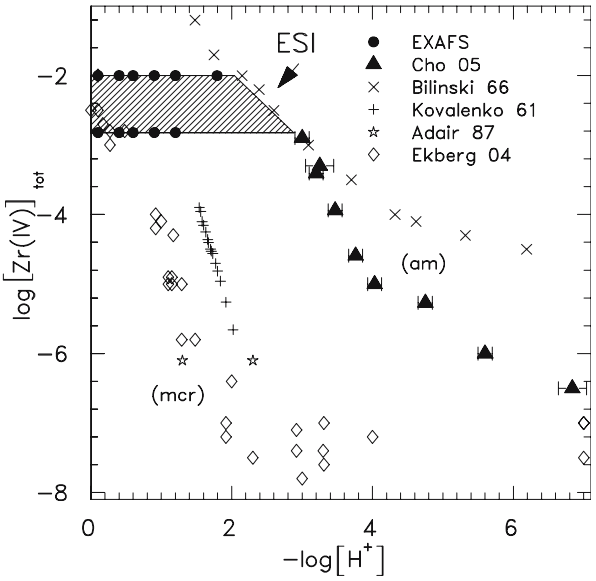

Fig. 2 Solubility data for microcrystalline $ZrO_2 \times H_2O$(mcr) [63–65] and amorphous zirconium hydroxide, $Zr(OH)_4$(am) [13, 22]

fixed at the first-derivative maximum in the individual spectra at ~18.016 keV. The *k*-range up to ~12 $Å^{-1}$ was investigated. EXAFS parameters (neighboring atomic distances R_i, EXAFS Debye–Waller factors σ_i^2, and coordination numbers N_i for different coordination shells *i*) were determined using the *feffit* code (v2.98). Backscattering amplitude and phase shift functions for single scattering paths in a 30-atom cluster of tetragonal $ZrOCl_2 \times 8H_2O$ ("zirconyl," crystallographic data taken from [59]) were obtained from FEFF8.2 [60, 61]. Prior to analysis, the k^3-weighted Zr K-EXAFS spectra were Fourier-transformed over a *k*-space range of ~2.5–12 $Å^{-1}$, using symmetric square windows with Δk=0.2 $Å^{-1}$ "Hanning sills". All fit operations were performed in *R*-space over the individual radial distance ranges given in Table 2. The amplitude reduction factor [62] S_0^2 was fixed at 0.9. This value has been found in the EXAFS analysis of crystalline $ZrOCl_2 \times 8H_2O$ in [12] to reproduce the Zr next-neighbor coordination numbers. The overall goodness of the fit, evaluated by *feffit*, was given as the "*R*-factor" (listed in the last column in Table 2).

Table 1 Summary of samples examined by XAFS in this study

ID	Sample description [Zr]	pH_C
a	10 mM	0.1
b	10 mM	0.4
c	10 mM	0.6
d	10 mM	0.9
e	10 mM	1.2
f	10 mM	1.8
g	1.5 mM	0.1
h	1.5 mM	0.4
i	1.5 mM	0.6
j	1.5 mM	0.9
k	1.5 mM	1.2

Results

Four series were measured by ESI-TOF at zirconium concentrations of 1.5 mM, 2.5 mM, 5 mM, and 10 mM. For each series, the pH_C was varied, starting at pH_C 0 and increasing to the highest pH_C that could be obtained by dilution without adding a base. Since approximately one H^+ is released per Zr ion dissolved, (Eq. 36), pH_C 2 is the highest pH_C that can be obtained for [Zr] = 10 mM. In the case of the 1.5-mM solutions, the preparation of a sample at pH_C 2.8 is possible. This highest pH_C coincides with the solubility of amorphous Zr hydroxide, $Zr(OH)_4$(am). In Fig. 2, the conditions of the present ESI measurements (hatched region) are plotted along with solubility data from [13, 22, 63–65] in a double logarithmic representation. As discussed in detail in [4, 13], there are two regions. Experiments from undersaturation with (micro)crystalline $ZrO_2 \times H_2O$(s) solid [63–65] lead to a low solubility, whereas experiments starting from oversaturated solutions produce $Zr(OH)_4$(am), which is more soluble (by several orders of magnitude). Below the solubility curve of $Zr(OH)_4$(am) (Fig. 2), the dissolution of zirconyl chloride leads to clear Zr(IV) solutions, despite the fact that the Zr(IV) concentration at a given pH may exceed the solubility of microcrystalline $ZrO_2 \times H_2O$(s), see Cho et al. [13].

The experimental procedure is explained below using two examples. For the nomenclature of the complexes and the formation constants used throughout the paper, refer to the "Appendix A." 1 is a solution at pH_C 0.2 and [Zr] = 2.5 mM. Figure 3, top, shows a portion of the mass spectrum of this sample, corresponding to mononuclear complexes of the Zr^{4+} ion. The natural isotope abundances of $^{90,91,92,94}Zr$ and $^{35,37}Cl$ result in a unique isotopic pattern for each complex in the mass spectrum. In Fig. 3, bottom, the region around *m*=341 amu is further magnified. Due to the low declustering conditions (see "The electrospray mass spectrometer"), the metal ion is embedded in a solvation shell (eight water molecules in the case of the blue peak). The quadruple charge of the Zr^{4+} ion is partly compensated for by three chloride ions, in the present example by two ^{35}Cl and one ^{37}Cl ions, which results in a singly charged complex. The second peak, which occurs 0.05 amu above this (green), corresponds to the first hydroxide complex $[Zr(OH)]^{3+35}Cl^{37}Cl$ with a solvation shell of nine water molecules. The two peaks are clearly distinguished, demonstrating that the high mass resolution of the

Table 2 Data range and metric parameters extracted by least-squares fit analysis of the Zr K-EXAFS spectra shown in Fig. 10

ID	Fit range R–Δ (Å)	Shell	R (Å)	N	σ^2 (Å^2)	ΔE (eV)	R-factor
a	1.10–3.50	O1	2.12(2)	4.0(2)	0.0030[f]	−0.99[a]	0.030
		O2	2.25(2)	4.0(2)	0.0030[f]	−0.99[a]	
		Zr	3.65(3)	1.3(4)	0.0032(5)	3.63	
b	1.14–3.50	O1	2.12(2)	4.0(2)	0.0030[f]	−0.67[a]	0.022
		O2	2.26(2)	3.5(2)	0.0030[f]	−0.67[a]	
		Zr	3.66(3)	0.9(4)	0.0024(5)	3.63[f]	
c	1.14–2.12	O1	2.12(2)	3.9(2)	0.0030[f]	−1.26[a]	0.015
		O2	2.26(2)	3.4(2)	0.0030[f]	−1.26[a]	
d	1.14–2.09	O1	2.12(2)	3.6(2)	0.0030[f]	−0.88[a]	0.009
		O2	2.25(2)	3.5(2)	0.0030[f]	−0.88[a]	
e	1.10–3.50	O1	2.13(2)	3.9(2)	0.0030[f]	−0.21[a]	0.035
		O2	2.26(2)	3.0(2)	0.0030[f]	−0.21[a]	
		Zr	3.63(3)	0.6(4)	0.0018(5)	3.63[f]	
f	1.07–3.65	O1	2.08(2)	3.0(2)	0.0011[f]	−0.94[a]	0.021
		O2	2.23(2)	4.5(2)	0.0011[f]	−0.94[a]	
		Zr	3.66(3)	1.5(4)	0.0022(5)	3.63[f]	
g	1.07–3.50	O	2.22(2)	7.6(2)	0.0062(2)	0.54	0.014
		Zr	3.78(3)	1.0(4)	0.0028(5)	5.50	
h	1.07–3.5	O	2.25(2)	7.1(2)	0.0072(2)	3.72	0.018
		Zr	3.74(3)	0.8(4)	0.0022(2)	5.50[f]	
i	1.10–3.28	O	2.24(2)	6.9(2)	0.0075(2)	3.72	0.018
		Zr	3.70(3)	0.8(4)	0.0018[f]	5.50[f]	
j	1.04–2.02	O	2.23(2)	6.6(2)	0.0073(2)	2.94	0.005
k	1.10–2.02	O	2.23(3)	6.7(2)	0.0071(2)	2.21	0.010

Values in parentheses are estimated uncertainties in the last digit of the fit value. ΔE for Zr shells is fixed at the best fit value obtained for pH_C 0.1 in the [Zr] = 10 mM (a–f) and [Zr] = 1.5 mM (g–k) series of samples, respectively.
[a] defined as a global parameter for both shells; [f] parameter is held constant during the fit procedure

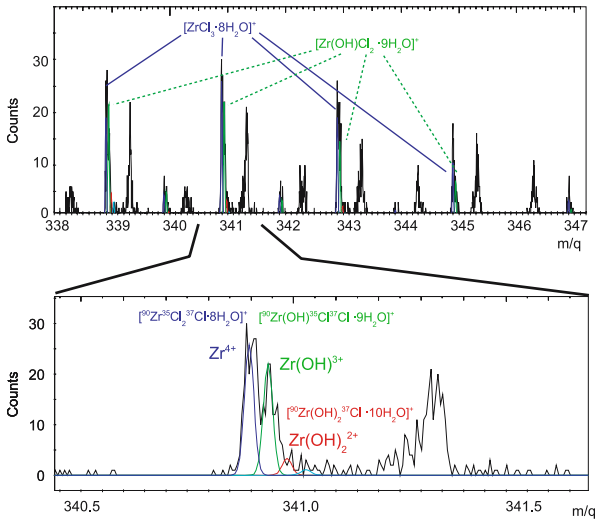

Fig. 3 Portion of the mass spectrum of Fig. 4 for the solution with [Zr] = 2.5 mM, pH_C 0.2. *Top*: Isotopic distributions of the complexes $[ZrCl_3{\cdot}8H_2O]^+$ and $[Zr(OH)Cl_2{\cdot}9H_2O]^+$ due to the natural isotopic abundances of Zr and Cl. *Bottom*: The isobars Zr^{4+},$^{35}Cl_2{}^{37}Cl{\cdot}8H_2O]^+$ (*blue*) and $[Zr(OH)]^{3+}$,$^{35}Cl^{37}Cl{\cdot}9H_2O]^+$ (*green*) are well resolved and can be evaluated separately. The peaks slightly above each mass unit (e.g., at m/z≈341.3) are due to organic contaminations, which are, however, clearly discriminated from the signals of the Zr species due to the high mass resolution

instrument allows the resolution of isobaric interferences. The dihydroxo-complex $[Zr(OH)_2]^{2+}$ is not present in significant amounts (red curve). This is in agreement with the hydrolysis model of the NEA-TDB [4] ($[Zr(OH)_2^{2+}] < 0.01 \times [Zr^{4+}]$ for the present conditions). The peaks slightly above each mass unit (e.g., at m/z≈341.3) result from organic contamination, which are, however, clearly discriminated from the signals of the Zr species due to the high mass resolution.

Monomers account for less than 20% of the mass fraction of the Zr species in solution. The full mass spectrum of sample 1 (Fig. 4, top) shows that the abundance of tetramers ($[Zr_4(OH)_y]^{16-y}$) far exceeds the fraction of monomers (note the logarithmic scale of the ordinate). Besides monomers (blue) and tetramers (red), pentamers ($[Zr_5(OH)_y]^{20-y}$, green) are present. No dimers or trimers are observed. As discussed in the "Introduction" and "Appendix B," the oligomers are highly charged species in solution; the tetramer is asummed to be octuply charged in highly acidic conditions [4]. In contrast, the mass spectra show only singly and doubly charged species. The excess charges on the oligomers are compensated for by chloride ions, as for the monomer (most likely in the second solvation shell [14, 66]), such that the measured species

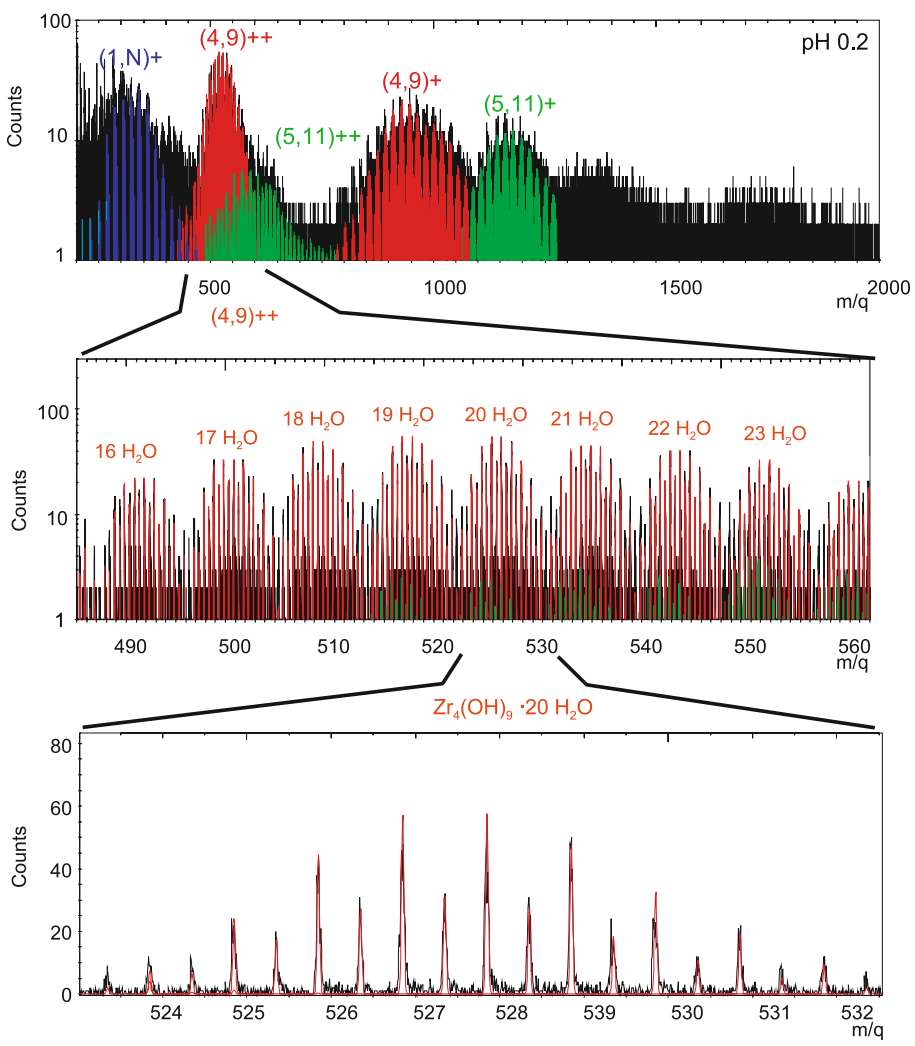

Fig. 4 Mass spectra of solution 1 with [Zr] = 2.5 mM, pH_C 0.2. *Top*: The full spectrum shows the monomers (*blue*), the tetramers (*red*), and the pentamers (*green*). *Middle*: Magnification of the peak cluster between m/q= 490–560 (doubly charged tetramers) reveals that this cluster is in turn composed of peak clusters representing different numbers of water molecules in the solvation shell. *Bottom*: The isotope distribution (chlorine and Zr isotopes, see text) of each group is shown by further magnification. The measured spectrum (*black*) agrees excellently with the theoretical distribution (*red*)

in sample 1 are the tetramers $[Zr_4(OH)_9Cl_6]^{+}\cdot nH_2O$, $[Zr_4(OH)_9Cl_5]^{2+}\cdot nH_2O$ (red) and the pentamers $[Zr_5(OH)_{11}Cl_8]^{+}\cdot nH_2O$, $[Zr_5(OH)_{11}Cl_7]^{2+}\cdot nH_2O$ (green), respectively. These "peak clusters" consist of groups of peaks with different numbers n of water molecules in the solvation shells. Such a sequence of peak clusters is shown for the doubly charged tetramer in Fig. 4 (middle).

Further magnification of the peak group representing $[Zr_4(OH)_9Cl_5]^{2+}\cdot 20H_2O$ shows almost 20 peaks (Fig. 4, bottom), which originate from the natural isotope distribution of chlorine (^{35}Cl: 24.2%, ^{37}Cl: 75.8%) and zirconium (^{90}Zr: 51.5%, ^{91}Zr: 11.2%, ^{92}Zr: 17.1%, ^{94}Zr: 17.4%, ^{96}Zr: 2.8%). The measured spectrum is plotted in black, the theoretical distribution convoluted with the spectrometer function (mass resolution) is plotted in red, and these show excellent agreement. Although the large number of isotopes complicates the spectrum, the isotope distribution is a fingerprint that can be used for the unequivocal identification of the polynuclear species.

The second example, 2, is a solution with the same concentration ([Zr] = 2.5 mM) but lower acidity (pH_C 1.0). In the mass spectrum (Fig. 5, top), the monomer is not detectable now (the peaks in the mass range m/q<400 amu are due to organic contaminations; however, these are well discriminated and do not hinder the quantification of mononuclear Zr(IV) ions; see the caption of Fig. 3). The amount of tetramers is strongly reduced compared to sample 1 at pH_C 0.2, and the pentamers are the dominant species. The pentamers are identified using the isotope pattern of $[Zr_5(OH)_{11}Cl_7]^{2+}\cdot 16H_2O$ in Fig. 5 (middle and bottom) in the same way as described for the tetramer in Fig. 4. Again, the measured data (black) agrees well with the theoretical distribution (green). Larger oligomers, such as hexamers, octamers, nonamers, and decamers, are

Anal Bioanal Chem (2007) 388:409–431 415

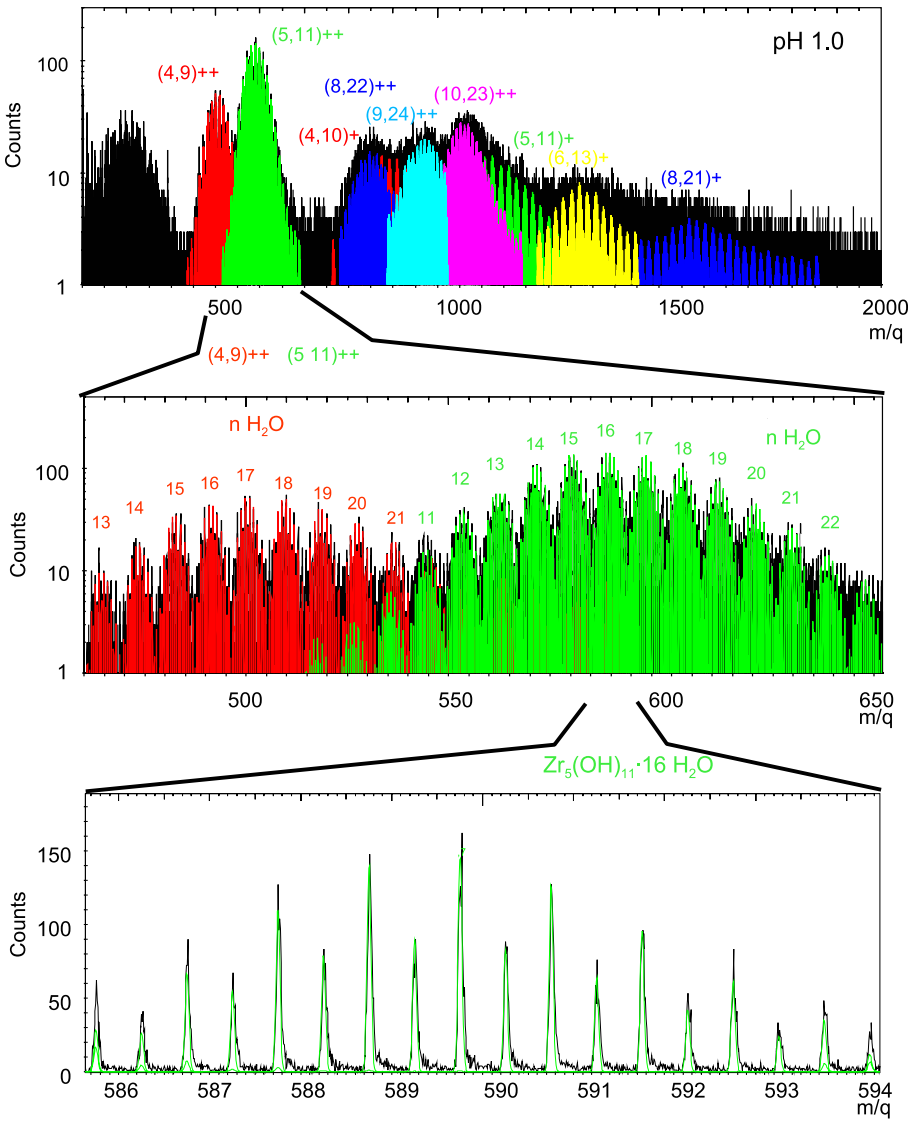

Fig. 5 Mass spectra of solution 2 with [Zr] = 2.5 mM, pH_C 1.0. *Top*: In contrast to Fig. 4, no monomer is observed. The fraction of tetramers (*red*) is reduced and the pentamers (*green*) dominate the spectrum. Larger oligomers like hexamers, octamers and decamers are identified. *Middle*: A magnification of the peak cluster between *m*/*q*=450–650 (doubly charged tetramers and pentamers) shows groups of peaks representing different numbers of water molecules in the solvation shell. *Bottom*: The isotope distribution of the $[Zr_5OH_{11}Cl_7]^{2+}\cdot 16H_2O$ group is shown by further magnification. The measured spectrum (*black*) agrees excellent with the theoretical distribution (*green*)

identified by the same method and contribute considerably to the total amount of zirconium in solution.

All measured spectra are evaluated in the following way. All possible combinations

$$[Zr_p(OH)_yCl_{4p-y-q'}]^{q'}nH_2O,\ p=1-20,\ q'=1-3,\ y=0-(4p-q'),\ n=0-50 \quad (1)$$

are fit to the data by a homemade C++-based fitting routine until a set of oligomers are found which fit the measured spectrum simultaneously. The natural isotope distributions of Zr, Cl, O, and H are taken into account by the fitting routine. The maximum charge observed in the mass spectra is q'=3, and the maximum number of water molecules is around 40. Doubly charged species carry more water molecules than singly charged ones, as illustrated for the pentamer in Fig. 6.

After all species are identified, the relative abundance of each polymer is calculated in three steps:

(1) For each species $\left[Zr_p(OH)_yCl_{4p-y-q'}\right]^{q'}\cdot nH_2O$ the peak areas of all isotope combinations and all different numbers of water molecules *n* are summed, giving a total number of ions

$$N\left(\left[Zr_p(OH)_yCl_{4p-y-q'}\right]^{q'}\right) = \sum_n N\left(\left[Zr_p(OH)_yCl_{4p-y-q'}\right]^{q'}\cdot nH_2O\right). \quad (2)$$

(2) Even for highly charged solution species (like for instance the tetramer $Zr_4(OH)_8^{8+}$), the corresponding species observed in the mass spectra are triply charged

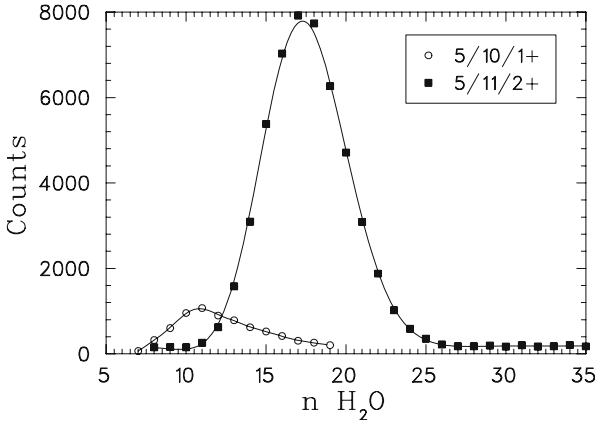

Fig. 6 Distribution of the number of water molecules attached to the pentamers $[Zr_5(OH)_{10}Cl_9]^{+}\cdot nH_2O$ and $[Zr_5(OH)_{11}Cl_7]^{2+}\cdot nH_2O$ for the sample at [Zr] = 2.5 mM

at most. The charge difference is compensated for by chloride ions (in the present example this would be $Zr_4(OH)_8Cl_6^{2+}$ and $Zr_4(OH)_8Cl_7^{+}$). However, chloride is not part of the oligomer but is instead located in the outer solvation shell [14, 66]. The oligomer (p,y) in solution is completely defined by the number of Zr ions (p) and OH groups (y), which is the sum

$$N\left(\left[\mathrm{Zr}_p(\mathrm{OH})_y\right]^q\right) = \sum_{q'=1}^{3} N\left(\left[\mathrm{Zr}_p(\mathrm{OH})_y\mathrm{Cl}_{4p-y-q'}\right]^{q'}\right); \quad q = 4p - y \tag{3}$$

The charge of the solution species is $q = 4p - y$ and differs from the charge q' of the species determined in the spectrometer.

(3) In many mass spectra, several different hydrolysis complexes with the same number of Zr atoms (degree of polymerization p) are present simultaneously; for instance $Zr_4(OH)_8^{8+}$, $Zr_4(OH)_9^{7+}$ and $Zr_4(OH)_{10}^{6+}$ [in short (4,8); (4,9) and (4,10)]. In this case, the total number of polymers with the same number of Zr nuclei p is obtained by the sum

$$N(p) = N(\mathrm{Zr}_p) = \sum_y N\left(\left[\mathrm{Zr}_p(\mathrm{OH})_y\right]^q\right) \tag{4}$$

Evaluation of the series at [Zr] = 1.5 mM, $0<pH_C<2.8$, according to Eq. 4, results in the species number distribution shown in Fig. 7 (top). At pH_C 0, some 65% of the Zr species are tetramers 25% are monomers, and the rest are pentamers. The percentages refer to the ion counts of the MS detector system and not to the concentrations in

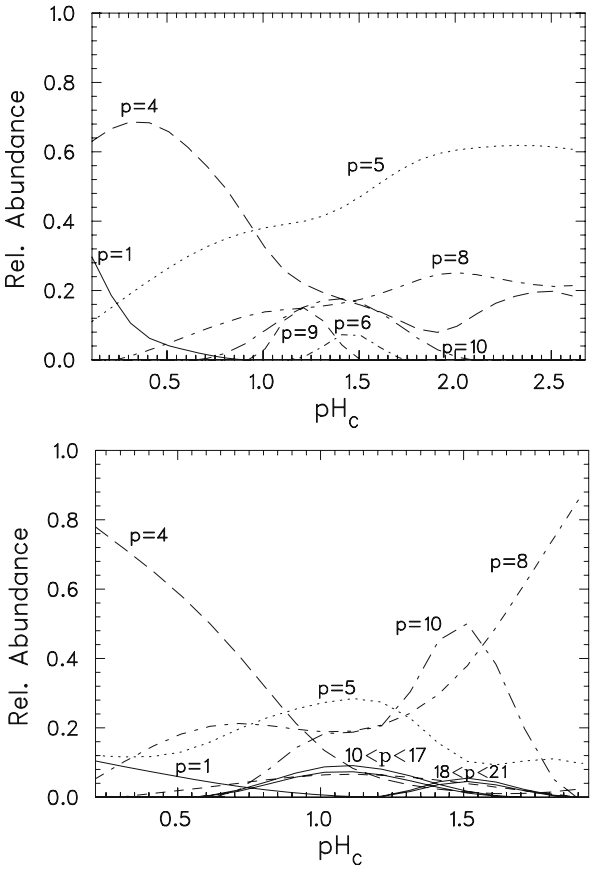

Fig. 7 Species distribution (relative number of detected ions). *Top*: [Zr] = 1.5 mM. *Bottom*: [Zr] = 10 mM

solution[1]. With increasing pH_C, the fraction of monomers decreases rapidly and falls below 1% at pH_C 1. The number of pentamers increases, and for $pH_C>0.5$ octamers form. Larger polymers form at pH_C~1.5, and 60% of the species are pentamers, 30% are octamers, and 10% are tetramers at pH_C 2.8.

The species distribution at [Zr] = 10 mM is shown in the lower part of Fig. 7. Due to H^+ release during the dissolution of zirconyl chloride, only the range $0<pH_C<2.0$ was measured. At pH_C 0, the species distribution resembles the one above but with a slightly higher fraction of tetramers and a lower fraction of monomeric species. The increase of the pentamer fraction with decreasing acidity is less pronounced; instead the octamers form and at pH_C 0.9 the number of octamers equals the number of

[1] Please note that this figure shows the relative numbers of ions, i.e., the number of detector counts of one species relative to the total number of counts of all Zr species. Hence, each molecule causes only one count irrespective of the number of Zr atoms it contains.

tetramers. Larger species form at pH_C 1.0, and at pH_C 1.5 the decamer accounts for 60% of all ions. At pH_C 2 the octamers are the dominant species.

With the premise that Cl^- ions belong to an outer shell, (Eq. 3) allows us to identify, as a function of pH_C, not only the size and polymerization p of the complexes, but also the number of hydroxide groups (y) and via $q = 4p - y$ the charge of each oligomer. Often several hydroxide complexes with the same degree of polymerization (p) but different numbers of hydroxide groups y are present simultaneously. In this case, a number-weighted mean charge is calculated. For the series at [Zr] = 1.5 mM (left) and 10 mM (right), the charges of the tetramers (top), pentamers (middle), and octamers (bottom) are plotted in Fig. 8. At pH_C 0 the tetramer is octuply charged for both concentrations, and the charge decreases only slightly as pH_C increases. However, the fraction of tetramers still present in solution at high pH_C decreases rapidly (Fig. 7). In the case of the pentamers and the octamers, a pronounced decrease in the charge q and hence an increase in the number of hydroxide groups y is observed, which is fitted empirically by the linear dependence

$$q = a + b\,pH_C \tag{5}$$

It is worth noting that in all four cases (pentamers and octamers at 1.5 mM and 10 mM) the mean charge approaches ≈2 close to the solubility curve (see "Discussion").

XAFS investigations

The Zr K-XANES of the samples specified in Table 1) are depicted in Fig. 9 (the spectra of intermediate samples b, d, h, and i have been omitted for clarity). They exhibit only slight differences between the different solutions. All samples show a pronounced resonance or "white line" (WL) following the rising edge. No WL splitting or pH-dependent broadening, as observed for the high pH titration series in [13] or in the XAFS investigation of various Zr(IV) oxide polymorphs in [67], is discernable. Based on the arguments made in these references, we have to assume that both sets of samples comprise molecular or oligomeric Zr oxide/hydroxide entities with rather high Zr absorber site symmetries. Nevertheless, there is a significant difference between the 10 mM and the 1.5 mM sets of Zr samples: the samples at higher Zr concentrations show a progressive decrease in the WL intensity with increasing pH, whereas those at 1.5 mM Zr exhibit constant WL normalized peak heights, equal to the maximum peak heights observed for the 10 mM series, independent of the solution pH. Intensity decreases and/or WL broadening in these sample systems are generally associated with increasing condensation of the aquatic metal oxide/hydroxide species (see e.g., [68]), i.e., the transition from a hydrated or hydrolyzed ionic species to oligomeric and colloidal species with bulk-like properties. According to this interpretation, Zr oxide/hydroxide species generally seem to be smaller in the low concentration series compared to the high concentration series. The somewhat different behaviors of both sets of samples is also reflected in the results from the EXAFS analysis (see below).

The Zr K-EXAFS of samples a through k and R-space EXAFS fit results are compared in Fig. 10. Qualitative inspection of the data shows that all samples exhibit a dominant FT peak centered at ~1.7 Å ($R-\Delta$, i.e., a radial distance of ~2.2 Å), and a less pronounced and broadened peak centered at ~3.1 Å (i.e., a radial distance of ~3.6 Å). However, the solutions c, d, j, and k exhibit a single dampened sinusoidal EXAFS oscillation (not shown), which is only slightly affected by interference patterns resulting from the backscattering of heavy atoms in a second shell. The fitting of a second shell contribution was not attempted for these samples. Considering the R-space fit results summarized in Table 2, we conclude that the first shell backscattering signal reflects the presence of oxygen atoms from hydroxo groups or the hydration spheres of the various Zr(IV) species. The oxygen peak is significantly broadened in the high concentration series (a–f). A satisfactory fit is achieved by including two oxygen single scattering paths. The distances and coordination numbers obtained for these paths, 4 O at 2.12 Å and 4 O at 2.26 Å, are in agreement with the oxygen coordination reported for bridging hydroxo groups and terminal waters in the tetrameric units of $ZrOCl_2{\times}8H_2O$, respectively [12]. Satisfactory fitting of the oxygen shell in the low concentration series (g–k) is achieved with just a single oxygen shell, resulting in a higher Debye–Waller factor. The fit is slightly improved by allowing for additional freedom using a third cumulant (not shown). These results point to the existence of several closely spaced oxygen neighbors which can no longer be resolved within the distance resolution $(\Delta R \sim \pi/2\Delta k = 0.16\,\text{Å})$ given in these experiments. This interpretation is also in accordance with the continuously decreasing apparent oxygen coordination number (from 7.6 to 6.6) observed for samples g through k. Fitting of the second shell contribution at around 3.1 Å ($R-\Delta$) with a single Zr shell is straightforward for both samples at pH_C 0.1 (a and g). The radial distance (3.65±0.03 Å) and coordination number (1.3±0.4) obtained for sample a are again in agreement with the assumption that tetrameric hydroxo-bridged Zr units dominate this sample. The deviation from the expected number of 2 for Zr–Zr pairs in the tetramer structure can be attributed to the influence of the remaining monomers at pH 0.1. The Zr–Zr distance in the low-concentration series, determined only for samples g–i, is somewhat increased (R_{ZrZr}≥3.7 Å). As a general trend for both series, we observe that the signal from the

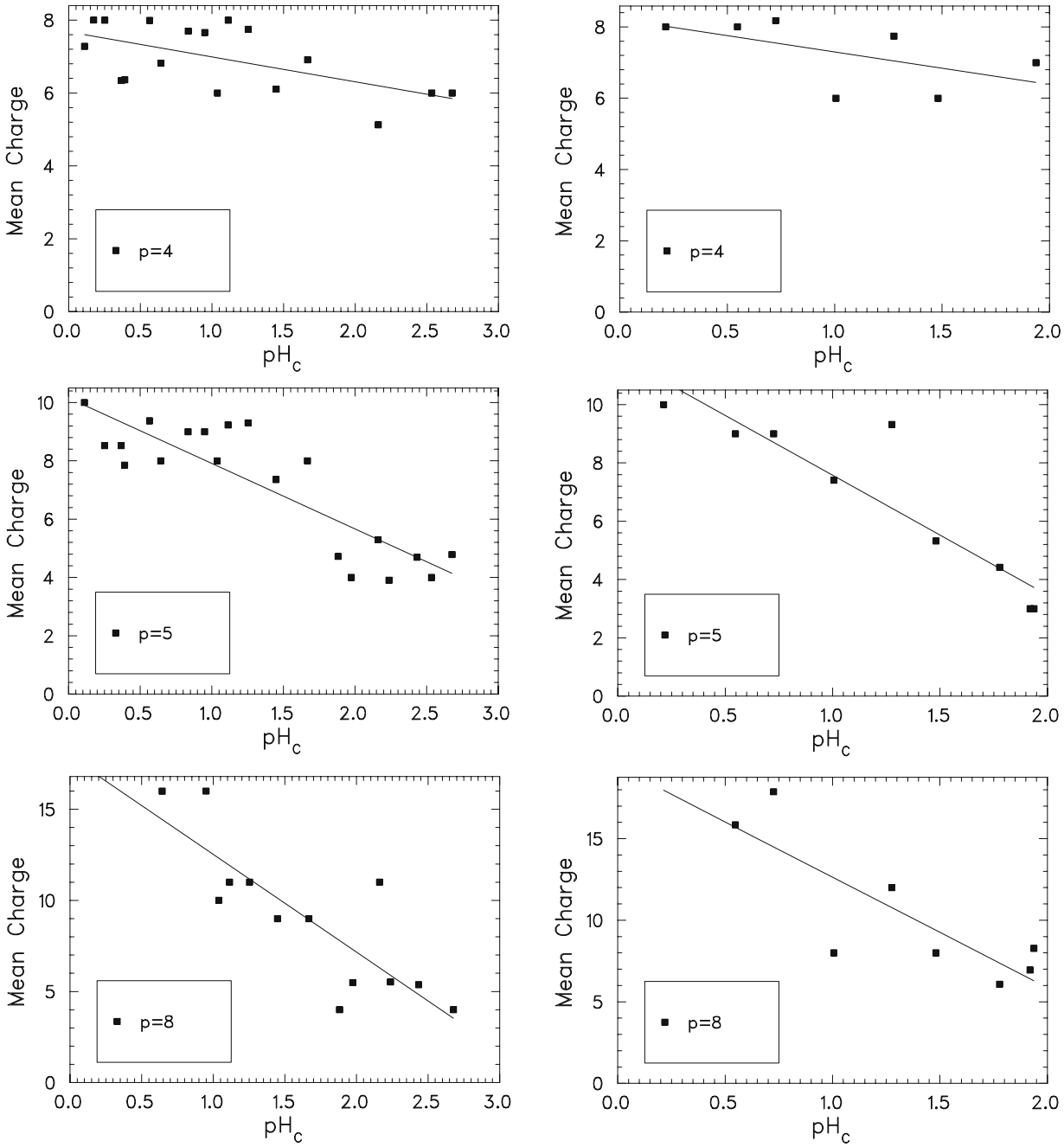

Fig. 8 Mean charge of tetramers (*top*), pentamers (*middle*), and octamers (*bottom*) as function of pH_C for [Zr] = 1.5 mM (*left*) and [Zr] = 10 mM (*right*). While the tetramer charge remains almost constant over the range of acidities investigated, the charges of the pentamers and octamers decrease almost linearly with increasing pH_C

more distant Zr shell becomes less pronounced or even disappears entirely as the number of different polymeric species in solution increases (see Fig. 7 and "Appendix B"). We assume the simultaneous presence of monomeric and polymeric species with different Zr–Zr distances is responsible for the suppression of the Zr backscattering contribution. This effect has been described before, by Conradson et al. [69], where the simultanous presence of many different Pu polynuclear species caused the destructive interference of the scattering signals, culminating in the disappearance of the metal–metal backscattering peak. Chlorine was not detected as a direct backscattering neighbor of Zr in these

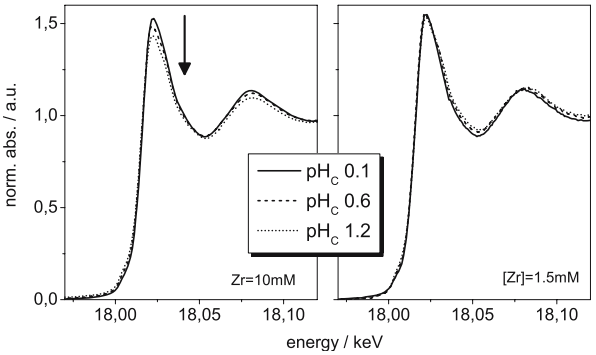

Fig. 9 Normalized Zr K-XANES spectra of samples a,c,e (*left*) and samples g,i,k (*right*). See Table 1 for sample descriptions

samples. However, it might be present in the second hydration sphere.

Discussion

How invasive is the electrospray process?

The present work has two objectives: to gain insight in the polymerization process during the hydrolysis of zirconium in acidic solutions, and, as a prerequisite, to show that ESI-TOF-MS is a suitable tool for investigating the polymerization of metal ions in solution and that the results obtained reflect the state in solution. This is not a trivial issue, since the electrospray process is invasive to a certain extent, as discussed in many books and reviews on these topics [29, 30]. The Zr(IV)–OH system was chosen as a model, since the presence of polynuclear species (in particular the tetramer) is unequivocally proven by various independent methods, and the recent NEATDB review [4] suggests well-founded formation constants. In addition to comparing the results with those in the literature, the EXAFS measurements ("XAFS investigations") provide a way to directly validate our findings using a nondestructive, noninvasive in situ method. EXAFS cannot measure the relative abundances of a complex mixture of different species. However, it is possible to use it to distinguish unequivocally mononuclear species from polymers by observing the Zr–Zr backscattering signal. The high number of coexisting polynuclear species leads to a dispersion in next-neighbor distances and coordination numbers which leads to higher Debye–Waller factors. Although it is not possible to deduce the specific structures from these data, one can correlate—as the acidity decreases—the increasing disorder indicated by the EXAFS spectra with the increasing mean size and number of different polynuclear species identified with the ESI-TOF measurements.

During the electrospray process, droplet formation is followed by shrinkage due to solvent evaporation and

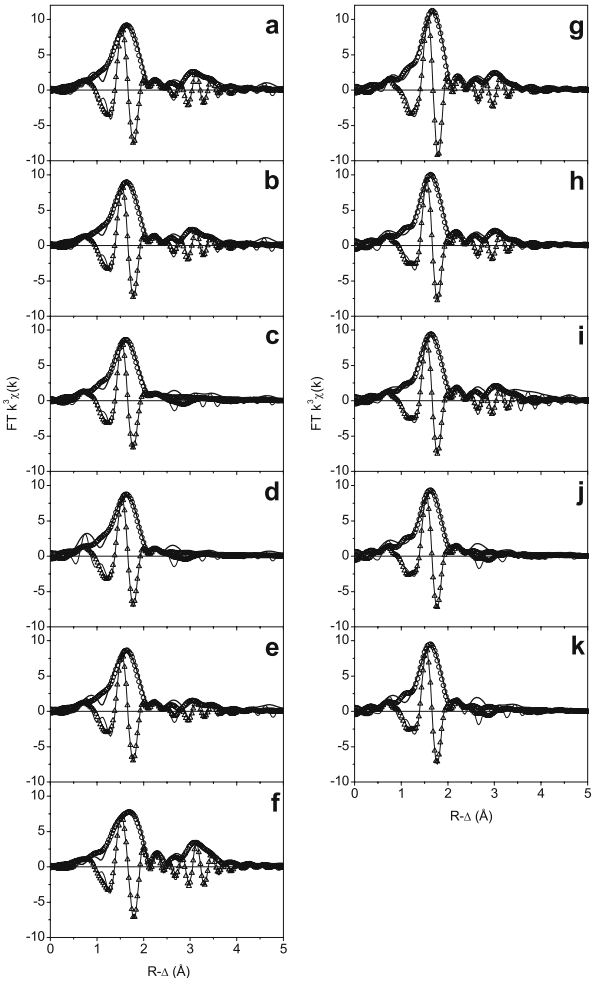

Fig. 10 Zr K-EXAFS *R*-space fit results for samples a–k (*left panel* [Zr] = 10 mM, *right panel* [Zr] = 1.5 mM). FT magnitude of EXAFS data (*thick solid line*), and corresponding fit (*open circles*) are shown, as well as the real part of the FT data (*thin line*) and the corresponding fit (*open triangles*). See Table 1 for sample descriptions

subsequent coulomb explosion of the highly charged droplets [29]. Two competing models describe the generation of water-free molecular ions in the gas phase. Dole [26] proposed the charge residue model, i.e., that extremely small droplets are produced by successive fission until solvent evaporation leads to a gas phase ion. Iribarne [70] and Thomson proposed a second model, which predicts that, after the radii of the droplets decrease below a certain size, direct ion emission from the droplets becomes possible. This process was assumed to become dominant over coulomb fission for droplet radii below ≈10 nm. A consequence of solvent evaporation is that the concentrations of nonvolatile species such as the metal ions increase [71]. Concentration-dependent effects like polymerization might hence be influenced. In the case of nano-

ESI [72], droplets less than 100 nm in diameter form at the tip of the Taylor cone and shrink within a few microseconds. At [Zr] = 1 mM, a droplet of diameter D=50 nm contains $N = N_A[Zr]\pi D^{3/6} \approx 39$ mononuclear ions or, in the case of polymers, a factor of p less (tetramer: N=10). A 25-nm droplet contains only one ion. In principle, enhanced polymerization due to upconcentration effects might be possible at [Zr] > 0.1 mM; however, the polymerization of highly concentrated zirconium solutions ([Zr] ≫ 1 mM) is known to proceed on a time scale of at least minutes [10], even at elevated temperatures. Hence it is very unlikely that the electrospray process alters the species due to polymerization reactions within microseconds [73]. The small water clusters observed in the mass spectrum consist of up to 50 water molecules, and due to the coulombic repulsion involved, it is physically impossible that two separate highly charged Zr species, whether monomer or polymer, are confined in such a tiny droplet. The fact that polynucleation is not caused by the source conditions was verified by investigating 1–10 mM Eu(III) and Th(IV) solutions at pH_C 0–2 (Walther C, Fuss M, Buechner S, Geckeis H, 2007, in preparation). Polymers were not detected in any of these samples, in agreement with thermodynamic data [74] and earlier experiments [47].

A second interfering effect is the electrolytic oxidation of water in the capillary due to the high voltage applied, which leads to H^+ generation and acidification of the solution. Acidification of near-neutral solutions by more than one pH unit was observed by fluorescence spectroscopy [75, 76] in conventional ESI studies. A local pH increase [77] at the tip of "nanoESI wire-in-capillaries" was observed within 1–2 h using pH indicators. In the present work, tips with exterior metal coatings are used. The metal is in contact with the solution only at the tip of the capillary, so electrolytic reactions can only take place in a very small boundary layer. Nevertheless, it is worth estimating the maximum possible pH change in solution. A typical current of 50 nA and a measurement cycle of one hour results in a total charge of 1.8×10^{-4}C, which can produce 1.8×10^{-9} mol H^+ ions, corresponding to $[H^+] = 1.8 \times 10^{-4}$ M in 10 µl of sample volume as an upper limit. In praxis the number is lower, since most of the charges are carried away by the droplets and do not acidify the solution, which remains in the capillary. A near-neutral solution might still be acidified by this effect; however, for the highly acidic solutions (pH_C< 2.8) of the present study, no severe pH change is expected. Indeed, upon spraying a pH_C 2.5 sample containing the pH indicator thymol blue, as suggested in [77], no color change and hence no acidification of the pH_C 2.5 sample was observed after four hours of continuous spraying. Further proof that the present measurements were not affected by a pH change is the stability of the spectra collected directly after the capillary is filled and after four hours of spraying: no difference between the species distributions was found.

Finally, the declustering conditions used (electric field strength between capillary tip and sampling plate, curtain gas flow rate) have a large influence when using electrospray. More and more solvent molecules evaporate from the droplet with increasing electric field, increasing gas flow rate (and/or heating) [31], eventually resulting in a molecular ion without any solvent (water) shell. However, very delicate molecules might be altered or even destroyed or fragmented by such strong declustering conditions. For this reason, very mild conditions were used in the present work, and the source was operated at room temperature (flow rate <0.1 l/min, field strength <20 V/cm). The mass spectra of Figs. 4 and 5 show that the detected metal ion complexes carry a solvation shell of typically 10–25 water molecules (Fig. 6). Under these mild conditions, the spectra contain up to 5000 peaks, depending on the number of species, but fragmentation of the solution species is rather unlikely.

Comparision of ESI-TOF data with EXAFS results

The ESI-TOF and EXAFS samples were both prepared by dissolving zirconyl chloride in hydrochloric acid and subsequent ultrasonification. The measurement was started as quickly as possible. In the case of ESI, this was within one hour, and the measurements were finished typically after <4 h. The EXAFS measurements were started within 4 h and were completed within <12 h (3–7 scans). No significant changes were observed between the first and subsequent EXAFS scans.

In the case of the samples at [Zr] = 10 mM and pH_C 0.1, the tetramers account for 80% of the Zr concentration (Fig. 7, bottom), which agrees very well with the EXAFS findings ("XAFS investigations") for samples a (pH_C 0.1) and b (pH_C 0.4) (see discussion on tetrameric Zr–Zr and Zr–O distances in [13]). At pH_C>0.5, ESI-TOF detects increasing amounts of pentamers (Fig. 7). Accordingly, in the EXAFS spectra the Zr–Zr backscattering peaks broaden and eventually vanish [samples c (pH_C 0.6) to e (pH_C 1.2)]. Based on the EXAFS data alone, one might erroneously conclude from the absence of a Zr–Zr backscattering signal that mononuclear Zr–hydroxide complexes $\left(Zr(OH)_y^{4-y}\right)$ are present. However, the vanishing Zr–Zr peak is caused by the presence of many different Zr–Zr distances, and this interpretation is strengthened by the results from sample f at pH_C 1.8; at this pH the number of different species is strongly reduced, and according to the ESI-TOF results (Fig. 7, bottom) the octamer accounts for more than 80% of the Zr solution species. In good agreement with this, the EXAFS data (Fig. 10f) show a distinct Zr–Zr backscattering signal and yield a Zr–Zr distance of 3.66(3) Å, with a

mean coordination number of close to two (1.5(4)). This corroborates previous findings on the solubility of amorphous Zr hydroxide [1, 13].

The low-concentration samples at [Zr] = 1.5 mM (Fig. 7, top) show the same trend of decreasing oxygen coordination number, which suggests ongoing hydrolysis and polymerization. However, the Zr–Zr backscattering signal is clearly visible up to higher pH (samples g–i) than in the samples at [Zr] = 10 mM, indicating that the size dispersion at pH_C 0.6 is smaller in the low-concentration sample. Indeed, according to ESI, the pentamer and the tetramer account for ≈90% of the Zr concentration at [Zr] = 1.5 mM, but at [Zr] = 10 mM tetramers, pentamers, and octamers are present at roughly equal amounts. The variety of species present at pH_C 0.9 and pH_C 1.2 explains why the Zr–Zr peak broadens and vanishes. It should be noted that EXAFS data at [Zr] = 1 mM and pH_C 1 was misinterpreted in our previous work [13]. The absence of a Zr–Zr backscattering signal was explained by the dominance of mononuclear Zr(IV) species in solution, which is clearly not the case and would be in conflict with most of the data summarized in Table 5. The mean Zr–Zr distances of all samples at [Zr] = 10 mM (3.63–3.66 Å) are significantly smaller than at [Zr] = 1.5 mM (3.70–3.78 Å). While 3.64 Å is in good agreement with the Zr–Zr distance of the tetramer [1, 12, 13, 19], various Zr polymorphs are known to have a bigger distance of ≈3.75 Å) (SAXS [67]). In an early review, one of them was described as being $Zr_5O_8Cl_4{\cdot}nH_2O$ precipitate [5]. It is hence reasonable to attribute the larger distance to the pentamers, which are the most abundant species at [Zr] = 1.5 mM over a wide pH range. In the case of [Zr] = 10 mM, tetramers and octamers account for >80% of the Zr concentration up to pH_C 0.5. Both are likely to have similar structures, since the octamers probably form via tetramer stacking [1, 9, 12, 14] and this should cause the shorter Zr–Zr distance observed by EXAFS.

The good correlation of the EXAFS findings with the species distribution inferred from ESI-TOF (Fig. 7), in particular the fact that the Zr–Zr backscattering peak (Fig. 10) broadens and vanishes when multiple species are detected, suggests that the species were not significantly disturbed by the electrospray process. In particular, since no clustering effects were observed, the mass spectra should reflect the species distribution in solution to a good approximation.

The Zr(IV) hydroxo species distribution

In this section the species distribution shown in Fig. 7 is compared with data in the literature. Figure 7 shows the relative *number* of ions obtained from peak area evaluations of the mass spectra (gained via Eq. 4). In a first step, these numbers are converted to Zr mass concentrations, noting that a polymer of nucleation p contains p Zr atoms and hence its molar concentration is $[\mathrm{Zr}]_{(p)} = p\left[\mathrm{Zr}_p(\mathrm{OH})_y^q\right]$. The Zr fraction within each size class of species $\mathrm{Zr}_p(\mathrm{OH})_y^q$ is calculated according to

$$[\mathrm{Zr}]_{(p,y)} = [\mathrm{Zr(IV)}]_{\mathrm{tot}} \frac{pN\left(\mathrm{Zr}_p(\mathrm{OH})_y^q\right)}{N(\mathrm{Zr}_{\mathrm{tot}})} = [\mathrm{Zr(IV)}]_{\mathrm{tot}} \frac{pN\left(\mathrm{Zr}_p(\mathrm{OH})_y^q\right)}{\sum_{p=1}^{\infty}\sum_{y=1}^{4p} pN\left(\mathrm{Zr}_p(\mathrm{OH})_y^q\right)} \quad (6)$$

and a summation over all hydroxide complexes with an equal degree of nucleation p gives

$$[\mathrm{Zr}]_{(p)} = \sum_{y=1}^{4p} [\mathrm{Zr}]_{(p,y)}. \quad (7)$$

These quantities are plotted for the mononuclear, tetrameric, pentameric, and octameric species as function of the $[H^+]$ concentration in a double logarithmic representation in Fig. 11 ([Zr] = 1.5 mM: top and [Zr] = 10 mM: bottom).

This representation allows us to compare the results to the model of the NEA-TDB review. The species distribution is calculated according to Eq. 18 using the constants summarized in Table 3. Since the samples do not contain a background electrolyte, the ionic strength I varies with pH and is determined by the concentration of the acid (HCl) and the concentration of the highly charged Zr ions. I is calculated according to

$$I = [\mathrm{H}^+] + 0.5\sum_{p,q} q^2\left[\mathrm{Zr}_p(\mathrm{OH})_y^q\right]. \quad (8)$$

Due to the q^2 weighting, the highly charged Zr polymers contribute significantly to the ionic strength, particularly at "low" acidity. It should also be noted that due to the ionic strength correction, Eq. 19 implies that each individual hydrolysis constant depends implicitly on the concentrations of all highly charged Zr species:

$$\log\left[\mathrm{Zr(OH)}^{3+}\right] = \log\left[\mathrm{Zr}^{4+}\right] + \log[\mathrm{OH}^-] + \log\beta'_{1,1} \quad (9)$$

$$\log\left[\mathrm{Zr(OH)}_2^{2+}\right] = \log\left[\mathrm{Zr}^{4+}\right] + 2\log[\mathrm{OH}^-] + \log\beta'_{1,2} \quad (10)$$

$$\log\left[\mathrm{Zr}_3(\mathrm{OH})_4^{8+}\right] = 3\log\left[\mathrm{Zr}^{4+}\right] + 4\log[\mathrm{OH}^-] + \log\beta'_{3,4} \quad (11)$$

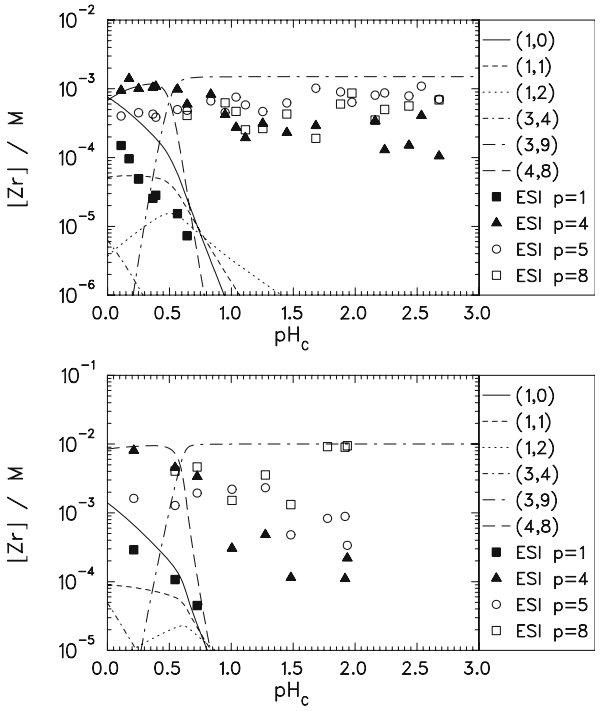

Fig. 11 Species distribution in units of molar Zr concentration within each size class $\left(\sum_{y=1}^{4p}\left[\mathrm{Zr}_p(\mathrm{OH})_y^q\right]\right)$. Formation constants of mononuclear, trimeric and tetrameric hydrolysis species are taken from the literature (NEA-TDB [4]). (p,y) denotes the complex $\mathrm{Zr}_p(\mathrm{OH})_y^{4p-y}$. For a more detailed discussion, see text. *Top*: [Zr] = 1.5 mM. *Bottom*: [Zr] = 10 mM

$$\log\left[\mathrm{Zr}_3(\mathrm{OH})_9^{3+}\right] = 3\log\left[\mathrm{Zr}^{4+}\right] + 9\log\left[\mathrm{OH}^-\right] + \log\beta'_{3,9} \tag{12}$$

$$\log\left[\mathrm{Zr}_4(\mathrm{OH})_8^{8+}\right] = 4\log\left[\mathrm{Zr}^{4+}\right] + 8\log\left[\mathrm{OH}^-\right] + \log\beta'_{4,8} \tag{13}$$

$$[\mathrm{Zr}]_{\mathrm{tot}} = \sum_{p,y} p\left[\mathrm{Zr}_p(\mathrm{OH})_y^q\right] = \mathrm{const.} \tag{14}$$

This system of (nonlinear) equations was solved numerically (using FORTRAN code and the open source SLATEC library). The results are included in Fig. 11. The measured species distribution (denominated ESI) shows that polymers are the dominant species over the pH range investigated for both concentrations, [Zr] = 1.5 mM (top) and [Zr] = 10 mM (bottom). The fraction of mononuclear species is very small. This behavior agrees well with the prediction from the NEA hydrolysis model (solid line: Zr^{4+}). At pH_C<0.5, the tetramer $\left(\mathrm{Zr}_4(\mathrm{OH})_8^{8+}\right)$ is the dominant species. At pH_C>0.5, we get the formation of pentamers and octamers, the latter dominating the species distribution,

Table 3 Equilibrium constants and interaction coefficients for Zr(IV) hydroxide complexes

Species	$\log\beta^{\circ}_{p,y}$ [a]	$\log *\beta^{\circ}_{p,y}$	$\log\beta'_{p,y}$ [c]	$\epsilon_{i,\mathrm{Cl}^-}$	$\epsilon_{i,\mathrm{OH}^-}$
Zr^{4+}	–	–	–	0.33[d]	0.64[g]
$Zr(OH)^{3+}$	14.1	0.32	13.5	0.18[e]	0.36[g]
$Zr(OH)_2^{2+}$	27.8	0.30	26.8	0.08[e]	0.18[g]
$Zr_3(OH)_4^{8+}$	55.4	0.4	56.3	0.18[e]	0.64[g]
$Zr_3(OH)_9^{9+}$	12.2	135.75	132.3	1.7[e]	0.38[g]
$Zr_3(OH)_8^{8+}$	9.0	7.93[b]	118.47	3.0[f]	0.64[g]
H^+	–	–	–	0.12[h]	–

[a] Reaction $p\mathrm{Zr}^{4+} + y\mathrm{OH}^- \rightleftharpoons \mathrm{Zr}_p(\mathrm{OH})_y^{4p-y}$
[b] Taken from [16]. In [4] $*\beta^{\circ}_{p,y} = (6.52 \pm 0.65)$
[c] Value at $[H^+] = 2$ M, [Zr] = 10 mM
[d] From [4]
[e] Estimated from $\varepsilon_{Zr^{4+},Cl^-}$ and quadratic charge/radius dependence [4]
[f] From [4]
[g] Estimated from value in [13] and quadratic charge/radius dependence [4]
[h] From [78]

especially at higher Zr concentrations (bottom). In contrast, the NEA model predicts the formation of a triply charged trimer[2] $\left(\mathrm{Zr}_3(\mathrm{OH})_9^{3+}\right)$ above pH_C 0.5. However, no direct proof of this species exists. The authors of the NEA-TDB review state that: "The species $\mathrm{Zr}_3(\mathrm{OH})_9^{3+}$ has been introduced to increase the quality of the global fit of the hydrolysis data (...). This species has not yet been identified or proposed in the experimental literature." However, it is not necessary to introduce $\mathrm{Zr}_3(\mathrm{OH})_9^{3+}$ in order to obtain a good fit. This species can be replaced by the octamer detected with ESI-MS, which has a similar p/q ratio and is also in agreement with X-ray scattering experiments [10, 14] (see Fig. 13 and discussion below).

Hydrolysis model including polynuclear species with continuously varying numbers of OH^- ligands

Experimental data from indirect methods (e.g., potentiometric titrations) are usually evaluated by keeping the number of species as low as possible in order to minimize the number of adjustable parameters. Several experiments at low metal concentrations have been modeled using mononuclear complexes $\mathrm{M}(\mathrm{OH})_y^{4-y}$ with $y = 0 - 4$ [74, 79–81]. For polynuclear hydrolysis species, the variation in the number of OH^- ligands and hence the charge is usually not considered. In most of these studies performed at higher metal concentrations, only a very limited number of polynuclear species, partly selected based on structural

[2] The *octuply* charged trimer $\left(\mathrm{Zr}_3(\mathrm{OH})_4^{8+}\right)$, which was used to model titration experiments of highly concentrated solutions at acidities >1 M, does not play a role under the present conditions (dashed dotted line).

Anal Bioanal Chem (2007) 388:409–431 423

considerations, are taken into account. In contrast to the majority of papers on the hydrolysis of metal ions, a very recent empirical model for estimating hydrolysis constants of actinide ions proposed a continuous series of polynuclear hydroxide complexes $An_p(OH)_y^{4p-y}$ with $1<p<10$ [81, 82]. This model was also applied to the hydrolysis of Zr(IV) [80], yielding formation constants for polynuclear species up to tetramers. The present experiments support the idea of a continuous series of Zr(IV) hydroxide complexes. Polynuclear species are dominant at Zr and H^+ concentrations of solutions saturated with $Zr(OH)_4$(am). Mononuclear hydroxide complexes are minor species under these conditions. Since the slope of the solubility curve of $Zr(OH)_4$(am) is between −2 and −1 at pH 3–6 (Fig. 2), the *dominant* species must be singly or doubly charged (see Eq. 32) and cannot be highly charged, for example $Zr_4(OH)_8^{8+}$. Indeed, Fig. 8 shows that the number of OH^- ligands increases with increasing pH, especially for the pentamers and octamers. The charges of the complexes decrease accordingly and approach $q=2$ close to the solubility curve. The tetramer, an exception, remains at a higher charge state, but it is not a dominant species since its abundance strongly decreases with increasing pH (Fig. 11) and its concentration is at least a factor of 10 below those of the larger polymers close to the solubility curve. In the following model, the complexity of the system Zr(IV)–OH is approximated by selecting nine polynuclear species.

The model (Eq. 15) includes different tetramers [(4,8), (4,10)], pentamers [(5,11), (5,12), (5,16)], and octamers [(8,19), (8,22), (8,27)], and in addition the trimer (3,4) proposed in the literature [4] and the mononuclear species (1,*y*) with $y = 0 - 4$. However, even for this reduced number of species, the experimental data does not allow us to fit all hydrolysis constants and ion interaction (SIT) parameters. The latter are estimated as described in Table 4. We do not claim that the equilibrium constants used here are appropriate or sufficient for an extended range of H^+ and Zr concentrations; nor can the accuracy of the equilibrium constants be judged due to the only roughly estimated SIT coefficients. The qualities of the corresponding equilibrium constants in Table 4 cannot be compared with the values deduced for instance in the NEA-TDB review [4] from a wide basis of literature data. However, we wish to point out that a realistic description of Zr(IV) hydrolysis requires a much larger number of complexes, in terms of both degree of polymerization and number of OH^- ligands, which increases continuously with increasing pH.

The species distribution is calculated as above by simultaneously solving the system of coupled equations.

$$\log\left[Zr_p(OH)_y^{4p-y}\right] = p\,\log\left[Zr^{4+}\right] + y\,\log\left[OH^-\right] + \log\beta'_{p,y} \quad (15)$$

Table 4 Equilibrium constants (at zero ionic strength: $\beta^o_{p,y}$ and ${}^*\beta^o_{p,y}$ and SIT coefficients $(\varepsilon_{i,Cl^-}, \varepsilon_{i,OH^-})$) for the Zr(IV) hydroxide complexes used in Fig. 12. For the applicability of these constants, refer to text

Species	$\log\beta^o_{p,y}$ [a]	$\log{}^*\beta^o_{p,y}$	ϵ_{i,Cl^-}	ϵ_{i,OH^-}
Zr^{4+}	–	–	0.33[d]	0.64[g]
$Zr(OH)^{3+}$	14.1	0.32	0.18[e]	0.36[g]
$Zr(OH)_2^{2+}$	27.8	0.30	0.08[e]	0.18[g]
$Zr(OH)_3^{+}$	37.1	−4.1	0[e]	0.04[d]
$Zr(OH)_4$	45.8	−9.2	0[e]	0[g]
$Zr_3(OH)_4^{8+}$	55.4	0.4	0.18[e]	0.64[g]
$Zr_4(OH)_8^{8+}$	121.5	*11.5*	*0.5*	2.56[g]
$Zr_4(OH)_{10}^{6+}$	149	*11.5*	*0.28*	1.44[g]
$Zr_5(OH)_{11}^{9+}$	165.4	*14.2*	*0.3*	3.6[g]
$Zr_5(OH)_{12}^{8+}$	180	*15*	*0.2*	2.5[g]
$Zr_5(OH)_{16}^{4+}$	230	*10*	*0.1*	0.6[g]
$Zr_8(OH)_{19}^{13+}$	281.3	*20*	*8*	6.7[g]
$Zr_8(OH)_{22}^{10+}$	324.5	*22*	*3*	4[g]
$Zr_8(OH)_{27}^{5+}$	385.75	*14.5*	*1*	1[g]

[a] Reaction $pZr^{4+} + yOH^- \rightleftharpoons Zr_p(OH)_y^{4p-y}$
[d] From [13]
[e] Estimated from $\varepsilon_{Zr^{4+},Cl^-}$ and quadratic charge/radius dependence [4]
[f] From [4]
[g] Estimated from value in [13] and quadratic charge/radius dependence [4]

$$[Zr]_{tot} = \sum_{p,y} p\left[Zr_p(OH)_y^q\right] = \text{const.} \quad (16)$$

for the species
$p = 1 \quad y: 0, 1, 2, 3, 4$
$p = 3 \quad y = 4$
$p = 4 \quad y = 8, 10$
$p = 5 \quad y = 11, 12, 16$
$p = 8 \quad y = 19, 22, 27$

The equilibrium constants and SIT parameters used are summarized in Table 4. In contrast with the model of Fig. 11, more species are included to account for the hydrolysis and decreasing charge of the Zr polymers, according to Fig. 8. However, far from all of the 53 $\left(Zr_p(OH)_y^{4p-y}\right)$ hydroxide complexes detected by ESI-TOF were included, since the amount of data available does not suffice to fit such a large number of equilibrium constants. The biggest species that are considered are the octamers, although polymers up to the eicosamer ($p=20$) were observed at high pH. For one degree of polymerization *p*, up to three hydrolysis species were taken into account. The equilibrium constants for the monomeric species and the trimer were taken from the literature (Table 4), and only the constants in *italic* font were varied. In order to account for the varying ionic strengths of the samples (lack of background electrolyte, see above), SIT coefficients ($\varepsilon_{(cation,Cl^-)}$ and $\varepsilon_{(cation,OH^-)}$) are needed. For those species with

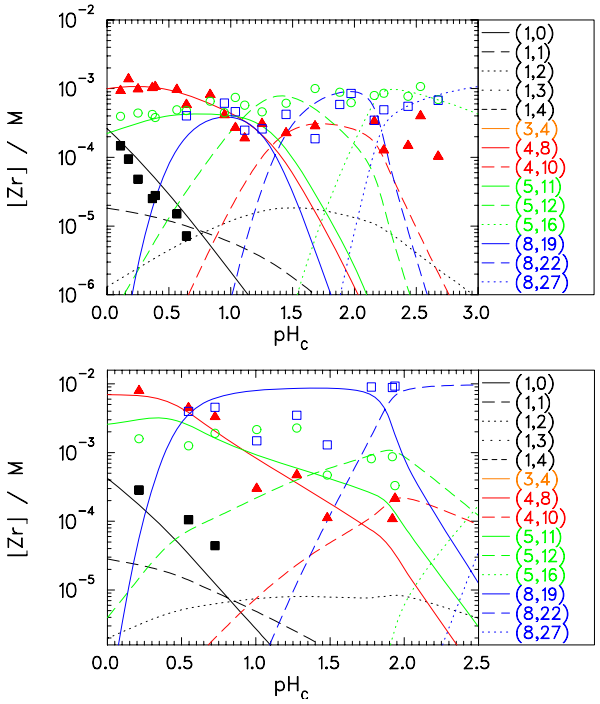

Fig. 12 Species distribution in units of molar Zr concentration within each size class $\left(\sum_{y=1}^{4p}\left[Zr_p(OH)_y^q\right]\right)$ for the ESI-TOF data (*filled squares*, monomers; *triangles*, tetramers; *circles*, pentamers; *unfilled squares*, octamers). The speciation model of Fig. 11 is extended in order to account for the observation of a reduction in charge with increasing pH (see Fig. 8). Monomer (*black lines*) and trimer (*orange*) data were taken from the literature (NEA-TDB [4]), the constants for the tetramer (*red*), pentamer (*green*) and octamer (*blue*) hydroxide complexes were estimated (for discussion see text). (p,y) denotes the complex $Zr_p(OH)_y^{4p-y}$ *Top*: 1.5 mM. *Bottom*: 10 mM

no values available in the literature, estimates were made according to the semi-empirical model in the NEA-TDB review, assuming that the interaction coefficients scale linearly with the ratio (charge of the complex/square root of the radius) q/R. To reduce the number of free parameters, the SIT coefficients were *not* fitted to the data. Using these assumptions, the measured data are reproduced satisfactorily for both concentrations ([Zr] = 1.5 mM and 10 mM, Fig. 12). When a lower number of species was used, the data for [Zr] = 1.5 mM could not be reproduced satisfactorily, due to the wider pH range and hence the stronger variation in charge of the pentamers and octamers (see Fig. 8).

The present model is compared with SAXS measurements obtained under similar conditions. Singhal et al. [14] measured 50 mM zirconyl chloride solutions in hydrochloric acid ($0<pH_C<1.7$) at I=1 M (see the "Appendix B"). The dominant solution species and their respective abundances were identified via small-angle X-ray scattering (SAXS): $[Zr_4(OH)_8 16H_2OCl_6]^{2+}$ at $pH_C<0.6$ and $[Zr_8(OH)_{20}24H_2OCl_{12}]$ at lower acidity. The proposed species distribution is plotted in Fig. 13 (dashed lines). The solid lines show the prediction of the present model. The pH that gives equal numbers of tetramers and octamers is predicted very well. The difference in absolute concentration compared to the present model originates from the additional pentamers, which account for the remaining Zr concentration and were not included by Singhal et al. It is worth mentioning that Singhal et al. found that the aggregation of two tetramers was accompanied by some charge compensation due to hydrolysis. The SAXS measurements were modeled by the complex $Zr_8(OH)_{20}^{12+}$, which agrees well with the dominant species of the present work in the respective pH range, the complex $Zr_8(OH)_{19}^{13+}$.

In the following, the results from the present model are compared with those from experiments reported in the literature that were performed at metal concentrations and acidities similar to the present work. The respective degrees of polymerization (p) or, if available, the concrete species $Zr_p(OH)_y^{4p-y}$ are listed in Table 5. Some important details about the experimental method applied are given as footnotes (see also the "Appendix B").

The general trends may be summarized as follows:

(a) At a given Zr(IV) concentration, and with increasing pH, the degree of polymerization p increases.
(b) At Zr concentrations in the mM range and for $pH_C>0$ the monomers are only a minor species.
(c) Many authors report a decrease in the charge of the polymers with decreasing acidity [11], and the present work suggests a limiting value of −2. This finding correlates with the slope of the solubility curve for freshly formed amorphous Zr(IV) hydroxide,[3] which requires the charge of the dominant species to approach q=2 [13, 22].

With increasing zirconium concentration, the degree of polymerization increases, as expected, and the solubility limit shifts toward lower pH. Close to the solubility limit, continuous growth of the polymers is found, which leads to the formation of large polynuclear species of 1000–10000 Da [88] and colloids. Most authors agree that no Zr dimers exist in solution; the exception is the potentiometric titration work of Veyland [25]. However, the latter can be interpreted in terms of higher polymers, as discussed above and in the NEA-TDB review [4]. Trimers are observed at elevated Zr concentrations and acidities exceeding 1 M. There are two papers that report trimers at

[3] Different results are obtained for aged or microcrystalline zirconium solid phases, see Fig. 2, and recent results indicate that aging of freshly precipitated amorphous zirconium hydroxide leads to phase transformation towards a more crystalline solid [85; Kobayashi T, Sasaki T, Takagi I, Moriyama H, 2006, submitted]. Futhermore, the dependence of the solubility on particle size needs to be considered. Small particles have a higher solubility than large ones, and a bulk solid composed of a highly disperse mixture of grains might exhibit a fast dissolution of the higher soluble particles followed by a slow dissolution of the larger ones [86, 87].

Table 5 Average degrees of polymerization (*p*) or, if given, assumed hydroxide complexes (p,y) obtained when investigating aqueous solutions by different methods, compared to the findings of the present work (ESI)

Reference			pH									
Method	Media	Concentration	-0.3	0	0.2	0.4	0.6	0.8	1.0	1.3	2.3	≥ 3
ESI	HCl	10^{-2}M		(4,8)	(4.8)	(4,8)	(4,8),(8,19)		(5,14)(8,22)		prec	prec.
(p.w)		1.5×10^{-3}M		(1,0), (4,8)	(4.8)	(4,8)	(4,8),(5,11)	(4,8),(5,12),(8,22)		(5,13),(8,22)	(5,16),(8,27)	prec.
TTA [15]	$HClO_4$	10^{-2}M		p= 10	infinte series of polynuclear species							
		10^{-3}M		p=3	infinte series of polynuclear species							
EX [16]	$HClO_4$	$> 10^{-4}$M	(3,4) and (4,8) [a)b)]									
IE [84]	$HClO_4$	10^{-2}M		p=4		p=6		p=8				
		1.5×10^{-3}M		p=2				p=4				
UC [20]	HCl	5×10^{-2}M		p=3-4,q=1-1.75			p=4-6	p=8	p=6-11	p=10[c)]		
XS [66]	HCl	5×10^{-2}M		p≥ 4								
TD [22]	$HClO_4$	$< 10^{-2}$M	p=1[d)]									q=1-2
CD [85]	HCl	$> 10^{-2}$M	increasing p with decreasing acidity									
TU [21]	HCl	$2 - 10 \times 10^{-2}$M	(3,9)		(6,18)[e)]							
CO [18]	HCl/$HClO_4$	$0.05 - 2 \times 10^{-3}$M		(3,7);(3,8) [f)]								
RA [23]	HCl	10^{-2}M		(1,0)						(4,8)	(4,12)[g)]	
NMR [24]	$HClO_4$	5.5×10^{-2}M		(1,0)						(4,8)[k)]		
PT [25]	$HClO_4$	5.5×10^{-2}M		(1,0)						(2,7)[i)j)]		
EXAFS [11]	NO_3^-	1M[k)]						(4,8)[l)]				
SAXS [14]	HCl	5×10^{-2}M		[m)]			(4,8)[n)]		(8,20)[n)]			
SAXS [10]	HCl	5×10^{-2}M		[o)]			(4,8)		(8,20)		[p)]	
TCSPS [19]	HCl	5×10^{-2}M	(4,8)						p=9-15[q)]		p>70	
EXAFS[r)] [12]	HCl	1M[s)]	(4,8)[t)]									
LIBD/EXAFS [13]	HCl	10^{-3}M[u)]		(4,8)[v)]						[w)]	p>4	q=1-2

p: average degree of polymerization; (p,y): concrete species:
Methods: ESI: electrospray, TTA: TTA complexation EX: extraction, IE: ion exchange, UC: ultracentrifugation, XS: X-ray scattering, TD: tyndallometry, CD: capillary diffusion, TU: turbidity, CO: monothiocyanatocomplexation and absorpt.spect., RA: Raman spectroscopy, NMR: ^{17}O nuclear magnetic resonance, PT: potentiometric titration, EXAFS: extended X-ray absorption fine structure, SAXS: small-angle X-ray scattering, TCSPS: time-correlated single-photon spectroscopy

[a] Refit in [4] yields equally good fits whether trimers are included or not
[b] *y* increases with increasing pH, not quantified
[c] pH calculated from H^+ release during dissolution of $ZrOCl_2$ in water
[d] The assumption of the authors that only monomers are present in solution is considered invalid by, e.g., [4]
[e] $q \sim p$
[f] Derived from the assumption that $ZrOH^{3+}$ dominates at very acidic conditions, which is most likely invalid since only Zr^{4+} exists in these solutions [4]
[g] In addition two unidentified species of presumably larger size were observed
[h] Two water coordination shells of eight molecules each were identified. Polymerization via double hydroxo bridges
[i] Reinterpretation in terms of larger polymers possible: (4,14),(4,16) [4] or (5,14). See "Appendix B"
[j] Release of 1 H^+ per Zr
[k] Gel precipitate
[l] Double hydroxo bridges, charge reduction during the polymerization process, up to colloidal size
[m] At high acidity this is a monodispersed species, at increased pH it forms larger aggregates. No species change from pH 0 to 0.4
[n] Cl^- complex exists in solution
[o] At [Zr] = 100 mM monodisperse polymers (tetramers) exist
[p] Colloids of fractal structure start forming
[q] pH 1.1–1.7
[r] And large-angle X-ray scattering
[s] From dissolution of 1 M $ZrOCl_2$ in water: $[H^+] > 1$ M
[t] Structure of $ZrOCl_2$ solid maintained in water
[u] Colloid formation detected for 10^{-8} M < [Zr] < 10^{-1} M
[v] At [Zr] = 0.1 M
[w] The authors deduced the presence of monomers from the very weak and broad Zr–Zr peak in the EXAFS spectra, which is wrong (see discussion of EXAFS data for the present work)

higher pH. Tribalat and coworkers [18] measured the decrease of the Zr^{4+} ion concentration with increasing pH by observing the 270 nm absorption band of the monothiocyanato complex. From a slope analysis, they concluded that the polynuclear species should be a trimer. However, the data could be interpreted differently if polymers were already present in their stock solutions (e.g., the tetramer, which is stable even in very acidic highly concentrated samples [12]) and/or the formation of several polynuclear species occurred at the same time, which is indeed observed in the present experiments. The relative fraction of polymers with respect to the total Zr concentration in solution reported by the authors agrees well with the present experiments. At [Zr] = 10 mM and pH 0, some 80% are polymerized, at pH 0.3 this is already 90%. At [Zr] = 1 mM and pH 0, the monomer accounts for 50% of the total Zr concentration. This fraction decreases to less than 25% at pH 0.3 (see ESI data in Fig. 12). In the NEA-TDB review, the trimer was introduced to obtain a better fit to the data, not because of direct observations (see above). The tetramer $Zr_4(OH)_8^{8+}$ is the dominant species over a wide range of concentrations at high to moderate acidities. In contrast to the general trend of charge compensation by hydrolysis, which is observed for all other polynuclear

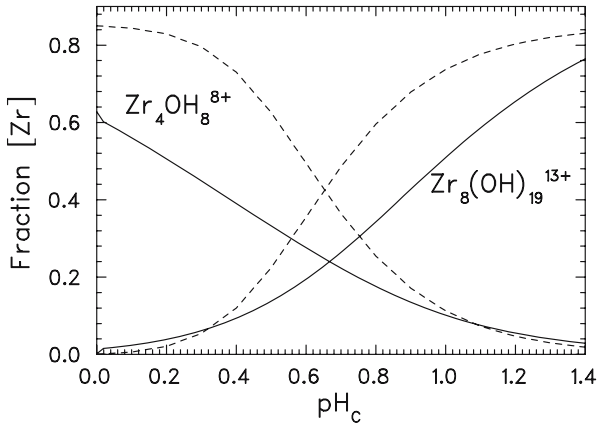

Fig. 13 The equilibrium between tetramers and octamers (*dashed lines*) proposed by Singhal et al. [14] on the basis of SAX measurements ([Zr] = 50 mM) is well reproduced by the present model of hydrolysis based on ESI-TOF measurements (*solid lines*)

species, the complex $Zr_4(OH)_8^{8+}$ remains stable up to pH_C~1.5, which might be a consequence of its high symmetry. At pH and Zr(IV) concentrations close to the precipitation of $Zr(OH)_4$(am), the existence of $Zr_4(OH)_{15}^{+}$ and $Zr_4(OH)_{16}$ is assumed in the NEA-TDB review [4]. The structure of the pentamer was investigated in 1956, and its presence in solution is discussed in Blumenthals monograph [5]. However, in more recent papers this polynuclear species has hardly been used to fit data obtained by "indirect" methods, and no direct proof for its existence has been reported since then to our knowledge. Bertin et al. [23], however, observed two unidentified peaks in the Raman spectra of zirconium solutions of >50 mM at pH_C> 1.3. The authors suggest that these peaks should be assigned to species larger than the tetramer. Angstadt [21] used hexamers to fit data obtained by turbidity measurements at pH 0.3 and Zr concentrations above 20 mM. Octamers are reported by several authors, including direct measurements of their structure by X-ray scattering [10, 14] as discussed above (Fig. 13). Their data prove that charge compensation occurs during hydrolysis with increasing pH. Furthermore, chloride ions were shown to interact with the zirconium species. Though not directly bound to the Zr ions, Cl^- ions were found by other authors to occupy well-defined positions within the second ligand sphere. This result agrees with our finding, that most of the zirconium species observed in the ESI-TOF spectra contain chloride ions. However, the extent to which these chloride ions coordinate to zirconium species already in solution or aggregate during droplet evaporation (see "How invasive is the electrospray process?") is not clear. The formation of strong zirconium complexes with Cl^- in the first coordination sphere is rather unlikely, as shown by the EXAFS investigations.

Conclusions

The present work demonstrates that ESI-TOF MS is suitable for quantifying charged hydroxide complexes of metal ions in acidic aquatic solutions. The use of nano-ESI capillaries allows aqueous samples to be investigated without the need for additives to lower the surface tension. The invasiveness of the ESI process is minimized by using very low declustering conditions (low flow rate and no heating of the nitrogen curtain, low potential of the sampling plate), and the metal ion hydroxide complexes are transferred to the mass spectrometer inside a ~20-molecule solvate shell. Changes in pH due to the ESI current are shown to be neglegible below pH_C 3. For selected samples, direct comparision of the ESI results with EXAFS measurements supports the assumption that the mass spectra reflect the species distribution in solution. For elements with more than one stable isotope, the natural isotope distribution permits unequivocal identification of the polynuclear species. The method allows the simultaneous detection of species which differ in abundance by two orders of magnitude (e.g., monomers in the presence of a 100-fold excess of tetramers). One shortcoming of our ESI spectrometer is its relatively low sensitivity for aqueous solutions, which limits the present investigations to the mM concentration range. However, for monoisotopic elements like Th, the sensitivity increases by several orders of magnitude (Walther C, Fuss M, Buechner S, Geckeis H, 2006, in preparation). Another limitation is that, in order to avoid capillary clogging, the electrolyte concentration must not exceed 10 mM. Therefore, it is impossible to study solutions from pH 0 to pH 3 (e.g., HCl/NaCl solutions) at constant ionic strength. For the same reason, oversaturated solutions cannot be measured since the formation of a solid precipitate clogs the capillary very rapidly.

The present results on the hydrolysis of Zr(IV) at pH 0–3 are consistent with observations reported in the literature; however, they provide additional information which is not available by other experimental methods. For Zr concentrations in the millimolar concentration range, mononuclear species are shown to be minor species at pH>0.1. The expected stability range of the tetramer $Zr_4(OH)_8^{8+}$ was confirmed, and the observed formation of octamers is in agreement with literature data based on X-ray scattering. In addition, it was shown that the degree of polymerization gradually increases if the conditions (Zr and H^+ concentrations) approach the solubility limit of $Zr(OH)_4$(am). The polymerization process culminates in the formation of colloids and finally precipitation. Simultaneously, the number of OH^- ligands per Zr(IV) ion increases with increasing pH (charge compensation). The charge of the polynuclear species found to be dominant under conditions close to the Zr and H^+ concentrations in solutions saturated

with $Zr(OH)_4(am)$ agrees with that obtained by slope analysis of solubility measurements. The simple models proposed for instance in the NEA-TDB review [4] provide adequate tools for modeling solubility data, but they do not reflect the complexity of the Zr(IV) hydrolysis process, which continuously produces a considerable number of polymers as a function of pH and total Zr concentration. On the other hand, it is not possible to construct an accurate set of thermodynamic constants for all of the species detected by nanoelectrospray mass spectrometry because of the large number of unconstrained model parameters.

Acknowledgements The authors acknowledge fruitful and helpful discussions with Marcus Altmaier, Horst Geckeis, Volker Neck, and Bernd Schimmelpfennig. We acknowledge the experimental assistance of Kathy Dardenne and Boris Brendebach. We are grateful for the many comments and suggestions of Enzo Curti, which greatly helped to improve this paper. C.W., M.F., and S.B. acknowledge financial support from the "Programm Nuklear" of the Helmholtz Gemeinschaft Deutscher Forschungszentren (HGF).

Appendix A

Hydrolysis, polymerization and solubility

The terminology used in the present work to describe the hydrolysis reaction of Zr^{4+} ions and the formation of polymers and hydroxide complexes $Zr_p(OH)_y^{4p-y}$ is briefly described in this Appendix.

$$pZr^{4+} + yOH^- \rightleftharpoons Zr_p(OH)_y^{4p-y} \tag{17}$$

The corresponding formation constants β'_{py} (in a given medium) and β°_{py} (at infinite dilution) are defined by

$$\beta'_{py} = \frac{\left[Zr_p(OH)_y^{4p-y}\right]}{\left[Zr^{4+}\right]^p[OH^-]^y} \tag{18}$$

$$\beta^\circ_{py} = \frac{\beta'_{py}\left(\gamma_{Zr_p(OH)_y^{4p-y}}\right)}{(\gamma_{Zr^{4+}})^p(\gamma_{OH^-})^y} \tag{19}$$

$[i]$ denotes the concentration of species i and γ_i its activity coefficient. The solubility products K'_{sp} (in a given medium) and K°_{sp} (at infinite dilution) of Zr(IV) oxides/hydroxides, formulated as $Zr(OH)_4(am)$, refer to the reaction

$$Zr(OH)_4(am) \rightleftharpoons Zr^{4+} + 4OH^- \tag{20}$$

with

$$K'_{sp} = \left[Zr^{4+}\right][OH^-]^4 \tag{21}$$

and

$$K^\circ_{sp} = K'_{sp}(\gamma_{Zr^{4+}})(\gamma_{OH^-})^4 \tag{22}$$

In solubility experiments (e.g., with freshly formed $Zr(OH)_4(am)$ [13, 22], see Fig. 2), the total Zr concentration is given by the sum of the species concentrations:

$$\log[Zr] = \log \sum p\left[Zr_p(OH)_y^{4p-y}\right] \tag{23}$$

The concentration of a distinct species $Zr_p(OH)_y^{4p-y}$ can be derived from the equilibrium

$$pZr(OH)_4(am) \rightleftharpoons Zr_p(OH)_y^{4p-y} + (4p-y)OH^- \tag{24}$$

with

$$\log K' = \log\left[Zr_p(OH)_y^{4p-y}\right] + (4p-y)\log[OH^-] \tag{25}$$

$$= p\log K'_{sp} + \log *\beta'_{p,y} \tag{26}$$

Alternatively, the reaction (Eq. 24) can be written as

$$pZr(OH)_4(am) + (4p-y)H^+ \rightleftharpoons Zr_p(OH)_y^{4p-y} + (4p-y)H_2O \tag{27}$$

with

$$\log K' = \log\left[Zr_p(OH)_y^{4p-y}\right] - (4p-y)\log[H^+] \tag{28}$$

$$= p\ \log {}^*K'_{s,0} + \log {}^*\beta'_{p,y} \tag{29}$$

The equilibium constants $\log {}^*K'_{s,0}$ and $\log {}^*\beta'_{p,y}$ are related to $\log K'_{sp}$ and $\log \beta'_{p,y}$ by the ion product of water $\left(K'_w\right)$ in the corresponding solution $\left(\log {}^*K'_{s,0} = \log K'_{sp} - 4\log K'_w\right.$ and $\left.\log {}^*\beta'_{p,y} = \log \beta'_{p,y} + y\ \log K'_w\right)$.

The Zr concentration arising from the species $Zr_p(OH)_y^{4p-y}$ is given by

$$\log[Zr]_{(p,y)} = \log\left(p\left[Zr_p(OH)_y^{4p-y}\right]\right) \tag{30}$$

$$= \log p + \log {}^*\beta'_{p,y} + p\log {}^*K'_{s,0} + (4p-y)\log[H^+] \tag{31}$$

$$= \log p + \log {}^*\beta'_{p,y} + p\log {}^*K'_{s,0} - (4p-y)pH_c \tag{32}$$

Accordingly, the concentration lines of species with the same charge $q = (4p–y)$ have the same slope $(-q)$ in a plot of $\log[Zr]$ against $pH_c = -\log[H^+]$. If the species $Zr_p(OH)_y^{4p-y}$ is dominant in saturated solution over a certain pH range, the solubility curve ($\log[Zr]$ vs. pH_c) decreases with a slope of $-q$ in that pH range, independent of whether the species is mononuclear or polynuclear.

The specific ion interaction theory (SIT) [89, 90] is used to calculate the activity coefficients, according to:

$$\log \gamma_i = -z_i^2 D + \sum_j \varepsilon_{ij} m_j \qquad (33)$$

where z_i is the charge of ion i, ε_{ij} is the interaction parameter for ion i and an oppositely charged ion j, and m_j (mol/kg H_2O) is the molal concentration of ion j. D is the Debye–Hückel term at 25 °C: $D = 0.509\sqrt{I}/\left(1 + 1.5\sqrt{I}\right)$, and I (mol/kg H_2O) is the molal ionic strength. In order to convert the equilibrium constants from I=0 to a given ionic strength, the ion interaction coefficients for mononuclear Zr(IV) species are set equal to those reported for analogous Pu(IV) species [91]. Most SIT coefficients of polymers $\varepsilon\left(\mathrm{Zr}_p(\mathrm{OH})_y^{4p-y}, \mathrm{Cl}^-\right)$ are not given in the literature and are estimated to convert the equilibrium constants $\log \beta^o_{py}$ to finite ionic strengths, as described in the "Discussion." The hydrolysis constants for the mononuclear complexes $\mathrm{Zr}(\mathrm{OH})_y^{4-y}$ and for the tetramer $\mathrm{Zr}_4(\mathrm{OH})_8^{8+}$ are taken from the NEA-TDB review [4].

Appendix B

Classification of literature in terms of experimental approaches

The literature cited in the present work, in particular those experiments used for Table 5, are classified in terms of the methodological approches in this section. Special attention is paid to whether a direct, unambiguous speciation of polynuclear species is possible, or whether only relative information on size, growth, etc., was obtained.

Phase equilibrium methods and complexation with organic ligands

A common approach used to quantify the relative abundance of the Zr^{4+} ion in solution is to study its complex formation by phase equilibrium methods like ion exchange, solvent extraction, etc. Distribution coefficients of the Zr^{4+} ion were obtained using complexation by thenoyltrifluoroacetone (TTA) [16]. The formation of Zr hydroxide tetramers and even larger species [15] was inferred from the decrease in the Zr^{4+} concentration in solution with increasing pH. A combination of visible light absorption spectroscopy (UV-VIS) and monothiocyanate complexation was used by Tribalat and coworkers [18]. From a slope analysis of the Zr^{4+} concentration as a function of the total Zr concentration and the acidity, the presence of the trimers $\mathrm{Zr}_3(\mathrm{OH})_7^{5+}$ and $Zr_3(\mathrm{OH})_8^{4+}$ was deduced. Complexation of the Zr^{4+} ion by pyrenecarboxylic acid (PCA) was combined with time-correlated single photon counting in a recent work by Tulock et al. [19]. The fluorescence decay rate is sensitive to pH, and hence the method can measure the pH change of the solution upon hydrolysis and the polymerization of zirconium. Furthermore, the rotational diffusion was measured from the fluorescence signal. This is sensitive to the shape of the polymer and allows its size to be estimated. At Zr concentrations of 50 mM in hydrochloric acid, Tulock et al. [19] obtained a polymerization of p=9–15 in the pH range 1.1–1.7. These results were interpreted in terms of the stacking of tetrameric units after charge compensation of the tetramer due to H^+ release

$$\left[\mathrm{Zr}_4(\mathrm{OH})_8 \cdot 16\mathrm{H_2O}\right]^{8+} \rightleftharpoons \left[\mathrm{Zr}_4(\mathrm{OH})_8(\mathrm{OH})_y \cdot (16-y)\mathrm{H_2O}\right]^{8-y} + y\mathrm{H}^+. \qquad (34)$$

Close to crystallization, polymers consisting of up to 70 tetramer units were found. A similar hypothesis had already been proposed in 1956 by Pokras [17] in his overview article on aqueous solutions of "salts" of polyvalent metals. Due to the stepwise hydrolysis and release of protons, the metal polymers were classified as Brønstedt acids, and the polymer formation was explained by a two-step process: "olation" (the formation of hydroxo bridges) followed by "oxolation" (the transformation of hydroxy-bound into oxo-bridges through the release of protons). However, the latter is no longer assumed to be correct [4].

Techniques based on diffusive processes

The diffusion of Zr polymers within a capillary [84] or into a KU1 resin [83] was studied, and by comparing the rates at different concentrations and acidities it was found that the degree of polymerization increases with decreasing acidity of the solution. Nabivanets et al. [83] gave a range of polymerization (average number of Zr atoms p per polymer Zr_p) from p=2 at mM Zr concentration and pH 0 to p=8 at [Zr] = 10 mM and pH 0.8.

Interaction with visible light

Johnson and Kraus [20] combined ultracentrifugation with measurements of the refractive index of the solution. In 50 mM Zr solutions at pH 0, a degree of polymerization p= 3–4 was determined with an average polymer charge of $\mathrm{Zr}_p(\mathrm{OH})_y^q$ for $q \approx p$ in hydrochloric acid and $q \approx 1.75p$ in perchloric acid. Light scattering and determination of the differential refractive index was applied by Angstadt [21] for Zr solutions at concentrations of between 20 and 100 mM in 2.8 M and 0.75 M hydrochloric acid. The data were interpreted in terms of trimers dominating in the first and hexamers in the second case.

Investigations on the solubility of zirconium hydroxide were conducted by Bilinski et al. [22] using tyndallometry (scattering of light by colloids and small particles). The authors did not interpret their data in terms of polymer formation, but rather assumed $Zr(OH)_3^+$ to be the dominant solution species, an assumption which is most likely not valid for the conditions of that study [4]. However, even if the interpretation of the authors was not correct, the data permits the charge state of the dominating solution species along the solubility curve to be determined: the slope of the solubility curve (log [Zr] vs. pH plot), which is between −1 and −2, indicates a charge $1<q<2$ of the species, independent of its degree of polymerization (see "The Zr(IV) hydroxo species distribution").

These findings were confirmed by Cho et al. [13] in a combined LIBD (laser-induced breakdown detection) and EXAFS (extended X-ray absorption fine structure) study on the solubility of $Zr(OH)_4$(am) in the concentration range 10^{-8} M < [Zr] < 10^{-3} M. Cho et al. were aware of the presence of polynuclear species but could not quantify the degree of polynucleation. They modeled their results using the specific ion interaction theory (SIT [89, 92]) for ionic strength corrections and calculated an "operative" solubility constant by assuming $Zr(OH)_2^{2+}$ and $Zr(OH)_3^+$ to be the dominant species, which most likely is not correct.

Potentiometric titration

Veyland investigated hydrolysis and the formation of complexes and polymers of Zr in perchlorate solutions by potentiometric titration [25]. When solutions of [Zr] = 4 mM and [Zr] = 8 mM were produced by the dissolution of $ZrOCl_2{\cdot}8H_2O$ in nitric acid, the release of one H^+ per Zr was observed in agreement with earlier observations [5, 20]. This observation confirms the presence of a singly charged solution species. The data was reinterpreted in [4] via the reaction

$$ZrOCl_2 \cdot 8H_2O \rightleftharpoons Zr(OH)_3^+ + H_3O^+ + 2Cl^- + 5H_2O. \quad (35)$$

However, the presence of monomers in the mM concentration range is not likely, and an alternative reaction scheme is proposed:

$$p(ZrOCl_2 \cdot 8H_2O) \rightleftharpoons Zr_p(OH)_y^{4p-y} + (y-2p)H_3O^+ + 2pCl^- + (11p-2y)H_2O \quad (36)$$

From potentiometric data, Veyland deduced the existence of the species $Zr_2(OH)_7^+$ and $Zr(OH)_4$(aq) from the equivalent points corresponding to the neutralization of 1.5 and two protons. However, the species assignment is ambiguous, since the species destribution in the initial solution is not known. The data could just as well be fitted by the formation of the tetramers $Zr_4(OH)_{14}^{2+}$ and $Zr_4(OH)_{16}$, as shown in [4].

Laser-based methods

Structural information on the Zr species is obtained from Raman spectroscopy. Bertin et al. investigated rather concentrated Zr solutions (0.04 M < [Zr] < 2.5 M) in hydrochloric and nitric acids [23]. The spectra suggested the presence of five species, but only three were identified: At pH<1.3, the Zr^{4+} ion and the tetramer $Zr_4(OH)_8^{8+}$ prevail. With increasing pH, the latter hydrolyzes and forms $Zr_4(OH)_{12}^{4+}$, until $Zr(OH)_4$(am) precipitates at pH 2.3. Two unidentified species are detected at high Zr concentrations and low acidity, and these are presumably larger than the tetramer. Aberg et al. [24] conducted a combined Raman/^{17}O-NMR study. A 55 mM Zr solution of pH 1.2 was prepared by dissolving $ZrO(ClO_4)_2$ in water. In agreement with Bertin, $Zr_4(OH)_8^{8+}$ was identified as the major species, with two solvation shells consisting of 8 H_2O molecules each. The eight terminal water molecules of the outer shell were found to slowly exchange protons (two per Zr atom), making the tetramer a strong Brønstedt acid. This allows further polymerization to larger units through the formation of hydroxo bridges.

Interaction with X-rays

Another useful technique is the interaction of solution species with X-rays. In 1960 Muha et al. [66] performed X-ray scattering experiments on two-molar solutions of zirconyl chloride in water (presumably pH<0 due to proton release according to Eqs. 35 or 36). The presence of the tetramer was confirmed and it was shown that the chloride ions, though not directly bound to the Zr atom, are fixed in place in the outer solvation shell. This result was supported by Turrillas et al. [9], who suggested a model of polymerization where tetrameric subunits are linked via OH^- groups, which leads to the formation of sheetlike zirconium hydroxide precipitates. The authors stressed that polymerization proceeds more slowly at low pH than at high pH due to the limited number of OH^- groups that are available, and this leads to more ordered structures. Singhal et al. [14] investigated 50 mM zirconium solutions in hydrochloric acid (0<pH<1.7) by small-angle X-ray scattering (SAXS). The authors stressed that SAXS is especially sensitive to the position of the chloride ions due to the high electron density of chlorine. At 0<pH<0.4, the presence of only one major species, $[Zr_4(OH)_8 16H_2OCl_6]^{2+}$, was deduced from the linear functionality of the radius of gyration. At pH≈0.6 ,the formation of the octamer $[Zr_8(OH)_{20}24H_2OCl_{12}]$ is observed, which dominates the

species distribution at higher pH. The authors assume an equilibrium of

$$2\left[Zr_4(OH)_8 16H_2OCl_6\right]^{2+} \rightleftharpoons \left[Zr_8(OH)_{20}24H_2OCl_{12}\right] + 4H^+ + 4H_2O. \quad (37)$$

This interpretation was adopted by Hu et al. [10], who investigated zirconium solutions of 0.025 M < [Zr] < 1 M at pH 1 in HCl by the same method (SAXS). All systems were dominated by only one oligomeric species, presumably the tetramer, with an increasing tendency towards octamer formation at lower acidity. The authors assumed that the octamers are formed by the stacking of two tetramers rather than by sheet formation. Upon heating, the formation of large polymers of fractal structure was observed. Hu et al. developed a model that involved the continuous generation of tetramers and octamers which are consecutively consumed to form large polymers (colloids). These colloids are polydisperse and not isometric. In the presence of additional electrolyte (NaCl), the particle growth rate is enhanced and the resulting colloids are less dense.

A combined EXAFS/SAXS study of 1 M zirconyl nitrate solutions at pH 0.8 by Southon et al. [11] proved the existence of double hydroxo-bridges between neighboring Zr atoms of a cyclic tetramer. For increasing pH (i.e., increasing OH^- abundance), the formation of polymers was described to occur by the conversion of coordinated water into hydroxo bridges and condensation between terminal OH^- groups. An important consequence of this reaction mechanism is that the average charge of the polynuclear species decreases with increasing pH.

Large-angle X-ray scattering and EXAFS measurements [12] revealed that the tetramer $Zr_4(OH)_8^{8+}$ is stable even at rather high concentrations ([Zr] = 2 M). The pH was not given by the authors, but due to the hydrolysis reaction of zirconyl chloride when dissolved in water, a pH of approximately –0.3 is assumed. Furthermore, the authors confirmed that the structure of the tetramer in solution equals the X-ray structure found for the $ZrOCl_2 \cdot H_2O$ solid. Rose et al. [1] investigated the possibitity of using Zr as a crosslinker to gel organic polymers. They found evidence for progressive polymerization with decreasing Zr concentration in the presence of lactates at pH 6 and 7. However, the Zr tetramer seems to be rather undisturbed, since Zr–Zr distances (3.55 Å) and coordination numbers (N_{Zr}=1.9 at [Zr] = 10 mM) agree with samples used in the present work where tetramers (a) or octamers (f) dominate.

References

1. Rose J, Bruin TJMD, Chauveteau G, Tabary R, Hazemann JL, Proux O, Omari A, Toulhoat H, Bottero JY (2003) J Phys Chem B 107:2910–2920
2. Chiavacci LA, Santilli CV, Pulcinelli SH, Bourgaux C, Briois V (2004) Chem Mater 16:3995–4004
3. Curti E, Degueldre C (2002) Radiochim Acta 90:801–804
4. Brown P, Curti E, Grambow B, Ekberg C, Mompean F, Perrone J, Illemassene M (2005) Chemical thermodynamics of zirconium (Chemical Thermodynamics Series vol. 8). OECD/Elsevier, Amsterdam
5. Blumenthal W (1958) The chemical behavior of zirconium. van Nostrand, Princeton, NJ
6. Clearfield A, Vaughan PA (1956) Acta Crystallogr 9:555–558
7. Peter D, Ertel T, Bertagnolli H (1994) J Sol-Gel Sci Tec 3:91–99
8. Helmerich A, Raether F, Peter D, Bertagnolli H (1994) J Mat Sci 29:1388–1393
9. Turrilas X, Barnes P, Gascoigne JD, Turner JZ, Jones SL, Norman CJ, Pygall CF, Dent AJ (1995) Radiat Phys Chem 45:491–508
10. Hu MZC, Zielke JT, Lin JS, Byers CH (1999) J Mat Res 14:103–113
11. Southon PD, Bartlett JR, Woolfrey JL, Ben-Nissan B (2002) Chem Mat 14:4313–4319
12. Hagfeldt C, Kessler V, Persson I (2004) Dalton Trans 14:2142–2151
13. Cho H, Walther C, Rothe J, Neck V, Denecke M, Dardenne K, Fanghänel T (2005) Anal Bioanal Chem 383:28–40
14. Singhal A, Toth LM, Lin JS, Affholter K (1996) J Am Chem Soc 118:11529–11534
15. Connick RE, Reas WH (1951) J Am Chem Soc 73:1171–1176
16. Zielen A, Connick R (1956) J Am Chem Soc 78:5785–5792
17. Pokras L (1956) J Chem Edu 33:152–161
18. Tribalat S, Schriver L (1975) Bull Soc Chim Fr 9:2012–2014
19. Tulock JJ, Blanchard GJ (2002) J Phys Chem B 106:3568–3575
20. Johnson JS, Kraus KA (1956) J Am Chem Soc 78:3937–3943
21. Angstadt R, Tyree S (1962) J Inorg Nucl Chem 24:913–917
22. Bilinski H, Branica M, Sillen L (1966) Acta Chem Scand 20:853–861
23. Bertin F, Bouix J, Hannane S, Paris J (1987) R Acad Sci Ser II 304:405–410
24. Aberg M, Glaser J (1993) Inorg Chim Acta 206:53–61
25. Veyland A (1999) Propriétés thermodynamiques, cinétiques et structurales de complexes simples et mixtes du zirconium(IV) avec les ions hydroxyle et carbonate. Ph.D. thesis, Univ. Reims Champagne-Ardenne
26. Dole M, Mack L, Hines R, Mobley R, Ferguson L, Alice M (1968) J Chem Phys 49:2240–2249
27. Yamashita M, Fenn J (1984) J Phys Chem 88:4451–4459
28. Fenn J (2002) J Biomol Tech 13:101–118
29. Cole R (1997) Electrospry ionization mass spectrometry. Wiley, New York
30. Pramanik B, Ganguly A, Gross M (2002) Applied electrospray mass spectrometry. Marcel Dekker, New York
31. Agnes GR, Horlick G (1995) Appl Spectr 49:324–334
32. Rosen AL, Hieftje GM (2004) Spectrochim Acta B 59:135–146
33. Gross J (2004) Mass spectrometry: a textbook. Springer, Berlin
34. Stewart I (1999) Spectrochim Acta B 54:1649–1695
35. Stewart I, Horlick G (1996) J Anal Atom Spectrosc 11:1203–1214
36. Rodriguez-Cruz S, Jockusch R, Williams E (1999) J Am Chem Soc 121:8898–8906
37. Sarpola A, Hietapelto V, Jalonen J, Jokela J, Laitinen RS, Ramo J (2004) J Mass Spectr 39:1209–1218
38. Sarpola A, Hietapelto V, Jalonen J, Jokela J, Laitinen RS (2004) J Mass Spectr 39:423–430
39. Hellmann H, Laitinen RS, Kaila L, Jalonen J, Hietapelto V, Jokela J, Sarpola A, Rämö J (2006) J Mass Spect 41:1421–1429
40. Peschke M, Blades AT, Kebarle P (1999) Int J Mass Spectr 187:685–699
41. Blades AT, Peschke M, Verkerk UH, Kebarle P (2004) J Am Chem Soc 126:11995–12003
42. Hartke B, Charvat A, Reich M, Abel B (2002) J Chem Phys 116:3588–3600
43. Moulin C (2003) Radiochim Acta 91:651–657

44. Plancque G, Maurice Y, Moulin V, Toulhoat P, Moulin C (2005) Appl Spectr 59:432–441
45. Vercouter T, Amekraz B, Moulin C, Giffaut E, Vitorge P (2005) Inorg Chem 44:7570–7581
46. Moulin C, Charron N, Plancque G, Virelizier H (2000) Appl Spectr 54:843–848
47. Moulin C, Amekraz B, Hubert S, Moulin V (2001) Anal Chim Acta 441:269–279
48. Moulin C, Amekraz B, Colette S, Doizi D, Jacopin C, Lamouroux C, Plancque G (2006) J Alloys Comp 408:1242–1245
49. Lamouroux C, Moulin C, Tabet JC, Jankowski CK (2000) Rapid Comm Mass Spectr 14:1869–1877
50. Veyland A, Dupont L, Pierrard JC, Rimbault J, Aplincourt M, Devoldere L (2000) Inorg Chem Comm 3:600–607
51. Lover T, Henderson W, Bowmaker GA, Seakins JM, Cooney RP (1997) J Mat Chem 7:1553–1558
52. Bergmann T, Martin TP, Schaber H (1989) Rev Sci Instrum 60:347–349
53. Bergmann T, Martin TP, Schaber H (1990) Rev Sci Instrum 61:2592–2600
54. Bergmann T, Goehlich H, Martin TP, Schaber H, Malegiannakis G (1990) Rev Sci Instrum 61:2585–2591
55. Denecke MA, Dardenne K, Marquardt CM (2005) Talanta 65:1008–1014
56. Sayers D, Bunker B (1988) In: Koningsberger DC, Prins R (eds) X-ray absorption: techniques of EXAFS, SEXAFS and XANES. Wiley, New York, pp 211–253
57. Ravel B, Newville M (2006) EXAFS analysis software: ATHENA. Accessed 13 March 2007. http://cars9.uchicago.edu/~ravel/software/aboutathena.html
58. Stern EA, Newville M, Ravel B, Yacoby Y, Haskel D (1995) Physica B 209:117–120
59. Mak C (1967) Can J Chem 46:3491–3497
60. Ankudinov AL, Ravel B, Rehr JJ, Conradson SD (1998) Phys Rev B 58:7565–7576
61. Ankudinov AL, Rehr JJ (1997) Phys Rev B 56:1712–1728
62. Lee P, Citrin P, Eisenberger P, Kincaid B (1981) Rev Mod Phys 53:769–806
63. Kovalenko P, Bagdasarov K (1961) Russ J Inorg Chem 6:272–275
64. Adair J, Denkewicz R, Arriagada F (1987) Ceramic Trans 1:135–145
65. Ekberg C, Kallvenius G, Albinsson Y, Brown PL (2004) J Sol Chem 33:47–79
66. Muha GM, Vaughan PA (1960) J Chem Phys 33:194–199
67. Li P, Chen IW, Pennerhahn JE (1993) Phys Rev B 48:10063–10073
68. Rothe J, Walther C, Denecke MA, Fanghänel T (2004) Inorg Chem 43:4708–4718
69. Conradson SD, Begg BD, Clark DL, den Auwer C, Ding M, Dorhout PK, Espinosa-Faller FJ, Gordon PL, Haire RG, Hess NJ, Hess RF, Keogh DW, Lander GH, Manara D, Morales LA, Neu MP, Paviet-Hartmann P, Rebizant J, Rondinella VV, Runde W, Tait CD, Veirs DK, Villella PM, Wastin F (2005) J Solid State Chem 178:521–535
70. Iribarne J, Thomson B (1976) J Chem Phys 64:2287–2294
71. Zhou SL, Cook KD (2000) Anal Chem 72:963–969
72. Wilm M, Mann M (1996) Anal Chem 68:1–8
73. Wortmann A, Kister-Momotova A, Wilhelm O, Zenobi R (2005) In: ANAKON 05, 15–18 March 2005, Regensburg, Germany
74. Neck V, Kim JI (2001) Radiochim Acta 89:1–16
75. Zhou SL, Edwards AG, Cook KD, Van Berkel GJ (1999) Anal Chem 71:769–776
76. Zhou SL, Prebyl BS, Cook KD (2002) Anal Chem 74:4885–4888
77. Van Berkel GJ, Asano KG, Schnier PD (2001) J Am Soc Mass Spectr 12:853–862
78. Grenthe I, Wanner H, Östhols E (2000) Guidelines for the extrapolation to zero ionic strength (Chemical Thermodynamics Series vol. 2). Elsevier, Amsterdam
79. Metivier H, Guillaumont R (1972) Radiochem Radioanal Lett 10:27–35
80. Baes CF, Mesmer RE (1976) The hydrolysis of cations. Wiley, New York
81. Moriyama H, Sasaki T, Kobayashi T, Takagi I (2005) J Nucl Sci Tech 42:626–635
82. Moriyama H, Sasaki T, Kobayashi T, Takagi I (2006) J Alloys Comp 408:1302–1306
83. Nabivanets B (1962) Russ J Inorg Chem 7:609–611
84. Lister B, McDonald L (1952) J Chem Soc 4315–4330
85. Sasaki T, Kobyashi T, Takagi I, Moriyama H (2006) Radiochim Acta 94:489–494
86. Schindler P, Althau H, Hofer F, Minder W (1965) Helvet Chim Acta 48:1204–1215
87. Schindler P (1967) Adv Chem Ser 67:196–221
88. Sasaki T, Kobayashi T, Takagi I, Moriyama H (2005) In: Actinides 2005—Recent Advances in Actinide Science, 4–8 July 2005, Manchester, UK
89. Ciavatta L (1980) Ann Chim (Rome) 70:551–562
90. Grenthe I, Fuger J, Konings R, Lemire R, Muller A, Nguyen-Trung C, Wanner H (1992) Chemical thermodynamics of uranium (Chemical Thermodynamics Series, vol. 1). OECD/Elsevier, Amsterdam
91. Neck V, Kim J, Seidel B, Marquardt C, Dardenne K, Jensen M, Hauser W (2001) Radiochim Acta 89:439–446
92. Neck V, Kim JI (2000) Radiochim Acta 88:815–822

4 Research and Development on Laser-Induced Breakdown Detection

Throughout the investigations compiled in the present work, laser-induced breakdown detection is the most important technique for colloid characterization. On the one hand, LIBD was used for size and concentration measurement of colloids which form in oversaturated solutions of Th(IV) (Sec. 3.3), Zr(IV) (Sec. 3.5), and Pu(IV) (Sec. 2.2,2.6). On the other hand, in the background but not less important, LIBD served as colloid contamination monitor in virtually all investigations discussed in Chapters 2-4, even if not mentioned explicitly. Formation of polynuclear species must be investigated in an environment extremely clean with respect to crystallization germs which could cause premature precipitation and formation of colloids. This requires the use of thouroughly cleaned containers, quartz cells, and tubing. All chemicals must be 'colloid free' which often requires ultrafiltration or ultracentrifugation. LIBD is the method of choice to decide on success or failure of the separation or cleaning procedures respectively.

LIBD was invented for monitoring the colloid contamination of process liquids in semiconductor industry [Kita88, Kita89b, Fuji92]. The light of a pulsed laser is focused into the sample where it induces a so called 'breakdown' (BD) and ignites a plasma. Within nanoseconds, the plasma is heated to temperatures of $> 20.000\,\mathrm{K}$ and expands rapidly causing a shock wave. This shock wave can easily be detected by an acoustic receiver (piezo detector or microphone). The second detection method makes use of the plasma cooling by emission of radiation. For the first some 100 ns, the plasma emits mainly black body radiation; after that time, the now lower temperature allows recombination of ions and electrons which is accompanied by emission of characteristic atomic line spectra. The emitted light can be imaged on a CCD camera and from the spatial distribution of plasma events, the mean size of the colloids can be obtained. Gated detection of the atomic emission lines allows to map the element composition of the sample.

Plasma ignition is possible in pure liquids as well as in solids, but, and this is the central idea behind LIBD, plasma formation occurs at several orders of magnitude lower power density in solids than in liquids. For LIBD, focus conditions and laser pulse energy are chosen such that no plasma is ignited in pure water, but every time a colloid - which is a tiny piece of bulk solid - enters the focal volume due to Brownian motion, a plasma is ignited. In dilute suspensions at sufficiently low power density, every plamsa (or breakdown) is caused by only one colloid. Hence, LIBD counts colloids one by one. The detection limit of LIBD (see Fig. 16 of [Kim07]) ranges from 10^4 particles/ml for micrometer sized particles to 10^6 particles/ml for 10 nm colloids – the latter corresponding to a mass concentration of only a few ppt (parts per trillion). This weak size dependence of the detection limit is one of the strong points of

LIBD and makes this method superior to most light-scattering based methods which become very insensitive for colloids smaller than one quart of the wavelength of the light they use (see Fig. 2 of [Walt03a]).

For the historical development of LIBD, the reader may refer to the introduction of [Kim07] (Sec. 4.2). Methodological details and basic physical principles of breakdown generation by a pulsed laser are the subject of the following papers: Sec. 4.1 comprises improvements of acoustical LIBD, *i.e.* detection of the shock wave caused by plasma expansion [Sche96]. A detailed model of LIBD including breakdown generation, spatial distribution of plasma events in the laser focus, and the functional description of so called 's-curves' [Sche96] is developed in Sec. 4.2. This model allows to deduce the colloid *size distribution* (not only a mean size) from acoustical LIBD data as presented in Sects. 4.3 and 4.4.

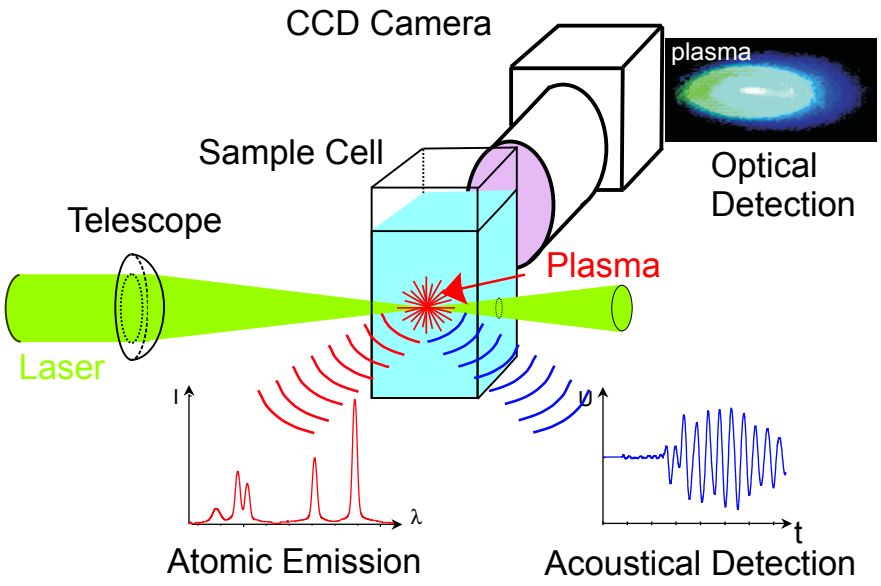

Figure 4.1: Schematic illustration of LIBD detection. The plasma created by a pulsed laser causes an acoustic wave, which is detected by a piezoelectric receiver. Alternatively, the emitted light can be detected by a spectrometer or spatially resolved by a microscope lens and a CCD camera.

4.1 APPARATIVE IMPROVEMENTS OF LIBD

(Summary of [Walt02] - Section 4.5.1)

In order to ignite a plasma by means of a short ($< 10\,\mathrm{ns}$) laser pulse, some few electrons need to be generated by simultaneous absorption of several (m) photons, a process called multi-photon ionization (MPI). This process depends non-linearly (with order m) on the power density (also called irradiance) or photon flux density, respectively, and hence even small deviations from the optimum laser beam profile cause a strong variance in breakdown generation: irregular maxima like 'hot spots' are highly undesirable, all the more if they are not constant in time but fluctuate from pulse to pulse. We hence have built an improved LIBD system applying a diode pumped Nd:YAG laser which generates a good spatial profile (TEM_{00}) and provides excellent pulse to pulse stability. The optics setup was completely redesigned in order to conserve the gaussian profile during all stages of beam manipulation, in particular during pulse energy variation. The manually operated gray wedge used in earlier instruments [Sche96, Knop99, Bund01b] was replaced by a motor driven polarization rotator combined with a Glan polarizer. All optics are aligned interferometrically by use of a counterpropagating HeNe laser beam. Two CCD cameras image the focal region from two directions perpendicular to each other allowing to locate the plasma plume's position within the laser focus in three dimensions. The apparatus combines acoustical detection [Kita88, Kita89b, Sche96] and optical detection [Fuji94, Bund01a]. For the latter, the particle size is appraised from the spatial distribution of the plasma events within the focal region while the laser pulse energy remains constant (details see Sec. 4.3 of [Kim07]). By means of two fast photodiodes, the temporal evolution of the plasma plume can be monitored by observing the obscuration of the late part of the laser pulse due to Thomson scattering [Hamm97, Fran00, Warn02] on the increasingly dense plasma (Fig. 3 of [Walt02]).

Of these three, the acoustical detection is described in more detail in [Walt02]: Increasing the pulse energy of the laser (increasing the power density in the focus) leads to an increasing number of breakdown events per number of laser pulses (BD probability, BDP). A plot of the BDP as a function of pulse energy is called 's-curve' [Sche96] due to its characteristic shape. The threshold[1] of the s-curve [Sche96] correlates with the size of the colloids (Fig. 8 [Walt02]) and the slope of the s-curve is a measure of colloid number density (Fig. 7 [Walt02]). If all colloids of a suspensions have equal size (monomodal suspension), the sample can be well characterized by this method but this simple evaluation is not suited for the characterization of suspensions containing a wide size distribution (multimodal suspension). In this case, the threshold of the s-curve reflects the largest size class which is present in the sample. Just inbetween these extremes is the bimodal suspension which contains colloids of two disjunctive

[1] In the present work, the threshold of the s-curve is defined as the pulse energy where the BDP exceeds 1% following the convention of [Sche96]. Various threshold definitions up to BDP 50%were suggested in literature [Kita89b, Sacc91, Sait99]. The difficulties arising from this somewhat arbitrary approach are discussed and an improved model is presented in the following sections.

sizes. In [Walt02] (Fig. 9), we show for the first time that in a suspension of 100 nm colloids a contribution of $> 1\%$ of 240 nm colloids is well detectable. These findings were used for the real time observation of ZrO_2 colloid aggregation in low concentrations [Bite03b].

The paper [Walt02] illustrates the technique by means of two examples. The first one is the investigation of Th(IV) colloids which was discussed already in Sec. 3.3. The second is the appraisal of colloid content of deep underground waters. Colloids are well known to facilitate transport of pollutants in the aquifer [Kim94], the maybe most sensational examples being the migration of plutonium near a nuclear detonation site in Nevada [Hone99] and the nuclear contamination of large areas around the Mayak reprocessing plant [Novi06]. Within the framework of safety assessment of a repository for the ultimate disposal of spent nuclear fuel in the Swedish Hard Rock Laboratory (HRL) Äspö, in-situ measurements of ground water between 69 m and 416 m below sea level were performed. Since pressure release and air intake may lead to oxidation of Fe(II) to Fe(III) and spontanous formation of iron hydroxide colloids in large concentrations, the samples were measured at the ambient (hydrostatic) pressures up to 33 bar by means of a homebuilt pressure cell. The mobile LIBD apparatus [Haus02] was operated in the s-curve mode in order to cover the full dynamic concentration range from a few ppt up to 1 ppm. This is not possible by fixed-pulse-energy optical-detection.
Surface near waters contain comparably large colloids probably originating from aggregation induced by organics (humic substances) in conjunction with the low salinity of these waters which increases the stability of large colloids against flocculation and precipitation. Though LIBD is less sensitive for organic material than for inorganic colloids, the net effect that inorganic colloids are coated by organics and then aggregate is very well observable and explains the high concentratoin of large colloids measured by LIBD. Deep underground waters in contrast, contain only small colloids of up to 10 nm in rather low concentration. High salinity leads to aggregation and precipitation of larger particles. However, the term 'rather low concentration' needs to be put into perspective: In the following, the total (reactive) surface area of the colloids in the two waters of Fig. 11 of [Walt02] is compared. The surface near water KR0012 contains 0.6 ppm colloids of some 600 nm diameter. For an assumed density $\rho = 1\,\mathrm{g/cm^2}$, this corresponds to a total colloid surface of $A_{tot} = 5.5 \times 10^{-7}\mathrm{m^2}$ per ml water. The deep underground water KA1755 contains some 20 ppt colloids of approximately 10 nm diameter which corresponds to $A_{tot} = 1.2 \times 10^{-8}\mathrm{m^2}$ per ml water. Though the mass concentration of colloids differs by a factor of 30.000, the reactive surface per ml differs only by a factor of < 50. This illustrates vividly that assessment of potential colloid mediated transport requires quantification of in particular the small colloids < 50 nm which are typically present in high numbers [Kim92] and contribute considerably to the reactive surface relevant for colloid mediated transport.

4.2 THE MODEL OF LIBD

(Summary of [Kim07] - Section 4.5.2)

It soon became evident that the pulse energy dependence of the breakdown probability contained more information than just the mean colloid size accessible by the more or less phenomenological correlation of colloid size with the 1%-threshold of the s-curves [Sche96]. In particular, the nearly constant detection efficiency for colloids of the wide size range 10 to 1000 nm should facilitate the measurement of size *distributions*. However, it became just as clear that a more detailed model of LIBD was needed to extract this information. The present chapter is part of the book *Environmental Colloids and Particles: Behaviour, separation and characterisation* edited by J. Lead and K. Wilkinson which adresses analytical and physical chemistry of environmental systems. As such, the chapter is written for the non-specialist and comprises an introduction on the historical development of LIBD, an overview of the different detection mechanisms, followed by a discussion of nine selected applications. In addition, we describe in this chapter (Sec. 3 of [Kim07]) a mathematical model of LIBD which is original work and was not published elsewhere before. This is the reason for including the book chapter as important part of the present work.

The model is based on the mathematical treatment of multi-photon ionization (MPI) in the focus of a gaussian laser beam [Morg75]. The probability for MPI scales strongly nonlinearly with the power density: $p \propto I^m$, and for the case of inorganic colloids, typical electron work functions range from 7-9 eV [Lide95] which requires $m = 4$ photons of a frequency doubled YAG laser ($h\nu = 2.3$ eV). Hence, small changes of the power density cause a strong variation of the MPI efficiency. The total ionization probability is calculated by integrating the product of {MPI cross-section} $\times I(\vec{x})^m \times$ {density of ionizable molecules} over the laser focus. After one first electron is generated by MPI, more are produced by 'inverse Bremsstrahlung'[2]. On theoretical grounds, we could stop at this point. However, in order to be detectable either by the shock wave or by emission of light, the plasma needs to be heated by absorption of a sufficient number of photons, which is only possible if the ignition happens early, within the first nanoseconds of the laserpulse, so that the remaining tail of the pulse can provide the heating. This condition, that the laser pulse must suffice to sustain the avalanche process of electron multiplication and heating, adds to the important threshold behavior of LIBD, often assigned to an irradiance threshold I_t. Combining all considerations above leads to an integral equation which describes the breakdown probability as a function of pulse energy and which is solved numerically.

This model allows to understand the functional pulse energy dependence of the acoustical detection and, moreover, correctly predicts the spatial distribution of plasma events within

[2]Bremsstrahlung denominates electromagnetic radiation produced by a sudden slowing down or deflection of charged particles (especially electrons) passing through matter in the vicinity of the strong electric fields of atomic nuclei. Inverse Bremsstrahlung means the opposite - the acceleration of electrons by an electromagnetic field (here the laser field) in the presence of ions.

the laser focus which is utilized for particle size measurements in the optical LIBD [Bund01a]. A concluding discussion compares the modeled ideal case of a gaussian beam focused by an aberration-free lens with real systems. We show that profound alterations of the beam profile at high pulse energies are due to self focussing effects which is a rather unexpected result since self focussing is mostly known from ps and fs lasers [Berg99]. However, the superposition of several longitudinal modes of a nanosecond TEM_{00} laser causes short spikes of $< 100\,ps$ in the temporal pulse profile [Main77] which can rise to self focussing even for ns pulses [Enge69]. This example underlines that a laser system used for LIBD must most carefully be characterized and controlled. Furthermore, distortions of the power density distribution in the focal region might arise from the use of unfavorable focus conditions. The influence of spherical aberrations is shortly dicussed in (Sec. 4.3 of [Kim07]) paving the way for the more detailed discussion in [Walt06] and Sec. 4.4 of the present work.

4.3 MEASUREMENT OF MULTIMODAL COLLOID SUSPENSIONS WITH LIBD

(Summary of [Walt04] - Section 4.5.3)

This paper describes the first successful measurements of particle size distributions (PSD) by a stand alone LIBD machine. By using LIBD as detector following flow field fractionation (FFF) [Than00, Boub01, Boub04], PSDs were measured before, but due to the high dilution factor of FFF, this combination is some three orders of magnitude less sensitive than LIBD alone and, moreover, FFF is very critical with respect to introducing colloidal contaminations.

The development of the new data evaluation algorithm required two tasks: (1) finding a substitute for the 1% threshold as a measure of colloid size and (2) modeling the superposition of s-curves which correspond to different colloid sizes. That it is not a sound concept to derive the colloid diameter from the pulse energy (or irradience respectively) where the s-curves exceed a certain BDP, *e.g* 1% is easy to understand by means of an example. When a colloid suspension of concentration C whose s-curve has the BDP=1% at pulse energy E_o is diluted 100 fold the BDP decreases by the same factor, so that the dilute suspension has only BDP=10^{-4} at E_o. The 1 % threshold is reached only for higher pulse energy. However, the colloid size of course did not change.

Since the efficiency of MPI scales with the fourth power of the irradience (power density, I^4) [Kim07] at $h\nu = 2.3\,eV$ for most solids, the same dependence of the breakdown probability on the pulse energy is expected (BDP$\propto E_o^4$) provided the pulse energy suffices to sustain the inverse Bremsstrahlung avalanche. Since the BDP cannot exceed '1', the E_o^4 functionality can only be valid for BDP$\ll 1$ and must evolve continuously into a function which asymptotically

approaches unity. As proven easily by Taylor expansion at $E_o = E_t + \delta$,

$$\begin{aligned} p(E_0) &= 1 - \Big\{(1 + C(E_0 - E_t) + \frac{1}{2}\big(C(E_0 - E_t)\big)^2 \\ &+ \frac{1}{6}\big(C(E_0 - E_t)\big)^3\Big\} \cdot \exp[-C(E_0 - E_t)] \end{aligned} \tag{4.1}$$

is such a function. E_t is the measure of colloid size and substitutes the 1 % breakdown threshold. C parametrizes the particle number density and is obtained from calibration with reference colloids.

We will now approach problem (2), the s-curve superposition: In a bimodal suspension (sizes A and B), a breakdown can be either due to the presence of a colloid of size A or of one of size B. Having no breakdown means neither a colloid of A nor a colloid of B was in the focal volume: $p(\text{noBD}) = (1 - p_A) \times (1 - p_B)$. The probability of no breakdown is one minus the probability of having a breakdown and we get $p_{Bi} = 1 - p(\text{noBD}) = 1 - (1 - p_A) \times (1 - p_B)$ which is the s-curve of the bimodal distribution. This summation of inverse probabilities is valid for an arbitrary number of colloid sizes. In practice, however, the number of size classes is limited by the statistics of the recorded s-curve and by the availability of reference colloids for calibration. In [Walt04], six size classes between $d = 20\,\text{nm}$ and $100\,\text{nm}$ are defined.

The feasibility of the method was demonstrated by mixing colloids of 20, 50 and 100 nm. The concentrations of all three sizes are well reproduced (Fig. 1 of [Walt04]) and the trimodal character of the suspension is very clear. This is not self-evident. It is a common phenomenon for single particle analytical techniques to produce so called phantoms, *i.e.* signals in size classes which should be empty (discussion in [Rose03]). LIBD does not suffer from this limitation.

Since the innovation of multimodal size measurement by LIBD does not concern hardware, but rather the *evaluation* of s-curve data, existing LIBD machines can be upgraded simply by using the new data evaluation. Moreover, even old data might be reevaluated, provided the data was sampled with sufficient statistics and a reliable calibration is available.

4.4 EXTENDING THE SIZE RANGE OF LIBD

(Summary of [Walt06] - Section 4.5.4)

The fitting routine described in the previuos section (4.3) allows to measure the PSD from 20 to 100 nm. Though being an improvement over measuring only a mean size, a method which covers not even one decade in colloid diameter is not appropriate for the investigation of natural waters whose PSD often ranges from a few nm to many microns. Now, the simple attempt to add more size classes for colloids larger than 100 nm by using Eq. 4.1 failed. Doing

so resulted in a significant underestimation of the lower size classes within a distribution. The reason is that the functional form of the s-curve changes from very small to large colloids: For pulse energies just above the respective threshold E_t of a given colloid size, the irradiance threshold I_t for breakdown ignition is exceeded only close to the central region of the focus where the intensity is highest. With increasing total pulse energy, this 'effective focal volume' increases and breakdown events appear in the outer parts of the focus region. Since I_t decreases for increasing colloid size, this growth effect is much more pronounced for large size fractions which leads to an increasing ignition length [Bund01a] for increasing colloid size (Sec. 4.3 of [Kim07]). The focal volume does not grow linearly with increasing pulse energy but shows a bend where its slope changes from $\mathrm{d}V/\mathrm{d}E_o = 4$ to a smaller value, depending on beam characteristics and focus conditions. For a gaussian beam focused by an aberration-free spherical lens, this second slope is 3/2 [Cerv75, Morg75]. This bend reappears in the s-curve, since the s-curve depends on the probability for MPI and the latter is proportional to the effective focal volume (Sec. 3.3 of [Kim07]).

These relations are illustrated in Fig. 1 of [Walt06] for the case of the diode pumped Nd:YAG laser of our setup [Walt02]. The power density distribution (isophotes) in the focus is calculated by numerical integration of the Huygens-Fresnel-Kirchhoff equation [Evan69, Born99] taking into account the gaussian intensity distribution of the laser beam *and* the aberrations caused by the telescope (two spherical lenses). The latter causes a pronounced asymmetry. Destructive interference of different parts of the beam cause Airy rings upstream (facing the laser) while the right part (downstream) resembles the ideal case of an aberration-free lens. This isophote plot is compared to the spatial distribution of breakdown events recorded by the CCD cameras for different pulse energies. At low E_o, all events are restricted to the central region but for increasing pulse energy, the distribution extends to the wings of the profile and resembles the asymmetric contour of the isophotes very well.

Fig. 4.2 compares the isophote contours for three types of LIBD systems which differ in intensity distribution of the laser beam, beam diameter, focusing lens (planoconvex *vs.* biconvex, diameter and focal length): Part (a) models the systems of [Knop99] and [Bund01a, Bund01c, Bund04, Bund05], part (b) the systems of [Haus02, Haus03, Mori03, Boub04], part (c) the laser of the present work [Walt02] focused by a single lens instead of a telescope and part (d) the ideal case. The flat top profiles of (a) and (b) differ considerably from the $\mathrm{TEM_{oo}}$ beams (c) and (d) and lead to different focal-volume growth functions (inlays). However, it is quite obvious that the approximation of any of the three real systems by the ideal case (d) leads to significant deviations.

In the present work, the s-curves for large colloids ($> 70\,\mathrm{nm}$) were fitted by a functional (Eq. 4 of [Walt06]) which includes the bend of the focal volume growth function (Fig. 3 of [Walt06]). The contributions of smaller colloids are well described by the simplified function (4.1) introduced in [Walt04]. The improved routine now comprises eight size classes which

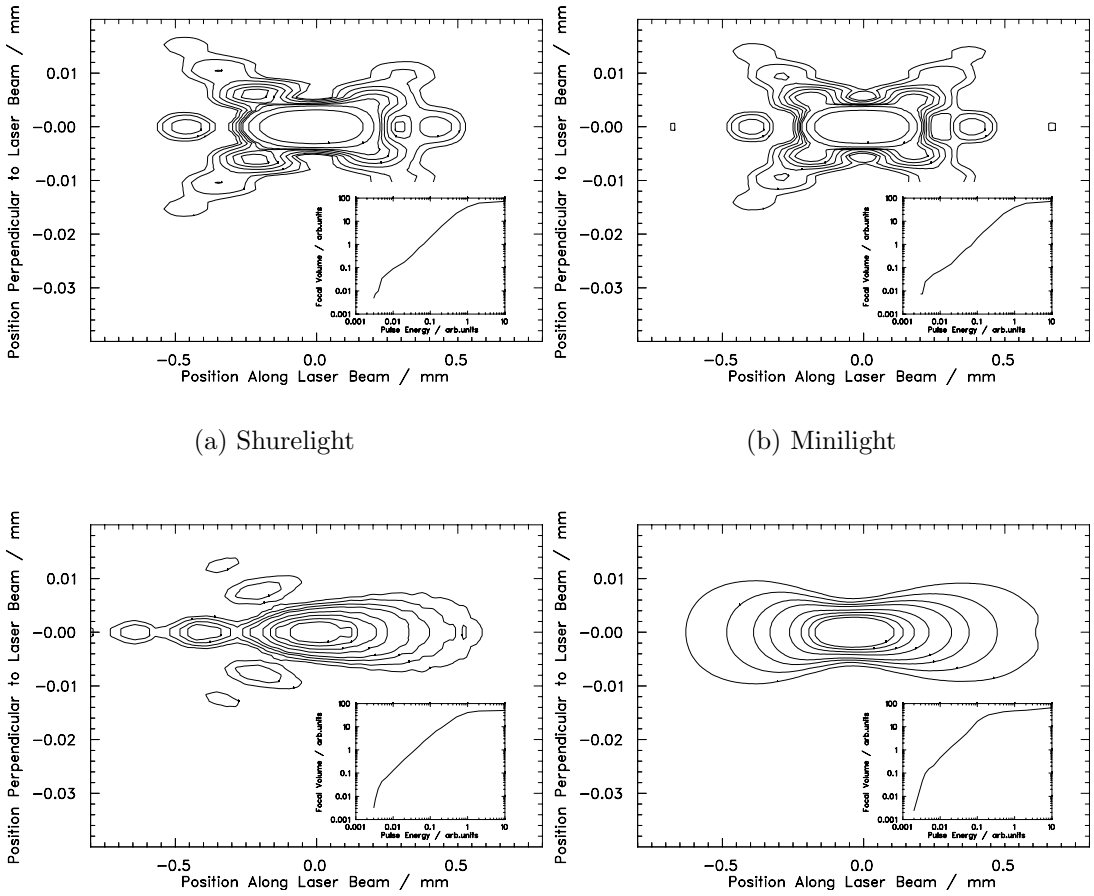

(a) Shurelight

(b) Minilight

(c) Diva

(d) Aberration-free Gaussian

Figure 4.2: Regions of equal power density I (isophotes) for the typical beam profile of different lasers. (a) Continuum Shurlight SL I-20 (similar to flat top, beam diameter 7 mm) focused by a plano-convex spherical lense (f=+60 mm, diameter 25 mm). (b) Continuum Minilight (similar to flat top, beam diameter 1 mm) focused by a bi-convex spherical lense (f=+8 mm, diameter 6 mm) (c) BMI Diva (beam diameter 8mm after beam expansion) focused by a 50 mm biconvex lens (d) gaussian beam focused aberration-free.

span the range from 15 nm to 400 nm plus one background function which accounts for larger particles.

For natural surface waters, however, even this extended operative size range is not sufficient. Considerable fractions of micrometer sized particles would remain undetected or even cause alterations of the LIBD measurement due to light scattering. Hence, in [Walt06], LIBD was combined with a single particle counter [Knol92, Degu01, Ross03]. For colloids < 200 nm,

this technique suffers from the usual restrictions applying for light scattering but for particles $> 200\,\text{nm}$, this ultrasensitive detector (LOD of ≈ 1 particle/ml) complements LIBD perfectly. First promising results on waters of the Pfinz channel (Karlsruhe) and Lake Brienz (Switzerland) show that a continuous detection of colloids from 15 nm to $> 2\,\mu\text{m}$ is feasible.
With this combination, we were able to show for the first time experimentally that Pareto's law (see p. 81) is valid down to 15 nm which was discussed controversely in the literature. Of course, a more comprehensive mapping of a greater variety of surface waters is needed to contribute to this discussion. The combination of LIBD and SPC has already been applied for the size measurements of Zr(IV) colloids formed in oversaturated solutions (Fig. 3.4) and size dispersion of colloids which travel through a synthetic column [Delo07]. Similar future applications are quite conceivable. Mobile versions of SPC as well as LIBD are available and both were successfully used in field campaigns which opens up the perspective of using this combination for future *in situ* projects such as investigations on colloid mediated transport and field studies of colloid size dispersion effects.

4.5 PUBLICATIONS

4.5.1 Laser-induced breakdown detection for the assessment of colloid mediated radionuclide migration [Walt02]

ELSEVIER

Nuclear Instruments and Methods in Physics Research B 195 (2002) 374–388

NIM B
Beam Interactions with Materials & Atoms

www.elsevier.com/locate/nimb

Laser induced breakdown detection for the assessment of colloid mediated radionuclide migration

C. Walther *, C. Bitea, W. Hauser, J.I. Kim, F.J. Scherbaum

Institut für Nukleare Entsorgung, Forschungszentrum Karlsruhe, Postfach 3640, D-76021 Karlsruhe, Germany

Received 12 February 2002; received in revised form 25 March 2002

Abstract

Colloids play an important role in the transport of pollutants in the environment. Harmful substances can undergo transport over large distances if bound to colloids in aqueous surrounding. One important example is the migration of Pu(IV) at unexpectedly high rates over several miles at a Nevada nuclear detonation test site. For long term safety assessments of radioactive waste repositories, it is hence crucial to know about the amount, size distribution and chemical composition of colloids in the ground water. Standard methods (e.g. light scattering) can be applied for high concentrations and large sizes of particles. Colloids smaller than 50 nm, however, are detected with very low efficiency. Laser induced breakdown detection (LIBD) can fill this gap. A new instrumentation is presented, which as compared to previous instruments, opens up a much wider operational dynamic range, now covering three orders of magnitude in size (5–1000 nm) and seven orders of magnitude in particle concentration (1 ppt – several ppm). The technique is based on plasma formation on colloidal particles inside the focus of a pulsed laser. The plasma plume is detected by three-dimensional optical observations and by means of its shock wave with a piezo-detector. For mathematical modelling, detailed knowledge on the photon fluence distribution in the focal region is indispensable. For the first time a true Gaussian TEM00 mode has been achieved in the focus of a LIBD apparatus and great care has been taken to guarantee long-term stability of the optical parameters. Automated control of the laser pulse energy and beam shape is introduced to allow routine reproducible measurement. The apparatus combines acoustic detection with three-dimensional optical monitoring of the focal region with two CCD cameras placed perpendicular to each other in order to gain additional size information. The breakdown events are systematically characterized with respect to the number density and size of aquatic colloids as a function of the laser pulse energy. Whereas the threshold energy (irradiance) only depends on the colloid size, the breakdown probability at higher pulse energies is a direct function of the number density of colloids. A correlation of the two facts allows the speciation of the colloidal size distribution.

1. Introduction

Aquatic colloids are of common interest to many different research fields. While their presence is undesired in clean process liquids e.g. for semiconductor manufacturing or for the primary coolant of nuclear power plants [1], they are

* Corresponding author. Tel.: +49-7247-826064; fax: +49-7247-82-3927.
E-mail address: walther@ine.fzk.de (C. Walther).

0168-583X/02/$ - see front matter © 2002 Elsevier Science B.V. All rights reserved.
PII: S0168-583X(02)01128-X

conveniently used for the design of 'new materials' [2] and also of catalysts [3]. In our case, working on the assessment of nuclear waste disposal, the center of interest is to appraise how aquatic colloids appear to play a carrier role for the migration of radionuclides in a given aquifer [4]. The risk of radionuclide migration into the environment has to be evaluated on time scales of the order of 100 000 years. Container materials cannot be expected to withstand corrosion for these time periods and eventually, radionuclide retention in the surrounding geological formation becomes an integral component of a multi-barrier safety system. However, in recent years plutonium was found to migrate fast over kilometer-distances in the aquifer near a Nevada nuclear detonation site [5] and this unexpected effect was attributed to colloid mediated transport. Aquatic colloids of organic or inorganic composition originating from mobilization of preformed colloid-sized materials or in situ precipitation of supersaturated mineral phases are omnipresent in natural groundwaters [6]. Obeying Pareto's power law, particle number density increases strongly as the size decreases ($\propto D^{-5}$) and natural ground waters may contain up to 10^{15} particles per liter below 50 nm [7]. They may form pseudocolloids by uptake of actinide ions and due to their large number may act as a very efficient carrier in the groundwater. But even a groundwater poor in natural colloids does not circumvent this problem entirely, because the tetravalent actinides are known to form stable eigencolloids by aggregation of the hydrolyzed species [8–10]. Destabilizing conditions lead to the formation of large aggregates and finally to immobile precipitates. If, however, only very small (<100 nm) colloids are formed, they remain suspended and migration is strongly enhanced [11]. Detailed knowledge on formation mechanisms and stability of the colloidal phase is hence of cardinal importance and the investigation of long term stability as a function of colloid concentration and geochemical parameters is a prerequisite for the assessment of actinide migration.

Such aquatic colloids are to be characterized without perturbation, since they are sensitive to change by elaborated handling. As they are small in size and low in concentration, conventional light scattering methods, e.g. photon correlation spectroscopy, are not capable of characterizing their size distribution and number density. Other methods, like scanning (SEM) or transmission (TEM) electron microscopy or field flow fractionation, perturb the initial state of aquatic colloids in the characterization procedure. Atom force microscopy is a non-decomposing method but requires a relatively concentrated colloid suspension, which means that a condensation of sample is necessary for the colloid characterization.

The method based on laser induced breakdown detection (LIBD) with its photo-acoustic [12,13] and optical detection [14] provides the possibility of characterizing aquatic colloids without perturbation. For LIBD, so far, dye lasers or flashlamp pumped Nd:YAG lasers were used, suffering from an ill defined spatial beam profile in the focal region (photon fluence distribution). Plasma detection was achieved by one CCD camera, using the dependence of the effective focal volume on particle size as the principal characterizing quantity. Laser induced plasma formation originates in non-resonant multi-photon ionization of matter, which is a highly non-linear process. Hence, LIBD is very sensitive to 'hot spots' and local deviations of the beam profile and a smooth, undisturbed spatial distribution of photon fluence is required. To compare particle suspensions of different elementary composition, mathematical simulations are applied, which call for a well defined photon flux dependence as input parameter. For the sake of simplicity and saving of computing time (to reduce the number of differential equations to be solved numerically) a simple parametrization of the flux density (i.e. a Gaussian) is very desirable. In the present work, a diode pumped Nd:YAG laser of single transversal mode (TEM00) serves as light source of a very good (>99%) Gaussian beam. Care was taken to preserve the profile during all stages of pulse-energy and beam-manipulation. Stability and reproducibility of the instrumentation is strongly enhanced by on-line monitoring of the beam shape in front of and behind the focal region. Knife edge measurements at different positions along the optical axis in the focus proved the beam to be diffraction limited ($M^2 <$ 1.1). In addition to the acoustical detection of the

breakdown events, the plasma plumes are observed by two CCD cameras perpendicular to each other resulting in a three-dimensional spatial distribution. Ambiguities of the so far standard observation of a two-dimensional projection onto a single camera are now avoided. Whereas the '2D-optical-detection' method is restricted to a dynamic range of ~100 in particle concentration for a given set of laser parameters, the instrumentation described here is capable of covering almost seven orders of magnitude without need for calibration.

After a detailed discussion of the experimental method two typical applications are presented: As mentioned above, migration of radionuclides, particularly of the tetravalent actinides, is strongly enhanced by either formation of eigencolloids or by sorption onto small suspended particles, omnipresent in groundwaters. Exemplary for the investigation of eigencolloids, the formation of thoriumhydroxide- and thoriumdioxide-particles in oversaturated Th(IV) solutions is discussed [15,16]. The second aspect, the characterization of natural colloids in groundwaters, is illuminated by means of experiments at the Swedish Äspö underground hard rock laboratory. This project is especially challenging due to strong variation of colloid content from a few ppt to well above 1 ppm and the requirement of in situ measurements, since the high pressure of the waters (up to 30 bar) had to be maintained in order to avoid precipitation of solvated species [17].

2. The breakdown process

The breakdown process has been described in detail before [18,19] and will be revisited briefly. When a pulsed laser is focused tightly into a medium and a certain pulse energy threshold is exceeded, a so called breakdown occurs. In the beginning at least one atom is ionized by multi-photon ionization (MPI), resulting in a seed electron which is accelerated by inverse bremsstrahlung in the high electric field of the laser pulse. After gaining sufficient energy additional atoms are ionized by collisions, multiplying the number of electrons. Hence, the density of free charge carriers increases in avalanche after a few consecutive iterations and a plasma is created. The threshold of this process depends on the phase of the matter in the focal region. The threshold irradiance is highest for the gas phase, lower for liquids and lowest for bulk matter. This is made use of for particle detection: the pulse energy is adjusted such that no breakdown occurs in pure water. Whenever a colloid enters the focal region, the threshold for the solid phase applies (which is exceeded) and a plasma is ignited. By counting the number of breakdown events relative to a predefined number of laser shots (breakdown probability), the particle number density in the sample can be evaluated.

Size information is gained by varying the laser pulse energy P_0: the creation of the first electron is of statistical nature, and consequently its probability depends on the number of ionizable electrons in the particle. More precisely, this depends on the number of electrons in a valence band or, if the bond character of constituents within the particle does not permit delocalization of electrons, this depends then on the number of outer shell electrons in the individual atoms or molecules involved. If there are N of these electrons, each having an MPI-cross section σ, the probability to excite one of them to an unbound state amounts to

$$P_{\mathrm{BD}} = N \int_0^{\Delta t} \int_{-\infty}^{\infty} \sigma(\Phi(t,\vec{x}))^n \,\mathrm{d}^3x\,\mathrm{d}t + \mathcal{O}(\sigma\Phi^n)^2, \tag{1}$$

$\Phi(t,\vec{x})$ being the photon flux density (time and space dependent), n the number of photons necessary to overcome the binding energy of an electron and Δt the laser pulse duration. σ is determined from MPI experiments in vacuum [20] or estimated using the Keldysh approach [21]. Neglecting electron loss processes as a first crude estimate, one can assume that the creation of every seed electron leads to a plasma formation. Due to the linear dependency on N, it is obvious that breakdown creation by a small particle requires a considerable higher pulse energy P_0 than by a larger one. For a single laser pulse starting at $t = 0$, P_0 and Φ are related by

$$P_0 = h\nu \int_0^\infty \int_{-\infty}^\infty \Phi(t,\vec{x})\,\mathrm{d}^3x\,\mathrm{d}t, \tag{2}$$

h is Planck's constant and ν the frequency of the light. Typical ionization energies of solids are $6\ \mathrm{eV} < E_\mathrm{I} < 10\ \mathrm{eV}$, hence n being 3–5 for visible light. This strong flux dependency (Φ^n) has important consequences. The photon flux density distribution in the focal region has to be reproducible and its characterization has to be very precise. Ideally one would like to work with a constant flux density confined to a well defined region of space, dropping to zero sharply outside. Unfortunately this is not possible to achieve by conventional optics. Even if one starts with a 'flat top' laser beam, it separates into Gaussian 'eigenmodes', when focused resulting in airy rings accompanying the central spot. Second best is a profile, the shape of which is conserved when focused by an ideal lens, because the time consuming characterization of the laser beam inside the focus can be substituted by easy measurements in front of and behind the cell. This is fulfilled by the Gaussian shaped TEM00 mode of a laser. Hence, special care is taken during the design of the described apparatus both to achieve such an intensity distribution and to conserve it during all stages of beam manipulation.

3. Optical setup

The setup of the optics system is shown in Fig. 1. In addition to the kernel – the focussing optics and the quartz cell containing the sample – there are various beam manipulation and detection units which are described in detail in the following in the order of beam travel. All optics are laser grade $\lambda/10$ surface roughness, unless specified otherwise.

A diode pumped Nd:YAG laser (BMI-Soliton DIVA II) is used as a light source, which provides a laser beam of 1 mm diameter and 0.5 mrad divergence. Pulses of 7 ns (FWHM) and up to 10 mJ at 532 nm are emitted at a repetition rate of 20 Hz. Besides the small dimension ($35 \times 17 \times 8$ cm) and low maintenance requirement (no flashlamp change, air cooled), the single transversal mode profile (TEM 00) was an important criterion to

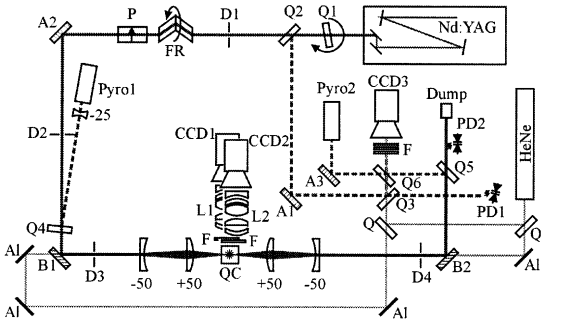

Fig. 1. Setup of the LIBD apparatus. The plasma is ignited inside the quartz cell (QC) containing the sample and observed by cameras CCD1 and CCD2. Details see text.

choose this model. Housing and optical mounts had to be modified considerably in order to improve the poor mechanical and thermal stability of the laser. However, due to the Z-design, a system inherent temperature drift cannot be avoided: the YAG rod serves as a mirror at one end and when it elongates due to heating, the laser beam shifts horizontally perpendicular to its propagation while the pointing direction is conserved. This effect is compensated for by passing the beam through a quartz plate (Q1; thickness 5 mm) which is tilted by a small angle ($\pm 5°$) relative to the beam and hence creates a parallel shift. The rotation is performed by a stepper motor (Newport SR50CC) controlled and programmed from the master PC (see Section 6). Some 5% of the beam is separated by a quartz wedge (Q2) and guided into a CCD camera for profile diagnostics (described in detail in Section 4) via mirror A1 (HR532) and quartz-plate Q3 (dashed line Fig. 1). The beam passes a diaphragm (D1) to avoid reflexes of the following optics, which can be backscattered into the laser.

The following two elements serve as pulse energy control. It is not advisable to tune the pulse energy by varying the diode current or the Q-switch delay, because pulse to pulse jitter of the laser is lowest and the beam profile is best when operated at maximum power ($\approx 2\%$). Therefore, the following external option was preferred. The initial horizontal polarization of the laser beam is rotated by a Fresnel rhomb (Fig. 1 FR) (the polarization rotation amounts to twice the angle of the Fresnel

rhomb relative to the incoming polarization plane). The resulting vertical component is separated by a Glan–Thompson polarizer (Fig. 1 P) and guided into a beam dump, while only the remaining horizontal component is transmitted. By varying the angle of the rhomb, the power passing through the polarizer is then controlled. This rotation also is performed and PC-controlled by a stepper motor (details see Section 6).

After 90°deflection by a HR 532 nm dielectric mirror (A2), the beam passes a second diaphragm (Fig. 1 D2) and some 2% of the light is deflected at 10° by a parallel quartz plate (Q4) into a pyroelectric detector (Pyro1, Newport 818J). At small angles, reflection is independent of the plane of polarization and allows to perform experiments with light of arbitrary polarization. Prior to entering the detector, the beam is expanded by a $f = -25$ mm fused silica lens in order to avoid damage of the delicate absorber surface by excessive power densities.

A dicroic mirror (B1: HR532, HT633) deflects the main beam by 90° through two diaphragms (D3 and D4) which define the principal axis of the experiment. In the center between these diaphragms a quartz cell containing the particle suspension is located. Beam focusing is achieved by a gallilean telescope of aspherical lenses: by a $f = -50$ mm planoconcave lens the beam is expanded by a factor of 3 and 100 mm behind collimated by a $f = +50$ mm planoconvex lens, resulting in an effective focal length of some 80 mm. All lenses can be translated and tilted along both axis perpendicular to the laser beam. Behind the cell the beam is collimated again by an exactly symmetric setup, deflected by 90° (mirror B2: HR532, HT633) and guided into a beam dump.

By use of quartz plates Q5 and Q6, 0.025% of the light enters the camera CCD3 for beam diagnostics. If necessary, the light can be further attenuated by neutral density filters (F). The light transmitted by plate Q6 is reflected via mirror A3 into a second pyroelectric detector (Pyro2, same model as Pyro1). The temporal pulse shape is measured by two photodiodes (Hamamatsu G4176) behind Q3 to characterize the pulse before entering the quartz cell and behind Q5 after passing the plasma region.

Along the principal axis the counter propagating light of a HeNe laser is superimposed on the Nd:YAG beam, guided by four aluminium coated mirrors (Al) and monitored by CCD3 before and after passing the quartz cell in analogy to the YAG beam. Its good spatial coherence is used to align the lenses exactly on axis and parallel to each other by observing interference fringes, which is not possible with the Nd:YAG. [1] In addition misalignments of the lenses (tilting or off axis positioning) can be detected on line during operation, due to the distortions of the far-field laser-profile they cause.

4. Characterization of the laser focal area

Within the focal region the beam diameter is too small to be observed directly by a CCD camera. On the other hand one can not rely solely on calculations assuming diffraction limited focusing conditions, because the (non-ideal) lenses cause aberrations of various kinds and also the laser beam might not be exactly diffraction limited. Therefore, the focus was characterized by use of the 'knife edge method'. A razor edge was guided through the beam along both directions (x- and y-axis) perpendicular to its direction of propagation (z) and the transmitted energy fraction was measured as a function of position. A model-curve assuming the shadowing of a spherical two-dimensional Gaussian by a square obstacle blocking its lower part was fitted to the data. From this fit the $1/e$ radius $r(z)$ was gained and by performing this measurement at various positions along the propagation (z-)axis, the beam waist was characterized. Comparison with the analytical expression for diffraction limited focussing

$$r(z) = r(0)\sqrt{1 + \left[\frac{z\lambda}{\pi r^2(0)n}\right]^2} \tag{3}$$

yields a focal diameter ($1/e$) of $r(0) = 5.0(1)$ μm (Fig. 2 solid line). n is the refractive index of the

[1] Due to its many longitudinal modes the coherence length is limited to some 30 cm.

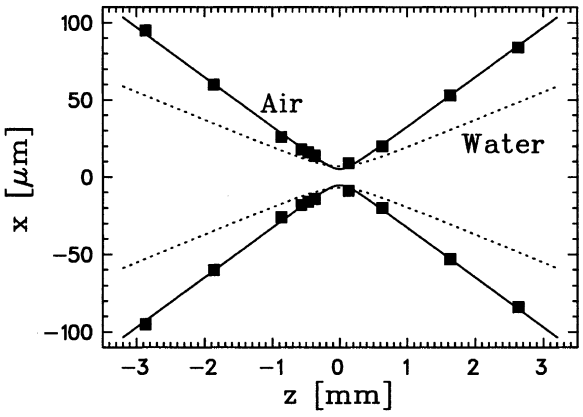

Fig. 2. The power contained in the laser beam near the focus is measured by guiding a razor edge through the beam along an axis (x) perpendicular to its propagation direction (z) at various positions z ('knife edge' technique). The solid line represents a fit of Eq. (3) to the data (in air), the dashed line shows the extrapolation to water as surrounding medium.

medium at wavelength λ. While the knife edge measurements were performed in air ($n = 1$), colloid detection takes place in water ($n = 1.336$ at 532 nm). Hence, the beam waist was further calculated for water (dotted line), which then yields a focal diameter of $r_W(0) = 6.7$ μm. Due to the good agreement of the measured data with diffraction limited focussing theory, constant conditions in front of the focussing telescope ensure a well defined focus quality. As mentioned above, the beam qualities of the two laser systems are observed for all stages of experiment in the near-field as well as in the far-field and all four profiles can be displayed simultaneously on the CCD array. The camera signal is read out and evaluated by commercial profiler software (Polytech, Spiricon), which allows extensive calculations and fitting routines. Typically a two-dimensional Gaussian is fitted to the data and the quality of the fit taken as a measure of the beam quality. Both near field profiles reflect the working conditions of each laser system. While the HeNe laser operates very reliable, the Nd:YAG laser has to be controlled frequently during the experiment due to the temperature dependent displacement of the beam as described above. In addition the profile tends to elongate and approaches an elliptical shape at room temperature exceeding 25 °C. Such an effect can only be obviated by air conditioning of the laboratory.

5. Detection of the plasma

A plasma ignition causes different observable signals which can be conveniently used for detection. Three of them are made use of here. The first is the shock wave caused by the thermal plasma expansion, which usually creates a strong sound audible even by the human ear and can easily be detected by a piezo crystal [13] attached to a quartz cell perpendicular to the laser beam [19] (Fig. 5, PZ). The second is represented by the gas bubbles created in consequence of the thermal expansion, which can be visualized by shining an additional light source through the breakdown area and displaying the shadow of the bubble [22]. Because in the case of plasmas created by ns-pulses only gross information is contained here, the gas bubble effect is not used for routine measurements. However, it was investigated in detail to characterize the plasma [23]. The third is the shadowing of the late part of the laser pulse by the plasma itself, that contains useful information. A plasma of electron density n_e is translucent for light above the critical (plasma) frequency

$$\nu_C = \frac{1}{2\pi}\sqrt{\frac{n_e e^2}{m_e \epsilon_0}}, \tag{4}$$

where e and m_e denote the electron charge and mass, respectively and ϵ_0 is the dielectric constant. Due to light scattering the opacity increases for the light of lower frequency and in consequence the more electrons are created by the laser pulse the lower becomes the percentage of transmitted light. By comparing the temporal pulse shape in front of and behind the quartz cell, as recorded by two photodiodes(Fig. 1 PD1, PD2) this shadowing can be observed directly (Fig. 3). During the first few ns of the laser pulse no significant extinction of light takes place. When the plasma has evolved to higher electron density, scattering weakens the light transmission and the integral of the difference between both curves (hatched area) is a measure of the total extinction. As shown by François and

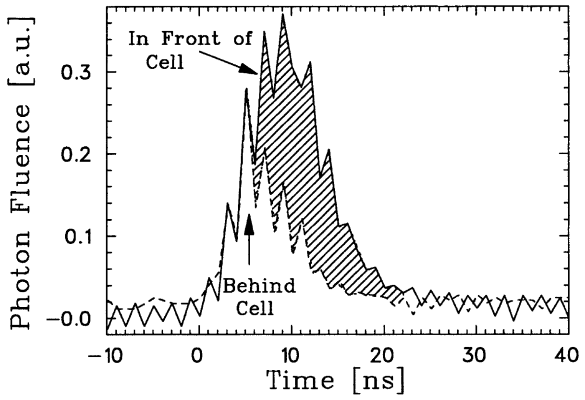

Fig. 3. Shadowing of the laser pulse due to scattering of the incoming laser beam at the plasma electrons. Details see text.

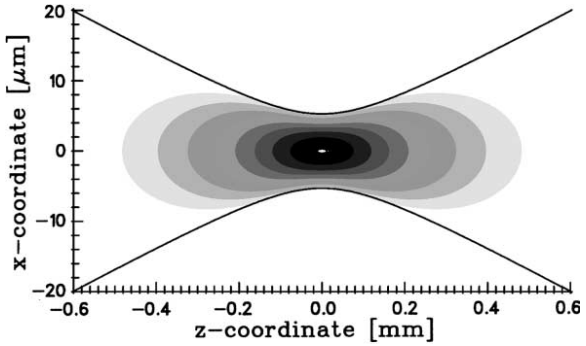

Fig. 4. Blow-up of the central region of Fig. 2. The gray contour scales indicate a two-dimensional cut through the three-dimensional double-club like photon flux density distribution (flux density increases from light to dark).

coworkers [24], such an 'induced optical density' contains information on size and chemical composition of colloids.

Additionally, the light emitted from the plasma is observed. Strong black body emission is superimposed by discrete emission lines of ionic and atomic energy levels. Information on the elementary composition of particles can be gained by analyzing the corresponding spectra. As was shown by Yun and coworkers, the discrete emission stems exclusively from the particle. The emission of hydrated metal ions of the same kind as in the colloids, is strongly suppressed and does not contribute to the spectra, even at concentrations exceeding the particle concentration by three orders of magnitude [25].

Of equal importance is the observation of the exact spatial position of each breakdown event within the focal volume [14] The photon flux resembles a double club with cylindrical symmetry. Fig. 4 shows a section through the three-dimensional distribution along a plane containing the laser beam axis. Dark contours correspond to high flux densities. The colloids of interest in natural water typically are <50 nm in diameter, while the focal region has a diffraction limited diameter of ≈ 13 μm and a length of some 2 mm (Section 4). In the case of translucent particles, there is little linear absorption inside the particle and the photon flux density is spatially constant, i.e. the 'front' of the particle facing the laser beam encounters the same flux as the 'backward' half. It is then a good approximation that the flux density is determined exclusively by the position within the laser focus. In the previous setups, the plasma plume is observed perpendicular to the beam axis with a microscope lens and a CCD camera [15,26]. Because only a two-dimensional projection of the three-dimensional focal region can be displayed, the assignment of a breakdown event to a certain flux density is ambiguous [14]. In the present experiment the plume is observed by two cameras from directions perpendicular to each other, both being at right angle to the laser beam axis (Fig. 5). The camera CCD1 (Pulnix 1040, 30 Hz, 10 bit, b/w, progressive scan) records a picture of the plume from the bottom of the quartz cell. The light is 90° deflected by a penta prism (PB) and magnified four

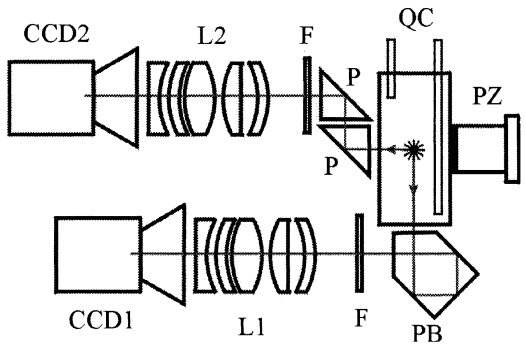

Fig. 5. The plasma plume is observed by two CCD cameras perpendicular to each other. Hence, the position of the plasma plume relative to the laser focus can be determined in three dimensions.

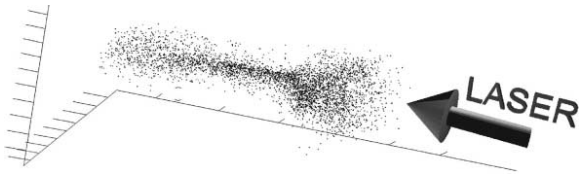

Fig. 6. Three-dimensional distribution of breakdown events. Each dot represents the center of mass of a plasma plume.

times by a microscope lens (Rodenstock, ZO 08-4) after 532 nm stray-light is suppressed by six orders of magnitude by a holographic filter (F). A second camera (CCD2) receives the light emitted in the horizontal plane via an identical setup. Because the two cameras are mounted on top of each other, the beam had to be shifted upward 6 cm, which is achieved by using two fused silica 90° prisms (P), instead of the penta prism in the light path.

Fig. 6 shows experimental data taken with polystyrene particles of 1000 nm diameter (500 ppb) at a breakdown probability of some 30%. The laser light enters the focal region from the right. Every dot corresponds to the 'center of mass' (i.e. center of luminosity) of a single plasma plume and 4000 events are displayed. The distribution reflects very well the flux density plotted in Fig. 4 and exhibits a good rotational symmetry confirming the assumption of a three-dimensional Gaussian profile in the focus. [2] However, a slight anisotropy is observed: the number of events in the right club facing the incoming laser beam exceeds the corresponding number in the opposite direction by almost a factor of two. This is due to light scattering weakening the flux density 'downstream' the laser and becomes significant for particles larger than 100 nm. A crude estimate can be given as follows: linear absorption measurements of the high concentrated sample used here show an extinction of $\rho = 30\%$ of the (unfocussed) laser beam passing the whole quartz cell. Considering the Φ^n, $n = 4$ dependency discussed in Section 2, a weakening of $w = (1 - \rho/2)^n = 0.5$ is expected, which agrees well with the experimental observation. When the length of the club is used for the determination of particle size [26], either a very dilute suspension has to be used, where scattering can be neglected, or just the right club has to be used for evaluation, which contains the full information due to symmetry arguments.

[2] This method also provides a powerful tool to measure the photon flux distribution of a small laser spot directly in the focal region.

6. Data acquisition

The experiment control comprises four PCs. The master PC runs a home built LabView program controlling a transient recorder card (TR; Spectrum PCI25, 40 MHz, 12 bit, 4 channels) for data acquisition, a digital I/O card, providing timing signals and a GPIB adapter for communication with the stepper motor controller and the image acquisition system comprising two additional PCs (Image1 and Image2) which are linked to each other via 100 MHz LAN. They record the three-dimensional picture of the plasma plume. Both contain a frame grabber card which receives a 10 bit gray scale camera picture at a rate of 20 Hz, after it is pre-processed by a DSP6000 processor (see Section 7). The picture is evaluated and written to hard disk in real time. Image1 contains a GPIB adapter and Image2 another transient recorder (same model as master PC). The fourth PC runs the profiler software (spiricon) which reads out camera CCD3 (CoHu), displays the four profiles (see Section 4) and evaluates the actual beam quality.

Time-critical trigger-signals (e.g. Q-switch of the laser, camera triggers, TR-signals) are provided by three delay generators (SI DG535). One of them serves as temperature stabilized 10 MHZ main clock for all timing requirements of the whole setup.

The laser pulses are too fast to be recorded by the TR and hence the two photodiodes are read out by a digital storage oscilloscope (HP5450) with a sample rate of 8GSs. The spectra are transferred to the master PC via a 10 MHz LAN.

7. Experimental sequence

The determination of the colloid content in a sample starts with several preparation steps. For

all cleaning and dilution purposes, ultra pure water with a resistivity of 18.2 MΩcm (millipore synthesis) is used. In order to reduce the surface sorption to minimum, containers and tubings used are made of perfluorated alcoxy compounds (PFA).

Several types of quartz cells are used, which are cleaned in concentrated (65%) nitric acid and rinsed thoroughly with ultrapure water before use. The choice of cell is disposed by the amount of sample liquid available. Best results are obtained, when the solution within the focal volume is exposed to the laser pulse only once. Thus, the effect of photon induced chemical reactions (e.g. built-up of radicals) is sufficiently dissipated and the gas bubbles built by the expanding plasma are dispersed out of the focus before the next laser pulse. This means that the solution within the focal volume has to be refreshed completely between two laser shots (within 50 ms) and drained afterwards. For optical reasons, $\lambda/10$ surface roughness is desired. According to the manufacturer, this requires a wall thickness of at least 2 mm and hence a $18 \times 18 \times 30$ mm cell is chosen, which is available as static and flow-through modification. For the static version, at least 10 ml solution is required and five times as much is needed to operate the flow through version. For limited amounts of sample, smaller cells are used (3 ml static or 450 μl flow through). The optical quality is specified to be $\approx\lambda$, which is sufficient for routine measurements. The cells are inserted into a home build mount designed specifically to secure precise centering and a reproducible positioning perpendicular to the laser beam. The optical path length inside the sample water is kept constant in order to maintain a constant focal volume.

The two principal observables to be recorded are the energy of the laser pulse entering the quartz cell (voltage output of Pyro1) and the photoacoustic signal from the plasma induced shock wave (breakdown event). These signals are amplified by voltage to current converters and connected to the transient recorder cards of both, 'Image1' and the master PC. The relatively large dynamics of the signals requires a careful background determination, which is performed in two consecutive steps. First, the DC-offset of all transient recorder channels is measured with the laser beam blocked. Due to a sensitive temperature drift of the TR's preamplifier (up to 1% of its maximum voltage) the measurement has to be repeated preceding every session. Second, the 'zero pulse energy' is determined, by measuring the amount of laser light transmitted through the attenuator even when the polarizer is exactly perpendicular to the plane of polarization (typically 0.1% of the maximum energy = 10 μJ). The actual run consists of 20–100 *sets* at different laser pulse energies and starts at a value to be chosen by the user. Depending on the statistical significance to be achieved, for an adjustable number of laser shots (typically 200–1000), the time dependent signals of the pyroelectric detector and piezo crystal are recorded as *transients* of 8192 channels. Noise is reduced by averaging several hundred channels of the absolute value of each transient (while the energy signal is strictly positive, the piezo signal oscillates to positive and negative fractions). Either the complete transients or just the averaged data are written to hard disk for offline evaluation. Afterwards the laser pulse energy is increased or decreased at defined intervals. Twice the standard deviation of the pulse energies of the preceding data set (≈2%) is taken as standard interval, but larger values can be taken to speed up the measurement. This procedure is repeated until 98% breakdown probability is attained or the laser pulse energy reaches its maximum. For each set the breakdown probability (ratio of piezo signals to total number of laser shots) is calculated and plotted against the mean laser pulse energy.

8. Calibration

A detailed offline evaluation is performed on a Linux machine running PHYSICA (a FORTRAN based data evaluation and graph plotting package of the TRIUMF group). In order to account for occasional strong deviations from the mean pulse energy within one set, all data is energy-rebinned to values centered at the respective mean energies of each data set (or to multiples hereof). These data (so called *s*-curves) contain the size and concentration information on the sample of the

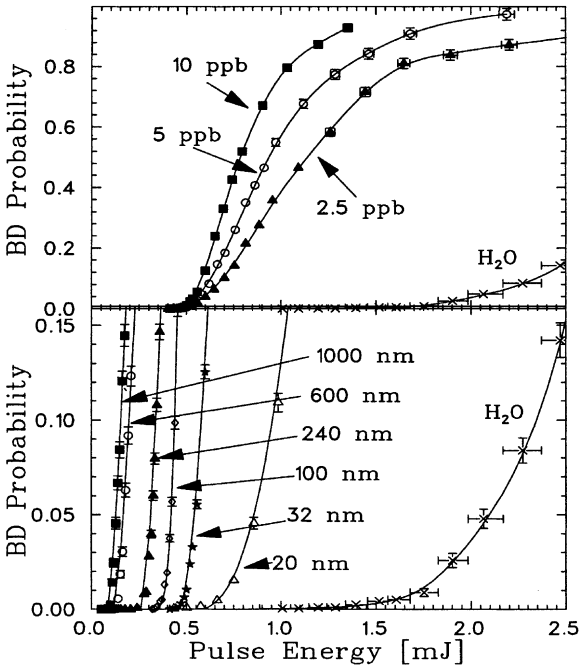

Fig. 7. Breakdown (BD) probability as a function of the laser pulse energy. Top: while the threshold remains unchanged, the slope changes with the colloid concentration (particle size 32 nm); bottom: the threshold of these '*s*-curves' increases with decreasing particle size.

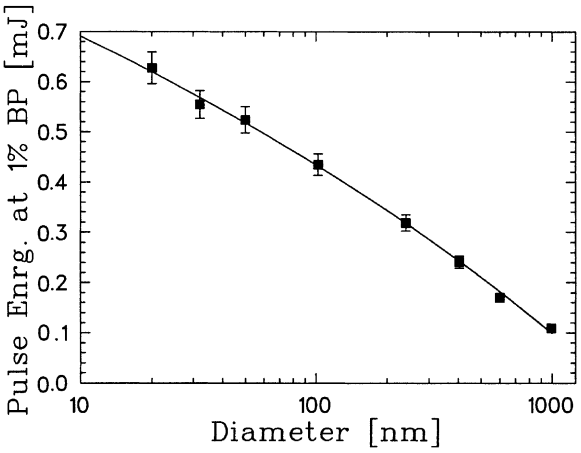

Fig. 8. The breakdown thresholds, i.e. the energy where the breakdown probability (PB) amounts to 1%, are plotted as function of particle size. Vice versa this calibration is used to determine the particle size of an unknown suspension from the PB threshold.

colloidal dispersion as described in detail before [19]. Fig. 7 (bottom) shows calibration measurement of polysterene reference particles. The threshold of the *s*-curve (i.e. the laser pulse energy where the first breakdown events occur) increases with decreasing particle size. If the breakdown threshold is plotted as a function of the particle size (Fig. 8), a calibration is achieved, with which an unknown size can be determined from its threshold energy. Strictly speaking this only holds for the very material the calibration is performed with. However, the material dependency is comparably weak and corresponding errors in particle size are in the order of 30% [15,19]. If two or three well defined particle sizes of different substances are available, the calibration can be adapted, and the precision can be improved considerably. The experiment for polysterene particles of 50 nm of four different concentrations is illustrated in Fig. 7 (top). Obviously, the threshold is common to all curves and they only differ in slope, which is then used to determine the particle concentration of an unknown solution. Here, it is important to take into account statistical effects: In order to determine a threshold of 1% breakdown probability, at least 10 breakdown events out of 1000 laser shots have to be observed. To perform the experiment on a suspension 100 times more dilute, the number of laser shots has to be increased accordingly. If the number of laser shots is adapted properly, the curves start at exactly the same position.

The calibration as shown in Fig. 8 is performed on well defined monodisperse suspensions with standard deviation of the mean colloid-diameter below 2%. In contrast Fig. 9 shows results for a bimodal dispersion as prepared by adding 240 nm particles to a suspension containing 10^8 ml^{-1} particles of 102 nm. The solid curve to the right (labeled 102 nm) corresponds to the pure monodisperse suspension. The dashed dotted curve to the left (240 nm is for the pure suspension of 240 nm particles at a concentration of 3×10^7 ml^{-1}. When 1% of the 240 nm particle suspension is added (i.e. 10^6 ml^{-1}) the threshold of the curve starts deviating from the one of the pure suspension (dashed curve, 1%) and corresponds to 240 nm particles, because the threshold is a measure of maximum particle size. When statistics is

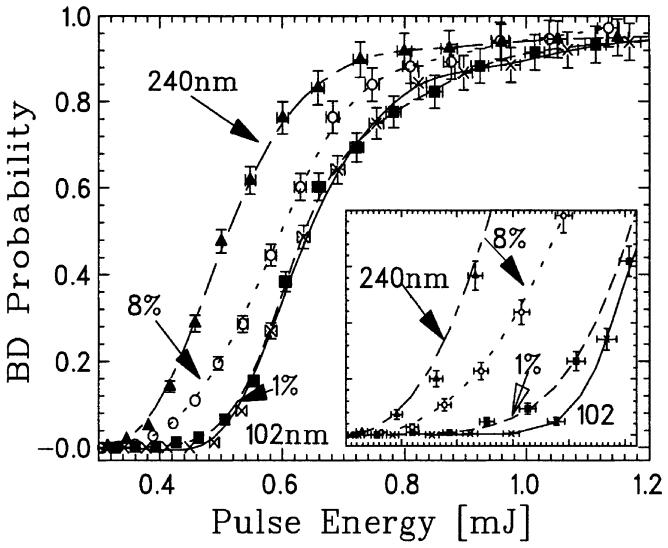

Fig. 9. Characterization of a bimodal suspension, consisting of a mixture of colloids of 102 and 240 nm diameter respectively. Even a contribution of 1% of the larger particles is distinguished by comparing the low energy parts of the *s*-curves. The insert represents a blow-up of the large graph, demonstrating the shift of BD threshold even for low admixture.

maintained at a high confidence level, the threshold shift is well in line with the calibration measurements (Fig. 8. In the further course of energy increase, the curve closely approaches that of the pure 102 nm suspension, because the slope is determined by the particle concentration, which is not changed considerably by adding the small fraction of large particles. Adding more of the large particles (dotted curve, 8%) results in a distinct enhancement of breakdown probability at the same pulse energy. The difference between the solid curve and the curve of the bimodal suspension reflects the concentration of larger particles.

9. Applications

Assessing underground storage of radioactive wastes, time scales on the order of several 100 000 years have to be considered. Any container will eventually undergo corrosion, leading to leakage or leaching of the contained waste form, which is most likely to take place after some 1000 years. By that time more than 90% of the radiotoxicity of highly radio active waste (HAW) is contributed by the actinides (Pu, Am, Cm) and hence their thermodynamics and interaction with the geological surroundings in a repository have to be considered thoroughly. Most actinides exhibit low solubility products at relevant pH and were considered immobile in the aquifer due to instantaneous precipitation. However, for dilute solutions as to be expected during leakage of a HAW-glass after influx of groundwater, rather than precipitation, formation of small mobile colloids is anticipated. It is therefore of cardinal importance, to understand formation mechanisms and long term stability of these colloids at groundwater conditions and the main focus of our present work aims at the tetravalent actindes. Representative, the investigation of oversaturated thorium solutions is discussed as first application [16]:

9.1. Formation of eigencolloids

Acidic solutions containing a well defined concentration of Th(IV) in 0.5 M HCl/NaCl were prepared. By coulometric titration the pH is increased in very small steps until the solubility is just exceeded, initiating the formation of small colloids. Titrations in the pH range 1.5–2.5 (regime A) lead to the formation of small ThO_2(s)

colloids which subsequently agglomerate to a microcrystalline precipitate [27]. At pH 3–5 hydrolysis and polynucleation causes the formation of amorphous thorium hydroxide colloids (regime B, C) and the H^+ and Th(IV) concentrations at the onset of colloid formation define the solubility of $Th(OH)_4$(am).

Three suspensions are discussed more closely in the following, denominated A, B and C. A refers to the 'ThO_2 domain', at a Th(IV) concentration of 2.5×10^{-3} M at pH = 1.9. Suspension B contains about the same amount of Th(IV) (3×10^{-3} M) at pH = 3.8, hence being in the '$Th(OH)_4$ colloid domain', at strong oversaturation but still showing no observable precipitation. Suspension C belongs to the same domain, but at lower concentration ($[Th(IV)] = 6.3 \times 10^{-5}$ M, pH = 4.1) and closer to the solubility curve. All suspensions were aged for at least six months in order to reach equilibrium. LIBD is applied to characterize the suspensions and the results are displayed in Fig. 10: Due to the inherent high sensitivity of the method, LIBD measurements are also sensitive to colloidal contamination stemming from primary chemicals. It is indispensable to perform 'background measurements' of all chemicals used in the experiments. In our case this is the matrix, a 0.5 M NaCl solution. After twofold recrystalization and ultrafiltration the matrix is of sufficient purity and does not contribute considerably to the total colloid content (Fig. 10, 'NaCl'). Sample A (ThO_2 colloids) shows a breakdown threshold corresponding to ~10 nm with a rather large saddle below 10% BD-probability, indicating some polydispersivity of the system. This is probably due to formation of small (2–5 nm) primary colloids which agglomerate in further course, as indicated by transmission electron microscope investigations. Suspension C ($Th(OH)_4$ colloids) exhibits a similar curve in the upper part, but with almost no saddle, hence suggesting a narrow size distribution of (<5 nm). Suspension B differs considerably: The colloids are of narrow distribution around 100 nm. The larger size is due to the strong oversatuartion of the solution, allowing the small colloids formed initially to grow further. Recent investigations seem to indicate a strong correlation of degree of oversatuartion and equilibrium colloid size and further long term experiments are being performed for validation.

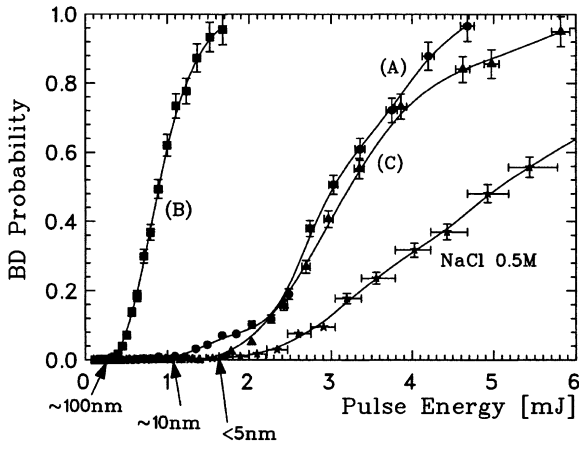

Fig. 10. Three samples of oversaturated Th(IV) solutions are probed by LIBD with respect to colloid content. B and C ($Th(OH)_4$ colloids) show a narrow size distribution centered at some 100 and 10 nm respectively. The saddle of A (ThO_2 colloids) indicates a higher polydispersivity in line with TEM observations of agglomerates of 3–5 nm units. Details see text.

9.2. Groundwater characterization

Apart from actinide oxide/hydroxide colloids, pseudocolloids can be formed by sorption of radioisotopes onto colloids released from backfill material (bentonite) and colloids naturally occuring in groundwater. As an example for this second group of investigations, work performed in collaboration with the Swedish 'Svensk Kärnbränslehantering AB' (SKB) at the Swedish Hard Rock Laboratory (HRL) is sketched in the following. In order to minimize disturbances by the sampling procedure, measurements were done in situ in the tunnel of the underground laboratory, applying a mobile version of the LIBD apparatus [28]. Depending on the respective elevation of the sampling site (depth under ground), the water leaks out of boreholes in the granite formation at pressures up to 33 bar. Since the flow through detection cell described above is not suited for pressures exceeding 4 bar, a home built high pressure cell was used.

The HRL is known to cross several aquifers originating from sea-water, meteoric, brine or

glacial sources respectively. Though well defined regarding chemical composition, little was known of their colloid content and for a first assessment eight different sampling sites were selected, located between 69 m and 416 m under sea level. From the large differences in metal ion concentrations (up to three orders of magnitude), quite some variations in colloid content were to be expected. Nevertheless, the degree actually found is remarkably high. Fig. 11 shows two extremes: The water from borehole KR0012 (the uppermost site at −69 m) contains large colloids at high concentration (▲). Included in the graph is a reference mesurement of 600 nm polystyrene particles (△) with a concentration of 0.6 ppm, which fits the data quite well below 50% breakdown probability. The deviation above indicates a considerable number of smaller particles in addition to the main fraction of some 600 nm in the natural system. However, the latter do not contribute considerably to the total particle mass-content. This large amount of colloids goes along with low salinity and a high content of organic substances (DOC 16 mg/l). Although LIBD is insensitive to pure humic/fulvic acids, these substances nevertheless might contribute to the observed colloids. Stability of inorganic or lignite particles is strongly enhanced by formation of mixed complexes and in conjunction with low ionic strength (which prevents further agglomeration followed by precipitation) even large particles are stable on long time scales.

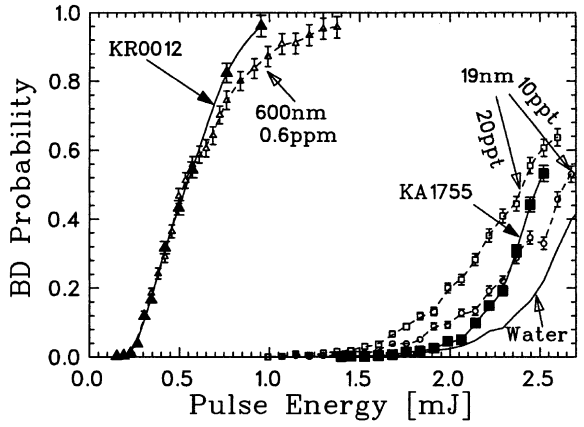

Fig. 11. Characterization of natural groundwaters in the Swedish Äspö Hard Rock Laboratory (HRL). KR0012 (▲) is a surface-near water (−69 m) containing a considerable amount of large particles. The corresponding '*s*-curve' is well fitted by a 600 nm reference suspension of 0.6 ppm. The second sample (KA1755, ■) is taken at 239 m below sea level. Comparison with 19 nm reference suspensions shows that colloid content is five orders of magnitude lower and the mean particle size amounts to some 10 nm.

Borehole KA1755 at −235 m below sea level contains a very pure water with colloidal contamination only slightly higher than it is the case for filtrated ultrapure deionized water shown for comparision ('water'). The natural sample (■) is confronted to reference measurements of 19 nm particle-suspensions with 10 ppt (○) and 20 ppt (□) content respectively. The higher threshold of the natural sample proves the colloids to be even smaller than that, with a concentration in the range of some 10 ppt (five orders of magnitude lower than in the case of borehole KR0012).

Since the transport capacity for colloid mediated migration scales proportional to the total active surface area of suspended particles, not only a water high in content of large colloids such as KR0012 adds a high risk of radionuclide-release into the environment. Even the apparent 'pure' water KA1755 due to their small mean diameter contains a high number of colloids ($\approx 10^{12}$ part/m^3) resulting in a large total surface area. Of course, colloid content of a groundwater is not the only safety criterion in the assessment of a nuclear waste repository. The character of the geological formations, pH, Eh and amount of species already solvated in the aquifer are just as important and have to be taken into account. However, the weight that is attributed to the colloid mediated transport might become apparent from the fact, that Sweden is about to make LIBD measurements an integral part of future repository assessments.

The latter example nicely demonstrates the flexibility of the method, spanning the dynamic range from ultra trace detection of some nm-sized colloids to quite dense suspension of micrometer particles, which are accessible by light scattering and allow a direct independent confirmation of the data.

Recently, ultra small Pd-colloids were investigated. Due to their sensitivity to oxygen they require degassed water conditions and hence are not suited to be compared directly to a natural water.

However, the capability of detecting 3–5 nm particles was clearly shown.

10. Summary

LIBD is applied to detect small aqueous colloids at trace concentrations. A reliable instrumentation allowing reproducible routine measurements was built, using a TEM00 Nd:YAG laser and a three-dimensional detection system. The latter allows to determine the spatial position of breakdown events relative to the laser focus. Exact information at which flux-density the breakdown is ignited can be used to image the profile of the highly focused laser in situ.

By automation of the laser pulse energy variation, a routine measurement of the breakdown probability ('*s*-curves') can be performed for the appraisal of particle size and concentration of colloidal suspensions. In addition to monodisperse samples, bimodal dispersions can be measured, which allow in situ observation of colloid size growth and colloid agglomeration down to very low concentrations [29].

For the assessment of nuclear waste repositories LIBD is of twofold importance. The method is used to determine thermodynamic properties of actinides under groundwater conditions. The solubility product is inferred from the onset of colloid formation in oversaturated solutions, and at the same time these data allow to estimate the relevance of transport via eigencolloids. Of equal importance for transport phenomena in the aquifer are pseudocolloids – radionuclides sorbed onto colloids of natural origin. A detailed characterization of groundwaters in the vicinity of a potential repository with respect to colloid content is needed, and LIBD represents a very sensitive detection method especially for suspension of small colloids.

Acknowledgements

The authors are indebted to V. Neck for many valuable discussions on the thermodynamics of Th(IV), R. Müller for backup in both word and deed during the experimental realization and R. Götz for his commitment during the Äspö campaign.

References

[1] M. Bolz, W. Hoffmann, W. Ruehle, F. Becker, Wat. Chem. Nucl. React. Sys. 7 (1996) 42.
[2] C.B. Murray, D.J. Norris, M.G. Bawendi, J. Am. Chem. Soc. 115 (1993) 8706.
[3] W. Moser, Advanced Catalysts and Nanostructured Materials, Academic Press, San Diego, 1996.
[4] J.I. Kim, MRS Bull. 19 (12) (1994) 47.
[5] B.D. Honeyman, Nature 397 (1999) 23.
[6] J.N. Ryan, Colloid. Surf. A. 107 (1996) 1.
[7] J.I. Kim, P. Zeh, B. Delakwitz, Radiochim. Acta 58 (1992) 147.
[8] R.E. Wildung, T.R. Garland, D.A. Cataldo, IAEA Viena 2 (12) (1979) 319.
[9] J.I. Kim, B. Kanellakopulos, Radiochim. Acta 48 (1989) 145.
[10] R. Knopp, V. Neck, J.I. Kim, Radiochim. Acta 86 (1999) 101.
[11] P. Zhao, S.A. Steward, Literature review of intrinsic actinide colloids related to spent fuel waste package release rates LLNL Report 126039, 1997, 2.
[12] T. Kitamori, K. Yokose, K. Suzuki, T. Sawada, Y. Goshi, Jpn. J. Appl. Phys. 27 (6) (1988) L983.
[13] W. Hauser, R. Götz, Druckwellensensor, Patent (Germany) DE 19602048C2.
[14] T. Bundschuh, W. Hauser, J.I. Kim, R. Knopp, F.J. Scherbaum, Colloid. Surf. A 180 (2001) 285.
[15] T. Bundschuh, R. Knopp, R. Müller, J.I. Kim, V. Neck, T. Fanghänel, Radiochim. Acta 88 (2000) 625.
[16] V. Neck, J.I. Kim, B.S. Seidel, C.M. Marquardt, K. Dardenne, M.P. Jensen, W. Hauser, Radiochim. Acta 89 (2001) 1.
[17] W. Hauser, R. Götz, H. Geckeis, B. Kienzler, In situ colloid detection in granite groundwater along the Äspö hard rock laboratory access tunnel, SKB International Report, 2002.
[18] L.J. Radziemski, D.A. Cremers, Laser Induced Plasmas and Applications, Marcel Dekker, Rochester, 1989.
[19] F.J. Scherbaum, R. Knopp, J.I. Kim, Appl. Phys. B 63 (1996) 299.
[20] C. Walther, A. Herlert, J.I. Kim, F.J. Scherbaum, L. Schweikhard, M. Vogel, Chem. Phys. 265 (2001) 243.
[21] J. Schwarz, P. Rambo, J.C. Diels, Appl. Phys. B 72 (3) (2001) 343.
[22] D.X. Hammer, R.J. Thomas, G.D. Noojin, B.A. Rockwell, P.K. Kennedy, W.P. Roach, IEEE J. Quantum Electron. 32 (4) (1996) 670.
[23] C. Walther, T. Fanghänel, G. Geipel, J.I. Kim, to be published.

[24] L. François, M. Mostafavi, J. Belloni, J.F. Delouis, J. Delaire, P. Feneyrou, J. Phys. Chem. B 104 (26) (2000) 6133.
[25] J.I. Yun, T. Bundschuh, V. Neck, J.-I. Kim, Appl. Spectrosc. 55 (3) (2001) 273.
[26] T. Bundschuh, R. Knopp, J.I. Kim, Colloid. Surf. A 177 (2001) 47.
[27] J. Rothe, M.A. Denecke, V. Neck, R. Müller, J.I. Kim, Inorg. Chem. 41 (2002) 249.
[28] W. Hauser, H. Geckeis, J.I. Kim, T. Fierz, Colloid. Surf. A 203 (2002) 37.
[29] C. Bitea, D. Cacuci, H. Geckeis, J.I. Kim, T. Rabung, F.J. Scherbaum, C. Walther, submitted for publication.

4.5.2 Laser-induced breakdown detection [Kim07]

12 Laser-induced Breakdown Detection

JAE-IL KIM AND CLEMENS WALTHER

Institut für Nukleare Entsorgung, Forschungszentrum Karlsruhe, PO 3640, D-76021 Karlsruhe, Germany

Environmental Colloids and Particles. Edited by K. J. Wilkinson and J. R. Lead

1 INTRODUCTION

Laser-induced breakdown detection (LIBD) is a colloid detection method utilising plasma formation in the high field of a focused laser beam. Size distributions of colloids between 5 and 1000 nm of mass concentrations down to 10^{-9} g dm^{-3} can be measured, often without sample pretreatment, both in the laboratory and in field experiments. The method is 'non-invasive' in the sense that the detected colloid itself is destroyed in the plasma of the microprobe, but since only a marginal fraction of the total colloid number is used for characterisation, the sample is virtually unaffected. This allows repeated measurements of a single sample, for instance when studying time resolved colloid stability.

This chapter starts with a historical overview of LIBD development and applications (Section 2) followed by details of the breakdown process and a short mathematical treatment (Section 3). Since LIBD is not yet a commercial method, this section instructs readers on how to build a machine and evaluate LIBD data themselves. Existing LIBD instrumentations are described (Section 4) and cross-referenced to the respective theoretical grounds of (Section 3). Selected applications are discussed (Section 5) and some important remarks on how to use LIBD in practice and in day-to-day operations follow (Section 6). The chapter closes with conclusions, future perspectives, a list of all variables and symbols used in this chapter and a glossary where the most important technical terms are explained.

2 THE DEVELOPMENT OF LIBD

The first laser-induced breakdown spectroscopy (LIBS) experiments were reported for the microanalysis of solids [1], shortly after the development of the ruby laser [2]. The analysis of liquids and gases followed (see, *e.g.* review by Rusak *et al.* [3]). In spite of the closely related principle, the investigation of colloids by LIBD required a different approach. In the late 1980s, Kitamori and co-workers tried to quantify the very low colloidal contamination of process liquids in semiconductor manufacturing. They made use of the photoacoustic effect, first observed by A. G. Bell in 1880: matter that absorbs light heats up, expands and generates an acoustic signal. Historically, the method was investigated first for bulk solids. However, the most important application in aquatic chemistry is laser-induced photoacoustic spectroscopy (LPAS) for the detection and speciation of solvated ions [4]: the signal scales linearly with the intensity of the light source, hence the intense light of a laser in combination with a very sensitive microphone results in very low detection limits. A similar principle was applied for colloid detection. The acoustic wave is picked up by a piezo-receiver, and particles in the sub-micrometre size range are detected at very low concentrations. Kitamori *et al.* [5] tried to lower the detection limit by focusing the laser beam. A continual increase in flux density lead to breakdown (BD) and plasma formation in water, which was a well known local phenomenon by that time [6]. Kitamori *et al.* were the first to ascertain the breakdown process on colloids in the laser focal region [7]. The expansion of the hot plasma gave rise to a shock wave which was easily detected by a piezo-receiver (Figure 1).

The number of BD events relative to the total number of laser pulses (breakdown probability, BDP) turned out to be directly proportional to the particle number density of colloids with a detection limit down to 10^4 particles cm^{-3} [8]. More detailed investigations

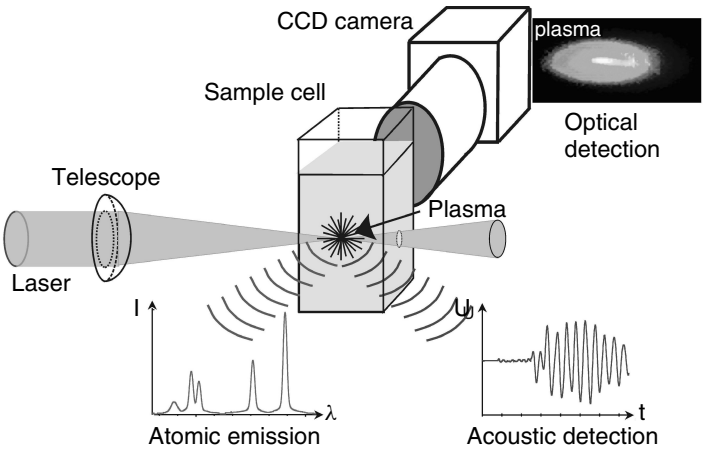

Figure 1. The plasma created by a pulsed laser causes an acoustic wave, which is detected by a piezoelectric receiver. In addition, the emitted light can be detected by a spectrometer or spatially resolved by a microscope lens and a CCD camera. Adapted from Walther, C. (2003). Comparison of colloid investigation by single particle analytical techniques – a case study on thorium-oxyhydroxides, *Colloids and Surfaces A*. **217**, 81–92, with permission from Elsevier

followed: an increase in detection volume and laser pulse energy led to a further improvement in sensitivity down to 10^{-11} g dm^{-3}, corresponding to only 100 particles cm^{-3} of 38 nm polystyrene particles [8]. Theoretical treatments of the breakdown process were based on previous work on plasma formation in pure water [9,10]. A size dependence of the BD threshold was reported shortly thereafter, allowing an appraisal of the mean particle size in addition to the number concentration [11]. The second part of this work focused on the optical emission. The plasma which typically is heated to 15 000–20 000 K, emits both blackbody radiation and atomic emission and, due to the high density of electrons, absorbs and scatters the late part of the laser pulse (Section 3). As observed by a streak camera, the time period between laser pulse and plasma emission was found to decrease with increasing particle size. However, the inherent scattering of data was very large and the size resolution too low to apply this correlation for particle sizing. The same holds for a functional dependence of the emission intensity on the delay time [12].

Even though the spectroscopic signal cannot be applied to particle sizing, it is possible to use it to gain information on the elemental composition of colloids. Kitamori *et al*. observed emission from $CaCO_3$ [13] and Ito *et al*. detected colloidal iron at concentrations below 10^{-3} g dm^{-3} with a coaxial nozzle arrangement, where a thin stream of liquid is surrounded by an atmosphere of argon [14]. The detection limit was lowered to 1.6×10^{-5} g dm^{-3} by using a second laser pulse for plasma heating [15], a technique well known for bulk solids [16] and taken up again by Pu *et al*. [17] for detection of $PbCO_3$ colloids down to 1.4×10^{-5} g dm^{-3}. Generally, the presence of colloids strongly enhances the LIBS signal. Knopp *et al*. demonstrated that Er^{3+} could not be detected as dissolved ion, even at g dm^{-3} concentrations. However, $ErBa_2Cu_3O_x$ colloids of 200 nm diameter gave rise to strong Er lines down to concentrations below 10^{-3} g dm^{-3} [18]. Yun *et al*. performed spectroscopy on europium(III) oxide and hydroxide colloids. The atomic emission intensity of the Eu_2O_3 suspension was about two orders of magnitude higher than that of the Eu^{3+} aquo ion and allowed spectroscopy down to 2×10^{-7} mol dm^{-3} [19].

The higher sensitivity facilitates selective detection for the colloids even in the presence of bulk ionic species. This principle is used for solubility measurements (see below and Section 5). The emission signal can even be enhanced by the presence of colloids of different composition, as reported for Eu ions sorbed on TiO_2 particles [19]. Plasma emission spectroscopy in liquids suffers from various line broadening effects and thus spectral resolution is typically limited to about 1 nm. However, Nakamura *et al*. showed that even the very small plasma generated on colloids can act as an 'optical gain medium' allowing amplified atomic emission [20]. They showed that laser action takes place in a plasma of polystyrene particles by measuring the isotope shifts of the hydrogen and deuterium Balmer Hα lines with a resolution of 0.1 nm [21].

The majority of work on laser-induced breakdown in colloidal suspensions has focused on particle sizing. Scherbaum *et al*. [22] published a statistical model, which described the BD probability as a function of the pulse energy using polystyrene beads of various sizes at different concentrations. Data gained by an excimer–dye system and acoustic detection corroborate this approach. In addition, the material dependence of the breakdown process has been investigated for polystyrene, thoria (ThO_2) and alumina (Al_2O_3) [22]. This technique was applied amongst others to investigate natural systems such as drinking waters, ground waters and water in waste repositories [23] as well as contaminants in the primary cooling circuit of a nuclear power reactor [24]. With the approach based on the same physical concept as given in [11], but with acoustic detection, Izumida *et al*. [25] made use of the variation in delay time between the laser pulse and acoustic wave for the appraisal of the size and composition of the colloids, namely for silica, polystyrene, iron (Fe_2O_3) and gold particles. In this study, gold and iron colloids were significantly smaller than both polystyrene and silica particles, as known from electron microscopy. Whereas polystyrene and silica particles behaved similarly, gold and iron colloids showed considerably lower thresholds. The authors explained this effect by the lower breakdown threshold of metal surfaces compared with optically transparent media. Saito *et al*. [26] suggested a further enhancement in detection efficiency: by the use of standing acoustic plane waves, colloids were accumulated in the nodes. When the laser focus was located inside one of these 'particle bands', the probability of particle detection was strongly enhanced over simple diffusion into the focal volume by Brownian motion.

The effect of various laser parameters on the detection efficiency was investigated by Bundschuh *et al*. [27], who compared an Nd:YAG-based system with an excimer–dye apparatus with various focusing optics. They claimed a detection limit of colloids as small as 0.64 ± 0.33 nm, based on model calculations. Partin [28] announced their intention to combine the LIBD and LIBS techniques in a single mobile apparatus that could be sold commercially; however, to our knowledge, such an instrument is not yet available.

Another approach for particle sizing, using spatially resolved imaging of the optical plasma emission, was reported in 1991 and patented in 1994 [29]. The focal region of the laser beam is imaged by a lens onto a two-dimensional array photodetector and the position of a plasma plume along the laser beam axis is recorded for every single breakdown. Small particles create plasma events solely in the centre region, whereas the events of large particles are spread over an extended volume, described as a large 'ignition length' or large 'effective focal length' (l_Z). This quantity can be calibrated versus particle size with some 20% precision. Bundschuh *et al*. [30] demonstrated a power law dependence of l_Z versus the colloid diameter between 20 nm and 1 μm, which is only weakly dependent

on the colloidal material (Section 3.3). The BDP increases roughly linearly with colloid concentration (Section 4). They applied the method for the characterisation of granitic ground water. Based on the same technique, Hauser *et al*. [31] built a mobile LIBD, which was used in field measurements. The groups of Hauser and Moeri reported real time, *in situ* observations of the colloid-mediated migration of trace elements in underground laboratories in Grimsel (Switzerland) [31,32] and Äspö (Sweden) [33]. The results were in agreement with off-line measurements (ICP-MS, light scattering and gamma-ray detection). Using a diode-pumped TEM_{00}-Nd:YAG laser[1], an optimal Gaussian profile in the focal region was realised [34], which is a prerequisite to verifying mathematical predictions on the BD probability and position. In order to locate the plasma in three dimensions, an image of the BD position in the laser focal volume was obtained by two CCD cameras, perpendicular to each other.

Recent applications of LIBD (Section 5) have included characterisation of bentonite colloids in ground water [35], the determination of particle contents of drinking water (Section 5.1) before and after purification [36,37] and *in situ* observation of ZrO_2–colloid aggregation down to 2×10^6 particles cm^{-3} [38]. Within the framework of nuclear waste disposal safety assessment, thermodynamic solubility data of actinides were gained by investigating colloid formation in oversaturated solutions, in particular plutonium(IV) [39–42], neptunium(IV) [43] (Section 5.2) and thorium [93,44–46]. Detection and spectroscopy of americium(III)–colloids was reported [47], and interaction of actinides (americium and curium) with nascent aluminosilicate colloids investigated in great detail [48,49] (Section 5.3). A combination of laser-induced fluorescence and LIBD has been applied for the sorption of curium(III) on cement and formation of curium-containing colloids [50].

In addition to the 'stand-alone' applications, LIBD has been used for sensitive detection in combination with a size fractionating method. This is particularly useful, when no reference colloids of a certain size fraction are available, *e.g.* in the range below 20 nm. Manh *et al*. [51] reported a three orders of magnitude sensitivity enhancement when LIBD replaced the light-scattering detector of a commercial flow field-flow fractionation (FFFF) instrument (Chapter 5). A multiple combination of UV–VIS, ICP-MS, LIBD and FFFF facilitated the characterisation of humic colloids in ground water in detail [52].

3 THE PHYSICS BEHIND THE TECHNIQUE

It is obvious from the name of the method, 'laser-induced breakdown detection', that breakdown plays a central role in the underlying physical processes [53]. But how do we define a 'breakdown'? The expression originates from the breakdown of classical dielectric properties of a given medium due to the presence of free charge carriers. As a common convention in the literature, the minimum density of electrons needed to speak of a breakdown is chosen to be 10^{18} electrons cm^{-3} [16]. In the following, the generation processes will be examined in a short overview in order to understand how LIBD works and provide sufficient information to apply correctly and understand the limitations of the method.

3.1 MULTI-PHOTON IONISATION OF ATOMS

When matter interacts with light of a pulsed laser beam, there are several possibilities of producing electrons. Direct photo-ionisation is a very efficient process as long as the

[1] Basic transverse mode; see Glossary.

photon energy $E_{\mathrm{Ph}} = h\nu$ (h is Planck's constant, ν- is the frequency of light) exceeds the energy to liberate one electron (ionisation energy, E_{I}). However, for visible light ($h\nu = 1.5 - 3$ eV) this is not the case, since most materials have an ionisation energy (work function, or band gap for solids[2]) between 6 and 10 eV [54]. The simultaneous absorption of $m > 1$ photons is required and one speaks of multiphoton ionisation (MPI) of order m [55,56].

In general this is a non-resonant process, which scales proportionally to the mth order of the photon flux-density and is very unlikely for 'long-pulse' lasers (nanoseconds and longer). This can be depicted as follows: in order to excite one electron of a molecule above the ionisation energy, all m photons have to be absorbed 'simultaneously', i.e., before the energy is dissipated on a picosecond time-scale. Below saturation, an increase in electron number N_{e}, equation (1), can be expressed in terms of the number of (neutral) molecules in the focal volume N_{M} [56], the power density I of the laser and the MPI cross-section μ_m [in general all quantities may depend on space coordinate and time (Section 4)].

$$\left(\frac{\partial N_{\mathrm{e}}}{\partial t}\right)_{\mathrm{MPI}} = -\frac{\partial N_{\mathrm{M}}}{\partial t} = N_{\mathrm{M}}(t)\mu_m I(t)^m \tag{1}$$

For nanosecond pulses, this process is very unlikely and can generate only a few electrons per laser shot. The majority of charge carriers have to be provided by a second process, cascade multiplication, which is also referred to as inverse bremsstrahlung[3] (IB) (Figure 2). Once free electrons are present in the focus, they will be accelerated by the

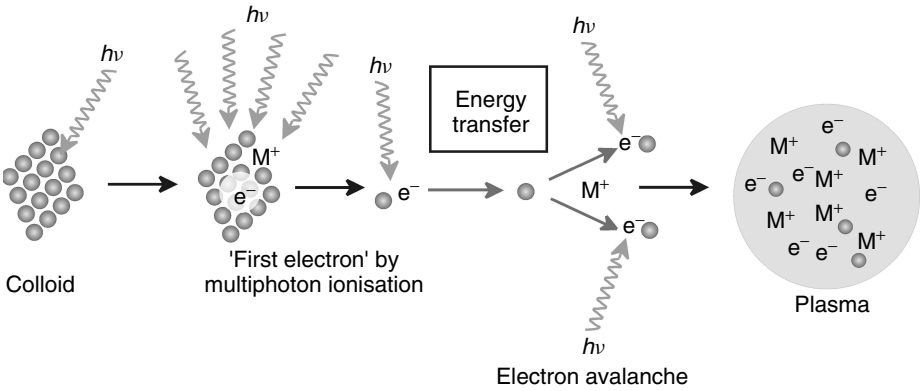

Figure 2. Nanosecond-laser induced plasma formation can be understood by the following model: a few 'first' electrons are produced by non-resonant multiphoton ionisation during the laser pulse. These electrons gain energy in the electric field of the laser by inverse bremsstrahlung which then produce further electrons via collisions with constituents of the colloid (atoms or molecules). Within a few nanoseconds, more than 10^{18} electrons cm^{-3} are generated and a dense, hot (15 000–20 000 K) plasma is formed. Drawing from [57]

[2] In the case of atoms or molecules in the gas phase, the energy to free one electron is referred to as ionisation energy (former expression: ionisation potential). For solids, this energy is named electron work function and in the case of (semi-)conductors the respective quantity is the gap between valence and conduction bands. In this chapter we will use the term *ionisation energy* irrespective of the medium.

[3] See glossary.

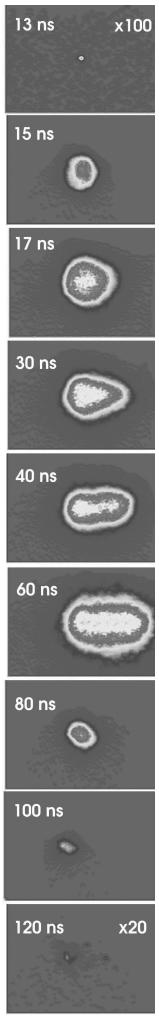

Figure 3. Evolution of the plasma plume induced by ns-laser pulses (532 nm), imaged by an ultrafast CCD camera

electric field of the laser and a few of them will gain energy that is greater than the ionisation energy of neighbouring atoms or molecules. In this case, a collision can ionise a molecule and detach one additional electron, which in turn is accelerated and may ionise further molecules. This repeated effect leads to an avalanche-like increase in the electron density within a few nanoseconds (Figure 3) and is the dominant electron production process for nanosecond pulses [58]. For gases [59], liquids [9] and solids [60], multiphoton ionisation and avalanche ionisation have been investigated in great detail and are well understood.

An increase of the electron density with time can be expressed by the following differential equation:

$$\frac{\partial N_\mathrm{e}}{\partial t} = \left(\frac{\partial N_\mathrm{e}}{\partial t}\right)_\mathrm{MPI} + \eta(E)N_\mathrm{e} - \left(\frac{\partial N_\mathrm{e}}{\partial t}\right)_\mathrm{loss} \tag{2}$$

where $\eta(E)$ is the rate at which an electron of energy E undergoes an ionising collision. The third term represents a decrease in electron number due to diffusion out of the focal region and recombination or trapping processes. The relative importance of these terms depends strongly on the laser pulse duration [58,61,62]. For nanosecond-laser pulses, diffusional loss can be neglected and the electron density increases exponentially, once some 'seed' electrons are generated by MPI. Two important conclusions drawn from this model should be noted:

1. The generation of the first electron represents the 'bottleneck' of plasma formation in the case of very pure materials without 'free' electrons, due to the polynomial dependence of equation (1) and a small value of the cross-section μ_m.
2. The cascade multiplication process has to be initiated early enough in the laser pulse to generate a high density of electrons. Only then will the plasma absorb laser light efficiently and become hot enough to be detected.

Both effects give rise to a *threshold behaviour* [63]. Below the lowest pulse energy, no plasma can be detected. The precise value of this threshold depends on the mechanism and efficiency of plasma detection, which are the most important criteria for LIBD, and on the plasma ignition material.

3.2 FLUX DENSITY DISTRIBUTION IN A LASER FOCUS AND 'FOCAL VOLUME'

Equations (1) and (2) are valid for a homogeneous distribution of molecules and a homogeneous photon flux. Unfortunately, the latter cannot be achieved by focusing a laser beam with refractive optics. Holographic elements, on the other hand, cannot handle the small spot size (typically $\lesssim$10 μm) required for breakdown generation. Hence one has to deal with photon flux that varies within the focal volume. The power density I and the absolute molecule and electron numbers (N_{M} and N_{e}) in equation (1) are replaced by the space-dependent power density $I(\vec{r}, t)$ and the respective number densities (ρ_{M} and ρ_{e}). Absolute electron numbers are calculated later on by integration over space [see equation (26)]:

$$\frac{\partial \rho_{\mathrm{M}}(t)}{\partial t} = -\rho_{\mathrm{M}}(t)\mu_m I(\vec{r}, t)^m \tag{3}$$

The power density in the focus must first be calculated. As detailed treatments can be found in basic textbooks [64,65], only a short description is given here in order to define the technical terms needed later on.

A laser pulse of energy E_0 and duration t_0 has a mean power of

$$P_0 = \frac{E_0}{t_0} \tag{4}$$

When the area of the spot is A, the mean power density is

$$I = \frac{E_0}{A\, t_0} \tag{5}$$

A common quantity for the treatment of linear processes is the photon flux density[4]:

$$\phi = \frac{\text{number of photons}}{\text{time area}} = \frac{E_0}{h\nu\, t_0\, A} \tag{6}$$

where $h\nu$ is the energy of one photon. Focusing a TEM_{00} laser beam by a spherical lens (neglecting aberration effects) results in a diffraction-limited Gaussian focus, which is parameterised as follows: r_0 is the radius perpendicular to the laser axis (*radial* dimension r), where the power density decreases to 1/e of the peak value:

$$P_0 := \int_0^{2\pi}\int_0^{\infty} I(r,\varphi) r \,\mathrm{d}\varphi \mathrm{d}r = I_0 \int_0^{2\pi}\int_0^{\infty} r\, \mathrm{e}^{-\frac{r^2}{r_0^2}} \,\mathrm{d}\varphi \mathrm{d}r \tag{7}$$

$$= I_0 \frac{2\pi r_0^2}{2} \quad \text{and} \;\Rightarrow I_0 = \frac{P_0}{\pi r_0^2} \tag{8}$$

with the peak power density I_0. Since the 1/e-radius varies with the position along the laser beam axis, $r_0 = r_0(z)$, the power density can be written as

$$I(r,z) = \frac{P_0}{\pi r_0^2(z)}\, \mathrm{e}^{-\frac{r^2}{r_0^2(z)}} \tag{9}$$

with the *longitudinal* dependence of the 1/e-radius $r_0(z)$, as given in [65, p. 27, equation (I.79)]

$$r_0(z) = r_0(0)\left[1 + \left(\frac{z\lambda}{n\pi r_0^2(0)}\right)^2\right]^{\frac{1}{2}} \tag{10}$$

where λ is the wavelength of light and n the refractive index of the medium into which the beam is focused [in general $n = n(\lambda)$]. The calculated $r_0(z)$ are compared with measured data (■) [34] in Figure 4.

Scherbaum *et al*. [22] approximated the focal volume by an ellipsoid with volume

$$V_{\mathrm{el}} = \frac{4}{3}\pi r_{\mathrm{C}}^2 z_{\mathrm{C}} \tag{11}$$

where r_{C} is the critical radius, i.e. the radius at $z = 0$ (perpendicular to the laser beam), where the power density decreases to a value below the breakdown threshold for a given particle. At the same time, r_{C} is the short half-axis of the (prolate) ellipsoid (Figure 5). By analogy, z_{C} is the critical distance from the focal centre along the laser axis, where the power density decreases below the breakdown threshold. The quantities are calculated as a function of the total power P_0 and the critical power density I_{C}, which in general depend on particle size and composition.

[4] Photon flux and photon flux density are used ambiguously in the literature. In this chapter, photon flux means number of photons per second and photon flux density is the differential quantity with respect to area. Some authors use photon flux for the number of photons per second and area, whereas photon flux density is the corresponding differential quantity with respect to the emission angle.

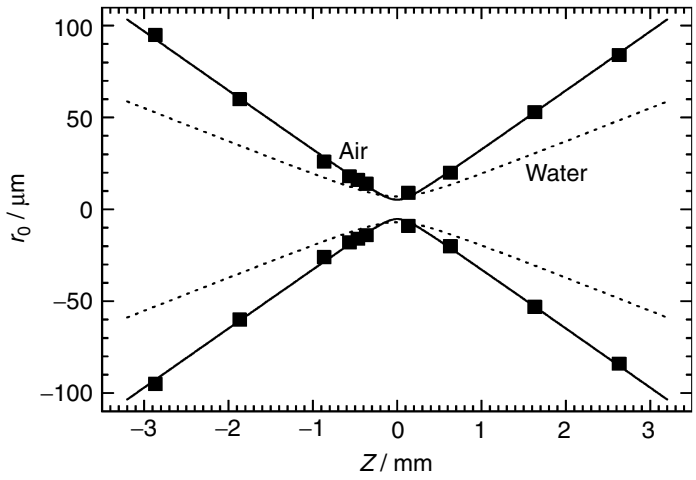

Figure 4. Measured data in air for the 1/e intensity isolines $[r_0(z)]$ of a focused Gaussian laser beam ($\lambda = 532$ nm, total focal length of telescope ($f_{tot} = 80$ mm) and calculation for water ($n_{H_2O} = 1.33$). Reprinted from Walther, C., Bitea, C., Hauser, W., Kim, J. I. and Scherbaum, F. J., (2002). Laser induced breakdown detection for the assessment of colloid mediated radionuclide migration, *Nuclear Instruments and Methods in Physics Research B*, **195**, 374–388, with permission from Elsevier

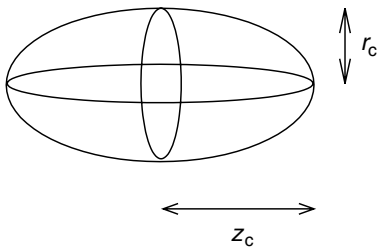

Figure 5. Approximation of the focal volume for a Gaussian beam, focused by a spherical lens without aberration as used in [22]

Inverting equation (9) yields

$$r_C = r_0(0)\sqrt{\ln\left[\frac{P_0}{I_C \pi r_0^2(0)}\right]}\Bigg|_{z=0} \tag{12}$$

By substituting equation (10) into equation (9) at $r = 0$ we obtain

$$I_C = \frac{P_0}{\pi r_0^2(0)} \frac{1}{1+\left[\frac{z_C \lambda}{n\pi r_0^2(0)}\right]^2}\Bigg|_{r=0} \tag{13}$$

which is inverted in order to obtain the critical distance along the laser axis, z_C:

$$z_C = \frac{n\pi r_0^2(0)}{\lambda}\left[\frac{P_0}{I_C \pi r_0^2(0)} - 1\right]^{\frac{1}{2}} \tag{14}$$

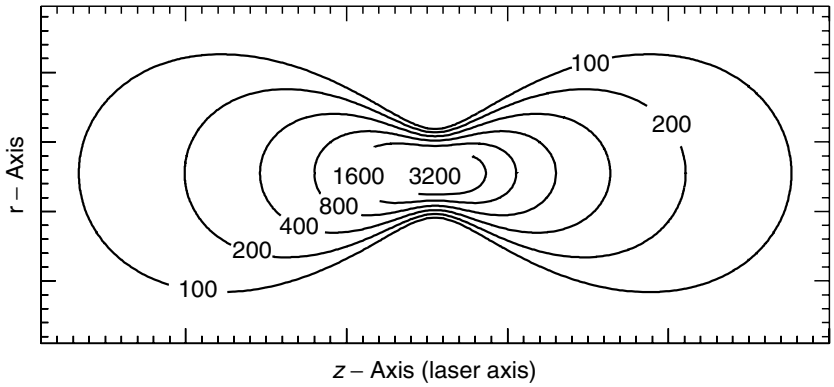

Figure 6. Contour plot of isoflux lines (regions of equal photon flux density or equal power area-density, respectively). The numbers indicate the relative photon flux density

The focal volume is then calculated as

$$V_{\mathrm{el}} = \frac{4}{3}\frac{n\pi^2 r_0^2(0)}{\lambda} r_0^2(0) \ln\left[\frac{P_0}{I_{\mathrm{C}}\pi r_0^2(0)}\right]\left[\frac{P_0}{I_{\mathrm{C}}\pi r_0^2(0)} - 1\right]^{\frac{1}{2}} \tag{15}$$

The volume scales with increasing power according to

$$V_{\mathrm{el}} \propto P_0^{\frac{1}{2}} \ln P_0 \tag{16}$$

The above simple treatment only holds in the limit of small laser pulse energy or high breakdown threshold. Outside this limit one has to take into account the non-elliptical (butterfly) shape of the breakdown region depicted in Figure 6. The mathematical treatment for spherical focus conditions is given in [66] and is briefly summarised below.

Equation (11) can be substituted by the more general formula in cylindrical coordinates:

$$V_{\mathrm{foc}} = 4\pi \int_0^{z_{\mathrm{C}}} \int_0^{r_{\mathrm{C}}(z)} r \, \mathrm{d}r \mathrm{d}z \tag{17}$$

and equation (12) is generalised by including the z-dependence of r_0:

$$r_{\mathrm{C}}(z) = r_0(z)\sqrt{\ln\left[\frac{P_0}{I_{\mathrm{C}}\pi r_0^2(z)}\right]} \tag{18}$$

Integration over r yields

$$V_{\mathrm{foc}} = \frac{4\pi}{2} \int_0^{z_{\mathrm{C}}} r_0^2(z) \ln\left[\frac{P_0}{I_{\mathrm{C}}\pi r_0^2(z)}\right] \mathrm{d}z \tag{19}$$

By introducing constants a and b, equation (10) can be written as follows:

$$r_0(z) = r_0(0)\sqrt{1 + b^2 z^2} \quad \Big| \quad a = \frac{P_0}{I_{\mathrm{C}}\pi r_0^2(0)}; \quad b = \frac{\lambda}{n\pi r_0^2(0)} \tag{20}$$

and equation (19) becomes

$$V_{\text{foc}} = 2\pi \int_0^{z_C} r_0^2(0)(1 + b^2 z^2) \ln\left(a \frac{1}{1 + b^2 z^2}\right) \mathrm{d}z \tag{21}$$

which is solved by integration by parts and simple integral calculus ([67], p. 156):

$$V_{\text{foc}} = \frac{4\pi^2 r_0^4(0) n}{9\lambda} \left[\frac{P_0}{I_C \pi r_0^2(0)} - 1\right]^{\frac{3}{2}} \tag{22}$$

The solid curve in Figure 7 is a fit of equation (22) to the calculated data of the 'butterfly' in the top of the figure. The isoflux areas are transformed well to isoflux volumes by weighting each area segment with its radius.[5]

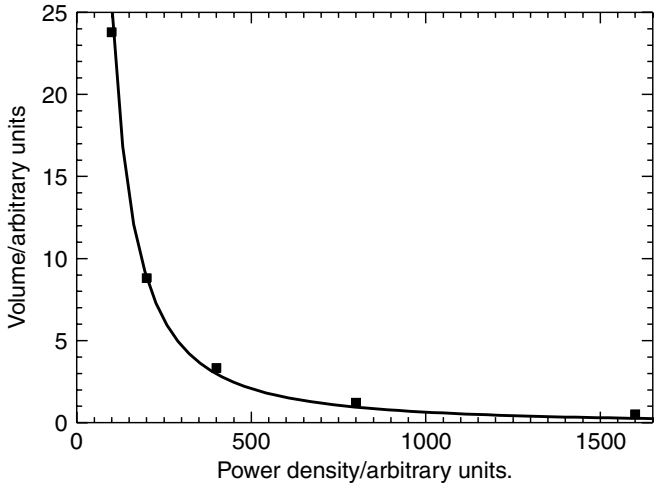

Figure 7. Cumulative relative volumes of the focal region, more precisely of the three-dimensional isoflux object depicted in Figure 6

[5] It is interesting to compare this exact result with the approximation of equation (15). At $\alpha = 1$, the ln can be approximated as a Taylor series:

$$\ln \alpha = (\alpha - 1) - \frac{(\alpha - 1)^2}{2} + \frac{(\alpha - 1)^3}{3} - \ldots$$

When the approximation is truncated at the second order term, we obtain the exact solution:

$$\ln\left[\frac{P_0}{I_C \pi r_0^2(0)}\right] \approx \frac{P_0}{I_C \pi r_0^2(0)} - 1 - \frac{1}{2}\left[\frac{P_0}{I_C \pi r_0^2(0)}\right] - 1^2 + \ldots$$

$$V_{\text{el}} \propto \left[\frac{P_0}{I_C \pi r_0^2(0)}\right] - 1^{\frac{3}{2}} - \frac{1}{2}\left[\frac{P_0}{I_C \pi r_0^2(0)}\right] - 1^{\frac{5}{2}} + \ldots$$

3.3 FROM THE ELECTRON NUMBER TO THE BREAKDOWN PROBABILITY

When the breakdown probability of colloids, i.e. the probability of igniting a plasma integrated over the total focal volume, is calculated, the temporal evolution of the electron density must be considered. It is assumed that the plasma formation is preceded by the generation of only *one* first free electron via non-resonant multiphoton ionisation (MPI). In the case of nanosecond-pulses, this process presents a bottleneck in plasma formation and its rate determines the total plasma generation. In due time, electrons are multiplied by inverse bremsstrahlung and the plasma is heated until it can be detected either by light emission or by the acoustic shockwave produced during expansion.

The power density at a fixed coordinate within the focal region is not constant but varies in time: $I = I(\vec{r}, t)$. For calculation of the MPI rate, equation (3) is used initially. In the following, a laser pulse of single transverse mode is assumed. In this case, $I(\vec{r}, t)$ can be separated into a spatial and a temporal part, $g(\vec{r})$ [equation (9)] and $h(t)$, respectively:

$$I(\vec{r}, t) = E_0 g(\vec{r}) \cdot h(t) \tag{23}$$

where E_0 is the total energy of the pulse (*e.g.* in joules). The combination of equations (3) and (23) and integration over time yield the number-density of electrons, ρ_e:

$$\frac{\rho_e}{\rho_M} = 1 - \exp\left\{ \int_{-\infty}^{\infty} \mathrm{d}t\, \mu_m \left[E_0 \frac{1}{\sqrt{\pi}\tau} \mathrm{e}^{-\frac{t^2}{\tau^2}} \frac{1}{\pi r_0^2} \mathrm{e}^{-\frac{r^2}{r_0^2}} \right]^m \right\} \tag{24}$$

where $\rho_{-\infty}$ is the density of educts before irradiation ($t = -\infty$). For the sake of simplicity, the temporal profile is approximated by a Gaussian with a '1/e lifetime' of τ. However, the mathematical treatment is valid for an *arbitrary* temporal dependence, since the time integration is independent of the space coordinates and yields a constant factor c_t. In the case of the temporal Gaussian, c_t amounts to:

$$c_t = \int_{-\infty}^{\infty} \mathrm{d}t \left[\frac{1}{\sqrt{\pi}\tau} \mathrm{e}^{-\frac{t^2}{\tau^2}} \right]^m = \frac{1}{\sqrt{m}(\tau\sqrt{\pi})^{m-1}} \tag{25}$$

In order to calculate the number of electrons N_e, the number-density ρ_e has to be integrated over space. One should note the z-dependence of the 1/e radius $r_0(z)$ [equation (10)] which, for the sake of readability, is not always written explicitly. In cylindrical coordinates, we obtain:

$$N_e = 2\pi \int_{-\infty}^{\infty} \mathrm{d}z \int_{0}^{\infty} r\, \mathrm{d}r \rho_M \left(1 - \exp\left\{ -\mu_m c_t \left[E_0 \frac{1}{\pi r_0(z)^2} e^{-\frac{r^2}{r_0(z)^2}} \right]^m \right\} \right) \tag{26}$$

By two-fold substitution:

$$u = m\,\frac{r^2}{r_0^2(z)} \text{ and } v = a\,\mathrm{e}^{-u} \tag{27}$$

we have

$$N_\mathrm{e} = -\frac{2\pi\rho_\mathrm{M}}{m}\int_0^\infty \mathrm{d}z\, r_0^2(z)\int_a^0 \mathrm{d}v\,\left(\frac{1}{v}-\frac{1}{v}\,\mathrm{e}^{-v}\right) \tag{28}$$

which is solved by using an integral table (*e.g.* [68], 8.21) to give

$$N_\mathrm{e} = \frac{2\pi\rho_\mathrm{M}}{m}\int_0^\infty \mathrm{d}z\, r_0^2(z)\,[\ln a + \boldsymbol{C} - \mathrm{Ei}(-a)] \tag{29}$$

$$a = \mu_m c_t\,\frac{P_0^n}{\pi^n r_0^{2n}(z)}$$

where $\boldsymbol{C} = 0.57721566490153$, i.e. Euler's constant, and $\mathrm{Ei}(-x)$ is the exponential-integral function[6].

Both $\ln a$ and $-\mathrm{Ei}(-a)$ diverge as $a \to 0$ ($z \to \infty$), but it can be shown ([68], 8.214) that

$$\lim_{a\to 0} \ln a - \mathrm{Ei}(-a) = -\mathbf{C} \tag{30}$$

and hence the second part of the integrand of equation (29) approaches 0.[7]

Equation (29) is visualised by an example with a set of parameters, which are typical for the experimental set-up of [34] (Table 1). The MPI cross-section [69] of polystyrene particle molecules were approximated by the measured value of toluene in the gas phase [70].

The transition from a free molecular gas to colloids in water is made by considering the following:

- 'Clustered' targets: one colloid consists of $N_m = \left[\frac{4}{3}\pi(\frac{d}{2})^3\right] \Big/ V_\mathrm{mol}$ molecules, with an MPI cross-section of μ_m^1 each. Under the assumption that the colloids are perfectly transparent, the cross-section of ionising at least *one* molecule inside the colloid amounts to $\mu_m = N_m\mu_m^1$. If colloids are not transparent and have a penetration depth for light d_p, only an outer layer with thickness d_p facing the laser beam contributes to electron production during the initial ionisation stage until vaporisation destroys the particle.
- The number density of colloids replaces the number density of gas molecules, with the important difference that having one colloid within a volume element means that there are N_m absorbers at a time. The absorption cross-section of the colloid is given by the sum of absorption cross-sections of clustered constituents justifying the introduction of the mesoscopic cross-section μ_m.

---

[6] $\mathrm{Ei}(x) = \int_0^x \mathrm{e}^{t^2}\,\mathrm{d}t$.

[7] Note that $\lim_{z\to\infty} r_0(z) = \infty$.

Table 1. Set of parameters used in Example 1

Parameter	Value	Comment
d_{coll}	0.1	Diameter of colloid in μm
ρ_{C}	4×10^5	Number of colloids cm^{-3}
m	4	Order of process
$r_0(0)$	6.7	Radius at Gaussian focus in μm
$n_{\mathrm{H_2O}}$	1.334	Index of refraction
λ	0.532	Wavelength in μm
μ_m^1	1.4×10^{-10}	MPI cross-section of one molecule in $\mu\mathrm{m}^8\mathrm{W}^{-4}\mathrm{s}^{-1}$
V_{mol}	1.7×10^{-10}	Volume of one molecule in $\mu\mathrm{m}^3$
τ	1×10^{-8}	1/e pulse duration in s
$\rho_{\mathrm{C}\mu\mathrm{m}^3}$	$\rho_{\mathrm{cm}^3}/10^{12}$	Colloids $\mu\mathrm{m}^{-3}$
C_{C}	$\rho_{\mathrm{C}\mu\mathrm{m}^3}\delta\left(\frac{4\pi}{3}r_{\mathrm{coll}}^3\right) \times 10^{12}$	Concentration in 10^{-9}g dm^{-3}(density colloid $= \delta$ g cm^{-3})
μ_m	$\mu_m^1\left(\frac{4\pi}{3}r_{\mathrm{coll}}^3\right)\Big/ V_{\mathrm{mol}}$	Cross-section of colloid
c_t	$[\sqrt{m}(\tau\sqrt{\pi})^{m-1}]^{-1}$	Integral over time dependence in s^{m-1} [equation (25)]

- Although the total number of molecules may still be large, the number of colloids per unit volume is considerably lower, due to clustering. Hence saturation effects occur already at moderate pulse energies (see below).
- Since colloids are suspended in water, light propagation is determined by the ratio of the respective indices of refraction $n_{\mathrm{H_2O}}/n_{\mathrm{Coll}} \approx n_{\mathrm{H_2O}}$ in the present work (polystyrene spheres: $n_{\mathrm{Coll}} = 1.59$).
- It is assumed that every electron that is generated by MPI is multiplied by avalanche generation, which is a good approximation for high pulse energies and small particles (see later).
- In the following example, we do not include focusing and field enhancement effects inside the colloid, which may become important for large particles of size $d \gtrsim \lambda$ (wavelength of the laser light) [71–73].

Figure 8 displays the inner function of equation (29), namely

$$\frac{\partial N_{\mathrm{e}}}{\partial z} = \frac{2\pi\rho_{\mathrm{M}}}{m} r_0^2(z)\,[\ln a + \boldsymbol{C} - \mathrm{Ei}(-a)] \;\Big|\; a = \mu_m c_t \frac{P_0^m}{\pi^m r_0^{2m}(z)} \tag{31}$$

i.e. the number density of electrons per unit z-axis which equals the number density of ionised molecules per unit z-axis as a function of the z-axis position ($\partial N_{\mathrm{c}}/\partial z$ has the one dimensional unit cm^{-1}). This quantity is observed directly by optical LIBD (Section 4, Figure 12), when the position of plasma plumes is imaged by one or two CCD cameras, and the relative number of events is plotted versus position along the laser beam (z-axis). Due to the small number of 'targets', a saturation effect occurs, most prominently in the focal area of high photon flux (central regions, Figure 6). At a certain level of photon flux density, an additional increase in pulse energy does not cause a higher number of events in the central region, because every colloid diffusing therein is ionised with a probability of 1. An increase can only be achieved at the outer regions due to the 'growth' of the effective

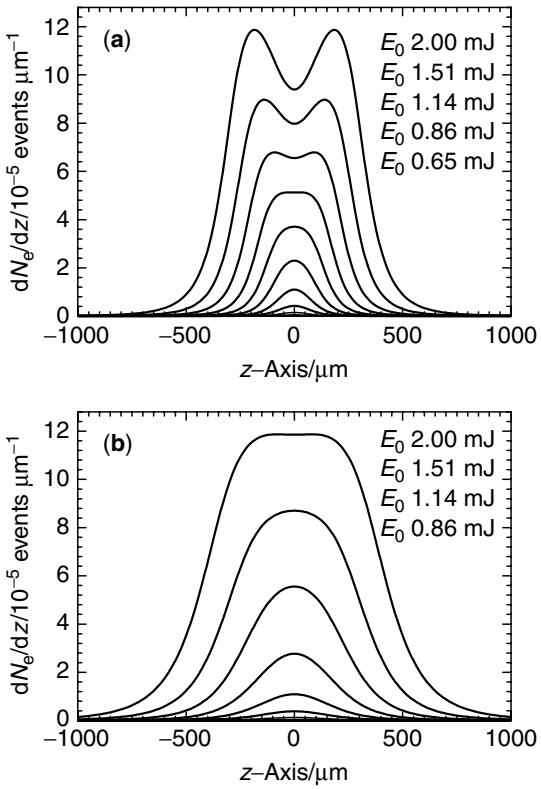

Figure 8. The number density of ionised molecules as a function of the z-axis (along the laser beam). This quantity is observed directly by optical LIBD (Section 4, Figure 12). (**a**) The higher the pulse energy E_0 (given in mJ), the more prominent is the saturation, causing a flat top or even 'hole burning' in the central region of the distribution. (**b**) The hole burning effect decreases as the radius of the Gaussian focus increases from 6.7 to 10 µm

focal volume at large z, as described earlier [equation (22)]. This effect causes a flattening of the distribution function of Figure 8 at the centre and can lead to a local minimum of breakdown events at $z = 0$ at very high pulse energies. For a given pulse energy, this effect is less pronounced for a laser beam of larger diameter in the Gaussian focal plane, because a larger focal volume contains more 'targets' and, accordingly, saturation does not play a role until the pulse energy is increased further.

The 'event density' equation (31) of Figure 8a is integrated numerically according to equation (29) and yields the total event number $N_e(z)$, which is plotted as a function of laser pulse energy E_0 on a double logarithmic scale in Figure 9a. The set of parameters for Example 1 (Table 1) and the pulse energies of Figure 8a were used again here. Deviating from the previous example, the number density of colloids was increased by a factor of 100 from $\rho_C = 4 \times 10^5$ to 4×10^7 particles cm^{-3}. At low pulse energy, in the absence of saturation, the curve has a slope $m = 4$, i.e. the order of the process. As the pulse energy increases and the central region no longer contributes to an event enhancement, the curve merges continuously differentiable into the characteristic growth dependence of the focal volume with a slope $s = 1.5$ [equation (22)] [66].

In the case of 'acoustic LIBD', i.e. the detection by a piezo-detector, the number of events for a single laser shot is not resolved. A single plasma cannot be discriminated

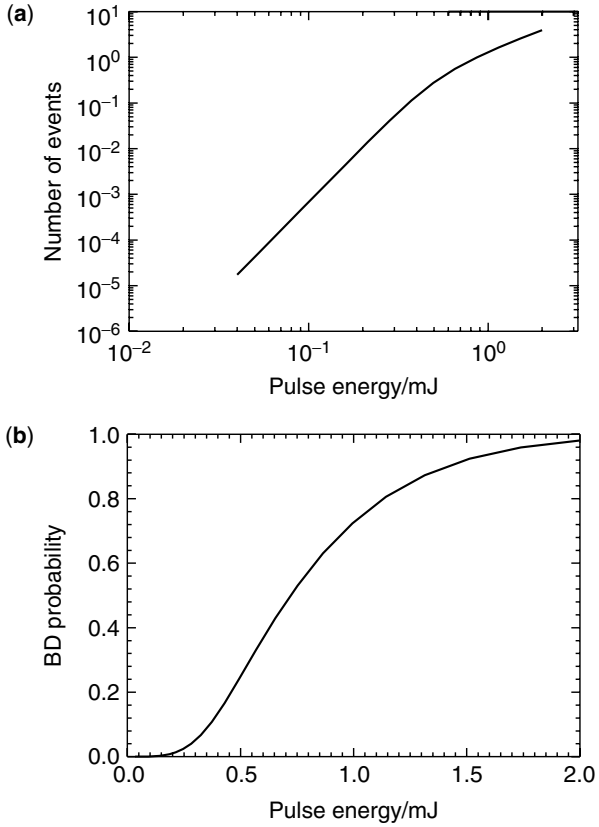

Figure 9. (**a**) Number of breakdown events versus laser pulse energy (log–log plot), taken from the limit as $z \to \infty$ of equation (29). (**b**) The probability of measuring at least one event per laser shot as a function of the laser pulse energy, the so called 's-curve' according to equation (35). These are is the data achieved by an acoustic LIBD experiment

from multiple events (two or more plasma plumes ignited by the same laser pulse). Hence the inverse probability, i.e. the probability of having no event, is taken as an unequivocal measure. Given a 'true' number of events $\overline{\mu}$, the probability (p_N) of measuring a value of N events can be calculated, according to Poisson statistics, as

$$p_N = \frac{\overline{\mu}^N}{N!} \mathrm{e}^{-\overline{\mu}} \tag{32}$$

In the present case, the probability of measuring $N = 0$ events, when the 'true' number should be $\overline{\mu}$, is given by

$$p_0 = \mathrm{e}^{-\overline{\mu}} \tag{33}$$

and the BD probability, which of course is the inverse of measuring *no* event, is

$$p_{\mathrm{BD}} = 1 - \mathrm{e}^{-\overline{\mu}}, \quad \text{with} \quad \overline{\mu} = N_{\mathrm{e}} \tag{34}$$

Figure 9b shows the breakdown probability p_{BD} as a function of the laser pulse energy E_0:

$$p_{\mathrm{BD}}(E_0) = 1 - \mathrm{e}^{-N_{\mathrm{e}}(E_0)} \tag{35}$$

This is the so called s-curve, the direct data one obtains with an acoustic LIBD apparatus (section 4).

Some remarks can be given for the applicability of this model and the restrictions formulated above.

- In the presence of electron donors [74], for particles with a large number of electrons in shallow states (low ionisation energy) [75], or for particles with a large total MPI cross-section ($\gtrsim$300 nm, depending on composition) 'first electrons' might be produced at a pulse energy not yet sufficient to sustain the avalanche process of electron multiplication. In these cases, the bremsstrahlungs term $\eta(E)N_e$ of equation (2) is added in equation (3) and an additional condition is introduced. After the first electron is generated, at least the threshold energy for detection has to be absorbed during the remaining laser pulse. A transition from MPI-dominated to avalanche-dominated breakdown is described for these cases [9]. Detailed investigations on electron multiplication and plasma growth [76] and heating processes [77,78] in aqueous media has been reported [63], mainly in the framework of eye surgery with short pulse lasers [79].
- The photon flux distribution of Figure 6 is only achieved when a perfect Gaussian beam is focused without diffraction by an aberration-free ideal lens. In the literature, most pulsed lasers used for LIBD do not deliver a satisfactory beam quality. In addition, as soon as spherical aberrations and diffraction become relevant, the profile changes drastically and small regions of higher photon flux density occur. Detailed calculations for plane and Gaussian wavefronts and various lens configurations have been discussed [53,80,81]. Within these regions, the probability for MPI is strongly enhanced due to the nonlinear character of the process [equation (1)] and the distribution of events observed by optical LIBD is altered (Section 4, Figure 14) [82].
- Of equal relevance is the evolution of the photon flux density with time. Some lasers do not have a smooth temporal profile but rather exhibit a peak structure enveloped by some kind of Gaussian function (see, for instance, Figure 10). The number and width of these peaks are, determined by the (longitudinal) mode structure of the laser. The strong enhancement of photon flux during the spikes of typically $<$100 ps leads to an increase in c_t [equation (25)] by up to $m!$ (m factorial, m-order of process = number of photons needed for ionisation) depending on coherence and whether or not these modes are locked [83].
- Self-focusing is an additional mechanism of flux density increase which must be considered. For laser pulses of high energy, the refractive index of matter, n_L, is no longer constant. It depends on the strength of the electric field $\mathcal{E}$: $n_L = n + \gamma_L|\mathcal{E}|^2$; γ_L is a material-dependent constant, which amounts to 0.5×10^{-22} m^2 V^{-2} in the case of water [65]. For Gaussian beams, the electric field is higher in the centre than outside, which gives rise to a more pronounced refractive index enhancement in the centre and an overall focusing of the light. It can be shown [65] that the focusing becomes important above a so-called 'critical power' of the beam L_C:

$$L_C = \frac{\varepsilon_0 c_0 \lambda_0^2}{8\pi\gamma_L} \tag{36}$$

where ε_0 is the electric permittivity, c_0 the velocity and λ_0 the wavelength of light in vacuum. The relevance of self focusing even for nanosecond lasers is demonstrated in Section 4, Figure 14.

4 EXPERIMENTAL APPROACHES

In the preceding section, we determined that a molecule of ionisation energy E_I can be ionised by the simultaneous absorption of $m = \mathrm{MOD}(E_\mathrm{I}/h\nu) + 1$ photons of energy $h\nu$, a process that scales with the mth power of the photon flux density. A typical electron ionisation energy (work function) of a solid ranges from 6 to 10 eV [54], and hence m-3–5 for visible light. This process describes the ionisation of a single atom or molecule[8]. For a system of many atoms, the probability of an ionisation process occurring scales linearly with the total number of atoms available. In addition, the efficiency of ionisation depends on the material properties, as does the electron multiplication process by inverse bremsstrahlung. For a dense solid, the process begins much more easily than for a liquid. This point is made use of for particle detection. The pulse energy is chosen to be just below the breakdown threshold of pure water [74]. Whenever a colloid enters the focal region, the threshold for a solid phase applies (which is exceeded) and a plasma is ignited. Because each plasma event corresponds to a single colloid, the relative number of events per predefined number of laser shots (breakdown probability) provides a measure of the colloid number density. The plasma generation mechanism becomes more efficient with increasing colloid size, leading to a pronounced size dependence[9], which is exploited for appraising the colloid size: *Small colloids require a higher photon flux density to ignite breakdown than larger ones, i.e. they have a higher 'breakdown threshold'*.

4.1 BUBBLE DETECTION

The plasma ignition causes different observable signals which can be conveniently used for detection (Figure 1). The first (and most sensitive, especially for ultra-short pulses) is the generation of gas bubbles due to the thermal expansion [77,84], which can be visualised by shining an additional light source through the breakdown area in order to display the shadow of the bubble [75]. In the case of plasmas created by nanosecond-pulses, the gas bubble effect is not used routinely, since the information is only rough.

4.2 DETECTION BY THOMSON SCATTERING

The second detection method is based on the extinction of laser light during the breakdown process. A plasma of electron density ρ_e is translucent for light above the critical (plasma) frequency:

$$\nu_\mathrm{C} = \frac{1}{2\pi}\sqrt{\frac{\rho_\mathrm{e} e^2}{m_\mathrm{e}\varepsilon_0}} \tag{37}$$

[8] More precisely, this depends on the number of electrons in a valence band or, if the bond character of constituents within the particle does not permit delocalisation of electrons, this depends on the number of outer shell electrons in the individual atoms or molecules involved.

[9] This is valid for colloids of different size and similar chemical composition. For limitations, see Section 6.

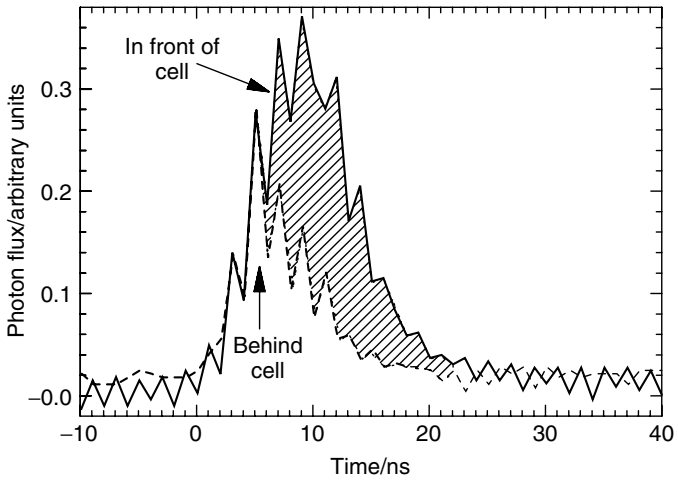

Figure 10. Shadowing of the laser pulse due to Thomson scattering of the incident laser beam at the plasma electrons. Reprinted from Walther, C., Bitea, C., Hauser, W., Kim, J. I. and Scherbaum, F. J. (2002). Laser induced breakdown detection for the assessment of colloid mediated radionuclide migration, *Nuclear Instruments and Methods in Physics Research B*, **195**, 374–388. with permission from Elsevier

where e and m_e denote the electron charge and mass, respectively, and ε_0 is the permittivity of free space. In other words, light of frequency $\nu < \nu_C$ undergoes Thomson scattering [85] and cannot pass the plasma region. By comparing the temporal pulse shapes in front of and behind the quartz cell, as recorded by two photodiodes, this shadowing can be observed directly (Figure 10). During the first few nanoseconds of the laser pulse, no significant extinction of light takes place. When the plasma has evolved to a higher electron density, Thomson scattering [85] weakens the light transmission [86] and the integral of the difference between both curves (hatched area, Figure 10) is a measure of the total extinction. As shown by François *et al.* [87], such an 'induced optical density' contains information on the size and chemical composition of colloids.

4.3 OPTICAL DETECTION

In a third approach, we make use of the photon flux density distribution inside the focal volume (see Section 3). The flux density increases as the beam diameter $r(z)$ decreases. Within the Gaussian laser focus, the isolines of flux distribution resemble a double club with a cylindrical symmetry or peanut-like shape as discussed in Section 3.2. Figure 11a shows a section through the three-dimensional distribution along a plane containing the laser beam axis (see also Figure 6). The focal region typically has a radius of $\sim$5–10 μm and a length of 1–2 mm along the laser axis, much larger than the colloids of interest for LIBD investigations (<100 nm in diameter). Therefore, the flux density is constant within the total volume of the colloid, to a very good approximation, and determined exclusively by the position of the colloid within the laser focus. In other words, different values of photon flux density are present within the focal volume for *fixed* pulse energy and the respective flux density to which a colloid is exposed depends on its position inside the focal volume. By using a microscope lens and a CCD camera, the exact position of the plasma plume can be imaged on a pulse-to-pulse basis for several thousand laser shots and a spatial distribution of BD events can be obtained. This detection scheme is referred to

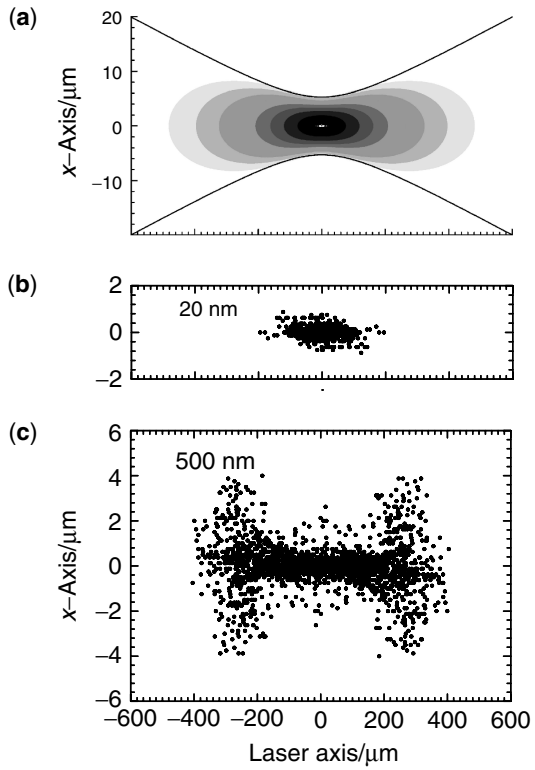

Figure 11. (**a**) Photon flux density distribution in the central region of the laser focus. The grey contour scales indicate a two-dimensional cut through the three-dimensional double-club-like distribution (flux increases from light to dark). Reprinted from Walther, C., Bitea, C., Hauser, W., Kim, J. I. and Scherbaum, F. J. (2002). Laser induced breakdown detection for the assessment of colloid mediated radionuclide migration, *Nuclear Instruments and Methods in Physics Research B*, **195**, 374–388, with permission from Elsevier. (**b**) Small colloids (polystyrene, 20 nm) are exclusively detected in the central region of high flux, whereas (**c**) large colloids (polystyrene, 500 nm) ignite also along the edges at lower flux (pulse energy 0.6 mJ)

as 'optical detection'. Typically, the plasma plume is observed with one camera which is mounted perpendicular to the beam axis [27]. A recent observation by two cameras from directions perpendicular to each other was also reported, allowing a true three-dimensional assignment of position and photon flux [34]. As discussed above, the smaller the colloids, the higher is the breakdown threshold, i.e. the higher is the photon flux density required for plasma formation. Applied to the spatially resolved observation, small particles are exposed to sufficiently high photon flux density only in the central region, whereas for large colloids the low flux density at the 'wings' of the focal area still suffices to ignite a plasma. Figure 11 illustrates this behaviour on polystyrene spheres of different diameters recorded at the same laser pulse energy (0.6 mJ). All events of 20 nm spheres are centred tightly around the Gaussian focus with a rather small spread along the laser axis. The plasma plumes ignited on 500 nm colloids are distributed over a much wider region along the iso-flux lines. For the same data, the number of events per unit length along the laser axis is shown in Figure 12. Adapting the evaluation method of [30], the 20 nm particles (a) are fitted by a Gaussian of $l_z = 92$ μm width (denoted 'ignition length'), whereas the 500 nm particles (b) result in an ignition length of $l_z = 334$ μm. The Gaussian function

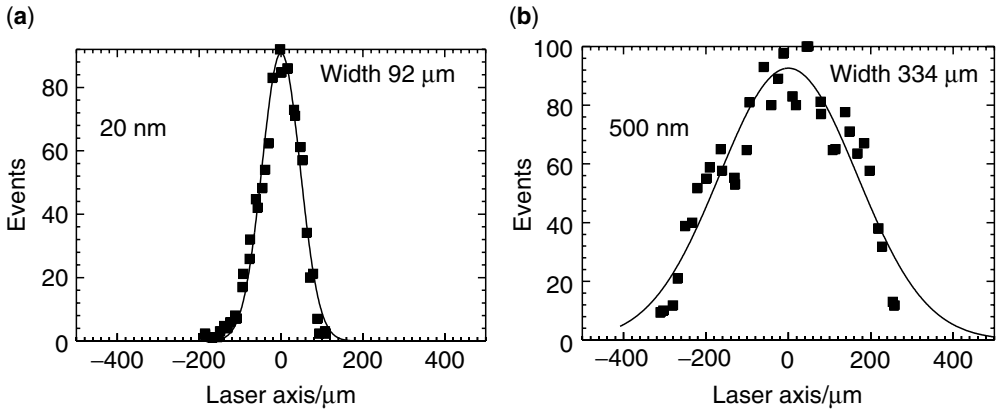

Figure 12. For the data of Figure 11, the number of events per unit length along the laser axis is shown. (**a**) The 20 nm particles are fitted by a Gaussian of 92 μm width (denoted 'effective focal length'), whereas the 500 nm particles (**b**) result in a focal length of 334 μm

was used for a convenient approximation in [30]. Since this plot represents the experimental counterpart of Figure 8, the distribution is more exactly described by equation (31). After an appropriate calibration with reference particles, the ignition length can serve as a measure of average particle size (for material dependence, see Section 6). The colloid concentration scales linearly proportional to the BD probability.

An example of an optical LIBD apparatus is the mobile version used for deep underground *in situ* measurements (Section 5.5). The light emission of each plasma event is recorded two-dimensionally (Figure 13a) and the 'centres of gravity' of these intensity profiles are plotted versus their position along the laser axis (*cf.* Figure 12). The resulting distribution can be approximated by a Gaussian curve of full width at half-maximum (FWHM) l_z (ignition length) (Figure 13b). l_z increases monotonously with the average size of colloids [30] and allows for the calibration of ignition length versus size (Figure 13c).

It is essential to preserve the spatial Gaussian profile of the laser beam. When using refractive optics, a major source of beam disturbance are spherical aberrations of the focusing lens(es). Morgan [53] calculated the isophotes (lines of equal photon flux density) for different values of the so called 'aberration function', Φ_{max} [64]. This function depends on focal length, refractive index and the ratio of unfocused beam diameter to lens diameter. Simplified, the aberration becomes stronger as the unfocused beam becomes larger relative to the size of the lens and the focal length becomes shorter. Hence the focusing of a large beam at short distances into the sample should be avoided. Figure 14 shows the calculation for $\Phi_{max} = 0.5\lambda$ [53]. Since for polystyrene the BDP depends on the fourth power of the power density, I^4, the fourth power of the isophotes is plotted and compared with respective measurements on 500 nm polystyrene particles (Figure 14a). For illustration purposes, an unfavourable optics configuration is chosen. The distribution of BD events reflects the asymmetry of the flux profile and the additional region of high flux at $z \approx -500$ μm results in additional events at the respective positions.

With increasing pulse energy, self-focusing can become important. As discussed above [equation (36)], this process depends on the power (energy/time) during the laser pulse. For the parameters given in Table 1, the critical power is $L_C = 6 \times 10^5$ J s^{-1}. For a smooth Gaussian temporal pulse profile, this corresponds to 6 mJ. In the case of short spikes due

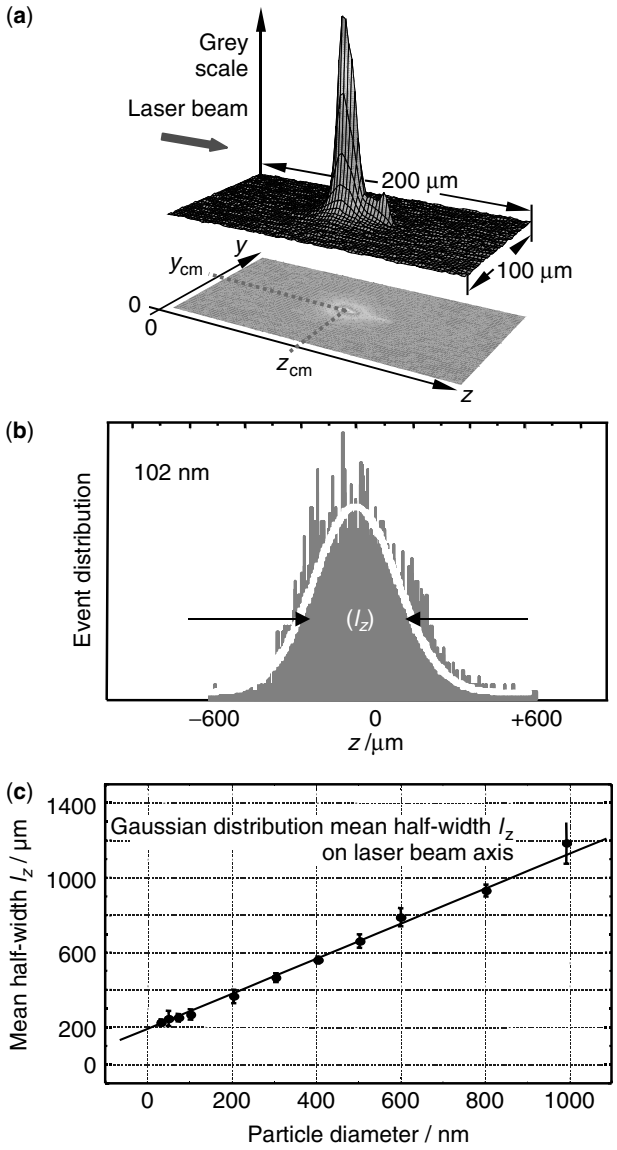

Figure 13. (**a**) A single particle breakdown event in a three-dimensional visualisation. (**b**) Breakdown events accumulated in the laser focus volume as they appear in a Gaussian distribution. (**c**) Calibration of FWHM (full width at half-maximum) values l_z (ignition length) as a function of particle diameter. Reprinted from Hauser, W., Geckeis, H., Kim, J.I. and Fierz, Th., A mobile laser-induced breakdown detection system and its application for the *in situ* monitoring of colloid migration, *Colloids and Surfaces A*, **203** 37–45, Copyright 2002, with permission from Elsevier

to coherence effects of the laser (see Figure 10 and the respective discussion), the temporary power, however, might be much higher: a 100 ps spike of 100 µJ energy corresponds to $P = 10^6$ W. The focal length of the self-focusing is calculated according to

$$z_f = \frac{\pi r_0^2}{\lambda_0 \sqrt{(P/L_c) - 1}} \tag{38}$$

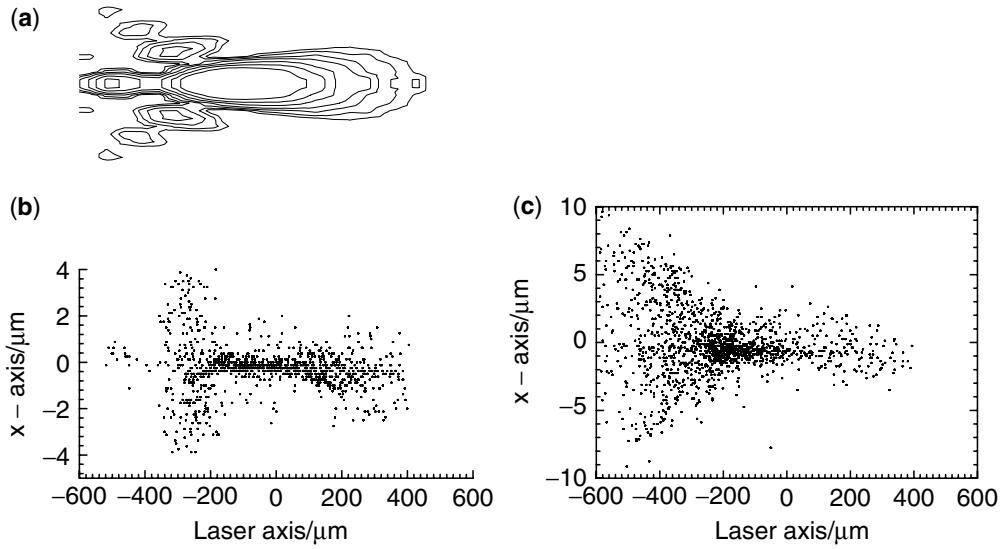

Figure 14. The position of plasma events within the focal volume, observed directly by a CCD camera as in Figure 12. (**a**) Spherical aberration disturbs the ideal flux profile of Figure 6 (according to Morgan, C. G. (1975). Laser-induced breakdown of gases, *Rep. Prog. Phys.*, **38**, 621–665.) and, as a consequence, the distribution of BD events is deformed (**b**) (polystyrene, 500 nm, $E_0 = 0.7$ mJ). (**c**) With increasing pulse energy of the laser, self-focusing occurs, which becomes prominent for the system of Table 1 at $E_0 = 2.6$ mJ (polystyrene, 500 nm)

Figure 14 shows the results of an experiment at $P = 1.1L_C$, which should lead to a focal length $z_f = 500$ μm. This is in accordance with the shift of breakdown events towards the laser.

Aberration and self-focusing complicate the determination of the ignition length and of the effective focal volume where a breakdown is generated. The optical layout, focusing conditions and pulse energies should be chosen in such a way as to minimise these effects when using LIBD as a quantitative tool for colloid detection.

4.4 LASER-INDUCED BREAKDOWN SPECTROSCOPY

In addition to detecting the position of a breakdown event, the optical emission can be analysed spectroscopically. For bulk samples, LIBS is well established as a standard method for quantitative element analysis [16]. Colloidal suspensions can be analysed in the same way [88], as discussed in the Introduction. The emission signal from the particles is well discriminated against the background from ionic species. By use of double pulse techniques and excitation of the evaporated material in the gas bubble, the detection limit is lowered to the 10^{-6} g dm^{-3} range. However, no true 'single-colloid spectroscopy' has been reported. In order to achieve a good background-to-noise ratio, many colloids have to be present either in the focal volume at a time, or the signals of many single events have to be averaged. While multi-element analysis of solids by LIBS has become a routine method, various line-broadening mechanisms (up to several nanometres) complicate speciation in aqueous media. LIBS on colloids in suspension is hence limited to samples of well-defined and homogeneous composition. For examples, see Section 5.9.

4.5 ACOUSTIC DETECTION

The fourth approach uses the shock wave caused by thermal plasma expansion [84], which creates a strong sound in the case of nanosecond-laser excitation, audible even to the human ear, that can easily be detected by a piezo crystal [89] attached to a quartz cell perpendicular to the laser beam. The BDP is measured by counting the number of shock waves [7,8,22,27,34] relative to the total number of laser shots (if 100 shock waves occur for 1000 laser shots, the BDP is 10%). In contrast to optical detection, BD events are not recorded with a spatial resolution and no information on the photon flux density of a single plasma is obtained. The weighted average flux density of the total focal volume is, however, known. When probing BD at different flux densities, the average pulse energy has to be varied by the use of devices such as crossed Glan polarisers [34]. The pulse energy is monitored by a pyroelectric detector and the energy is recorded along with the acoustic signal for every single laser shot by a transient recorder. In such a case, the BDP as a function of pulse energy E_0 results in an 's-curve', as discussed in Section 3 [equation (35)]. The total cross-sections for MPI and IB increase proportionally to the particle volume (proportional to the number of valence electrons in the particle) and hence the breakdown threshold E_T decreases with increasing particle size (Figure 15a) [25,34]. The slope of the curve scales with the particle concentration (Figure 15b); see also equation (39) and detailed discussion thereafter. At very low concentrations (50 ppt), the BDP increases strongly when the background due to the ultrapure water becomes effective (here ~3 mJ). The use of reference colloids of well-defined diameters provides a calibration for relating breakdown thresholds to particle size. For an unknown sample, the threshold is determined by recording the s-curve and subsequently converted to the particle diameter. If the sample contains colloids of more than one size (size distribution), the single 'diameter' obtained by this method is of limited value and should only be regarded as a mean diameter for fast comparative measurements (*e.g.* if one observes aggregation of colloids time resolved). It is highly recommended to use the multimodal evaluation instead (Section 4.7).

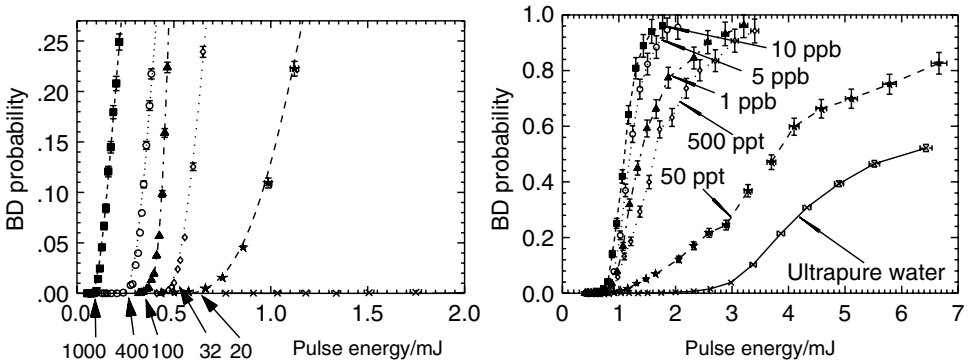

Figure 15. Acoustic detection: the breakdown probability (BDP) is plotted as a function of the laser pulse energy. (**a**) The threshold E_T of the so-called 's-curves' increases with decreasing particle size (polystyrene reference spheres). (**b**) While the threshold remains constant, the slope changes with colloid concentration (polystyrene, 20 nm). Reprinted from Walther, C., Bitea, C., Hauser, W., Kim, J. I. and Scherbaum, F. J., Laser induced breakdown detection for the assessment of colloid mediated radionuclide migration, *Methods in Physics Research B*, **195**, 374–388. 2002, with permission from Elsevier

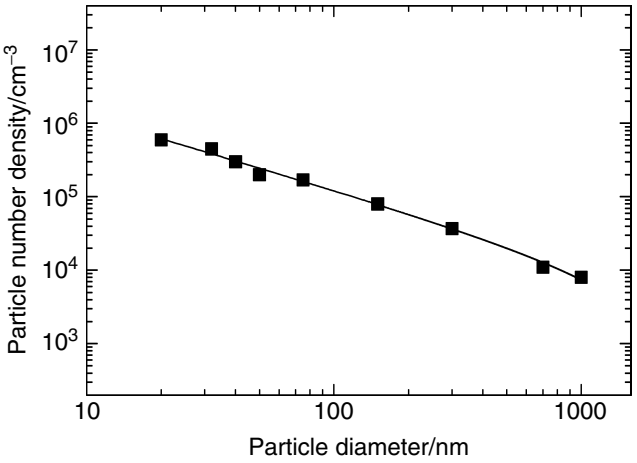

Figure 16. LIBD is capable of detecting particles with diameters between ~10 and 1000 nm. The limit of detection (LOD), plotted as particle number density versus diameter, scales almost linearly with size, allowing detection in the 10^{-9} g dm^{-3} concentration range. Reprinted from Walther, C. (2003). Comparison of colloid investigations by single particle analytical techniques – a case study on thorium-oxyhydroxides, *Colloids and Surfaces A*, **217**, 81–92, with permission from Elsevier

The limit of detection (for both optical and acoustic detection) is only weakly size dependent and determined by the probability of finding a colloid in the laser focal volume [22], crudely estimated by $\pi r^2 z \approx 10^{-6}$ cm^3 for small colloids. Since the effective focal length increases with increasing particle size, the effective focal volume for 1000 nm particles is 10-fold greater than for 20 nm colloids. Assuming a photon flux that is sufficient to induce a breakdown for every colloid entering the focal volume, we expect a BDP $p_{BD} = 0.1$ for a particle number density of 10^5 particles cm^{-3} (Figure 16). In the range <50 nm, the detection efficiency is comparable to that of fluorescence correlation spectroscopy (FCS, Chapter 11), which, however, requires fluorescing particles or the addition of dyes. For small colloids, the sensitivity is clearly superior to the widely used dynamic light-scattering techniques. Single particle counting [90,91] and other static light-scattering [71,72,92] methods are more sensitive for colloids >100 nm but the operational range becomes limited below *ca.* 80 nm [93,94] where concentrations are required which far exceed those of natural waters [95] (see also Section 6). Recently Particle Measuring Systems (PMS) [96] claimed to have reached a detection limit of 50 particles dm^{-3} for 30 nm particles. However, to our knowledge, no applications in environmental science have been reported so far.

4.6 COMPARISON OF OPTICAL AND ACOUSTIC LIBD

The acoustic set-up requires less equipment and is cheaper and easier to implement. In order to attain statistically sound measurements, a minimum of 1000 laser shots are needed for each of at least 20 different pulse energies. For a 20 Hz laser, this amounts to a total measurement time of >15 min. An optical system, which allows shorter measurement cycles to be used, requires a camera, a frame grabber, software and a microscope lens, which increase substantially the price of the instrument. One thousand events are sufficient for a satisfactory measurement; BDP = 0.2 corresponds to 5000 laser shots or 4 min.

However, speed is paid for by limitations of the dynamic range. Whereas the acoustic detection is applicable for colloid concentrations from approximately 10^{-9} g dm^{-3} to several 10^{-3} g dm^{-3}, optical detection can only cover three orders of magnitude without changing pulse energy. This is evident from the fact that, to a first approximation, the BDP scales linearly with concentration. If, for instance, a suspension of 50% BDP is diluted by a factor of 1000, the BDP decreases to 0.05%. Two million lasershots or 1 day would then be needed to achieve 1000 events. Increasing the pulse energy solves the problem only partially. The number of events will increase and the time required for the measurement will decrease. However, since the effective focal volume depends on the pulse energy, any change in the pulse energy requires a renewed calibration of the system. In order to achieve maximum sensitivity, the working pulse energy is chosen just below the threshold of ultrapure water, i.e. below 0.1% BDP. In this manner, dilute suspensions (*e.g.* 10^4–10^7 particles cm^{-3}) of size classes 10–1000 nm are accessible. In order to investigate more concentrated samples, the pulse energy should be lowered. Alternatively, for concentrations $>10^8$ particles cm^{-3}, complementary methods, *e.g.* photon correlation spectroscopy (PCS), can be applied, at least for particles larger than 100 nm.

4.7 MEASUREMENT OF SIZE DISTRIBUTION BY ACOUSTIC LIBD

Thus far, ideal, monodisperse samples have been discussed. Although these might be of interest in the laboratory, they are of less relevance in nature where size distributions extend over several orders of magnitude. In the case of optical detection, each size corresponds to an ignition length $l_z^{(i)}$ and for a given size distribution, one observes a superposition of various $l_z^{(i)}$. For the simple case of a bimodal distribution, a small Gaussian curve due to the small colloids is superimposed on a broad curve due to the large particles [29], much like summing the data of Figure 12a and b. So far, this effect has not been evaluated quantitatively for more than two size fractions. For polydisperse samples, an evaluation scheme based on s-curve detection has been developed recently [97].

In the following, the s-curves are described by a semi-empirical model with only two free parameters [equation (39)]. The breakdown threshold E_t is a measure of the particle size and the concentration determines the constant C:

$$p_{\text{mono}}(E_0) = 1 - \left\{(1 + C(E_0 - E_t) - \frac{1}{2}[C(E_0 - E_t)]^2 + \frac{1}{6}[C(E_0 - E_t)]^3\right\} \exp[-C(E_0 - E_t)] \tag{39}$$

In this case, the 'first electron' is generated by four-photon ionisation in the present case ($h\nu = 2.3$ eV, $IP_{\text{Polystyrene}} = 8.9$ eV) such that at low pulse energy E_0, a $p_{\text{mono}} \propto E_0^4$ dependence is required [98]. If one expands equation (39) in a Taylor series, the first three terms up to $(E_0 - E_t)^3$ cancel, which results in the $\propto E^4$ dependence. The negative sign of the quadratic term causes a weak second-order (E^2) dependence which approximates the increase in the effective focal volume $V_{\text{eff}} \propto E^{\frac{3}{2}}$ as the pulse energy is increased [66]. Since the probability of detecting a colloid scales linearly with the focal volume, the breakdown probability also increases. $p_{\text{BD}}(E_0)$ approaches unity asymptotically as $E_0 \to \infty$.

Strictly, equation (39) describes the BDP for a suspension containing colloids of only one size (monomodal). For a size distribution, it is possible to make use of the weak size dependence[10] of LIBD sensitivity (Figure 16). Whereas light scattering methods suffer from a decrease in signal proportional to d^{-6}, the detection limit of LIBD increases linearly with particle diameter from $\sim 10^3$ particles cm^{-3} at 1000 nm to $\sim 10^5$ particles cm^{-3} at 10 nm due to the increase in effective focal volume with increasing particle size [22]. As a consequence, size screening of small particles by the simultaneous presence of large ones is weak, a key to our approach of measuring size distributions. For a bimodal colloidal suspension containing particles of sizes d_1 and $d_2 < d_1$, with thresholds $E_t^{(2)} > E_t^{(1)}$, the s-curve will be identical with a pure sample of the first fraction of the colloids below the threshold of the second fraction. As the pulse energy increases and exceeds the threshold of the smaller size class $[E_t^{(2)}]$, the latter will contribute to the sum curve. Each point of the s-curve represents a probability. 'Adding' two s-curves is the equivalent of determining the probability of either the fraction of colloids with d_1 or the fraction of colloids with d_2 generating an event (logical OR). Such a probability is defined as one minus the product of the probabilities of no breakdown occurring:

$$p_{Bi} = 1 - (1 - p_1)(1 - p_2) \tag{40}$$

Combining equations (39) and (40), we obtain

$$p_{Bi} = 1 - \prod_{i=1}^{2} \left\{ 1 + C^{(i)}[E_0 - E_t^{(i)}] - \frac{1}{2}[C^{(i)}(E_0 - E_t^{(i)})]^2 + \frac{1}{6}[C^{(i)}(E_0 - E_t^{(i)})]^3 \right\} \exp[-C^{(i)}(E_0 - E_t^{(i)})] \tag{41}$$

where $E_t^{(i)}$ and $C^{(i)}$ are the threshold and the parameter of the colloid number density, respectively. Equation (11) is easily extended for any number of size classes. To appraise the size distribution of an unknown sample, the s-curve is measured and the above product of convoluted exponentials is fitted to the data.

In practice, it is necessary to limit the number of free fitting parameters. In the following example of six size classes, i.e. 20, 30, 40, 50, 70 and 100 nm, the thresholds $E_t^{(i)}$ are obtained by calibration with monodisperse polystyrene reference spheres and remain fixed thereafter. Monomodal suspensions of varying concentration are measured to calibrate the slope parameter $C^{(i)}$ versus the colloid number density per unit volume ρ_C according to the semi-empirical equation

$$\log C^{(i)} = a^{(i)} \log[b^{(i)} \rho_C^{(i)}] \tag{42}$$

To obtain the size distribution, the s-curve of a sample is measured with optimal statistics, especially in the low pulse energy region, i.e. the region that contains the size information. Increasing the particle size from 20 to 100 nm causes a decrease in threshold $E_t^{(i)}$ by a factor of 2 (from 0.5 to 0.28 mJ for the present optics set-up), which is

[10] This is valid for colloids of similar chemical composition. For limitations, see Section 6.

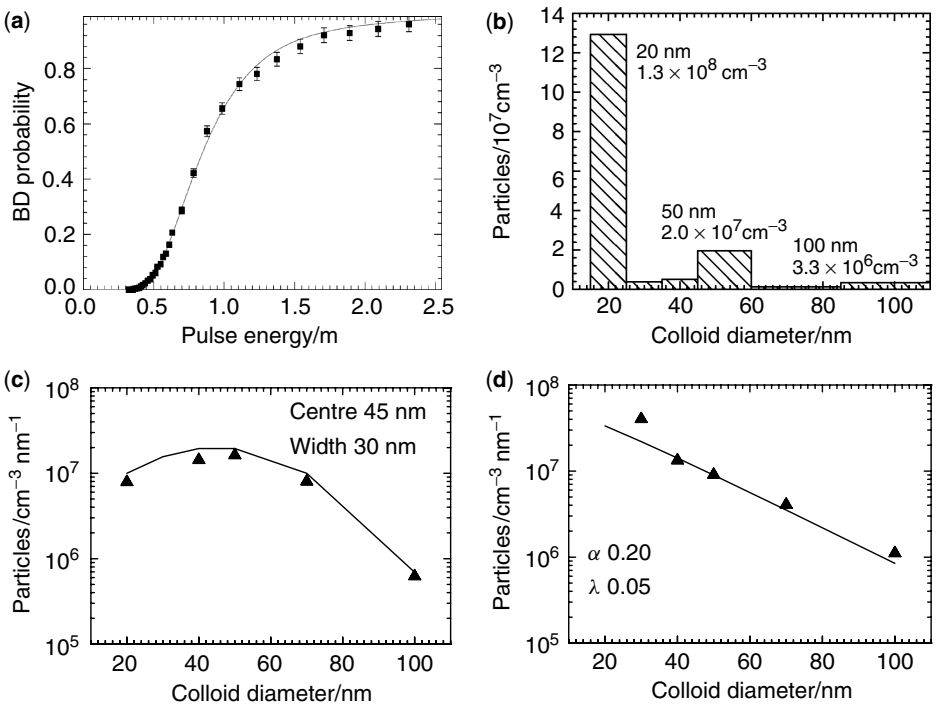

Figure 17. Particle size distribution (PSD) of polystyrene particles are reproduced typically within 20% error: **(a)** the relative number of breakdown events (BD probability) as a function of the laser pulse energy for a three modal colloid sample. **(b)** From the fitted curve the PSD is appraised. Reprinted with permission from Walther, C., Cho, H. R. and Fanghänel, Th. (2004). Measuring multimodal size distributions of aquatic colloids at trace concentrations. *Appl. Phys. Lett.*, **85**, 6329–6331. Copyright 2004, American Institute of Physics. Synthetic distributions (solid lines) following a Gaussian function **(c)** and a gamma function **(d)** are compared with the measured values (▲)

small compared with the typical energy interval of a complete 's-curve' (as depicted in Figure 17a). Equation (41) is then fitted to the data. The threshold parameters, $E_t^{(i)}$, remain fixed, since they determine the size classes, and only the concentration parameters $C^{(i)}$ are varied. In spite of six parameters being fitted simultaneously, the fit turns out to be robust. The parameters hardly affect one another, but rather each parameter is sensitive to a unique region of the s-curve. $C^{(1)}$ is determined solely in the region below $E_t^{(2)}$, the threshold of the second size class; $C^{(2)}$ is most sensitive at energies $E_t^{(2)} < E_0 < E_t^{(3)}$, and so forth. The size classes need to be separated sufficiently that several different pulse energies can be measured between $E_t^{(i)}$ and $E_t^{(i+1)}$. Typically the mean values of neighbouring size classes differ by at least 25%. Figure 17 illustrates the case of a trimodal sample of polystyrene reference beads: 1.5×10^8 particles cm^{-3} of 20 nm diameter, 2.0×10^7 particles cm^{-3} of 50 nm and 2.7×10^6 particles cm^{-3} of 100 nm. They are combined in order to simulate a Pareto-like particle size distribution as is found in natural waters. The differential number density of different sizes $\partial\rho_C(d)/\partial d$ scales as a power law of the particle diameter d:

$$\frac{\partial\rho_C(d)}{\partial d} \propto d^{-\beta}; \qquad 3 < \beta < 5 \tag{43}$$

In Figure 17a, the raw data, i.e. the number of breakdown events as a function of the laser pulse energy, are plotted. Note the high quality of the data at low pulse energies, which is crucial to achieve meaningful results. All six concentration parameters $C^{(i)}$ are varied and the results displayed in the histogram in Figure 17b. $C^{(1)}$, $C^{(4)}$ and $C^{(6)}$ yield finite values, whereas $C^{(2)}$, $C^{(3)}$ and $C^{(5)}$ remain close to zero, which demonstrates that little crosstalk[11] to lower channels exists. The particle number concentrations are reproduced with an approximately 20% error down to $\sim 10^8$ particles cm^{-3}, which is about two orders of magnitude more sensitive than the combination of FFFF and LIBD [51]. The method is applicable to continuous distributions with a size resolution of approximately 20% (i.e. 40 and 50 nm particles can be distinguished), as shown for the case of a synthetic gaussian distribution (Figure 17c):

$$\mathrm{d}N(d)/\mathrm{d}d \propto \exp[(d-\mu_\mathrm{G})^2/\sigma_\mathrm{G}^2],\ \mu_\mathrm{G} = 45\ \mathrm{nm},\ \sigma_\mathrm{G} = 30\ \mathrm{nm} \tag{44}$$

and for a gamma distribution (Figure 17d)

$$\mathrm{d}N(d)/\mathrm{d}d \propto d^{\alpha_\gamma} \exp[-d\lambda_\gamma],\ \alpha_\gamma = 0.2,\ \lambda_\gamma = 0.06 \tag{45}$$

If, however, a sample contains a predominant fraction of large colloids, some size-screening effects may occur. Colloids do not contribute to the sum curve below their specific threshold $E_\mathrm{t}^{(i)}$. In order for the contribution of small colloids (at comparatively high energy) to be of measurable relevance, the signal caused by the large colloids must remain sufficiently low. As the s-curve $p(E_0)$ approaches unity, an additional increase due to a fraction of very small sizes can no longer be resolved.[12]

5 APPLICATIONS

This chapter deals mainly with the characterisation of aquatic colloids by LIBD. In addition, some interesting applications of LIBD to aerosols will be mentioned briefly. As discussed in Chapters 1 and 2, colloids are ubiquitous in all kinds of natural waters [23,27,48, 90,99–101]. Variations of their size distribution, chemical composition and stability are attributed to their biogeochemical origin, either by nucleation or by dispersion. Natural aquatic colloidal systems generally contain very small particles at relatively low concentrations [48,49,91,102–107], and their detection may be complicated by the simultaneous presence of larger particles that have no enduring stability and hence may precipitate over time. The advent of LIBD [3,5–16,22,93] has made it possible to visualise such small and stable aquatic colloids. It is less well known that also in laboratory systems, even in chemicals of ultra-high purity, there are always colloids present [8–10]. Their presence is increasingly relevant when working in very dilute systems [39,41,43–45]. On the other hand, nanoscopic chemical reactions of actinides under environmental conditions can be masked by the presence of aquatic colloids [31,32,48,49]. LIBD is therefore applied to study the environmental significance of aquatic colloids [27–37].

[11] This crosstalk, i.e. a phantom signal in small size classes which results from large colloids, is a severe problem in the case of static light scattering [91].

[12] Recently, an increase of the size range and number of channels has been reported [82,84]. By taking into account the effects of spherical aberations, size distributions from 15–400 nm can be measured by LIBD.

5.1 AQUATIC COLLOIDS IN DRINKING WATER

LIBD allows the size and concentration of aquatic colloids present in potable water to be investigated. As the present book treats environmental colloids, it is appropriate to comment on the amount of aquatic colloids that we consume. LIBD facilitated the investigation of purified Bodensee waters (drinking water) with respect to their low colloid contents [108–110]. Bundschuh *et al*. measured the breakdown probability of several waters and found that river water (Hirschbach, Frauenau, Germany) contained far more colloids than mineral waters, which in turn had a higher colloid content than tap waters [27]. Figure 18 shows a similar comparison of different commercial mineral waters, laboratory tap water and ultrapure water (MilliQ). Their particle size range is measured as less than 200 nm, as equivalent to spherical diameter, and the predominant number density is in the range below 50 nm. Corresponding mass-weighted mean number densities varied from 10^{11} to 10^{14} particles dm^{-3} (Figure 18). Particle size distributions could not be measured by that time [27]. On average, water in plastic bottles contained less colloids than sparkling water in glass bottles. Carbonate may augment colloids but also glass leaching probably caused higher colloid concentrations.

5.2 COLLOID FORMATION AND THERMODYNAMIC EQUILIBRIA

An interesting application of LIBD in laboratory systems is in the determination of the solubility of sparingly soluble metal hydroxides [39,41,43–46]. Metal ions of higher oxidation state with $Z \geqslant 3+$ readily undergo hydrolysis in the acidic pH region and polynucleation leads to colloid formation with increasing pH. LIBD can be applied to monitor the pH edge at which such colloid formation begins [43–45]. If the hydrolysis constants of the metal ion are known, the solid–liquid equilibrium reaction can be evaluated from the pH edge of colloid formation.

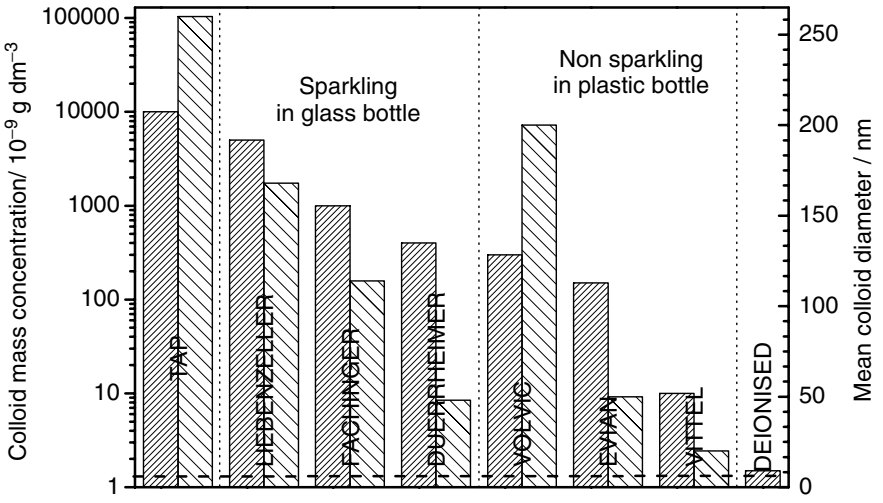

Figure 18. Aquatic colloids present in different kinds of drinking water as observed by LIBD. The mass concentration is estimated to be 10^{-5} g dm^{-3} in tap water down to 10^{-8} g dm^{-3} in Vittel bottled water (left bars) with average sizes range <200 nm in diameter (right bars). The horizontal dashed line indicates the detection limit of LIBD

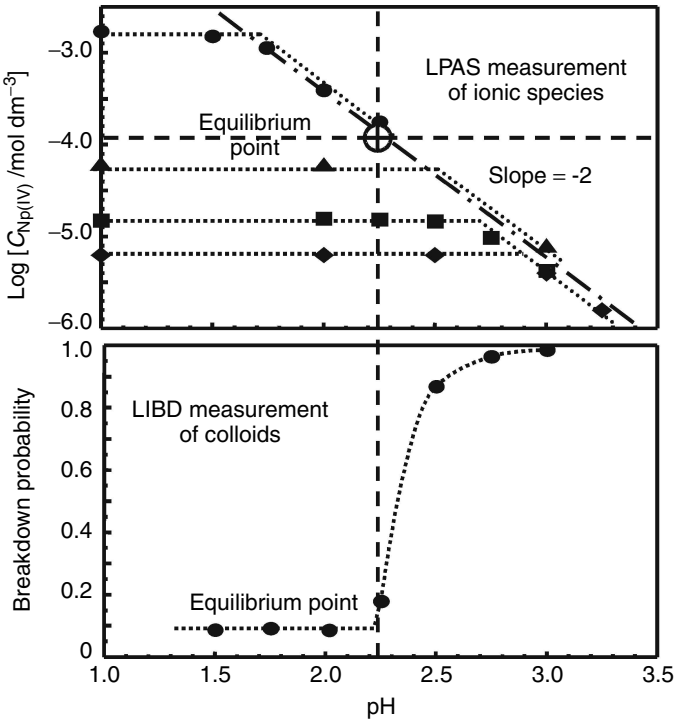

Figure 19. A combination of LPAS and LIBD experiments: the abundance of ionic Np(IV) relative to total Np concentration in solution shows a threshold-like decrease at a certain pH as measured by LPAS. The pH threshold depends on the total Np concentration **(a)**. It is shown by LIBD that at the pH threshold colloids form, which explains the decrease in ionic Np(IV) **(b)** [3×10^{-5} mol dm^{-3} Np(IV)]. Reproduced from Neck, V., Kim, J. I., Seidel, B. S., Marquardt, C. M., Dardenne, K., Jensen, M. P. and Hauser, W. (2001). A spectroscopic study of the hydrolysis, colloid formation and solubility of Np(IV). *Radiochim. Acta*, **89**, 439–446, by permission of Oldenbourg Wissenschaftsverlag GmbH

A typical example is demonstrated in Figure 19 for the hydrolysis of Np^{4+} either in H_2O or in D_2O [43]. The speciation of Np(IV) was performed by LPAS (laser-induced photoacoustic spectroscopy) as a function of pH (Figure 19a). The absorbance of Np(IV) at 724 nm (143 dm^3 mol^{-1} cm^{-1}) was observed with varying pH. A region of constant absorbance is followed by a sharp decrease at a pH edge. Simultaneously, the colloid content of the Np(IV) solution at 3×10^{-5} mol dm^{-3} was measured by LIBD as a function of pH (Figure 19b). With increasing pH, only the background signals of LIBD were observed up to pH 2. The first colloid signal appeared at pH 2.25, which then increased further with increasing pH. This pH edge coincided with the absorptivity decrease of LPAS measurements at $(3.0 \pm 0.5) \times 10^{-5}$ mol dm^{-3}. In previous studies, the absorptivity decrease was attributed to the formation of hydrolysed species, which were supposed to have a lower molar extinction coefficient than the free Np(IV) ion. However, in [43] the co-occurrence of an absorptivity decrease and colloid formation at the same pH edge suggested that all $Np(OH)_n^{4-n+}$, $n = 0$–2 have equal absorption coefficients and the decrease in absorptivity is rather due to the formation of (non-absorbing) polynuclear species.

The edges of colloid formation were shifted to higher pH with decreasing Np(IV) concentrations and led to a slope of 2 for all measurements, which showed that the

colloids were formed from the hydrolysed species $Np(OH)_2^{2+}$:

$$n[Np(OH)_2^{2+}] + 2H_2O \rightleftharpoons Np_nO_{2n-x}(OH)_{2+x}(\text{colloid}) + (2n + x)H^+$$

According to this reaction, the colloids may have evolved with time and formed precipitates such as $NpO(OH)_2$ or $Np(OH)_4$, or a mixture of both, depending on the pH. The solubility product of such a mixture was estimated to be $\log K_{sp} = -54.4 \pm 0.4$, obtained by use of the known hydrolysis constant for $Np(OH)_2^{2+}$. Similar work has been performed for Th(IV) [44–46], Pu(IV) [39,41] and Zr(IV) [117]. A comparable experiment for Eu(III) employing LIBS has also been published [19] (Section 5.9).

5.3 ALUMINOSILICATE COLLOIDS

Silicon and aluminium are omnipresent in natural water, the former in near mmol dm^{-3} concentrations and the latter in μmol dm^{-3} concentrations. Both elements are known as major components of various clay minerals in any geological environment and hence are present in all natural aquatic systems [48,49]. They readily form polynuclear species that may act as crystallisation cells (kernels) of larger aquatic colloids. In the course of the formation of such hydroxyl aluminosilicate colloids, many trace metal ions of high oxidation state (in particular actinides) can be incorporated [48,49]. The process results in the formation of actinide pseudo-colloids. Therefore, aquatic colloids may play a carrier role to facilitate the migration of metals (and other pollutants) in aquifer systems [105]. Consequently, the migration behaviour of colloid-borne metals is of environmental significance. Although the mass concentration of aquatic colloids is very low, their number density is in general high, particularly for small (<50 nm) colloids. The long-term safety assessment of nuclear waste repositories represents one example [111,112], where the possible migration of colloid-borne actinides in the course of time from a nuclear waste disposal site can be, for obvious reasons, of radiological importance.

A heterogeneous nucleation of aluminosilicate colloids with trace actinides has been investigated systematically [48,49] with LIBD and also other methods. A particular part of such an investigation is illustrated in Figure 20 [48]. Mixing of an acidic Al solution (10^{-5} mol dm^{-3}) containing 5×10^{-8} mol dm^{-3} Am with alkaline Si (10^{-3} mol dm^{-3}) resulted in a three-phase equilibrium: ionic phase, colloidal phase and an aluminosilicate precipitate. In order to separate solute species and small colloids from the precipitate, a 450 nm filtration was performed. The amount of Am found in the filtrate showed a minimum at pH 6 (Figure 20a), where the aluminosilicate solubility was the lowest. Am was found both in the colloidal and in the solute fraction. For pH > 5, most of the Am was incorporated into colloids (Figure 20b).

The formation of aluminosilicate colloids was examined under non-perturbed conditions (Figure 20c). Many laboratory chemicals of even the highest purity grade contain colloids typically at concentrations of the order of 10^{-6} g dm^{-3}. In particular, strong bases suffer from colloidal contaminations. In the present case this was true for one of the stock solutions for titration, i.e. Si in 0.03 mol dm^{-3} NaOH. In contrast, the second stock solution, i.e. Al in 0.03 mol dm^{-3} HCl, was prepared colloid free. Three titrations were performed. The Al–HCl mixture was titrated with NaOH to higher pH (Figure 20c, 'Al'). HCl was

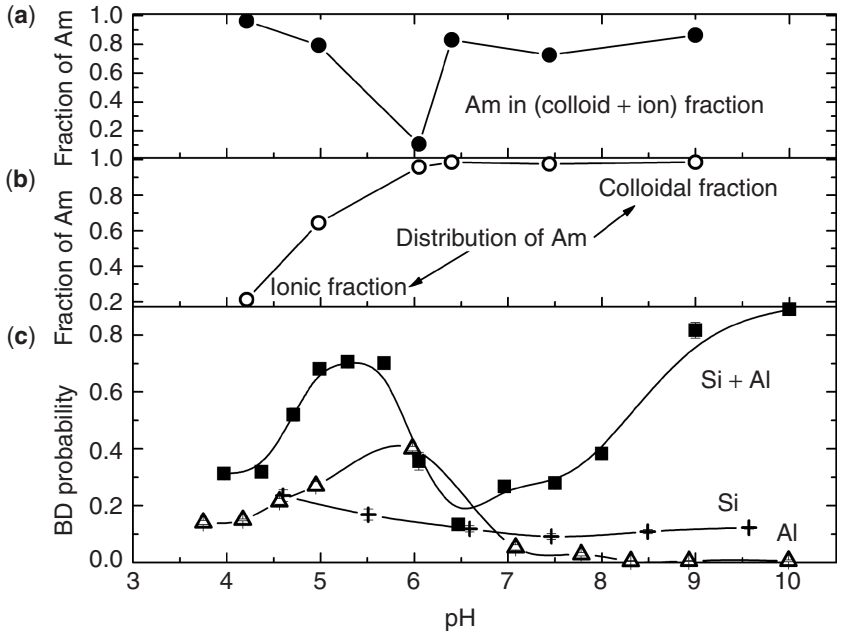

Figure 20. Formation of aluminosilicate colloids and colloid-borne Am in a mixture of 10^{-3} mol dm^{-3} Si, 10^{-5} mol dm^{-3} Al and 10^{-8} mol dm^{-3} Am. Am is distributed into three phases: ions, colloid and precipitate. **(a)** The amount of Am in either colloidal or ionic phase shows a minimum around pH 6. **(b)** Within the (colloid + ion) fraction, most Am is found incorporated or attached to colloids at pH> 5. **(c)** Colloid formation is observed in pure Si (10^{-3} mol dm^{-3}) and Al (10^{-3} mol dm^{-3}) solutions but is most pronounced in the mixture of both ($C_{Si}\,10^{-3}$ mol dm^{-3}, C_{Al} 10^{-5} mol dm^{-3}) . Reprinted from Kim, M. A., Panak, P. J., Yun, J. I., Kim, J. I., Klenze, R. and Kohler, K., Interaction of actinides with aluminosilicate colloids in *statu nascendi*. Part I: generation and characterisation of actinide (III)-pseudocolloids, *Colloids and Surfaces A*, 97–108, Copyright 2003, with permission from Elsevier

titrated with the Si–NaOH mixture towards higher pH ('Si') and finally the Al–HCl solution was titrated with the Si–NaOH solution ('Si + Al'). LIBD showed the formation of colloids in all three mixtures. However, in the third titration, where both Si and Al are present, the colloid generation was most pronounced. At pH < 5, the dissolution of aluminosilicates decreased the colloid formation, whereas the lowest solubility region at pH 6.5 also provided a minimal amount of colloids. The formation of aluminosilicate colloids was pronounced at pH 5.5 and at pH > 7. The concordance among Figure 20a,b and c is direct evidence for the formation of aluminosilicate colloid-borne Am. This is further corroborated by chemical speciation with TRLFS (time-resolved laser fluorescence spectroscopy), replacing Am by Cm. As confirmed further by LIBD, the mass concentration of aluminosilicate colloids formed under the given conditions ranged from 1×10^{-5} to 5×10^{-5} g dm^{-3} in the particle size range 10–50 nm. The corresponding number density varied in the range 10^{11}–10^{14} particles dm^{-3} water.

5.4 MIGRATION OF AQUATIC COLLOIDS

To understand further the migration of colloid-borne actinides, a field experiment was conducted in the Grimsel underground laboratory in Switzerland by using LIBD for *in situ*

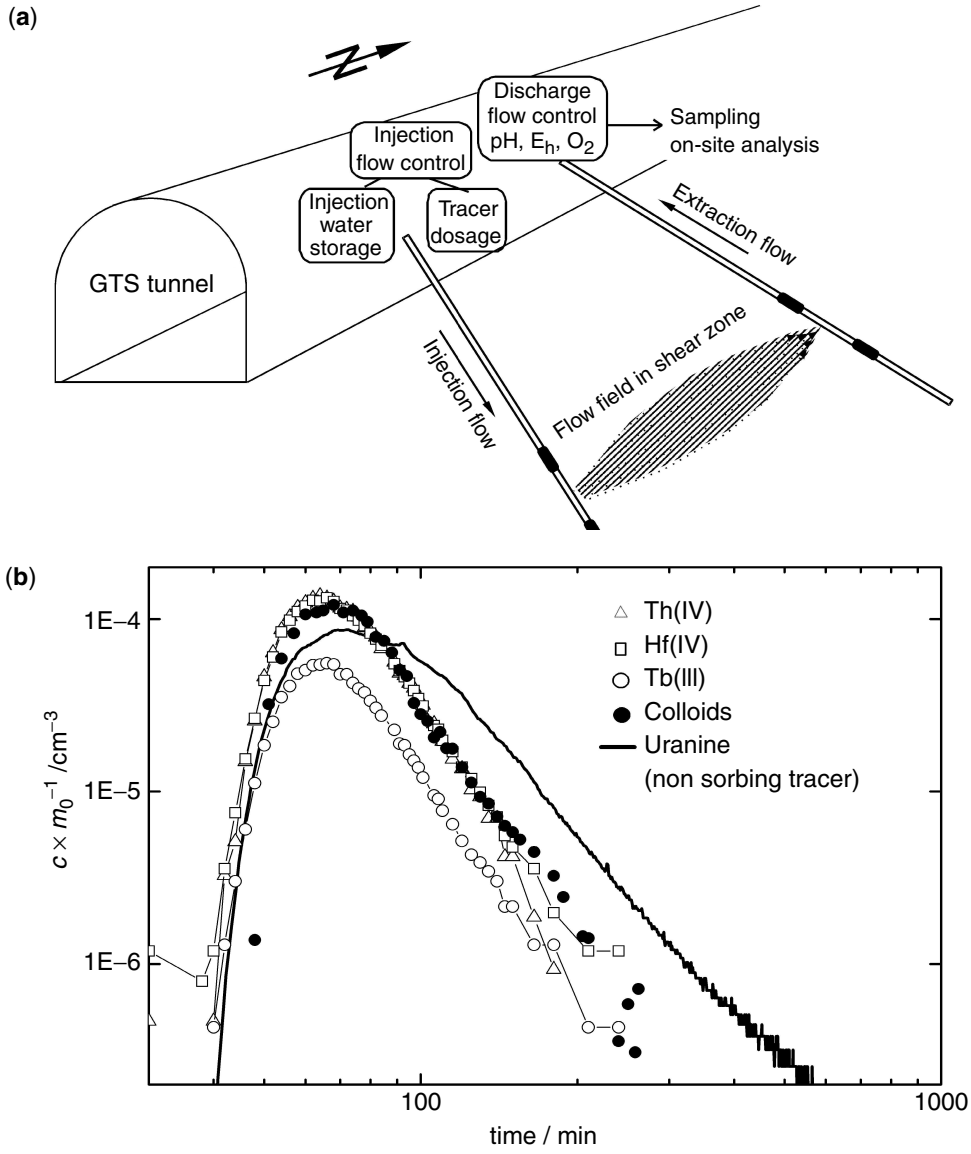

Figure 21. **(a)** Bentonite colloid migration through a 5 m long granite fracture was studied at the Grimsel test site (GTS). **(b)** An extraction profile of migrated colloids and colloid-borne trace elements. Colloids and uranine were monitored *in situ* by LIBD and fluorescence detection, respectively. The metals were analysed off-line by ICP-MS. Reprinted from Hauser, W., Geekeis, H., Kim, J. I. and Fierz, Th., A mobile laser-induced breakdown detection system and its application for the *in situ* monitoring of colloid migration, *Colloids and Surfaces A*, 37–45, Copyright 2002, with permission from Elsevier

monitoring [31,32,113]. For this purpose, a granite fracture of 5 m length was localised for a dipole aquifer flow path (Figure 21a) [31]. Bentonite colloids (smectite type) of concentration of 2×10^{-2} g dm^{-3} in about 100 cm^3 were injected into the fracture. The colloids showed a distribution between *ca.* 100 and 180 nm with a mean colloid size of 150 nm. The colloid content of the outflow of the dipole path was measured by time-resolved

LIBD. A background colloid level of 5×10^{-6} g dm^{-3} was found at an average size of 200 nm. After extracting 400 times the injection volume (100 cm^3), the injected colloid recovery was 55% in mass concentration and the average size of the extracted colloids decreased to 120 nm. From the mass concentration and the mean colloid diameter, the total colloidal surface area was calculated. Since mainly large colloids (with a lower surface to mass ratio) were lost [31] in the course of migration, the recovered colloidal surface area exceeded the mass recovery and appeared to be about 70%.

A further experiment was conducted with a cocktail of bentonite colloids spiked with about 10^{-7} mol dm^{-3} each of Th(IV), Hf(IV) and Tb(III). The mass concentration of the colloids exceeded the trace metal content by about 670-fold. This time colloid recovery was 55%, similar to the previous one. The extraction profile of all metals was the same as for the colloids (Figure 21b) [31]; radionuclide and colloid concentrations in the figure are normalised to the injected mass or activity (m_0). The peak maxima of the colloid and metal breakthrough curves appeared about 10 min ahead of the non-sorbing (conservative) tracer uranine. The shift suggested the existence of size and/or charge exclusion effects typical of colloid migration. The recovery was $78 \pm 8\%$ for both Th(IV) and Hf(IV) and $33 \pm 3\%$ for Tb(III). The tetravalent element recovery was related to the recovery of bentonite-colloid surface area ($\sim$70%)[13]. The agreement between surface recovery and trace recovery implied the surface-bound incorporation of tracers to colloids. The lower recovery of Tb suggested a rapidly reversible sorption on colloids and thus partial retention at surfaces of tubings or rock minerals.

5.5 COLLOIDS IN DEEP UNDERGROUND WATERS

Closely related to the investigations described in the previous section is the Äspö Hard Rock Laboratory (HRL) project of the Svensk Kärnbränslehantering AB (SKB) in Oskarshamn, Sweden. A granitic rock formation was assessed for the suitability of building a nuclear waste repository [114]. In contrast to the Swiss project in the Grimsel mountains, the Swedish Hard Rock Laboratory is located underneath the island of Äspö in the Baltic sea close to the Oskarshamn nuclear power plant. The rock formation contains several granitic shear zones, penetrated by aquifers of different origin (Figure 22) [33].

The laboratory is accessible via a tunnel 3.5 km long that descends 450 m below sea level, which allows one to measure *in situ* the ground waters at selected boreholes (depicted as 1–8 in Figure 22). The natural conditions of the water prior to and during the measurement have been conserved carefully; in particular, a high pressure LIBD cell was built which withstands the hydrostatic pressure up to 416 m below sea level (Table 2). The pressures given in the table reflect the heights of the water columns of the respective aquifers, which do not necessarily equal the total vertical depths of the sampling locations.

The variation in colloid content is remarkably high [34] (Figure 23), even considering the large difference in metal ion concentrations (up to three orders of magnitude). The water from the uppermost site at -69 m (borehole 1) contains large colloids (mean size 600 nm) at high concentrations. This large amount of colloids is found in concert with low salinity and a high content of organic substances (DOC 16 mg dm^{-3}). LIBD has a low sensitivity to pure humic/fulvic acids (see section 5.7), but these substances

[13] As defined previously, the surface area recovery is the ratio of total colloidal surface of recovered colloids to total colloidal surface of injected colloids.

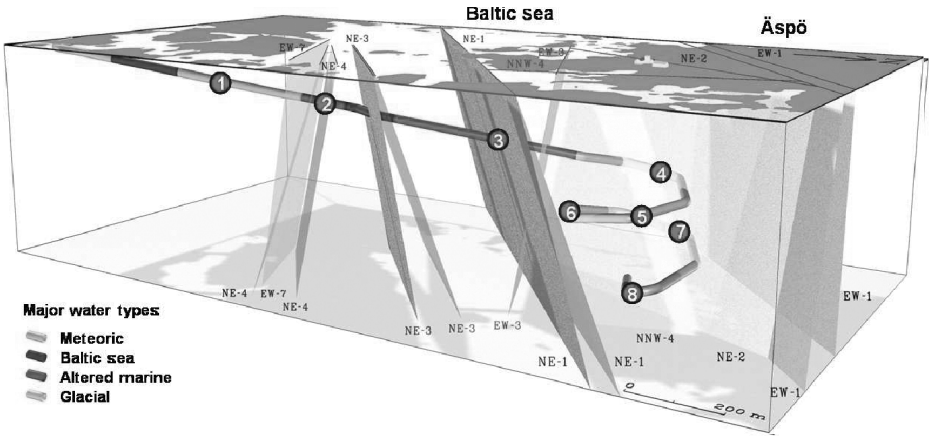

Figure 22. Sampling locations for LIBD. Different shades correspond to different origins of waters (meteoric water, seawater, altered marine water and glacial water). For parameters, see Table 2. Reprinted from *Äspö progress Report IPR 03-38*, 2003, with permission from Swedish Nuclear Fuel and Waste Management Company

Table 2. Borehole locations and water pressure

Location	Elevation/m	Pressure/10^5 Pa
1	−69	5.9
2	−168	12.9
3	−182	⩾8.0
4	−235	14.4
5	−282	21.3
6	−306	16.2
7	−370	14.3
8	−416	32.8

nevertheless might play an important modifying role towards the inorganic colloid concentrations [115,116]. The stability of inorganic or lignite particles is strongly enhanced by the formation of mixed complexes and at low ionic strength (which prevents further aggregation followed by precipitation) where even large particles are stable on long time-scales.

Borehole (4) at −235 m contains a very pure water of high salinity (Cl^- concentration 11 g dm^{-3}) with colloidal contamination similar to that observed for filtered ultrapure deionised water shown as the detection limit ('Ultra-Pure water'). Colloids were smaller than 20 nm with a concentration in the region of 10^{-8} g dm^{-3}, five orders of magnitude lower than in the case of borehole (1). The data below a Cl^- concentration of 12 g dm^{-3} followed a systematic decrease in colloid concentration with increasing salinity, suggesting a decrease in stability due to colloid aggregation and subsequent precipitation or sedimentation. Only the colloid content of borehole (7) deviated from this trend as it was too high by almost three orders of magnitude. However, the water of borehole (7) originated from a region disturbed by the tunnel driving. It is known that additional iron hydroxide colloids may be generated by oxygen permeation into these so called 'excavation disturbed zones'. In a more recent experiment, the water of the same aquifer

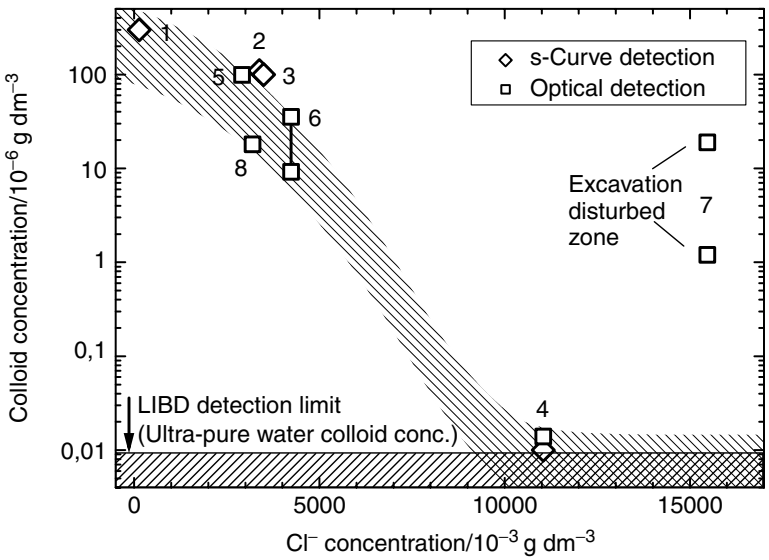

Figure 23. LIBD analysed colloid concentration as a function of the Cl^- concentration as an indicator for salinity (data points connected by bars indicate varying colloid concentrations due to pressure fluctuations). Reprinted from *Äspö progress Report IPR 03-38*, 2003, with permission from Swedish Nuclear Fuel and Waste Management Company

was sampled at a different position away from the disturbed zone and a colloid content close to the detection limit was found.

The change in colloid formation with experimental conditions was observed by varying the ground-water flow-rate and length of the tubing. Oxygen permeated the polyethylene (PE) tubing, which led to colloid formation in waters that were rich in Fe(II). The apparent colloid content increased with increasing length of the tubing (up to 100 m) and decreasing flow-rate. Sampling was hence performed as close to the boreholes as possible. Nonetheless, the flow-rate still is a critical parameter. Whereas at borehole (4) at 4 $cm^3\,min^{-1}$ the 'natural' colloid content of 10^{-8} $g\,dm^{-3}$ was measured, the colloid concentration increased 50-fold (5×10^{-7} $g\,dm^{-3}$) at a flow-rate of 1400 $cm^3\,min^{-1}$. This effect was caused by the erosion of the backfill material.

Since the transport capacity for colloid-mediated migration scales proportionally to the total specific surface area of suspended particles, a water containing high concentrations of colloids such as (1) increases the risk of radionuclide release into the environment. Even the low colloidal water (4) contains a large number of colloids ($\sim 10^9$ particles dm^{-3}), resulting in a large total surface area due to the small diameter. The importance attributed to colloid-mediated transport becomes apparent from the fact that Sweden is about to make LIBD measurements an integral part of future repository assessments.

5.6 AGGREGATION OF BENTONITE COLLOIDS

The multimode s-curve method discussed in section 4.7 is especially suited to observe changes in size distributions as a function of time, *e.g.* in the case of particle aggregation. Figure 24 shows the behaviour of bentonite colloids.

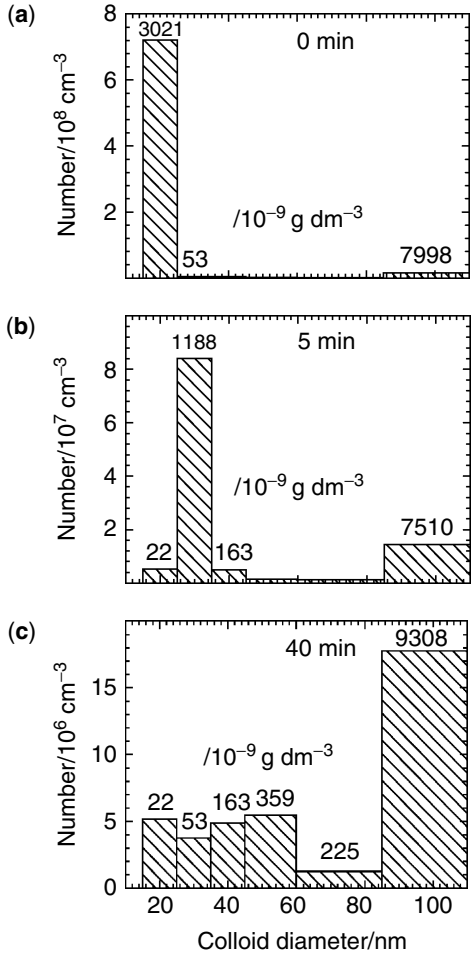

Figure 24. Time-resolved observation of aggregation in a multimodal bentonite colloid suspension (10^{-5}g dm^{-3}): **(a)** at pH 6 and **(b)** 5 min after the pH was adjusted to 2 and **(c)** 40 min after pH adjustment. Reprinted with permission from Walther, C., Cho, H. R. and Fanghänel, Th. (2004). Measuring multimodal size distributions of aquatic colloids at trace concentrations. *Appl. Phys. Lett.*, **85**, 6329–6331. Copyright 2004, American Institute of Physics

Figure 24a reflects the original, bimodal, size distribution at pH 6. The 100 nm size class[14] contains two-thirds of the total colloidal mass (7×10^{-6} g dm^{-3}); the rest (3×10^{-6} g dm^{-3}) has a size of approximately 20 nm. Due to their small mass (only 0.8% of a 100 nm colloid), the small fraction contributes the dominant colloid *number*. At pH 2 in 10 mmol dm^{-3} NaCl solution, the electric double layer of the colloids is neutralised and aggregation proceeds very fast, as can be seen from Figure 24b. The PSD is noticeably shifted to larger diameter after 5 min. The fraction of 100 nm particles remains constant (note the different scalings of Figure 24a and b) since collisions of two 100 nm particles are very unlikely due to their lower number density. After 40 min, practically all particles

[14] For non-spherical particles, the 'size' given by LIBD corresponds to a colloid of equal volume but spherical shape.

formed aggregates of 100 nm or larger (Figure 24c). The range for particle size distributions has now been extended from 15 to 400 nm. Combination with a single particle counter for the detection of colloids >100 nm [117] (Section 7) extends the size range from 15 nm to 2 μm [82].

5.7 LIBD ON ORGANIC COLLOIDS

LIBD is not commonly used for the detection of organic particles due to inherent difficulties. The colloid detection mechanism is based on the different breakdown thresholds of pure water and solid particles. Colloids of very high water content are difficult to discriminate from the background. Nonetheless, there have been a few reports on successful application of LIBD to organic substances. A systematic study on natural humic acid (HA) and fulvic acid (FA) substances isolated from deep groundwaters of the Gorleben site (Germany) was performed by Monsallier *et al*. [118]. It is well known from gel permeation chromatography (GPC) [119,120] that natural HA typically contain two fractions of hydrodynamic size equivalent to 1.5 kDa (globular protein calibration) and >100 kDa ($d \approx 6$ nm). Synthetic HA and FA do not contain the larger size fraction and cannot be detected by LIBD. By means of carefully designed blank experiments, the authors excluded possible artefacts from inorganic colloids and showed that LIBD signals originated in the HA content of the samples. Whereas LIBD was blind for the smaller size class and did not detect any colloids in the FA, the larger (colloidal) fraction in natural HA was detected by LIBD and a size of approximately 10 nm $m \approx 500$ kDa (according to a calibration with polystyrene particles) was assigned. The s-curves scaled correctly and reproducibly with increasing concentration. Aggregation and flocculation of HA was observed upon pH change from 3.5 to 9.3. Further proof that LIBD detected the large fraction only was given by centrifugation experiments. In a recent study [121], LIBD (called 'nano-particle analyser') was used to detect spores (*Bacillus subtilis*, 13–15% water content, 0.8 × 1.5 μm) and two types of bacteria (*Enterococcus faecalis*, 70–85%, 1 μm, and *Enterococcus durans*, 70–85%, 1–2 μm [37]). However, it is not possible to distinguish bacteria from inorganic particles by LIBD and little information is given on how background contamination was avoided, especially in the case of the bacteria with high water content. Possibly only metabolites of the bacteria were detected. In addition, it is not clear why the optical detection set-up was used to record s-curves (of low statistical quality) instead of obtaining size information from the ignition length. Globular proteins of mass 669 kDa in water were detected, the concentrations ranging from 10^{-6} to 10^{-3} g dm^{-3} [122]. The slope of the s-curves increased with increasing concentration, but no size information was obtainable from the thresholds due to poor reproducibility. Smaller proteins (<500 kDa) could not be discriminated against the background at all. Recently, particulate matter from diesel car engines was investigated by LIBD when the exhaust gas was bubbled through ultrapure water for 1 min [123]. Sooty particles of up to micrometre size were detected for conventional diesel engines, while only particles of <50 nm were found in the exhaust gas of a car with a particulate filter.

Although LIBD is sensitive to compact organic particles, it is evident from [118] that small or low-density proteins, FA and monomeric units of HA are not detectable. To our

knowledge, there are no systematic studies on how LIBD behaves in the transition region from compact organic particles to gelly particles and at what point the signal is lost.

5.8 LIBD AND LIBS ON AEROSOLS

In addition to colloid detection in aqueous media, LIBD has found applications in a variety of related research fields [124]. Particularly LIBD and LIBS have become standard methods in aerosol science, and have been used in this field longer than for the aquatic chemistry of colloids. The material and size of liquid aerosols were investigated for their breakdown thresholds [98]. A similar experimental and theoretical investigation followed [125,126] for plasma generation and evolution in droplets. By the use of intensified gated CCD cameras following a spectrograph, the elemental composition of aerosols could be determined by LIBS, since in air the perturbation of discrete emission lines is much less than in water. Various airborne particles have been analysed by a combination of LIBD and LIBS. Coal fire-ash particles [127] or seawater aerosols [128] were investigated and the size distribution of aerosols [129] or their chemical composition [88] was probed even in an *in situ* experiment [130]. Other examples include analyses of nanometre-sized carbon clusters [131], large biological aerosols [132] and spray droplets containing colloids [133]. This is an appealing scheme but it is hard to distinguish the contributions from true colloids and the signals from solvated species which form colloids during the evaporation process. Analyses by LIBS were also attempted on filtered colloids [134–136] and on aquatic colloids dispersed on the solid surface [137]. LIBS has been widely used mostly for solid surface characterisation [138–142] or performed on particulate material [143,144] and small particles [145,146], which is, however, outside the scope of this chapter.

5.9 LIBS ON AQUATIC COLLOIDS

It is well known that a colloid-borne element can be better recognised by LIBS than its ionic species [18,147,20], a fact that can be used for distinguishing the colloid formation of a particular element or for a solubility study (similar to section 5.2). An example for LIBS of aquatic colloids directly in suspension is the work of Yun *et al*. [19]. Figure 25a compares two different spectra of Eu in aqueous solution. Both samples contained an equal amount of Eu (concentration 2×10^{-4} mol dm^{-3} each) [19]. Trace (A) refers to a colloidal Eu_2O_3(s) suspension in neutral water and trace (B) depicts the emission signal of the solvated Eu^{3+}_{aq} ion in 0.7 mol dm^{-3} nitric acid. The Eu(I) emission lines at 495.4, 462.7 and 466.1 nm are clearly visible for the particles in water and about 100-fold weaker for the solvated ion. The peak at 306 nm originates from the O–H rotation–vibration transition of water [148]. For solvated species, and also colloids, the emission intensity shows a linear relation with concentration (Figure 25b) but is much weaker for solvated ions. This enhanced sensitivity for colloids was applied for the determination of Eu^{3+} solubility (Figure 25c). The pH of an Eu^{3+} solution (1.3×10^{-4} mol dm^{-3}) was increased by titration with NaOH. At pH $\approx$ 7.1 the emission intensity increased strongly due to the formation of colloids. This provides a possibility of assessing the solubility products of Eu oxy-hydroxide.

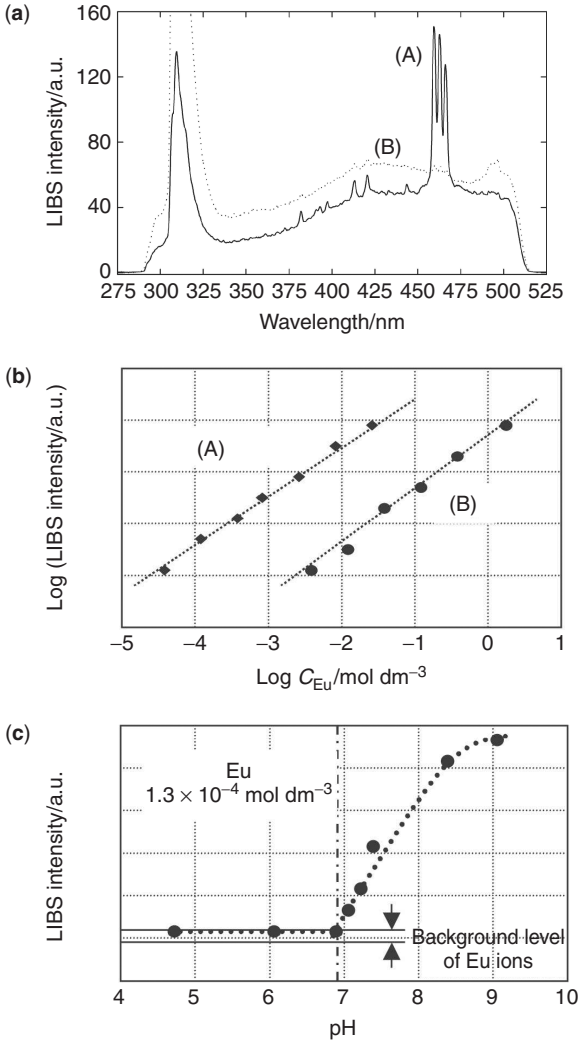

Figure 25. **(a)** LIBS spectra of samples with Eu concentrations of 2×10^{-4} mol dm^{-3}. Trace (A) shows a suspension of Eu_2O_3(s) particles in water and (B) Eu^{3+}_{aq} in 0.7 mol dm^{-3} nitric acid. **(b)** Calibration of the Eu concentration by LIBS in 10^{-3} mol dm^{-3} $HClO_4$ for ions or for solid suspension. **(c)** the pH edge of Eu colloid formation when an acidic ionic solution was titrated to higher pH. Reprinted from Yun, J. I., Bundschuh, T., Neck, V. and Kim, J.-I. (2001). Selective determination of europium(III) oxide and hydroxide colloids in aqueous solution by laser-induced breakdown spectroscopy. *Applied Spectroscopy* **55**, 273–278, with permission from the Society of Applied Spectroscopy

6 PRACTICAL REMARKS WHEN USING LIBD

Whereas the technical requirements on laser and optics are discussed in Sections 3.3 and 4, this section addresses some important issues for actual working with LIBD systems. It must be kept in mind that LIBD is an ultra-sensitive method for trace detection, inherently susceptible to contamination. Exposure of a dilute sample (10^{-9} g dm^{-3} regime) to air for a few minutes leads to an input of aerosols which may significantly increase the colloidal background signal. For this reason, sample preparation should be performed in a clean

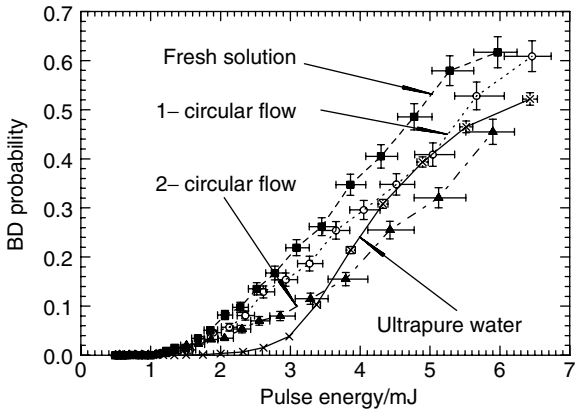

Figure 26. For very dilute samples (here polystyrene spheres, 20 nm, 5×10^{-8} g dm^{-3}), surface sorption plays an important role. In a closed-circle flow-through set-up, fresh sample is compared with once and twice recycled solutions. The colloid concentration decreased (lower slope) while the threshold as a measure of size remained unaffected. This effect can be avoided by proper choice of reactor and tubing material

air environment (laminar flow cabinet) and the colloid content of chemicals involved in the sample preparation has to be examined. If necessary, ultrafiltration, centrifugation or recrystallisation has to be applied for purification of the chemicals. Filters have to be soaked properly for cleaning and rinsed thoroughly prior to use. Containers and quartz cells have to be cleaned, *e.g.* in nitric acid, and rinsed thoroughly with colloid-free water.

On the other hand, the colloidal phase must not be perturbed and the usual care has to be taken for handling [99,100,104]. In particular, surface sorption has to be avoided. In a typical set-up, a sample is provided in a glass reactor, pumped through polyethylene tubing into the LIBD detection flow-through quartz cell and back into the reactor. Figure 26 shows s-curves of freshly prepared 5×10^{-8} g dm^{-3} 20 nm polystyrene suspensions along with measurements after the total volume has been pumped through once and twice. Whereas the threshold remains constant (the particle size, of course, does not change), the slope decreases, indicating colloid loss due to sorption. This problem is avoided by using Teflon-like materials, in particular PFA (perfluorinated alkoxy compounds) for containers and PEEK (polyether ether ketone) for capillaries.

The measurement cells are made of quartz (no metal tubing should be used, to avoid sorption) and the surface roughness has to remain below 100 nm in order not to alter the laser beam profile. Simple static cells (1–10 cm^3) with magnetic (Teflon-coated) stirrers are used for limited sample volume. If at least 20 cm^3 samples are available, flow-through measurements can be performed, with the optimum performance in a once-through cycle, where the sample is discarded after being exposed to the laser beam. LIBD is often referred to as being a non-invasive and non-destructive method. That is not true in an absolute sense. Of course, a colloid being detected by plasma ignition is completely destroyed and in addition a laser pulse of several GW cm^{-2}, even for a period as short as nanoseconds, can induce photochemical reactions. Nonetheless, the measurement of a sample with total absolute number of colloids exceeding 10^6 will not be altered considerably by destroying a few thousand of them. However, this might be a problem for extremely dilute samples. The same holds for photochemically produced radicals. Systems of exceptionally high redox sensitivity might even be influenced by a tiny amount of radicals. In such cases, a

once-through cycle should be used. Finally, the hot expanding plasma creates gas bubbles of millimetre size, which obstruct the laser pulse and cause an apparent decrease in BDP if not removed in time. This limits the pulse repetition rate of the laser to about 20 Hz and requires a sufficient flow-rate in a flow-through regime. Static cells should not be completely filled in order to allow the gas bubbles to escape to the surface.

In order to counteract sedimentation, samples containing particles >100 nm should be stirred. Nonetheless, care has to be taken not to abrade material from either stirrer or bottom of the cell or reactor. Even tiny fragments can contribute to the colloidal background considerably, hence stirring should be slow.

Further, the breakdown process depends on the material properties of the colloids [16, 22,38]. As shown above, the number of photons required to generate the first electron depends on the ionisation energy of the colloid [54,149]. Most materials, including the reference material polystyrene, require four photons of the frequency-doubled light (532 nm, $h\nu = 2.3$ eV) of an Nd:YAG laser, corresponding to an ionisation energy of 7 eV $< E_I <$ 9.3 eV. The cross-section for multi-photon ionisation is of similar magnitude [55,69,70, 150]. There are, however, exceptions, such as thoria (ThO_2) colloids [22], which are detected at lower sensitivity and require a calibration different from the four-photon case. Materials of high transparency (such as crystalline SiO_2) or low density and high water content (organics, see section 5.7) [52] hinder the inverse bremsstrahlung and are detected at higher photon flux or above 10^{-3} g dm^{-3} concentration.

Recent modifications of the mobile LIBD apparatus [31] have allowed measurements in a flow-through cell up to 3×10^6 Pa pressure and simultaneous recording of pH, redox potential (Eh), oxygen content and conductivity. Details on the technique are published and no restrictions apply to the use of LIBD for research purposes. For potential commercial use, it should be noted that LIBD detection is patented by Japanese inventors [29] and an additional German patent exists covering optical acquisition [151]. To date, no commercial system is available.

A concluding remark concerns light scattering. LIBD is many orders of magnitude more sensitive than light scattering for particles that are much smaller than the wavelength of light. However, for colloids larger than ~100 nm, static light scattering techniques [152,153] (such as the single particle counter, SPC [94,154,155]) become more sensitive, and for μm-sized particles, or at high concentrations, dynamic scattering (PCS) [103,156] is the method of choice due to a much faster measurement time and a less delicate set-up (in addition, both methods are available commercially). Suspensions which scatter light effectively cannot be measured by LIBD. The threshold evaluation relies on well-defined photon flux conditions in the focal area. If, however, a large fraction of light is scattered along the light path, this is no longer the case. For natural waters, containing a considerable fraction of large organics (≫1 μm) or strongly coloured substances, a fractionation prior to LIBD measurements may be inevitable.

7 CONCLUSIONS AND FUTURE PERSPECTIVES

LIBD is an essentially non-invasive method for measuring aquatic samples devoid of perturbation. Colloids submitted to breakdown processes are destroyed but for most natural samples the number is too small to be significant. The appraisal of colloid size distribution

by LIBD requires a large number of single measurements and subsequent statistical evaluation. Quantification of the colloid number density and the size distribution entails a proper calibration of the method. For this, there are not so many reference particles of wide size range available except for polystyrene particles which exist as well-defined monomodal particles, ranging from 20 to 1000 nm or greater. Therefore, an operational relationship of LIBD with respect to the material properties of the colloids has to be established.

Applications of LIBD can be made for laboratory experiments dealing with the presence of colloids or their formation and also for field experiments concerned with *in situ* monitoring of aquatic colloids or their migration behaviour. Recently, size dispersion effects were observed during colloid migration by means of multimodal s-curve evaluations [82]. Radioactive tracers may help to study the formation and dispersion of aquatic colloids with the help of LIBD. A combination of LIBD with LPAS or TRLFS (time-resolved laser fluorescence spectroscopy) allows speciation of metals in solution with respect to oxidation state (LPAS), chemical properties, binding states, complex formation or nature of ligands (TRLFS) and formation of polynuclear (LPAS) or colloidal (LIBD) species. A mobile LIBD facilitates the *in situ* monitoring of aquatic colloids under original natural conditions, without the need for colloidal sampling and transport, processes that perturb more often than not the original state of aquatic colloids.

Future developments are expected to take place in at least three fields. First, LIBD has already been applied to the sensitive detection of inorganic colloids following size fractionation by FFFF [51,52,157]. In these cases optical LIBD was used and, in addition to the size information obtained from FFFF, an evaluation of the BD event distribution presented a second independent size measurement (see Chapter 5). In order to lower the price and the complexity of the detection system, constant pulse energy acoustic detection can be used, acting as a 'yes/no' detector. Although the size information can be obtained from FFFF alone, the sensitivity can be enhanced by at least three orders of magnitude compared with light scattering. It should even be possible to commercialise such a system.

A second approach concerns size distributions. At present the evaluation of size distributions is limited to six channels in the size classes between 20 and 100 nm and only possible for acoustic detection. An analogue evaluation of the optical detection signal should be possible that could allow faster measurements. The size range could be extended and the number of size classes might be increased slightly. However, since the size information is not obtained from a single colloid but from the total distribution, the presence of many large particles will prevent the precise determination of the number of small colloids.

As a third development, LIBD can be combined with a single particle counter (SPC), as has been shown recently [117]. In a combined set-up, the sample can be measured in parallel by the SPC and LIBD in a flow-through cell. In such a case, the SPC detects large colloids (>100 nm) with very high sensitivity and LIBD can contribute its superior detection limit for smaller sizes. By combining these complementary techniques, one is able to cover a size range from 15 nm up to micrometres at concentrations down to 10-10^4 particles cm^{-3} [83].

SYMBOLS

α_γ	Parameter of Γ-distribution (dimensionless)
$\overline{\mu}$	Mean value of probability distribution (Poisson) (dimensionless)

δ	Mass density of a colloid g cm^{-3}
ε_0	Electric permittivity of free space $= 8.854187 \times 10^{-12}$ F m^{-1}
$\eta(E)$	Rate of ionisation of electrons (energy E) by IB. s^{-1}
γ_{L}	Self focusing constant. Water: $\gamma_L = 0.5 \times 10^{-22}$ m^2 V^{-2}
λ	Wavelength of light. nm
λ_0	Wavelength of light in vacuum. nm
λ_γ	Parameter of Γ-distribution. arbitrary; here, nm^{-1}
$\mathbf{C}$	Euler's constant $= 0.57721566490153$
$\mathcal{E}$	Electric field strength. Vm^{-1}
μ_m^1	MPI cross-section of one molecule inside a colloid. $\mu m^{2m} W^{-m} s^{-1}$
μ_{G}	Centre of Gaussian distribution. arbitrary; here, nm
μ_m	MPI cross-section. $\mu m^{2m} W^{-m} s^{-1}$
ν	Frequency of light. s^{-1}
ν_{C}	Critical (plasma) frequency. s^{-1}
ϕ	Photon flux density. cm^{-2} s^{-1}
$\Phi_{\max}$	Optical aberration function (dimensionless)
ρ_{C}	Concentration (number density) of colloids. cm^{-3}
ρ_{e}	Number density of electrons. cm^{-3}
ρ_{M}	Number density of molecules. cm^{-3}
ρ_{M}	Number density of educts (neutral molecules) before laser irradiation. μm^3
σ_{G}	Width of Gaussian distribution. arbitrary; here nm
τ	Pulse duration: 1/e width of the temporal laser profile. ns
φ	Azimuth angle of cylindrical coordinates (dimensionless)
A	Area. μm^2
a	Integration constant (dimensionless)
$a^{(i)}$	Calibration parameter for multimodal s-curve fitting (dimensionless)
b	Integration constant (dimensionless)
$b^{(i)}$	Calibration parameter for multimodal s-curve fitting (dimensionless)
C	Colloid concentration fit parameter (dimensionless)
c_0	Velocity of light in vacuum $= 299792458$ ms^{-1}
C_{C}	Mass concentration of colloids. g cm^{-3}
c_t	Temporal integration constant. ns^{-m+1}
d	Diameter of colloid. nm
d_{p}	Penetration depth of light. nm
E	Energy eV, J
e	Electron charge: 1.602177×10^{-19} C
E_0	Energy of a single laser pulse. mJ
E_{I}	Ionisation energy: see footnote 2, Section 3.1. eV
E_{t}	Threshold energy for breakdown. mJ
E_{Ph}	Photon energy. eV
$g(\vec{r})$	Spatial part of the power density: $I(\vec{r}, t = \text{constant})$ (dimensionless)
h	Planck's constant $= 6.626 \times 10^{-34}$ J s $= 4.135$ eV fs
$h(\vec{r})$	Temporal part of the power density: $I(\vec{r} = constant, t)$ (dimensionless)

$h\nu$	Photon energy. eV
I	Power density. W μm^{-2} $(= P/A)$
I_0	Peak power density. Wcm^{-2}
I_C	Critical power density. $W\,cm^{-2}$
K_{sp}	Solubility constant (dimensionless)
L_C	Critical power for self-focusing. W
l_Z	Ignition length = effective focal length. μm
m	Order of $\rightarrow$ *MPI*-process$\rightarrow$ *MPI*-ionisation by m photons (dimensionless)
m_0	Total injected mass or activity. g or Bq
m_e	Electron mass: 9.109389×10^{-31} kg
N	Number of colloids (dimensionless)
n	Refractive index (dimensionless)
N_e	Number of electrons (dimensionless)
n_L	Refractive index change during self-focusing (dimensionless)
N_M	Number of (neutral) molecules (dimensionless)
N_m	Number of molecules inside a colloid (dimensionless)
P	Power. W
p	Probability (dimensionless)
P_0	(Mean) power of a single laser pulse. W
p_N	Probability of measuring a value of N events (dimensionless)
P_t	Threshold power for breakdown. W
p_{BD}	Probability of a breakdown (dimensionless)
$r, \vec{r}$	Spatial coordinate(s). μm
r_0	Radius where power$\sim$/photon flux density decreased to 1/e of maximum. μm
r_C	Critical radius μm
s	Slope of growth of focal volume (dimensionless)
t	Time. s
t_0	Laser pulse duration. ns
u	Substitution variable (dimensionless)
V	Volume. cm^{-3}
v	Substitution variable (dimensionless)
V_{el}	Volume of ellipsoid. μm^3
V_{foc}	Focal volume of arbitrary shape. μm^3
x	1st axis perpendicular to laser beam propagation direction. μm
y	2nd axis perpendicular to laser beam propagation direction. μm
Z	Ionic charge. elementary charge e: 1.602177×10^{-19} C
z	Axis along laser beam propagation direction. μm
z_C	Critical distance along laser beam propagation. μm
z_f	Focal length induced by self-focusing. m
BD	Breakdown
BDP	Breakdown probability (dimensionless)
Ei(x)	Exponential-integral function
IB	Inverse bremsstrahlung

GLOSSARY

Cross-references are marked by an arrow (→) and *italic* font; '*cf.*' hints at a complimentary term.

Absorption The fraction of light that is lost and remains in a sample due to inelastic processes (*cf.* extinction).

Acoustic detection The breakdown is detected by means of a → *piezo detector*, which picks up the acoustic signal caused by the expansion of the hot laser induced → *plasma*.

Amplified atomic emission Prerequisite for laser action. In addition to spontaneous photon emission, an excited atom can be stimulated to emit a photon by the presence of a second photon of exactly the excitation energy. The emitted photon has the same properties as has the stimulating one, which results in monochromatic, coherent light.

Atomic emission Optical line spectra which are used for identifying elements quantitatively. In LIBS these are superimposed on and have to be discriminated against the background of → *blackbody radiation*.

Bimodal A suspension which contains colloids of two distinct, well-defined sizes.

Blackbody radiation Continuous electromagnetic radiation spectra of a body with absorptivity = 1 (ideal absorber/radiator) and defined temperature. Due to the quantum nature of light emission the *b.r.* spectra exhibit maxima at $\lambda = 0.2898\ \mathrm{cm\,K^{-1}}$ (Wien's law).

Breakdown Generation of a practically totally ionised gas (→ *plasma*) [16]. The experimental criterion generally used is the observation of a glow or flash or that the plasma becomes opaque for laser light (→ *Thomson scattering*) which corresponds to an electron density of $10^{19} - 10^{21}\ \mathrm{cm^{-3}}$.

Breakdown probability The number of BD events relative to the total number of laser pulses. E.g. if 100 laser pulses cause 10 breakdowns, the BDP = $p_{\mathrm{BD}} = 0.1$.

Breakdown threshold The lowest power density I_{t} that suffices to initiate a breakdown for a colloid of certain properties (size, → *MPI cross-section*, → *ionisation energy*). *B.t.* is also equally used for the lowest mean power (P_{t}) of a laser or the lowest pulse energy (E_{t}) which initiates a breakdown.

Cascade multiplication → *Inverse bremsstrahlung*

Colloid concentration The concentration of colloids in suspension is preferentially given in number per volume (particles $\mathrm{cm^{-3}}$). If available data only allow one to give the colloid content in mass concentration (if only average sizes, or no size information is available at all, for filtration experiments or in the case of quotations from the literature) this is explicitly stated by use of the units ($\mathrm{g\ cm^{-3}}$).

Critical power density See remark under *breakdown threshold*

Critical radius Critical distance from the focal centre along the laser axis, where the power density decreases below the → *breakdown threshold*.

Critical radius Radius at $z = 0$ (perpendicular to the laser beam), where the power density decreases to a value below the → *breakdown threshold* for a given particle.

Crosstalk General: unwanted signals in a communication channel (as in a radio) caused by transfer of energy from another circuit (as by leakage or coupling). Here: phantom signal in size classes that are not populated, for instance when a monomodal suspension of 100 nm causes signals in size classes <100 nm.

Destructive A detection method is referred to being destructive if the single colloid under investigation is destroyed and cannot be subjected to future investigations. *cf. Invasive*.

Detection limit The lowest number of detectable species that can be discriminated from background. In the case of LIBD for small colloids (< 100 nm), the *d.l.* is determined by the remaining colloid contaminations of the purest water that can be supplied in the laboratory and for large colloids it is determined by the finite size of the → *effective focal volume*.

Effective focal length → *Ignition length* (l_Z)

Effective focal volume The volume within the laser focus where the power density suffices to ignite a breakdown. Since, the → *breakdown threshold* decreases with increasing particle size, the *e.f.v.* also depends on particle size.

Extinction The weakening of light on passing through a sample. Sum of → *absorption* and → *scattering*.

Focal volume → *Effective focal volume*

Ignition length The width of the spatial distribution of → *breakdown* (plasma-) events along the laser beam axis. The *i.l.* increases monotonously with increasing colloid size and is applied for size measurements in the → *optical detection* of LIBD. See also Section 4, Figure 12 and Figure 13.

Invasive A detection method is referred to being invasive if the total sample is altered considerably or is completely destroyed by the measurement and it cannot be used for subsequent investigations. *cf. Destructive*.

Inverse bremsstrahlung From German Bremsstrahlung: 'Braking radiation'. Denotes electromagnetic radiation produced by a sudden slowing down or deflection of charged particles (especially electrons) passing through matter in the vicinity of the strong electric fields of atomic nuclei [158]. Inverse bremsstrahlung means the opposite–the acceleration of electrons by an electromagnetic field (here the laser field) in the presence of ions. For the sake of energy and momentum conservation, this needs to be a three-body process. Symbol $\eta(E)$.

Ionisation energy Energy to free one electron from an atom or molecule. See footnote 2, Section 3.1.

Isophote Line of equal photon flux density.

Kernels Oligomers or colloids which are too small to be detected by LIBD, but initiate crystallisation for formation of larger colloids.

Laser-induced breakdown spectroscopy See LIBS.

Laser-induced photoacoustic spectroscopy See LPAS.

LIBS Laser-induced breakdown spectroscopy. Technique used for the elemental analysis of solids, liquids and gases. The sample is heated and vaporised by the focused light of a pulsed laser. During the cooling of the hot (ionised) gas, recombination processes lead to the emission of ionic and → *atomic lines* (*cf.* atomic emission), which allow the quantitative determination of element content.

LPAS Laser-induced photoacoustic spectroscopy. Matter which absorbs light is heated, expands and causes an acoustic shock wave which can be detected by a sensitive microphone. The amplitude of the acoustic signal increases linearly proportionally with the concentration of absorbers and with the molar absorptivity (or photon absorption

cross-section). By scanning the excitation wavelength an optical absorption spectrum is obtained, which in turn is used to quantify the amount of species present in the sample. LPAS is applicable to solids and liquids. The detection limit depends on the absorptivity and is typically 1.5 orders of magnitude lower than for UV–VIS detection. In contrast to UV–VIS, the measurement is not disturbed by → *scattering* signals (*e.g.* due to colloids) since LPAS does not probe → *extinction* but → *absorption*.

Material dependency The → *photon flux density* required to generate a → *breakdown* depends on material properties such as → *multi-photon absorption cross-section* and → *ionisation energy*. Hence, the → *breakdown threshold* might be different for particles of the same size but different materials. See Section 3.1.

Monomodal A suspension which contains colloids of only one size.

MPI Ionisation of an atom or molecule by the 'simultaneous' (within picoseconds) absorption of several photons. This effect takes place when the → *ionisation energy* exceeds the energy of one photon. Depending on the → *MPI cross-section*, a very high → *photon flux density* is required.

MPI cross-section Cross-section for multiphoton ionisation. Symbol μ_m. The product of MPI cross-section times the mth power of the → *power density* I^m gives the ionisation rate (per unit time). Therefore, the unit of the MPI cross-section is length^{2m} power^{-m} time^{-1} (*e.g.* $\mu\mathrm{m}^{2m}\mathrm{W}^{-m}\mathrm{s}^{-1}$).

Multi-photon ionisation → MPI

Multimodal A suspension which contains colloids of many distinct sizes.

Optical detection Detection of the → *plasma* by means of its optical emission, which is observed by a microscope lens and a CCD camera. From the → *ignition length*, the particle size is appraised. The light originating from the hot → *plasma* is composed of → *blackbody radiation*, → *atomic emission* lines and → *Thomson scattering*. The very intense Thomson scattered light is filtered out by use of holographic notch filters. The blackbody emission is used for localising the plasma; the atomic emission lines can be used to measure the elemental composition of the colloid (*cf.* LIBS).

Photo-ionisation Ionisation of atoms or molecules by absorption of one or several photons. The former process is known as photoeffect and the latter as non-resonant → *multi-photon ionisation*.

Photon flux density Number of photons per second per unit area. Symbol ϕ.

Piezo receiver Microphone based on the piezoelectric effect. A piezo-crystal generates a voltage which is linearly proportional to the applied pressure.

Plasma An electrically conducting medium in which there are roughly equal numbers of positively and negatively charged particles, produced when the atoms in a gas become ionised. It is sometimes referred to as the fourth state of matter, distinct from the solid, liquid and gaseous states. The negative charge is usually carried by electrons; the positive charge is typically carried by atoms or molecules that are missing those same electrons. [158].

Power density Energy per second per unit area. Symbol I.

Pretreatment Here, pretreatment exclusively refers to fractionation methods such as filtration, centrifugation or FFFF in order to lower the fraction of large particles which alter the LIBD signal due to light → *scattering* or due to their low → *breakdown threshold*.

Scattering The fraction of light that is lost in a sample due to elastic processes and typically leaves the sample in arbitrary direction (*cf. extinction*).

Screening In the context of this chapter (size-)screening is used for the suppression of a signal originating from small colloids due to the simultaneous presence of large particles.

Size distribution If a sample contains colloids of more than one size, the term size distribution is used. In this chapter, the number of colloids in a certain size class (*e.g.* 30–40 nm) is given. Since the size classes of LIBD are not arbitrarily small absolute numbers are sometimes preferred over the common differential expression $\mathrm{d}N/\mathrm{d}V\mathrm{d}d$.

Size-screening → *Screening*.

TEM_{00} The basic transverse electromagnetic mode in a laser resonator, which has a Gaussian intensity distribution perpendicular to the laser axis.

Temporal profile Change of laser → *power density* (→ *photon flux density*) in time. Idealised this is a Gaussian function, but especially single transversal, multi-longitudinal mode lasers show short (<100 ps) spikes, where the power density is very high.

Thomson scattering A → *plasma* of electron density ρ_e becomes opaque for light of frequency $\nu < \nu_C(\rho_e)$ (critical plasma frequency). The light can no longer penetrate the plasma and is scattered effectively.

Threshold → Breakdown threshold

Work function Energy to free one electron from bulk material. See footnote 2, Section 3.1.

REFERENCES

1. Brech, F. and Cross, L. (1962). Optical microemission stimulated by a ruby laser, *Appl. Spectrosc.*, **16**, 59–61.
2. Maiman, T. H. (1960). Stimulated optical emission in ruby, *Nature*, **187**, 493–494.
3. Rusak, D. A., Castle, B. C., Smith, B. W. and Winefordner, J. D. (1997). Fundamentals and applications of laser-induced breakdown spectroscopy, *Crit. Rev. Anal. Chem.*, **27**, 257–290.
4. Kim, J.-I., Stumpe, R. and Klenze, R. (1990). Laser-induced photoacoustic spectroscopy for the speciation of transuranic elements in natural aquatic systems, *Top. Curr. Chem.*, **157**, 131–179.
5. Kitamori, T., Fujii, M., Sawada, T. and Gohshi, Y. (1985). Linear response theory in photoacoustic spectroscopy and characterization of turbid particles, *Jpn. J. Appl. Phys., Part 1*, **24**, 210–213.
6. Arushanov, S. Z., Bebchuk, A. S., Kosolobov, V. N. and Lomonosov, V. L. (1978). Laser induced breakdown of aqueous solutions of electrolytes, *Sov. Phys. Dokl.*, **23**, 587–588.
7. Kitamori, T., Yokose, K., Suzuki, K., Sawada, T. and Goshi, Y. (1988). Laser breakdown acoustic effect of ultrafine particle in liquids and its application to particle counting, *Jpn. J. Appl. Phys.*, **27**, L983–L985.
8. Kitamori, T., Yokose, K., Sakagami, M. and Sawada, T. (1989). Detection and counting of ultrafine particles in ultrapure water using laser breakdown acoustic method, *Jpn. J. Appl. Phys.*, **28**, 1195–1198.
9. Sacchi, C. A. (1991). Laser-induced breakdown in water, *J. Opt. Soc. Am. B*, **8**, 337–345.
10. Docchio, F., Avigo, A. and Palumbo, R. (1991). Characteristics of optical breakdown in ultrapure water induced by nanosecond Nd:YAG laser pulses., *Europhys. Lett.*, **15**, 69–73.
11. Fujimori, H., Matsui, T., Ajiro, T., Yokose, K., Hsueh, Y. M. and Izumi, S. S. (1992). Detection of fine particles in liquids by laser breakdown method, *Jpn. J. Appl. Phys., Part 1*, **31**, 1514–1518.
12. Ajiro, T, Fujimori, H, Matsui, T and Izumi, S. (1992). Particle size dependence of correlation between plasma emission delay time and plasma emission intensity of laser breakdown induced by a particle, *Jpn. J. Appl. Phys., Part 1*, **31**, 2760–2761.

13. Kitamori, T., Matsui, T. and Sakagami, M. (1989). Laser breakdown spectrochemical analysis of microparticles in liquids, *Chem. Lett*, **89**, 2205–2208.
14. Ito, Y., Ueki, O. and Nakamura, S. (1995). Determination of colloidal iron in water by laser-induced breakdown spectroscopy, *Anal. Chim. Acta*, **299**, 401–405.
15. Nakamura, S., Ito, Y. and Sone, K. (1996). Determination of an iron suspension in water by laser-induced breakdown spectroscopy with two sequential laser pulses, *Anal. Chem.*, **68**, 2981–2986.
16. Radziemski, L. J. and Cremers, D. A. (1989). *Laser-induced Plasmas and Applications*. Marcel Dekker, New York.
17. Pu, X. Y., Ma, W. Y. and Cheung, N. H. (2003). Sensitive elemental analysis of aqueous colloids by laser-induced plasma spectroscopy, *Appl. Phys. Lett.*, **83**, 3416–3418.
18. Knopp, R., Scherbaum, F. J. and Kim, J.-I. (1996). Laser induced breakdown spectroscopy (libs) as an analytical tool for the detection of metal ions in aqueous solutions, *Fresenius' J. Anal. Chem.*, **355**, 16–20.
19. Yun, J. I., Bundschuh, T., Neck, V. and Kim, J.-I. (2001). Selective determination of europium(III) oxide and hydroxide colloids in aqueous solution by laser-induced breakdown spectroscopy, *Appl. Spectrosc.*, **55**, 273–278.
20. Nakamura, M., Kitamori, T. and Sawada, T. (1991). Size and element dependence of amplified atomic emissions from laser breakdown plasma of ultrafine particles, *Anal. Sci.*, **7**, 563–564.
21. Nakamura, M., Kitamori, T. and Sawada, T. (1993). Highly anisotropic light emission from laser breakdown of microparticles in water, *Nature*, **366**, 138–141.
22. Scherbaum, F. J., Knopp, R. and Kim, J.-I. (1996). Counting of particles in aqueous solutions by laser-induced photoacoustic breakdown detection, *Appl. Phys. B*, **63**, 299–306.
23. Kim, J. I., Klenze, R. and Scherbaum, F.-J. (1996). Hochempfindiche quantifizierung von Aquatischen Kolloiden mit Hilfe der laser-induzierten Breakdown-detektion, *FZK Nachr.*, **28**, 321–328.
24. Bolz, M., Hoffmann, W., Ruehle, W. and Becker, F. (1996). Characterization of colloids in primary coolant, *Water Chem. Nucl. React. Syst.*, **7**, 42–46.
25. Izumida, S., Onishi, K. and Saito, M. (1998). Estimation of laser-induced breakdown threshold of microparticles in water., *Jpn. J. Appl. Phys., Part 1*, **37**, 2039–2042.
26. Saito, M., Izumida, S., Onishi, K. and Akazawa, J. (1999). Detection efficiency of microparticles in laser breakdown water analysis, *J. Appl. Phys.*, **85**, 6353–6357.
27. Bundschuh, T., Knopp, R. and Kim, J. I. (2001). Laser-induced breakdown detection (LIBD) of aquatic colloids with different laser systems, *Colloids Surf. A*, **177**, 47–55.
28. Partin, J. (2002). New instruments reveals information about colloids, *INEEL Newsl.*, **4**, 1–2.
29. Fujimori, H., Matsui, T., Ajiro, T., Yokose, K. and Izumi, S. (1994). Apparatus for analysis of particulate material, analytical method for same, apparatus for production of ultrapure water, apparatus for manufacturing of semiconductor, and apparatus for production of pure gas, *US Patent*, 5316983.
30. Bundschuh, T., Hauser, W., Kim, J. I., Knopp, R. and Scherbaum, F. J. (2001). Determination of colloid size by two-dimensional optical detection of laser induced plasma, *Colloids Surf. A*, **180**, 285–293.
31. Hauser, W., Geckeis, H., Kim, J. I. and Fierz, Th. (2002). A mobile laser-induced breakdown detection system and its application for the *in situ* monitoring of colloid migration, *Colloids Surf. A*, **203**, 37–45.
32. Mori, A., Alexander, W. R., Geckeis, H., Hauser, W., Schafer, T., Eikenberg, J., Fierz, T., Degueldre, C. and Missana, T. (2003). The colloid and radionuclide retardation experiment at the Grimsel test site: influence of bentonite colloids on radionuclide migration in a fractured rock, *Colloids Surf. A*, **217**, 33–47.
33. Hauser, W., Götz, R., Geckeis, H. and Kienzler, B. (2003). *In situ* colloid detection in granite groundwater along the Äspö hard rock laboratory access tunnel, *Äspö Progress report IPR*, 03–38, Swedish Nuclear Fuel and Waste Management Co..
34. Walther, C., Bitea, C., Hauser, W., Kim, J. I. and Scherbaum, F. J. (2002). Laser induced breakdown detection for the assessment of colloid mediated radionuclide migration, *Nucl. Instrum. Methods B*, **195**, 374–388.

35. Plaschke, M., Schäfer, T., Bundschuh, T., Thang, N. M., Knopp, R., Geckeis, H. and Kim J. I. (2001). Size characterization of bentonite colloids by different methods, *Anal. Chem.*, **73**, 4338–4347.
36. Bundschuh, T., Knopp, R., Winzenbacher, R., Kim, J. I. and Koster, R. (2001). Quantification of aquatic nano particles after different steps of Bodensee water purification with laser-induced breakdown detection (LIBD), *Acta Hydrochim. Hydrobiol.*, **29**, 7–15.
37. Wagner, T., Bundschuh, T., Schick, R., Schwartz, T. and Koster, R. (2003). Investigation of colloidal water content with laser-induced breakdown detection during drinking water purification, *Acta Hydrochim. Hydrobiol.*, **30**, 266–274.
38. Bitea, C., Walther, C., Kim, J. I., Geckeis, H., Rabung, T., Scherbaum, F. J. and Cacuci, D. (2003). Time resolved observation of ZrO_2-colloid agglomeration, *Colloids Surf. A*, **215**, 55–66.
39. Knopp, R., Neck, V. and Kim, J. I. (1999). Solubility, hydrolysis and colloid formation of plutonium(IV), *Radiochim. Acta*, **86**, 101–108.
40. Romanovski, V. V., Brachmann, A., Palmer, C. E., Shaw, H. F., Bourcier, W. L. and Jardine, L. J. (2000). Characterization of Pu colloidal and aqueous speciation in Yucca mountain groundwater surrogate, *Abstr. Pap. Am. Chem. Soc.*, **219**, U80.
41. Walther, C., Bitea, C., Yun, J. I., Kim, J. I., Fanghänel, Th., Marquardt, C. M., Neck, V. and Seibert, A. (2003). Nanoscopic approaches to the aquatic plutonium chemistry, *Actinide Res. Q.*, **3**, 12–16.
42. Rothe, J., Walther, C., Denecke, M. A. and Fanghänel, T. (2004). XAFS and LIBD investigation of the formation and structure of colloidal Pu(IV) hydrolysis products, *Inorg. Chem.*, **43**, 4708–4718.
43. Neck, V., Kim, J. I., Seidel, B. S., Marquardt, C. M., Dardenne, K., Jensen, M. P. and Hauser, W. (2001). A spectroscopic study of the hydrolysis, colloid formation and solubility of Np(IV), *Radiochim. Acta*, **89**, 439–446.
44. Bundschuh, T., Knopp, R., Müller, R., Kim, J. I., Neck, V. and Fanghänel, Th. (2000). Application of LIBD to the determination of the solubility product of thorium(IV)-colloids, *Radiochim. Acta*, **88**, 625–629.
45. Neck, V., Müller, R., Bouby, M., Altmaier, M., Rothe, J., Denecke, M. A. and Kim, J. I. (2002). Solubility of amorphous Th(IV) hydroxide–application of LIBD to determine the solubility product and EXAFS for aqueous speciation, *Radiochim. Acta*, **90**, 485–494.
46. Bitea, C., Müller, R., Neck, V., Walther, C. and Kim, J. I. (2003). Study of the generation and stability of thorium(IV) colloids by LIBD combined with ultrafiltration, *Colloids Surf. A*, **217**, 63–70.
47. Brachmann, A., Wruck, D. A., Palmer, C. E. A. and Terminello, L. J. (1998). Laser induced photoacoustic breakdown spectroscopy for colloid size distribution and colloid concentration analysis, *Abstr. Pap. Am. Chem. Soc.*, **216**, U634.
48. Kim, M. A., Panak, P. J., Yun, J. I., Kim, J. I., Klenze, R. and Kohler, K. (2003). Interaction of actinides with aluminosilicate colloids in statu nascendi. Part I: generation and characterization of actinide(III)-pseudocolloids, *Colloids Surf. A*, **216**, 97–108.
49. Panak, P. J., Kim, M. A., Yun, J. I. and Kim, J. I. (2003). Interaction of actinides with aluminosilicate colloids in statu nascendi. Part II: spectroscopic speciation of colloid borne actinides(III), *Colloids Surf. A*, **227**, 93–103.
50. Stumpf, T., Tits, J., Walther, C. and Fanghänel, Th. (2004). Uptake of trivalent actinides (Cm(III)) by cement: a time-resolved laser fluorescence spectroscopy (TRLFS) study, *J. Colloid Interface Sci.*, **276**, 118–124.
51. Manh, T. N., Knopp, R., Geckeis, H., Kim, J. I. and Beck, H. P. (2000). Detection of nanocolloide with flow-field flow fractionation and laser-induced breakdown detection, *Anal. Chem.*, **72**, 1–5.
52. Bouby, M., Manh, T. N., Geckeis, H., Scherbaum, F. J. and Kim, J. I. (2001). Characterization of aquatic colloids by a combination of LIBD and ICP-MS following size fractionation, *Radiochim. Acta*, **90**, 727–732.
53. Morgan, C. G. (1975). Laser-induced breakdown of gases, *Rep. Prog. Phys.*, **38**, 621–665.
54. Lide, D. R., ed. (1995). *Handbook of Chemistry and Physics*, 75th edn. CRC Press, Boca Raton, FL.

55. Keldysh, L. V. (1965). Ionization in the field of a strong electromagnetic wave, *Sov. Phys. JETP*, **20**, 1307–1314.
56. Chin, S. L. and Lambropoulos, P. (1984). *Multiphoton Ionisation of Atoms*. Academic Press, Toronto.
57. Walther, C., Hauser, W., Geckeis, H. and Fanghänel, Th. (2003). Die Laser induzierte Breakdown Detektion zur Analytik von aquatischen Kolloiden im Ultraspurenbereich, *FZK Nachr.*, **35**, 179–184.
58. Niemz, M. H. (1995). Threshold dependence of laser-induced optical-breakdown on pulse duration, *Appl. Phys. Lett.* **66**, 1181–1183.
59. Zeldovich, Ya. B. and Raízer, Yu. P. (1965). Cascade ionization of a gas by a light pulse, *Sov. Phys. JETP*, **20**, 772–780.
60. Bloembergen, N. (1974). Laser induced electric breakdown in solids, *IEEE J. Quantum Electron*, **10**, 375–386.
61. Kennedy, P. K. (1995). A first-order model for computation of laser-induced breakdown thresholds in ocular and aqueous media: Part I–theory, *IEEE J. Quantum Opt.*, **31**, 2241–2249.
62. Stuart, B. C., Feit, M. D., Herman, S. and Rubenchik, A. M. (1996). Nanosecond-to-femtosecond laser-induced breakdown in dielectrics., *Phys. Rev. B*, **53**, 1749–1761.
63. Noack, J. and Vogel, A. (1999). Laser-induced plasma formation in water at nanosecond to femtosecond time scales: calculation of thresholds, absorption coefficients and energy density, *IEEE J. Quantum Electron.*, **35**, 1156–1167.
64. Born, M. and Wolf, E. (1999). *Principles of Optics*, 7th edn. Cambridge University Press, Cambridge.
65. Bergmann, L. and Schaefer, C. (1999). *Optics*, 9th edn. Walter de Gruyter, Berlin.
66. Cervenan, M. R. and Isenor, N. R. (1975). Multiphoton ionization yield curves for gaussian laser beams, *Opt. Commun.*, **13**, 175–178.
67. Bronstein, I. N. and Semendjajew, K. A. (1996). *Taschenbuch der Mathematik*. Teubner, Leipzig.
68. Gradshteyn, I. S. and Ryzhik, I. M. (2000). *Table of Integrals Series and Products*, 6th edn. Academic Press, San Diego, CA.
69. Schwarz, J., Rambo, P. and Diels, J. C. (2001). Measurement of multiphoton ionization coefficients with ultrashort ultraviolet laser pulses, *Appl. Phys. B*, **72**, 343–347.
70. Walther, C., Herlert, A., Kim, J. I., Scherbaum, F. J., Schweikhard, L. and Vogel, M. (2001). Absolute cross-sections for the nonresonant multi-photon ionization of toluene and xylene in the gas phase, *Chem. Phys.*, **265**, 243–250.
71. Mie, G. (1908). Beiträge zur Optik trüber Medien, *Ann. Phys.*, **25**, 377–445.
72. Bohr, C. F. and Huffmann, D. R. (1998). *Absorption and Scattering of Light by Small Particles*. John Wiley & Sons, Inc., New York.
73. Mosbacher, M., Munzer, H. J., Zimmermann, J., Solis, J., Boneberg, J. and Leiderer, P. (2001). Optical field enhancement effects in laser-assisted particle removal, *Appl. Phys. A Mater. Sci. Proc.*, **72**, 41–44.
74. Schmidt-Kloiber, H., Paltauf, G. and Reichel, E. (1989). Investigation of the probabilistic behavior of laser-induced breakdown in pure water and in aqueous solutions of different concentrations, *J. Appl. Phys.*, **66**, 4149–4153.
75. Hammer, D. X., Thomas, R. J., Noojin, G. D., Rockwell, B. A., Kennedy, P. K. and Roach, W. P. (1996). Experimental investigation of ultrashort pulse laser-induced breakdown thresholds in aqueous media, *IEEE J. Quantum Electron.*, **32**, 670–678.
76. Noack, J., Hammer, D. X., Noojin, G. D. and Rockwell, B. A. (1998). Influence of pulse duration on mechanical effects after laser-induced breakdown in water, *J. Appl. Phys.*, **83**, 7488–7495.
77. Vogel, A., Noack, J., Nahen, K., Theisen, D., Busch, S., Parlitz, U., Hammer, D. X., Noojin, G. D., Rockwell, B. A. and Birngruber, R. (1999). Energy balance of optical breakdown in water at nanosecond to femtosecond time scales, *Appl. Phys. B*, **68**, 271–280.
78. Capitelli, M., Capitelli, F. and Eletskii, A. (2000). Non-equilibrium problems in laser-induced plasmas, *Spectrochim. Acta, Part B*, **55**, 559–574.

79. Feng, Q., Moloney, J. V., Newell, A. C. and Wright, E. M. (1997). Theory and simulation on the threshold of water breakdown induced by focused ultrashort laser pulses, *IEEE J. Quantum Electron.*, **33**, 127–137.
80. Evans, L. R. and Morgan, C. G. (1969). Lens aberration effects in optical-frequency breakdown of gases, *Phys. Rev. Lett.*, **22**, 1099–1102.
81. Evans, L. R. and Morgan, C. G. (1969). Intensity distribution of focussed laser beams in bio-medical studies, *Phys. Med. Biol.*, **14**, 205–212.
82. Walther, C., Buchner, S., Filella, M., Channdel, V. Probing particle size distributions in natural surface waters from 15 nm to 2 μm by a combination of LIBD and single particle counting, *J. Coll. Int. Sci.* **301**, 532–537 (2006).
83. Mainfray, G. (1977). Resonance and laser temporal coherence effects in multiphoton ionisation of atoms. In *Multiphoton Processes*, eds Eberly, J. H. and Lambropoulos, P., John Wiley & Sons, Inc., New York, pp. 253–266.
84. Sobral, H., Villagran-Muniz, M., Navarro-Gonzalez, R. and Raga, A. C. (2000). Temporal evolution of the shock wave and hot core air in laser induced plasma, *Appl. Phys. Lett.*, **77**, 3158–3160.
85. Warner, K. and Hieftje, G. M. (2002). Thomson scattering from analytical plasmas, *Spectrochim. Acta, Part B*, **57**, 201–241.
86. Hammer, D. X., Jansen, E. D., Frenz, M, Noojin, G. D., Thomas, R. J., Noack, J., Vogel, A., Rockwell, B. A. and Welch, A. J. (1997). Shielding properties of laser-induced breakdown in water for pulse durations from 5 ns to 125 fs, *Appl. Opt*, **36**, 5630–5640.
87. Francois, L., Mostafavi, M., Belloni, J., Delouis, J. F., Delaire, J. and Feneyrou, P. (2000). Optical limitation induced by gold clusters. 1. Size effect, *J. Phys. Chem. B*, **104**, 6133–6137.
88. Hahn, D. W., Flower, W. L. and Hencken, K. R. (1997). Discrete particle detection and metal emissions monitoring using laser-induced breakdown spectroscopy, *Appl. Spectrosc.*, **51**, 1836–1844.
89. Hauser, W. and Götz, R. (1999). Druckwellensensor, *German Patent*, DE-19602048.
90. Degueldre, C., Triay, I., Kim, J. I., Vilks, P., Laaksoharju, M. and Miekeley, N. (2000). Groundwater colloid properties: a global approach, *Appl. Geochem.*, **15**, 1043–1051.
91. Rosse, P. and Loizeau, J. L. (2003). Use of single particle counters for the determination of the number and size distribution of colloids in natural surface waters, *Colloids Surf. A*, **217**, 109–120.
92. Rayleigh, Lord (1871). On the light from the sky, its polarization and colour, *Philos. Mag.*, **41**, 107.
93. Walther, C. (2003). Comparison of colloid investigations by single particle analytical techniques–a case study on thorium-oxyhydroxides, *Colloids Surf. A.*, **217**, 81–92.
94. Degueldre, C., Bilewicz, A., Hummel, W. and L. Loizeau, J. (2001). Sorption behaviour of Am on marl groundwater colloids, *J. Environ. Radioactivity*, **55**, 241–253.
95. Borkovec, M. (2002). Measuring particle size by light scattering. In *Handbook of Applied Surface and Colloid Chemistry*, vol. 2, Holmberg, K. ed. John Wiley & Sons, Inc., New York, pp. 357–370.
96. http://www.pmeasuring.com/particleCounting/liquid/upw/ultraDI, Ultra DI ultra pure water laser particle counter, (2004).
97. Walther, C., Cho, H. R. and Fanghänel, Th. (2004). Measuring multimodal size distributions of aquatic colloids at trace concentrations, *Appl. Phys. Lett.*, **85**, 6329–6331.
98. Chylek, P., Jarzembski, M. A., Chou, N. Y. and Pinnick, R. G. (1986). Effect of size and material of liquid spherical-particles on laser-induced breakdown, *Appl. Phys. Lett.*, **49**, 1475–1477.
99. Buffle, J. and Leppard, G. G. (1995). Characterization of aquatic colloids and macromolecules. 1. Structure and behavior of colloidal matter, *Environ. Sci. Technol.*, **29**, 2169–2175.
100. Buffle, J. and Leppard, G. (1995). Characterization of aquatic colloids 2. Key role of physical structures on analytical results, *Environ. Sci. Technol.*, **29**, 2176–2184.
101. Evans, D. F. and Wennerström, H. (2000). *The Colloidal Domain*. VCH, New York.
102. Kim, J. I. (1994). Actinide colloids in natural aquifer systems, *Mater Res. Soc. Bull.*, **19**, 47–53.

103. Ledin, A., Karlsson, S., Düker, A. and Allard, B. (1994). Measurements *in situ* of concentration and size distribution of colloidal matter in deep groundwaters by photon correlation spectroscopy, *Water Res.*, **28**, 1539–1545.
104. Ledin, A., Karlsson, S., Dueker, A. and Allard, B. (1995). Characterization of the submicrometer phase in surface waters: a review, *Analyst*, **120**, 603–608.
105. Ryan, J. N. and Elimelech, M. (1996). Colloid mobilization and transport in groundwater, *Colloids Surf.*, **107**, 1–56.
106. Degueldre, C. (1997). Groundwater colloid properties and their potential influence on radionuclide transport, *Mater. Res. Symp. Proc.*, **465**, 835–846.
107. Filella, M., Zhang, J., Newman, M. and Buffle, J. (1997). Analytical applications of photon correlation spectroscopy for size distribution measurements of natural colloidal suspensions: capabilities and limitations, *Colloids Surf., A*, **120**, 27–46.
108. Wachter, U. (2004). *Die Schwebstofffracht des Bodenseetrinkwassers*. Diploma, University of Konstanz.
109. Wagner, T., Bundschuh, T., Schick, R. and Koster, R. (2004). Detection of aquatic colloids in drinking water during its distribution via a water pipeline network, *Water Sci. Technol.*, **50**, 27–37.
110. Bundschuh, T., Wagner, T., Weber, M. and Koster, R. (2004). Method of laser-induced breakdown detection and application examples, *Chem. Eng. Tech.*, **27**, 377–382.
111. Honeyman, B. D. (1999). Colloidal culprits in contamination, *Nature*, **397**, 23–24.
112. Kersting, A. B., Efurd, D. W., Finnegan, D. L., Rokop, D. J., Smith, D. K. and Thompson, J. L. (1999). Migration of plutonium in ground water at the Nevada test site, *Nature*, **397**, 56–59.
113. Geckeis, H., Schäfer, T., Hauser, W., Rabung, Th., Missana, T., Degueldre, C., Möri, A., Eikenberg, J., Fierz, Th. and Alexander, W. R. (2004). Results of the colloid and radionuclide retention experiment (CRR) at the Grimsel Test Site (GTS), Switzerland–impact of reaction kinetics and speciation on radionuclide migration, *Radiochim. Acta*, **92**, 9–11.
114. Laaksoharju, M. (2001). Äspö hard rock laboratory, project description of the Äspö project colloid with the aim to investigate the stability and mobility of colloids, *SKB International Progress Report IPR*, 3–38.
115. Tonner, B. P., Droubay, T., Denlinger, J., Meyer-Ilse, W., Warwick, T., Rothe, J., Kneedler, E., Pecher, K., Nealson, K. and Grundl, T. (1999). Soft x-ray spectroscopy and imaging of interfacial chemistry in environmental species, *Surf. Interface Anal.*, **27**, 247–258.
116. Rothe, J., Denecke, M. A. and Dardenne, K. (2000). Soft x-ray spectromicroscopy investigation of the interaction of aquatic humic acid and clay colloids, *J. Colloid Interface Sci.*, **231**, 91–97.
117. Cho, H. R., Walther, C., Rothe, J., Neck, V., Denecke, M. A., Dardenne, K. and Fanghänel, Th. (2005). Combined LIBD and EXAFS investigation of the formation and structure of Zr(IV) colloids, *Anal. Bioanal. Chem.*, **383**, 28–40.
118. Monsallier, J. M., Bitea, C., Scherbaum, F. J., Buckau, G. and Kim, J. I. (2000). Application of libd to humic size investigation, *Technical Report FZK*, Forschungszentrum Karlsruhe, PO 3640, 76021 Karlsruhe, Germany.
119. Artinger, R., Buckau, G., Kim, J. I. and Geyer, S. (1999). Characterization of ground-water humic and fulvic acids of different origin by GPC with UV/VIS and fluorescence detection, *Fresenius' J. Anal. Chem.*, **364**, 737–745.
120. Artinger, R., Buckau, G., Geyer, S., Fritz, P., Wolf, M. and Kim, J. I. (2000). Characterization of groundwater humic substances: influence of sedimentary organic carbon, *Appl. Geochem.*, **15**, 97–116.
121. Bundschuh, T., Wagner, T., Eberhagen, I., Hambsch, B. and Koster, R. (2005). Detection of biocolloids in aquatic media by nano-particle analyzer, *Spectroscopy*, **19**, 69–78.
122. Manh, T. N., Walther, C., Geckeis, H. and Kim, J. I. (2000). Detection of proteins by LIBD, unpublished results.
123. Walther, C. and Geckeis, H. (2005). Feinstaub Analyse von Diesel Abgasen in wasser, in preparation.

124. Panne, U. (2003). Laser induced breakdown spectroscopy (LIBS) in environmental and process analysis. In *Lasers in Environmental and Life Sciences*, eds. Hering, P., Lay, J.P. and Stry, S., Jan Springer, Berlin, pp. 99–123.
125. Zheng, J. B., Hsieh, W. F., Chen, S. C. and Chang, R. K. (1991). Laser-induced breakout and detonation waves in droplets. I. experiments, *J. Opt. Soc. Am. B*, **8**, 319–328.
126. Carls, J. C., Seo, Y. and Brock, J. R. (1991). Laser-induced breakout and detonation waves in droplets, *J. Opt. Soc. Am. B*, **8**, 329–336.
127. Singh, J. P., Zang, H., Yueh, F. Y. and Cook, R. L. (1993). Laser-induced breakdown spectra in a coal-fired MHD facility. In *Intersoc. Energy Convers. Eng.*, Vol. 1. American Chemical Society, Washington, DC, pp. 1.995–1.1000.
128. Poulain, D. E. and Alexander, D. R. (1995). Influences on concentration measurements of liquid aerosols by laser-induced breakdown spectroscopy, *Appl. Spectrosc.*, **49**, 569–579.
129. Hahn, DW. (1998). Laser-induced breakdown spectroscopy for sizing and elemental analysis of discrete aerosol particles, *Appl. Phys. Lett.*, **72**, 2960–2962.
130. Carranza, J. E., Fisher, B. T., Yoder, G. D. and Hahn, D. W. (2001). On-line analysis of ambient air aerosols using laser-induced breakdown spectroscopy, *Spectrochim. Acta, Part B*, **56**, 851–864.
131. Andreev, A. and Ueda, T. (2001). Detection of carbon particle and cluster parameters by laser-induced plasma line radiation. In *Fullerenes and Atomic Clusters, IWFAC' 2001*, St Petersburg, p. 288, http://www.ioffe.rssi.ru/IWFA/2001/index.html.
132. Hybl, J. D., Litngow, G. A. and Buckley, S. G. (2003). Laser-induced breakdown spectroscopy detection and classification of biological aerosols, *Appl. Spectrosc.*, **57**, 1207–1215.
133. Niida, T., Kousaka, Y. and Oda, S. (1988). Aerosol generation method for measuring particles suspended in water–detection of particulate impurities in ultrapure water and sizing of fine powders, *Part. Part. Syst. Charact.*, **5**, 139–143.
134. Panne, U., Haisch, C., Liermann, J. and Niessner, R. (1997). Characterization of aquatic colloids by laser-induced plasma spectroscopy (LIPS), *Wasser*, **88**, 227–241.
135. Haisch, C., Liermann, J., Panne, U. and Niessner, R. (1997). Characterization of colloidal particles by laser-induced plasma spectroscopy (LIPS), *Anal. Chim. Acta*, **346**, 23–35.
136. Haisch, C., Panne, U. and Niessner, R. (1998). Combination of an intensified charge coupled device with an echelle spectrograph for analysis of colloidal material by laser-induced plasma spectroscopy, *Spectrochim. Acta, Part B*, **53**, 1657–1667.
137. Wal, R. L. vander, Ticich, T. M., West, J. R. and Householder, P. A. (1999). Trace metal detection by laser-induced breakdown spectroscopy, *Appl. Spectrosc.*, **53**, 1226–1236.
138. Gornushkin, I. B., Ruiz-Medina, A., Anzano, J. M., Smith, B. W. and Winefordner, J. D. (2000). Identification of particulate materials by correlation analysis using a microscopic laser induced breakdown spectrometer, *J. Anal. At. Spectrom.*, **15**, 581–586.
139. Bulajic, D., Corsi, M., Cristoforetti, G., Legnaioli, S., Palleschi, V., Salvetti, A. and Tognoni, E. (2002). A procedure for correcting self-absorption in calibration free-laser induced breakdown spectroscopy, *Spectrochim. Acta, Part B*, **57**, 339–353.
140. Kim, T., Lin, C. I. and Yoon, Y. (1998). Compositional mapping by laser-induced breakdown spectroscopy., *J. Phys. Chem B*, **102**, 4284–4287.
141. Bauer, H. E., Leis, F. and Niemax, K. (1998). Laser induced breakdown spectrometry with an echelle spectrometer and intensified charge coupled device detection, *Spectrochim. Acta, Part B*, **53**, 1815–1825.
142. Beddows, D. C. S., Samek, O., Liska, M. and Telle, H. H. (2002). Single-pulse laser-induced breakdown spectroscopy of samples submerged in water using a single-fibre light delivery system, *Spectrochim, Acta, Part B*, **57**, 1461–1471.
143. Castle, B. C., Talabardon, K., Smith, B. W. and Winefordner, J. D. (1998). Variables influencing the precision of laser-induced breakdown spectroscopy measurements, *Appl. Spectrosc.*, **52**, 649–657.
144. Gornushkin, I. B., Smith, B. W., Potts, G. E. and Omenetto, N. (1999). Some considerations on the correlation between signal and background in laser-induced breakdown spectroscopy using single-shot analysis, *Anal. Chem.*, **71**, 5447–5449.

145. Huang, J.-S., Ke, C. B., Huang, L. S. and Lin, K. C. (2002). The correlation between ion production and emission intensity in the laser induced breakdown spectroscopy of liquid droplets, *Spectrochim. Acta, Part B*, **57**, 35–48.
146. Huang, J.-S., Ke, C.-B. and Lin, K. C. (2004). Matrix effect on emission/current correlated analysis in laser-induced breakdown spectroscopy of liquid droplets, *Spectrochim. Acta, Part B*, **59**, 321–326.
147. Hotokezaka, H., Tanaka, S., Suzuki, A. and Nagasaki, S. (2000). Speciation analysis on europium(III) using laser-induced breakdown spectroscopy, *Radiochim. Acta*, **88**, 645–648.
148. Pearse, R. W. B. and Gaydon, A. G. (1976). *The Identification of Molecular Spectra.* Chapman and Hall, London.
149. Burtscher, H., Mueller, U. and Schmidt-Ott, A. (1989). Monitoring adsorption on small particles, *Z. Phys. D*, **12**, 563–565.
150. Uiterwaal, C. J., Gebhardt, C. R., Schröder, H. and Kompa, K.-L. (2001). Analysis of nonlinear ionization of atoms and molecules based on their photoabsorption spectra in the ionization continuum, unpublished results.
151. Hauser, W. and Bundschuh, T. (1998). Verfahren zur Bestimmung der Größe von Partikein in einer Losung, *German Patent*, DE-19833339.
152. März, F., Scheer, R. and Graf, E. (1990). Use of a laser diffraction particle counter to monitor integrity of reverse osmosis membranes and its inefficiency to detect bacteria in product water, *Int. J. Pharm.*, **61**, 57–66.
153. Takanashi, S., Ishikawa, M. and Ohbayashi, K. (1998). Detection of submicron particles in water using Fabry-Perot interferometer, *Jpn. J. Appl. Phys., Part 1*, **37**, 2708–2711.
154. Alder, H. P., Degueldre, C. and Schenker, E. (1996). Non-invasive monitoring of corrosion in the light water reactor by optical methods, *Water Chem. Nucl. Reactor Syst.*, **7**, 272–276.
155. Degueldre, C., Pfeiffer, H. R., Alexander, W., Wernli, B. and Bruetsch, R. (1996). Colloid properties in granitic groundwater systems. I. Sampling and characterisation, *Appl. Geochem.*, **11**, 677–695.
156. Rees, T. F. (1987). A review of light scattering techniques for the study of colloids in natural waters, *J. Cont. Hydr.*, **1**, 425–439.
157. Bouby, M., Geckeis, H., Manh, T. N., Yun, J.-I., Dardenne, K., Schäfer, Th., Walther, C. and Kim, J.-I. (2004). Laser-induced breakdown detection combined with asymmetrical flow field-flow fractionation: application to iron oxy/hydroxide colloid characterization, *J. Chromatogr. A*, **1040**, 97–104.
158. DVD-ROM (2001). *Encyclopaedia Britannica*. www.Britannica.co.uk, London.

4.5.3 Measuring multimodal size distributions of aquatic colloids at trace concentrations [Walt04]

Measuring Multimodal Size Distributions of Aquatic Colloids at Trace Concentrations

C. Walther,* H.R. Cho, and Th. Fanghänel
Institut für Nukleare Entsorgung, Forschungszentrum Karlsruhe, Postfach 3640, D-76021 Karlsruhe, Germany
(Dated: November 11, 2004)

Many applications in research as well as industry require a highly sensitive detection of particulate matter in water or process liquids. We present a technique to measure the distribution of colloid sizes between 20 and 100 nm in situ at ultratrace concentrations. The method is based on laser-induced breakdown detection, which has been applied for trace detection of colloids and determination of the weighted mean size. Using a refined method of data evaluation, we are now able to measure the number density of inorganic colloids in six size classes between 20 and 100 nm simultaneously below ppb concentration.

PACS numbers: 82.70.Dd,82.80.-d,78.66.Vs
Keywords: colloid, aquatic, breakdown

The increasing demands for ultraclean process liquids of ever higher purity lead to the development of laser-induced breakdown detection (LIBD) for the quantification of aquatic colloids in trace concentration by Kitamori and coworkers [1–3] to detect trace contaminations of process liquids for the semiconductor industry. The method is now well known and finds application in a variety of research fields: size determination of aerosols in-situ [4, 5], microbubble formation in an aqueous solution of a silver/dendrimer nanocomposite [6], drinking water characterization [7], and in-situ groundwater colloid characterization, e.g., in Grimsel (Switzerland) and Äspö (Sweden) [8]. Colloids of tetravalent actinides formed in oversaturated solutions are investigated in order to determine thermodynamic solubility data [9, 10] and gain insight into their long-term stability. [11, 12]. Only a mean particle size could be obtained with LIBD in these experiments. However, knowledge of the size distribution would have been vitally important. For examples in [9, 10] small nascent colloids are observed, which increase the apparent solubility of a solution by many orders of magnitude; this effect strongly depends on particle size (Schindler equation)[13, 14]. Using a refined data evaluation method of LIBD we are now able to measure particle size distributions between 20 and 100 nm in sub-ppb concentration. This will help to improve future investigations of solubility and colloid migration.

When a pulsed laser is highly focused into a medium and exceeds a certain irradiance threshold, a so-called breakdown occurs [15]. In the case of nanosecond lasers [16], at least one atom is ionized by multiphoton ionization (MPI) at the beginning of the laser pulse. The resulting seed electron is accelerated due to inverse bremsstrahlung in the high electric field of the laser focus. After gaining sufficient energy, additional atoms are ionized by collisions, thereby multiplying the number of electrons. The density of free charge carriers increases as avalanche and after a few consecutive iterations a plasma is created. The energy density necessary to initiate this process (threshold) depends on the phase of the matter in the focal region. Breakdown thresholds for colloids (solid phases) are lower than for pure water, allowing their detection in aqueous solution. When a colloid in solution enters the focal region of a laser with sufficient irradiance, a plasma is then ignited [17]. The plasma can be detected by its optical emission [18] or by a piezo detector coupled to the sample cell, recording the acoustic signal of the plasma expansion [19, 20]. By counting the number of breakdown events relative to a predefined number of laser shots (breakdown probability), the particle number density in the solution can be determined [21, 22]. Size information is gained by measuring the breakdown probability as a function of pulse energy [23]. The ionization rate of a particle is proportional to the MPI-cross-section multiplied by an appropriate power of the photon-flux density. The cross-section increases proportional to the particle volume (proportional to the number of valence electrons in the particle), so the breakdown threshold decreases with increasing particle size [24]. For an unknown sample, the threshold is determined by recording the breakdown probability for increasing laser pulse energies (so called s-curves) and converted to a mean particle diameter. While the physical processes of breakdown generation on a small suspended colloid are quite complex, the s-curves can be described by a semi empirical model in eq.1 with only two free parameters. The breakdown threshold E_o is a measure of particle size and the concentration determines the constant C.

$$P_{mono} = 1 - \Big\{(1 + C(E - E_o) - \frac{1}{2}\big(C(E - E_o)\big)^2 + \frac{1}{6}\big(C(E - E_o)\big)^3\Big\} \cdot \exp[-C(E - E_o)] \quad (1)$$

Since the 'first electron' is generated by four-photon-ionization in the case of polystyrene ($h\nu = 2.3\,\mathrm{eV}$, $\mathrm{IP}_{Polystyrene} = 8.9\,\mathrm{eV}$) and in the case of most inorganic

*Electronic address: e-mail:walther@ine.fzk.de; URL: correspondingauthor:FAX:++49/7247/823927

colloids, at low pulse energy, a $P_{mono} \propto E^4$ dependence is required [25]. If one expands eq.1 in a Taylor series the first three terms up to $(E - E_0)^3$ cancel which results in the $\propto E^4$ dependence. The negative sign of the quadratic term causes a weak second order (E^2) dependency which describes the increase of the effective focal volume $V_{eff} \propto E^2$ as the pulse energy is increased [26]. Since the probability of a colloid to be detected scales linearly with the focal volume, the breakdown probability also increases. P approaches unity asymptotically as $E \to \infty$.

Strictly speaking eq.1 only describes narrow size distributions (monomodal), which can be prepared synthetically, but are of little relevance in nature. What happens in a 'real' system when the size distribution extends over several orders of magnitude? We now make use of the weak size dependency of breakdown detection. While light scattering methods suffer from a decrease in signal proportional to the sixth power of particle diameter (D^{-6}), the detection limit of LIBD scales linearly with D from $\sim 10^3 \mathrm{ml}^{-1}$ at 1000 nm to $\sim 10^5 \mathrm{ml}^{-1}$ at 10 nm, due to the increase in effective focal volume for increasing particle size [21]. As a consequence, screening of small particles by large ones is weak. This provides the key to our approach of measuring size distributions.

Let us consider a bimodal colloidal suspension containing particles of sizes D_1 and $D_2 < D_1$. Below the threshold for the fraction of colloids with size D_2 the 's-curve' will be identical to that of a pure sample colloids with size D_1. As the pulse energy increases and exceeds the threshold of the smaller sized colloids D_2, the latter will contribute to the sum-curve. Since the s-curve represents a probability, the sum is given by the product of the probabilities of the inverse, i.e., of no breakdown to occur.

$$P_{Bi} = 1 - (1 - P_1) \cdot (1 - P_2) \tag{2}$$

Combining eqs. (1) and (2), we get

$$\begin{aligned} P_{Bi} \;=\; & 1 - \prod_{i=1}^{2} \Big\{ 1 + C^{(i)}(E - E_o^i) - \frac{1}{2}\big(C^{(i)}(E - E_o^i)\big)^2 \\ & + \; \frac{1}{6}\big(C^{(i)}(E - E_o^i)\big)^3 \Big\} \cdot \exp[-C^{(i)}(E - E_o^i)] \end{aligned} \tag{3}$$

with $E_o^{(i)}$ and $C^{(i)}$ being the threshold and the parameter of colloid number density respectively. Equation (3) is easily extended for any number of size classes. In order to obtain the size distribution of an unknown sample, the s-curve is measured with high statistics and the product of convoluted exponentials in eq.3 is fitted to the data.

In praxis, we have to limit the number of free fitting parameters. In the following example we used six size classes, namely 20, 30, 40, 50, 70, and 100 nm . The thresholds $E_o^{(i)}$ are obtained by calibration with monodisperse polystyrene reference spheres of 21(1.5), 34(1.4), 41(1.8), 50(2), 73(1.6), and 101(3) nm and remain fixed thereafter. Monomodal suspensions of several concentrations are measured in order to calibrate the slope parameter $C^{(i)}$ versus colloid number density per unit volume N according to the semi-empirical eq.4

$$\log C^{(i)} = a^{(i)} \log (b^{(i)} N^{(i)}) \tag{4}$$

In order to obtain size distributions, we measure the s-curve of the sample with high statistics, especially in the low pulse energy region, which carries the size information. Increasing the particle size from 20 nm to 100 nm causes a decrease of threshold $E_o^{(i)}$ by a factor of three from 0.52 mJ to 0.30 mJ for the optics setup used. This is small compared to the typical energy interval of a complete 's-curve' (depicted in Fig.1(a)). Eq. (3) is then fit to the data by the MIGRAD algorithm of the CERNLIB MINUIT FORTRAN library [27]. The threshold-parameters $E_0^{(i)}$ remain fixed, since they determine the size classes, and only the the concentration parameters $C^{(i)}$ are varied. In spite of six parameters being simultaneously fit, the fit is quite robust, since the parameters hardly affect each other; each parameter is sensitive to a unique region of the s-curve. $C^{(1)}$ is determined in the region below $E_0^{(2)}$, the threshold of the second size class,

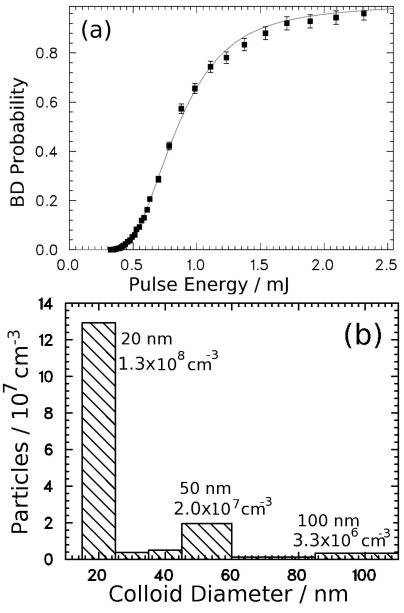

FIG. 1: The particle size distribution (PSD) of a synthetic three modal colloid sample of polystyrene spheres is reproduced within 20% error (see text): Viewgraph (a) shows the relative number of breakdown events (BD probability) as a function of laser pulse energy. From the curve fit the PSD is determined and is shown in the histogram (b).

$C^{(2)}$ at energies $E_0^{(2)} < E < E_0^{(3)}$ and so forth. Figure 1 illustrates the case of a trimodal sample of polystyrene reference beads containing $1.5{\cdot}10^8$part/ml with 20 nm diameter, $2.0{\cdot}10^7$part/ml with 50 nm, and $2.7{\cdot}10^6$part/ml with 100 nm in order to simulate a Pareto-like particle size distribution as found in natural waters [28–30]. The number density of different sizes scales as a power law of the particle diameter D:

$$N(D) \propto D^{-\beta} \qquad ; \qquad 3 < \beta < 5 \tag{5}$$

In Fig. 1(a) the raw data, i.e. the number of breakdown events as a function of laser pulse energy is plotted. Note the high quality of the data at low pulse energies, which is crucial. All six concentration parameters $C^{(i)}$ are varied and the result displayed in the histogram of

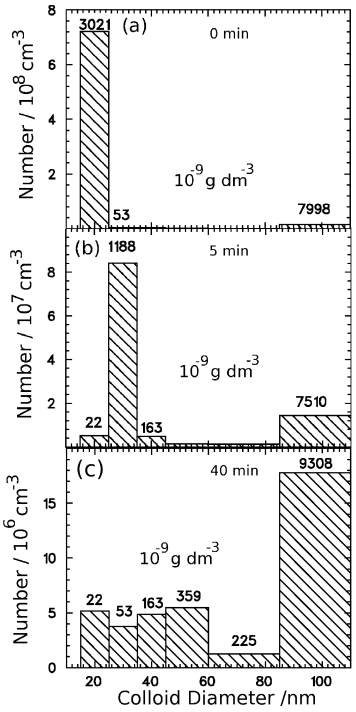

FIG. 2: Time resolved observation of agglomeration in a multimodal bentonite colloid suspension (10 ppb) at pH 6 and at pH 2 after 5 min and 40 min

Fig. 1(bottom) is obtained: $C^{(1)}$, $C^{(4)}$ and $C^{(6)}$ yield finite values, whereas $C^{(2)}$,$C^{(3)}$ and $C^{(5)}$ remain close to zero, which demonstrates that little crosstalk to lower size classes exists. This phantom signal which results from large colloids, is a severe problem in the case of static light scattering [31]. The particle number concentrations are reproduced within approximately 20% error. If, however, a sample contains a predominant fraction of large colloids, screening effects may occur. Colloids do not contribute to the sum-curve below their specific threshold $E_o^{(i)}$. In order for the contribution of small colloids (at comparatively high energy) to be of measurable relevance, the signal caused by the large colloids must remain sufficiently low. As the s-curve $P(E_o^{(i)})$ approaches unity, an additional increase due to a fraction of very small size can no longer be resolved. As a rule of thumb an excess up to the 10 fold weight concentration of particles larger than 1 μm is tolerated (example: the presence of 10 ppb colloids with 1 μm size does not affect the detection of 1 ppb colloids with 20 nm diameter)

The method is especially suited to observe changes in size distribution as a function of time, e.g., in the case of particle agglomeration. In Fig.2 we present results of investigations on FEBEX bentonite colloids [32, 33]. Histogram (a) reflects the original (bimodal) size distribution at pH 6. The size class of 100 nm contains two thirds of the total colloidal mass (7ppm), the rest (3ppm) has a size of approximately 20 nm. Due to their small mass ($^1/_{125}$ of a 100 nm colloid), the small fraction contributes to the dominant colloid *number*. Subsequently the acidity is increased to pH 2 in 10 mM NaCl solution. The electric double layer at the edges of the plate like colloids is neutralized [32] and agglomeration proceeds quickly, as can be seen from graph (b). The particle size distribution is noticeably shifted to larger diameters after 5 min. A rough estimate of the agglomeration constant yields a stability ratio W 4. The fraction of 100 nm particles remains constant. This is because collisions of two 100 nm particles are unlikely due to their lower number density. After 40 min virtually all particles formed agglomerates of 100 nm or larger (histogram c).

Future applications of this method lie in the field of colloid mediated transport of actinides. In particular, alteration products of backfill materials in a repository (e.g. bentonite) or corroding containers (e.g., magnetite) are subject to pseudocolloid formation. It is important to gain insight into the underlying chemical and physical processes. Recently, in situ experiments of colloid transport through granite fractures were performed in the Grimsel underground laboratory indicating a size fractionation of the transported colloids. However, the classical LIBD method allowed only to determine a weighted mean size of the colloids and the change in the particle size distribution could not be detected directly. By using the refined evaluation scheme we are now able to measure a change in size distributions. With the present calibration of our instrument we are restricted to a size region between 20 and 100 nm. Extension to a larger size range is presently under way.

Acknowledgments

The authors thank T. Schäfer for preparation of the bentonite samples, S. Büchner for LIBD measurements and M.A. Denecke, F.J. Scherbaum and J.I. Yun for valuable discussions.

[1] T. Kitamori, K. Yokose, K. Suzuki, T. Sawada, and Y. Goshi. Japanese J. Appl. Phys. **27(6)**, L983–L985 (1988).
[2] T. Kitamori, K. Yokose, M. Sakagami, and T. Sawada. Japanese J. Appl. Phys. **28(7)**, 1195–1198 (1989).
[3] H. Fujimori, T. Matsui, T. Ajiro, K. Yokose, Y.M. Hsueh, and S.S. Izumi. Jpn. J. Appl. Phys. **31(Part 1, 5A)**, 1514–1518 (1992).
[4] DW Hahn. Applied Physics Letters **72(23)**, 2960–2962 (1998).
[5] DE Poulain and DR Alexander. Applied Spectroscopy **49(5)**, 569–579 (1995).
[6] S. M. Milas, J. Y. Ye, T. B. Norris, L. P. Balogh, J. R. Baker, K. W. Hollman, S. Emelianov, and M. O'Donnell. Applied Physics Letters **82(6)**, 994–996 (2003).
[7] M Saito, S Izumida, K Onishi, and J Akazawa. Journal of Applied Physics **85(9)**, 6353–6357 (1999).
[8] W. Hauser, H. Geckeis, J.I. Kim, and Th. Fierz. Coll. Surf. A **203(1-3)**, 37–45 (2002).
[9] T. Bundschuh, R. Knopp, R. Müller, J.I. Kim, V. Neck, and Th. Fanghänel. Radiochim. Acta **88**, 625–629 (2000).
[10] V. Neck, R. Müller, M. Bouby, M. Altmaier, J. Rothe, M.A. Denecke, and J.I. Kim. Radiochim. Acta, **90**, 485–494 (2002).
[11] J. Rothe, C. Walther, M. A. Denecke, and T. Fanghanel. Inorganic Chemistry **43(15)**, 4708–4718 (2004).
[12] C. Bitea, R. Müller, V. Neck, C. Walther, and J.I. Kim. Coll. Surf. A **217**, 63–70 (2003).
[13] P. Schindler, H. Althau, F. Hofer, and W. Minder. Helvet. Chim. Acta **48**, 1204 (1965).
[14] P.W. Schindler. Advances in Chemistry Series **67**, 196 (1967).
[15] L. J. Radziemski and D.A. Cremers. *Laser induced Plasmas and Applications*. Optical Engineering. Marcel Dekker Rochester (1989).
[16] M. H. Niemz. Applied Physics Letters **66(10)**, 1181–1183 (1995).
[17] C.A. Sacchi. J. Opt. Soc. Am. B **8(2)**, 337–345 (1991).
[18] T. Bundschuh, W. Hauser, J.I. Kim, R. Knopp, and F.J.Scherbaum. Coll. Surf. A **180**, 285–293 (2001).
[19] W. Hauser and T. Bundschuh. Patent (Germany) DE **19833339** (1998).
[20] W. Hauser and R. Götz. Patent (Germany) DE **19602048C2** (1999).
[21] F.J. Scherbaum, R. Knopp, and J.I. Kim. Appl. Phys. B **63**, 299–306 (1996).
[22] T. Bundschuh, R. Knopp, and J.I. Kim. Colloids and Surfaces A **177**, 47–55 (2001).
[23] C. Walther, C.Bitea, W. Hauser, J.I. Kim, and F.J. Scherbaum. Nucl. Instr. Meth.B **195**, 374–388 (2002).
[24] S. Izumida, K. Onishi, and M. Saito. Jap. J. Appl. Phys. 1 **37(4A)**, 2039–2042 (1998).
[25] P. Chylek, M. A. Jarzembski, N. Y. Chou, and R. G. Pinnick. Applied Physics Letters **49(21)**, 1475–1477 (1986).
[26] M.R. Cervenan and N.R. Isenor. Optics. Comm. **13(2)**, 175–178 (1975).
[27] F. James. *Minuit, Function Minimization and Error Analysis* volume 94.1 of *Refernce Manual*. CERN Program Library (1994).
[28] J. Buffle and G.G. Leppard. Env. Sci. Technol. **29(9)**, 2169–2175 (1995).
[29] D.F. Evans and H. Wennerström. *The Colloidal Domain*. VCH New York (2000).
[30] C. Degueldre, I. Triay, J.I. Kim, P. Vilks, M. Laaksoharju, and N. Miekeley. Appl. Geochem. **15**, 1043–1051 (2000).
[31] P. Rosse and J.L. Loizeau. Coll. Surf. A **217**, 109–120 (2003).
[32] M.V. Villar, P.L. Martin, M. Pelayo, B. Ruiz, P. Rivas, E. Alonso, A. Lloret, X. Pintado, A. Gens, J. Linares, F. Huertas, E. Caballero, C. Jimenz de Cisneros, J. Obis, A. Perez, and J. Velasco. FEBEX bentonite: origin, properties and fabrication of blocks (full-scale engineered barriers experiment in crystalline host rock). Technical report 05/98 Enresa (empresa nacional de residuos radiactivos, s.a.) October 1998 1998.
[33] M. Plaschke, T. Schäfer, T. Bundschuh, N.M. Thang, R. Knopp, H. Geckeis, and J.I.Kim. Anal. Chem. **73**, 4338–4347 (2001).

4.5.4 Probing particle size distributions in natural surface waters from 15 nm to 2μm by a combination of LIBD and single-particle counting [Walt06]

Available online at www.sciencedirect.com
ScienceDirect
Journal of Colloid and Interface Science 301 (2006) 532–537
JOURNAL OF Colloid and Interface Science
www.elsevier.com/locate/jcis

Probing particle size distributions in natural surface waters from 15 nm to 2 μm by a combination of LIBD and single-particle counting

Clemens Walther [a,*], Sebastian Büchner [a], Montserrat Filella [b], Vincent Chanudet [b,c]

[a] *Institut für Nukleare Entsorgung, Forschungszentrum Karlsruhe, Postfach 3640, D-76021 Karlsruhe, Germany*
[b] *Department of Inorganic, Analytical and Applied Chemistry, University of Geneva, Quai Ernest-Ansermet 30, CH-1211 Genève 4, Switzerland*
[c] *Institut F.A. Forel, University of Geneva, Route de Suisse 10, CH-1290 Versoix, Switzerland*

Received 10 April 2006; accepted 18 May 2006
Available online 22 June 2006

Abstract

We present a technique for measuring colloid size distributions between 15 nm and 2 μm at concentrations relevant to natural surface waters. Two particle-measuring methods are combined: laser-induced breakdown detection (LIBD), which allows the quantification of colloid size distributions below 400 nm, and a commercial single-particle counter that extends the accessible size range up to two μm. Centrifugation was used in order to separate micrometer sized particles for the LIBD measurement. The feasibility is demonstrated on water of Lake Brienz (Switzerland) and the River Pfinz (Germany) and the particle size distributions follow Pareto's law even down to 15 nm in both cases.

Keywords: Colloid; Breakdown; Particle size distribution; LIBD; SPC; Fresh waters

1. Introduction

Solid particles are omnipresent in natural waters and the size distribution typically extends over many orders of magnitude from aquatic colloids in the lower nanometer domain to suspended particles many micrometers in diameter [1]. Detailed knowledge of the size distribution is mandatory in many different aspects of environmental and aquatic geochemistry [2,3], which might be illustrated by the prominent example of colloid-mediated transport of contaminants [4–10]. To quantify the sorption to colloids, their total reactive surface must be known and it does not suffice to measure the total mass of particulate matter, e.g., by filtration, since the surface-to-volume ratio of colloids increases linearly with decreasing size. However, it is not yet possible to cover the complete size range with one method [11]; rather, several techniques need to be combined. We report on the first results of combining a highly sensitive technique for submicrometer colloids, the laser-induced breakdown detection (LIBD), with a commercial light-scattering detection method, the so-called single-particle counter (SPC).

2. The method

In the late 1980s, the increasing demand for ultraclean process liquids of ever higher purity lead to the development of laser-induced breakdown detection for the quantification of aquatic colloids in trace concentrations [12–14]. The method made it possible to measure a mean diameter and a number density and is being applied in aerosol detection [15,16], nanotechnology [17], solubility measurements of metal oxides and metal hydroxides [18–21], drinking water characterization [22–24], and in situ groundwater colloid characterization [25–27]. An improved evaluation algorithm now allows the measurement of particle size distributions with LIBD [28], which was applied for characterization of zirconium colloids [29] and observation of size exclusion effects in colloid migration experiments [30]. In the present work we report a further extension of the size range from 15 to 400 nm for LIBD alone. Coupling with a single-particle counter allows the continuous measurement of the PSD from 15 nm to 2 μm, which is demonstrated on two natural systems.

* Corresponding author.
E-mail address: walther@ine.fzk.de (C. Walther).
URL: http://www.fzk.de.

0021-9797/$ – see front matter
doi:10.1016/j.jcis.2006.05.039

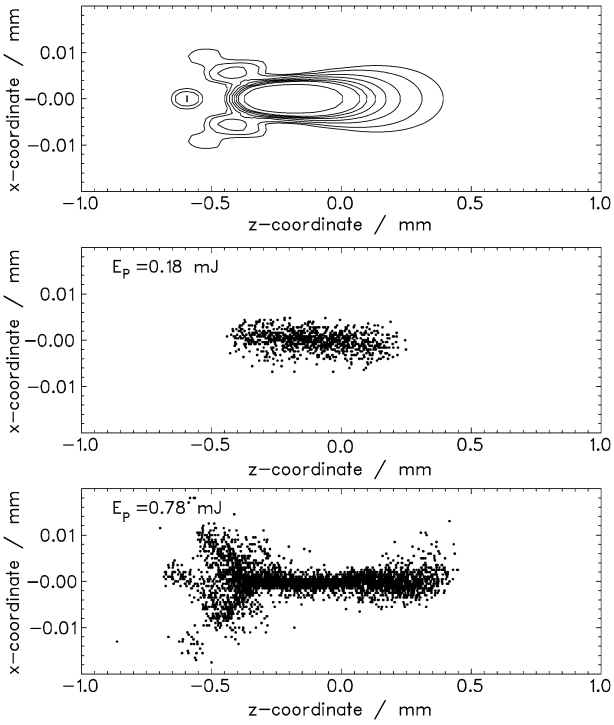

Fig. 1. Top: Regions of equal power density I (isophotes) for a Gaussian laser beam (TEM_{oo}) focused by a telescope of spherical lenses (−50 mm, +50 mm). Middle: A suspension of model colloids (polystyrene, diameter 500 nm, 1.5×10^6 part ml^{-1}) is imaged using a microscope lens and a CCD camera. At low laser pulse energy ($E_P^{(1)} = 0.18$ mJ), the events are distributed in a well-confined region around the center. Bottom: For $E_P^{(2)} = 0.78$ mJ the power density increases everywhere by a factor of $E_P^{(2)}/E_P^{(1)}$ and breakdown ignition becomes possible in regions where the power density did not exceed the threshold I_T before.

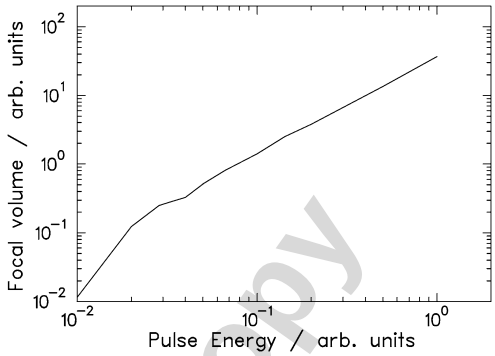

Fig. 2. Integration of the isophotes in Fig. 1 gives the spatial volume as a function of the power density I. This integrated volume where the power density suffices to ignite a breakdown ($I > I_T$) is called the effective focal volume (V). When plotted against the pulse energy E_P, the function shows an initial steep increase that evolves into an almost linear dependence (slope 1.3).

While the reader might refer to [31] for a detailed description on laser-induced breakdown and [27,32] for application to s-curve colloid detection, one important aspect of breakdown generation needs to be mentioned in order to describe the recent improvements. The breakdown is initiated selectively when a colloid is present in the focal region of the laser. At least one atom needs to be ionized by multiphoton ionization (MPI) [33] and the resulting seed electron is multiplied by inverse bremsstrahlung [34,35] in the high electric field of the laser focus and a hot plasma is formed. As a good approximation, breakdown ignition follows threshold behavior; i.e., above a certain power-density threshold I_T, plasma formation is possible (the power density I is defined by pulse energy per pulse length per area):

$$I = E_P/\tau A. \tag{1}$$

Consequently, a breakdown is ignited when a colloid enters a region with $I > I_T$. We now determine the exact geometry of the power density distribution of the focused Gaussian TEM_{oo} laser beam of our setup [27], using numerical integration of Bessel functions [36]. This method takes into account the spherical aberration of the telescope (−50 mm, +50 mm). In the upper part of Fig. 1, the isophotes, which enclose regions of equal power density I, are shown (the laser beam enters from the left). The volume inside each isophote, V_I, is numerically integrated, keeping in mind that the isophote plot of Fig. 1 (top) is a 2-dimensional lateral cut through a 3-dimensional, cylindrically symmetric distribution. This integrated volume, where the power density suffices to ignite a breakdown ($I > I_T$), is called the effective focal volume (V):

$$V_{I_T}(I) = 2\pi \int_{-\infty}^{\infty} \int_{0}^{\infty} H\big(I(x,z) - I_T\big) x \,\mathrm{d}x \,\mathrm{d}z. \tag{2}$$

The inner integral sums over all space where the critical power density for breakdown ignition, I_T, is exceeded (mathematically formulated by use of Heaviside's step function H). Of course this quantity is a function of the position along the beam axis z and depends on the power density (I). By use of Eq. (1) one obtains the expression $V(E_P)$, which describes the size of the effective focal volume as a function of pulse energy (Fig. 2). The function shows an initial steep increase that evolves into an almost linear dependence (slope 1.3).

The focal volume can be visualized by imaging the spatial positions of the plasma events inside the focus. A suspension of model colloids (polystyrene, diameter 500 nm, 1.5×10^6 part ml^{-1}) is imaged using a microscope lens and a CCD camera [27]. At low laser pulse energy ($E_P^{(1)} = 0.18$ mJ), the events are distributed in a well-confined region around the center (Fig. 1, middle), which corresponds to the isophote of highest flux (top). For $E_P^{(2)} = 0.78$ mJ (Fig. 1, bottom), the power density increases everywhere by a factor of $E_P^{(2)}/E_P^{(1)}$ and breakdown ignition becomes possible in regions where the power density did not exceed the threshold I_T before. The events distribute over a much wider range and reflect the outer isophote of Fig. 1 (top). Even the small local maximum at the left is reproduced.[1]

[1] Please note that the colloid size is 500 nm for both Fig. 1 (middle) and (bottom). This discussion should not be mistaken for the colloid size dependence of the effective focal volume, which was reported, e.g., by Bundschuh et al. in [37].

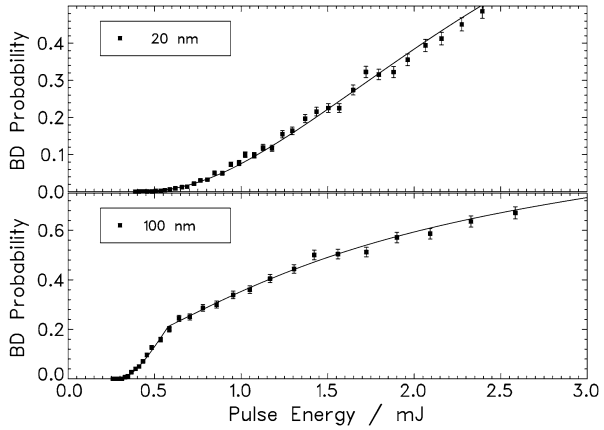

Fig. 3. Breakdown probability as a function of laser pulse energy E_P. Top: 20 nm polystyrene spheres (10^8 part ml^{-1}) show a pronounced E_P^4-dependence. Bottom: For 100-nm polystyrene spheres (2×10^8 part ml^{-1}), the curve flattens at approximately twice the threshold energy (see text).

To model the breakdown probability, i.e., the relative number of plasma-events per number of laser shots, as a function of laser pulse energy (s-curve), an additional effect must be considered. For visible light ($h\nu = 1.5$–3 eV) the simultaneous absorption of $m = 4\pm1$ photons is required [38] for exceeding the electron work function, which ranges from 6 to 10 eV for most solids [39]. This fourth-order process causes a fourth-order dependence of the plasma generation probability on the power density I [40–42]. For small colloids this effect dominates the laser-pulse-energy (E_P) dependence of the s-curve [28]. This is illustrated for the case of 20-nm polystyrene spheres in Fig. 3 (top). Larger particles consist of a greater number of molecules and have a large cross-section for MPI. Additional electrons are generated by thermal emission due to heating of the particle [43], which weakens the E_P-dependence of the s-curve (Fig. 3, bottom). In this case, when electrons are produced at a high rate, the breakdown generation is no longer limited by MPI but by the probability of colloids entering the focal region and hence by the increase of the effective focal volume $V(E_P)$.

This is now taken into account for the semiempirical model described in [28]. The s-curve of a monodisperse suspension of small colloids is described by the function

$$P_{\text{small}} = 1 - \left\{1 + C(E_P - E_T) - \frac{1}{2}\big(C(E_P - E_T)\big)^2 + \frac{1}{6}\big(C(E_P - E_T)\big)^3\right\}\exp\big[-C(E_P - E_T)\big]. \quad (3)$$

The particle size determines the breakdown threshold E_T and the particle concentration determines the constant C. If one expands Eq. (3) in a Taylor series the first three terms up to $(E_P - E_T)^3$ cancel, which results in the $\propto E_P^4$ dependence. P approaches unity as $E_P \to \infty$.

For large particles, the $\propto E_P^4$ dependence merges into a linear slope at about twice the pulse energy threshold ($E_P = 2E_T$). This is modeled by defining the breakdown probability function in two intervals:

$$\begin{aligned} P_{\text{large}} &= 1 - \left\{1 + C(E_P - E_T) - \frac{1}{2}\big(C(E_P - E_T)\big)^2 + \frac{1}{6}\big(C(E_P - E_T)\big)^3\right\} \\ &\quad\times \exp\big[-C(E_P - E_T)\big] \mid E_T < E_P < 2E_T \\ &= 1 - \exp\big[-B(E_P)\big] \qquad \mid E_P > 2E_T \end{aligned}$$

$$\text{with} \quad B = -\frac{\ln(1 - P(2E_T - E_T))}{2E_T}. \quad (4)$$

The constant B is determined from the condition that both parts of P_{large} should merge at the transition energy $E_P = 2E_T$. The solid lines in Fig. 3 represent fits of Eqs. (3) and (4) to the data, respectively. It is obvious that the s-curve of 100-nm particles (bottom) is well reproduced by Eq. (4), but it would not be possible to fit these data by Eq. (3).

To describe polydisperse samples, the s-curves are convoluted as described in [28]:

$$P_{\text{multi}}(E_P) = 1 - \prod_{i=1}^{N}\big(1 - P^{(i)}(E_P)\big). \quad (5)$$

For size fractions below 100 nm, $P^{(i)}$ has the form of Eq. (3), and for larger particles $P^{(i)}$ is described by Eq. (4). We use $N = 9$ size classes (10–20, 20–30, 30–40, 40–50, 50–70, 70–100, 100–200, and 200–400 nm) and each is represented by a unique threshold $E_T^{(i)}$. The thresholds $E_T^{(i)}$ and the slope parameters $C^{(i)}$ are calibrated by use of polystyrene reference spheres as described in [28].

In order to obtain size distributions of an arbitrary sample, we measure the s-curve of the sample with high statistics, and the product of convoluted s-curves in Eq. (5) is fit to the data by the MIGRAD algorithm of the CERN-LIB MINUIT FORTRAN library [44]. The threshold-parameters $E_T^{(i)}$ remain fixed, since they determine the size classes, and only the concentration parameters $C^{(i)}$ are varied. In spite of nine parameters being simultaneously fit, the fit is quite robust, since the parameters hardly affect each other; each parameter is sensitive to a unique region of the s-curve. $C^{(1)}$ is determined in the region below $E_T^{(2)}$, the threshold of the second size class, $C^{(2)}$ at energies $E_T^{(2)} < E < E_T^{(3)}$ and so forth. For polystyrene reference spheres, the particle number concentrations typically are reproduced within approximately 20% error.

If a sample contains a predominant fraction of large colloids, screening effects may occur: Colloids do not contribute to the sum-curve below their specific threshold $E_T^{(i)}$. If large particles, with low threshold, cause a high breakdown probability already below the threshold of the small ones, the latter can no longer contribute to the s-curve and are not detected. To some extend the contamination by large particles can be compensated for by background subtraction similar to the second part of Eq. (4):

$$P_{\text{back}}(E_P) = 1 - \exp\big[-C^{(B)}\big(E_P - E_T^{(B)}\big)\big]. \quad (6)$$

However, if the mass concentration of particles larger than 1 µm exceeds the mass concentration of the small particles which are to be detected considerably, prefractionation is necessary.

In parallel to the LIBD, particle size distributions were measured with a single-particle counter (SPC) in the nominal range from 50 to 2000 nm (for restrictions see below). The core instruments consist of two single-particle counters from PMS (Particle Measuring Systems, Boulder, CO): a high-sensitivity liquid in situ monitor (HSLIS) M50 and a LiQuilaz-S02 volumetric spectrometer. Both instruments are based on the principle of light scattering by single particles. The particularity of single-particle counters is that colloids cross the light beam one after the other. Each particle produces a light flash converted to an electrical pulse by a photodiode, the colloids being counted and sized by a pulse analyzer [45–47]. The intensity of the scattered light depends on the wavelength of the laser, the refractive index of the particle, its size, and its form. When the particle has a size close to that of the laser wavelength and the intensity is measured according to a sufficiently large angle, the intensity of the scattered light is, in an unequivocal way, a function of the size of the particles [45,47]. The HSLIS M50 allows the measurement of colloids in the range 50–200 nm separated into four channels (50–100, 100–150, 150–200, >200 nm). The LiQuilaz S02 measures colloids in the range 200–2000 nm in 15 adjustable size classes. These detectors were initially designed to count particles in ultrapure water. Dilution of the sample before the analysis is necessary to be able to make measurements in natural waters. A filtration system (Polygard-CR 0.5 m, Durapore 0.2 m, Optimizer DI 0.05 m) is needed to produce the ultrafiltered water used for the online sample dilution. High dilution factors allow better measurement of small particles (high number), whereas low dilution factors are preferred for larger particles (low number). The SPC makes it possible to measure the absolute number of colloids per unit volume in a broad range of concentrations covering the majority of natural surface waters. It has the advantage of being transportable and does not require any preparation of the samples. However, it is known from calibration measurements with polystyrene spheres [47] that the detection efficiency of the SPC decreases rapidly for small colloids (2.5% for 50–100 nm, ≈40% for 100–200 nm). Hence, LIBD provides important additional information not only below 50 nm but also for the size classes 50–200 nm.

3. Natural samples

The measurements of two natural samples are presented in the following. Example 1 is water from the Pfinz channel, close to Karlsruhe (Germany), which was measured within 2 h of sampling. The water was not characterized by additional methods but rather served as an example for a natural system.

The LIBD measurements were performed on 3-ml aliquots in static quartz cells with stirring. The laser pulse energy was increased stepwise by an automated system [27] and the breakdown probability measured for 1000 laser shots at each of 50–70 pulse energies. The breakdown probability as a function of pulse energy (s-curve) was fitted as described in Section 2, resulting in a particle size distribution [28]. An additional 100 ml of the sample was measured by the SPC. Both detectors were operated in parallel (HSLIS M50 and LiQuilaz S02) with a total constant flow (after dilution) of 150 ml min^{-1} (100 ml min^{-1} for the HSLIS M50 and 50 ml min^{-1} for the LiQuilaz). Samples were injected into the dilution line with a high-precision volumetric pump (Desaga KP2000) at different flow rates in order to be able to measure the particle size distribution at different dilution factors [47].

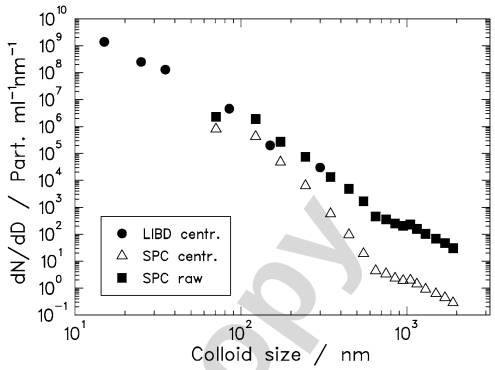

Fig. 4. Natural sample of the Pfinz channel close to Karlsruhe (Germany). The size distribution of the raw sample measured by the SPC (■) reveals a rather high concentration of large particles. After centrifugation (△) particles larger than 80 nm are suppressed (for details see text). The latter data agrees well with the LIBD measurement of the centrifuged sample (●). A slight overestimation of the 300-nm size class is observed for the LIBD, whereas the 50-nm size class is underestimated by the SPC. Since colloids <80 nm are only weakly suppressed by centrifugation, the LIBD curve merges well with the raw data of the SPC (■).

Measurements of the untreated water with the SPC revealed a rather high content of large particles (Fig. 4). Measurement of the untreated sample by LIBD resulted in screening effects of the small particles. Preexperiments with various filter types revealed severe losses of small particles due to sorption and hence we centrifuged the sample for 60 min at 2630g (4000 rpm, $r = 15$ cm) and used only the upper 4 cm of supernatant of a 10-cm vial. According to the centrifugation equation [48],

$$v = D^2(\rho_P - \rho_0)\frac{\omega^2 r}{18\eta}, \tag{7}$$

the cutoff size is about 80 nm for particles of density $\rho_P = 2.0$ g cm^{-3} (settling of 4 cm in 3600 s). v is the settling velocity (cm s^{-1}), D is the particle diameter, ρ_P and ρ_0 the density of particle and medium, respectively, ω the angular frequency, r the radius of the sample center in the centrifuge, and $\eta = 8.9 \times 10^{-4}$ kg m^{-1} s^{-1} the viscosity of water. The theoretical cutoff size agrees well with measurements by the SPC before (■) and after (△) centrifugation (Fig. 4). For particles of 50 nm the theoretical loss according to Eq. (7) is less than 30%, and for 20-nm particles less than 5%.

Hence, the small size classes that are measured by LIBD should reflect the original concentration to a good approximation. Fig. 4 shows the combined results of SPC (centrifuged: △, raw: ■) and LIBD (●). Both sets of data merge into a consistent curve. As expected from Eq. (7), the distribution of small particles (<80 nm) that are measured by LIBD is only slightly affected and also fits well to the SPC data of the raw sample (■). The differential number density as a function of particle diameter D shows the Pareto-like power law dependence [4,49–51],

which is typical for natural waters:

$$\frac{dN}{dD\ \mathrm{ml}} \propto D^{-\beta}, \quad \beta \approx 3. \tag{8}$$

The second sample is water of Lake Brienz and was collected near Iseltwalt (Canton of Bern, Switzerland). Water was taken directly from the shore (10-cm depth) and directly placed in thermostated bottles. The sample was measured within 48 h of sampling. We are aware of the fact that the colloid size distribution might have changed by that time, but the objective of our work was not to study the actual particle size distributions in Lake Brienz but to investigate whether LIBD and SPC applied at the same time to the same samples gave meaningful results.

Lake Brienz is a typical, deep, perialpine, ultraoligotrophic lake [52]. Colloids in Lake Brienz have been systematically studied for more than a year [53,54] by simultaneously applying on-site particle size distribution measurements by SPC and chemical and mineralogical characterization of the colloids present by a combination of a nonperturbing sampling preparation method and transmission electron microscopy, energy dispersive spectroscopy, and selected area electron diffraction [55]. Colloids are nearly exclusively formed by aluminosilicates of glacial origin [53]. The colloid concentration and particle size distribution shown in Fig. 5 are representative of Lake Brienz inorganic colloids in winter.

The colloid size distribution is measured as described for the Pfinz sample (Fig. 4). By SPC the raw sample was measured (■) and compared to the water after 60 min centrifugation at 2630g (△). Only the centrifuged sample was measured by LIBD (●). A Pareto-like distribution is obtained, with a total colloid concentration one order of magnitude less than for the Pfinz sample. However, in contrast to the Pfinz water (Fig. 4), the cutoff is shifted to smaller colloid size, which is apparent from the comparison of the SPC data (Fig. 5) before (raw, ■) and after centrifugation (centrifuged, △). After 1 h centrifugation, about 85% of the particles of 70 nm were eliminated in the Lake Brienz sample as compared to only 65% for the Pfinz River water; i.e., the elimination of particles by centrifugation

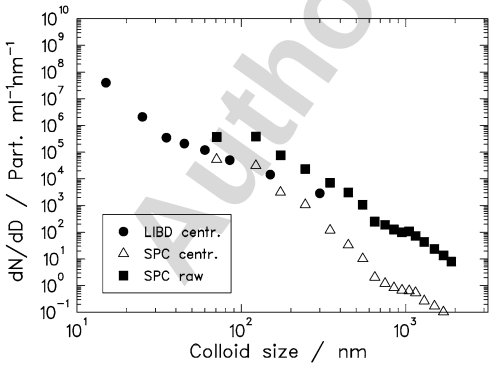

Fig. 5. Natural sample of Lake Brienz (Switzerland). The colloid size distribution is measured as described for Fig. 4, by SPC (raw: ■, centrifuged: △) and LIBD (centrifuged: ●). A Pareto-like distribution is found (for discussion see text). The total colloid concentration is one order of magnitude less than for the Pfinz sample.

is more efficient in the case of Lake Brienz. Consequently, the LIBD data (after centrifugation) fit well the SPC data of the centrifuged sample but not the raw water. The correspondent particle densities were obtained by centrifugation and measurement of the remaining colloid fraction by the SPC. Equation (7) gives apparent densities of $\rho_P = 2.2\ \mathrm{g\,cm^{-3}}$ for Lake Brienz and $\rho_P = 2.0\ \mathrm{g\,cm^{-3}}$ for the Pfinz River, respectively. This difference can be explained by a difference in the nature and/or shape of these colloids. Since the small colloids seem to have a higher density in Lake Brienz, the fraction of colloids eliminated by centrifugation below 80 nm might be nonnegligible in this sample. This fact can be a reason that LIBD data apparently fit SPC data of centrifuged water better than SPC data of noncentrifuged water. An additional uncertainty arises from nonspherical shapes of the particles. Equation (7) assumes spherical shape and hence the calculated density is an "effective" density. Conversion of an oblate particle to a spherical shape would result in a lower density (sedimentation is more slow).

In addition, it must be considered that the Brienz samples were analyzed much later after collection than the Pfinz River samples. Coagulation processes in this type of water, in particular for small colloids, can be very fast [52] and aggregation processes may have reduced colloid numbers by increasing their size, resulting in a deviation from an undisturbed Pareto distribution.

4. Conclusions and future perspectives

In this work we demonstrated for the first time a direct measurement of the particle size distribution from 15 to 2000 nm by combining an SPC with LIBD and using centrifugation to remove very large particles. The results of the Pfinz channel water indicate that Pareto's law is valid down to 15 nm. Since the stability of inorganic particles <50 nm in natural waters remains a controversial issue, this result can be considered as being very relevant from an environmental point of view. Some model calculations have shown that very small particles coagulate very fast to form bigger aggregates to the point that, in the absence of a continuous source, they should not be present in any natural water [56]. However, the model used was a very simple one based on very simple mechanisms of particle contact; more recent papers [57] suggest that this model probably overestimates Brownian coagulation for small particles. In [56] was already mentioned that inorganic colloids smaller than 50 nm had been measured in some systems; the explanation that these colloids could be attached on some kind of organic mesh was given as a hypothesis. Some authors [58] think that the DLVO theory does not apply to nanoparticles. It is also clear from the second measurement on the lake Brienz water, that the influence of the centrifugation must be carefully considered. In particular, a wide distribution of densities may result in an unwanted removal of colloids <100 nm.

Future applications of this method besides investigating surface waters are in the field of pseudocolloid formation and colloid mediated transport, size fractionation, and dispersion of

.

5 Time-Resolved Laser-Induced-Fluorescence Spectroscopy on Cm(III) and Pa(IV)

The present chapter comprises three papers on time-resolved laser-induced-fluorescence spectroscopy (TRLFS), a technique which is frequently used for the speciation of trace amounts of actinide ions in solution and solids [Beit91, Beit94]. In contrast to the light metal ions, lanthanide and actinide ions are spectroscopically active in the aqueous phase due to their special electron configuration. The energy gap between ground state and first excited state is rather large for many actinide ions [Bell68, Carn75b] making overtone quenching (energy transfer to solvent molecules or complexing ligands) less likely and increasing the life time (Judd-Ofelt theory [Katz86]). Moreover, in the case of the higher actinides ($Z \geq 94$), the optically active f-shell is well shielded against the solvent by the outer d-electrons further reducing quench processes.
The parity allowed f-d transitions of the actinide ions are in the ultraviolet, sometimes even in the hard to access vacuum UV. *E.g.*, the $5f^7 \rightarrow 5f^6 6d$ transition of the Cm^{3+} ion is close to $\tilde{\nu}$=69.000 cm^{-1}, the $5f^7 \rightarrow 5f^6 7p$ transition at $\tilde{\nu}$ =126.000 cm^{-1} and the $5f^3 \rightarrow 5f^2 7p$ transition of U^{3+} still has an energy of $\tilde{\nu}$ =30.000 cm^{-1} [Blai92]. Much easier to observe are the f-d intra band transitions of the $5f^N$ configuration in the UVA to near infrared part of the spectrum ($\tilde{\nu} < 30.000\,cm^{-1}$). Quantum mechanics tells us that transitions from pure d states to pure f states are parity forbidden. However, admixtures of $5f^{N-1}6d$ states due to symmetry breaking in the ligand field cause finite transition rates ranging from $\Gamma = 10 - 1000000\,s^{-1}$: $Cm^{3+}: \Gamma = 250\,s^{-1} (\tau = 4.8\,ms)$, $Am^{3+}: \Gamma = 530.000\,s^{-1}\,(\tau = 1.875\,\mu s)$. The $5f^n \rightarrow 5f^n$ transitions are rather weak but spectroscopically well structured with narrow characteristic lines. The (really) parity allowed $5f^n \rightarrow 5f^{n-1}6d$ transitions, on the other hand, are highly intense but extremely broad and poor in characteristic spectral features.

First applied to the speciation of rare earth metals (Ce^{3+}, Sm^{3+}, Eu^{3+},Gd^{3+},Tb^{3+}, Dy^{3+}, Yb^{3+}) (review in [Stei75]), TRLFS was successfully used to investigate the actinide ions UO_2^{2+} [Moul98, Ruts99, Bern01], Cm^{3+} [Beit80, Beit91, Kim91, Klen91], and, to some extent, Am^{3+} [Beit88, Thou93]. In particular, Cm^{3+} can be detected at very low concentrations down to $[Cm^{3+}] > 10^{-9}$ M. It is quite striking to note that with the exception of UO_2^{2+} the above listing solely comprises *tri*valent ions, which might appear out of place in the present work which focuses on the properties of *tetra*valent ions in solution. However, after a short digression concerning Cm^{3+} (Sec. 5.2), we will return to the actual subject in Sec. 5.3 and report on first TRLFS measurements of a tetravalent actinide ion in solution: Pa(IV).

5.1 A SHORT DESCRIPTION OF HOW TRLFS WORKS

As its name 'time-resolved laser-fluorescence-spectroscopy' implies, molecules, atoms, or ions are excited by absorption of photons from a short laser pulse [Beit80]. As an example, let us consider the Cm^{3+} ion in aqueous solution. Following excitation, the ion decays radiationless to the lowest excited level (for Cm^{3+} this is the ${}^6D'_{7/2}$ state) and from there to the ${}^8S'_{7/2}$ ground state (Fig. 5.1a) by emitting a photon. This fluorescent light is detected time resolved by a gated intensified CCD camera following a spectrometer. Interaction of the Cm^{3+} ion with ligands (chemical bond) alters the outer orbitals (ligand field / crystal field) causing an energy change of the respective electronic levels, which in turn causes a spectral shift of the fluorescence emission lines (Fig. 5.1b). *Vice versa*, a change in the chemical environment of the Cm^{3+} ion can be deduced from the spectral shift of the fluorescence. Moreover, the presence of ligands may have an additional effect on the fluorescence: If the excitation energy of the Cm^{3+} ion (${}^6D'_{7/2}$ - ${}^8S'_{7/2} \approx 16.900\,cm^{-1}$ [Grub66, Carn75a]) equals an integer multiple of the energy of a vibronic mode of the ligand, the energy may rapidly be transferred to the ligand. This quenching by overtone excitation is quite effective and shortens the lifetime considerably.

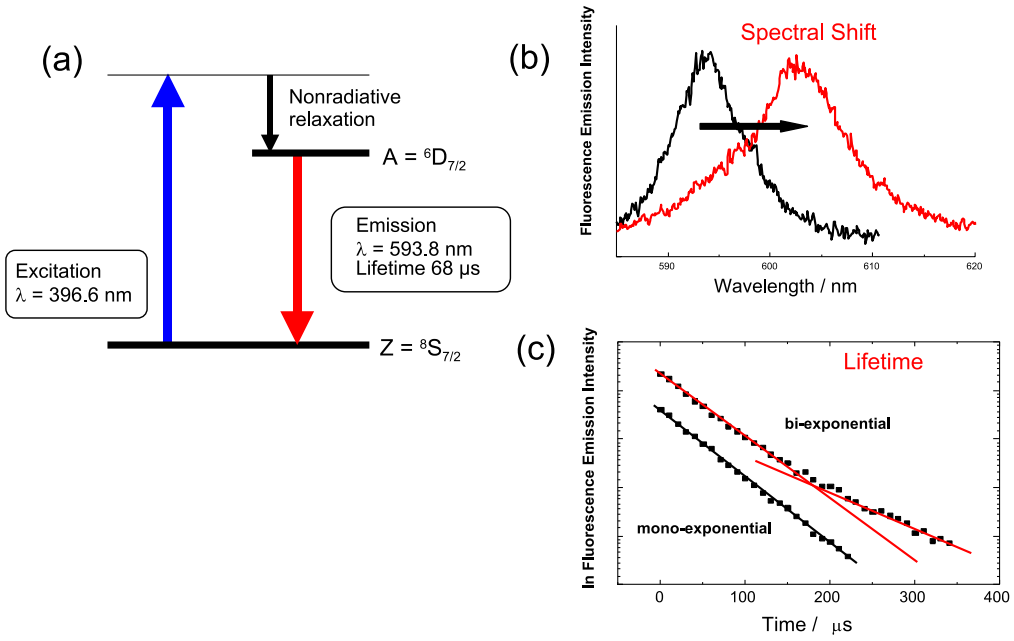

Figure 5.1: **(a)** Excitation scheme of Cm^{3+} **(b)** Bathochromic shift ('redshift') of the fluorescence emission caused by a change of the ligand field **(c)** The number of coordinated quenching ligands determines the fluorescence lifetime. A biexponential decay indicates the simultaneous presence of two species with different numbers of quenching ligands [Beit91].

Water, for instance, is a very effective quencher of Cm^{3+}: the fifth overtone excitation of the symmetric O-H stretching vibration (3400 cm^{-1}, width $\pm 250\,cm^{-1}$[Mare91]) perfectly matches the $^6D'_{7/2}$ - $^8S'_{7/2}$ energy difference of $\approx 16.900 cm^{-1}$ [Carn75b]. For a Cm^{3+} ion with nine H_2O molecules in its first coordination sphere, the lifetime is reduced to $\tau = 69 \pm 4\,\mu s$ as compared to $\tau = 1/\Gamma \approx 4\,ms$ of the free Cm^{3+} ion in vacuum. A decreasing number of coordinated water molecules (for instance in the case of inner sphere surface sorption) causes a decreasing decay rate as the number of quenching ligands is linearly related to k_Q (Kimura's equation, [Kimu94]). Moreover, the number of non-equivalent complexes can be determined from the time dependence of the fluorescence: A monoexponential decay with characteristic lifetime $\tau = 1/k_T = 1/(\Gamma + k_Q)$ indicates the presence of only one metal-ligand complex whereas the simultaneous presence of two species with different quench rates yields a biexponential decay (Fig. 5.1c).

The triple selectivity (excitation wavelength, emission wavelength, time resolution) makes TRLFS a very sensitive and at the same time element selective speciation method. Speciation (measurement of lifetimes and spectral shifts) is possible down to concentrations of $[Cm(III)]_{aq} = 10^{-9}\,M$. A detection limit of as low as $[Cm(III)]_{aq} = 10^{-12}\,M$ is achieved by adding organic ligands which act as an 'antenna' for the excitation light and transfer the energy to the metal ion. However, the formation of the complexes alters the speciation. Typical applications of TRLFS are speciation of different complexes, measurement of formation constants, determination of the thermodynamic reaction quantities ΔG, ΔH and ΔS and effects of the chemical environment on the metal ion (matrix effects).

5.2 WHAT CAN WE LEARN FROM CM^{3+} DOPED HYDRATED CRYSTALS FOR THE CHEMISTRY OF ACTINIDE AQUO IONS?

(Summary of [Lind05b] - Section 5.4.1)

Not only is TRLFS a valuable tool for the speciation of aquo ions, but also a useful method for investigations of bulk solids which contain - or are doped with - fluorescing metal ions. In the latter case, the selectivity of TRLFS can be strongly enhanced by cooling the sample ($T < 10\,K$) which reduces the linewidth from several nm at room temperature to $\Delta\tilde{\nu} < 1 cm^{-1}$. At this low temperature, a fine structure of the emission lines is observed which originates from the crystal field splitting of both $^8S'_{7/2}$ and $^6D'_{7/2}$ states (Fig. 5.2) and allows to deduce the symmetry of the ligand field [Görl96]. The $^8S'_{7/2}$ ground state splits into up to four Kramers doublets as does the $^6D'_{7/2}$ multiplet state, with the respective energy gaps depending on the symmetry of the ligand field. The total splitting of the four levels reflects the strength of the crystal field and ranges from 2 to 50 cm^{-1} [Edel06]. It was an appealing idea to apply this experimental methodology for shedding light on the still discussed question of the water

coordination of Cm^{3+} in aqueous solution [Beit91, Kimu94, Kimu96, Skan07], in particular at elevated temperatures where the determination of the number of water molecules by use of Kimura's equation is not possible [Lind05a]. Cm is located right in the center of the actinide series close to the transition from nine-fold to eight-fold coordination [Rösc90] which is an result of the actinide contraction. In the present work, we used Cm^{3+} doped *hydrated* crystals, *i.e.* crystals where the metal ion is embedded in a water coordination sphere. Use of these compounds allows to perform low temperature high resolution spectroscopy on hydrated Cm^{3+} ions which is not possible in aqueous samples.

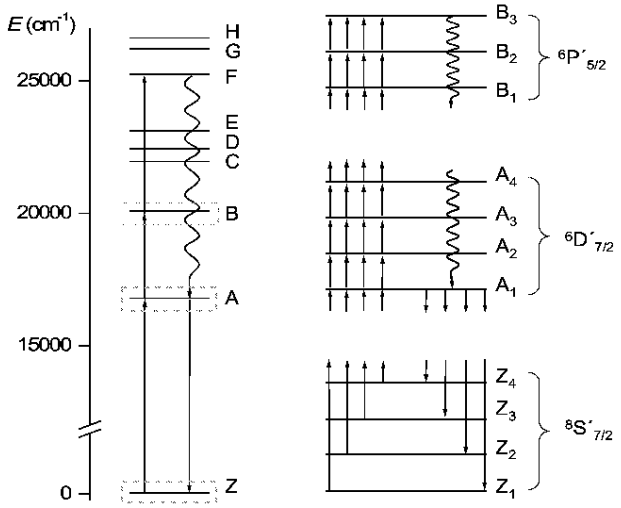

Figure 5.2: Jablonsky diagram of (left) the free Cm^{3+} ion and (right) crystal field splitting (not to scale) of the ${}^8S'_{7/2}$ ground state (Z_{1-4})and the excited states ${}^6D'_{7/2}$ (A_{1-4}) and ${}^6P'_{5/2}$ (B_{1-3})

Cm^{3+} is excited to the F or G state[1] followed by radiationless decay to the ${}^6D'_{7/2}$ state (A-band) and fluorescing decay to the ${}^8S'_{7/2}$ ground state. This excitation scheme combines the high absorption cross section of the F-band with the sensitivity of the ${}^6D'_{7/2}$ state on the chemical environment. However, the F-excitation is not site-specific, *i.e.* if the Cm^{3+}-ion is present in different non-equivalent sites simultaneously, a superposition of several emission lines will be observed.
It is nonetheless possible to select single sites spectroscopically by direct excitation to the ${}^6D'_{7/2}$ fluorescing state (instead of the F-band) and observe the D-S emission thereafter [Liu93, Brun96]. To this end, the excitation laser is suppressed either by means of a monochrometer

[1]The states of Cm^{3+} are named alphabetically in increasing order: A (${}^6D'_{7/2}$):$\approx 16.900\text{cm}^{-1}$, B (${}^6P'_{5/2}$):$\approx 20.000\text{cm}^{-1}$, (...), F: $\approx 25.200\text{cm}^{-1}$,G: $\approx 26.600\text{cm}^{-1}$ [Carn75b]

[Murd96] or by gated detection with a CCD camera [Lind05b] which blocks the first ≈100 ns after the laser pulse and records the fluorescence light for the following tens of μs up to ms.

Water ligands were assumed to generate only a weak crystal field which should lead to a rather small ground state splitting of ca. 2 cm^{-1} at most[Edel06]. In strong contrast in the present work [Lind05b], a splitting of 35 cm^{-1} was reported for eight-fold coordinate Cm^{3+} embedded in a crystalline yttrium trichloride crown-either host $[Cm^{3+}:Y(H_2O)_8]Cl_3$15-crown-5 (Fig. 5 of [Lind05b]). This apparent discrepancy called for further evidence that the four lines observed in the spectrum of (Fig. 5a of [Lind05b]) were due to ground state splitting of one single site and did not originate from a superposition of non-equivalent binding sites of the Cm^{3+} ion in the crystal host. Selective excitations at each of the four possible $^8S'_{7/2}$ - $^6D'_{7/2}$ transitions as well as excitation to the B level $^8S'_{7/2}$ - $^6P'_{5/2}$ (at some 20.050 cm^{-1})[2] lead to identical emission spectra (Fig. 5b,c of [Lind05b]). Neither number nor position of the spectral lines changed. The emisson lines were hence unequivocally attributed to the electronic transition from the $^6D'_{7/2}$(A=1) state to the four $^8S'_{7/2}$ groundstate doublets Z_1-Z_4.

Identical spectra were obtained when the excitation wavelength was tuned and the integral intensity of the fluorescence emission was plotted against the excitation wavelength. In principle this so called excitation spectroscopy is the measurement of the photon-absorption cross-section multiplied by the Clebsch Gordon coefficients for the respective crystal field transitions. Figure 5a of [Lind05b] compares the excitation spektrum for the $^8S'_{7/2} \rightarrow^6 D'_{7/2}$ transition (dashed line) and the emission spectrum (solid line). Though peak positions are identical, the relative strengths of the peaks differ clearly for emission and excitation spectra. At the low temperature (10 K) used for this measurement, the higher Z-crystal field levels are only weakly populated and the respective absorption is as weak (population according to Boltzmann's law). The emission, in contrast, does not depend on the populations of the ground state crystal field levels but only on those of the excited states ($^6D'_{7/2}$) and the respective matrix elements for the transition from the excited state to the crystal field levels of the ground state.

The excitation spectrum for the $^8S'_{7/2} \rightarrow^6 P'_{5/2}$ transition is shown in Fig. 5b of [Lind05b]). A small energy gap between $^6P'_{5/2}$ and $^6D'_{7/2}$ leads to a short lifetime of the $^6P'_{5/2}$ level (according to Judd-Ofelt, [Katz86]), even further reduced by energy transfer to the coordinated water molecules, whose vibrational frequency of the O-H stretching vibration equals the energy gap. Hence, the Cm^{3+}-ion decays to the fluorescing $^6D'_{7/2}$ state within tens of nanoseconds which in turn decays to the ground state. The integral fluorescence intensity of the latter transition ($^8S'_{7/2} \rightarrow^6 D'_{7/2}$) is detected and serves as signal for the excitation spectrum. The spectrum consists of four peaks with exactly the same relative distances as observed for the S-D excitation and emission spectra. The total of 35 cm^{-1} makes this ground state splitting

[2] which is followed by fluorescence emission from the $^6D'_{7/2}$ state

one of the largest ever observed for Cm^{3+} second only to the one of Cm^{3+} incorporation into ThO_2 [Edel06] and suggests a strong crystal field caused by the rather short Cm-O distance of (2.46 Å) in conjunction with the bicapped trigonal prismatic coordination geometry.

In [Lind05a], the fluorescence emission of the Cm^{3+} aquo ion was measured as a function of temperature between 20 and 200 ^{o}C. Spectral deconvolution yielded two components centered at $\tilde{\nu}$ =16700 cm^{-1} and $\tilde{\nu}$ =16900 cm^{-1} whose relative strength varied as a function of temperature. For high temperature, the relative intensity of the $\tilde{\nu}$ =16700 cm^{-1} component increased and additional hot bands at $\tilde{\nu}$ =17100 cm^{-1} and $\tilde{\nu}$ =17450 cm^{-1} evolve. The authors proposed that the $\tilde{\nu}$ =16700 cm^{-1} and $\tilde{\nu}$ =16900 cm^{-1} components correspond to the nine-fold and eight-fold coordinated Cm^{3+} aquo ion, respectively, and the change in relative abundance of these components arose from the transition from nine to eightfold coordinate Cm^{3+} with increasing temperature. Indeed, by means of the excitation spectra displayed in Fig. 4 of [Lind05b], we prove that eight-fold coordinate Cm^{3+} has transitions from the $^8S'_{7/2}$ to the $^6D'_{7/2}$ A_1 crystal field level at $\tilde{\nu}$ =16800 cm^{-1} and to the A_2,A_3,A_4 levels at $\tilde{\nu}$ =16915 cm^{-1}, $\tilde{\nu}$ =17054 cm^{-1} and $\tilde{\nu}$ =17460 cm^{-1}, respectively, in good agreement with the observed hotbands. We performed analogue low temperature studies on hydrated crystals where the Cm^{3+} is nine-fold coordinated, *e.g.*, on lanthanum triflate ($[Cm^{3+}{:}La(H_2O)_9](CF_3SO_3)_3$) which was very recently also studied by X-ray absorption spectroscopy [Skan07]. The $^8S'_{7/2}$ - $^6D'_{7/2}$ A_1 transition is shifted to higher energy ($\tilde{\nu}$ =16934 cm^{-1}) which is in agreement with the central wavenumber of the Cm^{3+} aquo ion room temperature emission. The splitting of the $^6D'_{7/2}$ A_{1-4} crystal field levels of only $\Delta\tilde{\nu} \approx 360 cm^{-1}$ is too small to explain the observed hotband positions at elevated temperatures, in contrast to the good agreement of the crystal field levels of the eight-fold coordinate system. These findings add evidence to the suggested hypothesis of coordination number change upon heating and prove once more that low temperature spectroscopy on Cm^{3+} doped hydrated crystals is a powerful tool which helps to understand coordination chemistry of actinide aquo ions.

5.3 TRLFS ON A TETRAVALENT ACTINIDE ION: HYDROLYSIS OF PA(IV)

(Summary of [Marq04, Marq05] - Sections 5.4.2,5.4.3)

The present chapter now returns to tetravalent actinide ions – in particular to protactinium. Recent interest in Pa chemistry arose from its role in ^{232}Th breeder reactors and accelerator driven transmutation reactors [Bowm92, Rubb95], where it is an intermediate in the reaction $^{232}\mathrm{Th} + \mathrm{n} \longrightarrow {}^{233}\mathrm{Th} \xrightarrow{\beta^-} {}^{233}\mathrm{Pa} \xrightarrow{\beta^-} {}^{233}\mathrm{U}$.
The development of separation techniques requires profound knowledge of its chemical behavior in aqueous as well as organic solvents. However, investigations focused mainly on

Pa(V) which exhibts an extraordinary high tendency to undergo hydrolysis and form polymers (see review on Pa in [Myas06]). There are little experimental investigations on the aqueous chemistry of tetravalent Pa, which arises from the low stability of this oxidation state: Pa(IV) is readily oxidized to Pa(V) by air or by absorption of UV light but the rate of oxidation can be reduced by exclusion of oxygen. Absorption spectroscopy on $Pa(IV)_{aq}$ in different acid solutions was reported (summary in [Guil66]) revealing characteristic absorption bands in perchloric acid at $\lambda = 225\,nm$, 256 nm and 278 nm [Eber77]. However, up to now, no fluorescence spectroscopy was performed on the Pa(IV) aquo ion which is surprising, for Edelstein and coworkers studied Pa^{4+} doped crystals in great detail using TRLFS [Edel88, Pieh91, Edel92, Edel93].

The two papers summarized in the present section focus on complexation of Pa(IV) in acidic aqueous media. Purified ^{231}Pa was used to prepare a $[Pa]_{tot} = 3.3 \times 10^{-4}\,M$ stock solution in 9.5 M HCl. Samples were diluted to a final protactinium concentration of ca. $1 \times 10^{-5}\,M$ and finally Pa(V) was reduced to Pa(IV) in a glove box under oxygen free argon atmosphere by adding Zn-amalgam [Eber77]. The solution was characterized by UV absorption spectroscopy and TRLFS utilizing the $5f^1$ - $6d^1$ transition of Pa(IV). In contrast to TRLFS on Cm^{3+} where f-f *intra*band transitions are observed, in the case of Pa(IV), the f-d *inter*band transition is monitored. As mentioned in the introduction of this chapter, the f-d transitions are short lived and strong, but featureless and spectrally broad. Excitation at 308 nm by an excimer laser and at 278 nm by a frequency doubled dye laser in [Marq04] and [Marq05], respectively, lead to fluorescence emission around $\lambda = 450\,nm$. In contrast to the great number of transitions reported by the Edelstein group for Pa^{4+} doped crystals, only one broad fluorescence band (FWHM $\approx 60\,nm$) is observed for the aquo ion.

Depending on type and concentration of the acid, we observed peak shifts due to the varying ligand field. It is, however, surprising that the fluorescence shifts to shorter wavelengths upon complexation (hypsochromic shift) whereas for Cm^{3+}, always a bathochromic shift is observed. The shift is strongest for SO_4^{2-} complexation, less pronounced for Cl^-, and almost no shift is observed for $HClO_4^-$ which reflects the decreasing complexation capacity of the respective ligands. No parity forbiddence hinders the f-f transition which leads to a short fluorescence lifetime of 16 ± 2 ns. The measurement of these lifetimes experiences two technical difficulties. For one, the pulse length of our excimer pumped laser system is ca. 26 ns so that the temporal pulse profile must be deconvoluted from the measured decay curve [Brab99, Jame94] (see also discussion in [Walt07a]). The second obstacle arose from photooxidation of Pa(IV) due to the illumination by the UV laser light. A continuous scan of the time delay between laser and fluorescence detection would have overestimated the decay rate since the amount of Pa(IV) in the sample decreased with increasing illumination. Hence, the measurement cycles were alternated with reference cycles at fixed delay time which were used for off line normalization. The lifetime remained constant independent of the ligands which is in line with expectations: for such short lifetimes, no significant energy transfer to the ligands is

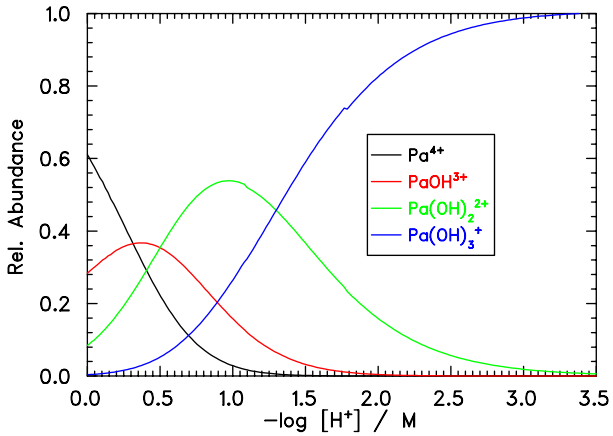

Figure 5.3: Calculated distribution of mononuclear hydroxide complexes ($HClO_4/NaClO_4$ solutions of I=3 M) in the absence of polynuclear species *e.g.* at very low metal ion concentration. Hydrolysis constants from Guillaumont [Myas06].

expected and no fluorescence quenching occurs.

In continuation of the work presented in [Marq04], the complexation of Pa(IV) by fluoride was investigated in [Marq05]. A solution containing $[Pa(IV)] = 1.5 \times 10^{-5}$ M in 1 M $HClO_4$ was titrated with a NaF solution. With increasing fluoride concentration from $[F^-] = 0 - 0.11$ M, the formation of the complexes PaF_y^{4-y} up to $PaF_{4(aq)}$ and finally formation of dispersed crystallite $PaF_{4(s)}$ lead to distinct changes in the absorption spectra which were well explained by a species distribution based on the formation constants of Guillaumont given in [Eber77]. However, in none of the samples a change of the fluorescence emission band at $\lambda = 469$ nm was observed; only the intensity increased with increasing fluoride concentration up to $[F^-]$=0.025 M and decreased strongly for higher fluoride concentration. This fall is probably due to the formation of $PaF_{4(s)}$.

The second part of [Marq05] is focused on hydrolysis of Pa(IV). First results in [Marq04] indicated a strong 'blue shift' of the emission band of a Pa(IV) sample in 2M H_2SO_4 upon pH increase to 3.6 by addition of NaOH. In [Marq05], NaOH was added stepwise to a solution of $[Pa(IV)] = 1.4 \times 10^{-5}$ M in 1 M $HClO_4$, and the change in the absorption and emission spectra was observed. From pH 0 - 1.6, the peak position of the fluorescence band remained constant but the intensity increased up to pH 0.38 and decreased continuously thereafter. Further pH increase lead to a pronounced spectral shift from $\lambda = 469$ nm to $\lambda = 422$ nm at pH 3.6. The intensity variation correlates with the variation in relative abundance of the $Pa(OH)^{3+}$ complex and the peak shift coincides with the formation and dominance of the third hydrolysis complex $Pa(OH)_3^+$ at pH 1.6 as calculated using the formation constants for

mononuclear hydroxide complexes from Guillaumont [Myas06] displayed in Figure 5.3. The most plausible explanation of this observation is that structural changes in the first hydration sphere and resulting changes of the crystal field upon the third hydrolysis step cause the large peak shift. Further pH increase lead to a strong decrease of Pa in solution as measured by liquid scintillation counting, which was either due to sorption onto the walls of the quartz cuvette - possibly after oxidation to Pu(V) which is known for its extraordinary pronounced sorption behavior - or due to precipitation. We refrained from giving an estimate of the solubility since literature data of solubity constants scattered considerably: $\log K^o_{sp} = -48.2$ [Brow87], $\log K^o_{sp} = -52.9$ [Tara05], $\log K^o_{sp} = -53.4$ [Dupl77]. Using the experimental value $\log K^o_{sp} = -53.4$ [Dupl77] one estimates[3] that up to pH 4, [Pa(IV)] $\approx 10^{-4}$ M should be soluble and precipitation should not play a role for [Pa(IV)] $= 1.4 \times 10^{-5}$ M.

Concluding, we demonstrated for the first time that TRLFS lends itself to the investigation of the tetravalent actinide ion Pa(IV) in solution. Hydrolysis, which affects the absorption spectra only weakly, causes a significant shift of the fluorescence emission and can hence be observed with high selectivity. The most important advantage of TRLFS over UV VIS, however, is its superior sensitivity which allows to perform speciation at [Pa(IV)] $= 10^{-7}$ M.

[3]The estimate approximates the ion interaction by the Debye-Hückel term only since no SIT coefficients are available.

5.4 PUBLICATIONS

5.4.1 Large ground-state and excited-state crystal field splitting of 8-fold-coordinate Cm^{3+} in $[Y(H_2O)_8]Cl_3 \cdot$15-crown-5 [Lind05b]

J. Phys. Chem. B **2006,** *110,* 5279−5285 **5279**

Large Ground-State and Excited-State Crystal Field Splitting of 8-fold-Coordinate Cm^{3+} in $[Y(H_2O)_8]Cl_3 \cdot 15$-crown-5

Patric Lindqvist-Reis,*,† Clemens Walther,† Reinhardt Klenze,† Andreas Eichhöfer,‡ and Thomas Fanghänel†,§

Institut für Nukleare Entsorgung and Institut für Nanotechnologie, Forschungszentrum Karlsruhe, P.O. Box 3640, 76021 Karlsruhe, Germany, and Physikalisch-Chemisches Institut, Ruprecht-Karls Universität, Im Neuenheimer Feld 253, 69120 Heidelberg, Germany

Received: December 20, 2005; In Final Form: January 23, 2006

The optical spectra of Cm^{3+} incorporated into the crystalline host structure of $[Y(H_2O)_8]Cl_3 \cdot 15$-crown-5 (**1**) is investigated by using laser spectroscopic methods at temperatures between 20 and 293 K. The coordination geometry of the $[Y(H_2O)_8]^{3+}$ entity in **1** is a distorted bicapped trigonal prism with $\sim C_2$ point symmetry, as confirmed by single-crystal X-ray diffraction at 200 K. The crystal-field splitting of the $^8S'_{7/2}$ ground state and the $^6D'_{7/2}$ and $^6P'_{5/2}$ excited states of the hydrated Cm^{3+} ion are measured by high-resolution fluorescence emission and excitation spectroscopy at various temperatures. The transitions between the ground state and the respective lowest crystal-field levels of the excited states exhibit narrow fluorescence lines, resolving the four crystal-field levels of the ground state as sharp, well-resolved lines at about 0, 10, 19, and 35 cm^{-1}. The total splittings of the $^6D'_{7/2}$ and $^6P'_{5/2}$ states are 670 and 170 cm^{-1}, respectively. Thermal population of the ground-state crystal-field levels is observed and quantified in the excitation spectra in the temperature range of 20−70 K. All spectroscopic results are consistent with the presence of one unique $[Cm(H_2O)_8]^{3+}$ site. The ground-state splitting of Cm^{3+} in **1**, 35 cm^{-1}, is comparable to that of Cm^{3+} in solid ThO_2, 36 cm^{-1}, which shows the strongest crystal field for Cm^{3+} reported so far. For this reason the present results are different than the findings for Ln^{3+} aqua ions, which show rather weak crystal field strengths.

Introduction

In analogy to the trivalent gadolinium ion, which has seven unpaired electrons in the half-filled 4f shell, the trivalent curium (Cm^{3+}) ion has a $5f^7$ electron configuration. Characteristic for the f^7 configuration is the large separation between the ground $^8S_{7/2}$ state and the higher excited states, which appear at ~32 000 for Gd^{3+} and ~17 000 cm^{-1} for Cm^{3+}.[1] While the ground state of Gd^{3+} has nearly pure (~97%) $^8S_{7/2}$ character, due to the stronger spin−orbit coupling in Cm^{3+}, this contribution is considerably lower (~78%) with an admixture of other LS states such as $^6P_{7/2}$ (19%). A direct consequence of the mixing of the higher lying excited states into the ground term by the spin−orbit interaction is a large ground-state splitting for Cm^{3+} (~10−20 cm^{-1}), which exceeds that of Gd^{3+} by more than 1 order of magnitude for a given crystal host.[2] While the ground-state splitting of Cm^{3+} has been quantified satisfactorily using ordinary crystal-field models, this approach fails in the case of Gd^{3+}.[3] In all but centrosymmetric crystal-field symmetries the ground state $^8S'_{7/2}$ multiplet of Cm^{3+} splits into four Kramers doublets, as does the $^6D'_{7/2}$ multiplet state located at ~17 000 cm^{-1} above the ground level, while the $^6P'_{5/2}$ multiplet at ~20 000 cm^{-1} splits into three doublets (see Figure 1). As expected, the total splitting of the excited-state multiplets is much larger than for the ground state.

The splitting of the multiplets is very sensitive to the strength and symmetry of the local crystal field. The strength depends on factors such as the metal to ligand distance and the character of the metal−ligand bonds.[4,5] Auzel and Malta showed that the scalar crystal-field strength parameter, N'_v, is proportional to the total splitting (ΔE) of a distinct $^{2S+1}L_J$ multiplet for a rare-earth ion in a crystal.[6] Similar correlations have been used for actinide ions, including Cm^{3+}, where N'_v is found to be about

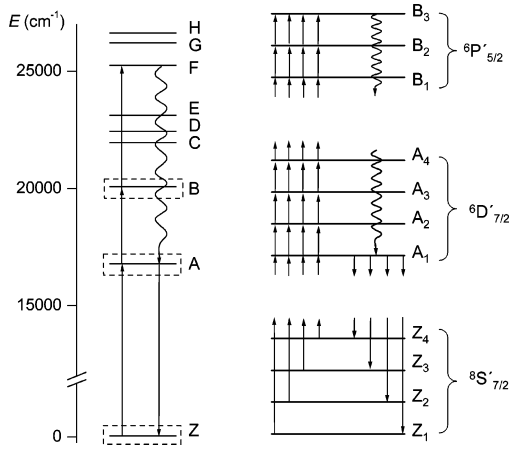

Figure 1. (Left) Free ion energy levels of the Cm^{3+} $5f^7$ configuration below 27 000 cm^{-1}, showing the absorption bands as energy levels Z, and A−H. (Right) Crystal-field splitting of the multiplets is shown schematically for the $^8S'_{7/2}$ ground state (Z_{1-4}) and the two excited-state levels $^6D'_{7/2}$ (A_{1-4}) and $^6P'_{5/2}$ (B_{1-3}). Excitation and fluorescence emission between ground- and excited-state levels are represented by vertical up- and down-pointing arrows, respectively, and nonradiative deexcitation by wavelike arrows.

* Corresponding author. Phone: +49-7247-822389. Fax: +49-7247-823927. E-mail: plr@ine.fzk.de.
† Institut für Nukleare Entsorgung, Forschungszentrum Karlsruhe.
‡ Institut für Nanotechnologie, Forschungszentrum Karlsruhe.
§ Ruprecht-Karls Universitat.

10.1021/jp0574100 CCC: $33.50
Published on Web 03/01/2006

twice the corresponding value for a rare-earth ion.[7,8] Among the most extensively studied Cm^{3+}-doped systems are hexagonal $LaCl_3$ with C_{3h} point symmetry,[9−11] tetragonal $LuPO_4$ (D_{2d} symmetry),[12,13] and cubic ThO_2 (O_h symmetry),[14] where the total splitting of the ${}^8S'_{7/2}$ ground state (and N'_v) are 2.0 (628), 9.5 (1302), and 36 (2953) cm^{-1}, respectively.

Detailed knowledge about the $5f^7$ ground- and excited-state electronic structures for Cm^{3+} as an impurity ion in various anhydrous inorganic crystals, including those mentioned above, has been obtained from their optical spectra. Electron-paramagnetic resonance (EPR) studies have provided data on the splitting of the ${}^8S'_{7/2}$ multiplet. Apart from an early EPR study on Cm^{3+} in $[La(H_2O)_9](C_2H_5SO_4)_3$, where no details about the zero-field splitting of the ${}^8S'_{7/2}$ multiplet were given,[15] there are no optical spectroscopic studies on the electronic structure of Cm^{3+} in crystalline hydrates or solvates. Such data would be very valuable, e.g., for elucidation of time-resolved laser-induced fluorescence spectroscopy (TRLFS) data of Cm^{3+} in various aquatic systems. TRLFS has proven to be a powerful tool for the speciation of Cm^{3+} at trace level concentration.[16] The only study showing the structure of excited-state electronic levels of hydrated Cm^{3+} is that of the absorption spectrum of an aqueous curium perchlorate solution by Carnal and Rajnak.[17] Since this spectrum consists of several narrow bands in the region of 375−450 nm, corresponding to transitions from the ground state to different excited-state levels, it was concluded that these bands were not affected appreciably by the ground-state splitting, which was considered to be of similar magnitude as in $LaCl_3$ (~2 cm^{-1}) and hence negligible.[17] This view, of a relatively small ground-state splitting for the Cm^{3+} aqua ion, is widely accepted and serves as a central assumption in many investigations dealing with TRLFS on trivalent curium.[18,19]

In this paper, we present high-resolution emission and excitation data of the 8-fold-coordinate $[Cm(H_2O)_8]^{3+}$ ion incorporated into the crystal host of $[Y(H_2O)_8]Cl_3$·15-crown-5 (**1**) (Cm/Y ~ 10^{-6}). This host was used in a recent TRLFS study of the temperature dependency of Cm^{3+}(aq) from 20 to 200 °C, where the spectrum of the Cm^{3+} aqua ion at 200 °C was found to be very similar to that of the octahydrated species in **1** at room temperature.[20] The spectroscopic results in the present study show that water ligands may strongly influence the electronic structure of the ${}^8S'_{7/2}$ and ${}^6D'_{7/2}$ states, by causing unusually large splitting of these states. These results are therefore in sharp contrast with the current view of the curium aqua ion as portrayed above. As will be shown in the following, the ground-state splitting is enhanced in **1**, but preliminary results show that also in nine-coordination the extent of the ground-state splitting is quite significant. Whereas the hydrated Cm^{3+} ion in aqueous solution is in general coordinated by nine water molecules in the first hydration shell,[20] eight-coordination is found under certain conditions in aqueous solution, e.g., at high temperature or at high ionic strength.[20,21]

Experimental Section

Sample Preparation. Crystals of the $[Y(H_2O)_8]Cl_3$·15-crown-5 host were grown from an acetonitrile:methanol (3:1) solution as described elsewhere.[21] Parts of the crystal material were used for single-crystal X-ray diffraction and chemical analysis, i.e., ethylenediaminetetraacetic acid (EDTA) titration (indicator: xylene orange) and cation exchange (Dowex 50W-X8, H^+-form) for checking the Y^{3+} and Cl^- contents, respectively. The other part of the crystal material was recrystallized by addition of Cm-248 stock solution (i.e., 50 μmol/L Cm^{3+} in 0.1 mol/L aqueous $HClO_4$) to give a final Cm^{3+} concentration of less than

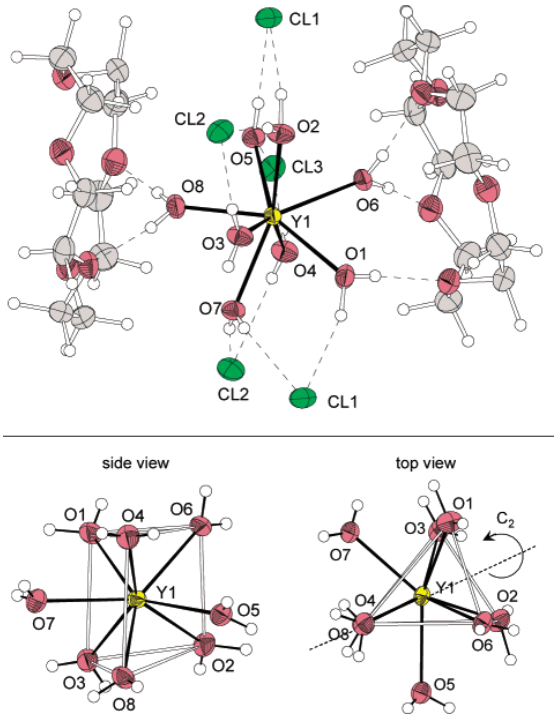

Figure 2. (Top) The local structure around the $[Y(H_2O)_8]^{3+}$ cation, showing its hydrogen bonding to two adjacent crown ether molecules and several chloride ions in **1** at 200 K. The thermal ellipsoids are drawn at the 40% probability level for non-hydrogen atoms. (Bottom) Bicapped trigonal prismatic (BTP) coordination geometry representation of the $[Y(H_2O)_8]^{3+}$ ion in **1**, as viewed from the side and from the top. The thin lines connecting the oxygen atoms have no chemical significance but help in recognizing the BTP geometry. The point symmetry of the YO_8 entity is ~C_2 (the pseudo C_2 axis is indicated). The Y−O bond distances (Å) are as follows: Y1−O8, 2.317(3); Y1−O4, 2.328(3); Y1−O2, 2.342(3); Y1−O6, 2.356(3); Y1−O3, 2.370(3); Y1−O1, 2.372(3); Y1−O7, 2.411(3); Y1−O5, 2.433(3). The mean Y−O prism and capping bond distances are 2.348 and 2.422 Å, respectively. Similar coordination geometry is assumed for the CmO_8 entity in the Cm^{3+}-doped compound (see text).

1 ppm. The Cm-248 ($t_{1/2}$ = 3.40 × 10^5 years), which includes ~9 wt % Cm-246 and some minor amounts of Cm-243 and Cm-244 isotopes, was obtained previously at FZK-INE by reprocessing of a used up Cf-252 neutron source.

Crystallography. Single-crystal X-ray diffraction data were collected using graphite-monochromatized Mo-Kα radiation (λ = 0.710 73 Å) on a STOE IPDS II (imaging plate diffraction system) at 200 K. The structure of **1** was solved with direct methods using the program SHELXS[23] of the SHELXTL PC suite programs and refined using the full-matrix least-squares program SHELXL. All hydrogen atoms were located and their positions refined with isotropic displacement parameters, while all non-hydrogen atoms were refined with anisotropic displacement parameters.[24] The molecular structure of **1** depicted in Figure 2 was obtained using the program DIAMOND.[25]

Laser System and Fluorescence Detection. TRLFS measurements were performed using a XeCl-excimer laser (Lambda Physics, EMG, 308 nm) pumped dye laser (Lambda Scanmate) for excitation (pulse width, 20 ns; spectral width, 0.2 cm^{-1}; wavelength accuracy, 0.5 cm^{-1}). Emission spectra were recorded by an optical multichannel analyzer consisting of a Czerny-Turner polychromator (Jobin Yvon, HR 320) with three gratings, 300, 600, and 1200 lines/mm, and a gated, intensified photodiode array (Spectroscopy Instruments, ST 180, IRY 700G).

To measure the decay time of the fluorescence emission, the intensifier was opened for typically 1 ms at delay times of 1−400 μs between laser excitation and detection in steps of 5 μs. For the excitation spectra, a fixed delay time of 10 μs and gate of 3.5 ms were used. In contrast to earlier measurements (see, e.g., refs 9 and 10), no monochromator was used to select a single emission wavelength, but rather for each excitation wavelength the full emission spectrum was recorded. To cover the $^6D'_{7/2}$ and $^6P'_{5/2}$ multiplets in the excitation spectra, the dye laser was scanned from 16 650 to 17 650 cm^{-1} using rhodamin B and coumarin 153, and from 20 030 to 20 650 cm^{-1} using coumarin 102. Depending on the width of the spectral features in the "overview" spectra and the high-resolution spectra of the ground-state splitting, the step size of the excitation wavelength was adapted to typically 20 and 0.2 cm^{-1}, respectively. The measured spectral resolution of the CzernyTurner polychromator was found to be ∼12 cm^{-1}. High-resolution emission spectra were recorded by an Echelle spectrometer (LLA, ESA 3000) with spectral resolution of $\lambda/\Delta\lambda > 10\,000$, corresponding to 1.7 cm^{-1} at 17 000 cm^{-1}. Its intensified CCD camera, 11 μs after the laser pulse, was opened for 10 ms.

Only polycrystalline samples were measured; hence, the orientation relative to the linearly polarized laser beam does not play any role. Samples were mounted on an in-house constructed copper sample holder, attached to the cold head of the cryostat (Cryodyne Cryocooler model 22C, compressor 8200, CTI-Cryogenics, USA), which allows temperatures down to ∼15 K (see ref 26 for details about this setup). However, the actual temperature at the sample was ca. 20 K, which was verified by comparing high-resolution excitation spectra at 15 and 20 K, which were found to be identical.

Results and Discussion

Host Structure. Figure 2 shows the $[Y(H_2O)_8]^{3+}$ ion hydrogen-bonded to the crown ether molecules and the chloride ions in the crystal lattice of **1** at 200 K. Detailed descriptions of the crystal structure at 295 and 120 K are given elsewhere.[22] The YO_8 polyhedron is recognized as a distorted bicapped trigonal prism (∼C_2 point symmetry) with a mean Y−O bond distance of 2.366 Å; the mean Y−O bond distances to the prismatic waters are shorter than those to the two capping ones, 2.35 and 2.42 Å, respectively. The coordination geometry of the $[Cm(H_2O)_8]^{3+}$ entity is expected to be similar to that of yttrium at all temperatures.[27] The mean Cm−O bond distance is estimated to be ca. 2.445 Å from the difference in the ionic radius between Cm^{3+} (1.094 Å)[28] and Y^{3+} (1.015 Å).[29] The size mismatch between the ions should generate a distortion of the crystal lattice in the vicinity of curium; however, this may be compensated for by the flexibility of the hydrogen bond network.

Emission Spectra. Figure 3 shows the $^6D'_{7/2} \rightarrow {}^8S'_{7/2}$ emission spectra of $[Cm(H_2O)_8]^{3+}$ in **1** upon excitation into the F level (λ_{ex} = 397.0 nm, 25 200 cm^{-1}) at three different temperatures, 293, ∼200, and 20 K. The room temperature (293 K) spectrum appears as a fairly broad and asymmetric band with peak maximum at 16 770 cm^{-1} and full width at half-maximum (fwhm) of about 140 cm^{-1}. With decreasing temperature from 293 to 20 K the bandwidth decreases severalfold, accompanied by an increase of the intensity and a peak shift of about 35 cm^{-1} toward higher energy (note that the spectra in Figure 3 are normalized to the same peak height). The emitting metastable $^6D'_{7/2}$ state (lifetime ∼ 70 μs) splits into four crystal field levels (A_i, i = 14; see Figure 1) which are in thermal equilibrium.

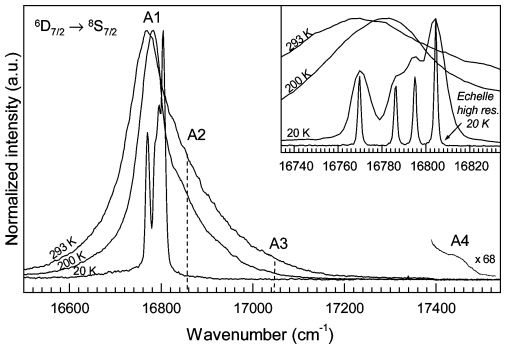

Figure 3. $^6D'_{7/2} \rightarrow {}^8S'_{7/2}$ emission spectra of Cm^{3+} in **1** (λ_{ex} = 397.0 nm, 25 200 cm^{-1}) at 293, ∼200, and 20 K, recorded using the Czerny-Turner polychromator. The inset shows a blow-up of the emission spectra in comparison with a high-resolution spectrum obtained by an Echelle spectrometer at 20 K.

Since the total splitting of these crystal field levels exceeds k_BT considerably at room temperature, the lowest level A_1 is by far the most populated and thus accounts for the strong emission band at about 16 770 cm^{-1}. Emissions from the second (A_2, 16 860 cm^{-1}) and third (A_3, 17 040 cm^{-1}) crystal-field levels are not well-resolved but give rise to the asymmetry at the high-energy flank of the band at 293 and 200 K. Emission from the fourth level (A_4, 17 050 cm^{-1}) is negligible (Figure 3). The decrease in the bandwidth upon cooling is to some extent a result of the decreasing emission contributions from A_2 to A_4; the intensities of these bands relative to that of A_1 are essentially Boltzmann ratios at a given temperature. Other important sources for broadening are the vibrational movements of the water ligands and the intrinsic, temperature-independent, ground-state splitting (see below). The spectrum at 20 K is composed of four overlapping bands with different intensities. In the high-resolution spectrum obtained using the Echelle spectrometer, these component bands are narrow (fwhm ≈ 1.7 cm^{-1}) and well-resolved with peak maxima at about 16 770, 16 786, 16 795, and 16 805 cm^{-1} (Figure 3, inset).

There are two possible origins for the multiple emission lines. Either they originate from four nonequivalent Cm^{3+} sites within the host matrix with different energy differences between the lowest excited state and the degenerate ground state or from a single site where Cm^{3+} is emitting from the lowest excited-state level to the four crystal-field levels of the $^8S'_{7/2}$ ground state. A combination of both mechanisms is also possible. To differentiate between these alternatives, additional investigations are undertaken.

Excitation Spectra. When Cm^{3+} is excited to the $^6D'_{7/2}$ state instead of the F state, which was the case in the previous section, a very similar emission spectrum is observed due to the radiative relaxation $^6D'_{7/2} \rightarrow {}^8S'_{7/2}$.[30] We recorded emission spectra in the range of 16 660−17 860 cm^{-1} by exciting at more than 200 wavelengths between 480 and 680 nm. In addition to conventional excitation spectroscopy, where the intensity of only one emission wavelength is monitored by use of a monochromator while scanning the excitation laser, we obtain by using an optical multichannel analyzer a complete emission spectrum at each excitation wavelength, which allows comparing the emission spectra for many excitation wavelengths (see below). The integrated intensity of the emission bands at about 16 770 cm^{-1} is taken as a measure of fluorescence intensity at a given excitation energy and plotted against wavenumber in Figure 4. Contrary to the emission spectra, all four energy levels (A_i) of the $^6D'_{7/2}$ multiplet give significant contributions to the excitation

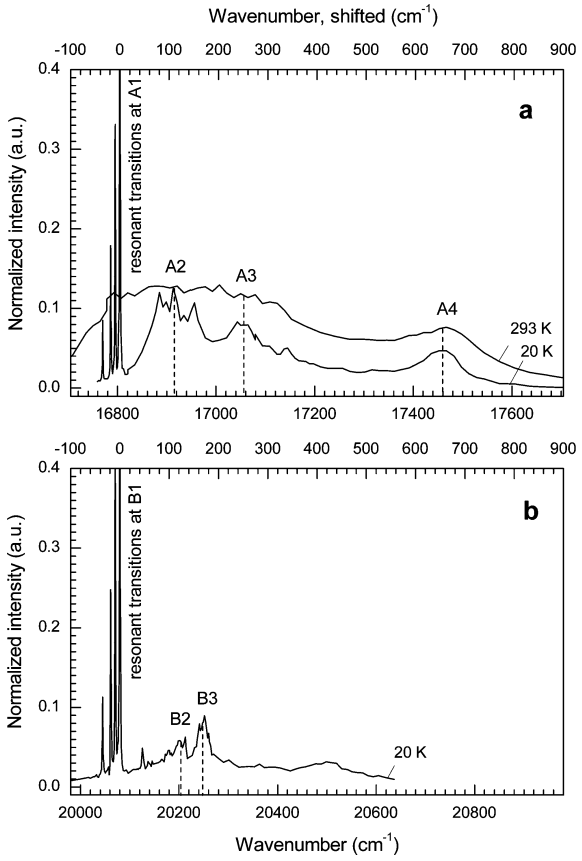

Figure 4. (a) $^8S'_{7/2} \rightarrow {}^6D'_{7/2}$ and (b) $^8S'_{7/2} \rightarrow {}^6P'_{5/2}$ excitation spectra of Cm^{3+} in **1** at 293 and 20 K. The $^6D'_{7/2} \rightarrow {}^8S'_{7/2}$ emission is monitored. The shifted wavenumber scales (top) have the shifts 16 804.7 and 20 083.7 cm^{-1} relative to the absolute wavenumber scales (bottom) in a and b, respectively. Note that the low-temperature spectra are normalized to the highest peak intensity of the resonant transition lines, but, for clarity, are shown only up to 0.4 intensity units (cf. Figure 5).

spectra independently of temperature, indicating a similar transition probability for all these transitions. Following excitation, rapid relaxation to the lowest $^6D'_{7/2}$ substate occurs, which is obvious from the fact that the emission spectra do not change as a function of excitation wavelength, with the exception of the resonant fluorescence line narrowing effect as discussed below.[31] The sum of all $^6D'_{7/2}(A_i) \rightarrow {}^8S'_{7/2}$ emission is taken as a measure of photoabsorption, and hence the excitation spectra are proportional to the photoabsorption cross-section $\sigma(E)$ of Cm^{3+}. The A_4 band, which is barely observed in the emission spectrum, is here rather pronounced (cf. Figures 3 and 4). The A_1-A_3 absorption bands appear as one broad feature at 293 K but are resolved at 20 K.

At low temperature the spectrum exhibits additional structure not present at room temperature and therefore merits further discussion. The most prominent feature is a resonant fluorescence line narrowing effect at the A_1 level near 16 800 cm^{-1}, which comprises four narrow lines (fwhm $\approx$ 1.35 cm^{-1}) with enhanced intensities, corresponding to the transitions from four different energy levels (Z_1-Z_4) of the ground-state $^8S'_{7/2}$ multiplet to the lowest energy level of the $^6D'_{7/2}$ multiplet, i.e., $Z_{1-4} \rightarrow A_1$ (cf. Figures 1 and 4). These lines are of Lorentzian shape, and the width is limited by the coherence of the excited-state alone. However, if nonradiative relaxation to a lower excited state occurs prior to fluorescence, the line is broadened

TABLE 1: Energy (cm^{-1}) of Identified Crystal-Field Levels of the $^8S'_{7/2}$ Ground State and the $^6D'_{7/2}$ and $^6P'_{5/2}$ Excited States of Cm^{3+} in 1 at 20 K

$^8S'_{7/2}$			$^6D'_{7/2}$[a]	$^6P'_{5/2}$
$^6D'_{7/2} \rightarrow {}^8S'_{7/2}$	$^8S'_{7/2} \rightarrow {}^6D'_{7/2}$	$^8S'_{7/2} \rightarrow {}^6P'_{5/2}$	$^8S'_{7/2} \rightarrow {}^6D'_{7/2}$	$^8S'_{7/2} \rightarrow {}^6P'_{5/2}$
0.0	0.0	0.0	16 804.7	20 083.7
9.4	9.6	9.7	16 915	20 200
18.4	18.5	18.6	17 054	20 252
34.7	34.9	35.2	17 461	

[a] Note that the energies of the A_1-A_4 levels are slightly higher (blue-shifted) at 20 K than at 293 K, as given in Table 1 in ref 20.

due to the limitation of the correlation time between the energies of the two excited states involved. This will mask the contribution of the coherence time to the fluorescence line width.[31] The positions of these lines, at 16 769.8, 16 786.2, 16 795.1, and 16 804.7 cm^{-1}, match those of the emission spectrum in Figure 3. Excitation into the higher levels of the $^6D'_{7/2}$ multiplet does not result in fluorescence line narrowing, although the A_2 band contains some sharp features that could reflect the ground-state splitting.

In a second step, the next higher state, $^6P'_{5/2}$, is excited by using the laser light of 19 950−20 650 cm^{-1}. The fluorescence between 480 and 680 nm is monitored, and, as described previously, the peak area of the $^6D'_{7/2} \rightarrow {}^8S'_{7/2}$ emission band at ~16 770 cm^{-1} is taken as a measure of fluorescence intensity. Again, four narrow lines, centered at 20 048.5, 20 065.1, 20 074.0, and 20 083.7 cm^{-1}, dominate the excitation spectrum at 20 K (Figure 4b); these lines are ascribed to the fluorescence line narrowing effect of the lowest crystal-field level (B_1) of the $^6P'_{5/2}$ multiplet. The transition from the lowest energy level of the $^8S'_{7/2}$ multiplet (Z_1) gives rise to the most intense band, while those from thermally populated levels appear with lower intensities. The second (B_2, 20 200 cm^{-1}) and third (B_3, 20 250 cm^{-1}) $^6P'_{7/2}$ crystal-field levels do not exhibit fluorescence line narrowing, and the corresponding excitation bands have comparably lower intensities and are relatively broad. The sharp features superimposed on these bands may originate from the different crystal-field levels of the ground-state $^8S'_{7/2}$ multiplet, as suggested for the analogous features at A_2. The energies of the identified crystal-field levels of the $^8S'_{7/2}$, $^6D'_{7/2}$, and $^6P'_{5/2}$ multiplets are given in Table 1.

Ground-State Splitting. A synopsis of the spectroscopic results relevant for the ground-state splitting is given in Figures 5 and 6. Parts a and b of Figure 5 show the resonant transition in the $^8S'_{7/2} \rightarrow {}^6D'_{7/2}$ (from Figure 4a) and $^8S'_{7/2} \rightarrow {}^6P'_{5/2}$ (from Figure 4b) excitation spectra at high resolution at 20 K, respectively. The observed energy splitting in both spectra (0, 10, 19, and 35 cm^{-1}) is in perfect agreement with each other, indicating that the splitting has the same origin and is associated to the electronic structure of the ground state rather than to the excited states. Also included in Figure 5a is the high-resolution $^6D'_{7/2} \rightarrow {}^8S'_{7/2}$ emission spectrum (from Figure 3, inset) at 20 K, showing the corresponding resonant transitions between the lowest crystal-field level of the $^6D'_{7/2}$ excited state to the four levels of the ground state.

The perfect match of the peak positions in the emission and excitation spectra is further evidence that there is only one major Cm^{3+} site, that of Y^{3+} in **1**. If, for instance, Cm^{3+} ions were incorporated into two structurally different sites, *M* and *N*, giving rise to different crystal field splitting, resonance of the excitation wavelength with the *M* $^8S'_{7/2} \rightarrow {}^6D'_{7/2}$ transitions would give rise to emission of the *M* $^8S'_{7/2}$ (Z_n) $\rightarrow {}^6D'_{7/2}$ lines but not to the *N* $^8S'_{7/2}$ (Z_n) $\rightarrow {}^6D'_{7/2}$ series, and vice versa. This strategy was successfully applied for distinguishing between structurally

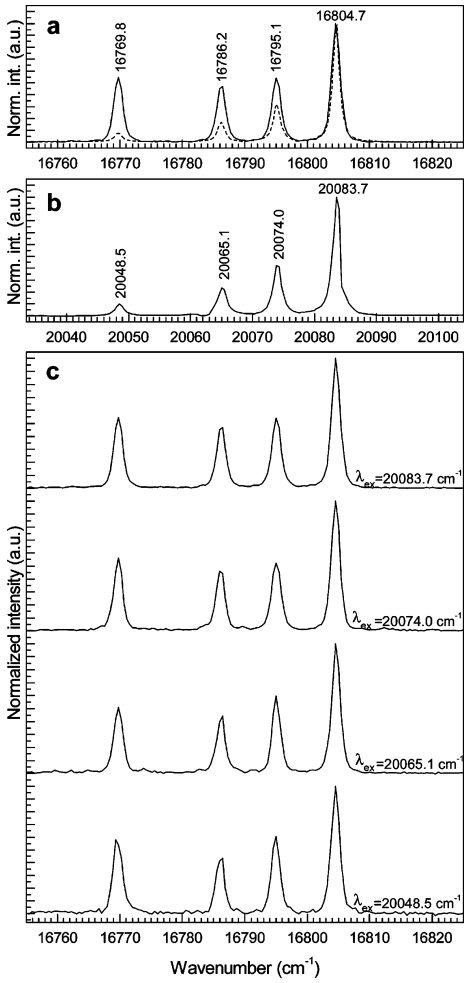

Figure 5. High-resolution excitation and emission spectra of the resonant transitions of Cm^{3+} in **1**: (a) $^6D'_{7/2}(A_1) \rightarrow {}^8S'_{7/2}(Z_{1-4})$ emission (solid line) and $^8S'_{7/2}(Z_{1-4}) \rightarrow {}^6D'_{7/2}(A_1)$ excitation (dashed line) spectra at 20 K. (b) $^8S'_{7/2}(Z_{1-4}) \rightarrow {}^6P'_{5/2}(B_1)$ excitation spectrum at 20 K. (c) $^6D'_{7/2}(A_1) \rightarrow {}^8S'_{7/2}(Z_{1-4})$ emission spectra at 20 K by selectively exciting the $^6P'_{5/2}(B_1)$ level at the four peak maxima at 20 048.5, 20 065.1, 20 074.0, and 20 083.7 cm^{-1} in b. Note that the resulting emission spectra are identical independently of the excitation wavelength.

different Cm^{3+} sites in crystalline YPO_4 and $LuPO_4$.[13] If Cm^{3+} ions were present in nonequivalent sites also in **1**, excitation at different resonant lines would result in emission spectra containing fewer lines than excitation into the F band (~397 nm), which is not the case, but rather the emission spectra remain constant for all excitation wavelengths. This is shown in Figure 5c as an example of selectively exciting the four ground-state levels on the transitions to the lowest crystal-field level of the $^6P'_{5/2}$ multiplet at 20 048.5, 20 065.1, 20 074.0, and 20 083.7 cm^{-1} while recording the individual $^6D'_{7/2} \rightarrow {}^8S'_{7/2}(Z_n)$ emission spectra at high resolution. The four spectra are identical and match that of the $^8S'_{7/2}(Z_n) \rightarrow {}^6D'_{7/2}$ excitation spectrum in Figure 5a.

Although the peak positions of the excitation and emission spectra match very well, the relative strengths of the lines are different. The emission bands result from the fluorescence transition from the $^6D'_{7/2}(A_1)$ state terminating at the four crystal-field levels (Z_n) of the ground-state multiplet. The peak areas of the bands reflect the probabilities of the emission and are proportional to the transition matrix elements of the electric and

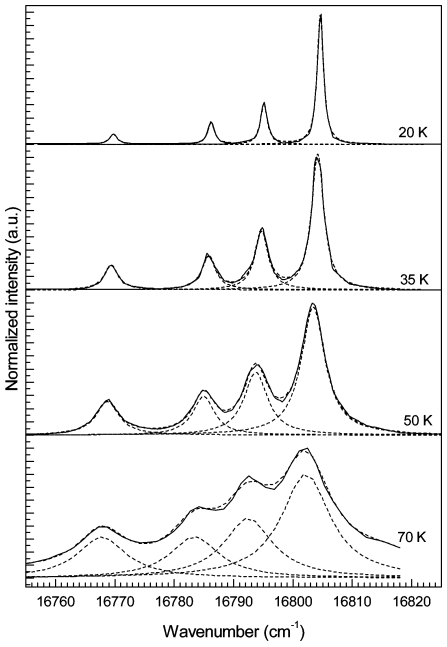

Figure 6. $^8S'_{7/2}(Z_{1-4}) \rightarrow {}^6D'_{7/2}(A_1)$ excitation spectra of Cm^{3+} in **1** at 20, 35, 50, and 70 K (solid lines) and curve-fitted spectra using Lorentzian functions (dashed lines). Note that with increasing temperature the bands broaden and shift slightly to lower energy (ca. 4 cm^{-1}), and their relative intensities change as the higher crystal-field levels become thermally populated (cf. Figure 7).

magnetic dipole operator (magnetic transitions are strongly suppressed; they are weaker but not forbidden). The relative intensities of the respective $^6D'_{7/2}(A_1) \rightarrow {}^8S'_{7/2}(Z_n)$ transitions at 20 K are 1.00, 0.58, 0.51, 0.59 for $n = 1, 2, 3, 4$, respectively (cf. Figures 5a and S1 of the Supporting Information).

The intensity of the excitation for the reverse transition $^8S'_{7/2}(Z_n) \rightarrow {}^6D'_{7/2}(A_1)$ depends not only on the transition matrix elements but also on the population of the respective crystal-field levels, *n*. While in thermal equilibrium, the distribution $P(n)$ of the states *n* of excitation energy $E(n)$ at temperature *T* is expected to follow the Boltzmann law

$$P(n) = g_n e^{-E(n)/k_B T} \quad (1)$$

where k_B is the Boltzmann's constant and g_n is the statistical weight of state *n* (here, $g_n = 1$). Hence, the transitions from the second, third, and forth ground-state levels are much weaker at low temperature than from the lowest crystal-field level. This agrees well with the excitation spectrum at 20 K in Figure 5a, where the intensity decreases with decreasing wavenumber.

The thermal population of the crystal-field levels of the ground state provides a powerful tool to exclude the presence of multiple sites (if present). Suppose, again, the presence of two nonequivalent sites *M* and *N*. Some of the observed bands would correspond to the crystal-field levels of *M* (Z^M_n) and the remaining bands to *N* (Z^N_n). Upon increasing temperature the intensities of the bands corresponding to the respective lowest crystal-field levels (Z^M_1 and Z^N_1) would not change significantly, while the transition probabilities from the higher states (Z^M_{2-4} and Z^N_{2-4}) would increase due to the higher thermal population. However, evaluation of the $^8S'_{7/2} \rightarrow {}^6D'_{7/2}(A_1)$ excitation spectra at 20, 35, 50, and 70 K in Figure 6 draws a different picture. Each spectrum shows the four bands, broadened and slightly shifted to lower energy with increasing temperature, but with

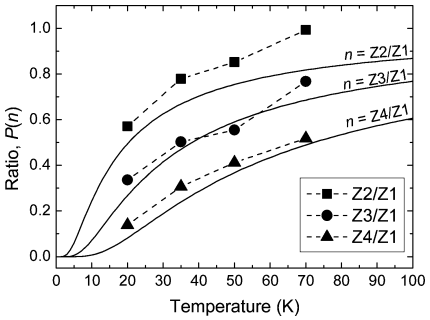

Figure 7. Temperature dependency of the excitation intensity of the ${}^8S'_{7/2}(Z_{1-4}) \rightarrow {}^6D'_{7/2}$ (A_1) transitions at 20, 35, 50, and 70 K, expressed as intensity ratios, $P(n)$, relative to the Z_1 band: Z_2/Z_1, Z_3/Z_1, and Z_4/Z_1. The solid lines represent the calculated ratios from the Boltzmann equation (eq 1).

constant differences between the peak maxima of about 0, 10, 19, and 35 cm^{-1}; i.e., the ground-state splitting remains unaltered with temperature. The high-energy band at ~16 805 cm^{-1} with the largest intensity corresponds to the transition from the ground level (Z_1) to A_1, while the bands at lower energies with lower intensities correspond to transitions from the thermally populated second (Z_2), third (Z_3), and fourth (Z_4) levels of the ground-state ${}^8S'_{7/2}$ multiplet to A_1. The intensity contributions from these higher levels are relatively small at low temperature but increase with temperature as they progressively become populated. Since all but the most energetic band increases in intensity with increasing temperature, the assumption of nonequivalent sites is definitively ruled out. Figure 7 plots the intensity ratios Z_{2-4}/Z_1 (corrected for differences in transition probability as described above) deduced from Figure 6, together with the theoretical Boltzmann ratios from eq 1 versus temperature. The ratios follow a single Boltzmann distribution, confirming the presence of one unique site.

Emission Decay Rate. The emission decay rate of the ${}^6D'_{7/2}$ level is monoexponential at 293 and 20 K with decay rate constants, k_{obs}, of 14.7 ± 0.5 and 14.5 ± 0.5 ms^{-1}, respectively; the corresponding lifetimes, τ ($=k_{obs}^{-1}$), are 68 ± 2 and 69 ± 2 μs at 293 and 20 K, respectively (Figure S2, Supporting Information). These lifetimes are essentially determined by nk_{H_2O} (the number of coordinated water molecules times the rate constant by each water molecule) rather than by the radiative decay constant, k_r ($k_r \leq 0.73$ ms^{-1} and $k_{H_2O} \approx 1.66$ ms^{-1} for the Cm^{3+} aqua ion at 293 K [20]). It is well-known that the very efficient quenching by ligated H_2O molecules is due to coupling with overtones of high-frequency OH vibrations. It should be emphasized that the shapes and the relative intensities of the four bands in the high-resolution ${}^6D'_{7/2} \rightarrow {}^8S'_{7/2}$ emission spectra at 20 K are constant at different delay times, indicating that these bands indeed originate from structurally identical $[Cm(H_2O)_8]^{3+}$ ions with identical decay rate constants (Figure S2, Supporting Information).

It is worth noting that, in contrast to some anhydrous Cm^{3+}-doped crystals, e.g., $LaCl_3$,[9,12] no direct fluorescence emission is observed from the different crystal-field levels of the ${}^6P'_{5/2}$ multiplet to the ground state for $[Cm(H_2O)_8]^{3+}$ in **1**. This is not surprising, since the energy difference between the lowest ${}^6P'_{5/2}$ and ${}^6D'_{7/2}$ levels, 3279 cm^{-1}, matches that of the OH-stretching vibration of coordinated water molecules.[32] The resulting fast nonradiative decay to the lowest crystal-field level of the ${}^6D'_{7/2}$ multiplet, which takes place probably within sub-nanosecond time scales, will strongly suppress the emission from the ${}^6P'_{5/2}$ multiplet.

Summary and Conclusions

This paper presents the level structure of the 8-fold-coordinate $[Cm(H_2O)_8]^{3+}$ ion in the crystal host of $[Y(H_2O)_8]Cl_3 \cdot$15-crown-5 (**1**) investigated by means of optical emission and excitation laser spectroscopy. It is the first study ever showing the crystal-field effects on the ground- and excited-state electronic structure of a hydrated Cm^{3+} ion. We find unusually large crystal-field splitting of the ${}^8S'_{7/2}$ ground state, 35 cm^{-1}, but also the excited ${}^6D'_{7/2}$ and ${}^6P'_{5/2}$ multiplets exhibit large splitting, 670 and 170 cm^{-1}, respectively. Resonance fluorescence line narrowing occurs on transitions between the ground-state multiplet and the lowest crystal-field levels of the ${}^6D'_{7/2}$ and ${}^6P'_{5/2}$ multiplets. These transitions give rise to very intense fluorescence bands, comprising four narrow lines separated by about 0, 10, 19, and 35 cm^{-1}, all of which are unambiguously assigned to transitions either commencing or terminating at the four crystal-field levels of the ${}^8S'_{7/2}$ multiplet. By carefully comparing emission spectra at different excitation wavelengths and after different delay times, and by evaluating relative peak areas of excitation spectra at four different temperatures, the simultaneous presence of Cm^{3+} ions in nonequivalent sites can be excluded definitely as an alternative explanation for the observed multiple lines.

The magnitude of the crystal field strength for $[Cm(H_2O)_8]^{3+}$ in **1** can be estimated using the scalar crystal field strength parameter, N'_v, as this parameter is proportional to the total splitting (ΔE) of the J-term. The ground-state splitting of 35 cm^{-1} in **1** is comparable to that of the 8-fold-coordinate Cm^{3+} in O_h site symmetry in ThO_2, 36 cm^{-1} ($N'_v = 2953$ cm^{-1}),[14] which is the largest value reported so far. This is much larger than for the 9-fold-coordinate Cm^{3+} with C_{3h} symmetry in $LaCl_3$, ~2 cm^{-1} ($N'_v = 628$ cm^{-1}),[9-11] which is known to be the weakest crystal-field for Cm^{3+}.

The coordination geometry of $[Cm(H_2O)_8]^{3+}$ in **1** is a distorted bicapped trigonal prism with rather low symmetry (cf. Figure 2). The estimated Cm−O mean bond distance, 2.445 Å, is similar to that of the $[Cm(IO_3)_8]$ unit in anhydrous $Cm(IO_3)_3$, 2.431(4) Å,[33] and only slightly shorter than that of the 9-fold-coordinated Cm^{3+} aqua ion, 2.46−2.47 Å, as determined by EXAFS.[34,35] The reason for the strong crystal field, causing the unusually large splitting of the ground- and excited-state multiplets, may be due to the distorted bicapped coordination geometry and the relatively short mean Cm−O bond distance of the $[Cm(H_2O)_8]^{3+}$ ion in **1**.

Recently, it was shown that the fluorescence spectrum of the Cm^{3+} aqua ion at 200 °C closely resembles the room-temperature spectrum of Cm^{3+} in **1**, with regard to peak positions and peak shapes, both of which are broadened and red-shifted relative to the aqua ion spectrum at room temperature.[20] It was concluded that the coordination geometry, and hence the ligand field, of the Cm^{3+} aqua ion at 200 °C is similar to that of $[Cm(H_2O)_8]^{3+}$ in **1**. As clearly shown in this work, the large ground-state splitting in **1** contributes significantly to the line width of the fluorescence band even at room temperature (cf. Figure 3). Thus, the 8-fold symmetry of the Cm^{3+} aqua ion at elevated temperature should cause a ground-state splitting of similar magnitude as that observed in **1** and, consequently, cause a much broader emission band than for the aqua ion at room temperature, which experiences a much weaker ligand field. The same way of reasoning led Carnal and Rajnak to the conclusion that the rather narrow bands observed in the absorption spectrum of Cm^{3+}(aq) at room temperature were not appreciably influenced by the ground-state splitting, which they considered to be comparably small as that for Cm^{3+} in $LaCl_3$.[17] However, our preliminary results on $[Cm(H_2O)_9]^{3+}$ in different

crystalline rare-earth nonahydrates suggest that this statement, about a small ground-state splitting of the Cm^{3+} aqua ion, is an underestimation. Future work may give a more precise estimate on this matter.

Acknowledgment. We thank S. Büchner for technical assistance and T. Rabung and N. Edelstein for helpful discussions.

Supporting Information Available: Crystallographic data in CIF format for **1**, high-resolution emission spectrum (Figure S1), and time-resolved spectra of the emission decay at 20 K (Figure S2). This material is available free of charge via the Internet at http://pubs.acs.org.

References and Notes

(1) Sytsma, J.; Murdoch, K. M.; Edelstein, N. M.; Boatner, L. A.; Abraham, M. M. *Phys. Rev. B* **1995**, *52*, 12668−12676.

(2) See e.g.: Edelstein, N. M. *J. Alloys Compd.* **1995**, *223*, 197−203, and references therein.

(3) (a) Wybourne, B. G. *Phys. Rev.* **1966**, *148*, 317−327. (b) Bernstein, E. R.; Dobbs, G. M. *Phys. Rev. B* **1975**, *11*, 4623−4638.

(4) Binnemans, K.; Görller-Walrand, C. *J. Phys.: Condens. Matter* **1996**, *8*, 1267−1279.

(5) Görller-Walrand, C.; Binnemans, K. In *Handbook of the Physics and Chemistry of Rare Earths*; Gschneidner, K. A., Jr., Eyring, L., Eds.; North-Holland: Amsterdam, 1996; Vol. 23, pp 121−183.

(6) Auzel, F.; Malta, O. L. *J. Phys.* **1983**, *44*, 201−206.

(7) For comparison of crystal-field strengths for different f^N ions in a given crystal host, or for a particular f^N ion in different hosts, the parameter N_v' is used, which is linearly related to N_v (defined in ref 6) according to $N_v' = N_v/(2\sqrt{\pi}) = (\sum_{k,q}(B^k_q)^2/(2k+1))^{1/2}$.

(8) Murdoch, K. M.; Cavellec, R.; Simoni, E.; Karbowiak, M.; Hubert, S. Illemassene, M.; Edelstein, N. M. *J. Chem. Phys.* **1998**, *108*, 6353−6361.

(9) Liu, G. K.; Beitz, J. V.; Huang, Jin *J. Chem. Phys.* **1993**, *99*, 3304−3311.

(10) Illemassene, M.; Murdock, K. M.; Edelstein, N. M.; Krupa, J. C. *J. Lumin.* **1997**, *75*, 77−87.

(11) Gruber, J. B.; Cochran, W. R.; Convay, J. G.; Nicol, A. T. *J. Chem. Phys.* **1966**, *45*, 1423−1427.

(12) Murdoch, K. M.; Edelstein, N. M.; Boatner, L. A.; Abraham, M. M. *J. Chem. Phys.* **1996**, *105*, 2539−2546.

(13) Liu, G. K.; Li, S. T.; Zhorin, V. V.; Loong, C.-K.; Abraham, M. M.; Boatner, L. A. *J. Chem. Phys.* **1998**, *109*, 6800−6808.

(14) Thouvenot, P.; Hubert, S.; Edelstein, N. M. *Phys. Rev. B* **1994**, *50*, 9715−9720.

(15) Abraham, M.; Judd, B. R.; Wickman, H. H. *Phys. Rev.* **1963**, *130*, 611−612.

(16) Billard, I. Lanthanide and Actinide Solution Chemistry Studied by Time-Resolved Laser-Induced Spectroscopy (TRLS). In *Handbook on the Physics and Chemistry of Rare Earths*. Gschneidner, K. A., Jr., Bünzli, J.-C., Pecharsky, V. K., Eds.; Elsevier: Amsterdam, 2003; Vol. 33, Ch. 216.

(17) Carnal, W. T.; Rajnak, K. *J. Chem. Phys.* **1975**, *63*, 3510−3514

(18) Beitz, J. V. *Radiochim. Acta* **1991**, *52/53*, 35−39.

(19) Beitz, J. V. *J. Alloys Compd.* **1994**, *207−28*, 41−50.

(20) Lindqvist-Reis, P.; Klenze, R.; Schubert, G.; Fanghänel, T. *J. Phys. Chem. B* **2005**, *109*, 3077−3083.

(21) Lindqvist-Reis, P.; Klenze, R.; Fanghänel, T. In *Advances in Actinide Science*; Alvares, R., May, I., Bryan, N. D., Eds.; Royal Society of Chemistry: Letchworth, U.K., in press.

(22) Rogers, R. D.; Kurihara, L. K. *Inorg. Chim. Acta* **1986**, *116*, 171−177; **1987**, *129*, 277−282.

(23) Sheldrick, G. M. *SHELXTL PC, version 5.1, An Integrated System for Solving, Refining, and Displaying Crystal Structures from Diffraction Data*; Bruker Analytical X-ray Systems: Karlsruhe, Germany, 2000.

(24) Crystal structure determination of **1**: $C_{10}H_{36}Cl_3O_{13}Y$, fw = 559.65 g mol^{-1}, orthorhombic, a = 9.1848(18) Å, b = 17.229(3) Å, c = 15.229-(3) Å, β = 92.80(3)°, V = 2418.1(8) Å^3, T = 200(2) K, space group $P2_1/n$ (No. 11), Z = 4, crystal size = 0.16 × 0.12 × 0.07 mm, ρ_{calc} = 1.537 g cm^{-1}, μ(Mo Kα) = 2.795 mm^{-1}, θ_{max} = 27.08° (99.3%), 18 808 reflections measured, 5280 independent reflections (R_{int} = 0.0917), 388 parameters, 1 restraint, GOF = 0.886, final R1 = 0.0472 (for 5280 data $I > 2\sigma(I)$), and wR2 = 0.1338 (all data).

(25) Brandenburg, K. *DIAMOND 2.1*; Crystal Impact GbR: Bonn, Germany, 2001.

(26) Tits, J.; Stumpf, T.; Rabung, T.; Wieland, E.; Fanghanel, T. *Environ. Sci. Technol.* **2003**, *37*, 3568−3573.

(27) XRD data at 295, 200, and 120 K show that no phase transition occurs in this temperature range; fluorescence emission data on the isomorphous $[Eu(H_2O)_8]Cl_3 \cdot$15-crown-5 compound show that there is only one type of Eu^{3+} ions with $\sim C_2$ symmetry at 20 K.

(28) David, F. H.; Vokhmin, V. *New J. Chem.* **2003**, *27*, 1627−1632.

(29) Shannon, R. D. *Acta Crystallogr.* **1976**, *A32*, 751−767.

(30) Liu, G. K.; Li, S. T.; Beitz, J. V.; Abraham, M. *J. Alloys Compd.* **1998**, *271−273*, 872−875.

(31) Brundage, R. T.; Powel, R. L.; Beitz, J. V.; Liu, G. K. *J. Lumin.* **1996**, *69*, 121−129.

(32) ν_1(OH) for isotopically dilute HDO molecules in solid hydrates appears at ~3300−3700 cm^{-1} depending on the hydrogen bond strength; see, e.g., Berglund, B.; Lindgren, J.; Tegenfeldt, J. *J. Mol. Struct.* **1978**, *43*, 169−177.

(33) Sykora, R. E.; Assefa, Z.; Haire, R. G.; Albrecht-Schmitt, T. E. *J. Solid State Chem.* **2004**, *177*, 4413−4419.

(34) Allen, P. G.; Bucher, J. J.; Shuh, D. K.; Edelstein, N. M.; Craig, I. *Inorg. Chem.* **2000**, *39*, 595.

(35) Weigl, M.; Denecke, M. A.; Panack, P.; Gompper, K. *Dalton Trans.* **2005**, 1281−1286.

5.4.2 Fluorescence spectroscopy on protactinium(IV) in aqueous solution [Marq04]

Radiochim. Acta **92**, 445–447 (2004)

Rapid communication

Fluorescence spectroscopy on protactinium(IV) in aqueous solution

By C. M. Marquardt[1,*], P. J. Panak[1], C. Apostolidis[2], A. Morgenstern[2], C. Walther[1], R. Klenze[1] and Th. Fanghänel[1]

[1] Forschungszentrum Karlsruhe, Institut für Nukleare Entsorgung, D-76021 Karlsruhe, Germany
[2] European Commission, Joint Research Centre, Institute for Transuranium Elements, P.O. Box 2340, D-76125 Karlsruhe, Germany

(Received January 20, 2004; accepted in revised form March 3, 2004)

Pa(IV) / *Time-resolved fluorescence spectroscopy* / *Absorption spectroscopy*

Summary. This work focuses on time-resolved laser fluorescence spectroscopy (TRLFS) of Pa(IV) in aqueous solution. Excitation at 308 nm causes a fluorescence emission with a peak maximum at about 460 nm. Thereby, the position of the band's maximum depends on the concentration, the type of the acid, and the pH value. Increasing complexation of the Pa(IV) ion leads to an increasing hypsochromic shift of the emission band up to 46 nm. In contrast to the band position the half-width (61.6 ± 1.4 nm) and the lifetime (16 ± 2 ns) of the fluorescence emission do not change significantly with changes in the chemical environment of the Pa(IV). The results of this work show that speciation of Pa(IV) can be performed even in aqueous solution by using TRLFS.

Introduction

In recent years a lot of work has been done on the spectroscopic properties of $4f^1$ and $5f^1$ elements like Ce(III), Pr(IV), Th(III) and Pa(IV) [1–4]. In case of the first elements of the lanthanide and actinide series the energy level of the $4f$, $5d$, or $5f$, $6d$, are very close in energy and transitions of the electrons from f to d levels are possible by excitation with UV light [5, 6]. In contrast to $f \rightarrow f$ transitions the $f \rightarrow d$ transitions are very intense (no Laporte forbiddance), very broad (crystal field splitting of the d-level: 10 000–20 000 cm^{-1}) and sensitive to changes in the chemical environment. Fluorescence spectroscopy on $f^1 \rightarrow 6d^1$ elements has been performed so far only with solid phases and in organic solutions, but not in aqueous solutions [3, 4]. The emission from the lowest crystal field level of the $6d^1$ configuration to the electronic levels of the $5f^1$ configuration of Pa^{4+} diluted into single crystals of Cs_2ZrCl_6 are studied after excitation with UV light. The objective of the present work is to demonstrate whether tetravalent protactinium shows fluorescence emission in aqueous solutions and whether the fluorescence bands are sensitive to changes in the chemical environment and can be used for speciation of Pa(IV) by time-resolved laser fluorescence spectroscopy (TRLFS).

Experimental

The isotope Pa-231 (3.3×10^4 y half-life) was used for all experiments. It was purified from decay products by sorption on silica gel from 8 M HNO_3 and elution with 5% H_2O_2/3 M HNO_3. This method is described in [7]. After purification the Pa-231 was dissolved in 9.5 M HCl with a final concentration of 3.3×10^{-4} M. The purity of the solution was checked by α-spectrometry. The concentration of Pa-231 solutions were measured by liquid scintillation counting for all succeeding experiments. The preparation of various Pa(IV) solutions was performed in a glove-box under oxygen-free argon atmosphere.

The protactinium of the stock solution was pentavalent. Aliquots were diluted with 2 M and/or 5 M $HClO_4$, HCl and H_2SO_4 to final Pa concentrations between 8.6×10^{-6} and 1.3×10^{-5} M. By adding 1–2 ml of liquid Zn-amalgam and vigorous shaking for 10 min all Pa(V) was reduced to Pa(IV). The solution was separated from the Zn-amalgam and characterized by UV spectroscopy and TRLFS.

UV spectroscopy was performed with a Cary5 spectrophotometer (Varian). The protactinium solutions were measured in 1 cm inert-gas quartz cuvettes (Hellma).

TRLFS measurements were performed using a XeCl-eximer laser (Lambda Physics, LPX 202, 308 nm, 24 ns) for excitation. Since no frequency doubling crystal was available, the output of the excimer laser was used directly for excitation instead of 278 nm, where the absorption cross section of Pa(IV) is tenfold higher (Fig. 1). Emission spectra were recorded from 350 to 570 nm. The fluorescence emission is detected by an optical multi-channel analyzer consisting of a polychromator (Acton Research 275) with a 300 lines/mm grating and a photodiode array (Spectroscopy instruments, ST 180, IRY 700GR). For measuring the decay time of the fluorescence emission the delay time was shifted in steps of 5 or 10 ns within a time interval of 1–121 ns, yielding 10 to 15 data points. Since the exciting laser pulse and lifetime are of similar duration a deconvolution of the decay curve assum-

*Author for correspondence (E-mail: marquardt@ine.fzk.de).

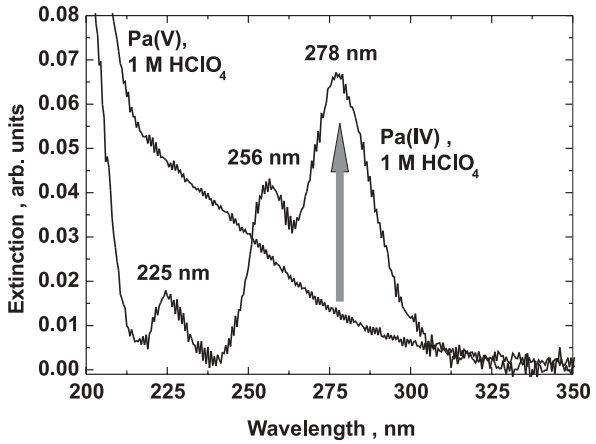

Fig. 1. Change of the absorption spectrum of Pa(V) in 1 M $HClO_4$ after reduction to Pa(IV) with liquid Zn-amalgam.

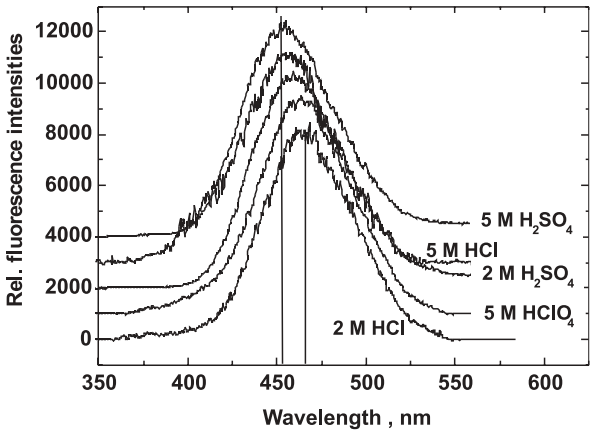

Fig. 2. Fluorescence spectra of Pa(IV) in different acidic solutions by excitation with laser light at 308 nm.

ing a gaussian temporal profile of the laser pulse was performed.

Results and discussion

The UV absorption spectra of pentavalent Pa showed a monotonous increase of the absorption with decreasing wavelength in the range between 210 and 400 nm, which is consistent with the literature data [8]. After treatment of Pa(V) with the Zn-amalgam three characteristic absorption bands emerge with maxima at about 225 nm, 256 nm and 278 nm. Fig. 1 shows the absorption spectrum of Pa in 1 M $HClO_4$ before and after the treatment with Zn-amalgam. The three bands are very well in accordance with results from the literature [8] and are ascribed to the tetravalent protactinium ion (Pa(IV)). The Pa(IV) is relatively stable under argon atmosphere and only 10% is oxidized to Pa(V) after 20 hours. The position of the maxima of the absorption bands varies with type and concentration of the acid. Generally, the shift of the bands to longer wavelengths increases (see Table 1) with increasing concentration and complexation strength of the anion.

The fluorescence spectra of Pa(IV) in different acids are shown in Fig. 2. In contrast to the spectra of Pa(IV) imbedded into a solid matrix [1–4] displaying various transitions, only one broad band with a half width of 61.6 ± 1.4 nm is observed in solution. The peak maximum varies between 455 and 465 nm depending on the type and concentration of the acid (see Table 1). Pa(IV) in 2 M HCl shows a peak maximum of 465 nm. In order to gain further insight, fluorescence spectra at shorter wavelengths have to be recorded. Increasing the HCl concentration to 5 M causes a peak shift of 9 nm to smaller wavelength. A similar trend is observed for H_2SO_4. The position of the emission band in 5 M H_2SO_4 (455 nm) occurs at lower wavelength compared to the spectrum in 2 M H_2SO_4 (460 nm). Comparing different mineral acids, we find that the hypsochromic shift is bigger for sulfuric acid than for HCl at equal acid concentrations. This leads to the conclusion that the hypsochromic shift corresponds with the complexation capability of the acid anion. This is also confirmed by the fact that Pa(IV) in 5 M $HClO_4$ displays a fluorescence band at 464 nm, because the perchlorate ion is considered as a very weakly complexing anion. The spectroscopic parameters of the absorption spectroscopy and fluorescence spectroscopy are summarized in Table 1.

Table 1. Maxima of the absorption and fluorescence band and the fluorescence lifetime of Pa(IV) in various acidic solutions.

	Maximum of absorption band (nm)	Maximum of fluorescence band (nm)	Fluorescence life-times of Pa(IV) (ns)
1 M $HClO_4$	278	–	–
5 M $HClO_4$	279	464	18.3
2 M HCl	279	465	14.7
5 M HCl	284	456	12.6
2 M H_2SO_4	288	460	16.5
5 M H_2SO_4	290	455	17.3

Contrary to $f \rightarrow f$ transitions with fluorescence lifetimes in the μs range, the decay of the fluorescence emission of Pa(IV) occurs within nanoseconds. Furthermore, the determination of the fluorescence lifetime of Pa(IV) is very difficult, because of an additional decrease of fluorescence intensity with increasing number of laser shots. This might be caused by photo-oxidation of Pa(IV) to Pa(V). This effect has to be taken into account by normalizing the fluorescence signal. Measurement cycles with increasing delay time Δt are alternated with reference cycles at $\Delta t = 0$ in order to correct for the decreasing Pa(IV)-fraction and hence decreasing fluorescence intensity. The corrected lifetimes of Pa(IV) in different acids are also given in Table 1. In contrast to the peak position, the lifetime of the Pa(IV) fluorescence emission does not change significantly with concentration and type of the mineral acid and a mean lifetime of 16 ± 2 ns is deduced.

To estimate effects of Pa(IV) hydrolysis on the fluorescence band, we added NaOH to the Pa(IV) in 2 M H_2SO_4 up to a pH of 3.5. Compared to the small shifts in acid solution the fluorescence band at pH 3.5 is shifted 46 nm to a smaller wavelength (see. Fig. 3). This result confirms that strongly complexing ligands cause a large “blue shift”, which enables

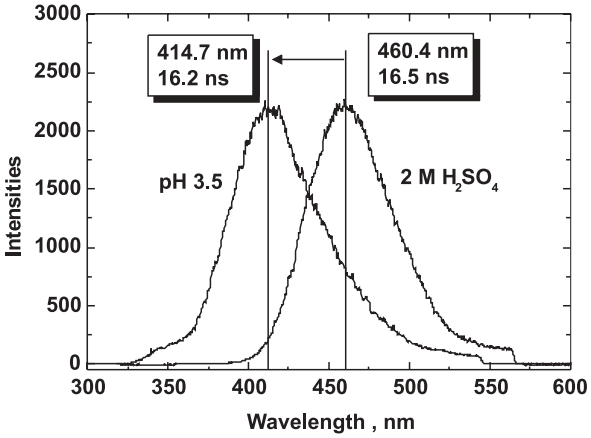

Fig. 3. Influence of the pH value on the fluorescence band of Pa(IV).

us to use fluorescence spectroscopy for further speciation of Pa(IV) complexes in aqueous solution. However, the width of the band and the lifetime of the species do not change significantly with the increase in the pH value.

Conclusions

TRLFS on Pa(IV) shows a broad intense fluorescence band which is sensitive to changes in the chemical environment of the Pa(IV) resulting in a hypsochromic shift of the fluorescence band. Even weak complexing ligands like ClO_4^-, Cl^- and SO_4^{2-} cause a significant "blue shift" of several nanometers, whereas strong complexing ligands like OH^- show a large "blue shift" up to 46 nm. Therefore, speciation studies are possible by TRLFS at Pa(IV) concentrations of 10^{-7} M. The fluorescence emission of Pa(IV) will be studied in more detail in future activities.

References

1. Edelstein, N. M., Kot, W. K.: Spectroscopic and magnetic studies of tetravalent Pa and trivalent Th compounds. J. Alloys Compd. **193**, 82 (1993).
2. Edelstein, N. M., Kot, W. K., Krupa, J. C.: The $5f \rightarrow 6d$ absorption spectrum of Pa^{4+}/Cs_2ZrCl_6. J. Chem. Phys. **96**, 1 (1991).
3. Piehler, D., Kot, W. K., Edelstein, N. M.: The $6d \rightarrow 5f$ fluorescence spectra of $PaCl_6^{2-}$ in a Cs_2ZrCl_6 crystal. J. Chem. Phys. **94**, 942 (1991).
4. Edelstein, N. M., Krupa, J. C., Naik, R. C., Rajnak, K., Whittaker, B., Brown, D.: Analysis of the $5f^1 \rightarrow 6d^1$ transitions in PaX_6^{2-} (X = Cl, Br) and $Pa^{4+}/ThBr_4$. Inorg. Chem. **27**, 3186 (1988).
5. Fred, M. S.: Spectra and Electronic Structure of Free Actinide Atoms and Ions. In: *The Chemistry of the Actinide Elements*. Vol. 2 (Katz, J. J., Seaborg, G. T., Morss, L. R., eds.) Chapt. 15 (1986).
6. Edelstein, N. M.: Comparison of the electronic structure of the lanthanides and actinides. J. Alloys Compd. **223**, 197 (1995).
7. Morgenstern, A., Apostolidis, C., Mayer, K.: Age determination of highly enriched uranium: separation and analysis of ^{231}Pa. Anal. Chem. **74**, 5513 (2002).
8. Eberle, S. H.: Chemie des Protactiniums in wässriger Lösung. In: *Gmelin Handbuch der anorganischen Chemie. 8, System-Nr 51, Erg. Bd 2*. Chapt. 13 (1977).

5.4.3 Fluorescence spectroscopy of protactinium(IV) [Marq05]

FLUORESCENCE SPECTROSCOPY OF PROTACTINIUM(IV)

C.M. Marquardt,[1] P.J. Panak,[1] C. Walther,[1] R. Klenze[1] and Th. Fanghänel[1,2]

[1]Forschungszentrum Karlsruhe GmbH, Institut für Nukleare Entsorgung, Postfach 3640, 76021 Karlsruhe, Germany
[2]Physikalisch-Chemisches Institut, Ruprecht-Karls-Universität
Im Neuenheimer Feld 253, D-69129 Heidelberg, Germany

1 INTRODUCTION

In a previous publication[1] we showed that fluorescence spectroscopy of tetravalent protactinium (Pa(IV)) in aqueous solution is possible. This might open up new vistas for spectroscopic speciation of tetravalent actinides at trace concentrations. In this paper we show that fluorescence spectroscopy is applicable for complexation studies with tetravalent protactinium. The fluoride and the hydroxide anion were chosen as complexing ligands.

2 EXPERIMENTAL

2.1 Chemicals

A stock solution of Pa-231 (3.3×10^4 y half-life) in 9.5 M HCl was used for all experiments with a concentration of 3.3×10^{-4} M. The protactinium was pentavalent in the stock. For the complexation studies aliquots were diluted with 1 M $HClO_4$ to final Pa concentrations between 8.6×10^{-6} and 1.3×10^{-5} M. The preparation of all Pa(IV) solutions was performed in a glove-box under oxygen-free (p_{O2}<10ppm) argon atmosphere. By adding 1-2 ml of liquid Zn-amalgam and vigorous shaking for 10 min all Pa(V) was reduced to Pa(IV). The Zn-amalgam was removed from the solutions before characterising by UV spectroscopy and TRLFS. After the spectroscopic measurements and before adding the next aliquot of NaF or NaOH, the sample was treated again with Zn-amalgam for two minutes to remove Pa(V), that had been produced meanwhile. Liquid scintillation counting was used for measuring the Pa concentration in solution.

The UV spectra of the solutions were recorded in 1 cm quartz cuvettes with a gas-tight screw cap (Hellma, Germany) by a Cary5 spectrophotometer (Varian).

TRLFS measurements were performed using a XeCl-excimer laser (Lambda Physics, LPX 202, 308 nm, 24 ns) for excitation. Details are described elsewhere.[1] The Pa(IV) was excited either at 308 nm by direct output of the laser light or at 278 nm by using a dye laser with a frequency doubling crystal. The absorption cross-section of Pa(IV) is about tenfold higher at 278 nm than at 308 nm. Emission spectra were recorded from 350 to 570 nm.

3 RESULTS AND DISCUSSION

3.1 Studies on Fluoride Complexation

The initial concentration of Pa(IV) used for complexation studies with F^- was 1.56 x 10^{-5} M in 1 M $HClO_4$. This sample was titrated with a 0.8 M NaF solution. Thus the total fluoride concentration varied from 0 to 0.11 M. In Figure 1 the absorption spectra of the samples are shown. It is discernable that with increasing fluoride concentration the absorption band at 279 nm of the free Pa^{4+}-ion is shifted to higher wavelengths. At higher fluoride concentrations (7 mM and higher) a new absorption band evolves at 340 nm. From thermodynamic calculations with complexing constants $\log\beta_1 = 7.91$ and $\log\beta_2 = 14.62$ from Guillaumont[2] at ionic strength of 3 and $\log\beta^\circ_3 = 21.89$, $\log\beta^\circ_4 = 26.34$, and the solubility product $\log K^\circ_{s,0} = 29.4$ for the analogues metal ion U(IV),[3] four regions of dominant species (fractions > 25%) can be defined with increasing F^- concentrations: 1. Pa^{4+}, 2. (PaF^{3+} + PaF_2^{2+}), 3. (PaF_2^{2+} + PaF_3^{+}) 4. (PaF_3 + PaF_4(s)). It must be pointed out that the species distribution is only an estimation, because of the uncertainties in the complexing constants at given experimental conditions. But nevertheless, these regions comply qualitatively with the shifts of the absorption band in the spectra: 1. 279 nm, 2. 284 nm, 3. 286 nm, and 4. 340 nm.

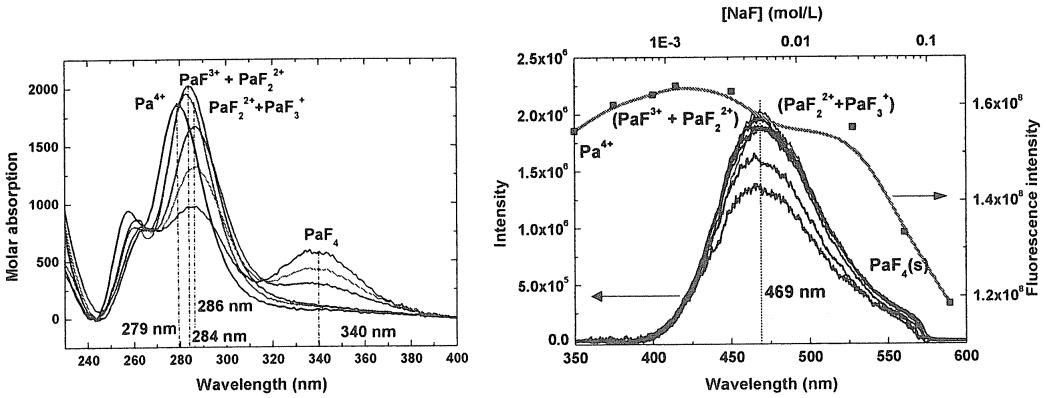

Figure 1 *Absorption (left) and fluorescence(right) spectra of Pa(IV) at various fluoride concentrations. In the graph on the right, the peak areas are plotted against the NaF concentration (grey line)*

However, the band at 340 nm may not solely be caused by the solved species PaF_4 (aq), because its concentration is too low for such high absorbances. We assume that it is rather caused by dispersed crystalline PaF_4 (s). This is in good agreement with the abrupt and enormous shift observed for NaF at concentrations higher than 0.025 M. In contrast to the absorption band the fluorescence spectra show no significant shift of the band at 469 nm with fluoride complexation. With increasing fluoride concentration the fluorescence intensity increases up to a concentration of 0.003 M and then decreases with an abrupt fall at 0.025 M NaF. This fall is correlated to an increase of the absorbance band at 340 nm and confirms the formation of PaF_4 (s).

3.2 Studies on the Hydrolysis Reaction

Small portions of concentrated NaOH solution were added stepwise to a solution of 1.4 x 10^{-4} M Pa(IV) in 1 M $HClO_4$ until pH 3.6. After each step the solution was characterised by spectroscopy. The absorption band of Pa(IV) shows a red shift from 280 nm at 1 M H^+

to 284 nm at pH 1.8. At higher pH it turns to a slight blue shift with a maximum at 281 nm at pH 3.6. This turn to shorter wavelengths is in accordance with a blue shift of the Pa(IV) fluorescence band at pH values higher than 1.6. A huge blue shift of 47 nm from 469 to 422 nm is observed at pH 3.6. The maximum of the fluorescence band remains constant at 469 nm at pH < 1.6. The absorbance declines steadily with increasing pH values, whereas the fluorescence increased until pH 0.38 and then dropped down at higher pH values. Only very low amounts of protactinium (< $1x10^{-7}$ M) were measured in solution by LSC in the last sample at pH 3.6. That means that almost all of protactinium is sorbed onto the quartz wall. An additional uncertainty arises about the amount of Pa(IV) that is oxidised to Pa(V). Also Pa(V) shows tremendous sorption behaviour at higher pH values.

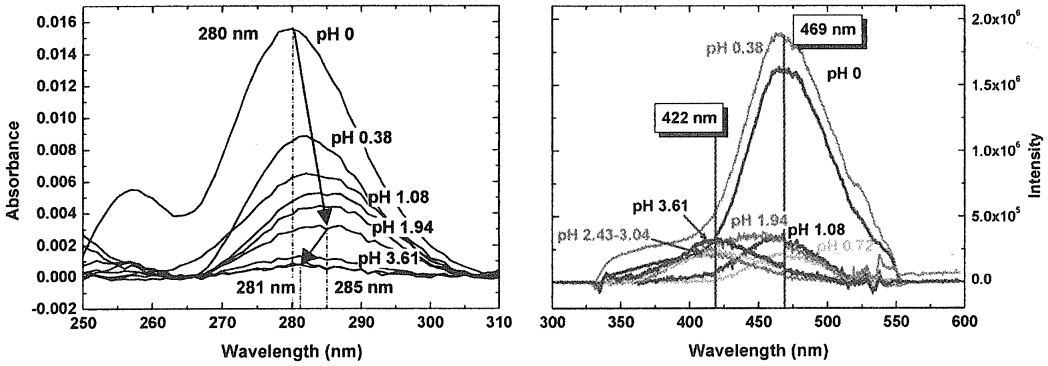

Figure 2 *Absorption (left) and fluorescence (right) spectra of Pa(IV) at various pH values in $HClO_4$ medium*

4 CONCLUSIONS

Fluorescence spectroscopy is a versatile tool for speciation of Pa(IV) in aqueous solution. The shifts of the fluorescence bands of Pa(IV) species among each other depends strongly on the ligand system. Speciation requires sufficiently large band shifts such that the bands of various species can be differentiated. For the fluoride system these shifts are very small contrary to UV absorption spectroscopy. Therefore, the latter is better applicable for fluoride complexation studies. For the hydrolysis reaction the shifts of the fluorescence bands are large for the complexes with OH^-, that is in contrast to the UV bands. Hence, fluorescence spectroscopy is the choice for hydrolysis studies. The most striking advantage of fluorescence spectroscopy is its high sensitivity, that allows the measurement of trace concentrations of Pa(IV) (< $1x10^{-7}$ M) in solution, as it was shown for the Pa(IV) hydrolysis species.

References

1 C.M. Marquardt, P.J. Panak, C. Apostolidis, A. Morgenstern, C. Walther, R. Klenze and Th. Fanghänel, *Radiochim. Acta,* 2004, **92**, 445.

2 S.H. Eberle, 'Chemie des Protactiniums in wässriger Lösung' in *Gmelin Handbuch der anorganischen Chemie. 8, System-Nr 51, Erg. Bd 2*, 1977, Chapter 13, p. 139.

3. I. Grenthe, J. Fuger, R.J.M. Konings, R.J. Lemire, A.B. Muller, C. Nguyen-Trung and H. Wanner, *Chemical Thermodynamics of Uranium,* Nuclear Agency Organisation for Economic Co-operation and Development (OECD), NEA Data Bank, 2004, p. 173.

6 Conclusions

The investigations on aquo species forming in solutions of tetravalent metal ions which are compiled in the present work are subdevided into three categories. Experiments performed on Pu(IV), those performed on the homologes Zr(IV) and Th(IV), and first results on the hydrolysis of Pa(IV). There are numerous parallels of polymer and colloid chemistry of Pu(IV), Zr(IV), and Th(IV), but it is as clear, that there exist pronounced differences.
The solubility experiments reported on Th(IV) in Sects. 3.2, 3.3, on Zr(IV) in Sec. 3.5, and on Pu(IV) in Sects. 2.2, 2.3, illustrate how experience which is gained from experiments on homologes facilitates the interpretation of Pu(IV) data. The investigations on Th(IV) showed unambiguously that colloids are formed in two different domains of pH and Th(IV) concentration and that these colloids differ in structure. In the more acidic range, colloid formation is strongly enhanced by addition of seeds, be it Th colloids or impurtities (dust) of any kind. Electron diffraction revealed clearly the crystalline nature of these colloids whereas at higher pH, amorphous colloids form spontaneously from the oversaturated solution. Early attempts to explain the existence of these two domains were based on the hydrolytic behavior of thorium. In the crystalline-colloid domain (low pH), Th does not yet hydrolyse, *i.e.* Th_4^+ is the dominating species. In the less acidic domain, the monohydroxo complex $ThOH^{3+}$ forms and, as further evidenced from the slope analysis of the solubility plot, $ThOH^{3+}$ is consumed during the formation of amorphous $Th(OH)_4$ precipitate or colloids. A plausible explanation for the formation of amorphous hydroxo colloids in the second domain seemed to be the presence of already hydrolyzed ionic Th(IV) species. However, analogous investigations on Zr(IV) revealed (Sec. 3.5) a very similar behavior, *i.e* two domains of colloid formation exist also for Zr(IV) colloids but, in sharp contrast to Th, hydrolysis of the $Zr(IV)_{aq}$ ions starts at much higher acidity and hence, even in the domain of microcrystalline colloids, hydrolyzed ions dominate the species distribution. For dilute samples, this is Zr^{4+}, for higher concentration, the tetramer $Zr_4(OH)_8^{8+}$. It became clear at this point that microcrystalline colloids can form whether the metal ions are hydrolyzed or not. Among others, this observation lead to the conclusion that an alternative explanation should be favored, the particle size effect. It is now proposed [Rand07] that in case of the Th colloids, small primary particles of ThO_2 structure exist, which can associate and form larger aggregates. The solubility of the different colloids is a function of the primary particle size [Rand07]. This is further corroborated by the TEM investigations in Sec. 3.2 which reveal that the amorphous $Th(OH)_{4(am)}$ particles are composed of small subunits. *Vice versa*, the solibility of Th solids of different homogeneity is backtracked to the inclusion of smaller or bigger particulate inclusions.
For the case of Pu(IV) colloids, this is a very valuable information. Due to the low solubility of Pu(IV), the domain of oxidic particle formation shifts to high acidities and low Pu(IV) concentrations [Kim84a], too low to perform a comprehensive solubility study com-

parable to the work on Th. However, it is well known that nm-sized colloids of either PuO_2 fluorite structure or amorphous '$Pu(OH)_{4(am)}$' composition form in sol gel processes ($[Pu(IV)]_{tot} > 10\,mM$)[Lloy78]. Freshly formed amorphous particles can be redissolved by acidification but eventually transform to 'insoluble' PuO_2 particles upon aging. Our recent XAFS data (Sec. 2.6) show that the PuO_2 fcc structure evolves from a rigid Pu-O-Pu backbone of polymeric Pu(IV) species. A model is proposed how these polymers form by stacking of cubic $Pu(OH)_2^{2+} \cdot 6H_2O$ units which in turn link the polymeric growth to the consumption of twofold charged solution species required by the slope of the solubility curve.
These small crystalline particles are still detectable in 'amorphous precipitates' formed upon addition of base [Lloy78] but their role in the solubility of precipitates is not as clear as in the case of thorium, since it might be hidden by the dominating effect of formation of PuO_{2+x} causing the solid to be in equilibrium with the much more soluble pentavalent Pu. The correlation between colloid dissolution and formation of plutonyl ions in oversaturated Pu(IV) (Sects. 2.3, 2.4) prove that also freshly formed colloids are in equilibrium with Pu(V) – and via the Pu(V)/Pu(VI) couple with Pu(VI) – a concept suggested already for explaining solubility data at near neutral pH [Rai81]. Plutonium redox reactions in highly acidic colloidal suspensions were shown to be well described by a two step model of simultaneous equilibration of the redox couples Pu(III)/Pu(IV) and Pu(V)/Pu(VI). This approach is strengthened by the excellent consistency of redox potentials obtained by direct measurement and calculated from the oxidation state distributions, in particular from the redox couple $Pu(V)/Pu(IV)_{coll}$ (Sec. 2.5). Going one step further, plutonium redox chemistry can be reformulated by including polymeric plutonium as a link between trivalent and tetravalent Pu on the one hand, and the plutonyl ions PuO_2^+ and PuO_2^{2+} on the other [Neck07].
Though the dominant Pu(IV) solution species in highly acidic media are monomers, polynuclear complexes might be present over a wide range of concentrations and acidities. The existence of a {Pu(III)-Pu(VI)-Pu(III)} trimer was recently proposed [Hasc07] and many more species might exist, like in the case of Zr(IV) and Th(IV) solutions where these polynuclear hydroxide complexes were detected directly by ESI-TOF (Sec. 3.6). However, in contrast to the continuous transition from monomers via growing polynuclear complexes to a well defined onset of colloid formation for Zr(IV) (Sec. 3.5, 3.6) and Th(IV) (Sec. 3.7), Pu(IV) once more seems to behave differently. In undersaturated solutions, well below the critical pH for spontaneous colloid formation, light scattering and observation of a very small number of breakdown events close to the detection limit of LIBD ($\approx 10^4$ particles/ml) (Sec. 2.2 and 2.6) suggests the presence of colloids sized some tenths of a micron at extremely low number. It might be that the equilibrium and hence coexistence of colloids and solution species which was proven for Th(IV) (Sec. 3.3) spans a much wider range in the case of Pu(IV) solutions and that monomeric ions coexist with colloids [Thiy90] and polymers of considerable size up the billions of amu [Ocke56]. This coexistence would underline the extraordinary role of colloids and polymers in the Pu(IV) chemistry.
Only by direct measurements it will be possible to quantify the abundance of polymeric

species and if – as expected and demonstrated for Th(IV) down to [Th(IV)]=6×10^{-6} M (Sec. 3.7) – the stability field of polymers will narrow more and more with decreasing Pu(IV) concentration. Moreover, it will be interesting to learn if prominent, geometrically stabilized, polymers of plutonium exist, like the trimer predicted in [Hasc07] and which would parallel the Zr(IV) tetramer $Zr_8(OH)_8^{8+}$ in highly acidic media, or if a wide variety of different sizes forms as described in Sec. 3.6 for Zr(IV) solutions of increasing pH. However, the ESI-TOF measurements for Zr(IV) and Th(IV) supply direct evidence that the hydrolysis of solution species be it monomer or polymer is a continuous process which leads to charge compensation with decreasing acidity, a concept which most likely will also be valid for plutonium polymers and which already was implicit part of the polymerization model developed in Sec. 2.6.

Besides the further routine use of LIBD (Ch. 4) and the application of the new technique ESI-TOF, TRLFS will most likely help in future investigations on hydrolysis and polymerization of tetravalent actinides. The nice spectroscopic properties of protactinium (Sec. 5.3) will be used for further investigation of its hydrolytic behavior. Pa(IV) might even be incorporated as a sensor ion in solids or solutions of different tetravalent actinides maybe even up to the point of investigating hydrated crystals including tetravalent ions similar to the study performed on Cm^{3+} (Sec. 5.2).
The bottomline of the present studies, however, is that investigations on homologes are extraordinary helpful for the development of methods, for first estimates on chemical behavior, and for basic insights in polymer and colloid chemistry, but never can fully substitute experiments on plutonium.

Formation constants and chemical properties for polynuclear An(IV) complexes and colloids are needed in order to develop realistic and reliable models for the prediction of potential radionuclide release from nuclear repositories in case of accidents. The first direct observation of the continuous hydrolysis of polynuclear metal hydroxide complexes (Zr(IV) and Th(IV)) opens up a novel approach of determining formation constants by means of ESI-TOF. Furthermore, the present work contributes precise data on the solubility of Pu(IV), formation constants of mononuclear Pu(IV) hydrolysis complexes, and new insights in the formation processes of Pu(IV) colloids and the structure of Th(IV) colloids. *Inter alia*, these results helped to refine the understanding of equilibrium chemistry and solubility of Th(IV) and Pu(IV). In the case of Th(IV), the new insights were already included in the NEA database, and hence might contribute to the continuous improvement of radionuclide transport modelling.

Appendix

A Proportional Equations Describing Pu Disproportionation

Silver published several papers on how to describe the disproportionation reactions by a system of balanced equations which are easily solved numerically [Silv99, Silv02b]

$$2Pu^{4+} + 2H_2O \leftrightharpoons Pu^{3+} + PuO_2^+ + 4H^+. \quad (P) \tag{A.1}$$

$$Pu^{4+} + PuO_2^+ \leftrightharpoons Pu^{3+} + PuO_2^{2+} \quad (Q) \tag{A.2}$$

$$K_1 = \frac{[Pu^{3+}][PuO_2^+][H^+]^4}{[Pu^{4+}]^2} = 6.97 \times 10^{-4} \tag{A.3}$$

$$K_2 = \frac{[Pu^{3+}][PuO_2^{2+}]}{[Pu^{4+}][PuO_2^+]} = 13.2 \tag{A.4}$$

The consumption and production of each oxidation state in reactions (A.1) and (A.2) is expressed in terms of P,Q, and the total concentration T: For instance, Eqs. (A.1) and (A.2) both produce one ion (or one part Pu^{3+}), so the amount of Pu^{3+} that appears after the sequence of both reactions is $P + Q$. PuO_2^+ is produced by (A.1) and consumed by (A.2) so both reactions lead to a production of $P - Q$ ions of PuO_2^+

$$K_1 = \frac{[P+Q][P-Q][H^+]^4}{[T-2P-Q]^2} \tag{A.5}$$

$$K_2 = \frac{[P+Q][Q]}{[T-2P-Q][P-Q]} \tag{A.6}$$

Since only Pu^{4+} and not $Pu(OH)^{3+}$ takes part in reactions (A.1) and (A.2), the amount of Pu(IV) must be corrected for hydrolysis (Eq. 2.3):

$$Pu^{4+} + OH^- \leftrightharpoons PuOH^{3+} \quad (R) \tag{A.7}$$

$$K'_{11} = \frac{R[H^+]}{T - 2P - Q - R} \tag{A.8}$$

The change in total acidity by the H^+ consumption or production by reactions (A.1) and (A.7) can be neglected for $[Pu]_{tot} \ll [H^+]$. Silver assumed $K'_{11} = 0.03$, [Yun07] suggested a higher value of $K'_{11} = 0.086$ in 0.5M NaCl/HCl.

Bibliography

[Aber93] M. Aberg and J. Glaser, ^{17}O and ^{1}H NMR study of the tetranuclear hydroxo zirconium complex in aqueous solution. *Inorg. Chim. Acta* **206** 53–61 (1993)

[Agne95] G.R. Agnes and G. Horlick, Effect of operating parameters on analyte signals in elemental electrospray mass-spectrometry. *Appl. Spectr.* **49** 324–334 (1995)

[Albr93] D. Albright, F. Berkhout and W. Walker, *World inventory of plutonium and highly enriched uranium*. Oxford University Press, Oxford (1993)

[Alle96] P.G. Allen, D.K. Veirs, S.D. Conradson, C.A. Smith and S.F. Marsh, Characterization of aqueous plutonium(IV) nitrate complexes by extended X-ray absorption fine structure spectroscopy. *Inorg. Chem.* **35** 2841–2845 (1996)

[Alte06] U. Alter, C. Götz, W. Mester, W. Koch and S. Mohr, Management of Radioactive Waste and Spent Fuel, Balance of Reprocessing, in *Joint Convention on the Safety of Spent Fuel Management and on the Safety of Radioactive Waste Management. Second Review Meeting*, Wien (2006). Internationalen Atomenergie Organisation (IAEO):

[Amar06] E. Amaral, K. Brockmann and H.G. Forsström, International perspectives on spent fuel management, in *Management of Spent Fuel from Nuclear Power Reactorsr*, pages 17–30, Vienna (2006). IAEA

[Amba05] C. Ambard, A. Delorme, N. Baglan, J. Aupiais, F. Pointurier and C. Madic, Interfacing capillary electrophoresis with inductively coupled mass spectrometry for redox speciation of plutonium. *Radiochim. Acta* **93** 665–673 (2005)

[Anku98] A.L. Ankudinov, B. Ravel, J.J. Rehr and S.D. Conradson, Real-space multiple-scattering calculation and interpretation of x-ray-absorption near-edge structure. *Phys. Rev. B* **58** 7565–7576 (1998)

[Arti98] R. Artinger, B. Kienzler, W. Schüßler and J.I. Kim, Effects of humic substances on the ^{241}Am migration in a sandy aquifer: column experiments with Gorleben groundwater/sediment systems. *J. Cont. Hydr.* **35** 261–275 (1998)

[Arti00] R. Artinger, C.M. Marquardt, J.I. Kim, A. Seibert, N. Trautmann and J.V. Kratz, Humic colloid-borne Np migration: influence of the oxidation state. *Radiochim Acta* **88** 609–612 (2000)

[Arti02] R. Artinger, T. Rabung, J. Kim, S. Sachs, K. Schmeide, K. Heise, G. Bernhard and H. Nitsche, Humic colloid-borne migration of uranium in sand colums. *J. Cont. Hydr.* **58** 1–12 (2002)

[Arty59] P. Artyukhin, V. Medvedovskii and A. Gelman, Disproportionation of Pu(IV) and Pu(V) in nitric acid solution. *Russ. J. Inorg. Chem.* **4** 596–599 (1959)

[Atte98] O. Atteia, D. Perret, T. Adatte, R. Kozel and P. Rossi, Characterization of natural colloids from a river and spring in a karstic basin. *Environm. Geol.* **34** 257–269 (1998)

[Avog84] A. Avogadro and G. de Marsily, The role of colloids in nuclear waste disposal, in *Scientific basis for nuclear waste management VII*, Vol. 26, pages 495–505. North Holland, New York (1984)

[Barr84] E. Barringer, B. Novich and T. Ring, Determination of colloid stability using photon correlation spectroscopy. *J Coll. Interf. Sci* **100** 584–586 (1984)

[Baum00] T. Baumann, N. Huber, S. Müller and R. Niessner, Qauntification of the colloidal transport through laboratory and field experiments. *Vom Wasser* **95** 151–166 (2000)

[Beit80] J.V. Beitz, D.L. Bowers, M.M. Doxtader, V.A. Maroni and D.T. Reed, Oxidation state specific detection of transuranic ions in solution. *Nucl. Tech.* **51** 169–177 (1980)

[Beit88] J.V. Beitz, D.L. Bowers, M.M. Doxtader, V.A. Maroni and D.T. Reed, Detection and speciation of trans-uranium elements in synthetic groundwater via pulsed-laser excitation. *Radiochim. Acta* **44** 87–93 (1988)

[Beit91] J.V. Beitz, Laser induced fluorescence studies of Cm^{3+} complexes in solution. *Radiochim. Acta* **52/53** 35 (1991)

[Beit94] J. Beitz, f-state luminescence of trivalent lanthanide and actinide ions in solution. *J. Alloys Comp.* **207/208** 41–50 (1994)

[Bell68] J.T. Bell and R.E. Biggers, Absorption spectrum of the uranyl ion in perchlorate media III. Resolution of the ultraviolet band structure; some conclusions concerning the excited state of UO_2^{2+}. *J. Mol. Spectr.* **25** 312–329 (1968)

[Bell73a] J.T. Bell, C.F. Coleman, D.A. Costanzo and R.E. Biggers, Plutonium polymerization. III. Nitrate precipitation of plutonium (IV) polymer. *J. Inorg. Nucl. Chem.* **35** 629–632 (1973)

[Bell73b] J.T. Bell, D.A. Costanzo and R.E. Biggers, Plutonium polymerization. II. Kinetics of the plutonium polymerization. *J. Inorg. Nucl. Chem.* **35** 623–8 (1973)

[Berg99] L. Bergmann and C. Schaefer, *Optics*, Vol. 3. Walter de Gruyter, Berlin, 9 edition (1999)

[Bern01] G. Bernhard, G. Geipel, T. Reich, V. Brendler, S. Amayri and H. Nitsche, Uranyl(VI) carbonate complex formation: Validation of the $Ca_2UO_2(CO_3)_3$(aq.) species. *Radiochim. Acta* **89** 511–518 (2001)

[Bert87] F. Bertin, J. Bouix, S. Hannane and J. Paris, Etude de l'hydrolyse de l'oxychlorure de zirconium en solution aqueuse par spectrométrie Raman. *C. R. Acad. Sci., Ser. II: Mec., Phys., Chim., Sci. Terre Univers,* **304** 405–410 (1987)

[Bili66] H. Bilinski, M. Branica and L. Sillen, Precipitation and hydrolysis of metallic ions II Studies on zirconium hydroxide in dilute solutions and in 1M $NaClO_4$. *Acta Chem. Scand.* **20** 853–861 (1966)

[Bite03a] C. Bitea, R. Müller, V. Neck, C. Walther and J.I. Kim, Study of the generation and stability of thorium(IV) colloids by LIBD combined with ultrafiltration. *Coll. Surf. A* **217** 63–70 (2003)

[Bite03b] C. Bitea, C. Walther, J.I. Kim, H. Geckeis, T. Rabung, F.J. Scherbaum and D. Cacuci, Time resolved observation of ZrO_2-colloid agglomeration. *Coll. Surf. A* **215** 55–66 (2003)

[Blai92] J. Blaise and J.F. Wyart, *Energy levels and atomic spectra of actinides*, Vol. 20 of *International tables of selected constants*. Universite P. et M. Curie, Paris, France (1992)

[Blum58] W.B. Blumenthal, *The chemical behavior of zirconium*. D. van Nostrand Company, Princeton (1958)

[Born99] M. Born and E. Wolf, *Principles of Optics*. Cambridge University Press, Cambridge, 7 edition (1999)

[Boub01] M. Bouby, T.N. Manh, H. Geckeis, F.J. Scherbaum and J.I. Kim, Characterization of aquatic colloids by a combination of LIBD and ICP-MS following the size fractionation. *Radiochim. Acta* **90** 727–732 (2001)

[Boub04] M. Bouby, H. Geckeis, T.N. Manh, J.I. Yun, K. Dardenne, T. Schäfer, C. Walther and J.I. Kim, Laser-induced breakdown detection combined with asymmetrical flow field-flow fractionation: application to iron oxy/hydroxide colloid characterization. *J. Chromat. A* **1040** 97–104 (2004)

[Bowm92] C.D. Bowman, E.D. Arthur, P.W. Lisowski, G.P. Lawrence, R.J. Jensen, J.L. Anderson, B. Blind, M. Capiello, J.W. Davidson, T.R. England, L.N. Engel, R.C. Haight, H.G. Hughes, J.R. Ireland, R.A. Krakowski, R.J. LaBauve, B.C. Letellier, R.T. Perry, G.J. Russel, K.P. Staudhammer, G. Versamis and W.B. Wilson, Nuclear energy generation and waste transmutation using an accelerator-driven intense thermal neutron source. *Nucl. Instr. Meth. A* **320** 336–367 (1992)

[Brab99] A. Brablec, D. Trunec and F. Stastny, Deconvolution of spectral line profiles: solution of the inversion problem. *J. Phys. D* **32** 1870–1875 (1999)

[Brow87] P.L. Brown and H. Wanner, *Predicted formation constants using the unified theory of metal ion complexation*. OECD Nuclear Energy Agency, Paris (1987)

[Brow05] P.L. Brown, E. Curti, B. Grambow, C. Ekberg, F.J. Mompean, J. Perrone and M. Illemassene, *Chemical Thermodynamics of Zirconium*, Vol. 8 of *Chemical Thermodynamics*. Elsevier, North-Holland, Amsterdam (2005)

[Brun96] R.T. Brundage, R.L. Powell, J.V. Beitz and G.K. Liu, Measurement of homogeneous line widths and ground-state splittings of trivalent curium in fluoride glasses. *J. Lumin.* **69** 121–129 (1996)

[Buff92] J. Buffle, D. Perret and M. Newman, *Environmental particles*, Vol. 1 of *IUPAC series on Environmental Analytical and Environmental Chemistry*. Lewis Publishers, Chelsea, MI (1992)

[Buff95a] J. Buffle and G. Leppard, Characterization of aquatic colloids 2. Key role of physical structures on analytical results. *Environ. Sci. Technol.* **29** 2176–2184 (1995)

[Buff95b] J. Buffle and G.G. Leppard, Characterization of aquatic colloids and macromolecules. 1. Structure and behavior of colloidal matter. *Env. Sci. Technol.* **29** 2169–2175 (1995)

[Bund00] T. Bundschuh, R. Knopp, R. Müller, J.I. Kim, V. Neck and T. Fanghänel, Application of LIBD to the determination of the solubility product of thorium(IV)-colloids. *Radiochim. Acta* **88** 625–629 (2000)

[Bund01a] T. Bundschuh, W. Hauser, J.I. Kim, R. Knopp and F.J. Scherbaum, Determination of colloid size by two-dimensional optical detection of laser induced plasma. *Coll. Surf. A* **180** 285–293 (2001)

[Bund01b] T. Bundschuh, R. Knopp and J.I. Kim, Laser-induced breakdown detection (LIBD) of aquatic colloids with different laser systems. *Coll. Surf. A* **177** 47–55 (2001)

[Bund01c] T. Bundschuh, R. Knopp, R. Winzenbacher, J.I. Kim and R. Koster, Quantification of aquatic nano particles after different steps of Bodensee water purification with laser-induced breakdown detection (LIBD). *Acta Hydrochi. Hydrobiol.* **29** 7–15 (2001)

[Bund04] T. Bundschuh, T. Wagner, M. Weber and R. Koster, Method of laser-induced breakdown detection and application examples. *Chem. Eng. Tech.* **27** 377–382 (2004)

[Bund05] T. Bundschuh, T. Wagner, I. Eberhagen, B. Hambsch and R. Koster, Detection of biocolloids in aquatic media by nano-particle analyzer. *Spectr. Int. J.* **19** 69–78 (2005)

[Bürg05] S. Bürger, *Spurenanalyse von Uran und Plutonium sowie Speziationsuntersuchungen an Plutonium mit massenspektrometrischen und kapillarelektrophoretischen Methoden*, Phd, JoGu Mainz (2005)

[Capd92] H. Capdevila, P. Vitorge and E. Giffaut, Stability of pentavalent plutonium - Spectrophotometric study of PuO_2^+ and Pu^{4+} disproportionation in perchloric media. *Radiochim. Acta* **58** 45–52 (1992)

[Capd95] H. Capdevila and P. Vitorge, Redox potentials of PuO_2^{2+}/PuO_2^+ and Pu^{4+}/Pu^{3+} at different ionic strengths and temperatures - entropy and heat-capacity. *Radiochim. Acta* **68** 51–62 (1995)

[Capd98] H. Capdevila and P. Vitorge, Solubility product of $Pu(OH)_4$(am). *Radiochim. Acta* **82** 11–16 (1998)

[Carn75a] W.T. Carnall, Absorption and luminescence spectra, in Edt.: G. Koch, *Gmelin: Handbuch der Anorganischen Chemie*, Vol. Transurane, pages 35–80. Springer, Berlin (1975)

[Carn75b] W.T. Carnall and K. Rajnak, Electronic energy level and intensity correlations in the spectra of the trivalent actinide aquo ions. II. Cm^{3+}. *J. Chem. Phys.* **63** 3510–3514 (1975)

[Cerv75] M. Cervenan and N. Isenor, Multiphoton Ionization yield Curves for Gaussian Laser Beams. *Optics. Comm.* **13** 175–178 (1975)

[Chia04] L.A. Chiavacci, C.V. Santilli, S.H. Pulcinelli, C. Bourgaux and V. Briois, Role of the surface state and structural feature in the thermoreversible sol-gel transition of a zirconyl aqueous precursor modified by sulfuric acid. *Chem. Mater.* **16** 3995–4004 (2004)

[Cho05a] H.R. Cho, C.M. Marquardt, V. Neck, A. Seibert, C. Walther, J.I. Yun and T. Fanghänel, Redox behavior of plutonium(IV) in acidic solutions, in Edt.: I. May, R. Alvarez and N. Bryan, *Recent Advances in Actinide Science*, Vol. 305, pages 602–604, Manchester (2005). RCS Publishing, Cambridge, UK

[Cho05b] H.R. Cho, C. Walther, J. Rothe, V. Neck, M.A. Denecke, K. Dardenne and T. Fanghänel, Combined LIBD and EXAFS investigation of the formation and structure of Zr(IV) colloids. *Anal. Bioanal. Chem.* **383** 28–40 (2005)

[Chop83] G.R. Choppin, Solution chemistry of the actinides. *Radiochim. Acta* **32** 43 (1983)

[Chop97] G. Choppin, A. Bond and P. Hromadka, Redox speciation of plutonium. *J. Radioanal. Nucl. Chem.* **219** 203–210 (1997)

[Chop99] G.R. Choppin and A. Morgenstern, Distribution and movement of environmental plutonium, in Edt.: A. Kudo, *Plutonium in the environment*, pages 91–105, Osaka, Japan (1999). Elsevier, Amsterdam

[Chop03] G.R. Choppin, Actinide speciation in the environment. *Radiochim. Acta* **91** 645–49 (2003)

[Clar02a] F. Claret, A. Bauer, T. Schäfer, L. Griffault and B. Lanson, Experimental investigation of the interaction of clays with high-pH solutions: A case study from the Callovo-Oxfordian formation, Meuse-Haute Marne underground laboratory (France). *Clays Clay Min.* **50** 633–646 (2002)

[Clar02b] S.B. Clark and C. Delegard, Plutonium in concentrated solutions, in Edt.: D.C. Hoffman, *Advances in plutonium chemistry, 1967-2000.* American Nuclear Society, La Grange park, Illinois (2002)

[Clar06] D.L. Clark, S.S. Hecker, G.D. Jarvinen and M.P. Neu, Chapter 7: Plutonium, in Edt.: L. Morss, N. Edelstein, J. Fuger and J. Katz, *The chemistry of actinide and transactinide elements*, Vol. 2, pages 813–1203. Springer, 3 edition (2006)

[Clea56] A. Clearfield and P.A. Vaughan, The crystal structure of zirconyl chloride octahydrate and zirconyl bromide octahydrate. *Acta Crystallogr.* **9** 555–558 (1956)

[Clev68] J.M. Cleveland, Sulfamate complexes of plutonium(IV). *Inorg. Chem.* **7** 874–878 (1968)

[Clev79] J.M. Cleveland, *The chemistry of plutonium.* American Nuclear Society, La Grange Park, Illinois, 2. edition (1979)

[Cole97] R.B. Cole, *Electrospry ionization mass spectrometry.* John Wiley and Sons, New York (1997)

[Conn49a] R.E. Connick, Mechanism of the disproportionation of plutonium(V). *J. Am. Chem. Soc.* **71** 1528–1533 (1949)

[Conn49b] R.E. Connick and W.H. McVey, The aqueous chemistry of zirconium. *J. Am. Chem. Soc.* **71** 3182–3191 (1949)

[Conn49c] R.E. Connick and W.H. McVey, The peroxy complexes of plutonium(IV). *J. Am. Chem. Soc.* **71** 1534–1542 (1949)

[Conn51] R.E. Connick and W.H. Reas, The hydrolysis and polymerization of zirconium in perchloric acid solution. *J. Am. Chem. Soc.* **73** 1171–1176 (1951)

[Conn53] R.E. Connick and W.H. McVey, Disproportionation equilibria and rates in perchloric and hydrochloric acid solutions of plutonium: Influence of α-particles. *J. Am. Chem. Soc.* **75** 474–479 (1953)

[Conr03] S.D. Conradson, B.D. Begg, D.L. Clark, C. Den Auwer, F.J. Espinosa-Faller, P.L. Gordon, N.. Hess, R. Hess, D.W. Keogh, L.A. Morales, M.P. Neu, W. Runde, C.D. Tait, D.K. Veirs and P.M. Villella, Speciation and unusual reactivity in PuO_{2+x}. *Inorg. Chem.* **42** 3715–3717 (2003)

[Conr04] S.D. Conradson, K.D. Abney, B.D. Begg, E.D. Brady, D.L. Clark, C. den Auwer, M. Ding, P.K. Dorhout, F.J. Espinosa-Faller, P.L. Gordon, R.G. Haire, N.J. Hess, R.F. Hess, D.W. Keogh, G.H. Lander, A.J. Lupinetti, L.A. Morales, M.P. Neu, P.D. Palmer, P. Paviet-Hartmann, S.D. Reilly, W.H. Runde, C.D. Tait, D.K. Veirs and F. Wastin, Higher order speciation effects on plutonium L-3 X-ray absorption near edge spectra. *Inorg. Chem.* **43** 116–131 (2004)

[Conr05] S.D. Conradson, B.D. Begg, D.L. Clark, C. den Auwer, M. Ding, P.K. Dorhout, F.J. Espinosa-Faller, P.L. Gordon, R.G. Haire, N.J. Hess, R.F. Hess, D.W. Keogh, G.H. Lander, D. Manara, L.A. Morales, M.P. Neu, P. Paviet-Hartmann, J. Rebizant, V.V. Rondinella, W. Runde, C.D. Tait, D.K. Veirs, P.M. Villella and F. Wastin, Charge distribution and local structure and speciation in the $UO2 + x$ and $PuO2 + x$ binary oxides for $x <= 0.25$. *J. Solid State Chem.* **178** 521–535 (2005)

[Cont97] C. Contado, G. Blo, F. Fagioli, F. Dondi and R. Beckett, Characterization of river Po particles by sedimentation field-flow fractionation coupled to GFAAS and ICP-MS. *Coll. Surf. A* **120** 47–59 (1997)

[Cost73] D.A. Costanzo, R.E. Biggers and J.T. Bell, Plutonium polymerization. I. A spectrophotometric study of the polymerization of plutonium(IV). *J. Inorg. Nucl. Chem.* **35** 609–622 (1973)

[Curt02] E. Curti and C. Degueldre, Solubility and hydrolysis of Zr oxides: a review and supplemental data. *Radiochim. Acta* **90** 801–804 (2002)

[Degu96] C. Degueldre, H. Pfeiffer, W. Alexander, B. Wernli and R. Bruetsch, Colloid properties in granitic groundwater systems. I: Sampling and characterisation. *Appl. Geochem.* **11** 677–695 (1996)

[Degu97] C. Degueldre, Groundwater colloid properties and their potential influence on radionuclide transport. *Mat. Res. Symp. Proc.* **465** 835–846 (1997)

[Degu00] C. Degueldre, I. Triay, J.I. Kim, P. Vilks, M. Laaksoharju and N. Miekeley, Groundwater colloid properties: a global approach. *Appl. Geochem.* **15** 1043–1051 (2000)

[Degu01] C. Degueldre, A. Bilewicz, W. Hummel and J. L.Loizeau, Sorption behaviour of Am on marl groundwater colloids. *J. Env. Radioact.* **55** 241–253 (2001)

[Delo07] A. Delos, C. Walther, T. Schäfer and S. Büchner, Laser-induced breakdown detection for the quantification of colloid size dispersion effects and colloid mediated radionuclide migration in a synthetic porous media. *submitted* (2007)

[Dick02] E. Dickinson, Food colloids. *Curr. Opin. Coll. Interf. Sci.* **7** 410–412 (2002)

[Ditl78] P. Ditl, R.W. Coughlin and E.H. Jere, Mass transfer kinetics of adsorption on suspended solid particles. *J. Coll. Interf. Sci.* **63** 410–420 (1978)

[Dole68] M. Dole, L.L. Mack, R.L. Hines, R.C. Mobley, L.D. Ferguson and M.A. Alice, Molecular beams of macroions. *J. Chem. Phys* **49** 2240–2249 (1968)

[Douc07] F.J. Douchet, J.R. Lead and P.H. Santschi, Colloid-trace element interactions in aquatic systems, in Edt.: J. Lead and K. Wilkinson, *Environmental colloids and particles: Behaviour, separation and characterisation*, Vol. 10 of *IUPAC series on Analytical and Physical Chemistry of Environmental Systems*, pages 95–157. John Wiley & Sons, West Sussex (2007)

[Dupl77] J. Duplessis and R. Guillaumont, Hydrolyse du Neptunium tetravalent. *Radiochem. Radioanal. Lett.* **31** 293 (1977)

[Dzim85] D.J. Dzimitrowicz, P.J. Wiseman and D. Cherns, An electron microscope study of hydrous thorium dioxide $ThO_2 \cdot nH_2O$. *J. Coll. Interf. Sci.* **103** 170–177 (1985)

[Dzom90] D.A. Dzombak and F.M.M. Morel, *Surface complexation modeling- hydrous ferric oxide*. Wiley & Sons, New York (1990)

[Eber77] S.H. Eberle, Chemie des Protactiniums in wässriger Lösung, in Edt.: Becke-Goehring, *Gmelin: Handbuch der anorganischen Chemie*. Springer, Berlin (1977)

[Edel88] N.M. Edelstein, J.C. Krupa, R.C. Naik, K. Rajnak, B. Whittaker and D. Brown, Analysis of the $5f^1 \rightarrow 6d^1$ transitions in $PaCl_6^{2-}$, $PaBr_6^{2-}$ and $Pa^{4+}/ThBr_4$. *Inorg. Chem.* **27** 3186–3189 (1988)

[Edel92] N.M. Edelstein, W.K. Kot and J.C. Krupa, The 5f→6d absorption spectrum of Pa^{4+} / Cs_2ZrCl_6. *J. Chem. Phys.* **96** 1–4 (1992)

[Edel93] N.M. Edelstein and W.K. Kot, Spectroscopic and magnetic studies of tetravalent Pa and trivalent Th compounds. *J. All. Comp.* **193** 82–87 (1993)

[Edel06] N.M. Edelstein, R. Klenze, T. Fanghänel and S. Hubert, Optical properties of Cm(III) in crystals and solutions and their application to Cm(III) speciation. *Coord. Chem. Rev.* **250** 948–973 (2006)

[Efur98] D.W. Efurd, W. Runde, J.C. Banar, D.R. Janecky, J.P. Kaszuba, P.D. Palmer, F.R. Roensch and C.D. Tait, Neptunium and plutonium solubilities in a Yucca Mountain groundwater. *Env. Sci. Tech.* **32** 3893 (1998)

[Ekbe04] C. Ekberg, G. Kallvenius, Y. Albinsson and P.L. Brown, Studies on the hydrolytic behavior of zirconium(IV). *J. Sol. Chem.* **33** 47–79 (2004)

[Enge69] W. Engelhardt, Self-focusing and plasma formation in transparent media. *Appl. Phys. Lett.* **15** 216–217 (1969)

[Evan69] L.R. Evans and C.G. Morgan, Lens aberration effects in optical-frequency breakdown of gases. *Phys. Rev. Lett.* **22** 1099–1102 (1969)

[Evan00] D.F. Evans and H. Wennerström, *The colloidal domain*. VCH, New York (2000)

[Ewin02] R. Ewing and A. Macfarlane, Nuclear waste: Yucca Mountain. *Science* **296** 659–660 (2002)

[Fang02] T. Fanghänel and V. Neck, Aquatic chemistry and solubility phenomena of actinide oxides/hydroxides. *Pure Appl. Chem.* **74** 1895–1907 (2002)

[Fenn02] J.B. Fenn, Review: Electrospray ionization mass spectrometry: How it all began. *J. Biomol. Tech.* **13** 101–118 (2002)

[File93] M. Filella and J. Buffle, Factors controlling the stability of submicron colloids in natural waters. *Coll. Surf. A* **73** 255–273 (1993)

[File97] M. Filella, J. Zhang, M. Newman and J. Buffle, Analytical applications of photon correlation spectroscopy for size distribution measurements of natural colloidal suspensions: capabilities and limitations. *Coll. Surf. A* **120** 27–46 (1997)

[File07] M. Filella, Colloidal properties of submicron particles in natural waters, in Edt.: J. Lead and K. Wilkinson, *Environmental colloids and particles: Behaviour, separation and characterisation*, Vol. 10 of *IUPAC series on Analytical and Physical Chemistry of Environmental Systems*, pages 17–94. John Wiley & Sons, West Sussex (2007)

[Flur02] M. Flury, J.B. Mathison and J.B. Harsh, In situ mobilization of colloids and transport of cesium in Hanford sediments. *Env. Sci. Technol.* **36** 5335–5341 (2002)

[Fouq06] F. Fouquet, Back end of the nuclear fuel cycle: The french choices, in *Management of Spent Fuel from Nuclear Power Reactorsr*, pages 17–30, Vienna (2006). IAEA

[Fran00] L. Francois, M. Mostafavi, J. Belloni, J.F. Delouis, J. Delaire and P. Feneyrou, Optical limitation induced by gold clusters. 1. Size effect. *J. Phys. Chem. B* **104** 6133–6137 (2000)

[Frie77] H.A. Friedmann, L.M. Toth and J.T. Bell, Photochemical reactions of aqueous plutonium species II. *J. Inorg. Nucl. Chem* **39** 123–126 (1977)

[Fuge76] J. Fuger and F.L. Oetting, *The chemistry thermodynamics of actinide elements and compounds part 2: The actinide aqueous ions*. IAEA, Vienna (1976)

[Fuji92] H. Fujimori, T. Matsui, T. Ajiro, K. Yokose, Y.M. Hsueh and S.S. Izumi, Detection of fine particles in liquids by laser breakdown method. *Jpn. J. Appl. Phys. Part 1* **31** 1514–1518 (1992)

[Fuji94] H. Fujimori, T. Matsui, T. Ajiro, K. Yokose and S. Izumi, Apparatus for analysis of particulate material, analytical method for same, apparatus for production of ultrapure water, apparatus for manufacturing of semiconductor, and apparatus for production of pure gas. *US-Patent* **5316983** 1–10 (1994)

[Fuji01] K. Fujiwara, H. Yamana, T. Fujii and H. Moriyama, Solubility product of plutonium hydrous oxide. *J. Nucl. Fuel Cycle Environ.* **7** 17–23 (2001)

[Fuji02] K. Fujiwara, H. Yamana, T. Fujii and H. Moriyama, Solubility product of plutonium hydrous oxide and its ionic strength dependence. *Radiochim. Acta* **90** 857–861 (2002)

[Fult70] R.B. Fulton, The kinetics of the oxidation of plutonium(III) by neptunium(VI). *J. Phys.Chem* **74** 1661–1669 (1970)

[Geck04] H. Geckeis, T. Schäfer, W. Hauser, T. Rabung, T. Missana, C. Degueldre, A. Mori, J. Eikenberg, T. Fierz and W.R. Alexander, Results of the colloid and radionuclide retention experiment (CRR) at the Grimsel Test Site (GTS), Switzerland - impact of reaction kinetics and speciation on radionuclide migration. *Radiochim. Acta* **92** 765–774 (2004)

[Gile04] J. Giles, Nanoparticles in the brain. *Nature* **401** 9 (2004)

[Gren00] I. Grenthe, H. Wanner and E. Östhols, *Guidelines for the extrapolation to zero ionic strength*, Vol. 2 of *Chemical Thermodynamics*. Elsevier, North-Holland, Amsterdam (2000)

[Grub66] J.B. Gruber, W.R. Cochran, J.G. Conway and A.T. Nicol, Optical spectra of tripositive curium in lanthanum trichloride. *J. Chem. Phys.* **45** 1423–1427 (1966)

[Guil66] R. Guillaumont, Contribution a l'etude des especes ioniques de protactinium en solution aqueuse. *Rev. Chim. Miner.* **3** 339–373 (1966)

[Guil03] R. Guillaumont, T. Fanghänel, J. Fuger, I. Grenthe, V. Neck, D.A. Palmer and M.H. Rand, *Update on the chemical thermodynamics of uranium, neptunium, plutonium, americium and technecium*, Chemical Thermodynamics. Elsevier, North-Holland, Amsterdam (2003)

[Guo06] Z. Guo, A. Jones and N. Li, Interpretation of the ultrasonic effect on induction time during $BaSO_4$ homogeneous nucleation by a cluster coagulation model. *J. Coll. Interf. Sci.* **297** 190–198 (2006)

[Görl96] C. Görller-Walrand and K. Binnemans, Rationalization of crystal field parametrization, in Edt.: K. Gschneidner and L. Eyring, *Handbook on the physics and chemistry of rare earths*, Vol. 23. North-Holland, Amsterdam (1996)

[Hagf04] C. Hagfeldt, V. Kessler and I. Persson, Structure of the hydrated, hydrolysed and solvated zirconium(IV) and hafnium(IV) ions in water and aprotic oxygen donor solvents. A crystallographic, EXAFS spectroscopic and large angle X-ray scattering study. *Dalton. Trans.* **14** 2142–2151 (2004)

[Hamm97] D.X. Hammer, E.D. Jansen, M. Frenz, G.D. Noojin, R.J. Thomas, J. Noack, A. Vogel, B.A. Rockwell and A.J. Welch, Shielding properties of laser-induced breakdown in water for pulse durations from 5 ns to 125 fs. *Appl. Optics* **36** 5630–5640 (1997)

[Harv47] B.G. Harvey, H.G. Heal, A.G. Maddock and E.L. Rowley, The chemistry of plutonium. *J. Chem. Soc.* **1** 1010–1018 (1947)

[Hasc00] J.M. Haschke, T.H. Allen and L.A. Morales, Reaction of plutonium dioxide with water: Formation and properties of PuO_{2+x}. *Science* **287** 285–287 (2000)

[Hasc02a] J.M. Haschke and R.G. Haire, Crystalline solids and corrosion chemistry, in Edt.: D.C. Hoffman, *Advances in Plutonium Chemistry, 1967-2000.* American Nuclear Society, La Grange park, Illinois (2002)

[Hasc02b] J.M. Haschke and V.M. Oversby, Plutonium chemistry: a synthesis of experimental data and a quantitative model for plutonium oxide solubility. *J. Nucl. Mat.* **305** 187–201 (2002)

[Hasc04] J.A. Haschke, Author's reply to "Comment on 'plutonium chemistry: a synthesis of experimental data and a quantitative model for plutonium oxide solubility' by J. M. Haschke and V. M. Oversby". *J. Nucl. Mat.* **334** 225–228 (2004)

[Hasc05] J.M. Haschke, Thermodynamics of water sorption on PuO_2: Consequences for oxide storage and solubility. *J. Nucl. Mat.* **344** 8–12 (2005)

[Hasc07] J.M. Haschke, Disproportionation of Pu(IV): A reassessment of kinetic and equilibrium properties. *J. Nucl. Mat.* **362** 60–74 (2007)

[Haus02] W. Hauser, H. Geckeis, J.I. Kim and T. Fierz, A mobile laser-induced breakdown detection system and its application for the in situ-monitoring of colloid migration. *Coll. Surf. A* **203** 37–45 (2002)

[Haus03] W. Hauser, R. Götz, H. Geckeis and B. Kienzler, Insitu colloid detection in granite groundwater along the Äspö hard rock laboratory access tunnel. *Äspö progress report IPR* **03-38** (2003)

[He94] S.L. He, J.E. Oddo and M.B. Tomson, The nucleation kinetics of calcium-sulfate dihydrate in NaCl solutions up to 6-M and 90-degrees-C. *J. Coll. Interf. Sci.* **162** 297 (1994)

[He96] Q.H. He, G.G. Leppard, C.R. Paige and W.J. Snodgrass, Transmission electron microscopy of a phosphate effect on the colloid structure of iron hydroxide. *Water Res.* **30** 1345–1352 (1996)

[Hoff01] J. Hoffmann(Red.), *Radioaktivität und Kernenergie.* Forschungszentrum Karlsruhe, Karlsruhe (2001)

[Holt96] H. Holthoff, S.U. Egelhaaf, M. Borkovec, P. Schurtenberger and H. Sticher, Coagulation rate measurements of colloidal particles by simultaneous static and dynamic light scattering. *Langmuir* **12** 5541–5549 (1996)

[Hone99] B.D. Honeyman, Colloidal culprits in contamination. *Nature* **397** 23–24 (1999)

[Horr79] W.D. Horrocks and D.R. Sudnick, Lanthanide ion probes of structure in biology. Laser-induced luminescence decay constants provide a direct measure of the number of metal-coordinated water molecules. *J. Ant. Chem. Soc.* **101** 334–340 (1979)

[Hu99] M.Z.C. Hu, J.T. Zielke, J.S. Lin and C.H. Byers, Small-angle x-ray scattering studies of early-stage colloid formation by thermohydrolytic polymerization of aqueous zirconyl salt solutions. *J. Mat. Res.* **14** 103–113 (1999)

[Humm02] W. Hummel, U. Berner, E. Curti, F.J. Pearson and T. Thoenen, Nagra/PSI chemical thermodynamic data base 01/01. *Radiochim. Acta* **90** 805–813 (2002)

[Irib76] J.V. Iribarne and B.A. Thomson, On the evaporation of small ions from charged droplets. *J. Chem. Phys.* **64** 2287–2294 (1976)

[Jame94] F. James, *Minuit, function minimization and error analysis*, Vol. 94.1 of *Reference Manual*. CERN Program Library (1994)

[Joha91] G. Johansson, M. Magini and H. Ohtaki, Coordination around thorium(IV) in aqueous perchlorate, chloride and nitrate solutions. *J. Sol. Chem.* **20** 775–792 (1991)

[John78] G.L. Johnson and L.M. Toth, Plutonium(IV) and thorium(IV) hydrous polymer chemistry, Technical Report TM-6365, Oak Ridge National Laboratory (1978)

[Kall87] N. Kallay, E. Barouch and E. Matijevic, Diffusional detachment of colloidal particles from solid/solution interfaces. *Advan. Coll. Interf. Sci.* **27** 1–42 (1987)

[Kall00] N. Kallay and S. Zalac, Charged surfaces and interfacial ions. *J. Coll. Inter. Sci.* **230** 1–11 (2000)

[Kash49] M. Kasha, Reactions between plutonium ions in perchloric acid solution: rate, mechanism, and equilibria, in Edt.: G.T. Seaborg, J.J. Katz and W.M. Manning, *The transuranium elements*, page 295. McGraw-Hill Inc., New York (1949)

[Katz86] J.J. Katz, *Chemistry of the actinide elements*. Chapman and Hall., London (1986)

[Kers99] A.B. Kersting, D.W. Efurd, D.L. Finnegan, D.J. Rokop, D.K. Smith and J.L. Thompson, Migration of plutonium in ground water at the Nevada test site. *Nature* **397** 56–59 (1999)

[Kim84a] J.I. Kim, G. Buckau, F. Baumgärtner, H.C. Moon and D. Lux, Colloid generation and the actinide migration in Gorleben groundwaters, in Edt.: G.L. McVay, *Scientific basis for nuclear waste management*, Vol. 7, pages 31–40. Elsevier, New York (1984)

[Kim84b] J.I. Kim, W. Treiber, C. Lierse and P. Offermann, Solubility and colloid generation of plutonium from leaching of a HLW glass in salt solutions, in Edt.: C.M. Jantzen, J.A. Stone and R.C. Ewing, *Scientific basis for nuclear waste management VIII*, Vol. 44, pages 359–368, Boston, MA (1984). MRS, Pittsburgh

[Kim88] J.I. Kim, Chap. 8, in Edt.: A. Freeman and C. Keller, *Handbook on the physics and chemistry of the actinides*, page 413. Elsevier, Amsterdam (1988)

[Kim89] J.I. Kim and B. Kanellakopulos, Solubility products of plutunium(IV) oxide and hydroxide. *Radiochim. Acta* **48** 145–150 (1989)

[Kim90] J.I. Kim, R. Stumpe and R. Klenze, Laser-induced photoacoustic spectroscopy for the speciation of transuranic elements in natural aquatic systems, in Edt.: K. Yoshihara, *Chemical applications of nuclear probes*, Vol. 157 of *Topics in Current Chemistry*, pages 131–179. Springer, Berlin (1990)

[Kim91] J.I. Kim, H. Wimmer and R. Klenze, A study of curium(III) humate complexation by time resolved laser fluorescence spectroscopy (TRLFS). *Radiochim. Acta* **54** 35–41 (1991)

[Kim92] J.I. Kim, P. Zeh and B. Delakwitz, Chemical interactions of actinide ions with groundwater colloids in Gorleben aquifer system. *Radiochim. Acta* **58** 147–154 (1992)

[Kim94] J.I. Kim, Actinide colloids in natural aquifer systems. *Mat. Res. Soc. Bulletin* **19** 47–53 (1994)

[Kim96] J.I. Kim, R. Klenze and F.J. Scherbaum, Hochempfindiche Quantifizierung von aquatischen Kolloiden mit Hilfe der Laser-induzierten Breakdown-Detektion. *FZK Nachrichten* **28** 321–328 (1996)

[Kim07] J.I. Kim and C. Walther, Laser-induced breakdown detection, in Edt.: J. Lead and K. Wilkinson, *Environmental colloids and particles: Behaviour, separation and characterisation*, Vol. 10 of *IUPAC series on Analytical and Physical Chemistry of Environmental Systems*, pages 555–612. John Wiley & Sons, West Sussex (2007)

[Kimu94] T. Kimura and G.R. Choppin, Luminescence study on determination of the hydration number of Cm(III). *J. Alloys Comp.* **213** 313–317 (1994)

[Kimu96] T. Kimura, G.R. Choppin, Y. Kato and Z. Yoshida, Determination of the hydration number of Cm(III) in various aqueous solutions. *Radiochim. Acta* **72** 61–64 (1996)

[Kiri04] A. Kirishima, T. Kimura, R. Nagaishi and O. Tochiyama, Luminescence properties of tetravalent uranium in aqueous solution. *Radiochim. Acta* **92** 705–710 (2004)

[Kita82] T. Kitamori and T. Sawada, Theoretical analysis of frequency characteristics of photoacoustic signal in liquids. *Jpn. J. Appl. Phys. 2* **21** 285–287 (1982)

[Kita88] T. Kitamori, K. Yokose, K. Suzuki, T. Sawada and Y. Goshi, Laser breakdown acoustic effect of ultrafine particles in liquids and its application to particle counting. *Jpn. J. Appl. Phys.* **27** L983–L985 (1988)

[Kita89a] T. Kitamori, T. Matsui and M. Sakagami, Laser Breakdown Spectrochimical Analysis of Microparticles in Liquids. *Chem. Lett* **89** 2205–2208 (1989)

[Kita89b] T. Kitamori, K. Yokose, M. Sakagami and T. Sawada, Detection and counting of ultrafine particles in ultrapure water using Laser Breakdown Acoustic Method. *Japanese J. Appl. Phys.* **28** 1195–1198 (1989)

[Klei96] T. Klein and R. Niessner, Characterization of heavy metal containing hydrocolloids from seepage water of a municipal waste disposal site with ultrafiltration and flow field-flow fractionation. *Vom Wasser* **87** 373–385 (1996)

[Klen91] R. Klenze, J.I. Kim and H. Wimmer, Speciation of Aquatic Actinide Ions by Pulsed Laser Spectroscopy. *Radiochimica Acta* **52-3** 97–103 (1991)

[Knau90] K.G. Knaus, T.J. Wolery and K.J. Jackson, New approach to measuring pH in brines and other concentrated electroytes. *Cosmochim. Geochim. Acta* **54** 1519–1523 (1990)

[Knol92] R.G. Knollenberg and D.L. Veal, Optical particle monitors, counters, and spectrometers - performance characterization, comparison, and use. *J. IES* **35** 64–81 (1992)

[Knop99] R. Knopp, V. Neck and J.I. Kim, Solubility, hydrolysis and colloid formation of plutonium(IV). *Radiochim. Acta* **86** 101–108 (1999)

[Korz04] P.A. Korzhavyi, L. Vitos, D.A. Andersson and B. Johansson, Oxidation of plutonium dioxide. *Nature Materials* **3** 225–228 (2004)

[Kral97] P.A. Kralchevsky, K.D. Danov and N.D. Denkov, Chemical physics of colloid systems and interfaces, in Edt.: K. Birdi, *Handbook of surface and colloid chemistry*, pages 333–477. CRC Press, New York (1997)

[Krau50] K.A. Kraus and F. Nelson, Hydrolytic behavior of metal Ions. I. The acid constants of uranium(IV) and plutonium(IV). *Journal of American Chemical Society* **72** 3901–3906 (1950)

[Krau56] K.A. Kraus, Hydrolytic behavior of the heavy elements, in *International conference on the peaceful use of atomic energy*, pages 245–257, Geneva, Switzerland (1956)

[Kret98] R. Kretzschmar, H. Holthoff and H. Sticher, Influence of pH and humic acid on coagulation kinetics of kaolinite: A dynamic light scattering study. *J. Coll. Interf. Sci.* **207** 95–103 (1998)

[Kucz03] B. Kuczewski, C.M. Marquardt, A. Seibert, H. Geckeis, J.V. Kratz and N. Trautmann, Separation of plutonium and neptunium species by capillary-electrophoresis inductively-coupled-plasma mass-spectrometry and application to natural groundwater samples. *Anal. Chem.* **75** 6769–6774 (2003)

[Laak01] M. Laaksoharju, Äspö hard rock laboratory, project discription of the Äspö project colloid with the aim to investigate the stability and mobility of colloids. *SKB International Progress Report IPR* **01-08** (2001)

[Lead07] J.R. Lead and K.J. Wilkinson, Environmental colloids and particles: current knowledge and future developments, in Edt.: J. Lead and K. Wilkinson, *Environmental colloids and particles: Behaviour, separation and characterisation*, Vol. 10 of *IUPAC series on Analytical and Physical Chemistry of Environmental Systems*, pages 1–16. John Wiley & Sons, West Sussex (2007)

[Ledi94] A. Ledin, S. Karlsson, A. Düker and B. Allard, Measurements in situ of concentration and size distribution of colloidal matter in deep groundwaters by photon correlation spectroscopy. *Wat. Res.* **28** 1539–1545 (1994)

[Ledi95] A. Ledin, S. Karlsson, A. Dueker and B. Allard, Characterization of the submicrometer phase in surface waters : a review. *Analyst* **120** 603–608 (1995)

[Lemi01] R.J. Lemire, J. Fuger, H. Nitsche, P. Potter, M.H. Rand, J. Rydberg, K. Spahiu, J.C. Sullivan, W.J. Ullman, P. Vitorge and H. Wanner, *Chemical thermodynamics of neptunium and plutonium*, Vol. 4 of *Chemical Thermodynamics*. Elsevier, North-Holland, Amsterdam (2001)

[Leto86] V.S. Letochov, *Laser analytical spectrochemistry*, Optics and Optoelectronics. Adam Hilger, Bristol (1986)

[Lide95] D. Lide, *Handbook of Chemistry and Physics*, aa. CRC, Boston, 75 edition (1995)

[Lin90] M.Y. Lin, H.M. Lindsay, D. Weitz, R.C. Ball, R. Klein and P. Meakin, Universality of fractal aggregates as probed by light scattering, in Edt.: M. Fleischmann, *Fractals in the natural sciences*, pages 71–89. Princeton University Press, Princeton (1990)

[Lind05a] P. Lindqvist-Reis, R. Klenze, G. Schubert and T. Fanghänel, Hydration of Cm^{3+} in aqueous solution from 20 to 200°C. A time-resolved laser fluorescence spectroscopy study. *J. Phys. Chem. B* **109** 3077–3083 (2005)

[Lind05b] P. Lindqvist-Reis, C. Walther, R. Klenze, A. Eichhöfer and T. Fanghänel, Large ground-state and excited-state crystal field splitting of 8-fold-coordinate Cm^{3+} in $[Y(H_2O)_8]Cl_3$·15-crown-5. *J. Chem. Phys.* **110** 5279–5285 (2005)

[Liu93] G.K. Liu, J.V. Beitz and J. Huang, Ground-state splitting of S-state ion Cm^{3+} in $LaCl_3$. *J. Chem. Phys.* **99** 3304–3311 (1993)

[Liu04] C.L. Liu, Z.M. Wang, S.S. Li, Y.E. Yang, B. Li, H. Jiang, L. Jiang, L. Wang and D. Li, Field study of the migration of ^{237}Np, ^{238}Pu and ^{241}Am in a weak loess aquifer. *J. Radioanal. Nucl. Chem.* **260** 193–197 (2004)

[Lloy78] M.H. Lloyd and R.G. Haire, The chemistry of plutonium in sol-gel processes. *Radiochim. Acta* **25** 139–48 (1978)

[Lu95] G.H. Lu, S.M. Bird and R.M. Barnes, Interface for capillary electrophoresis and inductively-coupled plasma-mass spectrometry. *Anal. Chem.* **67** 2949–2956 (1995)

[MacD73] T. MacDermott, The structural chemistry of zirconium compounds. *Coord. Chem. Rev.* **11** 1–20 (1973)

[Madi84] C. Madic, G.M. Begun, D.E. Hobart and R.L. Hahn, Raman spectroscopy of neptunyl and plutonyl ions in aqueous solution: Hydrolysis of Np(IV) and Pu(VI) and disproportionation of Pu(V). *Inorg. Chem.* **23** 1914–1921 (1984)

[Main77] G. Mainfray, Resonance and laser temporal coherence effects in mulitphoton ionisation of atoms, in Edt.: J.H. Eberly and P. Lambropoulos, *Multiphoton Processes*, pages 253–266, Rochester (1977). John Wiley & Sons, New York. buch

[Mare91] Y. Marechal, Infrared spectra of water. I.Effect of temperature and of H/D isotopic dilution. *J. Chem. Phys.* **95** 5565–5573 (1991)

[Marq04] C.M. Marquardt, P.J. Panak, C. Apostolidis, A. Morgenstern, C. Walther, R. Klenze and T. Fanghänel, Fluorescence spectroscopy on protactinium(IV) in aqueous solution. *Radiochim. Acta* **92** 445–447 (2004)

[Marq05] C.M. Marquardt, P.J. Panak, C. Walther, R. Klenze and T. Fanghänel, Fluorescence spectroscopy of protactinium(IV), in Edt.: I. May, R. Alvarez and N. Bryan, *Recent Advances in Actinide Science*, Vol. 305, pages 776–778, Manchester (2005). RCS Publishing, Cambridge, UK

[Mavr94] D. Mavrocordatos, C.P. Lienemann and D. Perret, Energy filtered transmission electron microscopy for the physico-chemical characterization of aquatic submicron colloids. *Mikrochim. Acta* **117** 39–47 (1994)

[McCa93] J. McCarthy and C. Degueldre, Sampling and characterization of colloids in groundwater for studying their role in contaminant transport, in Edt.: J. Buffle and H.P.v. Leeuwen, *Environmental particles*, Vol. 2 of *IUPAC series on Environmental Analystical and Environmental Chemistry*. Lewis Publishers, Chelsea, MI (1993)

[Meti72] H. Metivier and R. Guillaumont, Hydrolyse du Plutonium tetravalent. *Radiochem. Radioanal. Lett* **10** 27–35 (1972)

[Minc03] B.J. Mincher, R.V. Fox, D.C. Cooper and G.S. Groenewold, Neptunium and plutonium sorption to Snake River Plain, Idaho soil. *Radiochim. Acta* **91** 397 (2003)

[Moll99] H. Moll, M.A. Denecke, F. Jalilehvand, M. Sandstrom and I. Grenthe, Structure of the aqua ions and fluoride complexes of uranium(IV) and thorium(IV) in aqueous solution an EXAFS study. *Inorg. Chem.* **38** 1795–1799 (1999)

[Mons03] J.M. Monsallier, R. Artinger, M.A. Denecke, F.J. Scherbaum, G. Buckau and J.I. Kim, Spectroscopic study (TRLFS and EXAFS) of the kinetics of An(III)/Ln(III) humate interaction. *Radiochim. Acta* **91** 567–574 (2003)

[Morg75] C.G. Morgan, Laser-induced breakdown of gases. *Rep. Prog. Phys.* **38** 621–665 (1975)

[Mori03] A. Mori, W.R. Alexander, H. Geckeis, W. Hauser, T. Schafer, J. Eikenberg, T. Fierz, C. Degueldre and T. Missana, The colloid and radionuclide retardation experiment at the Grimsel test site: influence of bentonite colloids on radionuclide migration in a fractured rock. *Coll. Surf. A* **217** 33–47 (2003)

[Mori05] H. Moriyama, T. Sasaki, T. Kobayashi and I. Takagi, Systematics of hydrolysis constants of tetravalent actinide ions. *J. Nucl. Sci. Tech.* **42** 626–635 (2005)

[Moul98] C. Moulin, I. Laszak, V. Moulin and C. Tondre, Time-resolved laser-induced fluorescence as a unique tool for low-level uranium speciation. *Appl. Spec.* **52** 528–535 (1998)

[Muha60] G.M. Muha and P.A. Vaughan, Structure of the complex ion in aqueous solutions of zirconyl and hafnyl oxyhalides. *J. Chem. Phys.* **33** 194–199 (1960)

[Mura02] M.S. Murali and J.N. Mathur, Sorption characteristics of Am(III), Sr(II) and Cs(I) on bentonite and granite. *J. Radioanal. Nucl. Chem.* **254** 129–136 (2002)

[Murd96] K.M. Murdoch, N.M. Edelstein, L.A. Boatner and M.M. Abraham, Excited state absorption and fluorescence line narrowing studies of Cm^{3+} in $LuPO_4$. *J. Chem. Phys.* **105** 2539–2546 (1996)

[Myas06] B.F. Myasoedov, H.W. Kirby and I.G. Tananaev, Chapter 4: Protactinium, in Edt.: L.R. Morss, N.M. Edelstein, J. Fuger and J.J. Katz, *The chemistry of actinide and transactinide elements*, Vol. 1, pages 161–252. Springer, 3 edition (2006)

[Neck00] V. Neck and J.I. Kim, An electrostatic approach for the prediction of actinide complexation constants with inorganic ligands-application to carbonate complexes. *Radiochim. Acta* **88** 815–822 (2000)

[Neck01a] V. Neck and J.I. Kim, Solubility and hydrolysis of tetravalent actinides. *Radiochim. Acta* **89** 1–16 (2001)

[Neck01b] V. Neck, J.I. Kim, B.S. Seidel, C.M. Marquardt, K. Dardenne, M.P. Jensen and W. Hauser, A spectroscopic study of the hydrolysis, colloid formation and solubility of Np(IV). *Radiochim. Acta* **89** 439–446 (2001)

[Neck02] V. Neck, R. Müller, M. Bouby, M. Altmaier, J. Rothe, M. Denecke and J.I. Kim, Solubility of amorphous Th(IV) hydroxide - application of LIBD to determine the solubility product and EXAFS for aqueous speciation. *Radiochim. Acta,* **90** 485–494 (2002)

[Neck03] V. Neck, M. Altmaier, R. Müller, A. Bauer, T. Fanghänel and J.I. Kim, Solubility of crystalline thorium dioxide. *Radiochim. Acta* **91** 253–262 (2003)

[Neck07] V. Neck, M. Altmaier, A. Seibert, J.I. Yun, C.M. Marquardt and T. Fanghänel, Solubility and redox reactions of Pu(IV) hydrous oxide: Evidence for the formation of PuO_{2+x}(s,hyd). *Radiochim. Acta* **95** 193–207 (2007)

[Newt83] T.W. Newton and V.L. Rundberg, Disproportionation and polymerization of plutonium (IV) in dilute aqueous solutions, in *Materials Research Society annual meeting*, Vol. 26, pages 867–873, Boston, MA (1983). MRS, Pittsburgh

[Newt86] T.W. Newton, D.E. Hobart and P.D. Palmer, The formation of Pu(IV)-colloid by the alpha-reduction of Pu(V) or Pu(VI) in aqueous solutions. *Radiochim. Acta* **39** 139–147 (1986)

[Newt02] T. Newton, Redox Reactions of Plutonium IOns in Aqueous Solutions, in Edt.: D.C. Hoffman, *Advances in Plutonium Chemistry, 1967-2000*, pages 24–60. American Nuclear Society, La Grange park, Illinois (2002)

[Nits94] H. Nitsche, K. Roberts, R.H. Xi, T. Prussin, K. Becraft, I. Almahamid, H.B. Silber, S.A. Carpenter, R.C. Gatti and C.F. Novak, Long-term plutonium solubility and speciation studies in a synthetic brine. *Radiochim. Acta* **66-67** 3–8 (1994)

[Nits96] H. Nitsche and R.J. Silva, Investigation on the carbonate complexation of Pu(IV) in aqueous solution. *Radiochim. Acta* **72** 65–72 (1996)

[Nomi87] T. Nomizu, T. Nozue and A. Mizuike, Electron microscopy of submicron particles in natural waters - morphology and elemental analysis of particles in fresh waters. *Mikrochim. Acta* **2** 99–106 (1987)

[Nomi89] T. Nomizu, J. Nagamine and A. Mizuike, Electron microscopy of submicron particles in natural waters - detection of organic substances. *Mikrochim. Acta* **3** 69–73 (1989)

[Novi06] A.P. Novikov, S.N. Kalmykov, S. Utsunomiya, R.C. Ewing, F. Horreard, A. Merkulov, S.B. Clark, V.V. Tkachev and B.F. Myasoedov, Colloid transport of plutonium in the far-field of the Mayak production association, Russia. *Science* **314** 638–641 (2006)

[Ocke56] D.W. Ockenden and G.A. Welch, The preparation and properties of some plutonium compounds. V. Colloidal quadrivalent plutonium. *J. Chem. Soc* **1** 3358–3363 (1956)

[Olss06] M. Olsson, On the stability of Pu(III) at different pH under non-inert conditions. *Radiochim. Acta* **94** 575–578 (2006)

[Pain02] S. Painter, V. Cvetkovic, D. Pickett and D.R. Turner, Significance of kinetics for sorption on inorganic colloids: modeling and experiment interpretation issues. *Environ. Sci. Technol.* **36** 5369–5375 (2002)

[Pass97] G. Passler, N. Erdmann, H.U. Hasse, G. Herrmann, G. Huber, S. Kohler, J.V. Kratz, A. Mansel, M. Nunnemann, N. Trautmann and A. Waldek, Application of laser mass spectrometry for trace analysis of plutonium and technetium. *Kerntechnik* **62** 85–90 (1997)

[Pere65] J.A. Perez-Bustamante, Solubility product of tetravalent plutonium hydroxide and study of the amphoteric character of hexavalent plutonium hydroxide. *Radiochim. Acta* **4** 67 (1965)

[Pieh91] D. Piehler, W.K. Kot and N. Edelstein, The 6d → 5f fluorescence spectra of $PaCl_6^{2-}$ in a Cs_2ZrCl_6 crystal. *J. Chem. Phys* **94** 942–948 (1991)

[Pokr56] L. Pokras, On the species present in aqueous solutions of 'salts' of polyvalent metals. *J. Chem. Edu.* **33** 152–161 (1956)

[Pram02] B.N. Pramanik, A.K. Ganguly and M.L. Gross, *Applied electrospray mass spectrometry.* Marcel Dekker, New York (2002)

[Puls92] R.W. Puls and R.M. Powell, Transport of inorganic colloids through natural aquifer material: implications for contaminant transport. *Environ. Sci. Technol.* **26** 614–621 (1992)

[Quan03] R.D. Quang, V. Petitjean, F. Hollebecque, O. Pinet, T. Flament and A.Prod'homme, Vitrification of HLW produced by uranium/molybdenum fuel reprocessing in COGEMA's cold cubicle melter, in *Wate Management*, Tucson, AZ (2003)

[Rabi51] S.W. Rabideau and J.F. Lemons, The potential of the Pu(III)–Pu(IV) couple and the equilibrium constants for some complex ions of Pu(IV). *J. Am. Chem. Soc.* **73** 2895–2899 (1951)

[Rabi53] S.W. Rabideau, Equilibria and reaction rates in the disproportionation of Pu(IV). *J. Am. Chem. Soc.* **75** 798–801 (1953)

[Rabi55] S.W. Rabideau and H.D. Cowan, Chloride complexing and disproportionation of Pu(1V) in hydrochloric acid. *Journal Am. Chem. Soc.* **77** 6145–6148 (1955)

[Rabi56] S.W. Rabideau, Thermodynamic functions and formal potentials of the Plutonium(V)-(VI) couple. *J. Am. Chem. Soc.* **78** 2705 (1956)

[Rabi57] S.W. Rabideau, The kinetics of disproportionation of Pu(V). *J. Am. Chem. Soc.* **79** 6350–6353 (1957)

[Rabi58] S.W. Rabideau, Kinetics of oxidation rreduction reactions of plutonium. The reaction between plutonium(VI) and plutonium(III) in perchlorate solutions. *J. Am. Chem. Soc.* **62** 617–620 (1958)

[Rabi60] S.W. Rabideau and R.J. Kline, A spectrophotometric study of the hydrolysis of plutonium(IV). *J. Phys. Chem.* **64** 680–682 (1960)

[Rai81] D. Rai and J.L. Swanson, Properties of plutonium (IV) polymer of environmental importance. *Nucl. Tech.* **54** 107–111 (1981)

[Rai82] D. Rai and J.L. Ryan, Crystallinity and solubility of plutonium (IV) oxide and hydrous oxide in aged aqueous suspensions. *Radiochim. Acta* **30** 213–216 (1982)

[Rai84] D. Rai, Solubility products of Pu(IV) hydrous oxide and equilibrium constants of Pu(IV)/Pu(V), Pu(IV)/Pu(VI), and Pu(V)/Pu(VI) couples. *Radiochim. Acta* **35** 97–106 (1984)

[Rand07] M.H. Rand, J. Fuger, I. Grenthe, V. Neck and D. Rai, *Chemical thermodynamics of thorium.*, Vol. 11 (in print) of *Chemical Thermodynamics.* Elsevier, North-Holland, Amsterdam (2007)

[Reda07] Redakt, Kernenergie: Weltreport 2006. *atw, Int. J. Nucl. Power* **52** 273–277 (2007)

[Reed06] D.T. Reed, J.F. Lucchini, S.B. Aase and A.J. Kropf, Reduction of plutonium(VI) in brine under subsurface conditions. *Radiochim. Acta* **94** 591–597 (2006)

[Rees87] T.F. Rees, A review of light scattering techniques for the study of colloids in natural waters. *J. Cont. Hydr.* **1** 425–439 (1987)

[Rees91] T.F. Rees, Transport of contaminants by colloid-mediated processes, in Edt.: O. Hutzinger, *The handbook of environmental chemistry*, Vol. 2, Part F, pages 165–184 (1991)

[Rigl89] C. Riglet, P. Robouch and P. Vitorge, Standard potentials of the (MO_2^{2+} / MO_2^{+}) and (MO^{4+} / MO^{3+}) redox systems for neptunium and plutonium. *Radiochim. Acta* **46** 85–94 (1989)

[Roma00] V.V. Romanovski, A. Brachmann, C.E. Palmer, H.F. Shaw, W.L. Bourcier and L.J. Jardine, Characterization of Pu colloidal and aqueous speciation in Yucca mountain groundwater surrogate. *Abstr. Pap.Am. Chem. Soc.* **219** U80 (2000)

[Rose03] J. Rose, T.J.M.D. Bruin, G. Chauveteau, R. Tabary, J.L. Hazemann, O. Proux, A. Omari, H. Toulhoat and J.Y. Bottero, Aqueous zirconium complexes for gelling polymers. A combined X-ray absorption spectroscopy and quantum mechanical study. *J. Phys. Chem. B* **107** 2910–2920 (2003)

[Ross03] P. Rosse and J.L. Loizeau, Use of single particle counters for the determination of the number and size distribution of colloids in natural surface waters. *Coll. Surf. A* **217** 109–120 (2003)

[Roth95] G. Roth, INE's HLLW vitrification technology. *atw, Int. J. Nucl. Power* **40** 144–177 (1995)

[Roth00] J. Rothe, M.A. Denecke and K. Dardenne, Soft X-ray spectromicroscopy investigation of the interaction of aquatic humic acid and clay colloids. *J. Coll. Interf. Sci.* **231** 91–97 (2000)

[Roth02] J. Rothe, M.A. Denecke, V. Neck, R.Müller and J.I. Kim, XAFS investigation of the structure of aqueous Th(IV) species, colloids and solid Th(IV) oxide/hydroxide. *Inorg. Chem* **41** 249–258 (2002)

[Roth04] J. Rothe, C. Walther, M.A. Denecke and T. Fanghänel, XAFS and LIBD investigation of the formation and structure of colloidal Pu(IV) hydrolysis products. *Inorg. Chem.* **43** 4708–4718 (2004)

[Rubb95] C. Rubbia, The energy amplifier - a description for the non-specialist. *CERN/AT* **95** 44 (1995)

[Rund88] R.S. Rundberg, A.J. Mitchell, I.R. Triay and N.B. Torstenfelt, Size and density of a ^{242}Pu colloid, in Edt.: M.J. Apted and R.E. Westerman, *Mat. Res. Soc.*, Vol. 112, pages 243–248, Boston, MA (1988). MRS

[Rund99] W. Runde, S.D. Reilly and M.P. Neu, Spectroscopic investigation of the formation of PuO_2Cl^+ and PuO_2Cl_2 in NaCl solutions and application for natural brine solutions. *Geochim. Cosmochim. Acta* **63** 3443–3449 (1999)

[Rund00] W. Runde, The chemical interactions of actinides in the environment. *Los Alamos Sci.* **26** 392–410 (2000)

[Ruts99] M. Rutsch, G. Geipel, V. Brendler, G. Bernhard and H. Nitsche, Interaction of uranium(VI) with arsenate(V) in aqueous solution studied by time-resolved laser-induced fluorescence spectroscopy (TRLFS). *Radiochim. Acta* **86** 135–141 (1999)

[Ryan94] J.N. Ryan and P.M. Gschwend, Effect of solution chemistry on clay colloid release froman iron oxide-coated aquifer sand. *Environ. Sci. Technol.* **28** 1717–1726 (1994)

[Ryan96] J.N. Ryan and M. Elimelech, Colloid mobilization and transport in groundwater. *Coll. Surf.* **107** 1–56 (1996)

[Rösc90] F. Rösch and V.A. Khalkin, Ion mobilities of trivalent f-elements in aqueous electrolytes. *Radiochim. Acta* **51** 101–106 (1990)

[Sacc91] C.A. Sacchi, Laser-induced breakdown in water. *J. Opt. Soc. Am. B* **8** 337–345 (1991)

[Sait99] M. Saito, S. Izumida, K. Onishi and J. Akazawa, Detection efficiency of microparticles in laser breakdown water analysis. *J. Appl. Phys.* **85** 6353–6357 (1999)

[Sasa06] T. Sasaki, T. Kobyashi, I. Takagi and H. Moriyama, Solubility measuremen of zirconium(IV) hydrous oxide. *Radiochim. Acta* **94** 489–494 (2006)

[Savv61] S. Savvin, Analytical use of arsenazo III. Dertermination of thorium, zirconium, uranium and rare earth elements. *Talanta* **8** 673–685 (1961)

[Sche96] F.J. Scherbaum, R. Knopp and J.I. Kim, Counting of particles in aqueous solutions by laser-induced photoacoustic beakdown detection. *Appl. Phys. B* **63** 299–306 (1996)

[Schi65] P. Schindler, H. Althau, F. Hofer and W. Minder, Löslichkeitsprodukte von Metalloxiden und -hydroxiden. *Helvet. Chim. Acta* **48** 1204–1215 (1965)

[Schi67] P. Schindler, Heterogeneous Equilibria Involving Oxides, Hydroxides Carbonates, and Hydroxide Carbonates. *Advances in Chemistry Series* **67** 196–221 (1967)

[Schu97] M. Schudel, S.H. Behrens, H. Holthoff, R. Kretzschmar and M. Borkovek, Absolute aggregation rate constants of hematite particles in aqueous suspensions: A comperison of two different surface morphologies. *J. Coll. Interf. Sci.* **196** 241–253 (1997)

[Seam00] J.C. Seaman, Thin-foil SEM analysis of soil and groundwater colloids: Reducing instrument and operator bias. *Env. Sci. Techn.* **34** 187–191 (2000)

[Shan76] R.D. Shannon, Revised effective ionic radii and systematic studies of interatomic distances in halides and chalcogenides. *Acta Cryst.* **32** 751–767 (1976)

[Sill53] L.G. Sillen, Polynuclear complexes formed in the hydrolysis of metal ions, in *Symposium on Co-Ordination Chemistry*, pages 74–76, Copenhagen (1953). Danish Chemical Society

[Silv99] G.L. Silver, Rearrangement equations for plutonium. *J. Radioanal. Nucl. Chem.* **240** 231–235 (1999)

[Silv02a] R.J. Silva and H. Nitsche, Environmental chemistry, in Edt.: D.C. Hoffman, *Advances in Plutonium Chemistry, 1967-2000.* American Nuclear Society, La Grange park, Illinois (2002)

[Silv02b] G.L. Silver, Acidity changes and balanced equations for plutonium disproportionation reactions. *Appl. Rad. Isotopes* **57** 1–5 (2002)

[Sing96] A. Singhal, L.M. Toth, J.S. Lin and K. Affholter, Zirconium(IV) tetramer/octamer hydrolysis equilibrium in aqueous hydrochloric acid solution. *J. Am. Chem. Soc.* **118** 11529–11534 (1996)

[Skan07] S. Skanthakumar, M.R. Antonio, R.E. Wilson and L. Soderholm, The curium aqua ion. *Inorg. Chem.* **46** 3485–3491 (2007)

[Smol16] M.v. Smoluchowski, Drei Vorträge über Diffusion, Brownsche Molekularewegung und Koagulation von Kolloidteilchen. *Phys. Z.* **17** 557 (1916)

[Sout02] P.D. Southon, J.R. Bartlett, J.L. Woolfrey and B. Ben-Nissan, Formation and characterization of an aqueous zirconium hydroxide colloid. *Chem. Mat.* **14** 4313–4319 (2002)

[Stei75] G. Stein and E. Würzberg, Energy gap law in the solvent isotope effect on radiationless transitions of rare earth ions. *J. Chem. Phys.* **62** 208–213 (1975)

[Stum81] W. Stumm and J.J. Morgan, *Aquatic chemistry.* Wiley & Sons, New York, 2nd edition (1981)

[Stum84] R. Stumpe, J.I. Kim, W. Schrepp and H. Walther, Speciation of actinide ions in aqueous solution by laser-induced pulsed photoacoustic spectroscopy. *Appl. Phys. B* **34** 203–206 (1984)

[Stum93] W. Stumm, Aquatic colloids as chemical reactants: surface structure and reactivity. *Coll. Surf. A* **73** 1 – 18 (1993)

[Stum06] S. Stumpf, T. Stumpf, C. Walther, D. Bosbach and T. Fanghänel, Sorption of Cm(III) onto different feldspar surfaces: a TRLFS study. *Radiochim. Acta* **94** 243–248 (2006)

[Tam79] A.C. Tam and C.K.N. Patel, Optical absorptions of light and heavy water by laser optoacoustical spectroscopy. *Appl. Opt.* **18** 3348–3358 (1979)

[Tara05] P. Tarapcik, B. Fourest and E. Giffaut, Comparative approach of the solubility of protactinium oxy/hydroxides. *Radiochim. Acta* **93** 27–33 (2005)

[Than00] N.M. Thang, R. Knopp, H. Geckeis, J.I. Kim and H.P. Beck, Detection of nanocolloides with flow-field flow fractionation and laser-induced breakdown detection. *Anal. Chem.* **72** 1–5 (2000)

[Thiy90] P. Thiyagarajan, H. Diamond, L. Soderholm, E.P. Horwitz, L.M. Toth and L.K. Felker, Plutonium (IV) polymers in aqueous and organic media. *Inorg. Chem.* **29** 1902–7 (1990)

[Thou93] P. Thouvenot, S. Hubert, C. Moulin, P. Decambox and P. Mauchien, Americium trace determination in aqueous and solid matrices by time-resolved laser-induced fluorescence. *Rdiochim. Acta* **61** 15–21 (1993)

[Thou94] P. Thouvenot, S. Hubert and N. Edelstein, Spectroscopic study and crystal-field analysis of Cm3+ in the cubic-symmetry site of ThO2. *Phys.Rev.B* **50** 9715–9720 (1994)

[Tomb99] E. Tomb'acz, G. Filipcsei, M. Szekeres and Z. Gingl, Particle aggregation in complex aquatic systems. *Coll. Surf. A* **151** 233–244 (1999)

[Toth81] L.M. Toth, H.A. Friedman and M.M. Osborne, Polymerization of plutonium (IV) in aqueous nitric acid solutions. *J. Inorg. Nucl. Chem.* **43** 2929–2934 (1981)

[Town02] R.M. Town and M. Filella, Size fractionation of trace metal species in freshwaters: implications for understanding their behaviour and fate. *Env. Sci. BioTechn.* **1** 277–297 (2002)

[Trau04] N. Trautmann, G. Passler and K.D.A. Wendt, Ultratrace analysis and isotope ratio measurements of long-lived radioisotopes by resonance ionization mass spectrometry (RIMS). *Anal. Bioanal. Chem.* **378** 348–355 (2004)

[Tria91] I.R. Triay, D.E. Hobart, A.J. Mitchell, T.W. Newton, M.A. Ott, P.D. Palmer, R.S. Rundberg and J.L. Thompson, Size determinations of plutonium colloids using autocorrelation photon spectroscopy. *Radiochim. Acta* **52-3** 127–131 (1991)

[Tulo02] J.J. Tulock and G.J. Blanchard, Investigating hydrolytic polymerization of aqueous zirconium ions using the fluorescent probe pyrenecarboxylic acid. *J. Phys. Chem. B* **106** 3568–3575 (2002)

[Turr95] X. Turrilas, P. Barnes, J.D. Gascoigne, J.Z. Turner, S.L. Jones, C.J. Norman, C.F. Pygall and A.J. Dent, Synchrotron-related studies on the dynamic and structural aspects of zirconia synthesis for ceramic and catalytic applications. *Radiat. Phys. Chem.* **45** 491–508 (1995)

[VanB01] G.J. VanBerkel, K.G. Asano and P.D. Schnier, Electrochemical processes in a wire-in-a-capillary bulk-loaded, nano-electrospray emitter. *J. Amer. Soc. Mass Spectr.* **12** 853–862 (2001)

[Vird91] J.W. Virden and J.C. Berg, The use of photon correlation spectroscopy for estimating the rate constant for doublet formation in an aggregating colloidal dispersion. *J. Coll. Interf. Sci.* **149** 528–535 (1991)

[Walt02] C. Walther, C. Bitea, W. Hauser, J.I. Kim and F.J. Scherbaum, Laser-induced breakdown detection for the assessment of colloid mediated radionuclide migration. *Nucl. Instr. Meth. B* **195** 374–388 (2002)

[Walt03a] C. Walther, Comparision of colloid investigations by single particle analytical techniques - a case study on thorium-oxyhydroxides. *Coll. Surf. A, invited* **217** 81–92 (2003)

[Walt03b] C. Walther, C. Bitea, J.I. Yun, J.I. Kim, T. Fanghänel, C.M. Marquardt, V. Neck and A. Seibert, Nanoscopic approaches to the aquatic plutonium chemistry. *Actinide Research Quarterly* **11** 12–16 (2003)

[Walt04] C. Walther, H.R. Cho and T. Fanghänel, Measuring multimodal size distributions of aquatic colloids at trace concentrations. *Appl. Phys. Lett.* **85** 6329–6331 (2004)

[Walt06] C. Walther, S. Büchner, M. Filella and V. Chanudet, Probing particle size distributions in natural surface waters from 15 nm to 2μm by a combination of LIBD and single particle counting. *J. Coll. Interf. Sci.* **301** 532–537 (2006)

[Walt07a] C. Walther, H.R. Cho, C.M. Marquardt, V. Neck, A. Seibert, J.I. Yun and T. Fanghänel, Hydrolysis of plutonium(IV) in acidic solutions: No effect of hydrolysis on absorption-spectra of mononuclear hydroxide complexes. *Radiochim. Acta* **95** 7–16 (2007)

[Walt07b] C. Walther, J. Rothe, M. Fuss, S. Büchner, S. Koltsov and T. Bergmann, Investigation of polynuclear Zr-hydroxide complexes by nano-electrospray mass-spectrometry combined with XAFS. *Anal. Bioanal. Chem.* **388** 409–431 (2007)

[Warn02] K. Warner and G.M. Hieftje, Thomson scattering from analytical plasmas. *Spectrochim. Acta B* **57** 201–241 (2002)

[Weij02] L. Weijuan and T. Zuyi, Comparative study on Th(IV) sorption on alumina and silica from aqueous solutions. *J. Radioanal. Nucl. Chem.* **254** 187–192 (2002)

[Wick06] M. Wickleder, B. Fourest and P. Dorhout, Chapter 3: Thorium, in Edt.: L.R. Morss, N.M. Edelstein, J. Fuger and J.J. Katz, *The chemistry of actinide and transactinide elements*, Vol. 1, pages 117–129. Springer, 3 edition (2006)

[Wilm96] M. Wilm and M. Mann, Analytical properties of the nanoelectrospray ion source. *Anal. Chem.* **68** 1–8 (1996)

[Wils05] R.E. Wilson, Y.J. Hu and H. Nitsche, Detection and quantification of Pu(III, IV, V, and VI) using a 1.0-meter liquid core waveguide. *Radiochim. Acta* **93** 203–206 (2005)

[Wils07] R.E. Wilson, S. Skanthakumar, G. Sigmon, P.C. Burns and L. Soderholm, Structures of dimeric hydrolysis products of Thorium. *Inorg. Chem.* **46** 2368–2372 (2007)

[Wort05] A. Wortmann, A. Kister-Momotova, O. Wilhelm and R. Zenobi, Electrospray ionisation of noncovalent complexes investigated by laser induced fluorescence and doppler anemometry, in *Book of abstracts of conference: ANACON 05*, Regensburg (2005)

[Yama84] M. Yamashita and J. Fenn, Another variation on the free-jet theme. *J. Phys. Chem* **88** 4451–4459 (1984)

[Yun07] J.I. Yun, H.R. Cho, V. Neck, M. Altmaier, A. Seibert, C.M. Marquardt, C. Walther and T. Fanghänel, Investigation of the hydrolysis of plutonium(IV) by a combination of spectroscopy and redox potential measurements. *Radiochim. Acta* **95** 89–96 (2007)

[Yuso93] A.B. Yusov, Luminescence of transplutonium elements in solutions and its application. *Radiochemistry* **35** 1–14 (1993)

[Yuso02] A.B. Yusov, A.M. Fedoseev and L.N. Astafurova, Interaction of aluminium (III) with the f-family ions Np(VI), Np(V), Np(IV), Pu(IV), Nd(III), and Am(III) in the course of simultaneous hydrolysis. *Russ. J. Coord. Chem.* **28** 264–271 (2002)

[Yuso04] A.B. Yusov, A.M. Fedosseev and C.H. Delegard, Hydrolysis of Np(IV) and Pu(IV) and their complexation by aqueous $Si(OH)_4$. *Radiochim. Acta* **92** 869–881 (2004)

[Zhao97] P. Zhao and S.A. Steward, Literature review of intrinsic actinide colloids related to spent fuel waste package release rates. *LLNL Report* **126039** 2–13 (1997)

[Zhou99] S.L. Zhou, A.G. Edwards, K.D. Cook and G.J. Van Berkel, Investigation of the electrospray plume by laser-induced fluorescence spectroscopy. *Anal. Chem.* **71** 769–776 (1999)

[Zhou00] S.L. Zhou and K.D. Cook, Probing solvent fractionation in electrospray droplets with laser-induced fluorescence of a solvatochromic dye. *Analytical Chemistry* **72** 963–969 (2000)

[Zhou02] S.L. Zhou, B.S. Prebyl and K.D. Cook, Profiling pH changes in the electrospray plume. *Anal. Chem.* **74** 4885–4888 (2002)

[Ziel56] A.J. Zielen and R.E. Connick, The hydrolytic polymerization of zirconium in perchloric acid solution. *J. Am. Chem. Soc.* **78** 5785–5792 (1956)